# Graduate Texts in Physics

For further volumes:
www.springer.com/series/8431

# Graduate Texts in Physics

Graduate Texts in Physics publishes core learning/teaching material for graduate- and advanced-level undergraduate courses on topics of current and emerging fields within physics, both pure and applied. These textbooks serve students at the MS- or PhD-level and their instructors as comprehensive sources of principles, definitions, derivations, experiments and applications (as relevant) for their mastery and teaching, respectively. International in scope and relevance, the textbooks correspond to course syllabi sufficiently to serve as required reading. Their didactic style, comprehensiveness and coverage of fundamental material also make them suitable as introductions or references for scientists entering, or requiring timely knowledge of, a research field.

Udo W. Pohl

# Epitaxy of Semiconductors

## Introduction to Physical Principles

Springer

Prof. Dr. Udo W. Pohl
Institut für Festkörperphysik, EW5-1
Technische Universität Berlin
Berlin, Germany

ISSN 1868-4513 ISSN 1868-4521 (electronic)
Graduate Texts in Physics
ISBN 978-3-642-32969-2 ISBN 978-3-642-32970-8 (eBook)
DOI 10.1007/978-3-642-32970-8
Springer Heidelberg New York Dordrecht London

Library of Congress Control Number: 2012953380



Printed on acid-free paper

Springer is part of Springer Science+Business Media (www.springer.com)

# Preface

Epitaxy—the growth of a crystalline layer on a crystalline substrate—represents the basis for the fabrication of semiconductor heterostructures and devices. Textbooks on semiconductor physics and devices usually describe the design a heterostructure and subsequently measured data of a respective realization. The chain between these end points requires to solve many basic problems related to physics and technology. Such steps are generally described in specialized literature focusing on diverse aspects. Students and researchers starting in the field need to study papers and books on quite specific problems in a wide field. This textbook attempts to bridge the gap between well-established books on semiconductor physics on one side and texts on completed heterostructures like semiconductor devices on the other.

The book is based on a one-semester course held at Technical University of Berlin for undergraduate and graduate students in physics and engineering physics. It is primarily addressed to the non-specialist with some basic knowledge in solid state and semiconductor physics. The field of epitaxy is rapidly evolving and includes many materials and growth techniques. The text therefore focuses on basics and important aspects of epitaxy, emphasizing particularly the physical principles. Problems are illustrated for important semiconductors with zincblende and wurtzite structure.

The subject matter first covers properties of heterostructures. Structural aspects implying elasticity and strain relaxation by dislocations are addressed as well as electronic properties including band alignment and electronic states in low-dimensional structures. Then the thermodynamics and kinetics of epitaxial layer growth are considered, introducing the driving force of crystallization and paying special attention to nucleation and surface structures. Instructive examples are given for self-organized growth of quantum dots and wires. Afterwards aspects of doping, diffusion, and contacts are discussed. Eventually the most important methods used for epitaxial growth are introduced: metalorganic vapor-phase epitaxy, molecular-beam epitaxy, and liquid-phase epitaxy.

I am grateful to my students, who consistently engaged me in discussions about fundamentals of epitaxy and stimulated an active motivation to write this book. Our librarian Mrs I. Langenscheidt-Martens was always an invaluable help for

finding references difficult to retrieve. I am also indebted to A. Krost for critical manuscript reading, and I appreciated the cooperation with C. Ascheron, Springer Science+Business Media.

Berlin Udo W. Pohl
July 2012

# Contents

# Abbreviations

| | |
|---|---|
| 0D | zero-dimensional |
| 1D | one-dimensional |
| 2D | two-dimensional |
| 3D | three-dimensional |
| AIP | American Institute of Physics |
| APS | American Physical Society |
| AVS | American Vacuum Society—The Science & Technology Society |
| bcc | body-centered cubic |
| BEP | beam equivalent pressure |
| CB | conduction band |
| CBE | chemical beam epitaxy |
| CVD | chemical vapor deposition |
| DAS | dimer adatom stacking-fault (model) |
| DBR | distributed Bragg reflector |
| DOS | density of states |
| ELO | epitaxial lateral overgrowth (also: ELOG) |
| EMA | effective mass approximation |
| EXAFS | extended X-ray absorption fine-structure |
| fcc | face-centered cubic |
| FET | field-effect transistor |
| FWHM | full width at half maximum |
| GSMBE | gas-source molecular beam epitaxy |
| hcp | hexagonally closed packed |
| hh | heavy hole |
| HRTEM | high-resolution transmission electron microscopy |
| HRXRD | high-resolution X-ray diffraction |
| HUC | half unit cell |
| LED | light-emitting diode |
| lh | light hole |
| LPE | liquid phase epitaxy |
| MBE | molecular beam epitaxy |

| | |
|---|---|
| ML | monolayer |
| MOCVD | metal-organic chemical vapor deposition |
| MOMBE | metal-organic molecular beam epitaxy |
| MOVPE | metal-organic vapor-phase epitaxy |
| MRS | Materials Research Society |
| MWQ | multiple quantum well |
| PL | photoluminescence |
| PLE | photoluminescence excitation (spectroscopy) |
| PVD | physical vapor deposition |
| QD | quantum dot |
| QW | quantum well |
| QWR | quantum wire |
| RHEED | reflection high-energy electron diffraction |
| rms | root mean square |
| SEM | scanning electron microscopy |
| si | semi-insulating |
| SL | superlattice |
| slm | standard liters per minute |
| so | spin-orbit, also split-off |
| STM | scanning tunneling microscopy |
| TEC | thermal expansion coefficient |
| TEM | transmission electron microscopy |
| TLK | terrace-ledge-kink (model) |
| TSK | terrace-step-kink (model) |
| UHV | ultra-high vacuum |
| VB | valence band |
| VCA | virtual crystal approximation |
| VCSEL | vertical-cavity surface-emitting laser |
| ViGS | virtual gap states |
| VPE | vapor phase epitaxy |
| XRD | X-ray diffraction |
| XSTM | cross-sectional scanning tunneling microscopy |
| ZB | zincblende |

# Chapter 1
# Introduction

**Abstract** This introductory chapter provides a brief survey on the development of epitaxial growth techniques and points out tasks for the epitaxy of device structures. Starting from early studies of alkali-halide overgrowth in the beginning of the 20th century, basic concepts for lattice match between layer and substrate were developed in the late 1920ies, followed by the theory of misfit dislocations introduced about 1950. Major progress in epitaxy was achieved by technical improvements of the growth techniques, namely liquid phase epitaxy in the early, and molecular beam epitaxy and metalorganic vapor phase epitaxy in the late 1960ies. Current tasks for epitaxial growth are often motivated by needs for the fabrication of advanced devices, aiming to control carriers and photons.

Most semiconductor devices fabricated today are made out of a thin stack of layers with a typical total thickness of only some μm. Layers in such stack differ in material composition and may be as thin as a single atomic layer. All layers are to be grown with high perfection and composition control on a bulk crystal used as a substrate. The growth technique employed for coping with this task is termed epitaxy. In the following we briefly consider the historical development and illustrate typical issues accomplished using epitaxy.

## 1.1 Epitaxy

### *1.1.1 Roots of Epitaxy*

Crystalline solids found in nature show regularly shaped as-grown faces. The faces of a zinc selenide crystal grown from the vapor phase in the lab are shown in Fig. 1.1a. Mineralogists found that the angles between corresponding faces are always the same for different samples of the same type of crystal. They concluded already in the 18th century that such regular shape originates from a regular assembly of identical building blocks forming the crystal as indicated in Fig. 1.1b. In the early 19th century mineralogists noticed that naturally occurring crystals sometimes

U.W. Pohl, *Epitaxy of Semiconductors*, Graduate Texts in Physics,
DOI 10.1007/978-3-642-32970-8_1, 

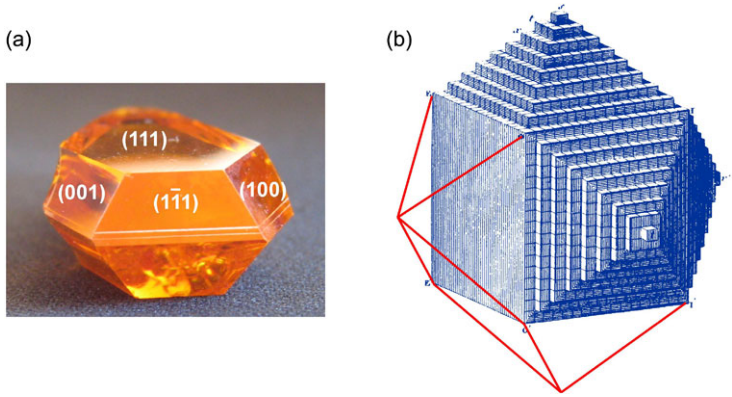


**Fig. 1.1** (**a**) ZnSe bulk crystal with {100} and {111} growth faces. (**b**) Faces formed from regularly repeating building blocks described around 1800 [3]. The complete shape of the displayed rhomb-dodecahedron is indicated by *red lines*

grew together with a unique relationship of their orientations [1]. A first successful artificial reproduction of this effect in a laboratory was reported by Moritz L. Frankenheim in 1836 [2]. He demonstrated a parallel oriented growth of sodium nitrate $NaNO_3$ from solution on a freshly cleaved calcite crystal $CaCO_3$.

First systematic studies on the crystal growth on top of another crystalline material were reported by Thomas V. Barker starting 1906 [4]. At that time growth from solution and optical microscopy were the only readily developed techniques for growth and characterization of samples, respectively. Baker investigated a large number of NaCl-type alkali halides like chlorides, bromides, iodides, and cyanides of, e.g., rubidium and cesium. He placed a drop of saturated solution of one halide onto a freshly cleaved surface of another halide and observed the nucleation of a crystalline structure under a microscope. Crystals of the solute appeared as a rule in a few seconds, but sometimes nucleation was too rapid to be observed or difficulties arose due to a greater solubility for the crystal than for the dilute dropped on top. He concluded that crystalline growth of alkali halides was more likely to occur if the molecular volumes of the two inter-growing materials were nearly equal. We note that such conditions often imply a similar size of the building blocks mentioned above and consequently a low misfit of the lattice constants of the two materials.

The discovery of X-ray diffraction (1912) and electron diffraction (1927) by crystals had a strong impact on the knowledge about crystal structure. When Louis Royer made his seminal comprehensive studies with a wide variety of layers and substrate materials in 1928, he could precisely report on the effect of substrate crystal structure on the crystalline orientation of the layer [5]. Royer introduced the term *epitaxy* from the Greek επι (*epi*, upon, attached to)—ταξισ (*taxis*, arrangement, order) and concluded general rules for epitaxy. He noted that oriented growth occurs only when it involves the parallelism of two lattice planes which have lattice networks of identical or quasi-identical form and closely similar spacing. More

precisely, he found that the differences between the lattice-network spacing (lattice parameters) for growth of alkali halides upon other alkali halides or mica (minerals of the form $XY_{2\text{-}3}Z_4O_{10}(OH,F)_2$) should be no more than 15 %. Such geometrical considerations are still prominent today, though it was established later that epitaxy may also occur for much larger misfits.

In the 1930ies, G.I. Finch and A.G. Quarrell concluded from a study of zinc oxide on sputtered zinc that the initial layer is strained in order to attain lattice matching parallel to the interface [6]. The layer lattice-parameter vertical to the interface was also considered to be changed to maintain approximately the bulk density. They named this phenomenon *pseudomorphism*. Though later the experimental evidence was pointed out to be by no means conclusive [1], the concept of pseudomorphic layers proved to be of basic importance for epitaxial structures.

The introduction of the theory of misfit dislocations at the interface between the substrate and the layer by F.C. Frank and Jan H. van der Merve in 1949 [7–9] extended the pseudomorphism approach and predicted a limit for the misfit of pseudomorphic growth. The incorporation of edge dislocations allows to accommodate misfit strain and consequently makes epitaxy possible also for structures with larger misfit. Conclusive experimental evidence for this was provided by John W. Matthews and co-workers in the 1960ies [10, 11]. Thin metal layers on single crystal metals with low misfit proved to grow pseudomorphic, while misfit dislocations were generated in thicker layers with a density depending on layer thickness. Later also conditions not included in the mentioned concepts like, e.g., interface alloying or surface energies were found to significantly affect epitaxial growth.

The emerging semiconductor industry in the early 1960ies had a strong impact on the interest in epitaxy. In addition, advancements in the technique of producing high vacuum and pure materials, and progress in experimental techniques like electron microscopy and X-ray diffraction allowed to efficiently develop methods for epitaxial growth. Liquid-phase epitaxy enabled epitaxial growth of multilayered device structures of high complexity like separate-confinement semiconductor lasers. The advancement of this technology was facilitated by its similarity to the well-studied growth of bulk single-crystals from seeded solution. In the 70ies the more sophisticated methods of molecular beam epitaxy and metalorganic vapor-phase epitaxy emerged. These techniques opened up epitaxy far from thermodynamic equilibrium and hence fabrication of structures with atomically sharp interfaces, which cannot be produced near equilibrium. Understanding and control of the epitaxial growth techniques was significantly advanced by the application of in-situ studies of the nucleation and growth process, and by the development of computational techniques. In the late 80ies the modern techniques attained a maturity to get in the lead of device mass-production. Today a large variety of electronic, optoelectronic, magnetic, and superconducting layer structures are fabricated using epitaxial techniques, including structures of reduced dimensionality on a nanometer scale.

### 1.1.2 Epitaxy and Bulk-Crystal Growth

Crystal growth in an epitaxial process proceeds basically in the same way as conventional growth of bulk crystals. In epitaxy, however, layer and substrate differ in the nature and strength of the chemical bond. Moreover, both materials may have a different crystal structure and generally have an unequal lattice parameter—at least if the temperature is varied. We may therefore say that crystals differ *energetically and geometrically* in epitaxy [12]. Crystalline deposition of different materials on each other is also termed *heteroepitaxy*.

Such definition does obviously not apply for an epitaxial deposition on a substrate of the same material. The process is usually referred to as *homoepitaxy* (sometimes also *autoepitaxy*). Let us consider a simple example to illustrate that there may still be a difference to conventional crystal growth. Epitaxy of electronic devices is usually performed on doped substrates and often starts by depositing a layer of the same material termed homoepitaxial buffer layer. Doping often alters the lattice parameter without significantly changing the chemical bond in bulk material. A $p$-type doping of, e.g., silicon with boron to a level of $2 \times 10^{19}$ cm$^{-3}$ induces a change of the lattice parameter by $-1$ %. An undoped layer on a doped substrate of the same material will hence not differ energetically but geometrically. This provides a clear distinction of homoepitaxy from conventional crystal growth. According this differentiation deposition of a layer of the same kind and doping like the substrate underneath should be termed crystal growth instead of epitaxy. Following the general usage we will, however, use the term homoepitaxy less strictly. Deposition of a layer of the same material as the substrate is usually just one of many layers to follow in the growth process of a device structure. Furthermore, fabrication of bulk crystals is usually performed applying a different growth regime than in epitaxy, allowing for much higher growth rates. Accordingly also different experimental setups are employed. The term homoepitaxy will be used here for deposition of the same material as the substrate, just to distinguish from heteroepitaxy.

## 1.2 Issues of Epitaxy

### 1.2.1 Convention on Use of the Term "Atom"

Solids are composed of atoms, which may be charged due to the character of the chemical bond. When used in a general way in this book, the word "atom" denotes both, an atom or an ion. Uncharged atoms are hence for simplicity usually not distinguished from charged atom cores in, e.g., ionic crystals or metals unless explicitly pointed out.

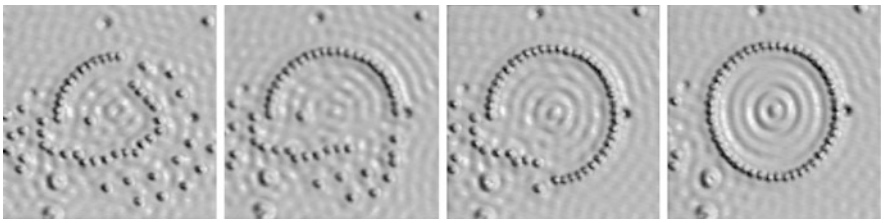

**Fig. 1.2** Gradual circular arrangement of 48 iron adatoms on a copper surface assembled using a low-temperature scanning tunnelling microscope. Interference ripples originate from electron surface states. From [14]

### *1.2.2 Assembly of Atoms*

Epitaxy denotes the regular assembly of atoms on a crystalline substrate. By inventing the scanning tunneling microscope (STM) a particular means has been developed to control the assembly of single atoms for forming an ordered structure. The method uses the finite force an STM tip always exerts on an adsorbed atom (adatom) attached to the surface of a solid [13]. The magnitude of the force can be tuned by adjusting the voltage and the position of the tip. Since generally less force is required to move an atom across a surface than to pull it away the tip parameters can be set to allow for positioning an individual adatom while it remains bound to the surface. The example given in Fig. 1.2 shows iron atoms on a (111) copper surface. The initially disordered Fe atoms were carefully positioned at chosen locations. May such procedure also be applied to deposit an epitaxial layer onto a substrate? Imagine a skillful operator placing one atom per second exactly on the correct site of a layer. For typically about $10^{15}$ sites per $cm^2$ such procedure requires 31 Mio. years for a single atomic layer being deposited on one $cm^2$. The fabrication of epitaxial structures hence requires other methods.

The problem of growing a layer by the assembly of single atoms is comparable to the issue of describing the behavior of a gas by formulating the equation of motion for each atom. This cannot be accomplished for exceedingly large ensembles like a considerable fraction of $6 \times 10^{23}$ atoms present in one mole. The approach of kinetic theory of gases hence solely describes averages of certain quantities of the vast number of atoms in the ensemble, concluded from the behavior of one single atom. These averages correspond to macroscopic variables. We will basically follow a comparable approach. In epitaxial growth we seek to establish favorable conditions for atoms of a nutrient phase to finding proper lattice sites in the solid phase. The macroscopic control parameters are governed by both thermodynamics and kinetics, and their effect depends on the materials and the applied growth method.

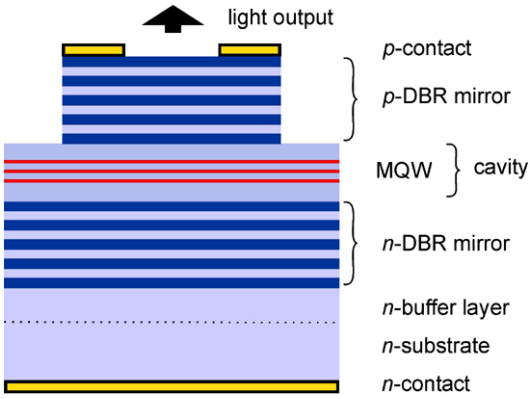


**Fig. 1.3** Schematic of a vertical-cavity surface-emitting laser indicating the sequence of differently alloyed and doped semiconductor layers

### *1.2.3 Tasks for Epitaxial Growth*

Semiconductor devices control the flow and confinement of charge carriers and photons. To fulfill its function a device is composed of crystalline layers and corresponding interfaces with different physical properties. Epitaxy is employed to assemble such layer structure. The precise control of the growth process in epitaxy requires the accomplishment of issues with quite different nature. We consider the example of a semiconductor device-structure to illustrate a number of tasks addressed during fabrication and indicate the connection to respective chapters of this book. The addressed concepts basically apply also for insulators and metals. In this book we focus on semiconductor materials.

The demand for increasing data-rate capacity in data-communication networks raised the need for suitable optical interconnects, particularly for light sources. Vertical-cavity surface-emitting lasers (VCSELs) have characteristics meeting ambitious requirements of fiber communication and recently emerged from the laboratory to the marketplace. VCSEL devices are also widely used in computer mice due to a good shape of their optical radiation field. A VCSEL is a semiconductor laser, which emits the radiation vertically via its surface—in contrast to the more common edge-emitting lasers. Like any laser it consists of an active zone where the light is generated, overlapping with a region where the optical wave is guided. Light is generated by recombination of electrons and holes which are confined in quantum wells (MQW, multiple quantum well). The generated photons contribute to the light wave which travels back and forth in an optical Fabry-Pérot resonator built by two mirrors, and a small fraction is allowed to emerge from the top mirror to form the laser radiation. Since the resonator in a VCSEL is very short, the reflectivity of the mirrors must be very high ($R > 99\ \%$) to maintain lasing oscillation. They hence are made from distributed Bragg reflectors (DBR) of many pairwise $\frac{1}{4}\lambda/n$ thick layers with a difference in the respective refractive index $n$, $\lambda$ being the operation wavelength. If the index step $\Delta n$ is low many pairs are required (a few tens). The basic design of a VCSEL is given in Fig. 1.3.

The realization of a semiconductor device is a complex process. The basic design layout is determined by a number of operation parameters like, e.g., the emission wavelength for an optoelectronic device. Already at this stage materials aspects play an important role. Obviously a wide-bandgap semiconductor material, e.g., must be used in the active region if the device is to radiate at high photon energy. The design stage comprises simulation work on electrical, optical, and other properties of the device depending on the employed materials and the specific purpose of the device. The design eventually yields a list of materials composition, thickness, and doping for each individual layer in the entire layer stack to be epitaxially grown.

The crystalline epitaxial growth on a single crystalline substrate requires a well-defined relationship of the substrate structure with respect to that of the layers grown on top. For this purpose the spacing of the atoms parallel to the interface between substrate and the layers of the device structure on top has to accommodate. Since the lateral lattice constants never match perfectly and the total layer thickness of the device structure is generally much below the substrate thickness, epitaxial layers are elastically strained. *Chapter 2* introduces into the structural and elastic properties of epitaxial layers and points out a critical limit for such strain. As a consequence of overcritical stress, plastic relaxation occurs by the introduction of misfit dislocations. Prominent species of such dislocations for the important crystal structures zincblende and wurtzite are treated. Prior to the growth of the device layers usually a buffer layer is grown on the substrate. This layer is introduced to keep defects located at the interface to the substrate and dislocations originating from large misfits away from the device layers. A further challenge occurs from a large change of composition within a layer sequence. The device depicted in Fig. 1.3 comprises Bragg mirrors, which require a large step of the refractive index between consecutive quarter-lambda thick layers. A large index step of the layer pairs in the mirror stack is connected not only to a large difference of the fundamental bandgap of the layers, but usually also to a large difference of lattice constants. To keep the strain below the critical limit, layers with a composition mix of materials are used to maintain the lattice constant while changing the refractive index. The change of lattice constant in mixed layers and means to compensate the total strain in a layer stack are also considered in Chap. 2.

Strain and interfaces between layers with different bandgap affect the electronic properties of the layer structure. In *Chapter 3* the effect of strain on valence and conduction-band states is outlined. Furthermore, the consequence of alloying on the fundamental bandgap is considered. The contact of two semiconducting layers raises the question how the uppermost valence bands mutually align. Models treating this problem and effects of interface composition are reviewed in Chap. 3. The band discontinuities determine the confinement of charge carriers in a sandwich structure and are also affected by strain. This is particularly important for the active layers which are usually formed by quantum wells as depicted in Fig. 1.3. Structures with a reduced dimensionality—quantum wells, quantum wires, and quantum dots—form the active core of many advanced devices. Chapter 3 points out the basic electronic properties of such quantum structures to indicate the required dimensions, which have to be realized in the epitaxial growth process.

Growth occurs at some deviation from thermodynamic equilibrium. Epitaxy is a controlled transition from the gas or liquid phase to a crystalline solid. The nature of the driving force depends on the particular material system and growth conditions. *Chapter 4* introduces into the thermodynamics of growth for simple one- and two-component systems. Nucleation of a layer, epitaxial growth modes, and a thermodynamic approach to surface energies is described. Even though epitaxial growth processes may occur under conditions far from equilibrium, thermalization times of atoms arriving from the nutrition phase on the surface can be much less than the time required to grow a single monoatomic layer. In such cases thermodynamic descriptions are often successfully applied to model the growth process. For the device structure illustrated in Fig. 1.3 thermodynamics may constitute limits for the stability of mixed crystals used to meet the requirements for lattice constants, bandgaps, band alignments, and doping. In such cases epitaxy may still be possible in a restricted temperature range.

The fabrication of atomically sharp interfaces between two dissimilar solids requires a significant deviation from equilibrium to suppress interdiffusion. This is particularly important for quantum structures like the active layers in the VCSEL structure shown in Fig. 1.3, usually realized using multiple quantum wells. Under such nonequilibrium conditions growth is strongly affected by kinetic influences. Kinetics and atomistic aspects of epitaxial growth are addressed in *Chapter 5*. A kinetic description of nucleation and layer growth accounts for the detailed steps atoms experience on the growing surface. They depend on the structure of the surface, where the arrangement of atoms may differ strongly from that found in the solid bulk underneath. Such surface reconstructions are specific for the given material and change with growth conditions—they are pointed out for specific examples. Growth modes depending on strain or specific surface states are often employed in epitaxy to fabricate low-dimensional structures by self-organized processes. The basics of such self-organized formation of quantum dots and quantum wires is considered in Chap. 5. VCSEL devices like that depicted in Fig. 1.3 are also fabricated using quantum dots in the active region, formed in the self-organized Stranski-Krastanow growth mode.

Electronic and optoelectronic devices require control of charge carriers in semiconductors and a contact of the semiconductor structure to a metal for a connection to the electric circuit. *Chapter 6* gives a brief introduction to problems in epitaxy connected to doping and contact fabrication. For a given semiconductor material thermodynamics may impose limits in the doping level originating from restricted solubility of the dopants, an amphoteric behavior of the dopants, or compensation by native defects. Nonequilibrium epitaxial growth may relieve some restrictions. Growth far from equilibrium also enables delta-like doping profiles, used to fabricate devices employing a two-dimensional electron gas with a high mobility. Doping and heterostructure composition profiles may be affected by redistribution of atoms due to diffusion phenomena. Mechanisms of diffusion in semiconductors are considered and examples are given for dependences on the ambient atmosphere and on doping. Ohmic contacts between semiconductor and metal are a classical subject, but epitaxy also enables the growth of specific contact structures to achieve a low contact resistance. Some examples are outlined in Chap. 6.

Various techniques for epitaxial growth have been established and are described in *Chapter 7*. The first method which attained maturity to produce complex devices was liquid-phase epitaxy. It operates close to thermodynamic equilibrium and may hence be well described by thermodynamics. More versatile control is achieved using the more sophisticated methods of molecular-beam epitaxy and metalorganic vapor-phase epitaxy, which both operate far from thermal equilibrium. They hence both allow for a control of layer thickness down to a fraction of a single atomic layer and are used to fabricate devices with quantum structures in the active region. The two methods are also employed in VCSEL production on a large scale.

## References


1. D.W. Pashley, A historical review of epitaxy, in *Epitaxial Growth (Part B)*, ed. by J.W. Matthews (Academic Press, New York, 1975), pp. 1–27
2. M.L. Frankenheim, Über die Verbindung verschiedenartiger Kristalle. Ann. Phys. **113**, 516 (1836) (in German)
3. M. L'Abbé R. J. Haüy, *Traité élémentaire de physique*, 3rd edn. (Mme. V. Courcier, Libraire Pour Les Sciences, Paris, 1821) (in French)
4. T.V. Barker, Contributions to the theory of isomorphism based on experiments on the regular growths of crystals on one substance on those of another. J. Chem. Soc. Trans. **89**, 1120 (1906)
5. L. Royer, Recherches expérimentales sur l'epitaxie ou orientation mutuelle de cristaux d'espèces différentes. Bull. Soc. Fr. Minéral. Cristallogr. **51**, 7 (1928) (in French)
6. G.I. Finch, A.G. Quarrell, The structure of magnesium, zinc and aluminium films. Proc. R. Soc. Lond. A **141**, 398 (1933)
7. F.C. Frank, J.H. van der Merve, One-dimensional dislocations. I. Static theory. Proc. R. Soc. Lond. A **198**, 205 (1949)
8. F.C. Frank, J.H. van der Merve, One-dimensional dislocations. II. Misfitting monolayers and oriented overgrowth. Proc. R. Soc. Lond. A **198**, 216 (1949)
9. F.C. Frank, J.H. van der Merve, One-dimensional dislocations. III. Influence of the second harmonic term in the potential representation, on the properties of the model. Proc. R. Soc. Lond. A **200**, 125 (1949)
10. W.A. Jesser, J.W. Matthews, Evidence for pseudomorphic growth of iron on copper. Philos. Mag. **15**, 1097 (1967)
11. W.A. Jesser, J.W. Matthews, Pseudomorphic growth of iron on hot copper. Philos. Mag. **17**, 595 (1968)
12. I.V. Markov, *Crystal Growth for Beginners* (World Scientific, Singapore, 2003)
13. D.M. Eigler, E.K. Schweizer, Positioning single atoms with a scanning tunnelling microscope. Nature **344**, 524 (1990)
14. Details and the last STM image are reported in M.F. Crommie, C.P. Lutz, D.M. Eigler, Confinement of electrons to quantum corrals on a metal surface. Science **262**, 218 (1993). Image originally created by IBM Corporation, accessible at http://www.almaden.ibm.com/vis/stm/corral.html

# Chapter 2
# Structural Properties of Heterostructures

**Abstract** Structural properties of epitaxial layers are pointed out in this chapter with some emphasis on zincblende and wurtzite crystals. After a brief review on perfect, polytype, and mixed bulk crystals we focus on elastic properties of pseudomorphic strained-layer structures. Then the concept of critical layer thickness is introduced, and dislocations relieving the strain in epitaxial layers are presented. X-ray diffraction—the standard tool for structural characterization—is outlined at the end of the chapter.

## 2.1 Basic Crystal Structures

Atoms in an ideal solid have a regular periodic arrangement, which represents a minimum of total energy. The structure of such a crystalline solid is described by a *lattice*, which constitutes the translational periodicity, and a *basis*, which represents the atomic details of the recurring unit cell. In 1848 Auguste Bravais showed that there are only 14 lattices in three-dimensional space. These 14 *Bravais lattices* may be divided into 7 crystal systems, which differ in shape of their unit cell as shown in Table 2.1. The given unit cells reflect the symmetry of the structures. In most cases they are not primitive, i.e., they are larger than the smallest possible unit cell and contain more than one basis. Some important crystal structures are pointed out explicitly in this Chapter.

### *2.1.1 Notation of Planes and Directions*

Lattice planes and directions in crystals are generally denoted by triplets of integer numbers $h$, $k$, $l$ called *Miller indices*. To determine the Miller indices of a given plane, first a coordinate system is constructed using base vectors of the unit cell (regardless of being primitive or not). Then the intersection points of the plane with the axes are determined in units of the lattice constants, i.e., as multiples of the base vectors. Finally the reciprocal of these three values are expanded to the smallest set of integer values. Example: A plane intersects the three axes of a cubic coordinate system at $(3, 1, 2)$ yielding the reciprocals $(1/3, 1, 1/2)$, and consequently

U.W. Pohl, *Epitaxy of Semiconductors*, Graduate Texts in Physics,
DOI 10.1007/978-3-642-32970-8_2, 

**Table 2.1** The seven crystal systems and the 14 Bravais lattices. **a**, **b**, and **c** are lattice vectors spanning the unit cell; $\alpha$, $\beta$, and $\gamma$ are angles between these vectors

| System | Unit cell | Bravais lattices | Symmetry axes |
|---|---|---|---|
| Cubic | $\mathbf{a} = \mathbf{b} = \mathbf{c}$, $\alpha = \beta = \gamma = 90°$ | simple cubic, body-centered cubic, face-centered cubic | 4 threefold axes parallel to the diagonals of the unit cell |
| Tetragonal | $\mathbf{a} = \mathbf{b} \neq \mathbf{c}$, $\alpha = \beta = \gamma = 90°$ | simple tetragonal, body-centered tetragonal | 1 fourfold axes of rotation or inversion parallel to **c** |
| Rhombohedral | $\mathbf{a} = \mathbf{b} = \mathbf{c}$, $\alpha = \beta = \gamma \neq 90°$ | rhombohedral | 1 threefold axes of rotation or inversion parallel to $\mathbf{a} + \mathbf{b} + \mathbf{c}$ |
| Hexagonal | $\mathbf{a} = \mathbf{b} \neq \mathbf{c}$, $\alpha = \beta = 90°$, $\gamma = 120°$ | hexagonal | 1 sixfold axes of rotation or inversion parallel to **c** |
| Orthorhombic | $\mathbf{a} \neq \mathbf{b} \neq \mathbf{c}$, $\alpha = \beta = \gamma = 90°$ | simple orthorhombic, base-centered orthorhombic, body-centered orthorhombic, face-centered orthorhombic | 3 mutually perpendicular twofold axes of rotation or inversion parallel to **a**, **b**, and **c** |
| Monoclinic | $\mathbf{a} \neq \mathbf{b} \neq \mathbf{c}$, $\alpha = \gamma = 90°$, $\beta \neq 90°$ | simple monoclinic, face-centered monoclinic | 1 twofold axes of rotation or inversion, e.g. parallel to **b** |
| Triclinic | $\mathbf{a} \neq \mathbf{b} \neq \mathbf{c}$, $\alpha \neq \beta \neq \gamma$; $\alpha, \beta, \gamma \neq 90°$ | triclinic | none |

the Miller indices $(2, 6, 3)$. Parentheses are used to signify a specific plane. Curly brackets $\{hkl\}$ are used if a *set* of crystallographic equivalent planes is denoted. To specify a specific *direction* or a set of equivalent directions, square brackets $[hkl]$ or cuspid brackets $\langle hkl \rangle$ are used, respectively. The position of a point $hkl$ is labeled by giving the coordinates without brackets. Finally, negative values are denoted by a bar on top, e.g., $[\bar{h}\bar{k}l]$ means $[-h\,-k\,l]$. Position and nomenclature of some important low-index planes in cubic and hexagonal lattices are depicted in Fig. 2.1. In the hexagonal system often *four* indices are used, i.e., $hktl$. The index $t$ refers to a third vector in the base plane of the unit cell and depends on the indices of the vectors along **u** and **v** shown in Fig. 2.4d by the relation $t = -(h + k)$. The index $t$ is hence redundant and commonly replaced by a dot. It should be noted that sometimes even this dot is dropped, so that Miller indices of cubic and hexagonal lattices look similar. The directions of the hexagonal system given in Fig. 2.1 refer to the commonly used convention.

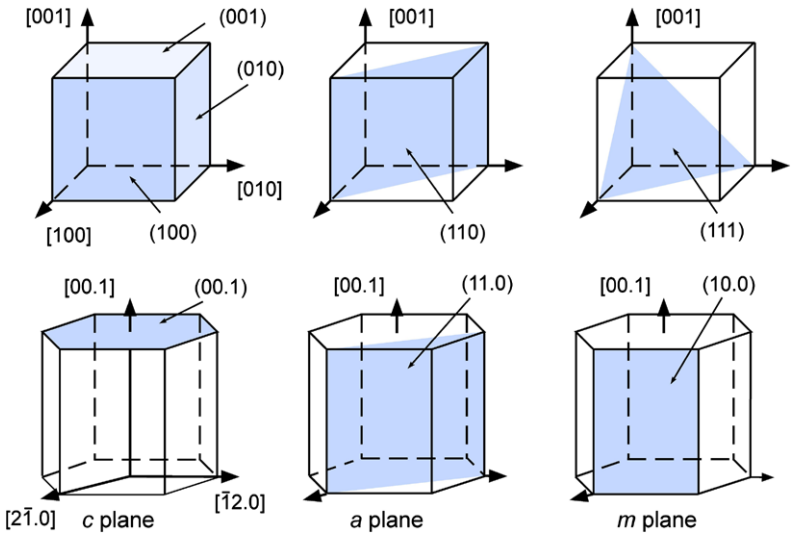


**Fig. 2.1** Position of important planes and their Miller indices for cubic and hexagonal lattices

### *2.1.2 Wafer Orientation*

Thin slices of bulk semiconductor crystals referred to as *wafers* are used for growth of epitaxial layers. Wafers made of Si, GaAs, and InP with surfaces vicinal to {100}, {111}, and {110} are most common and produced by cutting an on-axis crystal at the appropriate angle. Their cleavage planes are discussed in Sect. 2.1.4. The wafers are usually of circular shape with 2 to 6 inch diameter (silicon up to 300 mm) and 300 up to 1000 µm thick (depending on diameter). Information on the orientation of the crystallographic axes and the dopant type (*n*-type, *p*-type, or undoped) are indicated by location and number of *flats*, features machined at the perimeter of the wafer. Primary or major (orientation) flats and shorter secondary or minor (identification/index) flats are used according different standards. Common standards are the EJ (Europe/Japan), US, and SEMI options. Figure 2.2 shows some wafer geometries of semiconductors with cubic structure along with crystallographic orientations.

### *2.1.3 Face-Centered Cubic and Hexagonal Close-Packed Structures*

The face-centered cubic and the hexagonal structure are often found in metals, and the most important semiconductors crystallize in the related diamond, zincblende, or wurtzite structures. Let us consider the atoms as spheres, which do not prefer any direction of bonding. If such atoms are closely arranged in a plane, each one has contact to six next neighbors, cf. Fig. 2.3a. The atoms form a hexagonal net plane,

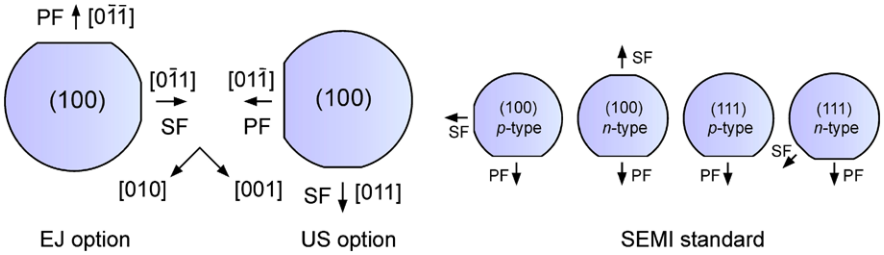


**Fig. 2.2** Semiconductor wafers with standard flat orientations according various options. *PF* and *SF* denote primary and secondary flats, respectively. The *arrows* along [010] and [001] refer to the coordinate system of the two wafers on the *left hand side*

which we label plane $B$. To obtain a closely stacked three-dimensional arrangement, atoms within a plane $A$ on top of plane $B$ must be arranged similarly, starting with an atom above the interstice of three $B$-atoms. Note that only 3 of the 6 hexagonally arranged interstices of $B$ are occupied by atoms in plane $A$. Hence there are two alternatives for a plane $C$ below plane $B$: Their atoms either use the interstices not used above in plane $A$, or they are arranged similar to plane $A$. These two different structures are referred to as *face-centered cubic* (fcc, stacking sequence $ABCABC$ along the [111] stacking direction) and *hexagonal close-packed* (hcp, sequence $ABAB$). Note that both structures have the *same* stacking density.

Figure 2.3b shows that the $ABC$-stacked atoms are located on a *cubic* lattice, with additional atoms centered on the six faces of the cube (the contour of the front half of the fcc unit cell is only partially drawn for clarity). This is not the case in the unit cell of the hcp structure, represented by the dark spheres in Fig. 2.4d.

### *2.1.4 Zincblende and Diamond Structures*

Many solids are composed of more than one kind of atoms. Crystal structures of some important binary bulk compounds with an at least partial ionic bond are given in Table 2.2. Some of these solids may crystallize also in another structure as noted in Table 2.3. ZnS and CdSe, e.g., have also a stable high temperature phase (here wurtzite), which may be preserved at room temperature by suitable growth conditions. Using epitaxy also structures which differ from that of the stable bulk crystal may be stabilized.

In the zincblende and wurtzite structures, the bases of the primitive unit cells consist of *two* atoms, which generally have different polarity. Their location is at $(0, 0, 0)$ and $(1, 1, 1) \times a/4$, $a$ being the lattice constant (cf. Fig. 2.4a). We will refer to these atoms as cations and anions (like zinc and sulfur in ZnS). The *zincblende structure* is composed of an fcc lattice of cations (represented by, e.g., dark spheres in Fig. 2.4a) and an fcc lattice of anions. These two sublattices are displaced by a quarter of the cube diagonal, i.e. by $(\sqrt{3}/4) \times a$. As a result, each ion is tetrahedrally surrounded by four ions of opposite polarity as depicted in Fig. 2.4a. $\langle 110 \rangle$ planes

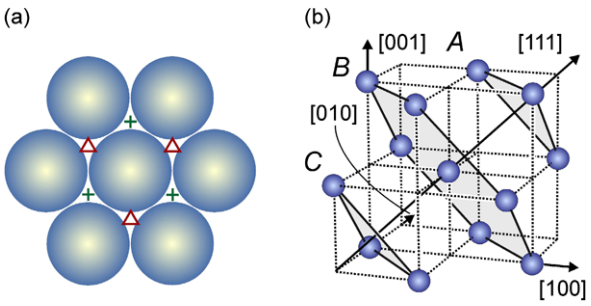


**Fig. 2.3** (**a**) Hexagonal net planes in a closed-packed crystal structure. $\Delta$ and + denote locations of atoms in the planes above and below, respectively, forming the fcc structure shown in (**b**). (**b**) Face-centered cubic structure. *A*, *B*, and *C* label different hexagonal lattice planes in a face-centered cubic lattice

of the zincblende structure contain an equal number of cations and anions, arranged along zig-zag chains. Since their charges balance, ⟨110⟩ crystal faces are non-polar. Crystals may usually be well cleaved parallel to non-polar planes, a fact used, e.g., in laser devices made from zincblende semiconductors to fabricate resonator facets by cleaving along two parallel ⟨110⟩ planes: Zincblende wafers with (100) orientation scribed along [011] and [01$\bar{1}$] form side facets perpendicular to the wafer surface and perpendicular to each other. In contrast, ⟨100⟩ and ⟨111⟩ planes contain only one kind of ions and hence form polar faces. The [111] direction is not equivalent to the [$\bar{1}\bar{1}\bar{1}$] direction. In *AB* compounds like zincblende ZnS (*A* an *B* generally denoting cations and anions, respectively, not to be confused with layer labels), wafers with (111) surface have a cation-terminated *A*-face and an opposing anion-terminated *B*-face, which can be distinguished, e.g., by different chemical etching behavior. Typical compounds with zincblende structure are ZnS, GaAs, InP, and CuCl.

If the atoms on the two fcc sublattices are identical, we obtain the *diamond structure* (consider *all* atoms in Fig. 2.4a to be blue). Crystal faces of this structure are non-polar, crystals may also be cleaved parallel to planes differing from ⟨110⟩. Elements crystallizing in diamond structure are C (diamond phase), Ge, Si, and Sn ($\alpha$ phase). In Si and Ge primary cleaving planes are ⟨111⟩ planes: They produce less dangling bonds than ⟨110⟩ planes upon cleaving. Si wafers with (100) orientation scribed along [011] or [01$\bar{1}$] form {111} side facets inclined to the wafer surface by an angle of 54.7°.

**Table 2.2** Stable crystal structures of *AB* compounds composed of either group II and VI, or group III and V elements. W, ZB, and Gr denote wurtzite, zincblende, and graphite structure, the compound marked by a star does not exist. From [1]

| Cation group II | Anion group VI | | | | Cation group III | Anion group V | | | |
|---|---|---|---|---|---|---|---|---|---|
| | O | S | Se | Te | | N | P | As | Sb |
| Be | W | ZB | ZB | ZB | B | Gr | ZB | ZB | * |
| Mg | NaCl | NaCl | NaCl | W | Al | W | ZB | ZB | ZB |
| Zn | W | ZB | ZB | ZB | Ga | W | ZB | ZB | ZB |
| Cd | NaCl | W | ZB | ZB | In | W | ZB | ZB | ZB |

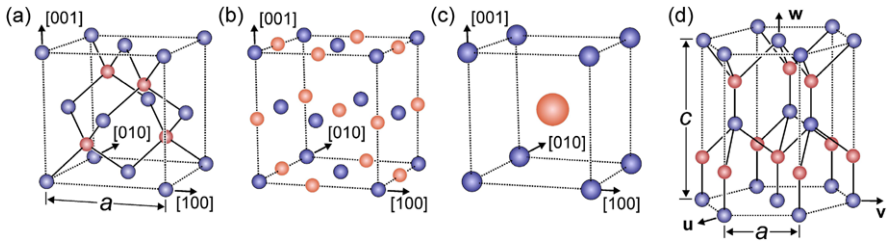


**Fig. 2.4** The crystal structures of (**a**) zincblende, (**b**) rocksalt (NaCl), (**c**) cesium chloride (CsCl), and (**d**) wurtzite

### *2.1.5 Rocksalt and Cesium-Chloride Structures*

The cubic *rocksalt structure* (also termed sodium-chloride structure) shown in Fig. 2.4b is composed of two fcc lattices for cations and anions, respectively, displaced by half of the cube diagonal, i.e., by $(\sqrt{3}/2) \times a$. The two ions of the basis are located at $(0, 0, 0)$ and $(1, 1, 1) \times a/2$. As a result, each ion is octahedrally surrounded by six ions of opposite polarity. Their charges balance on $\langle 100 \rangle$ crystal faces, which are hence non-polar and build cleavage planes of this structure. Compounds which crystallize in rocksalt structure are, e.g., NaCl, KCl, AgBr, FeO, PbS, MgO, and TiN.

The *cesium-chloride structure* depicted in Fig. 2.4c consists of a simple cubic lattice with a diatomic base. The two ions are located at $(0, 0, 0)$ and $(1, 1, 1) \times a/2$, similar to the rocksalt structure. Typical compounds with cesium-chloride structure are CsCl, $NH_4Br$, TlCl, AgZn, AlNi, and CuZn.

### *2.1.6 Wurtzite Structure*

The wurtzite structure shown in Fig. 2.4d is composed of two hcp sublattices, one for cations and one for anions. In the ideal structure these sublattices are displaced by $\mathbf{u} = 3/8\mathbf{c}$ along the [001] direction, $c$ being the vertical lattice parameter. The ideal ratio of vertical and lateral lattice parameters is $c/a = (8/3)^{1/2} = 1.633$. The $u/c$ ratio of wurtzite-type crystals often deviates from the ideal value 0.375, and likewise the $c/a$ ratio. The deviation gives rise to a macroscopic spontaneous polarization, which can cause strong internal electric fields—e.g. in group-III nitrides up to 3 MV/cm [2]. Lattice parameters for some crystal structures are listed in Table 2.3. In wurtzite crystals the zig-zag chains of bonding lie within a non-polar $\langle 11.0 \rangle$ plane (Fig. 2.6, $a$ plane Fig. 2.1). It is a cleavage plane perpendicular to the (00.1) $c$ plane. The top face of the unit cell represents the polar (00.1) plane. It is often referred to as *basal* plane, i.e., a plane which is perpendicular to the principal axis ($c$ axis) in a hexagonal or tetragonal structure. The [00.1] direction is not equivalent to $[00.\bar{1}]$; the (00.1) face is made up of cations and, e.g., in GaN referred to as (00.1)Ga face, while anions build the $(00.\bar{1})$ face ($(00.\bar{1})$N in GaN).

**Table 2.3** Lattice parameters of existing and hypothetical tetrahedrally coordinated crystals [1]. Italicized numbers are theoretical results from pseudopotential calculations, $\Delta E_{\text{W-ZB}}$ is the calculated energy difference between wurtzite and zincblende structures at $T = 0$

| Solid | Wurtzite | | | | Zincblende | $\Delta E_{\text{W-ZB}}$ (meV/atom) |
|---|---|---|---|---|---|---|
| | $a$ (Å) | $c$ (Å) | $c/a$ | $u/c$ | $a$ (Å) | |
| GaN | 3.192 | 5.196 | 1.628 | | 4.531 | |
| | *3.095* | *5.000* | *1.633* | *0.378* | *4.364* | *−9.9* |
| InN | 3.545 | 5.703 | 1.609 | | | |
| | *3.536* | *5.709* | *1.615* | *0.380* | *4.983* | *−11.4* |
| AlN | 3.112 | 4.980 | 1.600 | | 5.431 | |
| | *3.099* | *4.997* | *1.612* | *0.381* | *4.365* | *−18.4* |
| GaAs | | | | | 5.653 | |
| | *3.912* | *6.441* | *1.647* | *0.374* | *5.654* | *12.0* |
| AlAs | | | | | 5.660 | |
| | *3.979* | *6.497* | *1.633* | *0.376* | *5.620* | *5.8* |
| ZnS | 3.823 | 6.261 | 1.638 | | 5.410 | |
| | *3.777* | *6.188* | *1.638* | *0.375* | *5.345* | *3.1* |
| CdS | 4.137 | 6.716 | 1.624 | | 5.818 | |
| | *4.121* | *6.682* | *1.621* | *0.377* | *5.811* | *−1.1* |
| Si | | | | | 5.431 | |
| | *3.800* | *6.269* | *1.650* | *0.374* | *5.392* | *11.7* |
| C | 2.51 | 4.12 | 1.641 | | | |
| | *2.490* | *4.144* | *1.665* | *0.374* | *3.539* | *25.3* |

### *2.1.7 Thermal Expansion*

Epitaxy is performed at temperatures far above room temperature to provide sufficient mobility of adatoms on the growing crystal surface. Typical growth temperatures are around 600 °C, but materials may require substantially lower or higher temperatures (e.g., compound semiconductors containing Hg below 200 °C or nitrides well above 1000 °C). Cooling after epitaxy over a wide range to room temperature or cryogenic temperatures is accompanied by a significant diminution of the lattice constant due to anharmonic terms of the crystal potential. The difference in the thermal expansion of substrate and layer materials may induce large strain in the structure, leading to bending of the substrate and, in case of tensile strain, to cracks in the epitaxial layer. Large differences in the thermal expansion of layers within a heteroepitaxial structure may hence seriously affect structural properties and lead to the requirement of inserting suitable buffer layers to accommodate the thermal mismatch.

**Table 2.4** Linear thermal expansion coefficients and lattice parameters of some cubic and hexagonal semiconductors at 300 K. Data reported in literature have significant scatter, particularly for hexagonal structures. Listed values represent some mean data

| Semiconductor | Lattice parameter (Å) | | Thermal expansion coefficient ($10^{-6}$ K$^{-1}$) | |
|---|---|---|---|---|
| | $a$ | $c$ | $\alpha_a$ | $\alpha_c$ |
| GaAs | 5.6535 | – | 5.7 | – |
| AlAs | 5.660 | – | 5.2 | – |
| InAs | 6.058 | – | 4.5 | – |
| GaP | 5.4509 | – | 4.7 | – |
| InP | 5.8688 | – | 4.7 | – |
| ZnS | 5.410 | – | 7.1 | – |
| ZnSe | 5.668 | – | ∼7.4 | – |
| CdTe | 6.484 | – | 5.0 | – |
| Si | 5.4310 | – | 2.6 | – |
| Ge | 5.6576 | – | 5.7 | – |
| GaN | 3.183 | 5.185 | ∼4.5 | ∼4.0 |
| AlN | 3.11 | 4.98 | ∼4.2 | ∼5.3 |
| ZnO | 3.25 | 5.21 | ∼4.7 | ∼2.9 |

Within the thermal range of interest usually the description of a temperature-dependent lattice parameter $a(T)$ by a *linear* thermal expansion coefficient (TEC) $\alpha$ is applied according

$$\frac{a(T) - a(T_0)}{a(T_0)} = \alpha \times (T - T_0).$$

Usually room temperature is taken as reference temperature $T_0$. The thermal change of volume is in general anisotropic and $\alpha$ is consequently a second rank tensor. It is described by three components $\alpha_i$ the principal axes of which are along those of the strain tensor (Sect. 2.2.2). Along a principal axis the respective component $\alpha_i$ is defined by

$$\alpha_i = \frac{1}{a}\left(\frac{\partial a}{\partial T}\right)_P.$$

For cubic crystals the three components $\alpha_i$ are identical and the expansion coefficient becomes a scalar. Crystals with a hexagonal structure have two independent components, namely $\alpha_a = \alpha_\perp$ perpendicular to the $c$ axis and $\alpha_c = \alpha_\parallel$ along the $c$ axis. Linear expansion coefficients of semiconductors are typically of the order mid $10^{-6}$ K$^{-1}$. Data for some semiconductors are given in Table 2.4.

The thermal expansion is actually not a linear function of temperature. The expansion coefficients depend on temperature and are usually positive quantities. Below 100 K semiconductors with zincblende or diamond structure show a commonly not observed negative thermal expansion [3, 4]. Above 300 K coefficient values

slightly increase if the temperature is raised. An empirical relation by a polynomial fit is sometimes applied to account for the temperature dependence of the thermal expansion. In a specified temperature range a lattice parameter is then described by $a(T) = a(T_0)(1 + A + BT + CT^2 + DT^3)$, where $T_0$ is the reference temperature (generally 300 K) and $T$ is the absolute temperature in K.

### *2.1.8 Structural Stability Map*

Rules to predict crystal structures of solids from properties of atoms require first-principle calculations with a high degree of accuracy, because the difference in equilibrium energies of a given compound in two closely related structures is often less than 0.1 % of the cohesive energy. In the corresponding problem of the regularities of the periodic table of the elements, a scheme with the two integral coordinates principal and orbital quantum number was found. Starting from classical approaches using atomic radii and Pauling's electronegativity, today some largely universal schemes for predicting the structural stability of many intermetallic compounds of the form $A_xB_y$, of $sp$-bonded $A^nB^{p-n}$ ($p = 8$ or $2, \ldots, 6$) semiconductors and insulators, and of high-$T_c$ superconductors have been suggested. The success rate generally exceeds 95 %, and domains of different overlapping structure types could be related to polymorphic structural forms [1, 5–8]. Most schemes use orbital radii coordinates $R$, which are linear combinations of the $s$- and $p$-orbital radial functions $R^A$ and $R^B$ of the atoms building the $AB$ compound:

$$R_\sigma(A, B) = \left|\left(R_p^A + R_s^A\right) - \left(R_p^B + R_s^B\right)\right|, \tag{2.1a}$$

$$R_\pi(A, B) = \left|\left(R_p^A - R_s^A\right) + \left(R_p^B - R_s^B\right)\right|. \tag{2.1b}$$

$R_\sigma$ gives a measure of the size difference between atoms $A$ and $B$, and roughly scales with ionicity. $R_\pi$ scales with the atomic $s$ and $p$ energy difference and measures to some extent $sp$-hybridization. Figure 2.5 shows a structural stability diagram for binary compounds of the form $A^nB^{8-n}$ like $Ga^{III}As^{V}$, using radii of (2.1a)–(2.1b) at which the all-electron atomic radial orbitals $r \times R_{nl}(r)$ have their outer maxima.

Zincblende and wurtzite are the most common crystal structures of binary semiconductors. For these structures the orbital radii coordinates given in (2.1a)–(2.1b) were used to calculate the equilibrium energy difference $\Delta E_{\text{W-ZB}}$ between the ideal wurtzite and the zincblende structure, cf. Table 2.3. Calculated structural deviations from ideal wurtzite are small, the energy gain due to such relaxations is generally smaller than 1 meV per atom (except for AlN, −2.7 meV) [1]. The study confirms the phenomenological correlation, that wurtzite-stable compounds have smaller $c/a$ ratios than the ideal value, while zincblende and diamond-stable compounds have larger ratios. As a further rule of thumb, a large difference in electronegativity and atomic radii of atoms $A$ and $B$ favor the wurtzite structure.

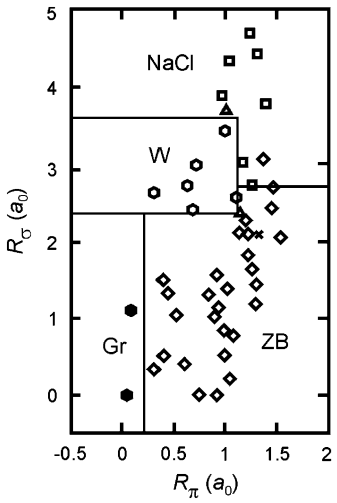


**Fig. 2.5** Structural stability map for binary $AB$ compounds, calculated using atomic orbital radial functions in units of the Bohr radius. NaCl, W, ZB, and Gr denote sodium-chloride, wurtzite, zincblende, and graphite structures, respectively. The misaligned cross in the zincblende range marks a NiAs structure, the triangles cinnabar (HgS) structure. From [1]

### *2.1.9 Polytypism*

Small values of equilibrium energy differences between wurtzite and zincblende structure $\Delta E_{\text{W-ZB}}$ given in Table 2.3 indicate an intrinsic low stability of the crystal structure of some solids. In fact many solids may crystallize in multiple crystal structures having identical stoichiometries, a phenomenon called polymorphism. Wurtzite and zincblende are two structures of a one-dimensional polymorphism referred to as *polytypism*. For a graphic representation of such polytypes of tetrahedrally coordinated $AB$ compounds a plot of the cation-anion zigzag chains, which lie in the (11.0) plane of the hexagonal lattice and in the (110) plane of the zincblende lattice, is useful. Figure 2.6 shows three prominent polytypes, the zincblende 3C structure, and the two structures 4H and 6H. The number in the notation refers to the periodicity, while C and H designate a cubic and hexagonal structure, respectively. Using this notation, the wurtzite structure is labeled 2H.

There are numerous such polytypes known from some compounds, more than, e.g., 100 for ZnS and about 170 for SiC; they build cubic (3C), hexagonal (H), and rhombohedral (R) structures. All these modifications have the same lateral lattice constant $a$ in the representation chosen above, while $c$ is an integer multiple of the layer thickness. All polytypes may be considered as mixtures of 3C and 2H. The 4H modification is then composed equally of cubic ($ABC$ next neighborhood) and hexagonal ($ABA$) bonds. The notation of a given polytype by periodicity is not unambiguous, e.g., periodic stacks of $ABCACB$ and $ABCBAB$ form inequivalent hexagonal 6H modifications.

The different polytypes of a given compound have widely ranging physical properties. The energy band gap generally becomes greater as the wurtzite component increases, see Table 2.5. The number of atoms within a unit cell and that of inequivalent atom sites increases with the size of the unit cell, and consequently also the number of phonon branches. The electron mobility of the high symmetry 3C

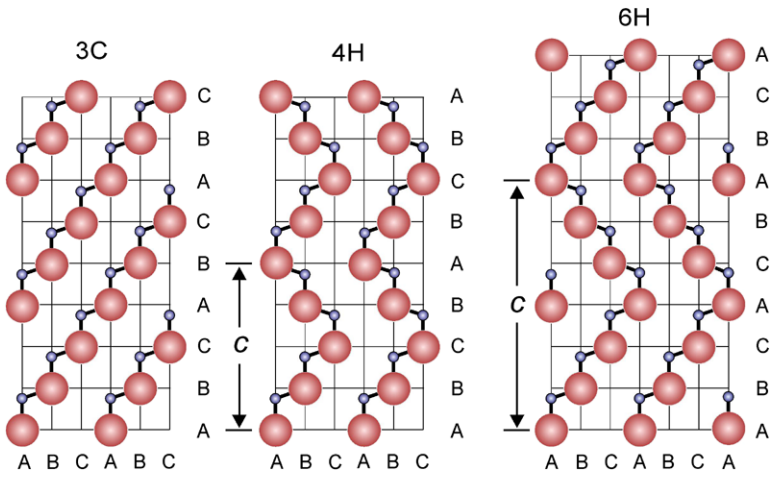


**Fig. 2.6** Stacking sequences of binary $AB$ compound polytypes depicted in the (11.0) plane of the hexagonal lattice. Labels $A$, $B$, and $C$ on the horizontal axis refer to atom sites, while such labels on the vertical axis denote net planes as shown in Fig. 2.3b

polytype may be higher due to reduced phonon scattering. Furthermore, a particular doping impurity on inequivalent sites has different electronic properties due to a more cubic or hexagonal environment.

A self-contained theory explaining the origin of polytypes with up to more than 100 planes within a period does not yet exist. The occurrence of long periods is often associated with dislocations (Sect. 2.3), e.g., screw dislocations which induce spiral growth. In such case the periodicity is determined by the step height of the growth spiral. Short-period polytypes may be stabilized by growth conditions given by temperature, pressure or gas-phase composition, due to different minima in formation energy.

### *2.1.10 Random Alloys and Vegard's Rule*

Mixing two or more solids to an *alloy*, i.e., a solid solution, is an old technique to modify properties of materials. Alloys with two, three, or four components are called *binary*, *ternary* or *quaternary* alloys, respectively. In substitution alloys atoms of comparable size are simply substituted for one another in the crystal structure. Such alloys are routinely made from semiconductors to engineer properties like lattice parameter or bandgap. Metals may also form interstitial alloys, where atoms of one component are substantially smaller than the other and fit into the interstices between the larger atoms.

Usually a random mixing of the atoms on the semiconductor lattice-sites of the alloy is intended. Limits in the miscibility of the components or ordering effects in the alloy may, however, lead to significant deviations from a random distribution

**Table 2.5** Physical properties of some polytypes, arranged in increasing order of wurtzite character. The number of atoms refers to the primitive unit cell, $E_g$ denotes the bandgap energy at 2 K. Data from [9–11]

| Polytype | | 3C | 15R | 6H | 4H | 2H |
|---|---|---|---|---|---|---|
| Space group symmetry | | $T_d$ | $C_{3v}$ | $C_{6V}$ | $C_{6V}$ | $C_{6V}$ |
| Atoms per unit cell | | 2 | 10 | 12 | 8 | 4 |
| Inequivalent sites | | 1 | 5 | 3 | 2 | 1 |
| SiC | $E_g^X$ (eV) | 2.390 | 2.906 | 3.023 | 3.265 | 3.330 |
| | $a$ (Å) | 4.349 | 3.08 | 3.081 | 3.073 | 3.076 |
| | $c$ (Å) | | 37.70 | 15.117 | 10.053 | 5.048 |
| ZnS | $E_g^\Gamma$ (eV) | 3.85 | | | | 3.91 |
| | $a$ (Å) | 5.410 | 3.83 | 3.82 | 3.81 | 3.823 |
| | $c$ (Å) | – | 46.88 | 18.72 | 12.46 | 6.260 |
| GaN | $E_g^\Gamma$ (eV) | 3.21 | | | | 3.503 |
| | $a$ (Å) | 4.50 | | | | 3.189 |
| | $c$ (Å) | – | | | | 5.185 |

and consequently to altered physical properties of the alloy. There are three extreme cases occurring in alloy formation.

- *Random alloy*: The probability of an atom next to a given atom in an $A_xB_{1-x}$ alloy is $x$ for an $A$-atom and $(1-x)$ for a $B$-atom. This is the case usually wanted for applications.
- *Ordered alloy*: Atoms in the alloy have a regular periodic structure. The crystal structure is then given by placing at each site of the Bravais lattice a multiatomic base, yielding translational symmetry of the Bravais lattice in the alloy. Examples are $\beta$-brass with alternating Cu and Zn atoms along [111] or CuPt structure of $In_{1-x}Ga_xP$ at $x \approx 0.5$. Since ordering requires a specific ratio in the number of the atom types forming such alloys, they are also referred to as *stoichiometric alloys*.
- *Phase separation*: Atoms of type $A$ and $B$ do not mix and are located at different regions in the solid.

We consider the technologically important *random alloy* in more detail. We assume two compound semiconductors $AC$ and $BC$ having the same crystal structure, $A$ and $B$ representing cations and $C$ an anion. Alloying leads to a semiconductor $A_xB_{1-x}C$ with a mixture of $A$ and $B$ atoms on the cation sublattice, while all sites on the anion sublattice remain occupied by $C$ atoms. Since the alloying forms a binary *sub*lattice (the unmixed materials $AB$ and $AC$ are already binary compounds themselves) such alloys are called *pseudobinary* (sometimes also referred to as ternary, though in a true ternary all components mix on the same lattice). The concept may be extended to compounds $A_xB_{1-x}C_yD_{1-y}$ usually termed quaternary compound.

The composition parameter $x$ in the pseudobinary alloy $A_xB_{1-x}C$ denotes that on the *average* an anion $C$ has $x$ neighbors of type $A$ and a fraction of $1-x$ neighbors of type $B$. A number of properties of true alloys are expected to scale by a smooth interpolation between the two endpoint materials. This is usually well fulfilled for the lattice constant. The empirical rule called *Vegard's rule* [12] states that a *linear* interpolation exists, at constant temperature, between the crystal lattice constant of an alloy and the concentrations of the constituent elements. The lattice constant $a_{\text{alloy}}$ from two materials $A$ and $B$ with the same crystal structure and lattice constants $a_A$ and $a_B$, respectively, is hence given by

$$a_{\text{alloy}} = xa_A + (1-x)a_B. \tag{2.2a}$$

The lattice constant of a (pseudobinary) ternary alloy with a mixture of compounds $AC$ and $BC$ is given by the same relation putting $a_A$ and $a_B$ to $a_{AC}$ and $a_{BC}$, respectively. The linear relationship also holds for quaternary alloys. For compounds of the type $A_xB_yC_{1-x-y}D$ the interpolation yields

$$a_{\text{alloy}} = xa_{AD} + ya_{BD} + (1-x-y)a_{CD}. \tag{2.2b}$$

The lattice parameter for alloys of the type $A_xB_{1-x}C_yD_{1-y}$, where atoms $A$ and $B$ mix on one sublattice and atoms $C$ and $D$ on another sublattice, is calculated from the ternary parameters $a_{ABC}$, $a_{ABD}$, $a_{ACD}$, and $a_{BCD}$,

$$a_{\text{alloy}} = \frac{x(1-x)[ya_{ABC}(x) + (1-y)a_{ABD}(x)] + y(1-y)[xa_{ACD}(y) + (1-x)a_{BCD}(y)]}{x(1-x) + y(1-y)},$$

$$a_{ABC}(x) = xa_{AC} + (1-x)a_{BC}, \tag{2.2c}$$

$a_{ABD}(x)$, $a_{ACD}(y)$, and $a_{BCD}(y)$ accordingly.

Using Vegard's rule (2.2a)–(2.2c) lattice matching to a substrate lattice parameter is achieved using an appropriate composition $x$ (and $y$) of materials with a larger and a smaller lattice parameter. Example: $In_{0.53}Ga_{0.47}As$ for epitaxy on InP ($a_{InAs} = 6.0584$ Å, $a_{GaAs} = 5.6533$ Å, $a_{InP} = 5.8688$ Å). It must be noted that the adjustment of lattice parameters by alloying is accompanied by a change of the bandgap energy and other properties. Often the composition is rather chosen for obtaining a desired band gap in the alloy. In a *quaternary* alloy lattice parameter and bandgap energy can be adjusted independently (Sect. 3.1.4). Note that exact lattice matching is generally met only for a given temperature, because the lattice parameter varies as the temperature is changed (e.g., from growth temperature to room temperature) and different materials like substrate and layer have usually different thermal expansion coefficients (cf. Sect. 2.1.7).

For stable two- and three-dimensional central-force networks (e.g. triangular net or fcc lattice) Vegard's rule was derived from quite general assumptions [13]. Deviations from the linear relation are always found in metallic alloys [14], but they are in practice usually negligible in miscible semiconductor alloys. Vegard's rule is therefore routinely used to measure the composition of a studied alloy from its lattice parameter $a_{\text{alloy}}$ using, e.g., X-ray diffraction.

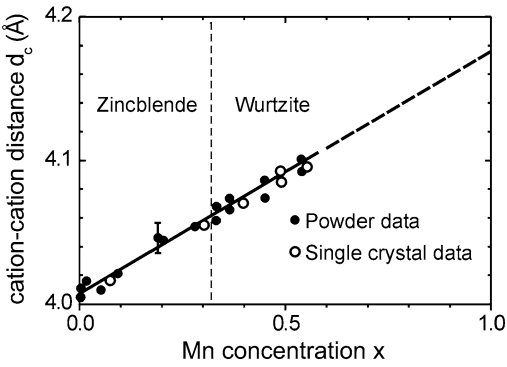


**Fig. 2.7** Mean cation-cation distance $d_c$ in $Zn_{1-x}Mn_xSe$ for varying Mn concentration $x$. The distance $d_c$ increases linearly with $x$ according Vegard's rule also across a change of crystal structure. From [15]

Vegard's rule may more generally apply for the average interatomic distances in solids if structural changes without change of the coordination number occur in an alloy. The example given in Fig. 2.7 shows the next-neighbor distance on the cation sublattice in the diluted magnetic semiconductor $Zn_{1-x}Mn_xSe$ with magnetic $Mn^{2+}$ ions substituting the nonmagnetic $Zn^{2+}$ cations. For a fraction exceeding $x \approx 0.3$ the crystal structure changes from zincblende to wurtzite. The $c/a$ ratio of wurtzite ZnMnSe is close to the ideal value of $\sqrt{8/3}$, indicating a close relationship to an ideal close packing arrangement [15]. The type of coordination does not change across the region in which the alloy changes between the crystal structures, which both are based on a closest packing of spheres. Such factors favor compliance with Vegard's rule.

The simple linear relation of the concentration-weighted average bond length expressed by Vegard's rule (2.2a), (2.2b) suggests that the chemical bond of atoms in an alloy smoothly changes between the values of the end-point materials. Such assumption is the premise of the virtual-crystal approximation (VCA) discussed below (Sect. 2.1.11). In real semiconductors this is not compelling. Experiments like extended X-ray absorption fine structure measurements (EXAFS) [16, 17] show that bond lengths in a semiconductor alloy are actually much closer to those of the end-point materials. The bond length calculated using Vegard's rule originates essentially from the weighted average of alternating bonds [18].

The difference between Vegard's rule and actual bond lengths is illustrated for the pseudobinary alloy $Ga_{1-x}In_xAs$. Both GaAs and InAs crystallize in zincblende structure. They are miscible over the entire range and form a random alloy. In X-ray diffraction (XRD) measurements the lattice constant of this alloy is found to vary linearly with the In composition $x$ according Vegard's rule. This behavior is shown in terms of the measured cation-anion bond length $\sqrt{3} \times a/4$ in Fig. 2.8a (squares) [19]. In contrast, a measurement of the local bond length using EXAFS

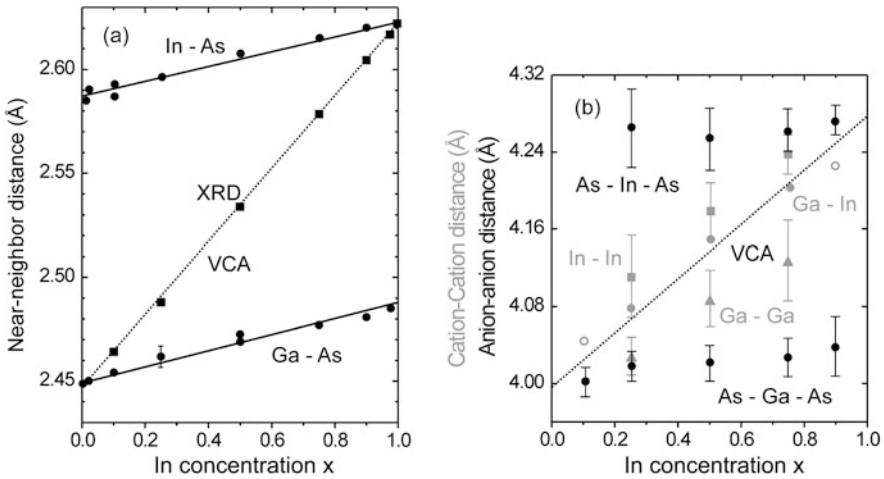


**Fig. 2.8** (**a**) Cation-anion near-neighbor distance as a function of In mole fraction in $Ga_{1-x}In_xAs$ alloys. *Circles* and *squares* refer to EXAFS and XRD data, respectively, the *dotted line* is the cation-anion bond length ($\sqrt{3} \times a/4$) according to the virtual-crystal approximation (VCA), calculated from the X-ray lattice constant. (**b**) As-As second-neighbor distance corresponding to As-Ga-As and As-In-As bonds (*black circles*) and Ga-Ga, In-In, and Ga-In second-neighbor distances, denoted by *gray triangles*, *squares*, and *circles*, respectively. The *dotted line* represents values expected from the VCA. Reproduced with permission from [16], © 1983 APS

demonstrates that actually two different types of bonds exist in the alloy: shorter Ga-As bonds and longer In-As bonds, yielding *in average* a bond length varying linearly with composition. Figure 2.8a shows that the actual individual bond lengths are close to those of GaAs and InAs, and that they vary only little. Consequently the two second-next neighbor distances of anions As-Ga-As and As-In-As given in Fig. 2.8b differ and remain almost constant for all compositions $x$. This is not the case for the second-next neighbor distances of *cations* depicted with gray symbols in the figure. The distances of atoms on the cation sublattice are all within ~0.05 Å of the linear interpolation suggested by Vegard's rule and the VCA considered below. Distances of In-In are above, Ga-Ga below, and Ga-In very close to the VCA line given in Fig. 2.8b. It should be noted that the bimodal near-neighbor distance shows a quite small width of the distribution, whereas all second-nearest neighbor distributions are rather broad [16]. The data demonstrate that the atomic scale structure of $Ga_{1-x}In_xAs$ alloys features a near-neighbor distribution which consists of two well defined distances. In contrast, the second-nearest neighbor mixed cation distances exhibit a single broadened distribution, and the corresponding common anion distribution is bimodal. The cation sublattice hence approaches a linearly interpolated VCA lattice, while the anions suffer a local displacement from the average position in the lattice. The origin of this behavior was explained in terms of differences in the distortion energy and the consequential mixing enthalpy [20].

### 2.1.11 Virtual-Crystal Approximation

The virtual-crystal approximation (VCA) assumes an ideal hypothetical crystal to model the properties of a random alloy formed by atoms $A$ and $B$ on a (sub-) lattice. In a VCA crystal atoms $A$ and $B$ are replaced by a single kind of atoms $C$ whose properties are assumed as a linear average of those of $A$ and $B$. The virtual alloy made of pseudo-atoms $C$ has hence a crystal structure common to the crystals made of either $A$ or $B$ atoms with a linearly averaged crystal potential. The assumption strongly reduces computational complexity and leads to a great popularity of the approach. The VCA has been applied to semiconductor alloys within various schemes like the semiempirical pseudopotential method or the empirical tight-binding method.

A VCA crystal contains solely a single type of bonds and yields the linear relationship of lattice parameters in the alloy expressed by Vegard's rule (2.2a)–(2.2c). The approximation succeeded in calculating a number of problems like the fact of an optical bandgap bowing discussed in Sect. 3.1.4. It must be noted that properties depending on local differences in the potentials of individual atoms like charge redistribution or polarization are precluded in the VCA approach. Effects arising from such differences as atom-$A$-like and atom-$B$-like features, also referred to as chemical disorder, are not correctly described by the VCA approach.

## 2.2 Elastic Properties of Heterostructures

An epitaxial layer with a chemically different composition and potentially also a different structure compared to the substrate represents a heterostructure. If the interface does not contain structural defects, the layer—and to some minor extent also the substrate—are *strained*, because the lattice parameters of layer and substrate will generally differ due to differences in bond lengths and thermal expansion coefficients. The elastic properties of the heterostructure can, to a very good approximation, be determined using continuum mechanics, i.e., a macroscopic theory. To assess the action of the structural and thermal misfits, we first consider the macroscopic effect of stress on the deformation of solids in general. An introduction into this classical subject may be found in, e.g., Refs. [21, 22].

### 2.2.1 Strain in One and Two Dimensions

Stress leads to a deformation (strain) of a solid. For a *one-dimensional* problem the effect of strain on a dilatable string is illustrated in Fig. 2.9. A point at an arbitrary position $x$ is displaced by $u$. In *homogeneous* stretching $u$ is a *linear* function of $x$, and the section $\Delta x$ is strained to $\Delta x + \Delta u$. The *strain* of the section $\Delta x$ can now be defined as $e = du/dx$. It is a dimensionless quantity and small compared to 1.

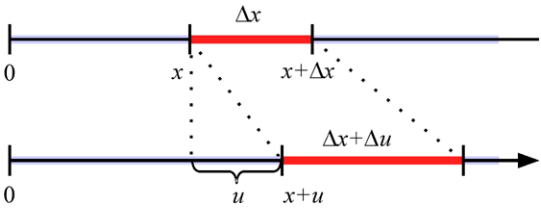


**Fig. 2.9** Deformation of a dilatable string in an unstrained (*top*) and strained state (*bottom*). The origin is assumed to be fixed

We now extend the problem to the *two-dimensional strain* of a plane sheet. Here, the strain is specified by the four quantities

$$e_{ij} = du_i/dx_j \quad \text{for } i, j = 1, 2. \tag{2.3}$$

The quantities $e_{ij}$ can be regarded as components of a second-rank tensor described by a $2 \times 2$ matrix. Without any distortion all components are expected to vanish. This is, however, not fulfilled for components defined in such a way; a simple rigid-body rotation leads to non-zero off-diagonal components. To meet the condition of zero components at zero distortion, the tensor is expressed as a sum of a symmetrical and an antisymmetrical tensor, yielding components $e_{ij} = \varepsilon_{ij} + \overline{\varepsilon_{ij}}$. Only the *symmetrical* part

$$\varepsilon_{ij} = \frac{1}{2}(e_{ij} + e_{ji}) = \varepsilon_{ji} \tag{2.4}$$

is defined as the strain (the antisymmetrical components are $\overline{\varepsilon_{ij}} = \frac{1}{2}(e_{ij} - e_{ji}) = -\overline{\varepsilon_{ji}}$). The two-dimensional strain tensor then reads

$$\boldsymbol{\varepsilon} = \begin{bmatrix} e_{11} & \frac{1}{2}(e_{12} + e_{21}) \\ \frac{1}{2}(e_{12} + e_{21}) & e_{22} \end{bmatrix}. \tag{2.5}$$

In absence of a rotation, the diagonal components $\varepsilon_{11}$ and $\varepsilon_{22}$ directly measure the extensions or compressions per length along the $x$- and $y$-axes, respectively. The off-diagonals $\varepsilon_{12} = \varepsilon_{21}$ measure the shear strain. The *anti*symmetrical tensor contains only the two off-diagonal elements $\frac{1}{2}(e_{12} - e_{21})$ and describes a pure solid-body rotation potentially connected to the deformation of the area.

The deformation of an area $(\Delta x_1, \Delta x_2)$ in the plane sheet is given by $(\Delta x_1 + \Delta u_1, \Delta x_2 + \Delta u_2)$ with the two displacement components

$$\Delta u_i = \frac{\partial u_i}{\partial x_1}\Delta x_1 + \frac{\partial u_i}{\partial x_2}\Delta x_2 = e_{i1}\Delta x_1 + e_{i2}\Delta x_2 \quad \text{for } i = 1, 2.$$

### 2.2.2 Three-Dimensional Strain

The description of *three-dimensional strain* is a generalization of the former cases. The three diagonal components $\varepsilon_{ii} = e_{ii}$ $(i = 1, 2, 3) = \varepsilon_{xx}, \varepsilon_{yy}, \varepsilon_{zz}$, are the tensile or compressive strains. They occur along the $x$, $y$, and $z$-axis, respectively, if no

rotation is connected to the deformation. The sum of the diagonal components yields the relative change of volume originating from the strain,

$$\frac{\Delta V}{V} = \sum_{i=1}^{3} \varepsilon_{ii}. \tag{2.6}$$

In the off-diagonal elements the quantities $e_{ij}$ describe rotations similar to the two-dimensional case. $e_{12}$ describes an anticlockwise rotation about the $z$-axis, $e_{21} = -e_{12}$. Similarly, $e_{13}$ and $e_{23}$ describe rotations about the $y$ and $x$-axes, respectively. The off-diagonal terms of $\boldsymbol{\varepsilon}$ are again symmetrized and represent shear strains,

$$\varepsilon_{ij} = \frac{1}{2}\left(\frac{\partial u_i}{\partial x_j} + \frac{\partial u_j}{\partial x_i}\right), \tag{2.7}$$

yielding the three-dimensional strain tensor

$$\boldsymbol{\varepsilon} = \begin{bmatrix} e_{11} & \frac{1}{2}(e_{12}+e_{21}) & \frac{1}{2}(e_{13}+e_{31}) \\ \frac{1}{2}(e_{12}+e_{21}) & e_{22} & \frac{1}{2}(e_{23}+e_{32}) \\ \frac{1}{2}(e_{13}+e_{31}) & \frac{1}{2}(e_{23}+e_{32}) & e_{33} \end{bmatrix}. \tag{2.8}$$

Since the strain tensor is symmetric, only 6 of the 9 components are independent. The 6 independent components are often written according the Voigt notation in form of a $6 \times 1$ matrix for short. This symbolic vector is formed by the index substitution $11 \to 1$, $22 \to 2$, $33 \to 3$, $23$ and $32 \to 4$, $31$ and $13 \to 5$, and $12$ and $21 \to 6$, yielding

$$\boldsymbol{\varepsilon} = \begin{bmatrix} \varepsilon_{11} & \varepsilon_{12} & \varepsilon_{13} \\ \varepsilon_{12} & \varepsilon_{22} & \varepsilon_{23} \\ \varepsilon_{13} & \varepsilon_{23} & \varepsilon_{33} \end{bmatrix} \to \boldsymbol{\varepsilon} = \begin{pmatrix} \varepsilon_1 \\ \varepsilon_2 \\ \varepsilon_3 \\ \varepsilon_4 \\ \varepsilon_5 \\ \varepsilon_6 \end{pmatrix}. \tag{2.9}$$

In the Voigt notation the shear components of the strain tensor are usually defined in terms of an *engineering convention* instead of the physical convention used above. The engineering quantities are $\varepsilon_{ij}^{\text{engin.}} = 2\varepsilon_{ij}$, $i \neq j$. This allows for writing Hooke's law in the simple notation with reduced indices (2.10). A $3 \times 3$ matrix composed of the off-diagonals $\varepsilon_{ij}^{\text{engin.}}$ and the diagonals $\varepsilon_{ii}$ of $\boldsymbol{\varepsilon}$ does, however, *not* form a tensor, because such array does not transform according the rules of a second-rank tensor [21]. This must be considered if the strain occurs not along the principal directions.

We briefly consider the three-dimensional *stress*, which gives rise to the strain treated above. Similar to the strain $\boldsymbol{\varepsilon}$ all stress components are combined in a symmetric second order stress tensor $\boldsymbol{\sigma}$, which often is likewise written in form of a vector. Any stress may be composed of three components: uniaxial stress, shear stress, and hydrostatic stress. Uniaxial tensile or compressive stresses $\sigma_{xx}$, $\sigma_{yy}$, and $\sigma_{zz}$, act along the axes $x$, $y$, and $z$, respectively. They are built by force pairs acting normal to the surfaces (see Fig. 2.10) and have the unit of a force per area, i.e.,

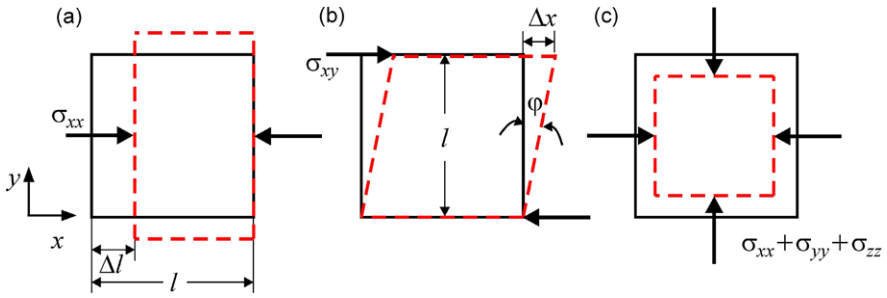


**Fig. 2.10** Deformation of a solid by (**a**) uniaxial stress, (**b**) shear stress, and (**c**) hydrostatic stress

N/m$^2$ or Pa. If the forces act tangentially, they create a shear stress and are labeled $\sigma_{xy}$, $\sigma_{yz}$, and $\sigma_{xz}$. The first and second index denote the axis of force direction and the normal of the surface where the force acts, respectively. In the Voigt notation the same index substitution is used as that applied for the strain, but no factor of 2 is put into the off-diagonal elements.

### *2.2.3 Hooke's Law*

If the strain is not too large, the interaction potential of the atoms in the solid is well described in the harmonic approximation, and we obtain a linear relationship between stress and resulting strain. For the analogous problem of a spring, Robert Hooke stated in the 17th century that the force exerted by a mass attached to a spring is *proportional* to the amount the spring is stretched. In the generalized Hooke's law the constant of proportionality in the one-dimensional case is replaced by the elasticity stiffness tensor $\mathbf{C}$. $\mathbf{C}$ is a fourth-order tensor comprising $3^4 = 81$ components $C_{ijkl}$. By considering all symmetries present in crystalline solids, the number of non-zero components is reduced to 36. $\mathbf{C}$ is usually written according Voigt's notation in form of a $6 \times 6$ matrix by putting $C_{ijkl} = C_{mn}$ ($i, j, k, l = 1, 2, 3$; $m, n = 1, \ldots, 6$). Using the Voigt notation for stress and strain defined in (2.9) and accordingly the $6 \times 6$ matrix representation for $\mathbf{C}$, Hooke's law reads

$$\begin{pmatrix} \sigma_1 \\ \sigma_2 \\ \sigma_3 \\ \sigma_4 \\ \sigma_5 \\ \sigma_6 \end{pmatrix} = \begin{pmatrix} C_{11} & C_{12} & C_{13} & C_{14} & C_{15} & C_{16} \\ C_{21} & C_{22} & C_{23} & C_{24} & C_{25} & C_{26} \\ C_{31} & C_{32} & C_{33} & C_{34} & C_{35} & C_{36} \\ C_{41} & C_{42} & C_{43} & C_{44} & C_{45} & C_{46} \\ C_{51} & C_{52} & C_{53} & C_{54} & C_{55} & C_{56} \\ C_{61} & C_{62} & C_{63} & C_{64} & C_{65} & C_{66} \end{pmatrix} \begin{pmatrix} \varepsilon_1 \\ \varepsilon_2 \\ \varepsilon_3 \\ \varepsilon_4^{\text{engin.}} \\ \varepsilon_5^{\text{engin.}} \\ \varepsilon_6^{\text{engin.}} \end{pmatrix}, \tag{2.10}$$

where $\varepsilon_i^{\text{engin.}}$ denotes shear components of the strain according the engineering convention. Equation (2.10) may be written $\boldsymbol{\sigma} = \mathbf{C}\boldsymbol{\varepsilon}$ for short. The inverse relation is given by the compliance matrix $\mathbf{S} = \mathbf{C}^{-1}$, yielding $\boldsymbol{\varepsilon} = \mathbf{S}\boldsymbol{\sigma}$. In Voigt's notation of $\mathbf{S}$

some factors appear, which are not necessary in $\mathbf{C}$ [21]: $S_{mn} = S_{ijkl}$ when $m$ and $n$ are 1, 2, or 3; $S_{mn} = 2S_{ijkl}$ for either $m$ or $n$ being 4, 5, or 6; $S_{mn} = 4S_{ijkl}$ when both $m$ and $n$ are 4, 5, or 6.

A particular stress component is given by

$$\sigma_i = \sum_{k=1}^{6} C_{ik}\varepsilon_k, \tag{2.11}$$

where $\varepsilon_k$ denotes the engineering quantities when $k > 3$. The components of the elasticity matrix $\mathbf{C}$ are called (second order) elastic stiffness constants. $\mathbf{C}$ is a symmetric matrix, which has at most 21 independent coefficients. The factor of 2 in $\varepsilon_k^{\text{engin.}}$ with respect to $\varepsilon_k$ had to be introduced in order to write Hooke's law in this simple form with reduced indices. If we write (2.11) in the initial full tensor notation

$$\sigma_{ij} = \sum_{k=1}^{3}\sum_{l=1}^{3} C_{ijkl}\varepsilon_{kl}, \tag{2.11a}$$

we obtain for the off-diagonals the summands $C_{ijkl}\varepsilon_{kl} + C_{ijlk}\varepsilon_{lk}$ $(k \neq l)$. In the shorter matrix notation (2.11) the corresponding summands $C_{mn}\varepsilon_n$ $(n = 4, 5, 6)$ only appear once. The missing factor of 2 is therefore put into the off-diagonal elements by introducing the engineering convention. The procedure has the disadvantage that it applies only for strain along the principal axes for the usually listed constants $C_{mn}$, e.g., along the [001] direction. For other orientations (2.11a) needs to be rotated to obtain a transformed elasticity tensor $C'_{ijkl}$ [23].

We return to the simplified $\mathbf{C}$ matrix of (2.10) with 21 independent coefficients. For crystal structures with high symmetry, many of these coefficients are 0. In addition, some coefficients are related to others. Any cubic crystal structure has only 3 independent elastic stiffness coefficients, namely $C_{11}$, $C_{12}$, and $C_{44}$. This strong reduction originates basically from the equivalence of the three cubic axes. Any hexagonal crystal structure has 5 independent coefficients. As an example, the matrix notations of the elasticity tensors of a cubic and a hexagonal structure are given by

$$\begin{aligned}
\mathbf{C}_{\text{cubic}} &= \begin{pmatrix} C_{11} & C_{12} & C_{12} & 0 & 0 & 0 \\ C_{12} & C_{11} & C_{12} & 0 & 0 & 0 \\ C_{12} & C_{12} & C_{11} & 0 & 0 & 0 \\ 0 & 0 & 0 & C_{44} & 0 & 0 \\ 0 & 0 & 0 & 0 & C_{44} & 0 \\ 0 & 0 & 0 & 0 & 0 & C_{44} \end{pmatrix}, \\
\mathbf{C}_{\text{hexagonal}} &= \begin{pmatrix} C_{11} & C_{12} & C_{13} & 0 & 0 & 0 \\ C_{12} & C_{11} & C_{13} & 0 & 0 & 0 \\ C_{13} & C_{13} & C_{33} & 0 & 0 & 0 \\ 0 & 0 & 0 & C_{44} & 0 & 0 \\ 0 & 0 & 0 & 0 & C_{44} & 0 \\ 0 & 0 & 0 & 0 & 0 & \frac{C_{11}-C_{12}}{2} \end{pmatrix}.
\end{aligned} \tag{2.12}$$

**Table 2.6** Elastic stiffness constants of some cubic and hexagonal solids at room temperature, given in units of $10^{10}$ Pa. Column 2 denotes structures as discussed in Sect. 2.1, values for carbon (C) refer to the diamond modification

| Material | Structure | $C_{11}$ | $C_{12}$ | $C_{13}$ | $C_{33}$ | $C_{44}$ |
|---|---|---|---|---|---|---|
| Au [24] | fcc | 19.0 | 16.1 | – | – | 4.2 |
| Al [25] | fcc | 10.9 | 6.3 | – | – | 2.8 |
| W [25] | bcc | 51.5 | 20.4 | – | – | 15.6 |
| Mg [24] | hcp | 5.9 | 2.6 | 2.1 | 6.2 | 1.6 |
| NaCl [24] | NaCl | 4.9 | 1.3 | – | – | 1.3 |
| CsCl [24] | CsCl | 3.7 | 0.9 | – | – | 0.8 |
| C [9] | D | 107.6 | 12.5 | – | – | 57.7 |
| Si [9] | D | 16.6 | 6.4 | – | – | 8.0 |
| ZnS [9] | ZB | 9.8 | 6.3 | – | – | 4.5 |
| ZnSe [9] | ZB | 9.0 | 5.3 | – | – | 4.0 |
| GaAs [9] | ZB | 11.9 | 5.4 | – | – | 6.0 |
| InAs [9] | ZB | 8.3 | 4.5 | – | – | 4.0 |
| GaN [26] | W | 39.0 | 14.5 | 10.6 | 39.8 | 10.5 |
| AlN [26] | W | 39.6 | 13.7 | 10.8 | 37.3 | 11.6 |
| InN [26] | W | 22.3 | 11.5 | 9.2 | 22.4 | 4.8 |
| ZnO [27] | W | 20.6 | 11.7 | 11.8 | 21.1 | 4.4 |

Values of $C_{mn}$ for some solids are listed according the engineering notation in Table 2.6.

For isotropic solids only 2 independent stiffness constants exist, describing the response on axial and shear stress. For such materials $\mathbf{C}$ is given by the cubic matrix in (2.12), putting $C_{44} = \frac{1}{2}(C_{11} - C_{12})$. The two independent elastic constants are called Lamé constants $\mu = G = C_{44}$ and $\lambda = C_{12}$. $G$ is the shear modulus. Often any other two constants are used, and a number of relations exist to express their dependences. If the elastic properties of isotropic solids are expressed in terms of components of the compliance matrix $\mathbf{S}$, the two independent components are $S_{11} = 1/E$ and $S_{12} = -\nu/E$; $S_{44} = S_{55} = S_{66}$ then equals $(2+2\nu)/E$. $E$ is Young's modulus (also referred to as elastic modulus) and represents the ratio stress/strain, and $\nu$ is Poisson's ratio considered below. The two quantities are related to the Lamé constants by

$$E = \frac{\mu(2\mu + 3\lambda)}{\mu + \lambda}, \qquad \nu = \frac{\lambda}{2(\mu + \lambda)}.$$

### *2.2.4 Poisson's Ratio*

Virtually all common materials undergo a transverse contraction when longitudinally stretched, and a transverse expansion when longitudinally compressed. The

quotient of such deformations is a material property termed *Poisson's ratio* $\nu$: $\nu = -(\text{transverse strain}/\text{longitudinal strain})$ for a uniaxial tensile stress applied in longitudinal direction. It is usually a positive quantity, though also negative Poisson's ratios were reported for novel foam structures called anti-rubber which have inter-atomic bonds realigning with deformation [28].

For isotropic solids comprising polycrystalline materials $\nu$ is given by the ratio of the two independent stiffness constants $C_{11}/C_{12}$. For non-isotropic materials like any crystalline solid $\nu$ depends on the stress direction. For cubic materials and stress along an axis of the unit cell, the ratio is $\nu = C_{12}/(C_{11} + C_{12})$, for other axes and symmetries the relation gets more bulky [29]. Values for Poisson's ratios range between 0.5 (incompressible medium) and $-1$ (perfect compressibility), values for ordinary materials are between 0.25 and 0.3 for common semiconductors, 0.45 for Pb, and 0.33 for Al.

### 2.2.5 Pseudomorphic Heterostructures

We consider a free standing crystalline structure consisting of two layers, which have a common interface as delineated in Fig. 2.11. We assume the layers to have the same cubic crystal structure, but—in absence of the common interface—different *unstrained* lattice constants $a$ and thicknesses $t$ labeled $a_1$, $t_1$, $a_2$, and $t_2$, respectively. If the difference in lattice constants is not too large (say, below 1 %), the layers may form an interface without structural defects and adopt a common in-plane lattice constant $a_\parallel$ parallel to the interface, with an intermediate value $a_1 > a_\parallel > a_2$. Since $a_\parallel$ is smaller than the relaxed (unstrained) lattice parameter $a_1$, layer 1 is compressively strained in lateral direction (i.e., parallel to the interface) by the contact to layer 2. Layer 1 consequently experiences a distortion also in the vertical direction to approximately maintain its bulk density. The vertical lattice constant $a_{1\perp}$ of the strained layer 1 is hence larger than the unstrained value $a_1$. Vice versa layer 1 exerts a laterally tensile stress on layer 2, leading likewise to a vertical strain $a_{2\perp} < a_2$. Such a heterostructure is called *pseudomorphic*, and the layers are designated *coherently* strained.

In the strained cubic heterostructure illustrated in Fig. 2.11, the strain in the two lateral directions, say $x$ and $y$, is equal, $\varepsilon_{xx} = \varepsilon_{yy} = \varepsilon_\parallel$. Such a biaxial strain results in a tetragonal distortion. Since the structure is assumed to be free-standing, no force is applied along the $z$-direction. The stress tensor component $\sigma_{zz}$ is thus always zero. Inserting the cubic elasticity tensor (2.12) into Hooke's law (2.10) and setting up (2.11) for $\sigma_{zz}$, we obtain a relation between the diagonal strain components and hence between $\varepsilon_\parallel$ and $\varepsilon_\perp$:

$$\begin{aligned} \sigma_{zz} &= 0 = C_{12}\varepsilon_{xx} + C_{12}\varepsilon_{yy} + C_{11}\varepsilon_{zz}, \\ \varepsilon_{zz} &= -\frac{C_{12}\varepsilon_{xx} + C_{12}\varepsilon_{yy}}{C_{11}} = -\frac{2C_{12}}{C_{11}}\varepsilon_{xx}, \\ \varepsilon_\perp &= -D_{001}\varepsilon_\parallel. \end{aligned} \tag{2.13}$$

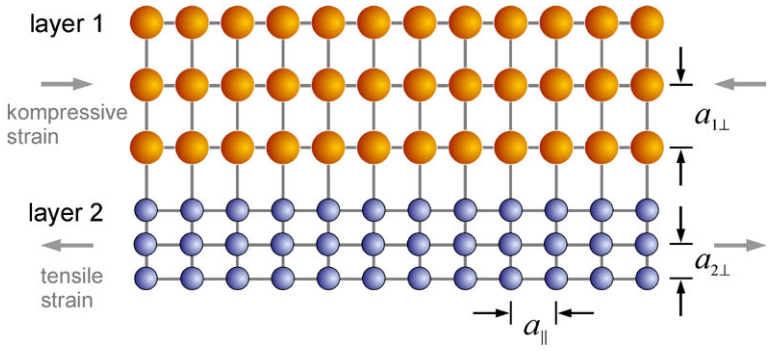


**Fig. 2.11** Schematic of a heterostructure consisting of two layers with a common interface. $a_{\parallel}$ is the common lateral lattice constant, $a_{1\perp}$ and $a_{2\perp}$ denote the vertical lattice constants of the strained layers 1 and 2

The distortion factor $D_{001}$ is given in (2.17) also for other orientations of the interface. Vertical strain $\varepsilon_{zz} = \varepsilon_{\perp}$ and lateral strain $\varepsilon_{\parallel}$ virtually always have opposite sign, since common stiffness constants $C_{ij}$ are positive quantities. The volume of the unit cell is usually not preserved during deformation: The effect of the counteracting strain perpendicular to the interface does not fully compensate the in-plane strain. In the case of a tetragonal distortion no in-plane shear strain occurs, the respective off-diagonal elements of the strain tensor are hence zero. According (2.6) the volume change is given by the trace of the strain tensor,

$$\Delta V/V = \varepsilon_{xx} + \varepsilon_{yy} + \varepsilon_{zz}. \tag{2.14}$$

The in-plane lattice constant $a_{\parallel}$ of the pseudomorphic heterostructure (Fig. 2.11) is given by a balance of the elastic strain minimizing the strain energy [30],

$$\begin{aligned} &a_{\parallel} G_1 t_1 + a_{\parallel} G_2 t_2 = a_1 G_1 t_1 + a_2 G_2 t_2, \\ &a_{\parallel} = \frac{a_1 G_1 t_1 + a_2 G_2 t_2}{G_1 t_1 + G_2 t_2}. \end{aligned} \tag{2.15}$$

$G$ denotes the shear modulus and depends on the crystal structure and the crystallographic orientation of the interface plane. $a$ and $t$ are the unstrained lattice parameter and the thickness of the respective layer. For a cubic structure, like e.g. zincblende, the shear moduli $G_i$ of layers 1 and 2 are given by

$$G_i = 2\big(C^i_{11} + 2C^i_{12}\big)(1 - D_i/2), \tag{2.16}$$

with the distortion factors $D$ of the respective orientations

$$\begin{aligned} D_{001} &= \frac{2C_{12}}{C_{11}}, \\ D_{110} &= \frac{C_{11} + 3C_{12} - 2C_{44}}{C_{11} + C_{12} + 2C_{44}}, \\ D_{111} &= \frac{2C_{11} + 4C_{12} - 4C_{44}}{C_{11} + 2C_{12} + 4C_{44}}. \end{aligned} \tag{2.17}$$

The factors $D$ represent the ratios $-\varepsilon_{i\perp}/\varepsilon_{i\parallel}$ for the respective orientations of the interface, i.e., the ratios of normal and lateral strains for a biaxial deformation. The assumption of a *constant* ratio in strained layers is based on the assumed validity of Hooke's law (2.10).

It should be noted that distortions along ⟨110⟩ or ⟨111⟩ reduce the crystal symmetry in a way that the atomic positions in the unit cell are not uniquely determined by strain. The shifts originate from changes in the bond strengths: Strain along [111] in zincblende or diamond structures, e.g., makes the [111] bond inequivalent to the other $[\bar{1}\bar{1}1]$, $[\bar{1}1\bar{1}]$, and $[1\bar{1}\bar{1}]$ bonds, leading to a static displacement of the sublattices. Introducing an internal strain parameter $\xi$ [31], the [111] bond is elongated by $(1-\xi)\varepsilon_{44}a\sqrt{3}/4$. $\xi = 0$ and 1 correspond to perfectly strained positions and rigid bond lengths, respectively [32].

Using the constants $D$ also the vertical change of the unit cell in layer $i$ can be calculated,

$$a_{i\perp} = a_i\big(1 - D_i(a_\parallel/a_i) - 1\big). \tag{2.18}$$

It should be noted that $a_\parallel$ and $a_\perp$ represent the actual lattice constants only for the (001) orientation of the interface plane. For other orientations these quantities express the change of the unit cell dimensions under strain. The lateral and vertical strains of layer $i$ are related to the respective strained lattice parameters by

$$\varepsilon_{i\parallel} = \frac{a_\parallel}{a_i} - 1, \tag{2.19a}$$

$$\varepsilon_{i\perp} = \frac{a_{i\perp}}{a_i} - 1, \tag{2.19b}$$

where the quantity $a_i$ denotes the unstrained lattice constant of layer $i$. In a corresponding *hexagonal* structure with a basal-plane interface, the lattice constants $a$ and $c$ of the considered layer are inserted in $a_\parallel$ and $a_\perp$ of (2.19a), (2.19b), respectively. Using analogous insertions made to obtain (2.13), the relation reads for hexagonal structures

$$\varepsilon_\perp = -\frac{2C_{13}}{C_{33}}\varepsilon_\parallel. \tag{2.19c}$$

### Pseudomorphic Layer

A thin epitaxial layer grown on a much thicker substrate is described by considering $t_1/t_2 \to 0$ in (2.15). We see that then $a_\parallel = a_2$. The unstrained lattice constant $a_\mathrm{L}$ of the layer ($a_1$ in (2.15)) laterally adopts the lattice constant of the substrate $a_\mathrm{S}$ ($a_2$ in (2.15)) at epitaxial growth and can be varied using different substrates. The substrate remains virtually unstrained due to its large thickness, and the *misfit* (or, *lattice mismatch*) $f$ between the two crystals is usually expressed by

$$f = \frac{a_\mathrm{S} - a_\mathrm{L}}{a_\mathrm{L}}. \tag{2.20a}$$

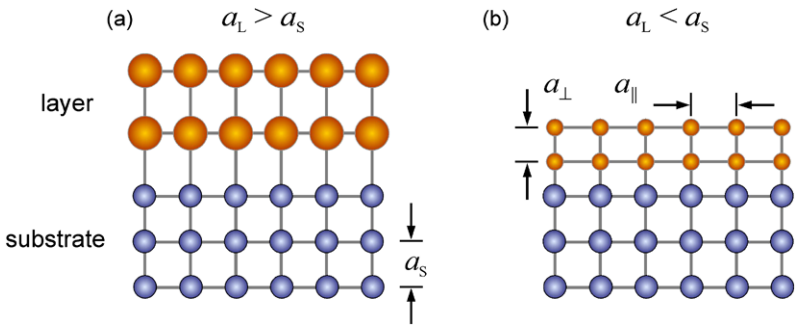


**Fig. 2.12** Biaxially strained layers (*yellow atoms*) on substrates (*blue atoms*) with another lattice constant $a_S$. In (**a**) the unstrained lattice constant of the layer $a_L$ is larger than $a_S$, and the layer is compressively strained in lateral direction; in (**b**) the layer is tensely strained

It must be noted that also other definitions for the lattice mismatch are used in literature, particularly the relations

$$f_{\text{alternative1}} = \frac{a_L - a_S}{a_S} \tag{2.20b}$$

and

$$f_{\text{alternative2}} = \frac{a_L - a_S}{a_L}. \tag{2.20c}$$

Note the change in sign of the alternative relations with respect to (2.20a).

If we compare (2.20a) with (2.19a), we notice that the misfit is equal to the lateral strain of the epitaxial layer: $f = \varepsilon_\parallel$. This applies for *coherent* growth, i.e., growth with an *elastic* relaxation of the strain without formation of defects. Such a layer is called *pseudomorphic*. $f$ may have either sign as illustrated in Fig. 2.12 by comparing a compressively and a tensely strained layer.

### 2.2.6 Critical Layer Thickness

A strained solid like the layers considered in Fig. 2.12 contains a strain energy per volume $E/V$. The differential work of deformation for a small increment of strain is given by

$$\frac{1}{V} dE = \sum_{i=1}^{6} \sigma_i d\varepsilon_i. \tag{2.21}$$

Integration of (2.21) using (2.11) yields the elastic energy density of a strained solid,

$$\frac{E}{V} = \frac{1}{2} \sum_{i=1}^{6} \sum_{k=1}^{6} C_{ik} \varepsilon_i \varepsilon_k. \tag{2.22}$$

For a cubic material (2.22) reads

$$\frac{E}{V} = \frac{1}{2}\big(C_{11}\big(\varepsilon_{xx}^2 + \varepsilon_{yy}^2 + \varepsilon_{zz}^2\big) + 2C_{12}(\varepsilon_{yy}\varepsilon_{zz} + \varepsilon_{zz}\varepsilon_{xx} + \varepsilon_{xx}\varepsilon_{yy}) + C_{44}\big(\varepsilon_{yz}^2 + \varepsilon_{zx}^2 + \varepsilon_{xy}^2\big)\big), \tag{2.23}$$

with the three respective terms of hydrostatic, uniaxial, and shear strains. We see that the homogeneous energy density increases quadratically with strain in the harmonic approximation of Hooke's law. If a cubic, biaxially strained pseudomorphic layer is considered, which is allowed to elastically relax according Poisson's ratio, the elastic energy density is given by [33]

$$\frac{E}{At_\mathrm{L}} = 2G\varepsilon_\parallel^2 \frac{1+\nu}{1-\nu}, \tag{2.24}$$

$A$, $t_\mathrm{L}$, $G$, $\varepsilon_\parallel$, and $\nu$ being the area, the *strained* layer thickness, the shear modulus, the in-plane strain parallel to the interface, and Poisson's ratio of the layer, respectively. According (2.24) the areal density of the elastic strain energy in the layer $E/A$ increases linearly with the layer thickness $t_\mathrm{L}$ and quadratically with $\varepsilon_\parallel$, i.e., the misfit $f$ for a pseudomorphic layer. Areal strain energy is hence accumulated as the layer thickness increases. At some critical thickness $t_\mathrm{c}$ this energy is larger than the energy required to form structural defects which *plastically* relax the strain. Such defects are dislocations, the nature of which is studied in more detail in Sect. 2.3. The plastic relaxation reduces the overall strain, but at the same time the dislocation energy increases from zero to a value determined by the particular dislocation.

Quite a few models were developed to calculate the critical thickness $t_\mathrm{c}$ of a pseudomorphic epitaxial layer depending on the misfit $f$ with respect to the substrate. They all consider some energy balance or, equivalently, a balance of forces or stresses, by comparing the amount of homogeneous strain energy relaxed by the introduction of a particular defect with the energy cost associated with the formation of this defect. Basic early work by Frank, Van der Merve, and co-workers described the plastic relaxation by an array of parallel, equally spaced misfit dislocations (Sect. 2.3.5) [34–36], or by a two-dimensional grid of such dislocations at the interface [37–40]. A more simple approach for predicting the critical thickness was developed by Matthews and Blakeslee [41, 42]. The model considers the force on a threading dislocation penetrating from the substrate through the epitaxial layer, which creates a dislocation at the interface and gives rise to a comparable scenario as considered by Van der Merve and co-workers.

The general picture is outlined below, assuming a structural lattice defect that can relax the strain of the layer by a plastic deformation. Such a dislocation formed by, e.g., the insertion of an extra lattice plane in the layer is depicted in Fig. 2.13. The end of the additional half-plane near the interface of the heterostructure builds a dislocation line with a locally highly strained region. The formation of this dislocation requires a formation energy $E_\mathrm{D}$. This energy cost is balanced by the elastic relief of homogeneous strain energy in the layer lattice outside the core region of the dislocation line.

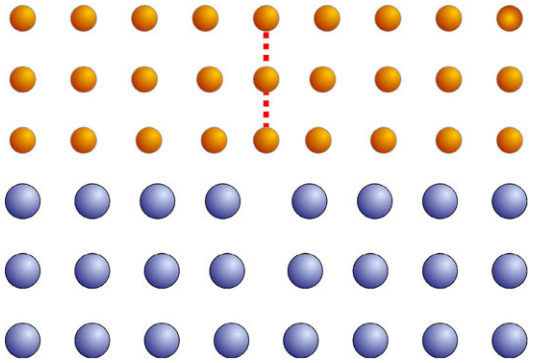

**Fig. 2.13** Scheme of a dislocation introduced into a layer, that plastically relaxes the strain. Layer and substrate are represented by *yellow* and *blue atoms*, respectively. The inserted extra plane is shown in cross section and represented by the *dashed red line*

Whether or not plastic relaxation occurs in the epitaxial layer depends on the minimum of the elastic energy $E_\mathrm{I}$ at the interface. $E_\mathrm{I}$ is given by the sum of homogeneous strain energy in the layer and dislocation energy. The dislocation energy $E_\mathrm{D}$ depends on the particular geometry and the amount of plastic relaxation as expressed by the Burgers vector (Sect. 2.3). The remaining mismatch $f$ of the (partially) relaxed layer refers to an *average* lattice constant of the layer. In the presence of dislocations $f$ is less than the natural misfit, which is defined by the *unstrained* lattice constants in (2.20a)–(2.20c) and denoted $f_0$ in the following. To a good approximation $f$ is given by the sum of $f_0$ and the lateral strain

$$\varepsilon = \frac{a_\mathrm{L} - a_{\mathrm{L},0}}{a_{\mathrm{L},0}}$$

which normally has opposite sign; $a_{\mathrm{L},0}$ denotes the unstrained lattice parameter of the layer. The dependence of $E_\mathrm{I}$ from $\varepsilon$ is then given by

$$\begin{aligned} E_\mathrm{I}/A &= E_\mathrm{H}/A + E_\mathrm{D}/A, \\ E_\mathrm{H}/A &\propto t_\mathrm{L}\varepsilon^2, \\ E_\mathrm{D}/A &\propto \varepsilon + f_0. \end{aligned} \tag{2.25}$$

The relation for the interface energy given by (2.25) is illustrated in Fig. 2.14 for a $GaAs_{0.9}P_{0.1}$ layer on GaAs substrate with a natural misfit $f_0 = -0.36$ % and a thickness below, just at, and above the critical value for plastic relaxation [39]. The homogeneous strain-energy density disappears at zero strain and increases quadratically with $\varepsilon$ (black curves), while the dislocation energy density gets zero at $f = \varepsilon + f_0 = 0$ (light gray curves). In any case the energy density at the interface $E_\mathrm{I}/A$ (gray curves) tends to attain a minimum. The criterion for the critical thickness $t_\mathrm{c}$ is [43]

$$\partial(E_\mathrm{I}/A)/\partial\big(|\varepsilon|\big) = 0, \tag{2.26}$$

evaluated at $|\varepsilon| = |f_0|$. For $t_\mathrm{L} > t_\mathrm{c}$ the homogeneous strain of the layer gets larger than the natural misfit $|f_0|$, and dislocations introduce a strain of opposite sign, thereby reducing $|\varepsilon|$ and hence $E_\mathrm{I}/A$. The critical thickness is usually inverse to the natural misfit in a wide range, cf. Fig. 2.15.

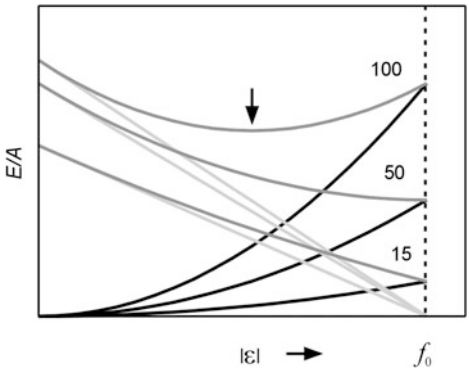


**Fig. 2.14** Areal energy densities occurring at a biaxially strained layer with a thickness of 15, 50 and 100 times the substrate lattice constant. $\varepsilon$ denotes lateral strain, $f_0 = -0.36$ % is the assumed natural misfit. The *black*, *gray*, and *light gray curves* are homogeneous strain, strain at the interface, and dislocation energy, respectively. The *arrow* denotes an energy minimum of a thick layer attained by plastic strain relaxation

For the evaluation of the critical thickness in a given heterostructure the geometry of the strain-relaxing dislocations must be specified. We consider the example of a semiconductor layer with diamond (or zincblende) structure and accommodating 60° dislocations, which are most prominent in such solids and are treated in detail in Sect. 2.3. We assume a biaxially strained layer with a given Poisson ratio $\nu$. Taking the dislocation energy $E_\mathrm{D}$ from (2.36), the energy at the interface $E_\mathrm{I}$ (2.25) reads

$$\begin{aligned} E_\mathrm{I}/A &= E_\mathrm{H}/A + E_\mathrm{D}/A \\ &= 2Gt\varepsilon^2 \frac{1+\nu}{1-\nu} + bG \frac{|\varepsilon + f_0|(1-\nu\cos^2\alpha)}{2\pi(1-\nu)\sin\alpha\cos\beta} \ln\left(\frac{\rho R}{b}\right). \end{aligned} \tag{2.27}$$

The strain denotes the in-plane components $\varepsilon = \varepsilon_{xx} = \varepsilon_{yy} = \varepsilon_\parallel$, and the geometry of the dislocation is expressed in terms of the absolute value $b$ of its Burgers vector $\mathbf{b}$, the angle $\alpha$ between the Burgers vector and the dislocation line vector, and the angle $\beta$ between the glide plane of the dislocation and the interface. $R$ is the cut-off radius defining the boundary of the strain field produced by the dislocation core, and the factor $\rho$ accounts for the strain energy of the dislocation core and is of the order of unity. We now apply condition (2.26) to the interface energy (2.27) and put $R = t_\mathrm{c}$, because the first dislocations are expected to appear if the cut-off radius is equal to the critical layer thickness. This gives the relation [39]

$$t_\mathrm{c} = b \frac{(1-\nu\cos^2\alpha)}{8\pi|f_0|(1+\nu)\sin\alpha\cos\beta} \ln\left(\frac{\rho t_\mathrm{c}}{b}\right). \tag{2.28}$$

The critical thickness $t_\mathrm{c}$ can be calculated numerically from this transcendent equation for a given natural misfit $f_0$. If the geometrical parameters of the 60° dislocation are inserted for the considered geometry, $b = a/2 \times [101] = a/\sqrt{2}$, $\alpha = 60°$, $\beta = 54.7°$, and assuming $\rho = 4$ for the dislocations and $\nu = 0.25$ for layer, we obtain

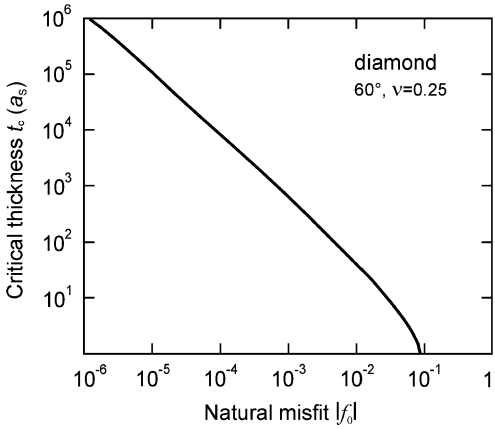


**Fig. 2.15** Critical thickness of a biaxially strained layer with diamond or zincblende structure in units of the substrate lattice constant $a_s$ for the introduction of accommodating 60° dislocations. From [39]

the dependence of $t_c$ shown in Fig. 2.15 [39]. The geometry of the 60° dislocation in zincblende crystals is depicted in Fig. 2.24b.

The dependence given in Fig. 2.15 follows approximately the relation $t_c \sim 1/|f_0|$. It should be noted that the actual degree of plastic relaxation does not solely depend on the misfit, but also on the growth procedure: Kinetic barriers for the generation and movements of misfit dislocations may lead to significantly larger values of the critical thickness than expected from equilibrium calculations. For metal layers, the experimentally determined values agree reasonably well with the predictions by equilibrium theory. For semiconductor layers, however, much larger values were observed. Equilibrium considerations are though useful to provide a reasonable measure for the lower limit of the critical layer thickness.

### *2.2.7 Approaches to Extend the Critical Thickness*

Epitaxy of heterostructures free of dislocations (at least within the diffusion length of charge carriers) is of particular importance for electronic and optoelectronic applications. Dislocations introduce local inhomogeneities, giving rise to a short lifetime and non-radiative recombination of charge carriers in semiconductors. Furthermore, piezoelectric effects associated with local strains change electronic properties. Dopants may precipitate at dislocations or strongly change diffusion characteristics. Fast degradation of devices often is connected to the action of dislocations. In device fabrication the reduction of the dislocation density in the active region below a level usually defined by the diffusion length of charge carriers is therefore an important issue. Typical values in semiconductor industry are in the range below $10^2$ cm$^{-2}$ for Si and $10^2$ to $10^3$ cm$^{-2}$ for III–V arsenides. Nitride semiconductors have much higher values in the range $10^4$ to $10^6$ cm$^{-2}$ for lasers and $10^7$ to $10^9$ cm$^{-2}$ for LEDs and electronic devices.

A number of concepts is applied to extend the critical thickness beyond the limit given by the natural misfit. In many cases *alloying* of the layer materials by mixing crystals of different lattice constants is used to closely match the substrate lattice constant. The lattice constants of alloys are generally found to vary linearly with composition, a relation expressed by Vegard's rule (Sect. 2.1.10). Since simultaneously the bandgap of the alloy varies, this may require mixing of more than two components with counteracting effects on bandgap and lattice constant (Sect. 3.1.4). Growth of such ternaries or quaternaries sometimes encounters thermodynamic limits, stimulating the search for alternatives.

**Buffer Layer**

A widely applied method to reduce the dislocation density of lattice-mismatched heterostructures is the introduction of a *buffer* between the epitaxial structure and the substrate [44]. Such layers or layer stacks confine misfit dislocations in a region below the active part and should in particular suppress the *penetration* of dislocation lines, i.e., the *threading dislocations*. A simple approach for a buffer is a *uniform buffer layer* (thick, μm range) with a high defect density near the interface to the substrate. The density of threading dislocations in a mismatched layer is usually found to decrease inverse to its thickness due to reactions of dislocations with opposite sign. Such buffer layers are referred to as *metamorphic*. They are to a large extend plastically relaxed and their lattice parameter approaches the unstrained value. Due to the thermal mismatch with respect to the substrate there will always remain some strain below growth temperature. A thick uniform buffer layer is also called *virtual substrate*.

The approach of a uniform buffer grown at low temperature is widely applied in nitride growth on sapphire [45, 46]. This systems is strongly structurally and thermally mismatched, giving rise to peeling off and cracking of epitaxial GaN layers grown without buffer. The basic idea is the deposition of a nitride layer with poor crystallinity at a low temperature where adatom mobility is low, and a subsequent crystallization by an annealing step. The interface to the substrate then contains numerous defects making the buffer compliant to accommodate misfits, while the surface consists of well oriented crystallites which can coalesce during overgrowth.

It should be noted that the epitaxial layer may have a different crystallographic orientation or a different crystal structure than the substrate. A prominent example is the prevalent growth of wurtzite (hexagonal) GaN on basal plane corundum (trigonal) $\alpha$-sapphire $Al_2O_3$. The [00.1] directions (or (00.1) planes, respectively) of GaN and $Al_2O_3$ coincide, but the [10.0] direction of GaN is parallel to the $[1\bar{1}.0]$ direction of the $Al_2O_3$ substrate [47, 48]. This corresponds to a rotation of the epitaxial unit cell by 30° around the [00.1] *c*-axis as compared to that of the substrate. *General matching conditions* for any pair of crystal lattices and any orientation may be found by considering interface translational symmetry [49]. The two lattices match if the two two-dimensional lattices, formed by the crystal translations of the paired

lattices parallel to the common interface, have a common superlattice. Such geometrical lattice match may induce epitaxial growth, but interface chemistry will always play a major role.

A drawback of the uniform relaxed buffer layer is the large thickness required to obtain a threading-dislocation density suitable for device-grade material of the epitaxial structure grown on top. Another approach is the *graded buffer* consisting of a continuously (or stepwise) change of the lattice constant by alloying with consecutive changing alloy parameters. Usually a *linear* grading of the composition—and consequently also of the lattice mismatch—is applied. The dislocation density at the surface of a graded buffer is expected to be inverse to the concentration gradient and also to the applied growth rate, if the gliding process of dislocations is not significantly impeded. Though such condition usually does not apply, strain relaxation in graded buffers was found to be more efficient than in uniform buffer layers.

A more sophisticated approach is the so-called dislocation filtering using a *strained-layer superlattice*. Multilayer structures with either alternating strain or alternating elastic stiffness were employed. Strains in the superlattice may cause bending of dislocation lines, leading to a meandering in alternating strain fields. Bending is also promoted when a dislocation line enters an elastically softer layer. The bending of dislocation lines increases the probability for defect reactions and favors annihilation. The thickness of the individual layers in the superlattice must be below the critical value for that particular layer, because the layers should induce a bending of dislocation lines without introducing new dislocations.

**Epitaxial Lateral Overgrowth**

A conceptual different approach is *epitaxial lateral overgrowth* (ELO or ELOG) [50]. The technique can be employed if the growth rate in lateral direction, i.e., parallel to the surface, is much larger than the vertical growth rate by choosing suitable growth parameters. Moreover, conditions for *selective* epitaxy must exist, where deposition occurs on the layer to be grown, but not on the material of a stable polycrystalline mask (made from, e.g., $SiO_2$), which covers a part of the substrate. In the ELO process the substrate is first covered with a mask layer which contains windows. In subsequent epitaxy, growth is controlled to occur only in the windows. When the layer thickness exceeds that of the mask, the mask is laterally overgrown. Since defects from the interface between substrate and layer cannot penetrate through the mask, the overgrowth region has a very low defect density. Using overgrowth of striped oxide masks, a smooth continuous layer with a linear array of low-defect areas may be achieved.

The ELO technique was applied in early work to chemical-vapor deposition and liquid-phase epitaxy of various semiconductors like, e.g., the conventional III–V compounds GaAs [50, 51] and GaP [52]. Later is was employed particularly in the epitaxy of GaN [53, 54].

**Compliant Substrate**

Concepts discussed so far use thick substrates which define the lateral lattice constant of the heterostructure in pseudomorphic growth. Considering (2.15), the critical layer thickness can be largely extended by using a thin and therefore *compliant substrate* [55–57]. The strain is then distributed between epilayer and substrate. For a sufficiently thin, free-standing substrate the epitaxial layer can virtually be arbitrarily thick.

Compliant substrates were implemented using various approaches. The compliant substrate is generally composed of a thin compliant layer, which is mechanically decoupled from a thicker substrate required for handling. On a small area thin free-standing membranes with a support at the side were realized. Approaches for larger area use various methods for bonding the thin layer to the mechanically stable support, in particular oxide bonding, borsilicate-glass-bonding, and twist-bonding. Reviews on this topic are given in [58, 59].

### *2.2.8 Partially Relaxed Layers and Thermal Mismatch*

The increase of elastic strain energy in a lattice-mismatched epitaxial layer up to a critical thickness $t_c$ was pointed out in Sect. 2.2.6. If the layer thickness exceeds $t_c$ misfit dislocations are formed in the layer and the strain is partially or, in sufficiently thick layers, fully relieved. We consider a cubic crystal. Usually strain relief of a biaxially strained and partially relaxed layer is symmetric and the two independent lateral lattice constants remain equal. The relief of strain may then be described by a strain parameter $\gamma$,

$$\gamma = 1 - \frac{a_{\parallel} - a_S}{a_L - a_S}, \tag{2.29}$$

$a_S$ and $a_L$ being the unstrained (natural) lattice constants of substrate and layer, respectively, and $a_{\parallel}$ the lattice constant of the layer in its strained state parallel to the interface. The fully strained pseudomorpic layer then corresponds to $\gamma = 1$ ($a_{\parallel} = a_S$), and $\gamma = 0$ to the fully relaxed layer ($a_{\parallel} = a_L$). Usually partial strain

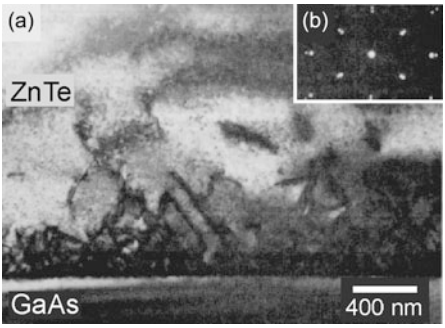


**Fig. 2.16** Transmission electron micrograph of a 1.8 µm thick ZnTe layer grown on (001)-oriented GaAs, imaged along the [110] direction. *Inset*: Diffraction pattern from the ZnTe/GaAs interface region. Reproduced with permission from [60], © 1993 Elsevier

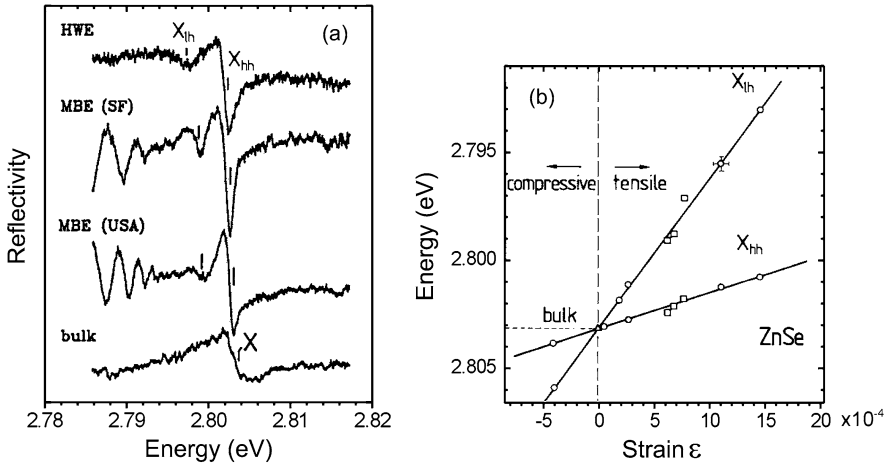


**Fig. 2.17** (**a**) Reflectivity spectra of free excitons in ZnSe/GaAs epitaxial layers which were grown at different temperatures. The lowest spectrum refers to a ZnSe bulk crystal. From [62]. (**b**) Energies of free light-hole ($X_{lh}$) and heavy-hole ($X_{hh}$) excitons in differently prepared ZnSe samples on GaAs substrate (*squares*) and ZnSe layers released from the substrate (*circles*). The triangle at the crossing point marks the exciton energy measured with a bulk crystal. Reproduced with permission from [61], © 1992 Elsevier

relief leads to a graded strain profile, i.e., $\gamma$ is not constant throughout the layer. An example is given in Fig. 2.16. The image shows a strongly mismatched zincblende ZnTe layer ($a_L = 6.123$ Å at $T_{growth} = 350$ °C) grown on GaAs substrate ($a_S = 5.665$ Å at 350 °C, $f = -7.5$ %) [60]. Dark lines indicate dislocation lines which form a dense network extending approximately 300 nm from the interface. Most of them are inclined by about 55° to the interface, equal to the angle of the intersection line of {111} planes with the (110) image plane. The angle indicates the occurrence of 60° dislocations (Sect. 2.3.4). The density of dislocations decreases as the ZnTe layer thickness grows, leading to regions with much lower defect density above 600 nm. The inset in Fig. 2.16 shows a diffraction pattern from the interface region, consisting of the superimposed response from the two zincblende crystals GaAs (outer points of each reflection due to a smaller lattice constant) and ZnTe. The pattern proves the epitaxial relation of layer and substrate.

The decreasing defect density for increased layer thickness is accompanied by a progressive strain relief ($\gamma \to 0$) and consequently by a gradual approach of the layer lattice constants $a_\parallel$ and $a_\perp$ toward the unstrained value $a_L$.

It must be noted that the unstrained lattice constant varies as the temperature is changed (e.g., from growth temperature to room temperature, Sect. 2.1.7), and that different materials (e.g., substrate and layer) have different thermal expansion coefficients.

An example of different built-in strains in ZnSe epilayers grown at different temperatures on GaAs is given in Fig. 2.17. The lattice mismatch (2.20a) at room temperature is $f = -0.27$ %, inducing laterally a biaxial compressive strain in the layer.

The studied ZnSe layers were thicker than the critical thickness $t_c$ ($\cong$150 nm) considered in Sect. 2.2.6 and were thus partially relaxed. Since the thermal expansion coefficient of GaAs is substantially smaller than that of ZnSe ($\sim 5.7 \times 10^{-6}$ K$^{-1}$ compared to $\sim 7 \times 10^{-6}$ K$^{-1}$ at RT, respectively), the ZnSe lattice contracts more pronounced when the heterostructure is cooled from growth temperature to the applied measurement temperature. The strain may be evaluated from the splitting of the valence band, reflected in the splitting of the free exciton (Sect. 3.1.2). The measurement of the free-exciton states in Fig. 2.17a shows that different strain states exist in samples which were prepared at different growth temperatures between 320 °C (molecular beam epitaxy) and 450 °C (hot wall epitaxy) [61, 62]. The exciton reflection-loops progressively split and shift to lower energy as the growth temperature is increased, indicating increasing *tensile* strain. The strain state was calculated from the difference of thermal expansion coefficients times the difference between growth and measurement temperature. The measurement of the near-surface strain state Fig. 2.17b derived from reflectivity spectra recorded at 1.6 K reveals a large range of values including also negative strain, i.e., still compressive in-plane strain of the ZnSe layer at 1.6 K. The crossing point agrees well with the energy of the unsplit free exciton of a ZnSe bulk crystal.

## 2.3 Dislocations

A crystalline defect is any region where the microscopic arrangement of atoms differs from that of a perfect crystal. Defects are classified into point defects, line defects, and surface defects, depending on whether the imperfect region is bounded in three, two or one dimensions, respectively. There is a very large variety of defects in solids, and for many of such imperfections their presence is a general thermal equilibrium phenomenon. We will focus on only two important kinds of defects, namely dislocations and substitutional impurities. The latter are point defects, which particularly govern electronic and optical properties of semiconductors and are studied in Chap. 6. In the following some basic properties of dislocations are outlined. More details are found in, e.g., Refs. [63, 64]. Examples are particularly considered for the fcc and hcp structures and their related important zincblende and wurtzite structures.

Dislocations are line defects which are present in virtually any real crystal. Dislocation densities in actual crystals range typically from $10^2$ cm$^{-2}$ in good semiconductors to $10^9$ cm$^{-2}$ in metals or highly defective semiconductors. The vector along

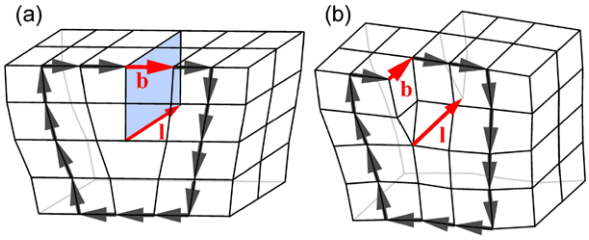


**Fig. 2.18** (**a**) Edge dislocation and (**b**) screw dislocation. **b** and **l** denote the Burgers vector and the dislocation-line vector, respectively

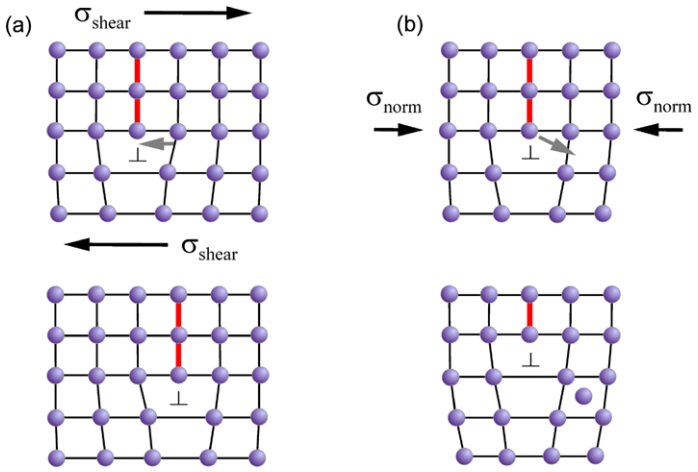


**Fig. 2.19** Edge dislocation performing (**a**) a gliding process and (**b**) a climbing process. $\sigma_{\text{shear}}$ and $\sigma_{\text{norm}}$ indicate shear and normal stresses acting on the solid

the dislocation line, i.e., along the core of the dislocation, is called *line vector* **l**. A dislocation is characterized by **l** and the *Burgers vector* **b**. **b** is the dislocation-displacement vector and determined by a closed path around the dislocation core, the burgers circuit. The procedure to find **b** is illustrated in Fig. 2.18. The Burgers vector completes the path around the dislocation line with respect to a similar path within a perfect reference crystal. According the *right-hand screw convention*, the Burgers circuit is formed *clockwise* around the dislocation line, when looking in the positive sense of the line vector (in Fig. 2.18 **l** points into the plane of projection; in many structures an arbitrariness in the sense of **l** cannot be avoided). If the path incloses more than one dislocation, the resulting Burgers vector is given by the sum of the Burgers vectors of all single dislocations.

### *2.3.1 Edge and Screw Dislocations*

There are two basic types of dislocations, edge dislocations and screw dislocations. In an *edge dislocation* **b** is perpendicular to **l**. Such dislocation may be formed by the insertion of an extra half-plane spanned by **l** and $\mathbf{b} \times \mathbf{l}$, see Fig. 2.18a. In a *screw dislocation* **b** is parallel to **l**. This kind of dislocation is built by a shift of one part of the solid by an amount **b** as shown in Fig. 2.18b. Most dislocations occurring in solids are of mixed character with an edge component and a screw component. They are generally denoted by specifying the angle between **b** and **l**. Pure edge dislocations obey $\mathbf{b} \cdot \mathbf{l} = 0$, for pure screw dislocations $\mathbf{b} \cdot \mathbf{l} = b$ (for a right-handed screw, $-b$ otherwise). The Burgers vector along a dislocation line is constant, if the dislocation line is a straight line. Consequently the type of dislocation does not change in this case, but it changes if the dislocation line bends.

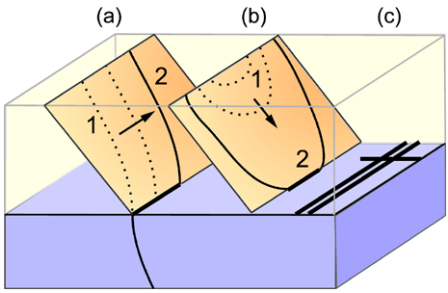


**Fig. 2.20** Generation of a misfit dislocation network (**c**) at the interface between layer (*upper part*) and substrate (*lower part*, *blue*) from (**a**) a preexisting threading dislocation of the substrate and (**b**) from the nucleation of a dislocation half loop

Geometrical considerations show that a dislocation line can neither begin nor end within the crystalline solid [63]. A dislocation line therefore either forms a closed loop within the crystal, or it begins and ends at an interface or grain boundary of the crystal. If a force acts on the crystal, the dislocation line can move along specific slip planes through the crystal. Since the position of individual atoms changes only a fraction of the lattice constant during such movements, the required energy is quite small. The presence of dislocations thereby accounts for the fact that real solids withstand much smaller shear strengths against slipping of atomic planes than perfect crystals would do (factor $\sim 10^{-4}$).

Two kinds of dislocation movements are distinguished: Glide and climb processes. They are illustrated in Fig. 2.19. During *gliding* the dislocation moves by turning crystal planes as illustrated in Fig. 2.19a. Such shear displacement is termed glide when it is produced by a single dislocation, and slip when it is produced by a number of dislocations. The total number of atoms and lattice sites is conserved in such motions. For pure edge dislocations the process can only occur along slip planes which contain both the Burgers vector and the dislocation line. Pure screw dislocations can glide along any plane, since **l** and **b** are parallel. *Climbing* occurs within a plane, which contains the dislocation line but is perpendicular to the Burgers vector. Climbing is accompanied by a material transport, i.e., emission or absorption of interstitials or vacancies (point defects), as indicated in Fig. 2.19b. The symbol to represent a general dislocation is $\perp$. For an edge dislocation the upwards pointing arm of the inverted T points to the direction of the added or removed material.

### *2.3.2 Dislocation Network*

Section 2.2 outlined how a strained epitaxial layer of a pseudomorphic heterostructure may relax strain energy by introducing a misfit dislocation. The process of this plastic strain relaxation is now considered in more detail. To reduce the tensile or compressive strain in an overcritical epilayer with thickness $t > t_c$, the introduction or omission of a lattice plane is favorable, respectively, creating a dislocation line at the layer/substrate interface. Since the dislocation line can neither begin nor end within a crystal, its ends must lie at the surface. There exist two possibilities which

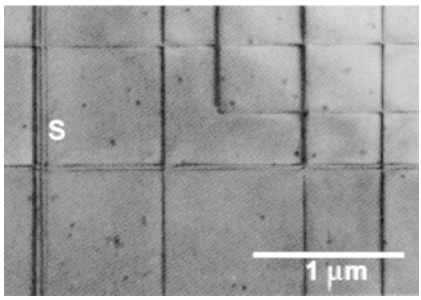


**Fig. 2.21** Plan view transmission-electron micrograph of a 2 µm thick Si layer on (001)-oriented GaP substrate. The parallel and closely spaced fringes denoted *S* originate from a stacking fault. Reproduced with permission from [65], © 1987 AIP

fulfill this condition [41]. One mechanism is based upon a dislocation line with a suitable Burgers vector already existing in the substrate and terminating at its surface. As illustrated in Fig. 2.20a the dislocation is replicated in the layer and forms a *threading dislocation*, i.e. a dislocation penetrating the layer. Under the action of coherency strain the dislocation line bends and glides along the interface (from position 1 to 2). Thereby a strain-relaxing misfit segment of the dislocation line is created at the interface. Another mechanism is the nucleation of a *dislocation half loop* at the layer surface, illustrated in Fig. 2.20b. The half loop represents the border of an extra plane (in tensely strained layers), which expands and glides towards the interface over slip planes. Both mechanisms lead to the formation of a *dislocation network* at the interface (Fig. 2.20c). The average spacing $p$ of the parallel line segments at the interface is given by (2.33).

The formation of a dislocation network at the layer/substrate interface of incoherent (plastically relaxed) epilayers may be observed in plan view micrographs. An example for an epitaxial layer with 0.5 % natural misfit at growth temperature is given in Fig. 2.21.

### *2.3.3 Dislocations in the fcc Structure*

The face-centered cubic and hexagonally close-packed structures are the two most common structures for metallic elements and—as constituents of the related zincblende and wurtzite structures—also for important semiconductors (Sect. 2.1). For these structures we consider simple reference schemes to denote Burgers vectors of possible dislocations and stacking faults. Figure 2.22 represents *Thompson's tetrahedron* used for fcc structures [66]. The side faces of the tetrahedron are the four equivalent {111} faces, which lie parallel to the corresponding close-packed planes of the fcc structure and represent the possible glide planes. The edges point towards ⟨110⟩ directions and correspond to the six glide directions denoted $BA$, etc. They represent vectors of the type $\frac{1}{2}\langle 110\rangle$, which are primitive translations of the fcc structure. Dislocations with such a Burgers vector are termed *perfect dislocations*. Vectors from a corner to the midpoint of a side facet are of the type $\frac{1}{6}\langle 112\rangle$ and are labeled $A\beta$, etc. Dislocations with a Burgers vector which does *not* correspond to primitive translations (like $A\beta$) are referred to as *partial dislocations*.

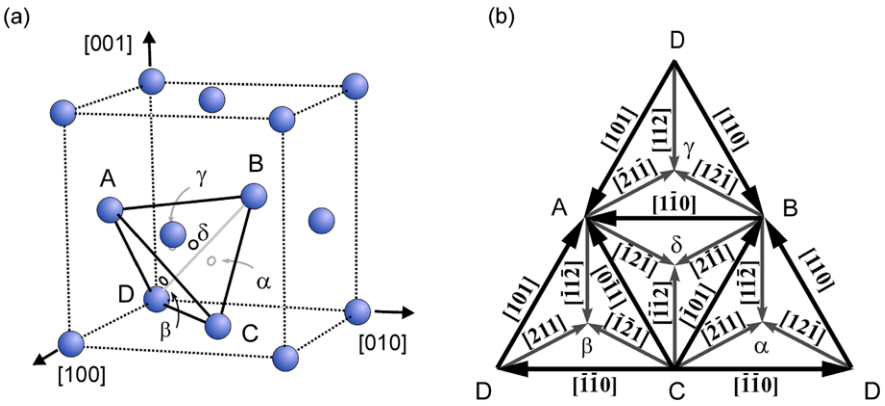


**Fig. 2.22** Thompson's reference tetrahedron (**a**) in the fcc unit cell and (**b**) in a planar development showing the different crystallographic directions

**Table 2.7** Burgers vectors and types of dislocations in the fcc structure, $a_0$ is the lattice constant of the unit cell

| Burgers vector (Thompson's notation) | Burgers vector (crystallographic notation) | Type of dislocation | $\lvert\mathbf{b}\rvert^2$ ($\times 36/a_0^2$) |
|---|---|---|---|
| $AB$ | $\frac{1}{2}a_0\langle 110\rangle$ | Perfect | 18 |
| $A\alpha$ | $\frac{1}{3}a_0\langle 111\rangle$ | Frank partial | 12 |
| $A\beta$ | $\frac{1}{6}a_0\langle 112\rangle$ | Shockley partial | 6 |
| $\alpha\beta$ | $\frac{1}{6}a_0\langle 110\rangle$ | Stair-Rod partial | 2 |
| $\delta\alpha/CB$ | $\frac{1}{3}a_0\langle 100\rangle$ | Stair-Rod partial | 4 |
| $\delta D/C\gamma$ | $\frac{1}{3}a_0\langle 110\rangle$ | Stair-Rod partial | 8 |
| $\delta\gamma/BD$ | $\frac{1}{6}a_0\langle 013\rangle$ | Stair-Rod partial | 10 |
| $\delta B/D\gamma$ | $\frac{1}{6}a_0\langle 123\rangle$ | Stair-Rod partial | 14 |

Partial dislocations lead to a change in the $ABC$ stacking order of the {111} planes of the fcc structure. The resulting planar defects are referred to as *stacking faults*. Possible Burgers vectors of dislocations in the fcc structure and the notation of the corresponding dislocation type are given in Table 2.7. Notations with two pairs represent the sum vector, e.g., $DB/CA \equiv DC + BA$ yields [100].

The energy of a dislocation is generally proportional to the square of the absolute value of its Burgers vector. A dislocation with Burgers vector **b** can, therefore, lower its strain energy and divide into two (or more) partial dislocations with Burgers vectors $\mathbf{b}_1$ and $\mathbf{b}_2$, if *Frank's rule* is satisfied:

$$|\mathbf{b}_1|^2 + |\mathbf{b}_2|^2 < |\mathbf{b}|^2. \tag{2.30}$$

The common validity of Frank's rule originates from the weak dependence of the line energy of a dislocation on its character (edge or screw type or mixed). In any

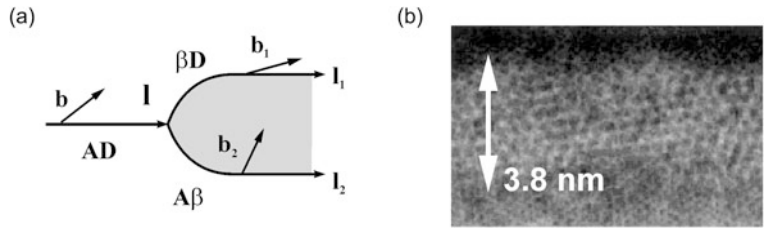


**Fig. 2.23** (**a**) Dissociation of a perfect dislocation into two Shockley partial dislocations. (**b**) High-resolution transmission electron micrograph of a stacking-fault ribbon in Ge bounded by two Shockley partial dislocations, the *double arrow* indicates the stacking fault width expected from the stacking fault energy. Reproduced with permission from [67], © 1998 Elsevier

case $E_{\text{dislocation}}/\text{length} \propto const \times Gb^2$, where $G$ is the shear modulus and the constant differs by less than a factor of 2.

Only dislocations with the shortest Burgers vectors are stable. Perfect dislocations with shortest Burgers vectors in the fcc structure are of the type $\frac{1}{2}a_0\langle 011\rangle$. Such a dislocation tends to dissociate into two (stable) partial dislocations with shorter Burgers vectors. From Thompson's tetrahedron Fig. 2.22 we read, e.g.,

$$AD = A\beta + \beta D, \quad \text{or}$$
$$\frac{a_0}{2}[\bar{1}0\bar{1}] = \frac{a_0}{6}[\bar{1}0\bar{2}] + \frac{a_0}{6}[\bar{2}\bar{1}\bar{1}].$$

This dislocation reaction describes the dissociation of a perfect dislocation into two energetically favorable Shockley partial dislocations, cf. Table 2.7. The process is illustrated in Fig. 2.23. The dislocation line of the perfect dislocation $AD$ splits into two lines of the partial dislocations. Since their Burgers vectors are not lattice vectors, they lead from a lattice site to a crystallographic not equivalent site: They produce a stacking fault. The two dislocation lines border a strip of stacking fault which keeps the partial dislocations together in some equilibrium distance and forms a so-called extended dislocation. In the stacking-faulted region the regular $ABCABC$ stacking order is changed by removal or insertion of one layer, e.g., to $ABABC$.

### *2.3.4 Dislocations in the Diamond and Zincblende Structures*

The diamond and zincblende structures result from the fcc structure by adding to each atom on the $ABC$-stacked fcc lattice one atom of another type in the distance $\frac{a}{4}[111]$, i.e., a corresponding $abc$-stacking. This yields a total $AaBbCc$ stacking, with different kind of atoms (charges) on the two sublattices in zincblende (Sect. 2.1). Dislocations in semiconductors which crystallize in diamond or zincblende structures are therefore also described using Thompson's tetrahedron. Mismatched layers of such semiconductors generally show larger values of the critical thickness for plastic relaxation and slower relaxation of the elastic strain than

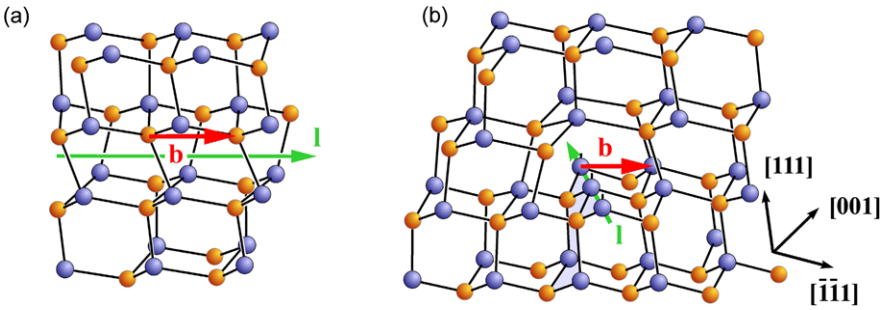


**Fig. 2.24** Perfect dislocations in the zincblende structure: (**a**) Screw dislocation, (**b**) 60° dislocation. The [001] direction shown in (**b**) lies in the plane spanned by [111] and [$\bar{1}\bar{1}$1]

metal films. This is due to a lower mobility of dislocations in semiconductors and a consequently reduced length of misfit segments along the interface. Furthermore, the larger perfection of semiconductor substrates necessitates the nucleation of new dislocations, instead of, as in metal films, glide of preexisting ones or heterogeneous nucleation at precipitates.

The three main types of perfect dislocations in diamond and zincblende semiconductors with $\frac{1}{2}\langle 110\rangle$ Burgers vectors are edge dislocations, screw dislocations, and 60°-mixed dislocations. The 60°-mixed type is the most common perfect dislocation, because the edge type has a high core energy and the screw type cannot relax tetragonal mismatch which arises from (001)-oriented heterostructure growth. The screw dislocation and 60°-mixed dislocation in zincblende structure are illustrated in Fig. 2.24. The respective dislocations of the diamond structure are obtained when all atoms are considered to be equal.

There are two different sets of dislocations due to the $AaBbCc$ double-layer atomic arrangement. Dislocations of the *shuffle set* (or type I) have glide planes lying between layers of the same index, e.g., $Aa$. Gliding of shuffle-set dislocations requires breaking of *one* bond per atom. Dissociation of perfect dislocations of such set into partials is not favorable, because it would produce a stacking fault of the type $AaBbC|bCcAa$ with a high energy of the $CbC$ sequence. Furthermore, the partial dislocations cannot glide like a perfect dislocation. On the other hand, dislocations of the *glide set* (or type II) dissociate into partials which are glissile by, e.g., forming a stacking fault of the type $AaBb|AaBbCc$. Gliding of perfect glide-set dislocations requires breaking of *three* bonds per atom. Dissociation and interactions of these dislocations are identical to those of the fcc structure. A glide-set dislocation can transform to the shuffle set and vice versa by climb. Dislocations in the zincblende structure require a further distinction with respect to those in diamond structure, because the dislocation line may either lie on a row of anions or cations. Dislocations with $l$ parallel to the $[1\bar{1}0]$ direction are termed $\alpha$ type. Their core comprises cations in the shuffle set and anions in the glide set. Accordingly, $\beta$ type dislocations have a dislocation line along the [110] direction with anions in the shuffle set and cations in the glide set.

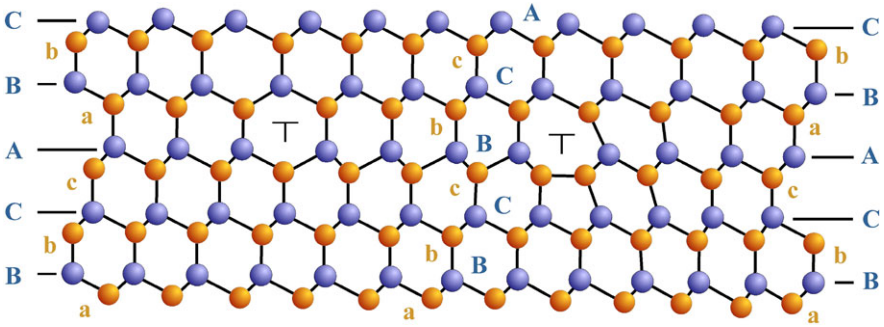


**Fig. 2.25** Dissociated perfect dislocation with a bounded stacking fault in zincblende structure viewed along $[1\bar{1}0]$

The dissociation of a perfect zincblende 60° dislocation with type II glide plane into an extended dislocation of a stacking fault bounded by two Shockley partial dislocations is shown in Fig. 2.25. This scheme corresponds to the stacking fault ribbon imaged in Fig. 2.23, if all atoms are considered to be of the same kind to obtain the diamond structure.

### 2.3.5 Dislocation Energy

Near a dislocation atoms are displaced from their equilibrium positions which they occupy in a perfect crystal. A corresponding cost of elastic energy is required to produce the dislocation and referred to as dislocation energy $E_\mathrm{D}$. To obtain an estimate for $E_\mathrm{D}$ we first consider the simple case of a *screw dislocation* in an isotropic continuum forming a coaxial cylinder as depicted in Fig. 2.26 [63]. The dislocation is produced by a shear displacement in the $z$ direction across the $xz$ glide plane and assumed to increase uniformly with the angle $\varphi$.

Displacements of this dislocation are given by $u_x = u_y = 0$, and $u_z = b \times \varphi/(2\pi) = b/(2\pi) \times \tan^{-1}(y/x)$. The only nonzero stresses of such displacement are $\sigma_{xz} = -Gb/(2\pi) \times y/(x^2 + y^2)$, and $\sigma_{yz}$ with $y$ in the enumerator being replaced by $-x$. $G$ is the shear modulus and $b$ the length of the Burgers vector. In polar coordinates the stress reads $\sigma_{\varphi z} = Gb/(2\pi r)$, and the strain resulting from Hooke's law is $\varepsilon_{\varphi z} = \varepsilon_{z\varphi} = \sigma_{\varphi z}/(2G) = b/(4\pi r)$. The strain field has a pure shear character and decays with $1/r$ from the dislocation line **l**. The elastic energy per length $L$ follows from the integration of the elastic energy density $E/V = 2G\varepsilon_{\varphi z}^2$, yielding

$$\frac{E_\mathrm{screw}^\mathrm{isotropic}}{L} = \int_{r_\mathrm{c}}^{R} 2G\varepsilon_{\varphi z}^2 r dr d\varphi = \frac{Gb^2}{4\pi} \ln(R/r_\mathrm{c}). \tag{2.31}$$

The lower bound $r_\mathrm{c}$ denotes the radius of the dislocation core. At a distance $r$ from the center of the dislocation below a value $r_\mathrm{c}$ the linear elastic theory cannot be applied. A somewhat arbitrary cutoff parameter $\rho$ is often used to account

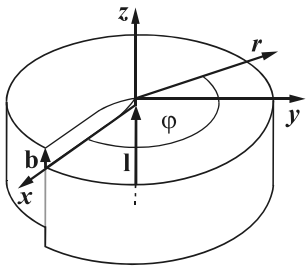


**Fig. 2.26** Screw dislocation along the axis of a cylinder

for the non-linear elastic energy and dangling bonds in the core, where $r_c = b/\rho$ with $\rho \approx 2, \ldots, 4$. Sometimes in literature instead of using $\rho$ a constant is added to the logarithm term of (2.31), yielding $(\ln(R/b) + const)$ instead of $\ln(\rho R/b)$. The divergence of $E_{\text{screw}}^{\text{isotropic}}/L$ for an infinite upper bound $R$ indicates that the dislocation does not have a specific characteristic energy, but depends on the size of the solid. An appropriate choice for $R$ is the shortest distance of the dislocation line to the surface or, in case of a solid with many dislocations of both signs, roughly their mutual average distance.

The strain field of an *edge dislocation* comprises all kind of strains. Considering the edge dislocation Fig. 2.18a with an inserted lattice plane above the line vector **l**, the strain field has dominant compressive and tensile hydrostatic components above and below **l**, respectively. At the right and left hand side of **l** we find predominantly shear strains of opposite sign, and on the diagonals compressive and tensile axial components. In isotropic media the tensile stress in radial direction $\sigma_{rr}$ and that along the circumference $\sigma_{r\varphi}$ should be proportional $1/r$ and change sign by exchanging $x$ and $y$. A continuum-mechanical deduction of the stress field of the edge dislocation yields $\sigma_{rr} = \sigma_{\varphi\varphi} = -Gb/(2\pi(1-\nu)) \times \sin\varphi/r$, and $\sigma_{r\varphi} = Gb/(2\pi(1-\nu)) \times \cos\varphi/r$ for the shear stress [63]. Integration leads to the elastic energy per length $E_{\text{edge}}^{\text{isotropic}}/L$, which, apart from an additional factor $1/(1-\nu)$, has the same form as that of the screw dislocation (2.31). The considerations likewise apply for anisotropic media, where the particular geometry examined introduces additional terms.

In a dislocation with *mixed character* the strain fields of the screw and edge components superimpose. We consider the example of the prominent 60° dislocation in crystals with diamond or zincblende structure, introduced at a (001) interface between a substrate and a layer to accommodate misfit strain. The angle $\alpha$ between line vector and burgers vector enters the elastic energy per unit length, yielding [39]

$$\frac{E_\alpha}{L} = \frac{Gb^2}{4\pi}\left(\cos^2\alpha + \frac{\sin^2\alpha}{(1-\nu)}\right)\ln\left(\frac{\rho R}{b}\right). \tag{2.32}$$

To evaluate the strain energy $E_D$ of *all* dislocations in a layer, their total number has to be considered. Figures 2.20 and 2.21 illustrate that the strain in a layer which exceeds the critical thickness is actually accommodated by a *network* of dislocations, which in many cases form a more or less regular grid at the interface. The average spacing $p$ in such an array of parallel misfit dislocations is related to the actual

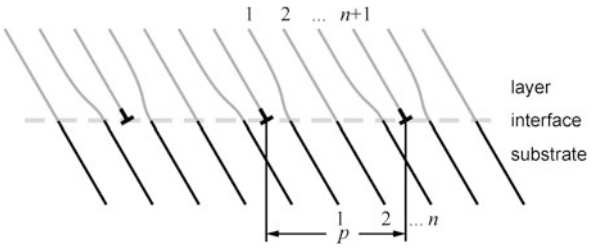


**Fig. 2.27** Equally spaced dislocations accommodating the strain in the layer of a mismatched, relaxed heterostructure. The *lines* represent lattice planes which lie perpendicular to the image plane and contain the dislocation line. Lattice planes in substrate and layer are drawn *black* and *gray*, respectively

misfit $f$. We consider the strongly mismatched, relaxed heterostructure depicted in Fig. 2.27 to obtain an expression for $p$. In Fig. 2.27 the lateral distance $p$ comprises $n$ planes of the substrate and $(n+1)$ planes of the layer (here $a_\mathrm{L} < a_\mathrm{S}$). The lateral spacing between the depicted planes of the substrate is then given by $a_\mathrm{S} = p/n$, and that of the layer planes is $a_\mathrm{L} = p/(n+1)$. Taking the definition of the misfit $f$ from (2.20a) we obtain for $a_\mathrm{L} < a_\mathrm{S}$

$$f = \frac{a_\mathrm{S} - a_\mathrm{L}}{a_\mathrm{L}} = \frac{\frac{p}{n} - \frac{p}{n+1}}{\frac{p}{n+1}} = \frac{1}{n}.$$

If $a_\mathrm{L} > a_\mathrm{S}$ there are only $n-1$ layer planes for $n$ substrate planes, yielding $a_\mathrm{L} = p/(n-1)$. Insertion into (2.20a) then leads to $f = -1/n$ $(f < 0)$. The spacing $p$ of the parallel misfit dislocations is hence

$$p = n a_\mathrm{S} = \frac{a_\mathrm{S}}{|f|}. \tag{2.33}$$

The inverse of $p$ is the (linear) density of the dislocations illustrated in Fig. 2.27.

A dense *regular* spacing of dislocations may occur, if a large lattice mismatch $f$ between epilayer (lattice spacing $d_\mathrm{L}$) and substrate ($d_\mathrm{S}$) is accommodated by a *coincidence lattice* fulfilling the condition $m \times d_\mathrm{S} \approx n \times d_\mathrm{L}$ with small integer numbers $m$ and $n$. The remaining mismatch is in this case $f = (m \times d_\mathrm{S} - n \times d_\mathrm{L})/n \times d_\mathrm{L}$. An example is given in Fig. 2.28. The lateral lattice constant of the AlN epilayer ($d_\mathrm{L} = 3.11$ Å) is much smaller than that of the (111)-oriented Si substrate ($d_\mathrm{S} = 5.43$ Å$/\sqrt{2} = 3.84$ Å), yielding a natural misfit $(d_\mathrm{S} - d_\mathrm{L})/d_\mathrm{L} = 0.23$. By introducing one step dislocation into each unit cell of the coincidence lattice on the epilayer side with a ratio $m : n = 4 : 5$ the mismatch is reduced to $f = -0.01$ [68].

The elastic dislocation energy $E_\mathrm{D}$ per area $A$ of a network of dislocations at the interface is

$$\frac{E_\mathrm{D}}{A} = \frac{2}{p}\frac{E_\mathrm{disloc}}{L}. \tag{2.34}$$

The factor 2 accounts for the two independent lateral directions assumed here to be equivalent, and $E_\mathrm{disloc}/L$ is the energy per length of one dislocation, like, e.g.,

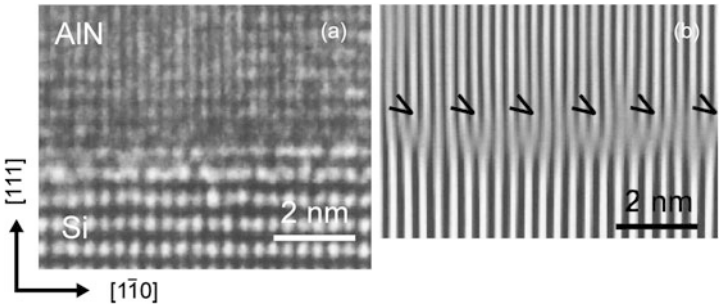


**Fig. 2.28** Equally spaced step dislocations at the interface between an AlN(0001) epilayer and the Si(111) substrate. (**a**) High-resolution transmission-electron micrograph taken along the [11 −2] axis of Si. (**b**) The fast-Fourier filtered image shows the Si(−110) and the AlN(−2110) net planes, respectively. Reproduced with permission from [68], © 1999 Elsevier

(2.32). If the degree of relaxation is anisotropic, as was observed for, e.g., 60° dislocations in zincblende type layers along the [110] and [1$\bar{1}$0] directions, (2.34) splits into a sum with *two* periods $p_i$ and two related $E_{\mathrm{disloc},i}/L_i$. An explicit relation of (2.34) also comprises the angle $\beta$ between the glide plane containing the Burgers vector and the interface. $\beta$ is related to the angle $\alpha$ between line vector **l** and Burgers vector **b**, and also to the substrate plane spacing $a_\mathrm{S}$ according to

$$a_\mathrm{S} = b \sin\alpha \cos\beta. \tag{2.35}$$

Using (2.32), (2.33), and (2.35) yields a general relation for the dislocation energy of a layer containing a dislocation network [39],

$$\frac{E_\mathrm{D}}{A} = bG \frac{|\varepsilon + f_0|(1 - \nu\cos^2\alpha)}{2\pi(1-\nu)\sin\alpha\cos\beta} \ln\left(\frac{\rho R}{b}\right). \tag{2.36}$$

The geometrical parameters for the 60° dislocation are the length of the Burgers vector $b = a/2 \times [101]$, the angle between Burgers vector and line vector $\alpha = 60°$, and the angle between the {111} glide planes and the considered (001) interface plane $\beta = 54.7°$. The critical thickness of a strained epitaxial layer accommodated by such misfits is given by the implicit relation (2.28), the solution of which is depicted in Fig. 2.15.

### *2.3.6 Dislocations in the hcp and Wurtzite Structures*

In the hcp structure the triangular bipyramid given in Fig. 2.29 is a widely used reference construction for classifying dislocations [69]. In this representation basal-plane lattice vectors are labeled $AB = \mathbf{a}_1$ $(= \frac{1}{3}[\bar{1}2\bar{1}0])$, $BC = \mathbf{a}_2$, and $CA = \mathbf{a}_3$. The lattice vector **c** (= [0001]) is given by $TS$, the line $\sigma S = T\sigma = \frac{1}{2}\mathbf{c}$ does not represent a lattice vector. Further vectors of interest are $TS + AB = \mathbf{c} + \mathbf{a}_1 = \frac{1}{3}[\bar{1}2\bar{1}3]$, and $A\sigma = \frac{1}{3}[01\bar{1}0]$.

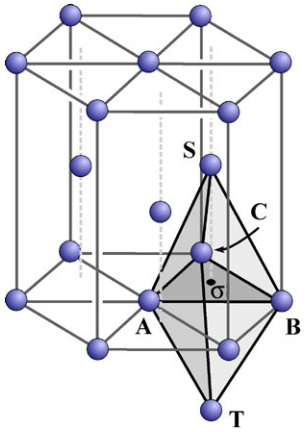


**Fig. 2.29** Triangular bipyramid used as reference system to describe dislocations in the hcp structure

In crystals with hcp structure the close-packed basal planes are the most frequently observed glide planes. Dislocations with a slip vector of the type $AB$ operating on these (0001) planes are therefore of particular importance. For vectors lying in the basal plane it is sufficient to use the base of the bipyramid as a reference system. As an example we consider the dissociation of a perfect glide dislocation with vector $AB$ into Shockley partial dislocations. From the reference bipyramid we read

$$AB = A\sigma + \sigma B. \tag{2.37}$$

The partial dislocation $A\sigma$ changes the layer sequence from the ordinary $abab$ stacking to a $bcbc$ sequence as illustrated in Fig. 2.30. The second partial $\sigma B$ in (2.37) restores the initial order. Thereby a stacking-fault ribbon bound by two partials is created, comparable to the case shown in Figs. 2.23 and 2.25. Another kind of such ribbon is formed from the same perfect glide dislocation if the order of the partial dislocations is reversed, i.e.

$$AB = \sigma B + A\sigma. \tag{2.38}$$

In this case the ribbon contains layers stacked in an $acac$ sequence, cf. Fig. 2.30b. Both kinds of ribbons have the same energy, although they are crystallographically distinguishable.

The wurtzite structure is formed from the hcp structure by adding to each atom a further atom of another kind, shifted by $\frac{3}{8}c$ along [0001], cf. Sect. 2.1. Dislocations in the resulting $AaBbAaBb$ stacking are described in the same framework as those of the hcp structure. The basic edge and screw dislocations in a wurtzite crystal are shown in Fig. 2.31. Panel (a) shows a high-resolution transmission-electron micrograph of a pure edge dislocation with a Burgers vector of $\frac{1}{3}[11\bar{2}0]$, determined from the Burgers cycle marked by open circles. The inserted plane is perceived by viewing the image at a glancing angle from the lower left corner. This type of threading dislocation is most common in GaN layers epitaxially grown on (0001) sapphire or on (111) Si.

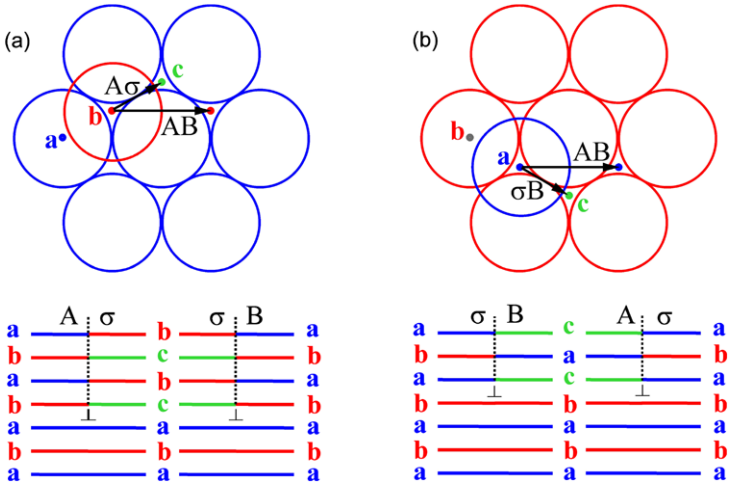


**Fig. 2.30** Dissociation of a perfect dislocation $AB$ in a hcp structure into two partial dislocations $A\sigma$ and $\sigma B$. (**a**) Displacement of an atom in the *b* layer (*red*) on *top* of the *a* layer (*blue circles*) by $A\sigma$. (**b**) Displacement of an atom in the *a* layer on *top* of the *b* layer by $\sigma B$. The stacking sequence of the ribbons bounded by the two partial dislocations is illustrated in the *bottom*

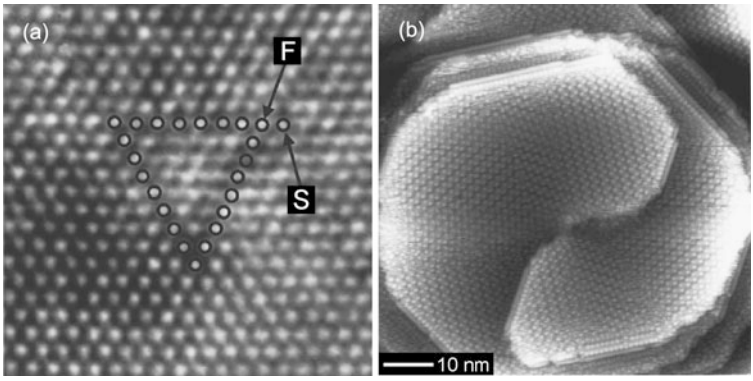


**Fig. 2.31** (**a**) Plan view transmission-electron micrograph of a pure edge dislocation in wurtzite GaN. *S* and *F* mark begin and end of a Burgers cycle which is indicated by *open circles*. Reprinted with permission from [70], © 2000 APS. (**b**) Scanning tunneling micrograph of a screw dislocation on the N-face of GaN. Reprinted with permission from [71], © 1998 AVS

Screw dislocations can provide a steady source of kinks on a growing crystal surface by producing kink sites and may thereby lead to high growth rates. Figure 2.31b shows an STM image of a pure screw dislocation at a GaN surface (N-face). The measured step heights at the two spiral growth fronts are each one GaN bilayer, yielding a Burgers vector of $c[000\bar{1}]$ for this dislocation.

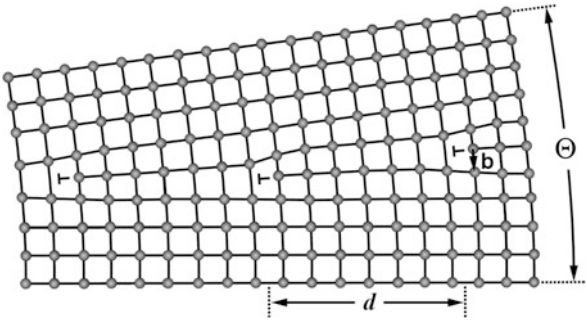


**Fig. 2.32** Scheme of a low-angle grain tilt boundary inducing a mutual tilt of adjacent crystalline regions by an angle $\Theta$

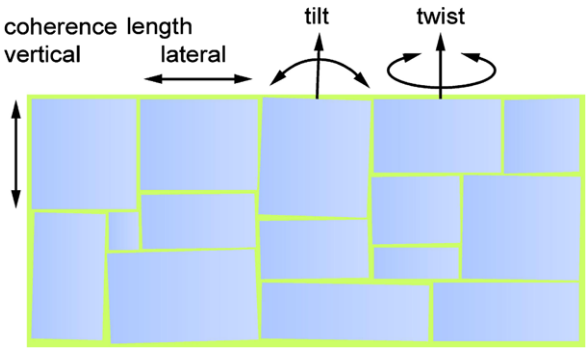


**Fig. 2.33** Characteristic parameters of mosaicity in single crystals

## *2.3.7 Mosaic Crystal*

Faults like the line defects considered in the last few pages exist in virtually any crystal. A periodic pattern of dislocations may form an interface between undistorted regions called low-angle grain boundary as depicted in Fig. 2.32. Such boundary leads to a local tilts or twists of crystal planes and separate regions with perfect crystal structure. The tilt angle $\Theta$ of a tilt boundary formed from a linear sequence of edge dislocations as shown in Fig. 2.32 is given by their average distance $d$ and the absolute value of their burgers vector $b$. From the figure follows $\tan(\Theta/2) = b/(2d)$ or, since $\Theta$ is small, $\Theta = b/d$. There exist also twist boundaries formed from a sequence of screw dislocations. Low-angle grain boundaries are normally composed of a mixture of tilt and twist boundaries.

In practice crystals usually consist of a mosaic of small blocks with undistorted structure. The single-crystalline blocks are typically of the order of a few microns in vertical and lateral dimensions (with respect to the growth plane), and they are randomly slightly misoriented with respect to each other. The finite size of the crystallites limits the coherence of scattered X-ray radiation. The dimensions are therefore called vertical and lateral coherence length, respectively. Out-of-plane rotation perpendicular to the surface leads to a mosaic tilt. In-plane rotation around the surface normal is referred to as mosaic twist. The characteristic parameters of mosaicity are illustrated in Fig. 2.33. It should be noted that the distortions are small and the

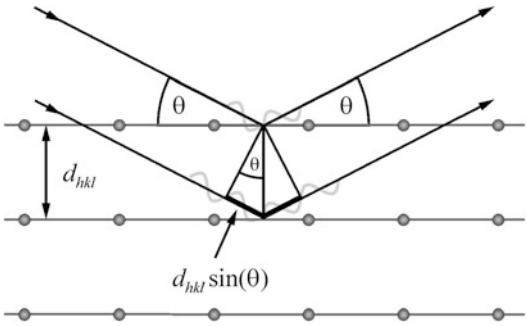


**Fig. 2.34** X-ray diffraction of two rays at neighboring lattice planes. For constructive interference the path difference of the diffracted waves $2d_{hkl}\sin\Theta$ must be equal an integral number of wavelengths

crystal is still considered as single crystal albeit with some mosaicity. In epitaxial layers with line defects mainly running parallel to the surface normal, the vertical coherence length is commonly related to the layer thickness.

## 2.4 Structural Characterization Using X-Ray Diffraction

X-ray diffraction is a powerful tool for investigating the structural properties of epitaxial layers and is employed in virtually any growth laboratory. Interatomic distances in a solid are typically on the order of some angstrom. A diffraction probe of the microscopic structure must hence have a wavelength at least this short. For an electromagnetic wave 1 Å corresponds to a photon energy $E = hc/\lambda = 12.40$ keV, a characteristical X-ray energy. High resolution X-ray diffraction (HRXRD) is the most commonly applied technique for analyzing lattice parameters, strains, and defects in epitaxial heterostructures. The technique is outlined in this section.

### *2.4.1 Bragg's Law*

The periodic arrangement of atoms in the solid leads to an elastic scattering of impinging X-ray waves. Diffracted waves have definite phase relations among each other. They interfere constructively, if the phase difference is an integral number $n$ of wavelengths $\lambda$. This is depicted in Fig. 2.34 for two rays which are diffracted at two parallel lattice planes spaced a distance $d_{hkl}$ apart. According this picture the waves behave as being reflected at the lattice planes.

The path of the lower ray is $2 \times d_{hkl} \times \sin\Theta$ longer, $\Theta$ being the angle of incidence (measured from the diffracting lattice plane). The condition for X-ray reflections was concluded by William L. Bragg and his father William H. in 1913 from characteristic patterns of X-rays reflected from crystalline solids and reads

$$2d_{hkl}\sin\Theta = n\lambda. \tag{2.39}$$

$n$ is called the order of the reflection. Note that *Bragg's law* (2.39) only defines the *direction* of a diffracted beam (not the intensity), and that it allows reflections

only for $\lambda \leq 2d_{hkl}$. The lattice-plane distance $d_{hkl}$ and hence $\Theta$ depend on shape and size of the unit cell and on the position of the planes with respect to the axes of the crystal system. They can be calculated for the seven crystal systems listed in Table 2.1 from the lattice vectors **a**, **b**, **c**, the angles $\alpha$, $\beta$, and $\gamma$ included by them, and the Miller indices of the lattice planes $h, k, l$. The result is given in Table 2.8 in terms of Bragg angles $\sin(\Theta)$ of allowed scattering directions.

### 2.4.2 The Structure Factor

The *intensity* of the diffracted beam depends on the spatial arrangement of the atoms in the unit cell. The intensity of the wave scattered by all $N$ atoms of the unit cell results from the sum of their individual contributions and their respective phases. This is expressed by the *structure factor* $F_{hkl}$,

$$F_{hkl} = \sum_{n=1}^{N} f_n \exp\big(i2\pi(hu_n + kv_n + lw_n)\big). \tag{2.40}$$

The *atomic scattering factor* $f_n$ expresses the scattering power of the $n$th atom in the unit cell and is determined by its inner electronic charge distribution. The exponential factor gives the phase relation of the $N$ contributions and depends on the positions of the atoms in the unit cell, expressed by the coordinates $u_n$, $v_n$, and $w_n$. The absolute value of the structure factor $|F_{hkl}|$ gives the amplitude of the diffracted wave, i.e., the amplitude of the wave scattered by all atoms of the unit cell with respect to the amplitude of a wave scattered by a free electron. The intensity $I_{hkl}$ of the scattered wave is eventually given by its square,

$$I_{hkl} \propto |F_{hkl}|^2 = F^*_{hkl} F_{hkl}. \tag{2.41}$$

We consider for example the structure factor of a solid with body centered cubic (bcc) structure. The unit cell contains 2 atoms located at 000 and $\frac{1}{2}\frac{1}{2}\frac{1}{2}$ (in units of the lattice constant $a$), which are identical ($f_1 = f_2 = f$). From (2.40) we obtain

$$\begin{aligned} F &= f\exp\big(i2\pi(0h + 0k + 0l)\big) + f\exp\big(i2\pi\big(\tfrac{1}{2}h + \tfrac{1}{2}k + \tfrac{1}{2}l\big)\big) \\ &= f\big(1 + \exp\big(i\pi(h + k + l)\big)\big), \end{aligned}$$

i.e., $F = 2f$ when $h + k + l$ is even, and $F = 0$ when $h + k + l$ is odd. For fcc structure we similarly obtain $F = 4f$ when $h, k, l$ are all even or all odd, and $F = 0$ when $h, k, l$ are mixed even or odd.

In *zincblende structure* we have two kinds of atoms with atomic form factors $f_1$ and $f_2$ ($> f_1$). In this case we find for the structure factor (with $n$ being an integer):

| | |
|---|---|
| $h, k, l$ all even and $h + k + l = 4n$, | $F = 4(f_1 + f_2)$, |
| $h, k, l$ all even and $h + k + l = 4n + 2$, | $F = 4(f_1 - f_2)$, |
| $h, k, l$ all odd, | $F = 4\big(f_1^2 - f_2^2\big)^{1/2}$, |
| $h, k, l$ are mixed even and odd, | $F = 0$. |

**Table 2.8** Bragg's equations for the seven crystal systems

| Crystal system | Angles $\sin(\Theta)$ of Bragg reflections |
|---|---|
| Cubic | $\sin(\theta) = \frac{\lambda}{2a}\sqrt{h^2 + k^2 + l^2}$ |
| Tetragonal | $\sin(\theta) = \frac{\lambda}{2a}\sqrt{h^2 + k^2 + (\frac{a}{c})^2 l^2}$ |
| Rhombohedral | $\sin(\theta) = \frac{\lambda}{2a}\sqrt{\frac{(h^2+k^2+l^2)\sin^2\alpha + 2(kl+lh+hk)(\cos^2\alpha - \cos\alpha)}{1-3\cos^2\alpha+2\cos^3\alpha}}$ |
| Hexagonal | $\sin(\theta) = \frac{\lambda}{2a}\sqrt{\frac{4}{3}(h^2 + k^2 + hk) + (\frac{a}{c})^2 l^2}$ |
| Orthorhombic | $\sin(\theta) = \frac{\lambda}{2a}\sqrt{h^2 + (\frac{a}{b})^2 k^2 + (\frac{a}{c})^2 l^2}$ |
| Monoclinic | $\sin(\theta) = \frac{\lambda}{2}\sqrt{\frac{h^2}{a^2\sin^2\beta} + \frac{k^2}{b^2} + \frac{l^2}{c^2\sin^2\beta} - \frac{2hl\cos\beta}{ac\sin^2\beta}}$ |
| Triclinic | $\sin(\theta) = \frac{\lambda}{2}\sqrt{h^2a^{*2} + k^2b^{*2} + l^2c^{*2} + 2klb^*c^*\cos\alpha^* + 2lhc^*a^*\cos\beta^* + 2hka^*b^*\cos\gamma^*}$, $a^* = \frac{1}{D}bc\sin\alpha,\ \cos\alpha^* = \frac{\cos\beta\cos\gamma - \cos\alpha}{\sin\beta\sin\gamma}$ $b^*,\ c^*,\ \cos\beta^*,\ \cos\gamma^*$ correspondingly with cyclic change of $a,\ b,\ c,\ \alpha,\ \beta,\ \gamma,$ and $D = abc\sqrt{1 + 2\cos\alpha\cos\beta\cos\gamma - \cos^2\alpha - \cos^2\beta - \cos^2\gamma}$ |

Note that all these structures belong to the cubic crystal system.

In the hexagonal *wurtzite structure* the structure factor has the following form:

$$\begin{aligned} &l = 2n \text{ and } h + 2k = (3m \text{ or } 3m \pm 1), && F = 2\left(f_1^2 + 2f_1 f_2 \cos(2\pi ul) + f_2^2\right)^{1/2}, \\ &l = 2n + 1 \text{ and } h + 2k = 3m, && F = 0, \\ &l = 2n + 1 \text{ and } h + 2k = 3m + 1, && F = \sqrt{3}\left(f_1^2 + 2f_1 f_2 \cos(2\pi ul) + f_2^2\right)^{1/2}. \end{aligned}$$

$n$ and $m$ are integers and $u$ ($\approx \frac{3}{8}c$) is the mutual displacement of the anion and cation sublattices.

A number of further factors determines the intensity of the scattered wave in addition to the structure factor $F$ which solely considers the geometric structure of the scattering unit cells. They account for the polarization of the scattered wave (polarization factor $P \propto (1 + \cos^2 2\Theta)$), deviations from a perfect parallel and monochromatic incident radiation (Lorentz factor $L \propto \lambda^2 / \sin^2 \Theta$), the effect of temperature (temperature factor or Debye-Waller factor $f_T \propto \exp(\sin^2 \Theta/\lambda)$), and absorption corrections depending on the measurement geometry (reflection or transmission setup). They are not included in this brief introduction.

### 2.4.3 The Reciprocal Lattice

For a detailed description of the scattering geometry the approach formulated by Max von Laue in 1911 is more appropriate than the simplified picture presented in Fig. 2.34. In this framework we regard the crystal as being composed of atoms which reradiate the incident radiation in all directions. Sharp reflections are obtained only in directions for which the rays from all lattice sites interfere constructively. We first consider scattering of only two atoms separated by a vector $\mathbf{r}$, see Fig. 2.35.

The incident X-ray beam along the direction $\mathbf{s}_0$ with wavelength $\lambda$ has the wave vector $\mathbf{k}_0 = (2\pi/\lambda)\mathbf{s}_0$, $\mathbf{s}_0$ being the unit vector $\mathbf{k}_0/k_0$. Constructive interference is obtained along a scattered direction $\mathbf{s} = \mathbf{k}/k$, if the path difference of the rays scattered by the two atoms is an integral number of wavelengths. From Fig. 2.35 we read that the path difference is composed by a sum of $a = r\cos\Theta_0 = -\mathbf{s}_0\mathbf{r}$ and $b = r\cos\Theta = \mathbf{sr}$, yielding

$$(\mathbf{s} - \mathbf{s}_0)\mathbf{r} = n\lambda. \tag{2.42}$$

$\lambda = \lambda_0$ because the scattering is assumed to be elastic. Multiplying (2.42) by $2\pi/\lambda$ we obtain

$$(\mathbf{k} - \mathbf{k}_0)\mathbf{r} = n2\pi. \tag{2.43}$$

We now consider many scattering atoms placed at the sites of a Bravais lattice. All lattice sites are displaced from one another by a Bravais lattice vector $\mathbf{R}$. Constructive interference of all scattered rays occurs if condition (2.43) holds simultaneously for all values of $\mathbf{r}$, i.e.

$$(\mathbf{k} - \mathbf{k}_0)\mathbf{R} = n2\pi. \tag{2.44}$$

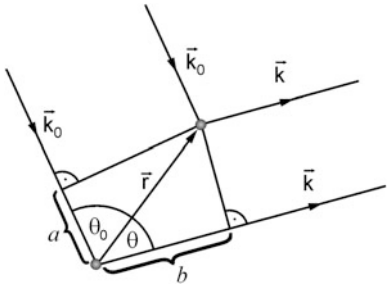


**Fig. 2.35** Path difference $a + b$ of X-rays scattered from two atoms separated by $\mathbf{r}$

Equation (2.44) may be rewritten by introducing the *reciprocal lattice*. A unique reciprocal lattice can be constructed for each particular Bravais lattice. It is a Bravais lattice for itself, and its reciprocal lattice is the original direct lattice. The base vectors $\mathbf{g}_i$ of the reciprocal lattice are defined by the condition

$$\mathbf{g}_i \mathbf{a}_j = 2\pi \delta_{ij}, \tag{2.45}$$

$\mathbf{a}_i$ being the base vectors of the corresponding Bravais lattice and Kronnecker's symbol $\delta_{ij} = 1$ for $i = j$ and 0 otherwise. The vector $\mathbf{g}_1$ is thus normal to $\mathbf{a}_2$ and $\mathbf{a}_3$, and can be calculated from

$$\mathbf{g}_1 = \frac{\mathbf{a}_2 \times \mathbf{a}_3}{\mathbf{a}_1(\mathbf{a}_2 \times \mathbf{a}_3)}. \tag{2.46}$$

The vectors $\mathbf{g}_2$ and $\mathbf{g}_3$ are obtained from (2.46) by a cyclic permutation of the indices. From the construction of the reciprocal lattice we conclude that each vector $\mathbf{G}_{hkl}$ is normal to a lattice plane of the real lattice with Miller indices $(hkl)$. Furthermore, the distance $d_{hkl}$ of two neighboring parallel lattice planes with Miller indices $(hkl)$ is inverse to the absolute value of the corresponding reciprocal lattice vector $\mathbf{G}_{hkl}$,

$$d_{hkl} = \frac{2\pi}{|\mathbf{G}_{hkl}|}. \tag{2.47}$$

Using the reciprocal lattice vectors defined in (2.45) and a reciprocal lattice vector $\mathbf{G}$ built from the base vectors $\mathbf{g}_i$ we represent (2.44) by the *von Laue condition*

$$(\mathbf{k} - \mathbf{k}_0) = \mathbf{G}. \tag{2.48}$$

Equation (2.48) means that constructive interference of scattered X-rays occurs if the change in wave vector (referred to as diffraction vector) $\Delta\mathbf{k} = \mathbf{k} - \mathbf{k}_0$ is a vector of the reciprocal lattice. Conditions (2.48) and (2.39) are equivalent criteria for constructive interference of X-rays. We may derive Bragg's law (2.39) from (2.48) by noting that $\mathbf{G}$ is an integral multiple of the shortest parallel reciprocal lattice vector, the length of which is $2\pi/d_{hkl}$, i.e., $G = n2\pi/d_{hkl}$. $G$ is also related to the Bragg angle $\Theta$. From (2.48) and the triangle built by the vectors $\mathbf{k}_0$, $\mathbf{k}$, and $\Delta\mathbf{k}$ in Fig. 2.36 we find the relation $G = \Delta k = 2 \times k \sin\Theta$. Putting this together we find

$$k \sin\theta = \frac{n\pi}{d_{hkl}}. \tag{2.49}$$

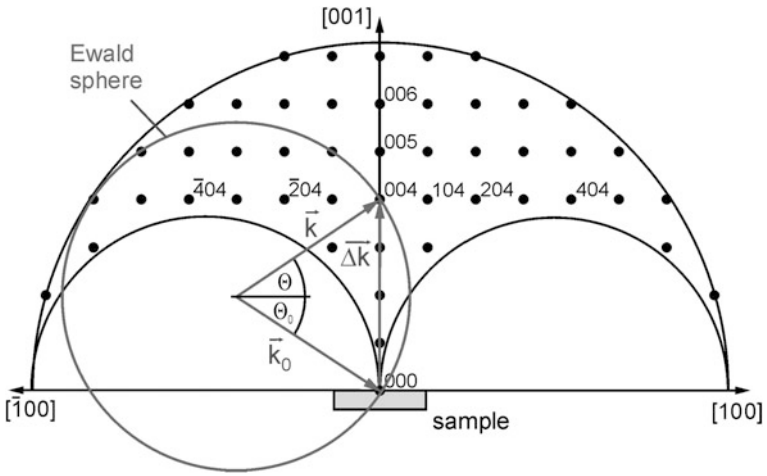


**Fig. 2.36** Reciprocal space map of all Bragg reflections accessible for an incident X-ray radiation with wave vector of length $k_0$. The *horizontal axis* denotes a diffraction vector $\Delta\mathbf{k}$ along a [100] direction lying in the sample surface, the *vertical axis* signifies a $\Delta\mathbf{k}$ normal to the surface. The *outer sphere* with radius $2k_0$ refers to a deflection angle $2\Theta = 180°$

By expressing $k$ in terms of $2\pi/\lambda$ we obtain Bragg's law from (2.49). We use here the convention, which is common in solid state physics. It should be noted that *in crystallography* the length of the wave vector is usually defined by $k = 1/\lambda$, i.e., without the factor $2\pi$; the reciprocal lattice spacing is then inverse to the associated lattice-plane spacing in real space.

The reciprocal lattice defined by (2.45) and (2.46) helps to find allowed Bragg reflections for a given crystal and the corresponding Bravais lattice. Such reflections fulfill the Bragg and von Laue conditions for a *set* of parameters consisting of lattice-plane distance $d_{hkl}$, angle $\Theta$, and X-ray wavelength $\lambda$. Methods of X-ray characterization differ in the parameters varied. They may be well represented using a simple geometric construction introduced by Paul P. Ewald.

### *2.4.4 The Ewald Construction*

To represent X-ray diffraction using the Ewald construction we first draw the reciprocal lattice, i.e., a collection of points derived from the real (direct) lattice of the crystal structure to be studied using (2.46). Now the incident wave vector $\mathbf{k}_0$ is added with the tip pointing to the origin $hkl = 000$, see Fig. 2.36. An *Ewald sphere* of radius $k_0$ $(= 2\pi/\lambda)$ centered on the origin of $\mathbf{k}_0$ is drawn. Scattered wave vectors $\mathbf{k}$ (with same length as $\mathbf{k}_0$) also starting at the center of the sphere satisfy the von Laue condition if and only if their tips end on a reciprocal lattice point, i.e., the lattice points lie on the surface of the sphere. In this case the diffraction vectors $\Delta\mathbf{k}$

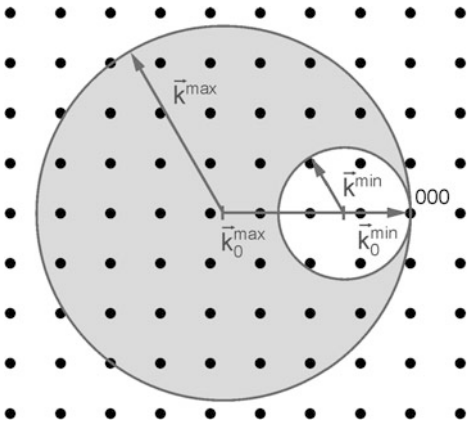


**Fig. 2.37** Ewald's construction of the von Laue method. The crystal is irradiated with a polychromatic X-ray beam

are vectors $\mathbf{G}_{hkl}$ of the reciprocal lattice. Note that each vector $\mathbf{G}_{hkl}$ represents a set of parallel lattice planes of the real crystal with Miller indices *hkl*.

The reciprocal space map shown in Fig. 2.36 is a representation of the real lattice in the reciprocal space. It is *fixed* with respect to the studied sample and its diffracting Bragg planes. Ewald's construction therefore provides a good survey of possible reflections for varied angles or wavelengths. For fixed $\lambda$ and consequently fixed lengths of $\mathbf{k}_0$ and $\mathbf{k}$ all possible reciprocal lattice points lie within a sphere of radius $2k$ (corresponding to Bragg scattering with $2\Theta = 180°$). Some points in the lower part of the map cannot be accessed since either $\Theta_0 < 0$ or $\Theta < 0$, i.e., $\mathbf{k}_0$ cannot enter the sample (the incident beam is below the surface) or $\mathbf{k}$ cannot emerge from the sample (the diffracted beam is below the surface).

If all angles are kept fixed and $\lambda$ is varied over all possible values we directly obtain an image of the reciprocal lattice. This technique was applied by von Laue and co-workers in 1912 to prove the wave nature of X-rays and is mainly used today to determine the crystallographic orientation of samples with a known structure. Ewald's construction of the *Laue method* provides spheres for all wavelengths between $\lambda_{min}$ (corresponding to $k_{max}$) and $\lambda_{max}$. They all have a common touch point at the origin because the crystal is kept stationary and the direction of incidence is hence fixed during data collection, see Fig. 2.37. Variation of $\lambda$ is performed by using white radiation, i.e., continuum Bremsstrahlung radiation of an X-ray tube or not monochromatized synchrotron radiation. The fraction of the reciprocal lattice filled by the shaded area then diffracts simultaneously.

### 2.4.5 High-Resolution Scans in the Reciprocal Space

X-ray diffractometers are widely employed for non-destructive structural analyses of crystalline samples. Epitaxial structures are usually characterized applying *high-resolution X-ray diffraction* (HRXRD). The large natural line width of the generally used $K_{\alpha 1}$ radiation ($\Delta\lambda/\lambda = 3 \times 10^{-4}$ for Cu) limits the resolution of a simple

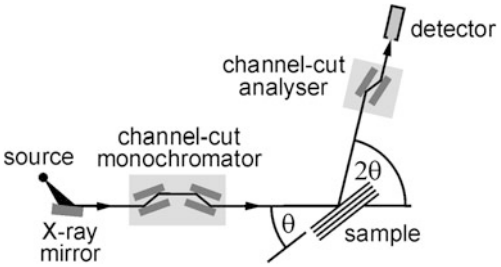


**Fig. 2.38** High-resolution X-ray diffractometer for structural analyses of heteroepitaxial structures. The studied sample is symbolized by its diffracting Bragg planes. These are not parallel to the sample surface in case of asymmetric reflections

single-crystal diffractometer to $\Delta\Theta/\Theta \cong 10^{-2}$. Furthermore, the close vicinity to the $K_{\alpha 2}$ line (1.5443 Å for Cu, with half the intensity of $K_{\alpha 1}$ at 1.5405 Å) complicates the analysis particularly for multilayer structures. In a modern HRXRD setup the incident X-ray radiation is therefore monochromized using Bragg reflections of a primary crystal (commonly a highly perfect Ge or Si crystal with a channel cut for multiple reflections). Such monochromator improves the resolution to typically $10^{-5}$. Often also a parabolic shaped multilayer mirror is used to convert the divergent radiation of the X-ray tube to an intense quasi-parallel beam. Such beam conditioning reduces the required measuring time significantly. A high-resolution X-ray setup is illustrated in Fig. 2.38.

The setup shown in Fig. 2.38 is also referred to as triple-axis diffractometer, the three rotation axes being the Bragg angles of the monochromator crystal, of the investigated sample, and of the analyzer crystal. Many other configurations of X-ray optics are used, depending on the required resolution. X-ray measurements are conveniently described in the reciprocal space illustrated in Fig. 2.36. Various types of scans are used to characterize or map a Bragg reflection. Commonly applied scan directions are depicted in Fig. 2.39.

The incident and diffracted wave vectors are denoted $\mathbf{k}_\mathrm{i}$ and $\mathbf{k}_\mathrm{f}$, respectively. Due to the elastic scattering their absolute values are equal and both given by the applied radiation wavelength, $k = 2\pi/\lambda$. The components of the diffraction vector $\Delta\mathbf{k} = \mathbf{k}_\mathrm{f} - \mathbf{k}_\mathrm{i}$ are

$$q_\parallel = k(\cos\alpha_\mathrm{f} - \cos\alpha_\mathrm{i}),$$
$$q_\perp = k(\sin\alpha_\mathrm{f} + \sin\alpha_\mathrm{i}).$$

In the X-ray diffractometer the angle of rotation of the sample surface is usually labeled $\omega$, and the angle of the detector rotation is labeled $2\Theta$. The goniometer angle $\omega$ represents the angle of incidence with respect to the sample surface $\alpha_\mathrm{i}$, and $2\Theta$ equals the sum of $\alpha_\mathrm{i}$ and the angle of the diffracted beam with respect to the sample surface $\alpha_\mathrm{f}$. The components of the diffraction vector are thus directly measured by scanning $\omega$ and $\Theta$.

In reciprocal space the $\omega - 2\Theta$ scan is oriented along the direction of the origin to the studied reciprocal-lattice point. The direction of $\Delta\mathbf{k}$ remains fixed, while the length changes. For such radial scan the sample is rotated by an amount $\Delta\omega$ and the detector is rotated by $\Delta 2\Theta = 2\Delta\omega$. In the case of a symmetric reflection, i.e., when the Bragg planes are parallel to the sample surface and $\alpha_i = \alpha_f$, the relation

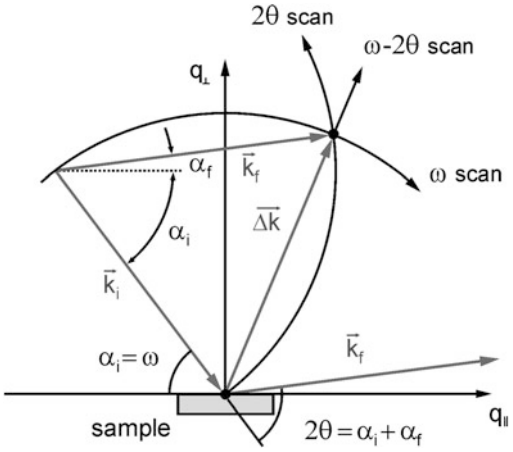


**Fig. 2.39** Scan directions in the reciprocal space commonly applied in high-resolution X-ray diffraction. $\mathbf{k}_i$ and $\mathbf{k}_f$ denote initial and final wave vectors of the monochromatic X-ray beams, respectively. Angles $\alpha$ represent angles of the incident and diffracted (final) beams with respect to the sample surface

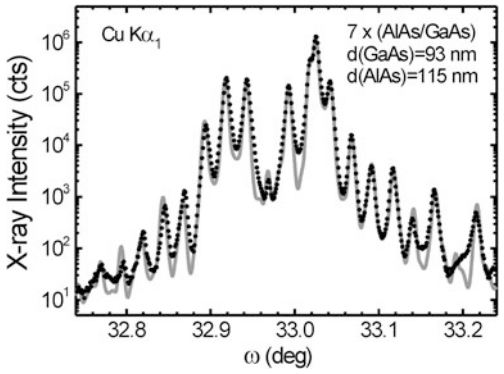


**Fig. 2.40** $\omega$ scan of the symmetric (004) reflection of a 7 period AlAs/GaAs superlattice structure grown on (001)-oriented GaAs. *Data points* and the *gray curve* are measured and simulated diffraction patterns, respectively

$\omega = 2\Theta/2$ applies. The diffraction vector $\Delta\mathbf{k}$ is then always normal to the surface as depicted in Fig. 2.36.

The $\omega$ scan traces a circle of radius $|\Delta\mathbf{k}|$ about the origin and is nearly oriented perpendicular to the $\omega - 2\Theta$ scan. The sample is rotated ('rocked') about the $\omega$ axis. The angle $2\Theta$ and hence the length of $\Delta\mathbf{k}$ remains fixed, while the direction of $\Delta\mathbf{k}$ changes. Usually no analyzer and no slit is attached to the detector for recording all intensity reflected from the sample. This scan is usually referred to as 'rocking curve' measurement, although also the $\omega - 2\Theta$ scan requires sample rotation.

The $2\Theta$ scan traces an arc on the Ewald sphere. The incident angle $\alpha_i$ and hence $\omega$ is kept fixed, and $\alpha_f$ is changed by varying the detector angle $2\Theta$. Both length and direction of the diffraction vector $\Delta\mathbf{k}$ change.

The $\omega$ scan is widely applied for the measurement of composition and layer thickness in coherent heterostructures. Data evaluation then applies Vegard's law (2.2a)–(2.2c) and a simulation of the intensity based on the dynamical theory of X-ray diffraction. In (001)-oriented structures of a cubic crystal system often the intense symmetric (004) reflection is used. A measured and simulated diffraction pattern of an AlAs/GaAs superlattice structure is shown in Fig. 2.40.

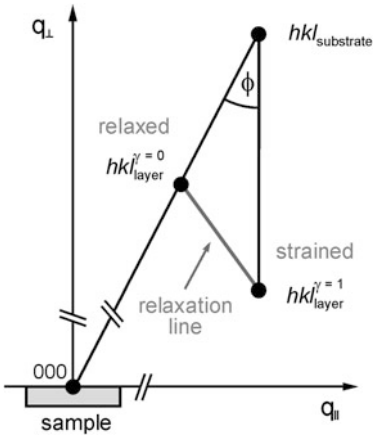


**Fig. 2.41** Positions of reciprocal-lattice points *hkl* of a fully strained ($\gamma = 1$) and fully relaxed ($\gamma = 0$) epitaxial layer

### *2.4.6 Reciprocal-Space Map*

The analysis of elastically relaxed heteroepitaxial structures requires the measurement of both, vertical and lateral lattice parameters. For the evaluation of lateral components asymmetric reflections must be used. Strain relief in the structure may be quite inhomogeneous as shown in Fig. 2.16. Furthermore, Bragg planes of an epitaxial structure may be tilted with respect to those of the substrate, and mosaicity of layers with tilted and twisted crystallites as illustrated in Sect. 2.3.7 may occur. The analysis of such imperfections is conveniently performed by combining a series of scans in reciprocal space to a map.

An analysis of the strain state in a partially relaxed epitaxial layer from reciprocal-space maps is illustrated in Figs. 2.41 and 2.42. For simplicity we assume an equal crystal structure for layer and substrate. Partial relaxation may be described by the relaxation parameter $\gamma$ (2.29) introduced in Sect. 2.2.8. The reflection $hkl_{\text{layer}}$ of a *coherently strained* pseudomorpic layer ($\gamma = 1$) has the same lateral component of the scattering vector as the corresponding reflection of the substrate, because the lateral lattice constant of the layer $a_\parallel$ adopts the value of the substrate $a_S$. In Fig. 2.41 a layer with a natural (unstrained) lattice constant $a_L$ larger than the substrate lattice constant $a_S$ is assumed. $hkl_{\text{layer}}$ therefore lies below $hkl_{\text{substrate}}$ in the reciprocal space map, i.e. at a *smaller* $q_\perp$ value. For a completely *relaxed* layer ($\gamma = 0$) the Bragg planes lie parallel to that of the substrate. Consequently the scattering vector $\Delta\mathbf{k}$ has the same direction for layer and substrate, i.e., $hkl_{\text{layer}}$ and $hkl_{\text{substrate}}$ lie on a common line starting at the reciprocal origin 000. Intermediate strain states of the layer lie on a *relaxation line* bounded by the points for $\gamma = 0$ and 1, cf. Fig. 2.41. This line is straight due to the assumed validity of Hook's law during the relaxation process.

The experimental result given in Fig. 2.42 represents a cut of the reciprocal space using the [110] axis of the cubic crystal lattice as azimuth reference:

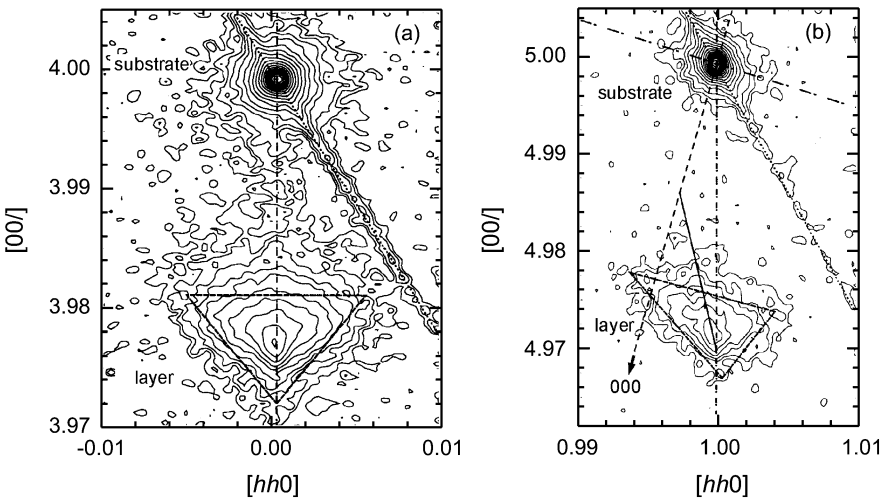


**Fig. 2.42** Reciprocal-space maps of the symmetrical (004) reflection (*left*) and the (115) reflection of a 310 nm thick epitaxial ZnSe layer on (001) GaAs substrate. *Contour lines* refer to scattered X-ray intensities on a logarithmic scale with steps of 0.2, coordinates are given in terms of non-integer Miller indices. The *straight line* in the *right* map indicates the relaxation line. The *dotted lines* in the maps indicate sections of Ewald spheres, the *streaks* along these lines are analyzer artefacts. Reproduced with permission from [72], © 1994 Elsevier

$q_{\parallel} = [hh0] \times \sqrt{2} a_S$, i.e., $h$ always equals $k$. The normal reference is $q_{\perp} = [00l] \times a_S$. The measurements show the scattered X-ray intensity near the (004) and (115) reflections of an epitaxial ZnSe layer on (001)-oriented GaAs substrate [72]. Both materials have zincblende structure.

The reciprocal-lattice points of the layer show a clear broadening with a non-circular shape indicated by triangles. The broadening along the *vertical* dash-dotted line (along the surface normal) demonstrates the coexistence of various strain states in the layer. Small $00l$ values refer to highly strained parts of the layer ($\gamma \to 1$), large values to relaxed parts. The distribution is asymmetric. Perpendicular to the scattering vector (i.e., the vertical line) another broadening mechanism originating from mosaicity occurs. The triangular shape of the reciprocal-lattice point indicates that this mosaicity is related to the strain state: small for large strains (lower triangle corner) and large for relaxed parts. The triangles referring to the (004) and (115) reflections are geometrically similar. The different shapes result from a transformation which depends on the inclination angle $\phi$ of the Bragg planes [72].

In the next example the mosaicity of an epitaxial layer is considered. Perturbations in the periodicity of the crystal lattice lead to incoherent scattering of X-rays and consequently to a broadening of reciprocal lattice points. From the broadening the average extension of coherently scattering regions in the crystal (i.e., regions free of defects) can be derived. The relation between this so-called coherence length $d$

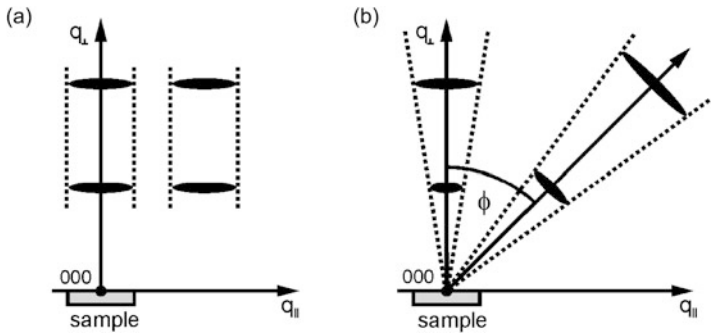


**Fig. 2.43** Scheme of broadened reciprocal-lattice points due to mosaicity in an epitaxial layer originating predominantly from (**a**) finite lateral coherence length and (**b**) tilts of mosaic blocks

and the broadening of a reciprocal lattice point due to the finite size of perfect crystallites is expressed by an equation formulated by P. Scherrer [73],

$$FWHM = \frac{K\lambda}{d \times \cos\Theta}. \tag{2.50}$$

In the *Scherrer equation* (2.50) *FWHM* denotes the full width at half maximum of an X-ray reflection scattered from crystallites with average dimension $d$, and $K$ is the Scherrer constant. $K$ is of order unity and usually put to 0.9 for a Gaussian function of the reflection shape. $\lambda$ and $\Theta$ are the X-ray wavelength and the Bragg angle, respectively. In addition to finite size effects in lateral and vertical direction expressed by Scherrer's formula mutual tilts and twists of the small crystalline blocks building the mosaic of a real crystal (Sect. 2.3.7) contribute to the broadening of reciprocal lattice points. The action of tilts differs from that of a finite size as illustrated in Fig. 2.43.

Finite sizes of mosaic blocks along the lateral and vertical directions lead to broadenings along $q_\parallel$ and $q_\perp$, respectively. This holds for symmetric and asymmetric reflections of any order in the same way as illustrated in Fig. 2.43a for a limited lateral size. Tilts induce a broadening which linearly increases with the order of the reflection. In symmetric reflections the superimposed broadening contributions due to lateral finite size and tilt can be separated by plotting the *FWHM* of rocking curves over the respective reflection order, yielding the tilt from the slope and the lateral coherence length from the inverse of the ordinate interception-point. Asymmetric reflections are broadened by pure tilts along an axis inclined by the angle $\phi$ which represents the angle between the diffracting Bragg planes and the sample surface. Superimposed finite size effects modify the angle.

Twists lead to a broadening of reciprocal lattice points in the plane spanned by $q_\parallel$ and a second independent lateral direction. An evaluation can be obtained from grazing incidence diffraction which uses scattering from Bragg planes lying perpendicular to the sample surface or from measuring the edge of the sample.

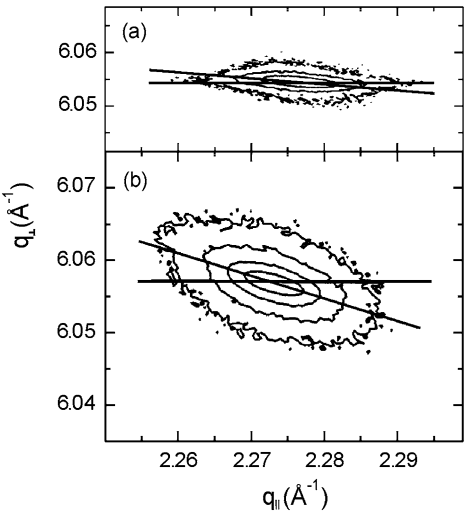


**Fig. 2.44** Reciprocal-space maps of the asymmetric (10.5) reflection of GaN layers with (**a**) 350 nm and (**b**) 4200 nm mosaic grains, epitaxially grown on (0001) sapphire substrate. *Contour lines* refer to equal X-ray intensities. Reproduced with permission from [74], © 2003 AIP

The effect of finite mosaic grain size and tilt on asymmetric reflections is illustrated in Fig. 2.44. The reciprocal-space maps show (10.5) reflections of wurtzite GaN grown on basal-plane sapphire [74]. The large lattice mismatch leads to very high dislocation densities in the range of typically $10^9$ cm$^{-2}$. The measured reflections have nearly elliptical shape with an inclination of the main axis with respect to the azimuth. The angle depends on the average size of mosaic grains in the epitaxial layer. Small angles are due to a dominant effect of lateral finite size. Pure tilts reproduce the inclination $\phi$ with respect to the surface (20.5° for the given reflection).

## 2.5 Problems Chap. 2

2.1 The stable modification of GaN is the wurtzite ($\alpha$) structure. Epitaxial layers can also be grown in the metastable cubic zincblende ($\beta$) structure.
   (a) Determine the lattice mismatch $f$ of $\beta$-GaN on (001)-oriented zincblende GaAs at room temperature.
   (b) Find a suitable ratio of small integers for a coincidence lattice and determine the respective coincidence-lattice mismatch.
   (c) On (111)-oriented GaAs the GaN layer tends to grow in the $\alpha$ phase. What is the wurtzite $a$ lattice parameter of the GaAs(111) plane? Prove that the lattice mismatch of $\alpha$-GaN/GaAs(111) is similar to that of $\beta$-GaN/GaAs(001), if $\alpha$-GaN is assumed to have the same bond length as $\beta$-GaN.

2.2 GaN is grown on various substrates due to a lack of well lattice-matched materials.
   (a) Calculate the lattice mismatch for growth on the most commonly used basal-plane sapphire $Al_2O_3$ in case of an epitaxial relation

$[0001]_{GaN} \parallel [0001]_{Al_2O_3}$ and $[1000]_{GaN} \parallel [1000]_{Al_2O_3}$ (i.e., $a$ and $c$ axes of substrate and layer are parallel). Compare this value to that often derived from the alterative definition $f_{alternative1}$ given in the text. The lattice parameters of $Al_2O_3$ are $a_{Al_2O_3} = 4.758$ Å, $c_{Al_2O_3} = 12.991$ Å.

(b) The $a$ axes of the GaN layer are actually rotated by 30° about the $c$ axis, yielding the relation $[1000]_{GaN} \parallel [1\,-100]_{Al_2O_3}$ (cf. figure below). What is the lattice mismatch for this epitaxial relation?

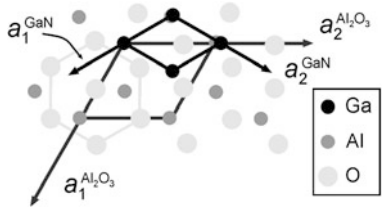


(c) The growth of $m$-plane wurtzite GaN (with a nonpolar surface) is often performed on $\gamma$-$LiAlO_2$, which has a tetragonal structure with lattice parameters $a = b = 5.169$ Å and $c = 6.268$ Å. Compute the lattice mismatch of the two edges of the GaN $m$-plane aligned along the two different axes of $\gamma$-$LiAlO_2$, when every second Ga atom along the $a$ axis of the GaN sublattice matches an Al atom along the $c$ axis of the $\gamma$-$LiAlO_2$ sublattice.

(d) An alternative $m$-plane substrate for $m$-plane wurtzite GaN is the readily available 6H-SiC polytype with $ABCABC$ stacking order. What is the lattice mismatch for an equal orientation of the unit cells? It should be noted that the GaN layers tend to grow in a 2H sequence and only partially adopt the 6H sequence (in contrast to AlN layers), yielding a high density of stacking faults.

2.3 (a) How does the Al composition parameter $x$ in the quaternary compound $Al_xGa_yIn_{1-x-y}As$ depend on the Ga composition parameter $y$ for a layer lattice-matched to InP according Vegard's law?

(b) What are the maximum of the Ga composition parameter $y$ and the maximum of the Al composition parameter $x$?

(c) Write the relation for a quaternary AlGaInAs layer lattice-matched to InP in terms of two ternary alloys $X_z$ and $Y_{z-1}$ which are both lattice-matched to InP.

2.4 Apply in the following problem *linear* expansion coefficients (which actually underestimate the thermal expansion at higher temperatures) and a linearly weighted quantity for the alloy.

(a) Calculate the lattice mismatch $f$ of a ZnS layer on Si substrate at a growth temperature of 360 °C.

(b) Determine the composition parameter $x$ of a $ZnS_{1-x}Se_x$ layer for lattice-matched conditions on Si at growth temperature.

(c) Calculate the thermally induced lateral strain of the $ZnS_{1-x}Se_x$ layer after cooling the lattice-matched $ZnS_{1-x}Se_x$ layer of (b) from 360 °C to room temperature (23 °C).

(d) Which composition parameter $x$ produces a strain-free $ZnS_{1-x}Se_x$ layer *at room temperature* for growth at 360 °C? How large is then the mismatch at growth temperature?

2.5 Consider a pseudomorphic ZnSe layer on (001)-oriented GaAs substrate at room temperature.

(a) Determine the strain of the ZnSe layer perpendicular to the interface.

(b) Calculate the relative change of the unit-cell volume induced by the strain.

(c) The strain in the layer changes the distance $d_{hkl}$ between nearest lattice planes. In crystal systems with orthogonal axes and lattice vectors of lengths $a$, $b$, and $c$ the distance can be expressed by $d_{hkl} = ((h/a)^2 + (k/b)^2 + (l/c)^2)^{-1/2}$. Use this relation to calculate the distances between nearest (111) planes in unstrained ZnSe and the pseudomorphically strained ZnSe/GaAs layer. Relate the factor $\sqrt{3}$ in the unstrained material to the stacking sequence of the zincblende structure.

(d) Express the thickness of a 285 Å thick layer in units of monolayers.

(e) Calculate the strain energy per unit area of a 285 Å thick layer. Which strain energy per unit area has a 114 nm thick layer?

(f) Which strain energy is stored in one unit cell of the pseudomorpic ZnSe layer?

2.6 The strain in pseudomorphic lattice-mismatched layers is sometimes compensated by inserting additional layers with opposite lattice mismatch, yielding layer stacks which are *in total* lattice-matched to a substrate.

(a) Determine the thickness of an $In_{0.15}Ga_{0.85}As$ layer, which is to be pseudomorphically grown on a 1 monolayer thick (001)-oriented GaP layer to obtain a total lateral lattice constant coinciding with that of GaAs. How many monolayers of $In_{0.15}Ga_{0.85}As$ correspond to this thickness? The stiffness coefficients of GaP are $C_{11} = 141$ GPa, $C_{12} = 62$ GPa; use a linearly weighted shear modulus for the $In_{0.15}Ga_{0.85}As$ layer determined similar to the unstrained lattice parameter of this layer.

(b) The strain in a pseudomorphic superlattice with 10 $In_xGa_{1-x}As$ quantum wells separated by GaAs barriers is to be compensated by the additional insertion of a counteracting $GaAs_{1-y}P_y$ layer into the center of each of these barriers. The entire layer stack of the strain-compensated superlattice should adopt the same lateral lattice parameter as the (001)-oriented GaAs substrate. Calculate the composition parameter $y$ for the case that in each of the 20 nm thick barrier layers 12 nm of GaAs is replaced by $GaAs_{1-y}P_y$. The quantum wells have a thickness of 10 nm and a composition of 22 % indium. Apply a linearly weighted shear modulus for the wells, but approximate the value for the barriers by that of GaAs (check if such simplification is justified).

2.7 Determine the energy per unit length for the following perfect misfit dislocations in GaAs within a radius of 300 nm around the dislocation line. A single dislocation with a dislocation-core radius of $\frac{1}{3}$ of the Burgers vector is assumed.
(a) Pure screw dislocation.
(b) Pure edge dislocation.
(c) 60° dislocation.

2.8 The composition parameter $x$ of a (001)-oriented alloy layer $A_xB_{1-x}$ with diamond structure was approximately adjusted for achieving lattice matching to a substrate with lattice parameter $a_S = 5.5$ Å, yielding a misfit $f = 10^{-3}$.
(a) Estimate the critical thickness for the introduction of 60° misfit dislocations for a Poisson ratio of the layer $\nu = 0.25$, using the graphical result given in the text.
(b) By which factor changes the layer thickness for $\nu = 0.35$?
(c) Which misfit must be achieved for extending the critical layer thickness by a factor of 5 for a Poisson ratio $\nu = 0.25$?

2.9 A ZnSe/GaAs(001) layer is characterized by X-ray diffraction using $CuK_{\alpha 1}$ radiation.
(a) Calculate the separation between the Bragg angles for the (004) reflections of the substrate and the layer for a completely relaxed layer and a pseudomorphically strained layer.
(b) Repeat (a) for the asymmetric (115) reflection.
(c) The intensity of the scattered radiation is largely determined by the square of the structure factor. Calculate the approximate intensity ratio $I(004)/I(115)$ of the two reflections, if the ratio of the atomic scattering factors $f_{Se}/f_{Zn} = 1.17$.

2.10 An $In_xGa_{1-x}N$ layer is to be grown lattice-matched on the basal plane of a ZnO substrate.
(a) Find the In composition $x_1$ and the Bragg angle of the (00.2) reflection of a lattice-matched $In_xGa_{1-x}N$ layer for $CuK_{\alpha 1}$ radiation.
(b) Calculate the In composition $x_2$ of a *relaxed* (not lattice-matched) $In_xGa_{1-x}N$ layer producing the (00.2) reflection at a Bragg angle 400 sec below the value of a lattice-matched layer. Compare this value to the composition $x_3$ of a *pseudomorphic* $In_xGa_{1-x}N$ layer, whose (00.2) reflection appears at the same Bragg angle (find $x_3$ by using $x_2$ and interpolation; use for simplicity elastic constants of pure GaN).

## 2.6 General Reading Chap. 2

J.F. Nye, *Physical Properties of Crystals* (Clarendon Press, Oxford, 1972)
A.S. Saada, *Elasticity Theory and Applications* (Pergamon Press, New York, 1974)
J.P. Hirth, J. Lothe, *Theory of Dislocations*, 2nd edn. (Wiley, New York, 1982)
D. Hull, D.J. Bacon, *Introduction to Dislocations*, 4th edn. (Butterworth-Heinemann, Oxford, 2001)

S. Amelinckx, Dislocations in particular structures, in *Dislocations in Solids*, vol. 2, ed. by F.R.N. Nabarro (North-Holland, Amsterdam, 1979)
J.E. Ayers, *Heteroepitaxy of Semiconductors: Theory, Growth, and Characterization* (CRC Press, Boca Raton, 2007)

## References

1. C.-Y. Yeh, Z.W. Lu, S. Froyen, A. Zunger, Zinc-blende–wurtzite polytypism in semiconductors. Phys. Rev. B **46**, 10086 (1992)
2. O. Ambacher, J. Smart, J.R. Shealy, N.G. Weimann, K. Chu, M. Murphy, W.J. Schaff, L.F. Eastman, R. Dimitrov, L. Wittmer, M. Stutzmann, W. Rieger, J. Hilsenbeck, Two-dimensional electron gases induced by spontaneous and piezoelectric polarization charges in N- and Ga-face AlGaN/GaN heterostructures. J. Appl. Phys. **85**, 3222 (1999)
3. H. Ibach, Thermal expansion of silicon and zinc oxide. Phys. Status Solidi **31**, 625 (1969)
4. K. Haruna, H. Maeta, K. Ohashi, T. Koike, The negative thermal expansion coefficient of GaP crystal at low temperatures. J. Phys. C **19**, 5149 (1986)
5. J.St. John, A.N. Bloch, Quantum-defect electronegativity scale for nontransition elements. Phys. Rev. Lett. **33**, 1095 (1974)
6. J.R. Chelikowsky, J.C. Phillips, Quantum-defect theory of heats of formation and structural transition energies of liquid and solid simple metal alloys and compounds. Phys. Rev. B **17**, 2453 (1978)
7. S.B. Zhang, M.L. Marvin, Determination of $AB$ crystal structures from atomic properties. Phys. Rev. B **39**, 1077 (1989)
8. P. Villars, K. Mathis, F. Hulliger, Environment classification and structural stability maps, in *The Structure of Binary Compounds*, ed. by F.R. de Boer, D.G. Pettifor (North-Holland, Amsterdam, 1989)
9. O. Madelung (ed.), *Semiconductors—Basic Data*, 2nd revised edn. (Springer, Berlin, 1996)
10. G.L. Harris (ed.), *Properties of Silicon Carbide*. EMIS Datareview Series, vol. 13 (INSPEC, London, 1995)
11. J.H. Edgar (ed.), *Properties of Group III Nitrides*. EMIS Datareview Series, vol. 11 (INSPEC, London, 1994)
12. L. Vegard, Die Konstitution der Mischkristalle und die Raumfüllung der Atome. Z. Phys. **5**, 17 (1921) (in German)
13. M.F. Thorpe, E.J. Garboczi, Elastic properties of central-force networks with bond-length mismatch. Phys. Rev. B **42**, 8405 (1990)
14. W.B. Pearson, *A Handbook of Lattice Spacing and Structures of Metals and Alloys*, vol. 1 (Pergamon Press, London, 1958)
15. D.R. Yoder-Short, U. Debska, J.K. Furdyna, Lattice parameters of $Zn_{1-x}Mn_xSe$ and tetrahedral bond lengths in $A^{II}_{1-x}Mn_xB^{VI}$ alloys. J. Appl. Phys. **58**, 4056 (1985)
16. J.C. Mikkelsen Jr., J.B. Boyce, Extended X-ray absorption fine-structure study of $Ga_{1-x}In_xAs$ random solid solutions. Phys. Rev. B **28**, 7130 (1983)
17. A. Balzarotti, N. Motta, A. Kisiel, M. Zimnal-Starnawska, M.T. Czyzyk, Model of the local structure of random ternary alloys: experiment versus theory. Phys. Rev. B **31**, 7526 (1985)
18. J.L. Martins, A. Zunger, Bond lengths around isovalent impurities and in semiconductor solid solutions. Phys. Rev. B **30**, 6217 (1984)
19. J.C. Mikkelsen Jr., J.B. Boyce, Atomic scale structure of random solid solutions: extended X-ray absorption fine-structure study of $Ga_{1-x}In_xAs$. Phys. Rev. Lett. **49**, 1412 (1982)
20. T. Fukui, Atomic structure model for $Ga_{1-x}In_xAs$ solid solutions. J. Appl. Phys. **57**, 5188 (1985)
21. J.F. Nye, *Physical Properties of Crystals* (Clarendon Press, Oxford, 1972)
22. A.S. Saada, *Elasticity Theory and Applications* (Pergamon Press, New York, 1974)

23. D.J. Dunstan, Strain and strain relaxation in semiconductors. J. Mater. Sci., Mater. Electron. **8**, 337 (1997)
24. K.-H. Hellwege, A.M. Hellwege, *Landolt-Börnstein New Series Group III, vol. 2, Elastic, Piezoelectric, Piezooptic, Electrooptic Constants, and Nonlinear Dielectric Susceptibilities of Crystals*, 6th edn. (Springer, Berlin, 1966)
25. K.-H. Hellwege, A.M. Hellwege, *Landolt-Börnstein New Series Group III, vol. 1, Elastic, Piezoelectric, Piezooptic and Electrooptic Constants of Crystals*, 6th edn. (Springer, Berlin, 1966)
26. I. Vurgaftman, J.R. Meyer, L.R. Ram-Mohan, Band parameters for III–V compound semiconductors and their alloys. J. Appl. Phys. **89**, 5815 (2001)
27. G. Carlotti, D. Fioretto, G. Socino, E. Verona, Brillouin scattering determination of the whole set of elastic constants of a single transparent film of hexagonal symmetry. J. Phys. Condens. Matter **7**, 9147 (1995)
28. R.S. Lakes, Foam structures with a negative Poisson's ratio. Science **235**, 1038 (1987)
29. A. Ballato, Poisson's ratio for tetragonal, hexagonal, and cubic crystals. IEEE Trans. Ultrason. Ferroelectr. Freq. Control **43**, 56 (1996)
30. C.G. Van de Walle, R.M. Martin, Theoretical calculation of heterojunction discontinuities in the Si/Ge system. Phys. Rev. B **34**, 5621 (1986)
31. L. Kleinman, Deformation potentials in silicon. I. Uniaxial strain. Phys. Rev. **128**, 2614 (1962)
32. O.H. Nielsen, R.M. Martin, Stress in semiconductors: *ab initio* calculations on Si, Ge, and GaAs. Phys. Rev. B **32**, 3792 (1985)
33. W.A. Jesser, D. Kuhlmann-Wilsdorf, On the theory of interfacial energy and elastic strain of epitaxial overgrowth in parallel alignment on single crystal substrates. Phys. Status Solidi **19**, 95 (1967)
34. F.C. Frank, J.H. van der Merve, Proc. R. Soc. Lond. A **198**, 205 (1949)
35. F.C. Frank, J.H. van der Merve, Proc. R. Soc. Lond. A **198**, 216 (1949)
36. F.C. Frank, J.H. van der Merve, Proc. R. Soc. Lond. A **200**, 125 (1949)
37. J.H. Van der Merve, Crystal interfaces. Part I. Semi-infinite crystals. J. Appl. Phys. **34**, 117 (1963)
38. J.H. Van der Merve, C.A.B. Ball, Energy of interfaces between crystals, in *Epitaxial Growth. Part B*, ed. by J.W. Matthews (Academic Press, New York, 1975), pp. 493–528
39. C.A.B. Ball, J.H. Van der Merve, The growth of dislocation-free layers, in *Dislocations in Solids*, vol. 6, ed. by F.R.N. Nabarro (North-Holland, Amsterdam, 1983)
40. W.A. Jesser, J.H. Van der Merve, An exactly solvable model for calculating critical misfit and thickness in epitaxial superlattices. II. Layers of unequal elastic constants and thicknesses. J. Appl. Phys. **63**, 1928 (1988)
41. J.W. Matthews, A.E. Blakeslee, Defects in epitaxial multilayers I. Misfit dislocations. J. Cryst. Growth **27**, 118 (1974)
42. J.W. Matthews, S. Mader, T.B. Light, Accommodation of misfit across the interface between crystals of semiconducting elements or compounds. J. Appl. Phys. **41**, 3800 (1970)
43. C.A.B. Ball, On bonding and structure of epitaxial bicrystals. Phys. Status Solidi **42**, 357 (1970)
44. R. Beanland, D.J. Dunstan, P.J. Goodhew, Plasic relaxation and relaxed buffer layers for semiconductor epitaxy. Adv. Phys. **45**, 87 (1996)
45. I. Akasaki, H. Amano, Y. Koide, K. Hiramatsu, N. Sawaki, Effects of a buffer layer on crystallographic structure and on electrical and optical properties of GaN and $Ga_{1-x}Al_xN$ ($0 < x = 0.4$) films grown on sapphire substrate by MOVPE. J. Cryst. Growth **98**, 209 (1989)
46. J.N. Kuznia, M. Asif Khan, D.T. Olson, R. Kaplan, J. Freitas, Influence of buffer layers on the deposition of high quality single crystal GaN over sapphire substrates. J. Appl. Phys. **73**, 4700 (1993)
47. R.C. Powell, N.-E. Lee, Y.-W. Kim, J.E. Greene, Heteroepitaxial wurtzite and zincblende structure GaN grown by reactive-ion molecular-beam epitaxy: growth kinetics, microstructure, and properties. J. Appl. Phys. **73**, 189 (1993)

48. P. Kung, C.J. Sun, A. Saxler, H. Ohsato, M. Razeghi, Crystallography of epitaxial growth of wurtzite-type thin films on sapphire substrates. J. Appl. Phys. **75**, 4515 (1994)
49. A. Zur, T.C. McGill, Lattice match: an application to heteroepitaxy. J. Appl. Phys. **55**, 378 (1984)
50. R.W. McClelland, C.O. Bozler, J.C.C. Fan, A technique for producing epitaxial films on reusable substrates. Appl. Phys. Lett. **37**, 560 (1980)
51. B.Y. Tsaur, R.W. McClelland, J.C.C. Fan, R.P. Gale, J.P. Salerno, B.A. Vojak, C.O. Bozler, Low-dislocation-density GaAs epilayers grown on Ge-coated Si substrates by means of lateral epitaxial overgrowth. Appl. Phys. Lett. **41**, 347 (1982)
52. S. Zhang, T. Nishinaga, LPE lateral overgrowth of GaP. Jpn. J. Appl. Phys. **29**, 545 (1990)
53. J.A. Smart, E.M. Chumbes, A.T. Schremer, J.R. Shealy, Single step process for epitaxial lateral overgrowth of GaN on SiC and sapphire substrates. Appl. Phys. Lett. **75**, 3820 (1999)
54. P. Gibart, Metal organic vapour phase epitaxy of GaN and lateral overgrowth. Rep. Prog. Phys. **67**, 667 (2004)
55. Y.H. Lo, New approach to grow pseudomorphic structures over the critical thickness. Appl. Phys. Lett. **59**, 2311 (1991)
56. D. Teng, Y.H. Lo, Dynamic model for pseudomorphic structures grown on compliant substrates: an approach to extend the critical thickness. Appl. Phys. Lett. **62**, 43 (1993)
57. W.A. Jesser, J.H. van der Merve, P.M. Stoop, Misfit accommodation by compliant substrates. J. Appl. Phys. **85**, 2129 (1999)
58. K. Vanhollebeke, I. Moerman, P. Van Daele, P. Demeester, Compliant substrate technology: integration of mismatched materials for opto-electronic applications. Prog. Cryst. Growth Charact. Mater. **41**, 1 (2000)
59. J.E. Ayers, Compliant substrates for heteroepitaxial semiconductor devices: theory, experiment, and current directions. J. Electron. Mater. **37**, 1151 (2008)
60. S. Bauer, A. Rosenauer, P. Link, W. Kuhn, J. Zweck, W. Gebhardt, Misfit dislocations in epitaxial ZnTe/GaAs (001) studied by HRTEM. Ultramicroscopy **51**, 221 (1993)
61. G. Kudlek, N. Presser, U.W. Pohl, J. Gutowski, J. Lilja, E. Kuusisto, K. Imai, M. Pessa, K. Hingerl, H. Sitter, Exciton complexes in ZnSe layers: a tool for probing the strain distribution. J. Cryst. Growth **117**, 309 (1992)
62. G. Kudlek, Struktur und Dynamik exzitonischer Komplexe in verspannten ZnSe- und ZnTe-Heteroschichten, PhD Thesis, Technische Universität Berlin, D83, Berlin, 1992 (in German)
63. J.P. Hirth, J. Lothe, *Theory of Dislocations*, 2nd edn. (Wiley, New York, 1982)
64. S. Amelinckx, Dislocations in particular structures, in *Dislocations in Solids*, vol. 2, ed. by F.R.N. Nabarro (North-Holland, Amsterdam, 1979)
65. P.M. Marée, J.C. Barbour, J.F. Van der Veen, K.L. Kavanagh, C.W.T. Bulle-Lieuwma, M.P.A. Viegers, Generation of misfit dislocations in semiconductors. J. Appl. Phys. **62**, 4413 (1987)
66. N. Thompson, Dislocation nodes in face-centred cubic lattices. Proc. Phys. Soc. B **66**, 481 (1953)
67. M. Inoue, K. Suzuki, H. Amasuga, M. Nakamura, Y. Mera, S. Takeuchi, K. Maeda, Reliable image processing that can extract an atomically-resolved line shape of partial dislocations in semiconductors from plan-view high-resolution electron microscopic images. Ultramicroscopy **75**, 5 (1998)
68. H.P.D. Schenk, G.D. Kipshidze, U. Kaiser, A. Fissel, J. Kräußlich, J. Schulze, Wo. Richter, Investigation of two-dimensional growth of AlN(0001) on Si(111) by plasma-assisted molecular beam epitaxy. J. Cryst. Growth **200**, 45 (1999)
69. A. Berghezan, A. Fourdeux, S. Amelinckx, Transmission electron microscopy studies of dislocations and stacking faults in a hexagonal metal-zinc. Acta Met. **9**, 464 (1961)
70. S. Vézian, J. Massies, F. Semond, N. Grandjean, P. Vennéguès, In situ imaging of threading dislocation terminations at the surface of GaN(0001) epitaxialy grown on Si(111). Phys. Rev. B **61**, 7618 (2000)
71. A.R. Smith, V. Ramachandran, R.M. Feenstra, D.W. Grewe, M.-S. Shin, M. Skowronski, J. Neugebauer, J.E. Northrup, Wurtzite GaN surface structures studied by scanning tunnel-

ing microscopy and reflection high energy electron diffraction. J. Vac. Sci. Technol. A **16**, 1641 (1998)
72. H. Heinke, M.O. Möller, D. Hommel, G. Landwehr, Relaxation and mosaicity profiles in epitaxial layers studied by high resolution X-ray diffraction. J. Cryst. Growth **135**, 41 (1994)
73. P. Scherrer, Bestimmung der Grösse und der inneren Struktur von Kolloidteilchen mittels Röntgenstrahlen. Nachr. Ges. Wiss. Gött. **26**, 98 (1918) (in German)
74. R. Chierchia, T. Böttcher, H. Heinke, S. Einfeldt, S. Figge, D. Hommel, Microstructure of heteroepitaxial GaN revealed by high resolution X-ray diffraction. J. Appl. Phys. **93**, 8918 (2003)

# Chapter 3
# Electronic Properties of Heterostructures

**Abstract** This chapter presents electronic properties of a junction between two semiconductors and electronic states in low-dimensional structures. First, we consider the valence and conduction bands of zincblende and wurtzite bulk semiconductors and illustrate the effects of strain and alloying. Then, models describing the band lineup of heterostructures are introduced and the effect of interface stoichiometry is illustrated. The characteristic scale for the occurrence of size quantization is discussed, and electronic states in quantum wells, quantum wires, and quantum dots are described.

## 3.1 Bulk Properties

A heterostructure is formed by a junction between two dissimilar solids. Before considering the electronic properties of such interface in more detail (Sect. 3.2) we briefly compile some electronic properties of a single constituent. We focus on the uppermost valence bands and the fundamental bandgap of bulk crystals with zincblende or wurtzite structure. Bulk denotes a size well above the limit of size-quantization effects (Sect. 3.3.2). In this sense a 100 nm thick epitaxial layer may be considered as a bulk crystal.

### *3.1.1 Electronic Bands of Zincblende and Wurtzite Crystals*

Energy bands in semiconductors may fittingly be described using the effective mass approximation in the framework of a multiband **kp** method, which requires only a small set of experimentally determined parameters [cf., e.g., Ref. [1]]. Tetrahedrally coordinated crystals with zincblende or wurtzite structure form three $p$-like valence bands and an $s$-like conduction band, leading to an 8 band **kp** Hamilton operator (4 bands $\times 2$ spin orientations) with terms linear and quadratic in $k$. The valence dispersions comprise bands for the heavy hole, the light hole, and the split-off hole (zincblende) or crystal hole (wurtzite). The effective mass $m^*$ at the edges of valence

U.W. Pohl, *Epitaxy of Semiconductors*, Graduate Texts in Physics,
DOI 10.1007/978-3-642-32970-8_3, 

and conduction bands near the center of the Brillouin zone is generally a tensor. Its components $m^*_{ij}$ are related to the energy dispersion $E(\mathbf{k})$ according

$$m^*_{ij} = \hbar^2 \left( \frac{\partial^2}{\partial k_i \partial k_j} E(\mathbf{k})|_{k_i, k_j = 0} \right)^{-1}. \tag{3.1}$$

In *zincblende semiconductors* the anisotropic effective mass of the heavy hole is usually expressed in terms of band parameters $A$, $B$, $C$, or the related Luttinger (or: Kohn-Luttinger) parameters $\gamma_1$, $\gamma_2$, $\gamma_3$. We apply the widely used Luttinger parameters, yielding along the different crystallographic directions for the effective heavy-hole mass the relations

$$\begin{aligned} \left(\frac{m_0}{m^*_{\mathrm{hh}}}\right)^{[100]} &= \gamma_1 - 2\gamma_2, \qquad \left(\frac{m_0}{m^*_{\mathrm{hh}}}\right)^{[110]} = \frac{1}{2}(2\gamma_1 - \gamma_2 - 3\gamma_3), \\ \left(\frac{m_0}{m^*_{\mathrm{hh}}}\right)^{[111]} &= \gamma_1 - 2\gamma_3. \end{aligned} \tag{3.2a}$$

The corresponding effective light-hole mass is given by similar relations,

$$\begin{aligned} \left(\frac{m_0}{m^*_{\mathrm{lh}}}\right)^{[100]} &= \gamma_1 + 2\gamma_2, \qquad \left(\frac{m_0}{m^*_{\mathrm{lh}}}\right)^{[110]} = \frac{1}{2}(2\gamma_1 + \gamma_2 + 3\gamma_3), \\ \left(\frac{m_0}{m^*_{\mathrm{lh}}}\right)^{[111]} &= \gamma_1 + 2\gamma_3. \end{aligned} \tag{3.2b}$$

The split-off hole mass is given by

$$\frac{m_0}{m^*_{\mathrm{so}}} = \gamma_1 - \frac{E_P \Delta_0}{3E_{\mathrm{g}}(E_P + \Delta_0)}, \tag{3.2c}$$

where $E_P$ is the momentum matrix-element between the $p$-like valence bands and the $s$-like conduction band. $E_{\mathrm{g}}$ and $\Delta_0$ are the direct bandgap energy and the spin-orbit splitting, respectively. Parameters for some technologically important zincblende semiconductors are given in [2]. The 8 band **kp** approximation provides a good description up to about a quarter of the way from the center to the boundary of the Brillouin zone. Additional bands may be included to improve the description or to describe also indirect-bandgap semiconductors.

The valence-band structure near the center of the Brillouin zone ($\Gamma$ point at $k = 0$) for a typical zincblende semiconductor (GaAs) is shown in Fig. 3.1a. The bands of heavy hole and light hole are degenerated at $k = 0$ in absence of symmetry-reducing strain. Away from the $\Gamma$ point non-parabolicity occurs due to an anti-crossing behavior of these holes with the split-off hole, which lies below the other two bands at $k = 0$ by the amount of the spin-orbit energy $\Delta_0$.

Crystals with *wurtzite structure* have a different dispersion in the basal plane and perpendicular, i.e., along the $c$ axis parallel [0001]. The valence band-structure of a typical wurtzite semiconductor (GaN) near $k = 0$ is shown in Fig. 3.1b. The degeneracy of the valence bands is lifted at the $\Gamma$ point. The splittings between heavy hole and light hole, and that between heavy hole and crystal hole essentially

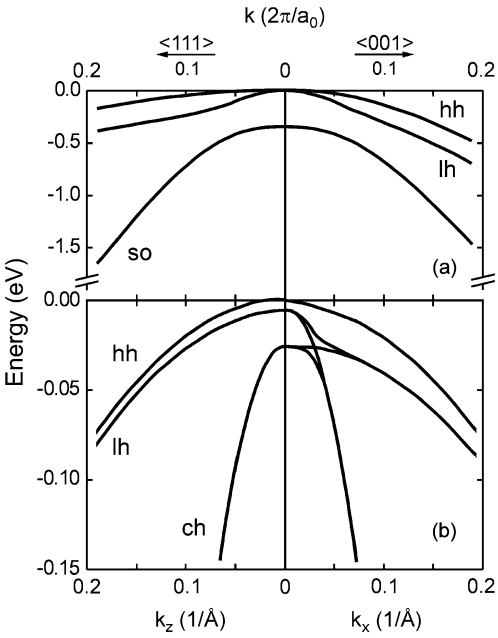


**Fig. 3.1** Valence-band structure of (**a**) a zincblende and (**b**) a wurtzite semiconductor near the center of the Brillouin zone. The labels *hh*, *lh*, *so*, and *ch* denote valence bands of heavy hole, light hole, split-off hole, and crystal hole, respectively

reflect the effects of spin-orbit and crystal-field interactions, respectively. A set of seven Luttinger-like parameters which accounts for the non-cubic symmetry was introduced to describe the bands of wurtzite semiconductors [3].

### *3.1.2 Strain Effects*

Virtually any heteroepitaxial structure is strained as pointed out in Sect. 2.2. Strain and the related atomic positions are determined by minimizing the elastic energy, under the constraint of a common lattice constant parallel to the interface $a_\parallel$ throughout the structure for pseudomorphic conditions. The resulting strain described by (2.13) to (2.19a)–(2.19c) affects the energy of the electronic bands. We first focus on *zincblende* semiconductors and consider wurtzite structures at the end of this section. Shear components of the strain lead to a splitting of degenerate cubic valence bands and indirect conduction bands, but they do not affect the *average* valence-band energy $E_{\mathrm{v,av}}$. The hydrostatic component of the strain changes the volume and leads to a shift of the bands with respect to $E_{\mathrm{v,av}}$ and also affects the average electrostatic potential itself.

The effect of strain in cubic semiconductors is expressed in terms of deformation potentials $a$, $b$, and $d$ [4, 5]. The total effect of hydrostatic strain on the valence band is described by the hydrostatic deformation potential $a_{\mathrm{v}}$ for the valence band,

$$a_{\mathrm{v}} = \frac{dE_{\mathrm{v,av}}}{d\ln V} = \frac{dE_{\mathrm{v,av}}}{\frac{1}{V}dV}. \tag{3.3}$$

The quantity $a_v$ expresses the shift of the average valence-band energy $E_{v,av}$ per relative change of the volume $V$. A similar relation applies for the shift of the conduction-band energy $E_c$ under the action of hydrostatic pressure, with $a_v$ and $E_{v,av}$ in (3.3) being replaced by the deformation potential of the conduction band $a_c$ and $E_c$, respectively. Consequently the change of the gap energy $E_c - E_{v,av}$ is also given by such a relation with a deformation potential $a$, which is equal to $a = a_c - a_v$. It must be noted that also another sign convention is widely used for $a_v$, yielding $a = a_c + a_v$. Furthermore, different conventions of the quantities $b$ and $d$ are used. They yield $d' = \sqrt{3}/2 \times d$ for trigonal distortions and refer to a term proportional $(J_x^2 \varepsilon_{xx} + \text{c.p.})$ instead of $((J_x^2 - 1/3J^2)\varepsilon_{xx} + \text{c.p.})$ for tetragonal distortions.

Using the deformation potential defined by (3.3), the influence of the hydrostatic strain component on the offsets of the average valence-band and the conduction band is given by

$$\begin{aligned} \Delta E_{v,av} &= a_v \frac{\Delta V}{V} \quad \text{and} \\ \Delta E_c &= a_c \frac{\Delta V}{V}, \end{aligned} \tag{3.4}$$

respectively, with the fractional volume change $\Delta V/V = (\varepsilon_{xx} + \varepsilon_{yy} + \varepsilon_{zz})$. Eventually the spin-orbit splitting of the valence band is considered. In semiconductors with zincblende or diamond structure the edge of the topmost valence band is

$$E_v = E_{v,av} + \frac{\Delta_0}{3}, \tag{3.5}$$

$\Delta_0$ being the spin-orbit parameter.

Splittings of the valence band in addition to those originating from the spin-orbit interaction arise from shear components of the strain. They depend on the strain direction and are proportional to the strain in the linear regime, which is expected to be a good approximation for pseudomorphic heterostructures. Taking the average valence-band energy $E_{v,av}$ as reference, the shifts of the heavy hole, the light hole, and the split-off band for uniaxial strain along the [001] direction are given by [5, 6]

$$\begin{aligned} E_{v,hh} &= \frac{\Delta_0}{3} - \frac{1}{2}\delta E_{001}, \\ E_{v,lh} &= -\frac{\Delta_0}{6} + \frac{1}{4}\delta E_{001} + \frac{1}{2}\sqrt{\Delta_0^2 + \Delta_0 \times \delta E_{001} + \frac{9}{4}\delta E_{001}^2}, \\ E_{v,so} &= -\frac{\Delta_0}{6} + \frac{1}{4}\delta E_{001} - \frac{1}{2}\sqrt{\Delta_0^2 + \Delta_0 \times \delta E_{001} + \frac{9}{4}\delta E_{001}^2}. \end{aligned} \tag{3.6}$$

In (3.6) the abbreviation

$$\delta E_{001} = 2b(\varepsilon_{zz} - \varepsilon_{xx}) \tag{3.7}$$

is used, with the shear deformation potential $b$ for biaxial strain which induces a tetragonal distortion of the cubic unit cell. Equation (3.6) also holds for uniaxial strain along [111], if $\delta E_{001}$ is replaced by

$$\delta E_{111} = 2\sqrt{3} d \varepsilon_{xy}, \tag{3.8}$$

where $\varepsilon_{xy} = 1/3(\varepsilon_\perp - \varepsilon_\parallel)$.

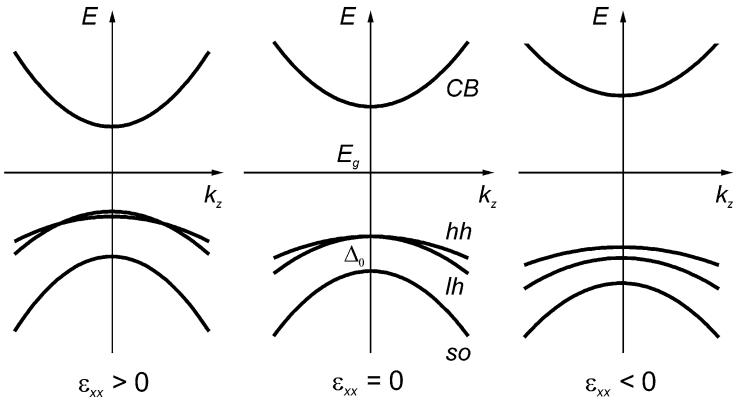


**Fig. 3.2** Effect of strain on the valence bands and the lowest conduction band (*CB*) of a zincblende-type semiconductor. *hh*, *lh*, and *so* denote heavy-hole, light-hole, and split-off hole valence bands, $\Delta_0$ is the spin-orbit splitting. $\varepsilon_{xx} = \varepsilon_{yy}$ is the in-plane strain

The effect of uniaxial strain along the [001] direction, or similarly by biaxial strain along [110] and [$\bar{1}$10], is shown in Fig. 3.2. The unstrained valence band of a zincblende semiconductor at the Brillouin zone center $k = 0$ is split by the spin-orbit interaction $\Delta_0$ into a fourfold degenerate heavy-hole (*hh*) and light-hole (*lh*) band with total angular momentum $J = 3/2$ ($M_J = \pm 3/2, \pm 1/2$), and a doubly degenerate split-off (*so*) band with $J = 1/2$ ($M_J = \pm 1/2$). The strain reduces the symmetry from $T_\mathrm{d}$ to $D_{2\mathrm{d}}$ and lifts the degeneracy of the $J = 3/2$ band, yielding a $J = 3/2$, $M_J = \pm 3/2$ *hh* band and a $J = 3/2$, $M_J = \pm 1/2$ *lh* band [7]. In addition, the hydrostatic component of the stress shifts the bandgap energy. In common zincblende materials the bandgap energy increases for compressive strain due to the nature of the atomic bonding. It is generally believed that most of the change occurs in the upward moving conduction band. Since the share of $a_\mathrm{c}$ and $a_\mathrm{v}$ is difficult to isolate experimentally it is usually based on theoretical predictions.

We illustrate strain effects in pseudomorphic structures for results obtained from the model-solid theory [8] outlined in Sect. 3.2.5. Calculated deformation potentials are given in Table 3.1 for some semiconductors. Data computed according (3.3) refer to the direct gap at the $\Gamma$ point of the Brillouin zone (index *dir*) or to the indirect gap (*indir*). The gap energies $E_\mathrm{g}$ are taken from low-temperature experiments, yielding with (3.5) the conduction-band values $E_\mathrm{c} = E_\mathrm{v} + E_\mathrm{g}$.

To illustrate the effect of strain on the valence and conduction bands, we consider data for a thin pseudomorphically strained ZnS layer on a ZnSe substrate [8]. Both solids have zincblende structure with lattice parameters of 5.40 Å and 5.65 Å, respectively. ZnS has a smaller unstrained lattice parameter, and is tensely strained parallel to the interface $(x, y)$ and compressively strained perpendicular $(z)$. According (2.19a)–(2.19c) the respective strains are $\varepsilon_{xx} = \varepsilon_{yy} = 0.046$ and $\varepsilon_{zz} = -0.058$, leading to a fractional volume increase $\Delta V/V = 0.035$. The change of the volume affects the energy of valence band and conduction band. The band energies of the strained ZnS layer follow from (3.4), yielding $E_{\mathrm{v,av}}^{\mathrm{ZnS}} = -9.07$ eV

**Table 3.1** Average valence-band energies $E_{v,av}$ and deformation potentials of the valence band $a_v$, the conduction band $a_c$, and the gap energy $a$ calculated from the model-solid theory. $\Delta_0$ and $E_g$ denote measured spin-orbit splitting and energy gap at 0 K, respectively. All values are given in eV. Data from [8]

| Solid | $E_{v,av}$ | $a_v$ | $a_c^{dir}$ | $a^{dir}$ | $E_g^{dir}$ | $E_c^{dir}$ | $a_c^{indir}$ | $a^{indir}$ | $E_g^{indir}$ | $E_c^{indir}$ | $\Delta_0$ |
|---|---|---|---|---|---|---|---|---|---|---|---|
| Si | −7.03 | 2.46 | 1.98 | −0.48 | 3.37 | −3.65 | 4.18 | 1.72 | 1.17 | −5.85 | 0.04 |
| Ge | −6.35 | 1.24 | −8.24 | −9.48 | 0.89 | −5.36 | −1.54 | −2.78 | 0.74 | −5.51 | 0.30 |
| GaP | −7.40 | 1.70 | −7.14 | −8.83 | 2.90 | −4.47 | 3.36 | 1.56 | 2.35 | −5.02 | 0.08 |
| AlAs | −7.49 | 2.47 | −5.64 | −8.11 | 3.13 | −4.27 | 4.09 | 1.62 | 2.23 | −5.17 | 0.28 |
| GaAs | −6.92 | 1.16 | −7.17 | −8.33 | 1.52 | −5.29 | | | | | 0.34 |
| InAs | −6.67 | 1.00 | −5.08 | −6.08 | 0.41 | −6.13 | | | | | 0.38 |
| ZnS | −9.15 | 2.31 | −4.09 | −6.40 | 3.84 | −5.29 | | | | | 0.07 |
| ZnSe | −8.37 | 1.65 | −4.17 | −5.82 | 2.83 | −5.40 | | | | | 0.43 |

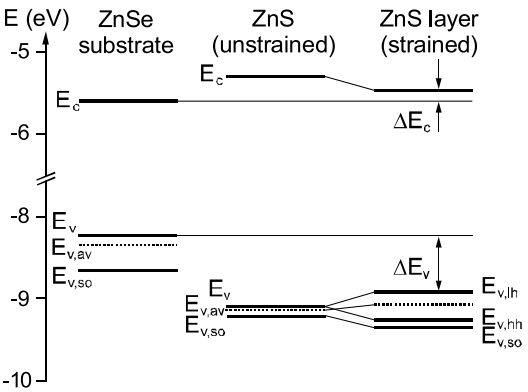


**Fig. 3.3** Band alignment of a biaxially strained pseudomorphic ZnS layer on a (001)-oriented ZnSe substrate, calculated according the model-solid theory using experimental values for gap energies and spin-orbit splittings. After [8]

and $E_c^{ZnS} = -5.43$ eV. The deformation potential $b$ of ZnS is $-1.25$ eV, yielding with (3.7) $\delta E_{001} = 0.26$ eV. From (3.6) we finally obtain the energy shifts of the heavy hole, the light hole, and the split-off hole of the strained ZnS layer with respect to $E_{v,av}^{ZnS}$ being $-0.11$ eV, $+0.26$ eV and $-0.16$ eV, respectively. The resulting alignment with $\Delta E_v = -0.50$ eV and $\Delta E_c = 0.03$ eV is depicted in Fig. 3.3.

Deformation potentials are experimentally obtained from optical spectroscopy. A comparison of the reflectivity and a two-photon absorption spectrum of a ZnSe bulk crystal is shown in Fig. 3.4a. The sharp nonlinear resonances of the $1S$ exciton allow for a direct measurement of splittings induced by stresses applied along various crystallographic low-index directions. The deformation potentials $a$, $b$, and $d$ are contained in the Hamiltonian of the $1S$ orthoexciton and are evaluated by assigning the measured energies to the eigenenergies [9]. Results for uniaxial stress along [001] are given in Fig. 3.4b.

Application of uniaxial stress to a biaxially strained 5.3 μm thick ZnSe layer on GaAs substrate is shown in Fig. 3.4c. In the lowest spectrum the splitting of light-

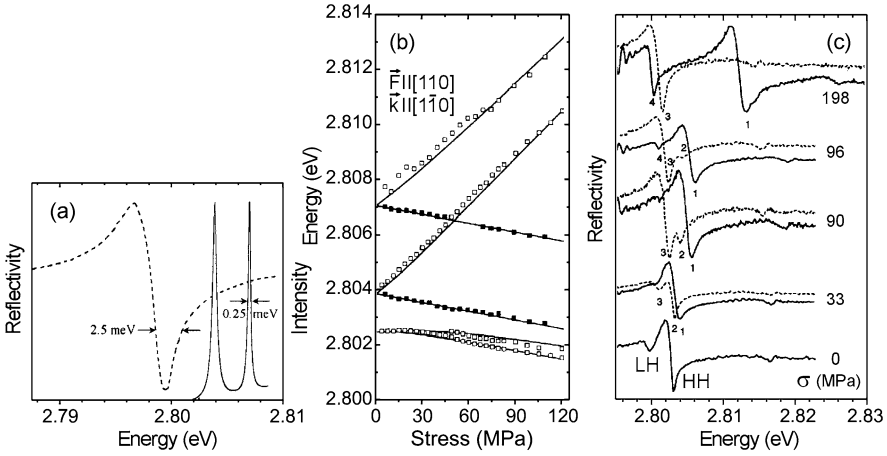


**Fig. 3.4** (**a**) Two-photon excitation spectrum (*solid lines*) and reflectivity (*dashed*) of a ZnSe bulk crystal, recorded at 5 K and 2 K, respectively. (**b**) Shift and splitting of two-photon resonances for uniaxial stress applied along [001], incident light along [1$\bar{1}$0], and polarizations parallel to [001] (*filled symbols*) and [110] (*open symbols*). Reproduced with permission from [9], © 1995 APS. (**c**) Reflectance spectra of a biaxially strained epitaxial ZnSe/GaAs layer under an additional external stress $\sigma$ applied along [110]. *Solid* and *dotted* curves refer to $\sigma$ and $\pi$ polarizations, respectively. Reproduced with permission from [10], © 1996 APS

hole and heavy-hole $1S$ exciton due to pure biaxial strain of the epilayer is seen. Four resonances of the $1S$ exciton appear when an additional stress is applied along [110]. They are linearly polarized either parallel ($\pi$) or perpendicular ($\sigma$) with respect to the axis of external stress. The stress-induced strain lowers the symmetry to $C_{2v}$ and creates dipole-allowed mixtures of paraexcitons with orthoexcitons, giving rise to $2 \times 2$ resonances [10].

Experimentally determined deformation potentials for some semiconductors are given in Table 3.2.

We now consider semiconductors with *wurtzite structure* like the Column III nitrides or ZnO. The unstrained valence-band structure of wurtzite crystals shown in Fig. 3.1b. Due to a weak spin-orbit coupling the dispersions of the $hh$-, $lh$-, and $ch$-valence-bands are not strongly affected by strain, in contrast to effects in zincblende materials. Under biaxial strain in the basal plane the $C_{6v}$ symmetry of the unit cell is preserved, but the crystal-field splitting changes. For compressive biaxial strain the energy which separates the crystal-hole band from the heavy-hole and light-hole bands is increased, for tensile strain it is decreased. Uniaxial strain in the basal plane reduces the symmetry to $C_{2v}$. Under compressive uniaxial strain along the $\Gamma$–$K$ direction in the first Brillouin zone ('$y$' direction) the $lh$ band in this direction and the $hh$ band in the perpendicular lateral $x$ direction move to higher energy. The same effect has a tensile strain along the $x$ direction, and a reverse effect has a tensile strain along the $y$ direction.

Wurtzite crystals have no inversion center in the unit cell. They consequently exhibit a non-zero macroscopic spontaneous polarization $\mathbf{P}_{SP}$. Strained wurtzite crystals additionally show a strong piezoelectric polarization $\mathbf{P}_{PE}$. Piezoelectricity is

**Table 3.2** Deformation potentials $a$, $b$, and $d$, experimentally determined for the lowest bandgap $E_g$ from optical spectroscopy (exp). Theoretical values (theo) are from the model-solid theory [8]. Solids denoted in gray have an indirect lowest bandgap. All values are given in eV

| Solid | $a^{\text{exp}}$ | $a^{\text{theo}}$ | $b^{\text{exp}}$ | $b^{\text{theo}}$ | $d^{\text{exp}}$ | $d^{\text{theo}}$ |
|---|---|---|---|---|---|---|
| Si | $+1.5 \pm 0.3$[a] | $+1.72$ | $-2.10 \pm 0.10$[a] | $-2.35$ | $-4.85 \pm 0.15$[a] | $-5.32$ |
| Ge | $-2.0 \pm 0.5$[b] | $-2.78$ | $-2.86 \pm 0.15$[b] | $-2.55$ | $-5.28 \pm 0.50$[b] | $-5.50$ |
| GaP | $-9.9 \pm 0.3$[c] | $+1.56$ | $-1.5 \pm 0.2$[c] | | $-4.6 \pm 0.2$[c] | |
| AlAs | $-8.2$[d] | $+1.62$ | $-2.3$[d] | | $-3.4$[d] | |
| GaAs | $-8.5$[d,e] | $-8.33$ | $-2.0$[d,e] | $-1.90$ | $-4.8$[d,e] | $-4.23$ |
| InAs | $-6.1$[d] | $-6.08$ | $-1.8$[d] | $-1.55$ | $-3.6$[d] | $-3.10$ |
| ZnS | $-4.56$[f] | $-6.40$ | $-0.75$[f] | $-1.25$ | | |
| ZnSe | $-4.7 \pm 0.2$[g] | $-5.82$ | | $-1.20$ | $-6.37 \pm 0.07$[g] | |

[a]Ref. [11], [b]Ref. [6], [c]Ref. [12], [d]Ref. [2], [e]Ref. [13], [f]Ref. [7], [g]Ref. [9] (factor $\sqrt{3}/2$ in $d$ taken into account)

also present in zincblende material, but the effect is negligible for strained-layer growth along the common [001] direction. Even for growth along [111] the effect is small for cubic heterostructures and was not discussed above; data of important III–V semiconductors may be found in [2].

In the Column III nitrides or ZnO heterostructures the strong piezoelectricity cannot be neglected. The piezoelectric polarization $\mathbf{P}_{\text{PE}}$ is obtained from the product of the piezoelectric tensor of wurtzite crystals and the strain $\boldsymbol{\varepsilon}$ with components along the axes,

$$\mathbf{P}_{\text{PE}} = \begin{pmatrix} 0 & 0 & 0 & 0 & e_{15} & 0 \\ 0 & 0 & 0 & e_{15} & 0 & 0 \\ e_{31} & e_{31} & e_{33} & 0 & 0 & 0 \end{pmatrix} \begin{pmatrix} \varepsilon_1 \\ \varepsilon_2 \\ \varepsilon_3 \end{pmatrix}. \tag{3.8a}$$

Here the piezoelectric forth-rank tensor is given in the Voigt notation. We restrict ourselves to polarizations along the $c$ axis, i.e., on the common (0001) growth direction. Biaxial strain in the basal plane is expressed by $\varepsilon_1 = \varepsilon_2 = \varepsilon_\parallel = (a_{\text{L}} - a_{\text{L},0})/a_{\text{L},0}$, and strain along the $c$ axis correspondingly by $\varepsilon_3 = \varepsilon_\perp = (c_{\text{L}} - c_{\text{L},0})/c_{\text{L},0}$. The indices L and L,0 denote the actual (strained) and natural lattice parameters of the layer. Using the relation between $\varepsilon_\parallel$ and $\varepsilon_\perp$ (2.19c) we obtain for the $z$ component of the piezoelectric polarization

$$\mathbf{P}_{\text{PE},z} = 2\varepsilon_\parallel \left( e_{31} - e_{33} \frac{C_{13}}{C_{33}} \right). \tag{3.8b}$$

Data of piezoelectric tensor components and the spontaneous polarization for some wurtzite semiconductors are given in Table 3.3. According the sign convention a positive $c$ axis points from the metal cation to the adjacent anion. The semiconductors listed in Table 3.3 show a negative spontaneous polarization. The sign of the strain-induced piezoelectricity depends on the sign of strain. Since the bracket in (3.8b) yields negative values, the piezoelectric polarization is positive for compressive strain. The total polarization $P_z = P_{\text{SP},z} + P_{\text{PE},z}$ may then have either sign.

**Table 3.3** Coefficients $e_{ij}$ of the piezoelectric tensor and spontaneous polarization $P_{SP}$ of wurtzite compound semiconductors. All values are given in C/m$^2$

| Semiconductor | $e_{15}$ | $e_{31}$ | $e_{33}$ | $P_{SP}$ |
|---|---|---|---|---|
| GaN | $-0.22\ldots-0.33$[a] | $-0.35$[b] | $1.27$[b] | $-0.029$[c] |
| AlN | $-0.48$[a] | $-0.50$[b] | $1.79$[b] | $-0.081$[c] |
| InN | | $-0.57$[b] | $0.97$[b] | $-0.032$[c] |
| ZnO | $-0.35\ldots-0.59$[d] | $-0.35\ldots-0.62$[d] | $0.96\ldots1.56$[d] | $-0.057$[c] |

[a]Ref. [14], [b]Ref. [2], [c]Ref. [15], [d]Ref. [16]

Piezoelectricity has a substantial effect on the electronic properties of devices made from GaN-based heterostructures. At the interface between two wurtzite semiconductors 1 and 2 the total polarization changes, giving rise to a sheet charge $\sigma$ determined by the difference in total polarization,

$$\sigma = (P_{SP,z1} + P_{PE,z1}) - (P_{SP,z2} + P_{PE,z2}).$$

High-electron-mobility transistors based on strained AlGaN/GaN heterostructures achieved very high sheet carrier concentrations in a two-dimensional electron gas formed at the interface, enabling devices with excellent performance. The high values could be assigned to an additive effect of spontaneous and piezoelectric polarization in structures with tensely strained AlGaN barriers [17].

### *3.1.3 Temperature Dependence of the Bandgap*

Energies of electronic bands are generally calculated for a temperature $T = 0$ K. To describe the temperature dependence of the important fundamental bandgap $E_g$ a number of approaches was developed. The usually observed decrease of $E_g$ for increased temperature originates from a change of both, the electron-phonon interaction and the interatomic bond distance. Instead of an explicit derivation from such interactions empirical formula are widely used to express the thermal behavior of $E_g$. Most popular is the empirical *Varshni formula* [18]

$$E_g(T) = E_g(T = 0) - \frac{\alpha T^2}{T + \beta}, \tag{3.9}$$

where the three parameters $E_g(T = 0)$, $\alpha$, and $\beta$ are fitted to experimental data. The dependence describes both, direct and indirect bandgaps. $E_g(T = 0)$ is the bandgap energy at 0 K. $\alpha$ is claimed to be related to the Debye temperature but may in certain cases be negative. Moreover, at very low temperatures a rather temperature-independent behavior of $E_g$ was found instead of the quadratic dependence predicted from (3.9). Typical values for $\alpha$ and $\beta$ are in the range (0.4–0.6) meV/K and (200–600) K, respectively. The thermal shift of the bandgap energy according (3.9) is illustrated in Fig. 3.5.

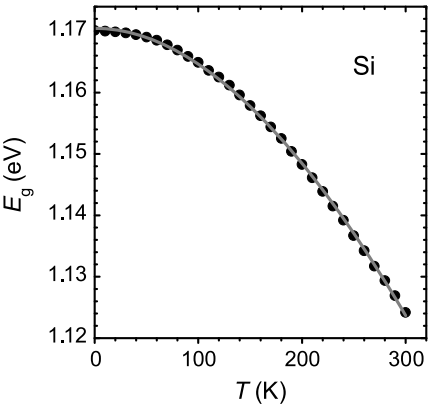


**Fig. 3.5** Dependence of the indirect bandgap energy of Si on temperature. The *gray curve* is a fit to Varshni's formula (3.9), data are from [22]

A number of better motivated models was developed later, based on the occupation of phonon states and assuming an average phonon energy [19–21]. They particularly improve the description of low-temperature data but did not yet gain comparable acceptance.

### *3.1.4 Bandgap of Alloys*

The bandgap energy of a miscible random alloy of two (or more) semiconductors may continuously be varied by changing the composition. Unlike the lattice constant discussed in Sect. 2.1.10 the bandgap of the alloy is usually not obtained by a linear interpolation. Instead, it can normally be described by a quadratic dependence using a *bowing parameter* $b$ which is mostly positive [23]. The bandgap energy $E_{\mathrm{g\ alloy}}$ of an alloy $A_xB_{1-x}$ from two materials $A$ and $B$ with the same crystal structure and bandgaps $E_{\mathrm{g}\ A}$ and $E_{\mathrm{g}\ B}$, respectively, is expressed by

$$E_{\mathrm{g\ alloy}} = xE_{\mathrm{g}\ A} + (1-x)E_{\mathrm{g}\ B} - bx(1-x), \tag{3.10a}$$

$x$ being the molar fraction of $A$ in the alloy (cf. Sect. 2.1.10). The bandgap energy of a (pseudobinary) ternary alloy $A_xB_{1-x}C$ from binaries $AC$ and $BC$ is given by the same relation putting $E_{\mathrm{g}\ A}$ and $E_{\mathrm{g}\ B}$ to $E_{\mathrm{g}\ AC}$ and $E_{\mathrm{g}\ BC}$, respectively. For quaternary compounds of the type $A_xB_yC_{1-x-y}D$ (i.e., mixing of $A$, $B$, $C$ atoms on the cation sublattice) the bandgaps are described by the weighted sum of the related ternary alloys $ABD$, $ACD$, and $BCD$, yielding [24]

$$\begin{aligned} E_{\mathrm{g\ alloy}} = {} & xE_{\mathrm{g}\ AD} + yE_{\mathrm{g}\ BD} + (1-x-y)E_{\mathrm{g}\ CD} \\ & - b_{AB}xy - b_{AC}x(1-x-y) - b_{BC}y(1-x-y). \end{aligned} \tag{3.10b}$$

Here $b_{AB}$, $b_{AC}$ and $b_{BC}$ are the three bowing parameters for the ternary alloys $A_xB_{1-x}D$, $A_xC_{1-x}D$, and $B_xC_{1-x}D$, respectively. The bandgap energy for quaternary alloys of the type $A_xB_{1-x}C_yD_{1-y}$ (i.e., mixing on the cation *and* anion

**Table 3.4** Bowing parameters $b$ of the direct bandgap of alloyed GaAs-based zincblende and GaN-based wurtzite semiconductors. Data from [2]

| Semiconductor | $b$ for alloy with GaAs (eV) | Semiconductor | $b$ for alloy with GaN (eV) |
|---|---|---|---|
| AlAs | $-0.127+1.310\times x_{\mathrm{Al}}$ | AlN | 1.0 |
| InAs | 0.477 | InN | 3.0 |
| GaP | 0.8 | | |

sublattice) is calculated from the ternary parameters $E_{\mathrm{g}\,ABC}$, $E_{\mathrm{g}\,ABD}$, $E_{\mathrm{g}\,ACD}$, and $E_{\mathrm{g}\,ABD}$,

$$E_{\mathrm{g\ alloy}} = \frac{x(1-x)[yE_{\mathrm{g}\,ABC}(x)+(1-y)E_{\mathrm{g}\,ABD}(x)]+y(1-y)[xE_{\mathrm{g}\,ACD}(y)+(1-x)E_{\mathrm{g}\,BCD}(y)]}{x(1-x)+y(1-y)},$$

$$E_{\mathrm{g}\,ABC}(x) = xE_{\mathrm{g}\,AC}+(1-x)E_{\mathrm{g}\,BC}-b_{ABC}x(1-x), \tag{3.10c}$$

$E_{\mathrm{g}\,ABD}(x)$, $E_{\mathrm{g}\,ACD}(y)$, and $E_{\mathrm{g}\,BCD}(y)$ accordingly.

We note that (3.10a)–(3.10c) are similar to (2.2a)–(2.2c) for $b=0$. Bowing parameters for some ternary (pseudo-binary) alloys are given in Table 3.4. The value given for $\mathrm{Al}_x\mathrm{Ga}_{1-x}\mathrm{As}$ indicates that a *constant* bowing parameter does not always yield an appropriate description.

Bandgap energies for a number of important semiconductors are given in Fig. 3.6. The lines representing the bandgap of alloys in Fig. 3.6 sometimes have a kink. Such features originate from a transition of a direct to an indirect semiconductor due to a crossing of the lowest $\Gamma$ conduction band and an X or L conduction band (for Si and Ge crossing of indirect X and L bands).

The bandgap energy of alloys composed of more than two semiconductors can be illustrated using diagrams with curves of constant energy versus composition parameters. A material of particular importance for optoelectronic devices is the quaternary alloy $\mathrm{Ga}_x\mathrm{In}_{1-x}\mathrm{As}_y\mathrm{P}_{1-y}$. The bandgap of such quaternaries may be choosen independently from the lattice parameter by a proper selection of the two independent composition parameters $x$ and $y$. For lattice matching conditions on InP substrates one composition parameter is independent and may be used to choose a bandgap energy, while the other parameter is given by

$$x = 0.1896y/(0.4176-0.0125y) \approx 0.47y \quad (0 \le y \le 1).$$

The diagram Fig. 3.7 shows the variation of the direct bandgap of $\mathrm{Ga}_x\mathrm{In}_{1-x}\mathrm{As}_y\mathrm{P}_{1-y}$ in the full range of compositions $x$ and $y$, along with lattice matching conditions for GaAs and InP substrates.

Equations (3.10a)–(3.10c) show that the bandgap energy of an alloy usually deviates from a linear concentration-weighted interpolation by a quadratic term described by the bowing parameter $b$. It should be noted that the virtual-crystal approximation (Sect. 2.1.10) which describes a lattice parameter variation *without* bowing also yields such bowing for the bandgap energy [23, 25–27]. The reason is that the

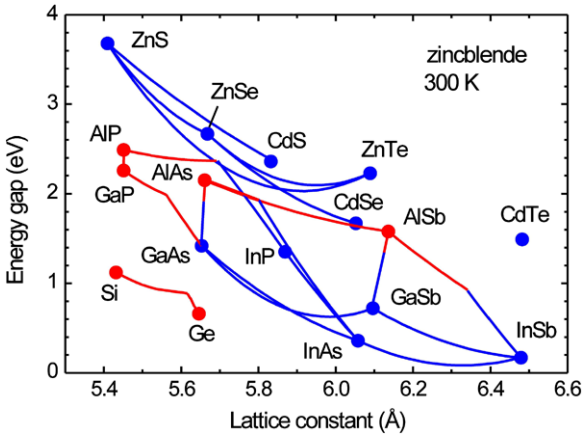


**Fig. 3.6** Bandgap energy as a function of lattice constant for pure (*dots*) and alloyed zincblende and diamond semiconductors at room temperature. *Blue* and *red* drawing denotes direct and indirect bandgap, respectively

eigenvalues produced by band-structure methods are mostly nonlinear in the potential matrix elements. It was, however, pointed out that a given set of band energies can be fitted by widely different potential parameters in semiempirical models, permitting almost any value of $b$ within the simple VCA approach [28].

The origin of optical bowing is widely associated with disorder in an alloy. The effect of alloy disorder alone may however be insufficient to describe bowing. In a first-principles approach evidence was given for three contributions to $b$ in tetrahedrally coordinated compound semiconductors: A modification of the band structure due to the change of the lattice constant, a relaxation of the anion-cation bond length in the alloy, and a contribution of chemical electronegativity due to charge exchange in the alloy [28]. Respective calculations provided a good description of bowing parameters experimentally obtained from zinc chalcogenes.

## 3.2 Band Offsets

Epitaxy allows to produce a pseudomorphic, atomically sharp transition from one solid to another. The intimate contact of two solids with different electronic properties forms a heterojunction. At the interface the electronic bands of the solids align on a scale of atomic nearest-neighbor distances. In addition, transfer of charges from one solid to the other and charge accumulation at the interface may lead to an electrostatic bending of the bands on a larger scale. The band alignment is of basic technological importance, because it controls the transport and confinement of charge carriers and hence the properties and performance of (opto-)electronic devices. Calculation and measurement of band offsets (also termed *band discontinuities*, *band lineups* or *band alignments*) are difficult, and a thorough understanding of the physics of semiconductor band-alignment is still missing. In the following we focus on the technologically important contact between two semiconductors. The junction between a semiconductor and a metal is treated in Sect. 6.3.

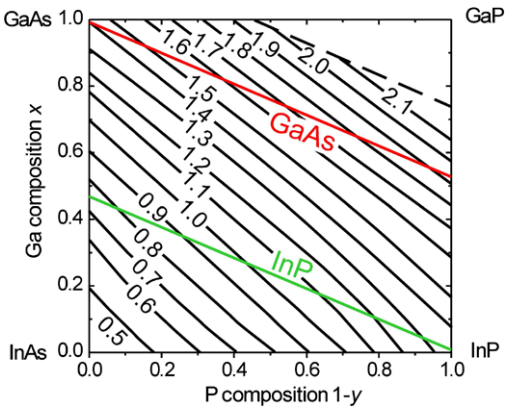


**Fig. 3.7** Bandgap energy of the quaternary alloy $Ga_xIn_{1-x}As_yP_{1-y}$ in eV at 300 K as a function of compositions $x$ and $y$. *Red* and *green lines* mark compositions which are lattice matched to GaAs and to InP. From [29]

Various types of band alignments may occur at semiconductor junctions, usually labeled type I and type II. In a *type I* alignment the bandgap of one semiconductor lies completely within the bandgap of the other. If such straddled type I offset is applied to a *BAB* double heterostructure, electrons and holes can both be confined in material $A$ with the smaller bandgap, see Fig. 3.8a. This feature is often employed in low-dimensional structures like quantum wells to tailor electronic properties, cf. Sect. 3.3. If the offset in the valence band and the conduction band has *the same sign* for an electron transfer from material $A$ to $B$ the band alignment is referred to as *type II*. In a *BAB* double heterostructure with such a staggered band lineup *either* electrons *or* holes are confined in material $A$. In Fig. 3.8b a lower conduction band edge in material $A$ leading to electron confinement is assumed. When the bandgaps of the two semiconductors do not overlap at all a *misaligned* (or *broken gap*) configuration occurs. Such alignment appears if in Fig. 3.8 $E_{v\,A}$ lies above $E_{c\,B}$ or $E_{c\,A}$ lies below $E_{v\,B}$.

A case analogous to the broken gap configuration occurs if a junction is formed by a semiconductor and a zero-gap semiconductor like, e.g., HgTe. This kind of alignment is occasionally referred to as *type III*.

The type of band alignment forming in a semiconductor heterostructure depends on the position of the respective band edges. The prediction of this alignment is not trivial, because there exists no natural common reference energy. Such reference should be a property of a bulk crystal. Much theoretical and experimental work was devoted to predict or measure offsets within the required precision of about 0.1 eV or better. A comprehensive review as of 1991 was given in Ref. [30]. In the following we will consider some rules and more recent theoretical and experimental results.

### *3.2.1 Electron-Affinity Rule*

If two semiconductors $A$ and $B$ are combined their Fermi levels $E_F$ tend to align by transferring electrons from the solid with higher Fermi energy to the other. In

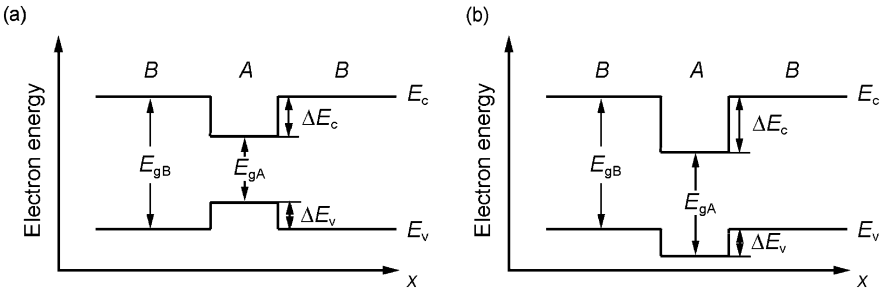


**Fig. 3.8** Alignment of band edges in (**a**) type I and (**b**) type II double heterostructures built from a small-bandgap semiconductor $A$ with a small extension along the spatial coordinate $x$ and a wide-bandgap semiconductor $B$

the ideal case the vacuum level $E_{\mathrm{vac}}$ is a common reference energy [31, 32]. In the framework of this so-called *electron-affinity rule* the alignment of the conduction bands follows from their electron affinities $e\chi = E_{\mathrm{vac}} - E_{\mathrm{c}}$, $E_{\mathrm{c}}$ being the band edge of the (lowest) conduction band and $e$ the elementary charge, see Fig. 3.9. The discontinuity of the conduction band at the interface is then

$$\Delta E_{\mathrm{c}} = e(\chi_A - \chi_B), \tag{3.11}$$

and the corresponding offset of the (uppermost) valence band is given by

$$\Delta E_{\mathrm{v}} = e(\chi_A + E_{\mathrm{g}\,A}) - e(\chi_B + E_{\mathrm{g}\,B}), \tag{3.12}$$

$E_{\mathrm{g}}$ being the bandgap.

Theoretical calculations suggest that only a single atomic layer away from the interface the electronic structure in a heterostructure becomes nearly bulk-like. The offset can hence be well assumed as being abrupt as illustrated in Fig. 3.9b. This does not apply for the long-range band bending (μm scale) originating from the electron transfer for aligning $E_{\mathrm{F}}$. Therefore double-heterostructures with semiconductors of small dimensions (nm scale) embedded in other semiconductors may be represented by flat bands as depicted in Fig. 3.8.

A drawback of the classical electron-affinity rule is that the reference energy $E_{\mathrm{vac}}$ is not a bulk property. The electron affinity $e\chi$ is determined by experiments involving the surface. Therefore the structure of the surface and related charges may strongly affect the potential. Consequently the vacuum level is not a reliable reference.

### *3.2.2 Common-Anion Rule*

Heterostructures are often fabricated from compound semiconductors like ZnS and ZnSe. In such cases a heuristic rule called *common-anion rule* has been applied to

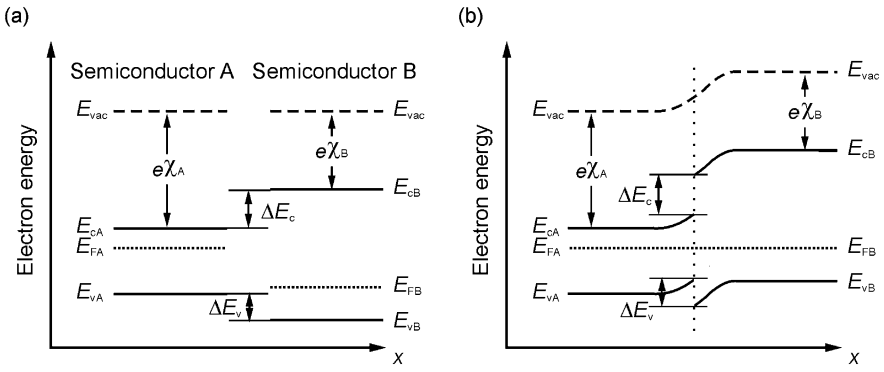


**Fig. 3.9** Band alignment at a heterointerface between two semiconductors in the ideal case in absence of dipoles and interface states. (**a**) Before and (**b**) after formation of a heterojunction in thermal equilibrium

estimate whether the offset essentially occurs in the valence band or in the conduction band. The rule arises from the evidence that the valence-band states are essentially derived from $p$-states of the anions in $sp$-bonded $AB$ compounds. The energy of the valence-band edge on an absolute scale is therefore expected to be basically determined by the valence electrons of the anions. Consequently the valence-band offset should be governed by the difference in anion electronegativity of the two semiconductors. A heterojunction with a common cation like Zn in a ZnS/ZnSe contact is expected to induce merely a small offset in the conduction band, leaving the majority of the bandgap difference for an offset in the valence band. Early models of band alignments largely complied with the common-anion rule [33, 34]. The models did not include $d$-orbitals of cations. Deviations from the common-anion rule were basically ascribed to contributions of these orbitals to the valence band [35]. It must, however, be noted that the rule fails in many cases. A basic shortcoming is the fact that the rule does not pay attention to an interface dipole formed from contributions of both, anions and cations [36].

### *3.2.3 Model of Deep Impurity Levels*

Experiments indicate the existence of some "natural" reference potential which adopts the role of the vacuum level in the classical approach. An indication for such a reference is the transitivity rule for the valence-band offset found for some combinations of semiconductors $A$, $B$, and $C$, i.e., $\Delta E_v^{AC} = \Delta E_v^{BC} - \Delta E_v^{AB}$ [37, 38]. Moreover, deep level impurities were found to have similar energy differences in different semiconductors. The observation was used for an empirical description of heterostructure band-offsets.

Transition metals like Fe form localized impurity states in semiconductors. They often possess several charge states separated by a fraction of the energy gap of the

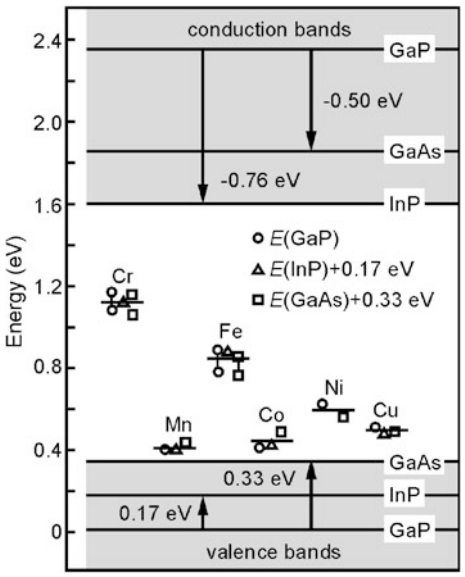


**Fig. 3.10** Average energy levels of transition metal impurities forming deep acceptor states in GaP, InP and GaAs, drawn with respect to the GaP valence band edge. After [39]

host crystal. A change of the impurity's charge state implies the transfer of a charge carrier from or to the host. This allows to determine the impurity level with respect to the band edges of the host material. Comparing such levels for a series of impurity ground states in various semiconductors yields an apparent similarity of both ordering and relative energy separations, cf. Fig. 3.10. The levels of transition-metal impurities are not pinned to either band edge like those of shallow impurities used as donors or acceptors (Sect. 6.1). This finding leads to the approach to take these levels within the bulk crystals as a reference for the alignment of the band edges in a heterojunction [39, 40]. The offset of the valence band at the interface $\Delta E_v$ is then given by the difference in the energy level positions of a given impurity in the two semiconductors forming the heterojunction. The constant separation of deep cationic impurity levels from the vacuum level was attributed to their antibonding character [40].

The energy levels of the transition-metal impurities depicted in Fig. 3.10 refer to a charge transition of an acceptor from a singly negative charge to the neutral state $(-/0)$. The measured transition energies were vertically shifted, so as to minimize the overall deviations, yielding the relative positions of the valence-band edges [39]. Positions of the conduction-band edges were experimentally obtained from low-temperature energy gaps. It should be noted that the method is restricted to heterojunctions formed by pairs of isovalent compound semiconductors, e.g., among III–V or among II–VI compounds, to ensure an electrically neutral interface without a dipole moment.

A comparable universal alignment of deep impurity levels as described above was also reported for hydrogen [41]. By computing the position of the Fermi energy where the stable charge state of interstitial hydrogen changes from the $H^+$ donor

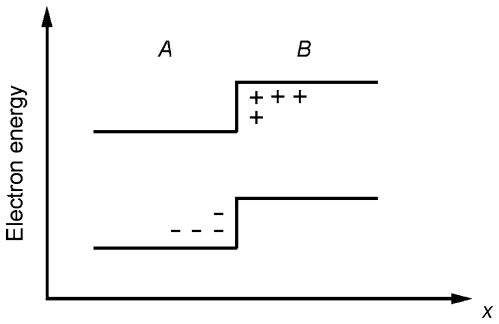


**Fig. 3.11** Scheme of band alignment at an interface artificially induced in a homogeneous semiconductor. (+) and (−) represent net charges of unoccupied states with electron deficit and occupied states with electron excess, respectively. After [42]

state to the $H^-$ acceptor state, predictions of band alignments for a wide range of host zincblende and wurtzite compound semiconductors were given.

### *3.2.4 Interface-Dipol Theory*

The dominant role of charge accumulation at the interface rather than the effect of bulk properties was emphasized in the *interface-dipol theory* for the prediction of heterojunction band-offsets [42]. The approach was also applied to the theory of Schottky barrier heights at a metal-semiconductor interface [43] considered in Sect. 6.3.2. The initial point of the approach is that the discontinuity at a semiconductor interface induces electronic states in the bandgap of at least one semiconductor. The formation of such states is illustrated in Fig. 3.11 for the artificial case of a band discontinuity created in a homogeneous semiconductor by an external step potential. States lying near the conduction-band edge at side $A$ of the interface have exponentially decaying tails into side $B$. At side $B$ they lie in the gap of the semiconductor. Any state in the gap has a mixture of valence- and conduction-band character. Occupying such state leads locally to an excess charge, according to its degree of conduction character. Filling a state which lies near the top of the gap gives a large excess charge of almost one electron due to a large conduction character. Leaving that state empty gives an only slight charge deficit. Conversely filling a state near the bottom of the gap at side $A$ results in a slight excess charge in proportion to its little conduction character, while leaving it empty leads to a charge deficit of almost one electron. Changing the band lineup hence induces a net dipole. The external potential assumed to create the potential step in Fig. 3.11 leads to an electron deficit at side $B$ and an electron excess at side $A$ of the interface. The resulting dipole tends to reduce the offset, i.e., the potential step is screened. By the action of the induced local charges the step is reduced by a factor of $\varepsilon$, the bulk dielectric constant.

The heterojunction of two different semiconductors is described analogous to the case considered above. Local states in the gap of one or both semiconductors lead to a dipole which screens the potential step and drives the lineup towards a value which minimizes the dipole. The zero-dipole lineup condition is not obvious. An

**Table 3.5** Differences of midgap energies $E_{B,A} - E_{B,B}$ according the interface-dipol theory and experimental valence-band discontinuities for some semiconductor heterojunctions. Data from [42]

| Heterojunction | | $E_{B,A} - E_{B,B}$ (eV) | $\Delta E_{\mathrm{v,exp}}$ (eV) |
|---|---|---|---|
| *A* | *B* | | |
| Si | Ge | $0.36 - 0.18 = 0.18$ | 0.20 |
| GaAs | Ge | $0.70 - 0.18 = 0.52$ | 0.53 |
| GaAs | InAs | $0.70 - 0.50 = 0.20$ | 0.17 |

effective midgap energy $E_B$ for each semiconductor is introduced at which the gap states, on the average, cross over from valence to conduction character [42]. States at $E_B$ are nonbonding on the average, the respective position is calculated from the band structure [43]. For a heterojunction $E_B$ plays a role in analogy to the Fermi energy in metals: $E_B$ is aligned for the respective semiconductors. Results of the interface-dipol theory are given in Table 3.5 for some heterojunctions, calculated values are claimed to be typically accurate to ∼0.1 eV. Extensions of the interface-dipol theory distinguish between the long-range tails of the gap states considered above and polarization of the bonds which form the interface.

### *3.2.5 Model-Solid Theory*

The more recently widely applied model-solid theory emulates the classical electron affinity rule illustrated in Fig. 3.9 by constructing a local reference level and avoiding dipoles. Within this approach the charge density in a semiconductor is composed by a superposition of neutral atoms [44]. The potential outside each such sphere goes exponentially to zero. This zero is taken as reference level. The construction leads to a well-defined electrostatic potential with respect to the vacuum level *in each atom*. By superposition the average electrostatic potential in a model solid composed of such atoms is hence specified on an absolute energy scale. The electron configuration of an atom in the solid is determined from a tight-binding calculation. This leads for, e.g., one Si atom in a silicon bulk crystal to $1.46s$ and $2.54p$ electrons, meaning that a part of the two $s$ electrons of a Si atom are excited into the $p$ band [44]. The result of the calculation is the position of the valence band on some absolute energy scale, allowing to relate it to the respective value of another semiconductor. For semiconductors with zincblende or diamond structure the value $E_{\mathrm{v,av}}$ represents an average of the heavy hole, light hole and split-off hole valence-bands. Spin-orbit effects are added a posteriori. Once $E_{\mathrm{v,av}}$ values are computed separately for a pair of semiconductors, their band discontinuities can be predicted for an unstrained heterojunction with a perfect interface, i.e., an abrupt change in the type of material without displacements of atoms from their ideal positions. The result of a calculation of the average valence-band energy $E_{\mathrm{v,av}}$ on an absolute scale in the framework of the model-solid theory is given in Fig. 3.12 for some unstrained semiconductors. Data are included in Table 3.1 along with the effect of strain.

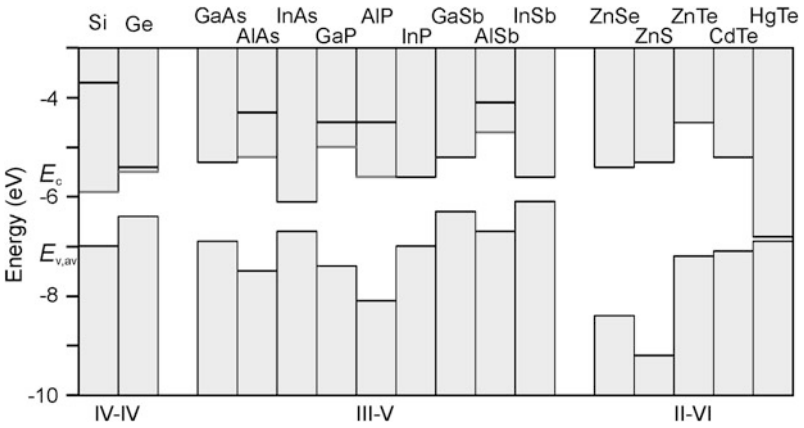


**Fig. 3.12** Average valence-band energy $E_{v,av}$ of unstrained semiconductors on an absolute scale resulting from the model-solid theory. Experimental values of bandgap energies are used to depict the conduction-band energy $E_c$, *black* and *gray lines* at the *bottom* of the conduction bands denote direct and indirect conduction band edges, respectively. Data taken from [8]

### *3.2.6 Offsets of Some Isovalent Heterostructures*

For many isovalent combinations of semiconductors with equal valence of the atoms on the two sides of a common junction the contribution of the interface dipole is not very large. In such cases the valence-band energy may be considered as a bulk property on either side, and the simple difference of electron affinities (3.2a)–(3.2c) is a reasonable approximation to evaluate the valence-band offset. Data for a number of technologically important III–V compound semiconductors are summarized in Fig. 3.13. The values do not include effects of strain. Furthermore, the valence-band offset is taken to be independent of temperature, basically due to a lack of reliable data. Valence-band offsets at a junction of two semiconductors of Fig. 3.13 are given by the energy difference of their plotted band positions. The same applies for the offset in the direct conduction band. The direct bandgap energy is represented by the vertical lines and is given for low temperature (0 K). Note that some of the binaries have a smaller *indirect* bandgap and that the three nitrides usually crystallize in the wurtzite structure.

### *3.2.7 Band Offset of Heterovalent Interfaces*

Models considered above in Sects. 3.2.1 to 3.2.5 considered abrupt interfaces and derived band offsets without detailed knowledge of the atomic interface structure. Theoretical work showed that the valence-band offset may actually depend on the microscopic arrangement of atoms at the interface [45]. A particularly strong effect was experimentally found for heterovalent interfaces, where—in contrast to isovalent systems—the atoms at the two sides of the interface have different chemical

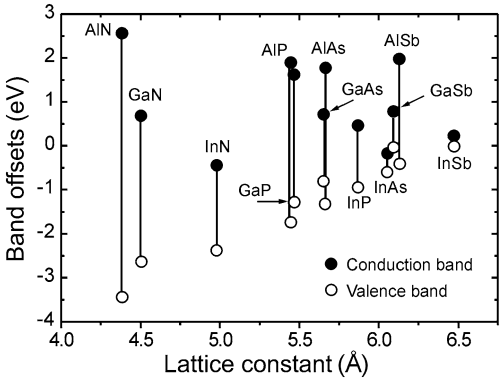


**Fig. 3.13** Valence-band offsets (*open circles*) of binary semiconductors with zincblende structure, plotted with respect to the valence-band maximum of InSb. *Filled circles* indicate corresponding offsets of the lowest direct conduction band. From [2]

valence. We will consider the well-studied ZnSe/GaAs interface in more detail. The same findings were observed in the similar system ZnSe/AlAs [46]. ZnSe and GaAs have both zincblende structure and are well lattice-matched with a misfit below 0.5 %. Due to the heterovalent nature of the II–VI and the III–V material an abrupt interface builds a strong dipole moment. Calculations indicate that such abrupt transition at a heterovalent interface is energetically unstable and structures consisting of one or two intermixed layers are more favorable [47–49].

Experimental evidence for the impact of growth conditions on the band offset of the ZnSe/GaAs interface are given in Fig. 3.14. Using molecular beam epitaxy (Sect. 7.3) ZnSe layers were epitaxially grown on (001)-oriented GaAs substrates [50, 51]. Non-stoichiometric growth conditions were applied by controlling the composition via the Zn/Se beam-pressure ratio (BPR). The valence-band offset at the interface was measured using X-ray photoemission (XPS) related to the Ga *3d* and the Zn *3d* core levels, see Fig. 3.14a. The observed Zn *3d* core-level separation with respect to the ZnSe bulk value (difference between dotted and solid lines in Fig. 3.14a) gives directly the valence-band offset across the heterojunction. The corresponding Zn/Se ratio at the interface $R_{\mathrm{Zn/Se}}$ was determined from the ratio of the integrated *3d* core-level emission intensities related to those of Zn and Se (Se not shown) for thin ZnSe layers. The measurements given in Fig. 3.14b clearly evidence a monotonous increase of the valence-band offset $\Delta E_{\mathrm{v}}$ with increasing Zn/Se ratio from 0.58 eV (Se-rich) to 1.2 eV (Zn-rich).

The apparent dependence of the band offset from the interface stoichiometry can be understood in terms of differently mixed layers formed at the interface for varied growth conditions [48, 50]. Let us consider the $sp^3$ bonds of a binary zincblende semiconductor like GaAs. Each atom has 4 hybrid orbitals directed to the surrounding four nearest neighbors (Fig. 2.4a). Each of these bonds comprises 2 electrons. The *primitive* unit cell of GaAs contains one cation (Ga) and one anion (As) with a total number of 8 valence electrons: 3 from the Column III element Ga and 5 from the Column V element As. Each atom can be considered to donate one quarter of its valence electrons to its four bond orbitals. The number of valence electrons in one orbital referring to one Ga atom is then $3/4$, and the corresponding number per orbital of an As atom is $5/4$. One Ga-As bond thus contains $3/4 + 5/4 = 2$

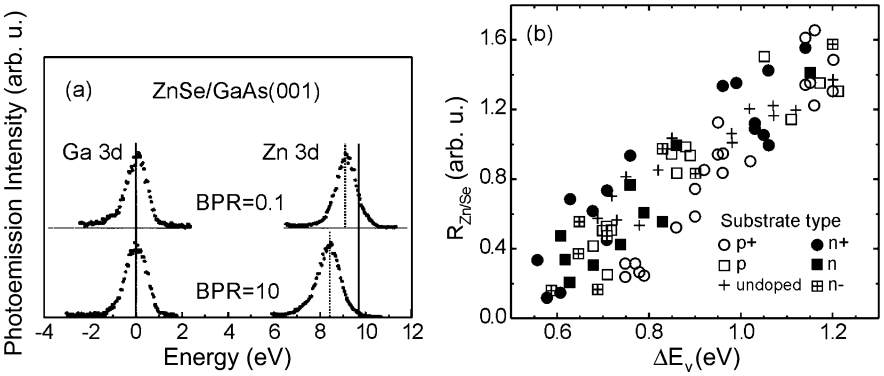


**Fig. 3.14** (**a**) X-ray photoemission spectra of ZnSe/GaAs heterojunctions grown with different Zn/Se beam-pressure ratios (BPR). The energy origin was set to the center of the Ga *3d* core-level emission. (**b**) Experimental valence-band offsets for ZnSe/GaAs(001) interfaces with different type of substrate doping versus Zn/Se ratio obtained from integrated XPS emission intensities for 0.3 nm thick ZnSe layers. Reproduced with permission from [50], © 1994 APS

electrons. The same applies for the II–VI semiconductor ZnSe: One Zn-Se bond contains $2/4 + 6/4 = 2$ electrons. At the heterovalent interface between GaAs and ZnSe we find Ga-Se or Zn-As bonds. A Ga-Se bond contains $3/4 + 6/4 = 2\frac{1}{4}$ electrons, i.e., it has an excess of a quarter electron. Such bond acts like a donor. Likewise a Zn-As bond has a quarter electron deficiency and acts like an acceptor. This unbalanced charge accounts for the dependence of the valence band offset from the stoichiometry at the interface.

An abrupt interface contains either solely Ga-Se bonds or Zn-As bonds. In both cases a strongly localized, two-dimensional charge is created at the interface. Such charge is connected to a high interface energy. Consequently the abrupt interface is thermodynamically unstable against intermixing [48]. Interface layers with a mixture of atoms from both semiconductors contain both kind of bonds; they accumulate less charge and are more stable. Figure 3.15 illustrates two examples of atomic configurations at intermixed heterovalent ZnSe/GaAs interfaces.

The total charge of an intermixed interface is reduced by charge transfer from donor-like to acceptor-like bonds. An interface with an equal number of uneven bonds is compensated. There may, however, remain a strong dipol moment at the interface: If the intermixed interface is built by a *single layer* of 50 % Ga and 50 % Zn cations (Fig. 3.15a) the acceptor-like Zn-As bonds lie towards the ZnSe and the donor-like Ga-Se bonds towards the GaAs. Note that the dipole moment is reversed, if such single-layer interface is formed on the anion sublattice (50 % As + 50 % Se, not shown in Fig. 3.15): The acceptor-like Zn-As bonds then lie towards the GaAs and the donor-like Ga-Se bonds towards the ZnSe. The valence-band offset is increased in the first case and decreased in the latter. Calculated values are +1.75 eV and +0.72 eV, respectively, when going from ZnSe to GaAs [48]. Formation of these mixings is favored in more Zn-rich growth conditions and Se-rich conditions, respectively, and describes correctly the experimentally observed tendency shown in

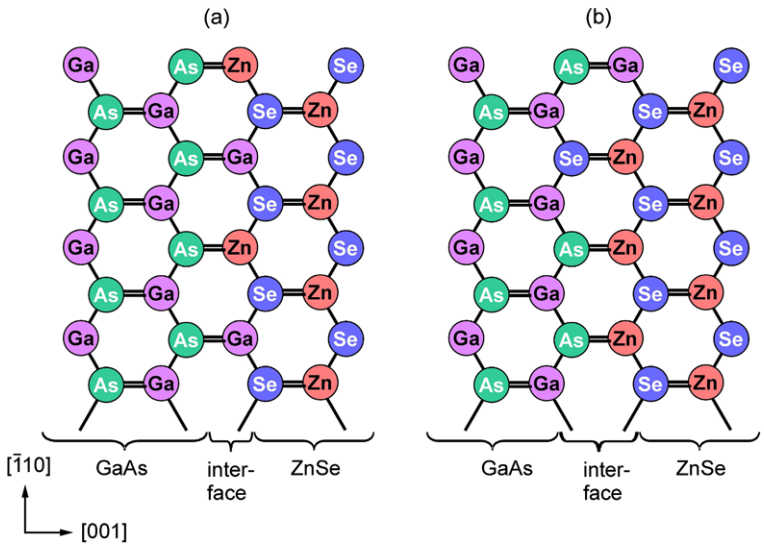


**Fig. 3.15** Schematic arrangement of atoms at the heterovalent ZnSe/GaAs interface, viewed along the [110] direction. Each atom is bond by two bonds in the figure plane and by two bonds, which are directed out of and into the figure plane—the *horizontal double lines*. (**a**) Interface with a single intermixed cation layer comprising 50 % Zn and 50 % Ga. (**b**) Interface with an intermixed double layer containing 75 % As and 25 % Se anions, and 25 % Ga and 75 % Zn cations

Fig. 3.14. The average of the two offsets (1.25 eV) is close to the experimental value of 1.22 eV [52]. This indicates the possibility to compensate the dipole moment, namely by interface layers comprising more than a single layer.

An interface consisting of an intermixed cation layer and an intermixed anion layer is illustrated in Fig. 3.15b. The Ga atoms and the Se atoms in the interface double-layer create a quarter charge excess each, while the two As-Zn bonds have a quarter charge deficiency each. The dipole moment in this intermixed double layer is hence fully compensated. It should be noted that the dipole moment is also compensated *in average* if small domains of single-layer interfaces of both polarities occur in a ratio of 1:1 [48].

The ZnSe/GaAs interface is well lattice-matched. Elastic relaxation as discussed in Sect. 2.2 does hence not play a significant role, and the effect was not considered here. Atomic relaxation does, however, play a crucial role in more mismatched heterostructures like GaN/SiC(001) [53].

Isovalent heterojunctions have, in contrast to the heterovalent interfaces discussed above, band offsets which are almost independent of the local atomic arrangement. This commonly accepted conclusion was initially established for common-ion systems, and later generalized [54]. It should be noted that intrinsic defects like antisites may limit the validity of this general statement and must be taken into account in case of low formation energies. The same applies for the formation of heterovalent interlayers at the interface.

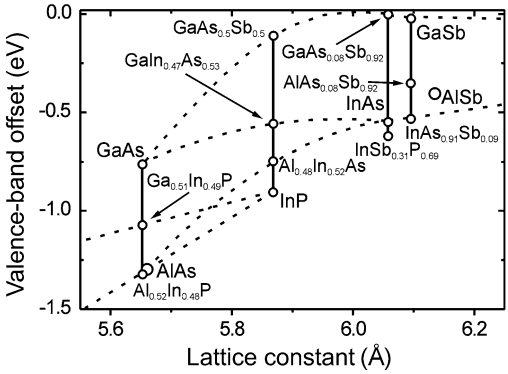


**Fig. 3.16** Valence-band offset of alloy semiconductors, plotted with respect to the valence-band maximum of InSb. *Vertical lines* mark common substrate materials, points signify offsets for binaries and lattice-matched ternary alloys. From [2]

### *3.2.8 Band Offsets of Alloys*

The observation of a constant energy with respect to the vacuum level of deep transition-atom impurities according the model of deep impurity levels (Sect. 3.2.3) was also used to measure the change of valence-band energy $E_v$ in alloys. Experiments reveal mostly a linear dependence of the valence-band maximum in the alloy with respect to the deep levels for varied composition $x$. Studied materials are, e.g., $Ga_{1-x}Al_xAs$:Fe [39, 55], $Ga_{1-x}Al_xAs$:Cu [56], $GaAs_{1-x}P_x$:Cu [57], $In_{1-x}Ga_xP$:Mn [58]. The slope of the linear dependence was found to be largely independent from the impurity. Such linear variation may also be inferred from the interface-dipol theory (Sect. 2.3.4), where the effective midgap energy $E_B$ of an alloy was estimated as a linear interpolation from the pure semiconductors [36]. Valence-band offsets of some zincblende semiconductor-alloys are summarized in Fig. 3.16 for composition parameters matching the lattice constants of the common substrate materials GaAs, InP, InAs, and GaSb.

## 3.3 Electronic States in Low-Dimensional Structures

The unique properties of low-dimensional structures originate essentially from the modification of the electronic density-of-states (DOS) produced by the confinement of charge carriers. To track such modification for the reduction of dimensionality from a three-dimensional (3D) bulk crystal to a 0D quantum dot we first recall the origin of 3D DOS and then consider the effect of potentials confining the mobility of charge carriers gradually to two, one, and eventually zero dimensions. Electronic properties of the solid are described in the framework of the effective-mass approximation by applying effective carrier masses and the relative permittivity as characteristic parameters.

### 3.3.1 Dimensionality of the Electronic Density-of-States

We first describe the energy of a single quasi-free electron confined in a bulk crystal by a simple square potential $W$ given by the dimensions of the crystal $L_x$, $L_y$, and $L_z$. The periodic potential of the atoms which leads to the band structure is neglected. It may be treated in a second step as a perturbation of $W$. If we assume $W$ being 0 inside the crystal and a constant $W_0 > 0$ outside we obtain energy and eigenstates of the electron inside the crystal by solving the Schrödinger equation

$$-\frac{\hbar^2}{2}\left(\frac{1}{m_x^*}\frac{\partial^2}{\partial x^2}+\frac{1}{m_y^*}\frac{\partial^2}{\partial y^2}+\frac{1}{m_z^*}\frac{\partial^2}{\partial z^2}\right)\psi(\mathbf{r})=E\psi(\mathbf{r}) \quad \text{(three dimensions)}. \tag{3.13}$$

The quantities $m^*$ are the electron's effective masses along the three spatial directions $x$, $y$, $z$. Using periodic boundary conditions like $\psi(x \pm L_x, y, z) = \psi(x, y, z)$ we obtain the solutions of (3.13) given by plane waves $\psi_{\mathbf{k}}(\mathbf{r})$ with eigenenergies $E_{\mathbf{k}}$:

$$\psi_{\mathbf{k}}(\mathbf{r}) = \frac{1}{\sqrt{V}} e^{i(k_x x + k_y y + k_z z)}, \tag{3.14}$$

$$E_{\mathbf{k}} = \frac{\hbar^2 k_x^2}{2m_x^*} + \frac{\hbar^2 k_y^2}{2m_y^*} + \frac{\hbar^2 k_z^2}{2m_z^*}. \tag{3.15}$$

In (3.14) $V = L_x \times L_y \times L_z$ is the volume of the bulk crystal. If we apply the boundary conditions to (3.14) we yield allowed values for $\mathbf{k}$,

$$k_x = \frac{2\pi}{L_x} n_x, \qquad k_y = \frac{2\pi}{L_y} n_y, \qquad k_z = \frac{2\pi}{L_z} n_z, \quad n_x, n_y, n_z = 0, \pm 1, \pm 2, \ldots. \tag{3.16}$$

Each electron state is hence described by *discrete* values of $\mathbf{k}$ as illustrated in the scheme of the reciprocal space depicted in Fig. 3.17a. Each state marked by a dot in the figure is occupied by 2 electrons with opposite spin. The spacing between allowed adjacent values along $k_x$ is $2\pi/L_x$. Since the crystal dimensions $L_x, L_y, L_z$ are macroscopic quantities, a finite region of $k$-space contains a very high number of dense lying allowed states. $\mathbf{k}$ and likewise $E_{\mathbf{k}}$ are therefore quasi-continuous quantities. The number of allowed $k$-values per unit volume of $\mathbf{k}$ space, i.e., the density of states in $\mathbf{k}$ space, is given by the constant quantity $V/(2\pi)^3$.

The electronic density of states $g(E)$—expressed in units of $\mathrm{m}^{-3} \times \mathrm{J}^{-1}$ or $\mathrm{cm}^{-3} \times \mathrm{eV}^{-1}$—is obtained from the number of electron states $dN$ per unit volume $V$ and per energy interval $dE$,

$$g(E) = 2 \times \frac{1}{V}\frac{dN}{dE}. \tag{3.17}$$

The factor 2 in (3.17) accounts for the spin degeneracy, allowing for a two-fold occupancy of each state. We obtain $dN$ from the volume in $\mathbf{k}$ space between two planes of constant energy at $E$ and $E + dE$ multiplied by the constant density of

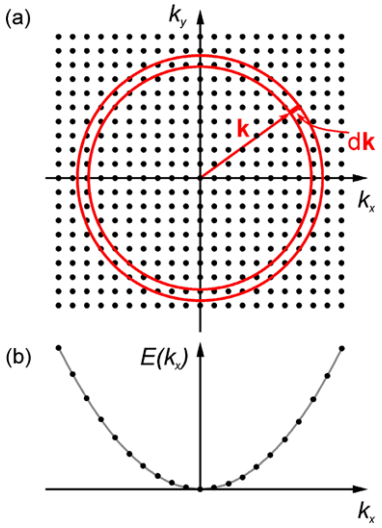


**Fig. 3.17** (**a**) Cross section of **k** space in the $k_x$–$k_y$ plane. (**b**) Values of $E(k_x)$ which fulfill the boundary condition for a quasi-free electron in a solid with finite dimension $L_x$

states in **k** space. Such volume is illustrated in Fig. 3.17a by the spherical shell of thickness $d\mathbf{k}$. We note that the volume increases for a given $dE$ (or correspondingly $d\mathbf{k}$) with the same power as the area of a sphere in **k** space increases as $k$ augments. For a quasi-free electron we obtain

$$dN = \frac{V}{(2\pi)^3}\int_E^{E+dE} d^3k = \frac{V}{(2\pi)^3} \times 4\pi k^2 dk. \tag{3.18}$$

To keep expressions simple we assume an isotropic medium with equal electron masses $m^*$ and equal crystal dimensions $L$ in all three spatial directions. We then may put $E = (\hbar^2/2)(k_x^2/m_x^* + k_y^2/m_y^* + k_z^2/m_z^*) = (\hbar^2/2m^*)k^2$. From this we obtain $k = (2m^*/\hbar^2)^{1/2}\sqrt{E}$ and $kdk = (m^*/\hbar^2)dE$, yielding for (3.18)

$$dN = \frac{V}{4\pi^2}\left(\frac{2m^*}{\hbar^2}\right)^{3/2}\sqrt{E}dE \quad \text{(isotropic medium)}. \tag{3.19}$$

Inserting (3.19) into the definition (3.17) we obtain the square-root dependence of the electronic DOS for bulk crystals

$$g(E) = \frac{1}{2\pi^2}\left(\frac{2m^*}{\hbar^2}\right)^{3/2}\sqrt{E} \quad \text{(three dimensions)}. \tag{3.20}$$

We now consider the *two-dimensional case* by assuming an additional contribution to the potential $W(z)$ which confines the mobility of the electron to the $xy$ plane. Within this two-dimensional plane it still moves quasi-free. The electron states are now described by the Schrödinger equation

$$-\left(\frac{\hbar^2}{2}\left(\frac{1}{m_x^*}\frac{\partial^2}{\partial x^2} + \frac{1}{m_y^*}\frac{\partial^2}{\partial y^2} + \frac{1}{m_z^*}\frac{\partial^2}{\partial z^2}\right) + eW(z)\right)\psi(\mathbf{r})$$
$$= E\psi(\mathbf{r}) \quad \text{(two dimensions)}. \tag{3.21}$$

Equation (3.21) can be separated into two equations describing movements either within the $xy$ plane or perpendicular by using the approach for the solution

$$\psi_{\mathbf{k}}(\mathbf{r}) = \frac{1}{\sqrt{V}} e^{i(k_x x + k_y y)} \varphi_n(z). \tag{3.22}$$

The plane-wave term in $\psi_{\mathbf{k}}(\mathbf{r})$ is analogous to the three-dimensional case described by (3.14) and yields correspondingly the eigenvalues

$$E_{xy} = \frac{\hbar^2 k_x^2}{2m_x^*} + \frac{\hbar^2 k_y^2}{2m_y^*}. \tag{3.23}$$

For the $z$ direction we obtain

$$-\left(\frac{\hbar^2}{2}\frac{1}{m_z^*}\frac{\partial^2}{\partial z^2} + eW(z)\right)\varphi_n(z) = E_n \varphi_n(z). \tag{3.24}$$

The eigenvalues $E_n$ depend on the characteristics of the potential $W(z)$. If we assume a square potential with infinite barriers separated by a spacing $L_z$ the eigenvalues follow from the condition for allowed waves $L_z = n\lambda_{z,n}/2$, $n = 1, 2, 3, \ldots$. Putting $k_{z,n} = 2\pi/\lambda_{z,n}$ the eigenvalues are given by

$$E_{z,n} = \frac{\hbar^2}{2m_z^*}\left(\frac{n\pi}{L_z}\right)^2, \quad n = 1, 2, 3, \ldots. \tag{3.25}$$

We note that the energy of the ground state with the quantum number $n = 1$ is increased by the *quantization energy* $\Delta E = E_{z,1}$. The eigenvalues of (3.21) are given by the sum of (3.23) and (3.25), $E = E_{xy} + E_{z,n}$. The band scheme $E(\mathbf{k})$ along $k_x$ and $k_y$ therefore consists of a series of parabola, each labeled by a particular value of $n$. The parabola are also referred to as *subbands*.

The two-dimensional electronic DOS follows from the equidistant states in $\mathbf{k}$ space similar to the three-dimensional case. For an area $L_x \times L_y$ the two-dimensional density of states in $\mathbf{k}$ space is given by $L_x L_y/(2\pi)^2$. The volume of a spherical shell in $\mathbf{k}$ space is replaced in 2D by the area of a circular ring bounded by $E(\mathbf{k}) = \text{const}$ and $E + dE = E(\mathbf{k} + d\mathbf{k}) = \text{const}$. We assume again an isotropic medium and use the isotropic energy dispersion $E(k) = (\hbar^2/2m_{xy}^*)k^2$. In analogy to (3.18) we obtain

$$dN = \frac{L^2}{(2\pi)^2}\int_E^{E+dE} d^2k = \frac{L^2}{(2\pi)^2} 2\pi k dk \quad \text{(isotropic medium)}. \tag{3.26}$$

The general expression for the two-dimensional DOS $g(E)$ is obtained by inserting this into the definition (3.17), yielding for the isotropic DOS of the $n$th subband

$$g_n = \frac{m_{xy}^*}{\pi\hbar^2} = \text{const} \quad \text{(two dimensions)}. \tag{3.27}$$

The two-dimensional DOS in (3.27) is expressed in units of $\text{cm}^{-2} \times \text{eV}^{-1}$. The total electronic DOS follows from the sum of all subband contributions, which all have the same magnitude given by (3.27): $g(E) = \sum g_n$. This results in the staircase-like

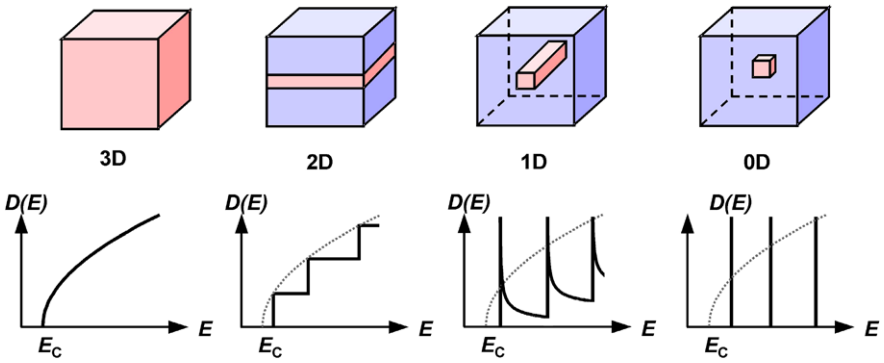


**Fig. 3.18** (**a**) Electronic density of states $g(E)$ in isotropic semiconductors (*red*) with different dimensionalities: 3D bulk semiconductor, 2D quantum well, 1D quantum wire, and 0D quantum dot. The environment drawn in *blue* provides potential barriers for the charge carriers. $E_C$ denotes the conduction-band edge in the semiconductor

function of the total DOS for a two-dimensional (2D) semiconductor illustrated in Fig. 3.18 and expressed by

$$g(E) = \sum g_n = \frac{m^*_{xy}}{\pi\hbar^2} \sum_n \Theta(E - E_n) \quad \text{(two dimensions)}, \tag{3.28}$$

$\Theta(E - E_n)$ being the unit step-function. The subbands are consecutively occupied as the energy is increased.

The one-dimensional case follows from the two-dimensional case by an additional confinement $W(y)$. This leads to a quasi-free mobility only along the $x$ axis. The energies along the $y$ and $z$ axes are quantized, and the subbands have two corresponding indices $l$ and $n$. Analogous to (3.23) and (3.25) we may write

$$E = E_{l,n} = \frac{\hbar^2 k_x^2}{2m^*_x} + l^2 \frac{\hbar^2}{2m^*_y}\left(\frac{\pi}{L_y}\right)^2 + n^2 \frac{\hbar^2}{2m^*_z}\left(\frac{\pi}{L_z}\right)^2 \quad \text{(one dimension)}. \tag{3.29}$$

The one-dimensional electronic DOS is obtained from a one-dimensional "volume" element in **k** space simply given by $dk$, yielding for the subband $l$, $n$

$$g_{l,n}(E) = \sqrt{\frac{m^*_x}{2\pi^2\hbar^2}} \frac{1}{\sqrt{E - E_{l,n}}} \quad \text{(one dimension)}. \tag{3.30}$$

The one-dimensional DOS in (3.30) is expressed in units of $\mathrm{cm}^{-1} \times \mathrm{eV}^{-1}$. The total DOS is again given by the sum of all subband contributions, $g(E) = \sum_{l,n} g_{l,n}(E)$. The resulting function of the one-dimensional (1D) semiconductor is illustrated in Fig. 3.18. Note that the peaks are not necessarily equidistant since $L_y$ and $L_z$ are independent.

Adding a further confining potential $W(x)$ to the one-dimensional semiconductor leads to the zero-dimensional case. The mobility is now restricted in all three spatial

dimensions. Accordingly the energy is quantized in all directions, and from (3.29) follows

$$E = E_{j,l,n} = \frac{\hbar^2\pi^2}{2}\left(\frac{j^2}{m_x^* L_x} + \frac{l^2}{m_y^* L_y} + \frac{n^2}{m_z^* L_z}\right) \quad \text{(zero dimensions)}. \tag{3.31}$$

The zero-dimensional electronic DOS is a sum of $\delta$ functions given by $g(E) = \sum 2\delta(E - E_{j,l,n})$. The function is shown in Fig. 3.18. Like in the two-dimensional case the peaks are not necessarily equidistant.

### 3.3.2 Characteristic Scale for Size Quantization

We considered above the modification of the electronic density-of-states for solids of reduced dimensionality. What is the characteristic scale required for the size quantization to become observable in experiment? Besides the size of the solid it is related to the effective mass of the considered charge carriers and to the temperature. For a quasi-free charge carrier with effective mass $m^*$ size quantization gets distinguishable if the motion is confined to a length scale in the range of or below the de Broglie wavelength $\lambda = h/p = h/\sqrt{2m^*E}$. Assuming a room temperature thermal energy $E = (3/2)k_\mathrm{B}T = 26$ meV and an effective mass of one tenth of the free electron mass, a typical length is in the 10 nm range. In semiconductors often effects of excitons, i.e., correlated electron-hole pairs, are studied instead of those referring to either electrons or holes. The relevant quantity of the two-particle states is the exciton Bohr-radius. The exciton Bohr-radius is given by

$$a_X = \frac{h^2\varepsilon\varepsilon_0}{\pi\mu e_0^2}, \tag{3.32}$$

where $\varepsilon$, $\varepsilon_0$, $\mu$, and $e_0$ designate the relative permittivity of the solid and that of vacuum, the reduced mass of the exciton and the electron charge, respectively. The reduced mass of the exciton is defined by $1/\mu = 1/m_\mathrm{e}^* + 1/m_\mathrm{h}^*$. The hole mass $m_\mathrm{h}^*$ is often much heavier than the electron mass $m_\mathrm{e}^*$, leading to a reduced mass close to $m_\mathrm{e}^*$. The value of the exciton Bohr-radius is related to the binding energy (also termed Rydberg constant) of the exciton

$$E_X = \frac{\mu e_0^4}{8h^2(\varepsilon\varepsilon_0)^2}. \tag{3.33}$$

The product $a_\mathrm{X} \times E_\mathrm{X}$ is constant for three-dimensional excitons. The relation remains a good estimate also for two-dimensional excitons [59]. Values for some semiconductors are given in Table 3.6. A typical length to observe size quantization for excitons is also in the 10 nm range. It must be noted that exciton binding-energy and Bohr radius are significantly modified by a spatial localization [59].

Size-quantization effects were observed at surfaces and in thin layers of both, metals and semiconductors. A review on early work was given in, e.g., Ref. [64].

**Table 3.6** Exciton Bohr radius $a_X$ and binding energy $E_X$ of excitons in some direct semiconductors with zincblende (ZB) or wurtzite (W) structure. A, B, and C in wurtzite material refer to the three valence bands

| Semiconductor | | $a_X$ (Å) | $E_X$ (meV) |
|---|---|---|---|
| GaAs[a] | ZB | 115 | 4.7 |
| InP[b] | ZB | 113 | 5.1 |
| ZnTe[c] | ZB | 11.5 | 13 |
| ZnSe[c] | ZB | 10.7 | 19.9 |
| ZnS[c] | ZB | 10.2 | 29 |
| ZnO[d] | W | | 60 (A) |
| | | | 57 (B) |
| GaN[e] | W | | 21 (A) |
| | | | 21 (B) |
| | | | 23 (C) |

[a]Ref. [60], [b]Ref. [61], [c]Ref. [1], [d]Ref. [62], [e]Ref. [63]

In the following we will focus on semiconductor heterostructures. Clear quantum-size effects are particularly observed in GaAs-based heterostructures. Their electronic properties can be described almost purely quantum mechanically using the effective-mass approximation, with constituent materials represented by a few band parameters.

### *3.3.3 Quantum Wells*

A quantum well is made from a thin semiconductor layer with a smaller bandgap energy clad by semiconductors with a larger bandgap forming barriers. Usually the same barrier material is used in such double heterostructure leading to a symmetrical square potential as illustrated in Fig. 3.8. The confinement is given by the band offsets. Since the potential is no longer infinite as assumed to obtain the eigenvalues (3.25) the wave functions of a confined charge carrier now penetrate into the barriers. For finite barrier energy $W(z) = W_0$ the eigenvalues are obtained from a transcendental equation

$$\tan\left(\sqrt{\frac{m_\mathrm{w} E_n L_z^2}{2\hbar^2}}\right) = \sqrt{\frac{m_\mathrm{w}}{m_\mathrm{b}} \frac{W_0 - E_n}{E_n}} \tag{3.34a}$$

for even wave functions, i.e. even values of quantum numbers $n$, and

$$\cot\left(\sqrt{\frac{m_\mathrm{w} E_n L_z^2}{2\hbar^2}}\right) = \sqrt{\frac{m_\mathrm{w}}{m_\mathrm{b}} \frac{W_0 - E_n}{E_n}} \tag{3.34b}$$

for odd wave functions, i.e., odd $n$ [65]. $m_\mathrm{w}$ and $m_\mathrm{b}$ are the effective masses of the charge carriers in the well and the barriers, respectively, and $L_z$ is the well width. Numerically obtained solutions are given in Fig. 3.19 [66]. Energies in the figure are scaled in units of the ground-state energy $E_1$ of a well with infinite barriers,

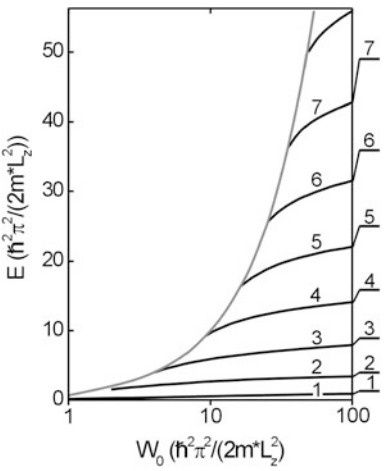


**Fig. 3.19** Calculated bound-state energies of a particle in a symmetrical rectangular potential well of finite depth $W_0$ indicated by the *gray line*. *Bars* at the *right-hand side* mark energy levels with quantum numbers $n$ for infinite high barriers. After [67]

cf. (3.25). The gray line signifies the top of the well at $E = W_0$. Discrete bound states are found for $E < W_0$, while continuum states exist for $E \geq W_0$. We note that the number of bound states of the confined particle decreases as $W_0$ decreases. Furthermore, the level spacing and consequently the energy of the levels decrease. The topmost bound level approaches the top of the well as $W_0$ is gradually reduced. It should be noted that at least one bound level exists in any quantum well.

A clear experimental observation of the quantum-size effect in quantum wells requires well-defined sharp interfaces. A vivid demonstration of subband formation was accomplished by imaging the local DOS in InAs/GaSb quantum wells [68]. Growth conditions ensured the formation of smooth InSb-like interfaces between InAs and GaSb. The two semiconductors form a misaligned staggered band alignment with the conduction-band edge of the InAs quantum well lying below the valence-band edge of the cladding GaSb. This broken-gap configuration provides a large confinement potential for electrons in the well. Using the tip of a low-temperature scanning tunneling microscope the local DOS was probed across the InAs well from the differential conductance $dI/dV$, cf. Fig. 3.20.

The differential conduction given in Fig. 3.20a clearly shows a standing-wave pattern originating from electron subbands in the InAs quantum well. The number of maxima increases with energy, i.e. sample bias voltage. The tunneling tip locally probes the probability amplitude of electrons across the well. The experimental result agrees remarkably well with the calculated subband wave-functions shown in Fig. 3.20b. The two-dimensional DOS of the quantum well given in Fig. 3.20c is experimentally deduced from integrating over the local DOS. The contributions of the subbands lead to apparent steps in the DOS being characteristic for a 2D heterostructure, cf. Fig. 3.18.

Features of both confined electrons and holes are observed in optical spectra. Transitions measured from nearly unstrained GaAs quantum wells with $Al_{0.2}Ga_{0.8}As$ barriers and from strained GaAs wells with $GaAs_{0.5}P_{0.5}$ barriers on GaAs substrates are shown in Fig. 3.21. The structures consist of multiple wells,

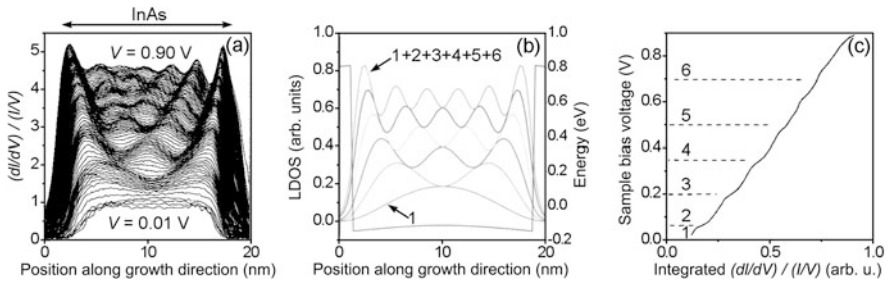


**Fig. 3.20** (**a**) Experimental scanning tunneling $(dI/dV)/(I/V)$ spectra locally probed across a 17 nm wide InAs/GaSb quantum well for bias varied from 0.01 V to 0.9 V in steps of 0.01 V. (**b**) Calculated local density-of-states given as the sum of the squared subband wave-functions. (**c**) Experimental density-of-states obtained from integration of each curve in (**a**) over the quantum well. Reproduced with permission from [68], © 2007 APS

i.e. superlattices with barriers sufficiently thick to prevent electronic coupling of the well states. They were grown using molecular-beam epitaxy [69] and metalorganic vapor-phase epitaxy [70], respectively. The curves show the intensity of the ground-state emission under excitation at the displayed varied photon energy. The spectra exhibit series of peaks labeled according the participating levels of the confined electrons and holes. Most intense peaks refer to allowed transitions between electron and hole states of two-dimensional excitons with an equal quantum number $n$. Such exciton states have largest electron-hole overlap if strain effects are not dominating. The strongest line labeled $E_{1\mathrm{h}}$ originates from the radiation of an exciton with the electron in the $n_\mathrm{e} = 1$ state and the $m_J = 3/2$ hole denoted heavy hole in the $n_\mathrm{hh} = 1$ state. The corresponding transition of an electron and an $m_J = 1/2$ light hole in the $n_\mathrm{lh} = 1$ state is labeled $E_{1\mathrm{l}}$. The energy difference $E_{1\mathrm{l}} - E_{1\mathrm{h}}$ reflects the splitting of the $m_J = 3/2$ and $1/2$ valence bands due to the biaxial shear strain in the GaAs well arising from the different lattice constants of barriers and well (Sect. 3.1.2). Note that excited states gradually broaden, as indicated in Fig. 3.21 for the heavy-hole series labeled $E_{n\mathrm{h}}$. The broadening is described by $\Delta E_n = \Delta E_1 \times n^2$ [69], reflecting a non-constant well width probed by a gradually increasing exciton diameter. Besides the two series of allowed transitions with $n_\mathrm{electron} = n_\mathrm{hole}$ for heavy and light hole there are also forbidden peaks associated with transitions where $n_\mathrm{electron} \neq n_\mathrm{hole}$: Lines $E_{\mathrm{f}1}$ and $E_{\mathrm{f}2}$ mark transitions $E_{1\mathrm{e}} - E_{3\mathrm{h}}$ and $E_{2\mathrm{e}} - E_{4\mathrm{h}}$, respectively [69, 71].

The transitions of the more strongly strained GaAs well clad by $GaAs_{0.5}P_{0.5}$ barriers shown in Fig. 3.21b exhibit a much larger splitting $E_{1\mathrm{l}} - E_{1\mathrm{h}}$ (44 meV) than observed for $Al_{0.2}Ga_{0.8}As$ barriers. Hydrostatic and shear-strain components of $\varepsilon_\mathrm{h} = 0.008$ and $\varepsilon_\mathrm{s} = 0.014$, respectively, were determined from the shift of the ground-state exciton with respect to a GaAs bulk exciton and from the light-hole—heavy-hole splitting [70]. The quantum-size effect is expressed in Fig. 3.21b by a blue shift of the excited-state transitions in the thinner quantum well (lower spectrum).

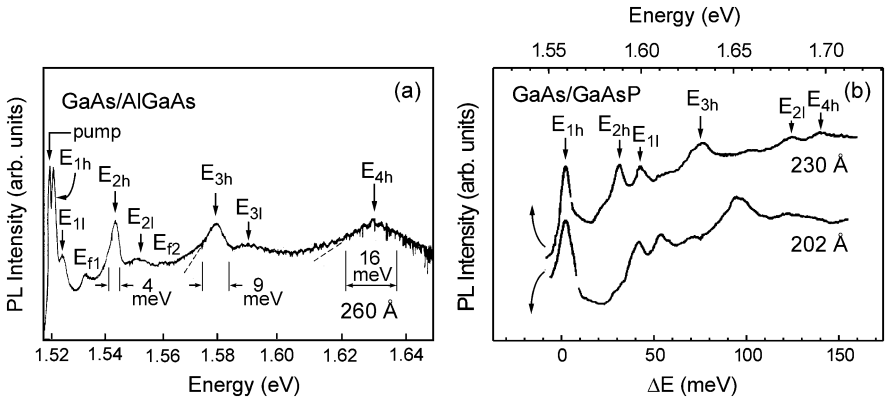


**Fig. 3.21** Photoluminescence excitation spectra of GaAs quantum wells clad by (**a**) $Al_{0.2}Ga_{0.8}As$ and (**b**) $GaAs_{0.5}P_{0.5}$ barriers, recorded at low temperatures and low excitation density. The well width is indicated at the spectra. Labeled energies refer to optical transitions of bound electron states to bound hole states, see text. Absolute energy scale on top of panel (**b**) refers to upper spectrum, the lower spectrum is shifted in energy to align the $E_{1h}$ transition. (**a**) After [69], (**b**) after [70]

The two-dimensional confinement changes spatial extension and binding energy of an exciton both within the quantum-well plane and perpendicular [59]. The effect is illustrated in Fig. 3.22 for an exciton confined in a $GaAs/Al_{0.4}Ga_{0.6}As$ quantum well. We note a strong increase of the binding energy $E_X$ (3.32) in Fig. 3.22a with a maximum for very thin quantum wells near 1 nm. The smaller binding energy of the heavy hole originates from a larger in-plane mass of the light hole [59]. The (degenerate) bulk values of the binding energies of light-hole and heavy-hole excitons are approached for the limits of zero and infinite well width $L_z$. The lateral and perpendicular extensions of the exciton given in Fig. 3.22b show a simultaneous squeezing inverse to the binding energy, according to the rule $a_X \times E_X = \text{const}$.

Heterostructure interfaces are usually not abrupt from a single atomic layer to the next layer in growth direction over a macroscopically large lateral scale. The resulting roughness of the interface is probed by excitons confined in a quantum well. Lateral fluctuations of the well thickness (and composition) are averaged within the spatial extent of the exciton which is given by twice the Bohr radius $a_X$. Such effect leads to the gradual broadening of the exciton series shown in Fig. 3.21. If the fluctuations occur on a scale larger than the exciton diameter discrete transitions may be found. A model for interface roughness due to growth steps with a height of a single monolayer (ML) at both barriers of a quantum well is illustrated in Fig. 3.23. Since a step position at the lower interface is not expected to be reproduced by the upper interface three thicknesses arise from such fluctuations, namely $L_z$, $L_z + 1$ ML, and $L_z - 1$ ML.

Interface disorder of the kind illustrated in Fig. 3.23 may be observed particularly in narrow quantum wells. A clear observation in photoluminescence spectra of $GaAs/Al_xGa_{1-x}As$ quantum wells is shown in Fig. 3.24 [72]. In the (001)-oriented zincblende material one monolayer corresponds to half a lattice constant: 1 ML

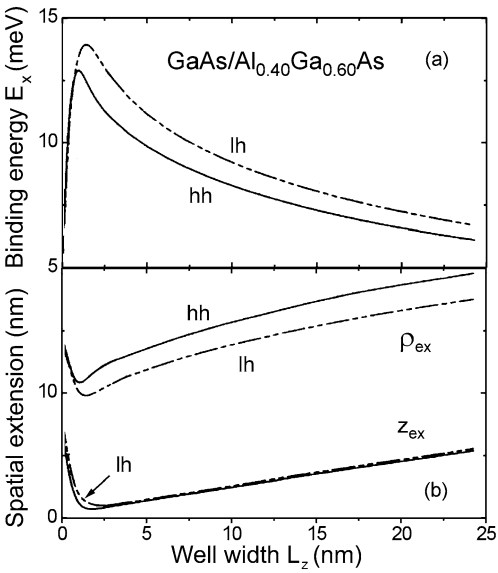


**Fig. 3.22** (**a**) Calculated binding energy and (**b**) both lateral ($\rho_{ex}$) and perpendicular ($z_{ex}$) spatial extension of an exciton confined in a $GaAs/Al_{0.4}Ga_{0.6}As$ quantum well. *Solid* and *dashed lines* refer to heavy and light-hole exciton, respectively. Reproduced with permission from [59], © 1988 APS

$= a/2$, $a$ being the lattice constant of both materials, the quasi-unstrained GaAs well and the $Al_{0.3}Ga_{0.7}As$ barriers.

The sample studied in Fig. 3.24 consists of a $GaAs/Al_{0.3}Ga_{0.7}As$ superlattice (SL) with $L_z = 50$ Å thick wells and 50 Å thick barriers. After growth of each 14 wells (1400 Å) one enlarged well (EW) with an additional thickness of three monolayers (50 Å + 8.6 Å) was introduced. The photoluminescence shows emissions from heavy-hole excitons of the superlattice and the enlarged wells, both split by an amount corresponding to about one-third of their mutual separation. (Corresponding transitions of the light-hole excitons were found in excitation spectra.) This agrees with an expected variation originating from a thickness difference of one monolayer ($a/2$). The position of the individual peaks matches calculated transitions energies of quantum wells with thicknesses $L_z + n \times a/2$, $n = 1$ to 4, and $a = 5.73$ Å, if the transition referring to $L_z$ of the SL well is taken as a reference. The poor agreement of the leftmost peak is attributed to an increased disorder in the extended well. We note that the peaks corresponding to $L_z + 2a/2$ (middle arrow) is missing. Also no peak is found referring to $L_z - a/2$ (above 1.62 eV, no arrow drawn). These transitions would arise from thinner parts of the enlarged well and the superlattice, respectively. They are not observed due to a negligible thermal occupation at the low measurement temperature of 1.7 K.

Size-quantization effects of excited states and interface roughness are frequently observed in quantum wells of various materials systems, albeit usually not as pronounced as in the examples given above.

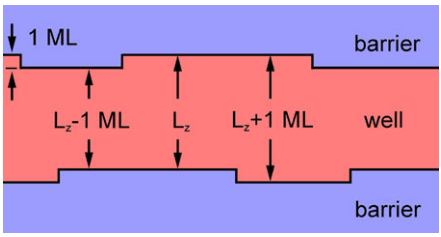


**Fig. 3.23** Cross section of a quantum well/barrier double-heterostructure. Interface roughness by growth steps of single monolayer height is depicted at both barriers of the quantum well

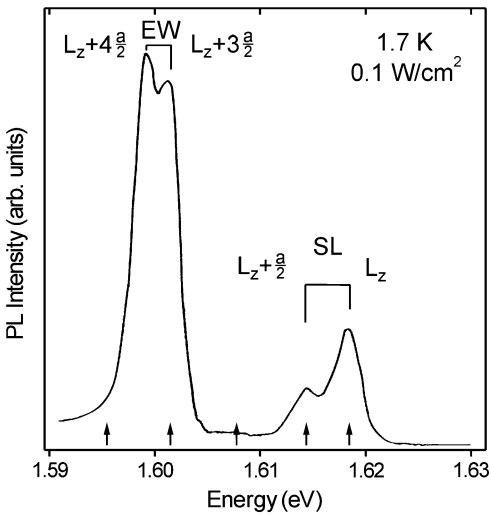


**Fig. 3.24** Photoluminescence spectrum of a $GaAs/Al_{0.3}Ga_{0.7}As$ heterostructure comprising a superlattice with wells of 50 Å (SL) width and also wells with a width enlarged by additional three monolayers to 58.6 Å (EW). The emission was excited non-resonantly with a low excitation density at low temperature. *Arrows at bottom* indicate calculated transitions energies referring to $L_z + n \times a/2$. After [72]

### *3.3.4 Quantum Wires*

Fabrication of a quantum well follows naturally from the two-dimensional epitaxy of a double heterostructure. The potential of such quantum well is basically defined by the well thickness and the (homogeneous) chemical composition of well and barrier materials, i.e., by the band discontinuities. A further reduction of dimensionality towards a one-dimensional quantum wire or a zero-dimensional quantum dot requires some patterning to define an additional lateral confinement. The small dimensions needed to obtain respective quantum size-effects (Sect. 3.3.2) can usually not be accomplished straightforward by patterning a quantum well structure using, e.g., lithography techniques [73]. The interface-to-volume ratio of 1D and 0D structures increases as compared to 2D quantum wells, and the electronic properties of such structures are largely governed by interface effects. A variety of techniques was developed instead to realize 1D and 0D structures with high optical quality, e.g., by employing growth on corrugated substrates [74] or whisker growth. Most of these techniques lead to complicate confinement potentials, and often an additional quantum well is coupled to the quantum wires or quantum dots. A few examples will be considered in this and the following sections.

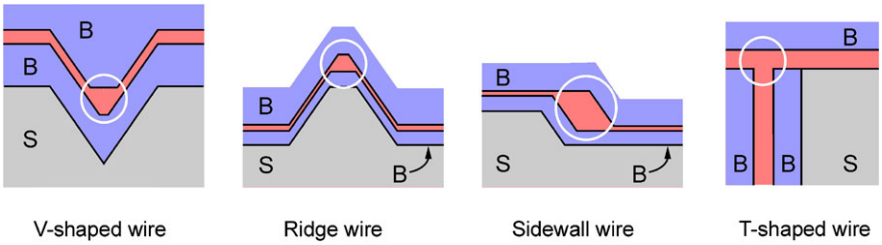


**Fig. 3.25** Cross-section view of typical types of epitaxial quantum wires (*encircled*). *B* and *S* signify barrier and substrate materials, respectively

Much progress in the formation of epitaxial 1D quantum wires was achieved using V-shaped wires or T-shaped wires. A schematic of some typical wire geometries is given in Fig. 3.25.

The V-shaped, ridge, and sidewall wires depicted in Fig. 3.25 are fabricated by employing the dependence of the growth rate on crystallographic orientation. Using patterned substrates with various facet orientations thereby a locally enhanced thickness of a wire material clad by barrier materials can be grown. The T-shaped wire depicted in Fig. 3.25 is formed from an overgrowth of the cleaved edge of a quantum-well structure. The fabrication process of low-dimensional structures is described in more detail in Sect. 5.3.

Early demonstrations of quantum wires in the late 1980s suffered from thickness fluctuations on a length scale of the exciton Bohr radius, leading to 0D behavior at low temperatures. Clear 1D behavior was proved later using improved structures and also by employing micro-photoluminescence on single wires. Photoluminescence (PL) and corresponding excitation (PLE) spectra of V quantum wires are shown in Fig. 3.26 [75]. The given wire thickness refers to the thickest part in the center of the crescent-shaped GaAs, which has parabola-like interfaces to the cladding AlGaAs barriers. The wire emission is labeled QWR in Fig. 3.26a, the dominating emission originates from the quantum wells formed at the side walls of the V groove.

The PLE spectra given in Figs. 3.26b, 3.26c show a number of features also observed with quantum wells, cf. Fig. 3.21. Basically optical transitions with an equal quantum number $n$ of electron and hole states are found. The $e_n$–$h_n$ transitions shift to the blue as the wire thickness decreases, and their mutual energy spacings increase. The assignment of the peaks to corresponding exciton states is not trivial due to the complicate crescent-shaped potential of the wire. The transition energies marked in Figs. 3.26b, 3.26c were calculated using a 16-band **kp** model and a potential shape extracted from transmission-electron micrographs. We note a pronounced oscillator strength of the usually forbidden $e_1$–$h_6$ transition in the thicker well. Moreover, no distinction is drawn between contributions of light holes and heavy holes. Calculations reveal a strong mixing of light- and heavy-hole character in the valence-band states, particularly involved in the mentioned transition. The wave function of the ∼70 % light-hole part of the $h_6$ state has its maximum in the wire center similar to the $e_1$ state, yielding a large overlap [76] (for separate *lh* and

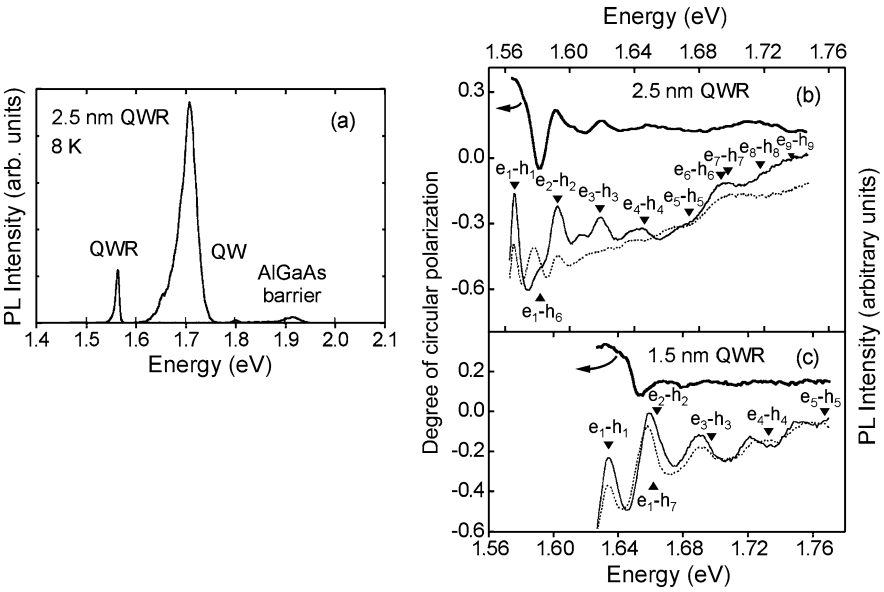


**Fig. 3.26** (**a**) Photoluminescence of a V-shaped GaAs/$Al_{0.3}Ga_{0.7}As$ quantum wire, non-resonantly excited at 2.4 eV with a low excitation density of 25 W/cm$^2$. (**b**) PLE spectra for 2.5 nm and (**c**) 1.5 nm thick wires polarized parallel (*thin solid line*) or perpendicular (*dotted line*) the [110]-oriented wires. Thick *solid curves* represent the degree of circular polarization. *Arrows* mark calculated positions of excitonic $e_n$–$h_m$ interband transitions. Reproduced with permission from [75], © 1997 APS

*hh* assignments cf. [77, 78]). The valence-band mixing also gives rise to the polarization behavior observed in the samples. It should be noted that such mixing and polarization anisotropy may also originate from other sources like structural inhomogeneity, and care was taken to ensure the 1D origin.

For crescent-shaped V groove quantum-wires a simple model with infinite barriers and hyperbolic boundaries was considered to obtain approximative energy separations of the subbands in the wires [79]. The assumed potential leads to analytical solutions given by

$$E_{n,m} \cong \frac{\hbar^2\pi^2 n^2}{2m^* t_0^2} + \frac{\hbar^2\pi\sqrt{\alpha}n}{m^* t_0 \overline{\rho}}(m - 1/2), \quad m, n = 1, 2, 3, \ldots, \tag{3.35}$$

where $m^*$ is the effective charge-carrier mass, $t_0$ is the crescent thickness at its center, and $\overline{\rho} = \sqrt{\rho_{\text{low}} \times \rho_{\text{up}}}$ is the geometric mean radius of the lower and upper radii of the crescent. The upper curvature $\rho_{\text{up}}$ is given by $\rho_{\text{up}} = \rho_{\text{low}} + \alpha t_0$, with $\alpha$ describing the linear increase of the curvature as the wire thickness increases. The second summand in (3.35) describes the energy separation of the 1D subbands due to the lateral confinement.

Size quantization effects of 1D wires are sometimes not well distinguished from those of a 2D well or a 0D dot. The lateral confinement potential of commonly

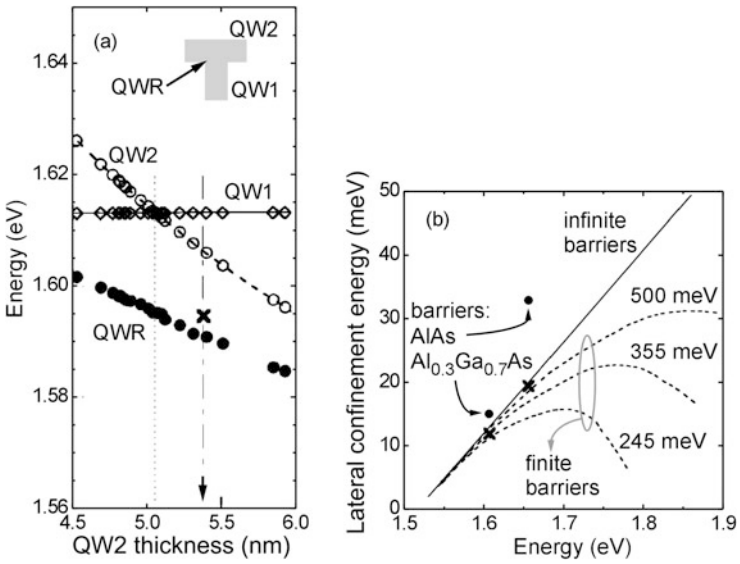


**Fig. 3.27** (**a**) PL peak energies of excitons confined in a T quantum wire (QWR) and the neighboring stem quantum well (QW1) and arm well (QW2) of a GaAs/$Al_{0.3}Ga_{0.7}As$ heterostructure. *Dash-dotted* and *dotted vertical lines* indicate identical QW1 and QW2 well thicknesses and QW2 thickness at identical QW1 and QW2 exciton energy, respectively. (**b**) Calculated lateral confinement energy of electrons in balanced T quantum wires as a function of QW2 exciton energy. *Solid* and *dashed lines* refer to energies for infinite and finite barriers as indicated. *Crosses* and *filled circles*, respectively, mark calculated and experimental confinement energies extracted from the measurement of GaAs/$Al_xGa_{1-x}As$ structures. Reproduced with permission from [80], © 1996 APS

used wire geometries (Fig. 3.25) is typically only of the order of 30–40 meV, giving rise to only 10 meV subband energy-separation [74]. The potential is hence much smaller than that of a quantum well. Furthermore, size fluctuations may give rise to an additional confinement along the wire axis in the same order of magnitude.

The potential depth of the lateral confinement in T-shaped GaAs/$Al_xGa_{1-x}As$ quantum wires was evaluated from sample series with varied well widths and Al compositions. Energies of exciton PL peaks related to the T quantum wire (QWR), the stem well QW1 (vertical quantum well in Fig. 3.25), and the arm well QW2 (horizontal) are shown in Fig. 3.27a for varied thickness of QW2 [80]. The exciton energy increases for thinner QW2 also in the quantum wire. Note that the slope of the QWR energy is smaller than that of the QW2 energy. The energy of the wire hence approaches that of QW1 for thinner QW2 and that of QW2 for thicker QW2. The reason is a convergence of QWR states into QW1 for $t_{QW2} \ll t_{QW1}$ and vice versa into QW2 for $t_{QW2} \gg t_{QW1}$. The spacings between the QWR PL peak energy and those of the quantum wells QW1 and QW2, i.e., the energy differences between the 1D exciton and the 2D exciton states of the neighboring wells, give directly the effective lateral confinement in the wire for given quantum well thicknesses. This value includes possible changes of the exciton binding-energy. The lateral confine-

ment gets maximal for identical thicknesses of QW1 and QW2. For such balanced T quantum wires Fig. 3.27b shows the dependence of the effective lateral confinement on the exciton energy in QW2.

The calculated dependence of lateral confinement energy on the recombination energy of well-excitons given in Fig. 3.27b shows a sublinear increase for finite barrier height. This feature arises from a penetration of the wave function into the wells. The dependence approaches linearity for increasing barriers. At infinite barriers both, QWR energy and QW2 energy scale according $t^{-2}$ leading to the linear relation. The strong experimental *super*linear increase found for increased barriers ($x_{\mathrm{Al}}$ from 0.30 to 1.00) is due to the substantial enhancement of Coulomb interaction in 1D excitons [80].

The excitonic absorption of a 1D quantum wire is expected to deviate significantly from that of a 2D quantum well or a 3D bulk crystal. For direct allowed transitions above band edge the intensity ratio of the unbound (continuum) exciton to the free electron-hole pair is found to be smaller than unity, in contrast to the 2D and 3D cases [81]. The feature may be understood by considering the eigenenergies of states bound in a bare Coulomb potential for $d$ dimensions ($d = 1, 2, 3, \ldots$). The analytical solutions of the Schrödinger equation yield in each dimension $d$ energies $E_n^d$ of eigenstates with $s$ symmetry in form of a Rydberg series [81]

$$E_n^d = -\mathrm{Ry}^* \left( n + \frac{d-1}{2} \right)^{-2}, \quad n = 0, 1, 2, \ldots, \tag{3.36}$$

$\mathrm{Ry}^*$ being the effective Rydberg energy. For the three-dimensional case ($d = 3$) we recognize the well-known Rydberg series of hydrogen. For 1D we note a singularity for the lowest state $n = 0$, corresponding to infinite binding energy, in contrast to the 3D and 2D case. This suggests the attractive force between electron and hole being stronger in 1D than in 2D or 3D. In a descriptive idea a particle may move *around* the origin of a Coulomb potential in 2D or 3D, while it moves *through* the origin in 1D. In fact, the $1/r$ singularity of the Coulomb potential is removed upon integration in 2D and 3D, but it remains as a logarithmic singularity in 1D.

The 1D nature of a quantum wire leads also to a characteristic dynamics of the radiative decay of exciton population after pulse excitation [82]. The population decay time was found to vary proportional to the square root of sample temperature, in contrast to the linear proportionality observed in quantum wells. The PL hence decays slower at low temperatures and faster at high temperatures in wires compared to wells.

### *3.3.5 Quantum Dots*

A quantum dot represents the ultimate limit in charge-carrier confinement, leading to fully quantized electron and hole states like the discrete states in an atom. The most successful approach for the fabrication of dislocation-free semiconductor quantum-dots is the self-organized (also referred to as self-assembled) technique

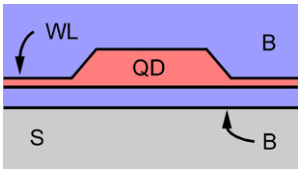


**Fig. 3.28** Cross-section view of a quantum dot grown self-organized in the Stranski–Krastanow mode. $QD$, $WL$, $B$, and $S$ signify quantum dot, wetting layer, barriers and substrate, respectively

of Stranski–Krastanow growth (Sect. 5.3.1). This kind of growth mode may be induced by epitaxy of a highly strained layer, which initially grows two-dimensionally and subsequently transforms to three-dimensional islands due to *elastic* strain relaxation. Some part of the layer material does not redistribute but remains as a two-dimensional layer, due to a low surface free energy compared to the covered material. Since this layer wets the surface of the material underneath it is referred to as wetting layer. For practical use such islands are covered by a cap layer, which builds an upper barrier in addition to the lower barrier provided by the covered material underneath, cf. Fig. 3.28. It must be noted that a minimum size of a quantum dot exists to allow for confining a charge carrier, in contrast to structures of higher dimensionality. For a dot with spherical shape the minimum diameter $D_{\min}$ required to confine at least one bound state of a particle is given by [83]

$$D_{\min} = \frac{\pi\hbar}{\sqrt{2m^* W_0}}, \tag{3.37}$$

where $W_0$ is the confining potential and $m^*$ the effective mass (assumed to be identical in dot and barrier). For a rough estimate of the minimum size to confine a single electron in a spherical InAs/GaAs dot we use an unstrained conduction band offset of $\sim$0.9 eV for $W_0$ and an effective electron mass in InAs of 0.03 $m_0$, yielding $D_{\min} \cong 6$ Å.

Quantum dots grown in the Stranski–Krastanow mode often have a shape of a truncated pyramid. Due to the persistence of the wetting layer in the formation process such dots are coupled to a quantum well, similar to the epitaxial quantum wires depicted in Fig. 3.25. Self-organized Stranski–Krastanow growth may be induced by a strong mismatch of the heterostructure. InAs dots on GaAs with 7 % mismatch represents the most studied model system. The type I band alignment to GaAs leads to a confinement of both, electrons and holes. The finite barrier height provided by the GaAs matrix allows for only few electronic states to be confined within the dot. Luminescence spectra of single quantum dots detected with high spatial resolution show radiative recombination of correlated electrons and holes, cf. Fig. 3.29. The narrow half-width of such confined-exciton recombination reflects the zero-dimensional DOS. Various lines from a single QD originate from states differently filled with few particles like, e.g., the negative trion ($X^-$) formed by two electrons and one hole, or the biexciton (XX) formed by two excitons.

The wave functions of the confined states can be calculated by considering realistic size, shape, and composition of the dot, in addition to material properties like dielectric constants, strain tensors and piezoelectric tensors [85]. Results for

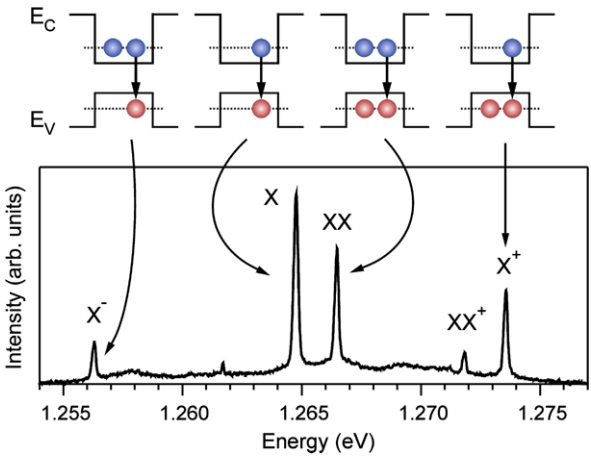


**Fig. 3.29** Luminescence of a single quantum dot showing sharp recombination transitions of neutral and charged confined excitons, as depicted above the spectrum. $E_C$ and $E_V$ denote conduction and valence band edge, respectively. Spectrum reproduced with permission from [84], © 2005 APS

one electron and one hole confined in an InAs dot with pyramidal shape of 11.3 nm base length and {101} side facets in a GaAs matrix are shown in Fig. 3.30. The iso-surfaces encase 65 % probability and resemble atomic $s$-like ground states (left column), and $p$- and $d$-like excited states. Corresponding wave functions of single-electron states in uncovered InAs/GaAs dots were experimentally imaged using a low-temperature scanning-tunneling microscope. The images were obtained from spatially resolved differential voltage-current curves $dI/dV$ taken at different sample voltage [86]. In the same way states of holes confined in InAs quantum dots embedded in GaAs matrix were imaged from cleaved samples [87].

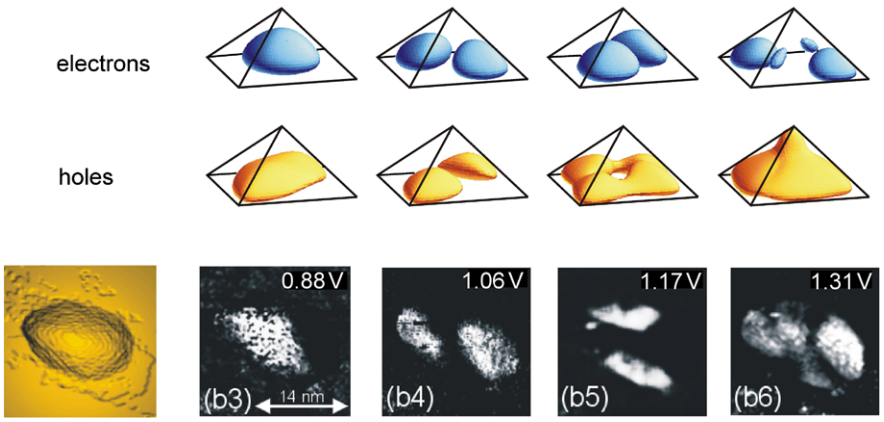


**Fig. 3.30** *Top*: Calculated probability densities of electron and hole wave-functions confined in a *pyramid-shaped* InAs quantum dot in a GaAs matrix. Reproduced with permission from [88], © 1999 APS. *Bottom*: Low-temperature STM images of an uncovered InAs quantum dot on GaAs. *Left image*: Constant-current image showing the dot shape. *Right four images*: Single-electron densities of different excitation states sampled at different bias voltage. Reproduced with permission from [86], © 2003 APS

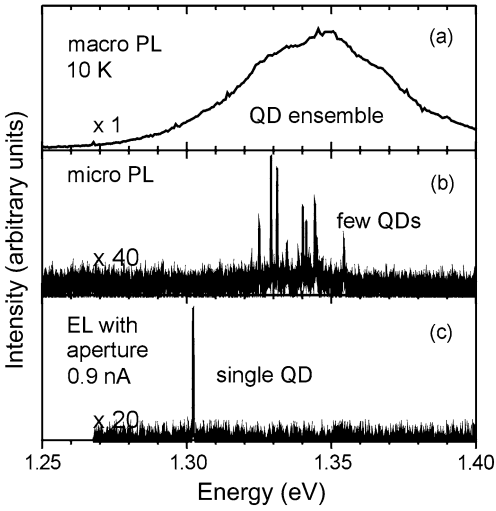


**Fig. 3.31** (**a**, **b**) Luminescence of an InAs/GaAs quantum dot ensemble with $\sim 10^8$ cm$^{-2}$ areal density, detected at 10 K using a conventional setup (**a**) and a setup with a small focus (**b**). (**c**) 10 K electroluminescence of a single dot of the same kind as in (**a**, **b**), integrated into a diode structure with a current-confining aperture of sub-micron diameter. Spectra (**b**) and (**c**) adapted from [89]

The discrete energies of confined charge carriers sensitively depend on size, shape, and composition of the dot. Since these quantities show some variation among individual dots within an ensemble comprising many dots the eigenenergies vary from dot to dot. Optical spectra detected as a response of the entire ensemble are consequently inhomogeneously broadened due to a superposition of numerous transitions of different energies. The discrete nature of the transitions, i.e. the *homogeneous* line width, becomes apparent when only a single dot of an ensemble is spatially selected by using, e.g., micro-photoluminescence (micro PL) or opaque masks with a small aperture. The luminescence spectra shown in Fig. 3.31 illustrate the effect of a gradually increased spatial selection of the detected or excited area in a planar field of a quantum-dot ensemble. The broad luminescence spectrum in Fig. 3.31a measured using a conventional PL setup (macro PL) originates from a large number ($\sim 10^6$) of dots. The full width at half maximum (FWHM) of an ensemble PL is typically several 10 meV broad. The micro-PL setup used in Fig. 3.31b probes the photo-excited quantum-dot ensemble solely within a small focus, thereby detecting only $\rho_{\mathrm{QD}} \times A_{\mathrm{focus}}$ dots simultaneously, $\rho_{\mathrm{QD}}$ being the areal dot density. Further selection eventually leads to the detection of a single dot of the ensemble, cf. Fig. 3.31c and Fig. 3.29.

The homogeneous line width of a single-dot emission is extraordinary small. In absence of inhomogeneous contributions (e.g., by spectral diffusion) it is given by the lifetime $\tau$ of the excited charge carrier according the $\Delta E \times \Delta \tau$ uncertainty relation. It is typically of the order of μeV and usually below the experimental detection limit.

The areal density of a quantum-dot ensemble grown using the Stranski–Krastanow mode is typically in the 1–10 $\times$ $10^{10}$ cm$^{-2}$ range, cf. Sect. 5.3.1. The number of states to be occupied by charge carriers in a single dot layer (or few dot layers) is much smaller than in bulk or a quantum well. Occupation of quantum dots with more than one exciton or charge carrier hence occurs already at reasonably

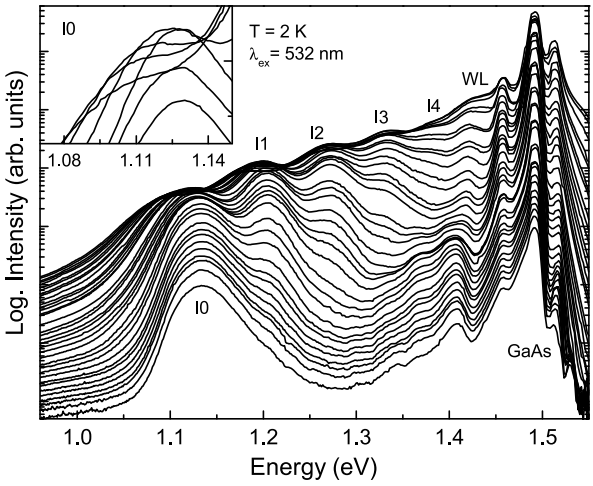


**Fig. 3.32** Photoluminescence spectra of an $In_{0.6}Ga_{0.4}As/GaAs$ quantum-dot ensemble, excited into the GaAs matrix with an excitation density gradually increasing from 0.2 W/cm$^{-2}$ (*bottom*) to 5 kW/cm$^{-2}$. *I0* marks ground-state emission, peaks *I2* to *I4* originate from excited states. *WL* and *GaAs* signify emission from the wetting layer and the *GaAs* matrix, respectively. *Inset*: Emission *I0* on a linear scale. Reproduced with permission from [90], © 2004 Elsevier

low optical or electrical excitation. Since the ground state may be occupied with only two charge carriers (of opposite spin) excited states are easily populated. Figure 3.32 shows the strong occupation of excited levels in a quantum-dot ensemble at increased excitation density. While at low excitation density only the inhomogeneously broadened emission from the ground state labeled I0 is observed, gradually additional emissions from excited states (I1 to I4) appear on the high-energy side for more intense excitation. The number of excited levels is high in this particular sample, because an $Al_{0.3}Ga_{0.7}As$ barrier was placed underneath the dot layer, separated by a 1 nm thick GaAs spacer, so as to increase the confinement potential. Taking the degeneracy $2(n+1)$ of an harmonic potential as a rough estimate for the exciton occupation in a quantum dot, the maximum overall occupation number of the confined excitonic states is about 30 in the studied case.

A close look to the energies of the quantum dot emission shows that the increasing occupation of levels with charge carriers is accompanied by a small energy decrease. The ground-state transition, e.g., exhibits a red shift by a total of 35 meV (inset Fig. 3.32). Such behavior cannot be described in a single-particle picture, because the Coulomb interaction between the confined particles alters the overall energy in the system. The effect is referred to as *renormalization* of the band gap. The origin was traced back in bulk semiconductors to the exchange-correlation energy in dense charge-carrier ensembles, being independent on the characteristics of the electronic band structure, i.e., on the material [91]. It is also pronounced in quantum-well structures [92]. In quantum wires [93] and quantum dots [94] such renormalization may be smaller in case of a dominating strong confinement.

An ensemble of self-organized quantum dots usually exhibits a single distribution of dot sizes and compositions, leading to a single inhomogeneously broadened ensemble emission. Under certain growth conditions also distributions with several well separated emission maxima are formed. An insight into the interplay between confined-particle interaction and confinement potential was obtained using dots with a multimodal size distribution, featuring a number of clearly resolved fairly narrow

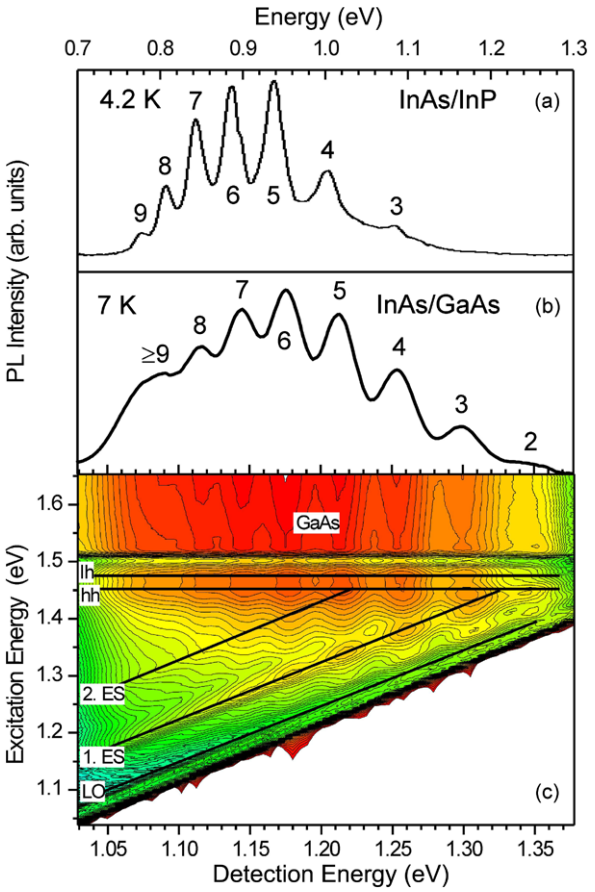


**Fig. 3.33** Ensemble emission of (**a**) InAs/InP and (**b**) InAs/GaAs quantum dots with a multimodal size distribution. Numbers at the peaks refer to a common dot height within a subensemble in units of monolayers. (**c**) Combined PL and PL-excitation contour plot of the ensemble measured in (**b**) on a logarithmic color scale, abscissa also applies for (**b**). *Horizontal lines* mark light-hole (*lh*) and heavy-hole (*hh*) resonances of the wetting layer, *inclined lines* indicate resonances of the first and second excited state of the dots and an *LO* phonon transition. Data in (**a**) adapted from [98], data in (**b**) and (**c**) reproduced with permission from [99], © 2007 Elsevier

emission peaks of the ensemble [95]. The multiple peaks refer to subensembles (or families) of dots within the ensemble, which differ in height by integral numbers of InAs monolayers. Peak labels given in Fig. 3.33 indicate the height of the dots in the corresponding subensemble in units of monolayers. The assignment was proved by both structural characterization [96] and calculated exciton energies [97], revealing a truncated pyramidal shape of the dots. Spectra shown in Fig. 3.33a, b were excited with a low excitation density to ensure emission solely from the ground state.

PL excitation spectra of a multimodal dot ensemble are given in the contour plot Fig. 3.33c: A horizontal cut represents a photoluminescence spectrum at fixed excitation energy, a vertical cut represents an excitation spectrum for the selected detection energy. For large quantum dots with low emission energy an excitation spectrum shows two excited states ES1 and ES2 below the excitation of the dot emission via the wetting layer (labels hh and lh). We note that smaller dots with a height between 5 and 3 monolayers—and correspondingly a higher emission energy between 1.22 eV and 1.32 eV—have only a single excited state. Dots with even higher emission energy ($>1.32$ eV) have no excited state at all.

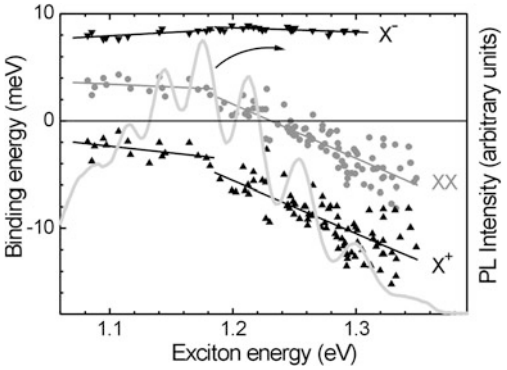


**Fig. 3.34** Binding energy of few-particle complexes confined in InAs/GaAs quantum dots as a function of the neutral exciton emission energy. *0* refers to the neutral exciton recombination energy. $X^-$, $X^+$, and *XX* refer to negative trion, positive trion, and biexciton. *Right ordinate* corresponds to the light-gray emission spectrum. Reproduced with permission from [99], © 2007 Elsevier

The well-defined size and shape of multimodal dots was employed to study the renormalization of few-particle transition energies acting when, e.g., one electron and hole recombine in the presence of additional charge carriers. Figure 3.34 shows relative binding energies of negative trions (consisting of 2 electrons and 1 hole), positive trions $(1e, 2h)$, and biexcitons $(2e, 2h)$ for many single-dot spectra recorded all over the inhomogeneously broadened ensemble peak [100]. The binding energy of these few-particle complexes is given with respect to the (neutral) exciton-recombination energy and the recombination energy of these complexes, i.e. by $E_{\mathrm{X}} - E_{\mathrm{complex}}$.

The three excitonic complexes show an obvious characteristic trend. The negatively charged exciton labeled $\mathrm{X}^-$ has always a positive binding energy being almost independent on the neutral exciton-recombination energy. Contrary the binding energies of the positively charged exciton $\mathrm{X}^+$ and the biexciton XX clearly decrease for increasing exciton-recombination energy (decreasing dot size). Moreover, for the biexciton a transition from positive to negative binding energies is observed.

The non-zero binding energies originate from the Coulomb interaction $C$ between the confined charge carriers. The binding energy of, e.g., $\mathrm{X}^-$ directly depends on the difference between the two direct Coulomb terms $C(e,h)$ and $C(e,e)$. The wave function of the hole is much stronger localized than that of the electron due to the larger effective mass of the holes, independent on the dot size as shown on top of Fig. 3.35. The absolute value of the Coulomb interaction between two electrons $|C(e,e)|$ is consequently smaller than that between two holes, and that between an electron and a hole is in between, i.e., $|C(e,e)| < |C(e,h)| < |C(h,h)|$, cf. Fig. 3.35a. All energies increase in smaller dots because the wave functions are slightly squeezed. A negative trion is formed by adding an electron to a dot which is filled with an exciton, thereby adding a repulsive interaction and additionally a (larger) attractive interaction. The negative trion has therefore a positive binding energy $E_{\mathrm{X}} - E_{\mathrm{X}^-}$, while the positive trion has a negative binding energy.

The simple picture does not account for the trend of the biexciton XX. Including three instead of one level for both, electron and hole states into the calculation (i.e., considering also effects of *correlation*) changes the result from a nearly constant negative binding energy (Fig. 3.35b) to a nearly constant positive binding energy

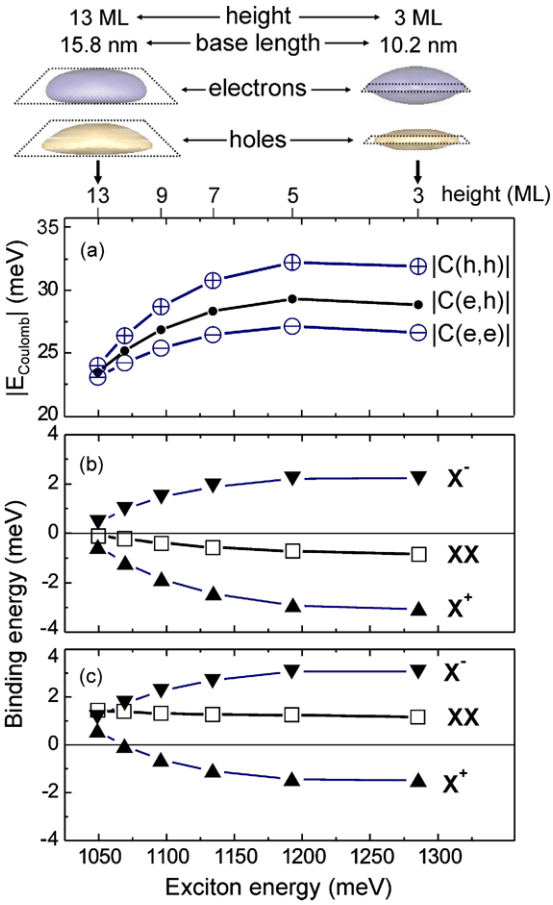


**Fig. 3.35** *Top*: Electron and hole wave-function (65 % probability surface) for confinement in a 15 monolayer high (*left*) and 3 monolayer high (*right*) InAs/GaAs quantum dot. (**a**) Absolute value of the Coulomb energy between two charge carriers confined in a quantum dot. (**b**, **c**) Calculated few-particle binding energies: (**b**) only ground state considered, (**c**) additionally 2 excited levels for both, electrons and holes included. Reproduced with permission from [101], © 2006 Elsevier

(Fig. 3.35c). Figure 3.33c demonstrates that large dots bind more confined levels than small dots. Consequently the degree of correlation decreases as the dot size decreases. We hence start with large dots (small exciton energy) in a case depicted in Fig. 3.35c, and end with small dots in a case similar to Fig. 3.35b. Thereby the XX binding energy changes from positive to negative values as found in the experiment Fig. 3.34. A more detailed consideration shows that the number of *hole* levels plays a major role in correlation [100].

## 3.4 Problems Chap. 3

3.1 The $Ga_{1-x}In_xP$ alloy is interesting due to its large bandgap energy compared to that of GaAs and InP.

(a) Calculate the bandgap energy of $In_xGa_{1-x}P$ at room temperature, assuming a layer which is lattice-matched on GaAs substrate. Check whether this

alloy has a direct or an indirect conduction-band minimum. Compare the order of these bandgap energies to that expected from the virtual crystal approximation. Room-temperature bandgap parameters $E^{\Gamma}$, $E^{\mathrm{X}}$, $E^{\mathrm{L}}$ (in eV) of GaP are 2.78, 2.27, 2.6, and parameters of InP are 1.34, 2.19, 1.93, respectively. The bowing parameters of the alloy are (in eV) $b^{\Gamma} = 0.65$, $b^{\mathrm{X}} = 0.20$, $b^{\mathrm{L}} = 1.03$.

(b) Determine the composition parameter $x$, where unstrained $Ga_{1-x}In_xP$ changes from a direct to an indirect semiconductor. Which bandgap energy exists at the crossing point?

3.2 Consider a lattice-matched InP/$In_xGa_{1-x}As$/InP double heterostructure on (001) InP substrate. Find the offset in the conduction band at 300 K and at 77 K, if the valence-band offset of +0.36 eV from InP to $In_xGa_{1-x}As$ is assumed temperature-independent, and effects of thermally induced strain can be neglected. Band parameters $E_g$ at 0 K (in eV), $\alpha$ (in meV/K), and $\beta$ (in K) are for InAs 0.417, 0.276, and 93, for GaAs 1.519, 0.541, and 204, and for InP 1.424, 0.363, and 162, respectively, $b_{\mathrm{InGaAs}} = 0.48$ eV.

3.3 A pseudomorphic hexagonal $Al_{0.2}Ga_{0.8}N$ layer grown on a relaxed thick GaN buffer layer produces a sheet charge-density at the interface induced by piezoelectric polarization. Apply in the following linearly weighted materials parameters.

(a) Calculate the sheet carrier-concentration per $cm^2$ of the AlGaN layer originating from the piezoelectric polarization.

(b) The piezoelectric polarization adds to the spontaneous polarization of a wurtzite semiconductors, the latter being $-0.029$ C/$m^2$ for GaN and $-0.081$ C/$m^2$ for AlN. Determine the lateral strain of the GaN layer required to yield a zero total polarization in the AlGaN layer. What is then the resulting total sheet carrier-density at the interface?

3.4 (a) Find the offset in the valence band and the conduction band for a transition from a GaAs (001) substrate to a thin pseudomorphic InP layer. Neglect the strain-induced splitting between heavy hole and light hole.

(b) What offsets occur in the inverse heterostructure of a thin pseudomorphic GaAs layer on InP(001) substrate, if the strain-induced splitting between heavy hole and light hole is neglected?

(c) Compare the energy splitting between the heavy-hole valence band and the light-hole valence band of GaAs in case (b) with the band offsets calculated for a neglected splitting. Which exciton has lowest energy? What are the actual band offsets obtained by including the energy splitting between heavy hole and light hole?

3.5 (a) The temperature dependence of the direct bandgap of GaAs is described by the parameters $\alpha = 0.54$ meV/K and $\beta = 204$ K. Which bandgap energy has GaAs at room temperature (300 K) and at the temperature of liquid nitrogen (77 K)?

(b) The effective bandgap changes in presence of a confining potential. It is then approximately given by the difference between the ground-state levels of the electron in the conduction band and the hole (with lowest energy)

in the valence band. Calculate the effective bandgap of an unstrained GaAs quantum well of 9 nm thickness for infinite barriers at room temperature. Effective electron and hole masses are $0.067m_e$ and $0.082m_e$, respectively.

(c) The thickness of the quantum well in (b) varies by $\pm$ one monolayer due to interface roughness. To which variations in the effective bandgap translates this thickness fluctuation?

## 3.5 General Reading Chap. 3

E.T. Yu, J.O. McCaldin, T.C. McGill, Band offsets in semiconductor heterojunctions, in *Solid State Physics*, vol. 46, ed. by H. Ehrenreich, D. Turnbull (Academic Press, Boston, 1992), pp. 1–146
P.Y. Yu, M. Cardona, *Fundamentals of Semiconductors* (Springer, Berlin, 1996)

## References


1. P.Y. Yu, M. Cardona, *Fundamentals of Semiconductors* (Springer, Berlin, 1996)
2. I. Vurgaftman, J.R. Meyer, L.R. Ram-Mohan, Band parameters for III–V compound semiconductors and their alloys. J. Appl. Phys. **89**, 5815 (2001)
3. M. Suzuki, T. Uenoyama, First-principles calculations of effective-mass parameters of AlN and GaN. Phys. Rev. B **52**, 8132 (1995)
4. G.L. Bir, G.E. Pirkus, *Symmetry and Strain-Induced Effects in Semiconductors* (Wiley, New York, 1974)
5. F.H. Pollak, M. Cardona, Piezo-electroreflectance in Ge, GaAs, and Si. Phys. Rev. **172**, 816 (1968)
6. C.G. van de Walle, R.M. Martin, Theoretical calculation of heterojunction discontinuities in the Si/Ge system. Phys. Rev. B **34**, 5621 (1986)
7. K. Shahzad, D.J. Olego, C.G. van de Walle, Optical characterization and band offsets in ZnSe-$ZnS_xSe_{1-x}$ strained-layer superlattices. Phys. Rev. B **38**, 1417 (1988)
8. C.G. van de Walle, Band lineups and deformation potentials in the model-solid theory. Phys. Rev. B **39**, 1871 (1989)
9. D. Fröhlich, W. Nieswand, U.W. Pohl, J. Wrzesinski, Two-photon spectroscopy of ZnSe under uniaxial stress. Phys. Rev. B **52**, 14652 (1995)
10. F. Kubacki, J. Gutowski, D. Hommel, M. Heuken, U.W. Pohl, Determination of deformation potentials in ZnSe/GaAs strained-layer heterostructures. Phys. Rev. B **54**, 2028 (1996)
11. L.D. Laude, F.H. Pollak, M. Cardona, Effects of uniaxial stress on the indirect exciton spectrum of silicon. Phys. Rev. B **3**, 2623 (1971)
12. H. Mathieu, P. Merle, E.L. Ameziane, B. Archilla, J. Camassel, Deformation potentials of the direct and indirect absorption edges of GaP. Phys. Rev. B **19**, 2209 (1984)
13. P. Pfeffer, I. Gorczyca, W. Zawadzki, Theory of free-electron optical absorption in $n$-GaAs. Solid State Commun. **51**, 179 (1984). Table 1 with references therein
14. O. Ambacher, J. Smart, J.R. Shealy, N.G. Weimann, K. Chu, M. Murphy, W.J. Schaff, L.F. Eastman, R. Dimitrov, L. Wittmer, M. Stutzmann, W. Rieger, J. Hilsenbeck, Two-dimensional electron gases induced by spontaneous and piezoelectric polarization charges in N- and Ga-face AlGaN/GaN heterostructures. J. Appl. Phys. **85**, 3222 (1999)
15. F. Bernardini, V. Fiorentini, D. Vanderbilt, Spontaneous polarization and piezoelectric constants of III–V nitrides. Phys. Rev. B **56**, R10024 (1997)

16. U. Rössler (ed.), *Semiconductor II–VI and I–VII Compounds; Semimagnetic Compounds*. Landolt-Börnstein III/41B, revised and updated edition of Vols. III/17 and 22 (Springer, Heidelberg, 1999)
17. O. Ambacher, B. Foutz, J. Smart, J.R. Shealy, N.G. Weimann, K. Chu, M. Murphy, A.J. Sierakowski, W.J. Schaff, L.F. Eastman, R. Dimitrov, A. Mitchell, M. Stutzmann, Two-dimensional electron gases induced by spontaneous and piezoelectric polarization in undoped and doped AlGaN/GaN heterostructures. J. Appl. Phys. **87**, 334 (2000)
18. Y.P. Varshni, Temperature dependence of the energy gap in semiconductors. Physica **34**, 149 (1967)
19. L. Viña, S. Logothetidis, M. Cardona, Temperature dependence of the dielectric function of germanium. Phys. Rev. B **30**, 1979 (1984)
20. K.P. O'Donnell, X. Chen, Temperature dependence of semiconductor band gaps. Appl. Phys. Lett. **58**, 2924 (1991)
21. R. Pässler, Parameter sets due to fittings of the temperature dependencies of fundamental bandgaps in semiconductors. Phys. Status Solidi B **216**, 975 (1999)
22. W. Bludau, A. Onton, W. Heinke, Temperature dependence of the band gap of silicon. J. Appl. Phys. **45**, 1846 (1974)
23. J.A. Van Vechten, T.K. Bergstresser, Electronic structures of semiconductor alloys. Phys. Rev. B **1**, 3351 (1970)
24. C.K. Williams, T.H. Glisson, J.R. Hauser, M.A. Littlejohn, Energy bandgap and lattice constant contours of III–V quaternary alloys of the form $A_x B_y C_z D$ or $A B_x C_y D_z$. J. Electron. Mater. **7**, 639 (1978)
25. A. Baldereschi, E. Hess, K. Maschke, H. Neumann, K.-R. Schulze, K. Unger, Energy band structure of $Al_xGa_{1-x}As$. J. Phys. C, Solid State Phys. **10**, 4709 (1977)
26. A.-B. Chen, A. Sher, Electronic structure of III–V semiconductors and alloys using simple orbitals. Phys. Rev. B **22**, 3886 (1980)
27. A.-B. Chen, A. Sher, Electronic structure of pseudobinary semiconductor alloys $Al_xGa_{1-x}As$, $GaP_xAs_{1-x}$, and $Ga_xIn_{1-x}P$. Phys. Rev. B **23**, 5360 (1981)
28. J.E. Bernard, A. Zunger, Electronic structure of ZnS, ZnSe, ZnTe, and their pseudobinary alloys. Phys. Rev. B **36**, 3199 (1987)
29. A.T. Gorelenok, A.G. Dzigasov, P.P. Moskvin, V.S. Sorokin, I.S. Tarasov, Dependence of the band gap on the composition of $In_{1-x}Ga_xAs_{1-y}P_y$ solid solutions. Sov. Phys. Semicond. **15**, 1400 (1981)
30. E.T. Yu, J.O. McCaldin, T.C. McGill, Band offsets in semiconductor heterojunctions. *Solid State Physics*, vol. 46 (Academic Press, New York, 1992), pp. 1–146
31. R.L. Anderson, Experiments on Ge-GaAs heterojunctions. Solid-State Electron. **5**, 341 (1962)
32. A.G. Milnes, D.L. Feucht, *Heterojunctions and Metal-Semiconductor Junctions* (Academic Press, New York, 1972)
33. W.R. Frensley, H. Kroemer, Theory of the energy-band lineup at an abrupt semiconductor heterojunction. Phys. Rev. B **16**, 2642 (1977)
34. W.A. Harrison, Elementary theory of heterojunctions. J. Vac. Sci. Technol. **14**, 1016 (1977)
35. S.-H. Wei, A. Zunger, Role of d orbitals in valence-band offsets of common-anion semiconductors. Phys. Rev. Lett. **59**, 144 (1987)
36. J. Tersoff, Band lineups at II–VI heterojunctions: failure of the common-anion rule. Phys. Rev. Lett. **56**, 2755 (1986)
37. A.D. Katnani, G. Margaritondo, Empirical rule to predict heterojunction band discontinuities. J. Appl. Phys. **54**, 2522 (1983)
38. A.D. Katnani, R.S. Bauer, Commutativity and transitivity of GaAs-AlAs-Ge(100) band offsets. Phys. Rev. B **33**, 1106 (1986)
39. J.M. Langer, H. Heinrich, Deep-level impurities: a possible guide to prediction of band-edge discontinuities in semiconductor heterojunctions. Phys. Rev. Lett. **55**, 1414 (1985)
40. A. Zunger, Electronic structure of 3d transition-atom impurities in semiconductors, in *Solid State Physics*, vol. 39 (Academic Press, New York, 1986), pp. 275–464

41. C.G. van de Walle, J. Neugebauer, Universal alignment of hydrogen levels in semiconductors, insulators and solutions. Nature **423**, 626 (2003)
42. J. Tersoff, Theory of semiconductor heterojunctions: the role of quantum dipoles. Phys. Rev. B **30**, 4874 (1984)
43. J. Tersoff, Shottky barrier heights and the continuum of gap states. Phys. Rev. Lett. **52**, 465 (1984)
44. C.G. van de Walle, R.M. Martin, Theoretical study of band offsets at semiconductor interfaces. Phys. Rev. B **35**, 8154 (1987)
45. R.G. Dandrea, S. Froyen, A. Zunger, Stability and band offsets of heterovalent superlattices: Si/GaP, Ge/GaAs, and Si/GaAs. Phys. Rev. B **42**, 3213 (1990)
46. S. Rubini, E. Milocco, L. Sorba, E. Pelucchi, A. Franciosi, A. Garulli, A. Parisini, Y. Zhuang, G. Bauer, Structural and electronic properties of ZnSe/AlAs heterostructures. Phys. Rev. B **63**, 155312 (2001)
47. W.A. Harrison, E.A. Kraut, J.R. Waldrop, R.W. Grant, Polar heterojunction interfaces. Phys. Rev. B **18**, 4402 (1978)
48. A. Kley, J. Neugebauer, Atomic and electronic structure of the GaAs/ZnSe (001) interface. Phys. Rev. B **50**, 8616 (1994)
49. R.G. Dandrea, S. Froyen, A. Zunger, Stability and band offsets of heterovalent superlattices: Si/GaP, Ge/GaAs, and Si/GaAs. Phys. Rev. B **42**, 3213 (1990)
50. R. Nicolini, L. Vanzetti, G. Mula, G. Bratina, L. Sorba, A. Franciosi, M. Peressi, S. Baroni, R. Resta, A. Baldereschi, Local interface composition and band discontinuities in heterovalent heterostructures. Phys. Rev. Lett. **72**, 294 (1994)
51. A. Bonanni, L. Vanzetti, L. Sorba, A. Franciosi, M. Lomascolo, P. Prete, R. Cingolani, Optimization of interface parameters and bulk properties in ZnSe-GaAs heterostructures. Appl. Phys. Lett. **66**, 1092 (1995)
52. N. Kobayashi, Single quantum well photoluminescence in ZnSe/GaAs/AlGaAs grown by migration-enhanced epitaxy. Appl. Phys. Lett. **55**, 1235 (1989)
53. M. Städele, J.A. Majewski, P. Vogl, Stability and band offsets of polar GaN/SiC(001) and AlN/SiC(001) interfaces. Phys. Rev. B **56**, 6911 (1997)
54. F. Bernardini, M. Peressi, V. Fiorentini, Band offsets and stability of BeTe/ZnSe(100) heterojunctions. Phys. Rev. B **62**, R16302 (2000)
55. Z.-G. Wang, L.-Å. Ledebo, H.G. Grimmeis, Optical properties of iron doped $Al_xGa_{1-x}As$ alloys. J. Appl. Phys. **56**, 2762 (1984)
56. Z.-G. Wang, L.-Å. Ledebo, H.G. Grimmeis, Nuovo Cimento **2D**, 1718 (1983)
57. L. Samuelson, S. Nilsson, Z.-G. Wang, H.G. Grimmeis, Direct evidence for random-alloy splitting of Cu levels in $GaAs_{1-x}P_x$. Phys. Rev. Lett. **53**, 1501 (1984)
58. A.A. Reeder, J.M. Chamberlain, Optical study of the deep manganese acceptor in $In_{1-x}Ga_xP$: evidence for vacuum-level pinning. Solid State Commun. **54**, 705 (1985)
59. M. Grundmann, D. Bimberg, Anisotropy effects on excitonic properties in realistic quantum wells. Phys. Rev. B **38**, 13486 (1988)
60. S. Adachi, GaAs, AlAs and $Al_xGa_{1-x}As$: material parameters for use in research and device applications. J. Appl. Phys. **58**, R1 (1985)
61. S. Adachi, *Physical Properties of III–V Semiconductor Compounds* (Wiley, New York, 1992)
62. D.C. Reynolds, D.C. Look, B. Jogai, C.W. Litton, G. Cantwell, W.C. Harsch, Valence-band ordering in ZnO. Phys. Rev. B **60**, 2340 (1999)
63. W. Shan, B.D. Little, A.J. Fischer, J.J. Song, B. Goldenberg, W.G. Perry, M.D. Bremser, R.F. Davis, Binding energy for the intrinsic excitons in wurtzite GaN. Phys. Rev. B **54**, 16369 (1996)
64. G. Dorda, Surface quantization in semiconductors, in *Festkörperprobleme*, ed. by H.J. Queisser. Advances in Solid State Physics, vol. 13 (Pergamon/Vieweg, Braunschweig, 1973), p. 215
65. G. Bastard, J.A. Brum, Electronic states in semiconductor heterostructures. IEEE J. Quantum Electron. **QE-22**, 1625 (1986)

66. R. Dingle, W. Wiegmann, C.H. Henry, Quantum states of confined carriers in very thin $Al_xGa_{1-x}As$-GaAs-$Al_xGa_{1-x}As$ heterostructures. Phys. Rev. Lett. **33**, 827 (1974)
67. R. Dingle, Confined carrier quantum states in ultrathin semiconductor heterostructures, in *Festkörperprobleme*, ed. by H.J. Queisser. Advances in Solid State Physics, vol. 15 (Pergamon/Vieweg, Braunschweig, 1975), p. 21
68. K. Suzuki, K. Kanisawa, C. Janer, S. Perraud, K. Takashina, T. Fujisawa, Y. Hirayama, Spatial imaging of two-dimensional electronic states in semiconductor quantum wells. Phys. Rev. Lett. **98**, 136802 (2007)
69. R.C. Miller, D.A. Kleiman, W.A. Nordland Jr., A.C. Gossard, Luminescence studies of optically pumped quantum wells in GaAs-$Al_xGa_{1-x}As$ multilayer structures. Phys. Rev. B **22**, 863 (1980)
70. P.L. Gourley, R.M. Biefeld, Quantum size effects in GaAs/$GaAs_xP_{1-x}$ strained-layer superlattices. Appl. Phys. Lett. **45**, 749 (1984)
71. R.C. Miller, D.A. Kleiman, O. Munteanu, W.T. Tsang, New transitions in the photoluminescence of GaAs quantum wells. Appl. Phys. Lett. **39**, 1 (1981)
72. B. Deveaud, J.Y. Emery, A. Chomette, B. Lambert, M. Baudet, Observation of one-monolayer size fluctuations in a GaAs/GaAlAs superlattice. Appl. Phys. Lett. **45**, 1078 (1984)
73. A. Forchel, H. Leier, B.E. Maile, R. Germann, Fabrication and optical spectroscopy of ultra small III–V compound semiconductor structures, in *Festkörperprobleme*, ed. by U. Rössler. Advances in Solid State Physics, vol. 28 (Pergamon/Vieweg, Braunschweig, 1988), p. 99
74. X.-L. Wang, V. Voliotis, Epitaxial growth and optical properties of semiconductor quantum wires. J. Appl. Phys. **99**, 121301 (2006)
75. F. Vouilloz, D.Y. Oberli, M.-A. Dupertuis, A. Gustafsson, F. Reinhardt, E. Kapon, Polarization anisotropy and valence band mixing in semiconductor quantum wires. Phys. Rev. Lett. **78**, 1580 (1997)
76. F. Vouilloz, D.Y. Oberli, M.-A. Dupertuis, A. Gustafsson, F. Reinhardt, E. Kapon, Effect of lateral confinement on valence-band mixing and polarization anisotropy in quantum wires. Phys. Rev. B **57**, 12378 (1998)
77. Z.-Y. Deng, X. Chen, T. Ohji, T. Kobayashi, Subband structures and exciton and impurity states in V-shaped GaAs-$Ga_{1-x}Al_xAs$ quantum wires. Phys. Rev. B **61**, 15905 (2000)
78. E. Martinet, M.-A. Dupertuis, F. Reinhardt, G. Biasiol, E. Kapon, O. Stier, M. Grundmann, D. Bimberg, Separation of strain and quantum-confinement effects in the optical spectra of quantum wires. Phys. Rev. B **61**, 4488 (2000)
79. E. Kapon, G. Biasiol, D.M. Hwang, E. Colas, M. Walther, Self-ordering mechanism of quantum wires grown on non-planar substrates. Solid-State Electron. **40**, 815 (1996)
80. T. Someya, H. Akiyama, H. Sakaki, Enhanced binding energy of one-dimensional excitons in quantum wires. Phys. Rev. Lett. **76**, 2965 (1996)
81. T. Ogawa, T. Takagahara, An exact treatment of excitonic effects. Phys. Rev. B **44**, 8138 (1991)
82. D. Gershoni, M. Katz, W. Wegscheider, L.N. Pfeiffer, R.A. Logan, K. West, Radiative lifetimes of excitons in quantum wires. Phys. Rev. B **50**, 8930 (1994)
83. D. Bimberg, M. Grundmann, N.N. Ledentsov, *Quantum Dot Heterostructures* (Wiley, Chichester, 1999)
84. S. Rodt, A. Schliwa, K. Pötschke, F. Guffarth, D. Bimberg, Correlation and few particle properties of self-organized InAs/GaAs quantum dots. Phys. Rev. B **71**, 155325 (2005)
85. A. Schliwa, M. Winkelnkemper, D. Bimberg, Impact of size, shape, and composition on piezoelectric effects and electronic properties of In(Ga)As/GaAs quantum dots. Phys. Rev. B **76**, 205324 (2007)
86. T. Maltezopoulos, A. Bolz, C. Meyer, C. Heyn, W. Hansen, M. Morgenstern, R. Wiesendanger, Wave-function mapping of InAs quantum dots by scanning tunneling spectroscopy. Phys. Rev. Lett. **91**, 196804 (2003)
87. A. Urbieta, B. Grandidier, J.P. Nys, D. Deresmes, D. Stiévenard, A. Lemaître, G. Patriarche, Y.M. Niquet, Scanning tunneling spectroscopy of cleaved InAs/GaAs quantum dots at low

temperatures. Phys. Rev. B **77**, 155313 (2008)
88. O. Stier, M. Grundmann, D. Bimberg, Electronic and optical properties of strained quantum dots modeled by 8-band kp theory. Phys. Rev. B **59**, 5688 (1999)
89. M. Scholz, S. Büttner, O. Benson, A.I. Toropov, A.K. Bakarov, A.K. Kalagin, A. Lochmann, E. Stock, O. Schulz, F. Hopfer, V.A. Haisler, D. Bimberg, Non-classical light emission from a single electrically driven quantum dot. Opt. Express **15**, 9107 (2007)
90. F. Guffarth, S. Rodt, A. Schliwa, K. Pötschke, D. Bimberg, Many-particle effects in self-organized quantum dots. Physica E **25**, 261 (2004)
91. P. Vashishta, R.K. Kalia, Universal behavior of exchange-correlation energy in electron-hole liquid. Phys. Rev. B **25**, 6492 (1982)
92. G. Tränkle, E. Lach, A. Forchel, F. Scholz, C. Ell, H. Haug, G. Weimann, G. Griffiths, H. Kroemer, S. Subbanna, General relation between band-gap renormalization and carrier density in two-dimensional electron-hole plasmas. Phys. Rev. B **36**, 6712 (1987)
93. R. Ambigapathy, I. Bar-Joseph, D.Y. Oberli, S. Haacke, M.J. Brasil, F. Reinhard, E. Kapon, B. Deveaud, Coulomb correlation and band gap renormalization at high carrier densities in quantum wires. Phys. Rev. Lett. **78**, 3579 (1997)
94. R. Heitz, F. Guffarth, I. Mukhametzhanov, M. Grundmann, A. Madhukar, D. Bimberg, Many-body effects on the optical spectra of InAs/GaAs quantum dots. Phys. Rev. B **62**, 16881 (2000)
95. U.W. Pohl, InAs/GaAs quantum dots with multimodal size distribution, in *Self-assembled Quantum Dots*, ed. by Z.M. Wang (Springer, New York, 2008), pp. 43–66, Chap. 3
96. U.W. Pohl, K. Pötschke, A. Schliwa, F. Guffarth, D. Bimberg, N.D. Zakharov, P. Werner, M.B. Lifshits, V.A. Shchukin, D.E. Jesson, Evolution of a multimodal distribution of self-organized InAs/GaAs quantum dots. Phys. Rev. B **72**, 245332 (2005)
97. R. Heitz, F. Guffarth, K. Pötschke, A. Schliwa, D. Bimberg, N.D. Zakharov, P. Werner, Shell-like formation of self-organized InAs/GaAs quantum dots. Phys. Rev. B **71**, 045325 (2005)
98. S. Raymond, S. Studenikin, S.-J. Cheng, M. Pioro-Ladrière, M. Ciorga, P.J. Poole, M.D. Robertson, Families of islands in InAs/InP self-assembled quantum dots: a census obtained from magneto-photoluminescence. Semicond. Sci. Technol. **18**, 385 (2003)
99. S. Rodt, R. Seguin, A. Schliwa, F. Guffarth, K. Pötschke, U.W. Pohl, D. Bimberg, Size-dependent binding energies and fine-structure splitting of excitonic complexes in single InAs/GaAs quantum dots. J. Lumin. **122–123**, 735 (2007)
100. S. Rodt, A. Schliwa, K. Pötschke, F. Guffarth, D. Bimberg, Correlation of structural and few-particle properties of self-organized InAs/GaAs quantum dots. Phys. Rev. B **71**, 155325 (2005)
101. U.W. Pohl, R. Seguin, S. Rodt, A. Schliwa, K. Pötschke, D. Bimberg, Control of structural and excitonic properties of self-organized InAs/GaAs quantum dots. Physica E **35**, 285 (2006)

# Chapter 4
# Thermodynamics of Epitaxial Layer-Growth

**Abstract** Growth requires some deviation from thermodynamic equilibrium. This chapter outlines the driving force for equilibrium-near growth of a crystal in terms of macroscopic quantities. We consider a thermodynamic description for the transition of a gaseous or liquid phase to the solid phase. The initial stage of layer growth requires a nucleation process. We discuss the energy of a surface and illustrate the nucleation of a layer and the occurrence of different growth modes.

Growth of a crystalline solid represents a transition from one phase, e.g., the vapor phase, to a crystalline phase. Such phase transition is phenomenologically described by *thermodynamics* using macroscopic quantities. Often the understanding of growth phenomena requires also consideration of the *kinetics*. A respective description considers transition states on an atomistic scale. Epitaxy may be performed close to thermodynamic equilibrium using, e.g., liquid phase epitaxy (Sect. 7.1). Growth is then well described in terms of thermodynamic properties of the system. Epitaxy far away from equilibrium, e.g., processes occurring during molecular beam epitaxy (Sect. 7.3) may often more appropriately be described in terms of kinetics. In this chapter basics of growth processes employed in epitaxial methods are discussed in terms of thermodynamics.

## 4.1 Phase Equilibria

Thermodynamics studies the effect of changes in, e.g., temperature on a system at a macroscopic scale by analyzing the collective motion of its particles. The term particles comprises both, atoms and molecules, and the term system denominates a large ensemble of particles which is marked-off from environment in some defined manner. The system may either contain a single kind of particles (single-component system) or a mixture of different kind of particles (multi-component system). If the system is completely *homogeneous* (regardless of being a single- or multi-component system) it is called to consist of a single phase. Growth occurs in *heterogeneous* systems which are characterized by interfaces separating different phases within the system.

U.W. Pohl, *Epitaxy of Semiconductors*, Graduate Texts in Physics,
DOI 10.1007/978-3-642-32970-8_4, 

### 4.1.1 Thermodynamic Equilibrium

If a system is left undisturbed by outside influences the interacting particles will share energy among themselves and reach a state, where the global statistics are unchanging in time. Parameters describing the system then have ceased to change with time. This allows single parameters like temperature or pressure to be attributed to the *whole* system.

Growth requires a force to drive particles from one phase of a system across the interface towards a solid phase. The crystal grower controls parameters in a way that a more volatile phase of the system is thermodynamically less stable than the crystalline phase, i.e., he adjusts some deviation from equilibrium. There are two kind of state variables which describe the system:

- *Intensive parameters* like temperature $T$, pressure $P$, mole fraction $x_i$ of component $i$, or chemical potential $\mu_i$ are independent on the size of the system.
- *Extensive parameters* like internal energy $U$, entropy $S$, volume $V$, or amount of substance $n_i$ do depend on system size.

The amount of substance $n_i$ designates the number of moles of component $i$ in the system and is given by the mass $m_i$ of the substance of component $i$ divided by its mole mass $M_i$. The corresponding mole fraction $x_i$ (also called *molar fraction*) denotes the number of moles of component $i$ as a proportion of the total number of moles of all components in the system, i.e.,

$$x_i = \frac{n_i}{\sum_{j=1}^{N_c} n_j} = \frac{n_i}{n}, \tag{4.1}$$

where $N_c$ is the number of components in the system and $n$ is the total number of moles in the system.

All thermodynamic properties of a system may be derived from its internal energy $U$. For a system composed of $N_c$ components this state function is given by

$$U = TS - PV + \sum_{i=1}^{N_c} \mu_i n_i. \tag{4.2}$$

$S$, $V$, and $n_i$ are the proper variables for the internal energy, and $\mu$ is the chemical potential introduced in (4.4) below. For crystal growers the direct access to the intensive parameters temperature and pressure is more convenient than control of the extensive parameters entropy and volume. Therefore the state function *Gibbs energy* $G$ with $T$, $P$, and $n_i$ as proper variables is introduced,

$$G = U + PV - TS. \tag{4.3}$$

Gibbs energy $G$—also referred to as Gibbs function or Gibbs free energy—is an extensive function like the internal energy $U$. The chemical potential of component $i$ in the system is given by the partial derivative of Gibbs energy,

$$\mu_i = \left(\frac{\partial G}{\partial n_i}\right)_{T,P,n_{j\neq i}} = \mu_i(T, P, x_1, \ldots, x_{N_c}). \tag{4.4}$$

Inserting (4.2) into (4.3), Gibbs energy can also be expressed by the $N_c$ amounts of substance $n_i$ and their respective chemical potentials,

$$G = \sum_{i=1}^{N_c} \mu_i n_i. \tag{4.5}$$

The total chemical potential $\mu$ then reads

$$\mu = \frac{G}{n} = \sum_{i=1}^{N_c} \mu_i x_i. \tag{4.6}$$

Thermodynamic equilibrium is characterized by the *minimum* of Gibbs energy $G$. Extensive functions of a system are similarly given as the sum of the corresponding quantities for each phase. For a system containing $N_p$ phases, $G$ is hence the sum of those for each phase $\sigma_i$,

$$\begin{aligned} G &= \sum_{j=1}^{N_p} G(\sigma_j) = G(\sigma_1) + G(\sigma_2) + \cdots + G(\sigma_{N_p}) \\ &= \sum_{j=1}^{N_p} \sum_{i=1}^{N_c} \mu_i(\sigma_j) n_i(\sigma_j) \\ &= \sum_{i=1}^{N_c} \mu_i(\sigma_1) n_i(\sigma_1) + \sum_{i=1}^{N_c} \mu_i(\sigma_2) n_i(\sigma_2) + \cdots + \sum_{i=1}^{N_c} \mu_i(\sigma_{N_p}) n_i(\sigma_{N_p}). \end{aligned} \tag{4.7}$$

The $\sigma_j$ and $n_i(\sigma_j)$ identify the phases and the amount of substance of component $i$ in phase $\sigma_j$, respectively. If $G$ is minimum at equilibrium, then condition

$$\left( \frac{\partial G}{\partial n_i(\sigma_j)} \right)_{T,P,n(\sigma_j)_{j \neq i}} = 0 \tag{4.8}$$

must apply for all $N_c$ components and all $N_p$ phases of the system. Under given (constant) conditions for $T$, $P$, and $n_i$, Gibbs energy $G$ hence assumes a minimum value with respect to any variation of these state parameters.

Let us assume a variation of one parameter, namely a transition of component 1 from phase $\alpha$ to phase $\beta$. The change is expressed by a variation of $n_1(\alpha)$ with the condition $n_1(\alpha) + n_1(\beta) = \text{constant}$. Applying condition (4.8) we obtain

$$\begin{aligned} \frac{\partial G}{\partial n_1(\alpha)} &= \frac{\partial (G(\alpha) + G(\beta) + G(\gamma) + \cdots)}{\partial n_1(\alpha)} \\ &= \frac{\partial G(\alpha)}{\partial n_1(\alpha)} + \frac{\partial G(\beta)}{\partial n_1(\alpha)} = \frac{\partial G(\alpha)}{\partial n_1(\alpha)} - \frac{\partial G(\beta)}{\partial n_1(\beta)} = 0. \end{aligned}$$

In the second fraction all apart from the first two summands are zero for all phases except for $\alpha$ and $\beta$ due to the assumed transition, and the negative sign of the second summand originates from $\partial n_1(\beta) = -\partial n_1(\alpha)$. Inserting (4.4) applied to component 1 yields the equilibrium condition

$$\mu_1(\alpha) - \mu_1(\beta) = 0.$$

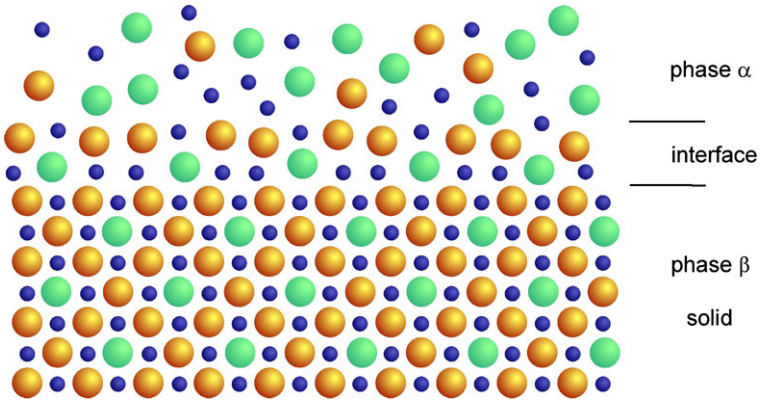


**Fig. 4.1** Schematic of a three-component system with two phases $\alpha$ and $\beta$ in equilibrium

This condition applies for pairs of *all* of phases and *all* components. The general conditions for equilibrium hence reads: The chemical potentials $\mu_i$ of all $N_c$ components are equal among each other in each of the $N_p$ phases,

$$\mu_i(\sigma_1) = \mu_i(\sigma_2) = \cdots = \mu_i(N_p), \quad i = 1, \ldots, N_c \quad \text{(equilibrium)}. \tag{4.9}$$

Equation (4.9) applies simultaneously for all $N_c$ components of the system, yielding a set of $N_c$ relations in case of an equilibrium between two phases. In equilibrium of a multi-component system much more phases than two may coexist. For $N_p$ coexisting phases a set of $(N_p - 1) \times N_c$ relations must be fulfilled at equilibrium. The *composition* of the $N_p$ phases is generally *not* equal at equilibrium to fulfill these conditions, i.e., usually $x_1(\sigma_1) \neq x_1(\sigma_2) \neq x_1(\sigma_3) \neq \cdots$.

Figure 4.1 illustrates the equilibrium between phase $\alpha$ and a solid phase $\beta$ of a three-component system. Different species of particles are depicted by different symbols. Note different compositions indicated in phases $\alpha$ and $\beta$. The interface between $\alpha$ and $\beta$ is the surface of the solid. Its structure is thermodynamically less favorable than that of the solid or of the more volatile phase $\alpha$. The surface hence tends to be thin. In practice, it extends over a few atomic layers. In a thermodynamic description the surface region is usually not regarded as a separate phase and assumed infinitely thin.

### *4.1.2 Gibbs Phase Rule*

The number of phases which can coexist at equilibrium is limited. According (4.4) a set of the variables $T$, $P$, and compositions $x_i$ of the $N_c$ components specifies a phase of a heterogeneous system. The chemical potential in this phase is fixed when $N_c - 1$ mole fractions are quoted besides $T$ and $P$: The last of $N_c$ mole fractions is given by the condition $\sum_i x_i = 1$ in each phase. We hence have $N_p \times (N_c - 1)$

independent mole fractions for a system with $N_\mathrm{p}$ phases. Therefore a total of $N_\mathrm{p} \times (N_\mathrm{c} - 1) + 2$ intensive variables are sufficient to fix all of the intensive variables of the system. Many of them are dependent, however. Considerations leading to (4.9) showed that $N_\mathrm{c}$ relations according $\mu_i(\alpha) = \mu_i(\beta)$ have to be fulfilled at equilibrium between two coexisting phases. For three coexisting phases $2 \times N_\mathrm{c}$ relations, and for $N_\mathrm{p}$ phases a number of $(N_\mathrm{p} - 1) \times N_\mathrm{c}$ relations have to be fulfilled. There remains thus a number $N_\mathrm{f}$ of *independent* intensive variables given by $(N_\mathrm{p} \times (N_\mathrm{c} - 1) + 2) - ((N_\mathrm{p} - 1) \times N_\mathrm{c})$ or

$$N_\mathrm{f} = N_\mathrm{c} - N_\mathrm{p} + 2. \tag{4.10}$$

This number of independent intrinsic state parameters may be used to control growth near thermodynamic equilibrium without changing the number of phases $N_\mathrm{p}$. $N_\mathrm{f}$ is called the *number of degrees of freedom* for a given thermodynamic condition and specifies how many control variables can be altered while maintaining this condition. This *Gibbs phase rule* was stated by Josiah Willard Gibbs in the 1870s. In literature the numbers of degrees of freedom, of components, and phases $N_\mathrm{f}$, $N_\mathrm{c}$, and $N_\mathrm{p}$, are also labeled as $F$, $C$, and $\pi$, respectively.

$N_\mathrm{f}$ may not be negative. Consequently a maximum of $N_\mathrm{p} = 3$ phases may coexist in equilibrium of a single-component system ($N_\mathrm{c} = 1$). Since in this case $N_\mathrm{f} = 0$ the variables $T$ and $P$ are fixed in a triple point. In a two-phase equilibrium of a single-component system we obtain $N_\mathrm{f} = 1$. We hence can choose one parameter independently (within some limits), say $T$, while the other, $P$, adjusts accordingly to accomplish equilibrium. In a single-phase range of a single-component system $N_\mathrm{f} = 2$. $T$ and $P$ may then be varied independently. In a two-component system a maximum of 4 phases may coexist, and in a two-phase equilibrium still two parameters may be controlled independently.

### *4.1.3 Gibbs Energy of a Single-Component System*

A single-component system has a maximum of three phases in equilibrium (Sect. 4.1.2), and a state is fixed by fixing temperature, pressure, and volume of the system. The equilibrium conditions between the thermodynamically distinct phases are clearly represented in a phase diagram. A simple illustration is the pressure-temperature diagram given in Fig. 4.2. The diagram is a projection of $P$–$V$–$T$ space on the $P$–$T$ plane for a fixed volume and shows the phase boundaries between the three equilibrium phases of solid, liquid, and gas. On a boundary two phases coexist, and in the triple point three phases coexist. Dashed curves near the triple point indicate metastable states (cf. Sect. 4.1.5). The solid-liquid phase boundary of most substances has a positive slope. This is due to the solid phase having a higher density than the liquid, so that increasing the pressure increases the melting point. Prominent exceptions are, e.g., water and silicon.

To study the behavior of the system at transitions from one phase to another we consider a variation of one of the variables $P$ or $T$ while keeping the other fixed [1].

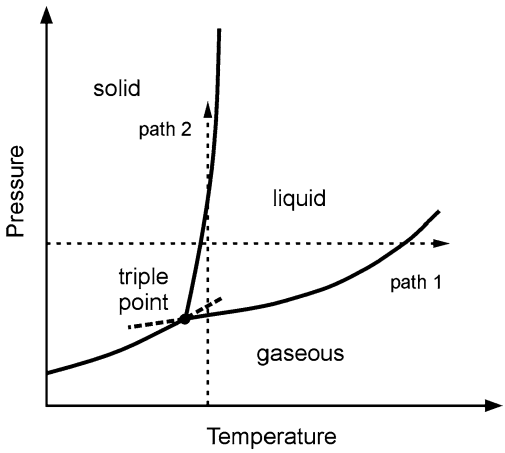


**Fig. 4.2** $P$–$T$ phase diagram for a single-component system. *Dashed curves* near the *triple point* indicate metastable states. The dependence of Gibbs energy $G(P, T)$ for variations along *paths 1* and *2* is discussed in the text

We first discuss the temperature dependence of Gibbs energy $G(T)_P$, i.e., $G(T)$ at constant pressure $P$, along path 1 drawn in Fig. 4.2. In a second step the pressure dependence $G(P)_T$ along path 2 will be discussed.

Considering a system consisting of one component yields a descriptive dependence of Gibbs energy $G$ from temperature and pressure. There is only a single chemical potential,

$$\mu = \frac{\partial G}{\partial n} = \frac{G}{n} \equiv g \quad \text{(single-component system)}.$$

The relation shows that the chemical potential is identical to the Gibbs energy per mole $g$. Both $\mu$ and $G$ depend solely on $T$ and $P$.

We first consider $G(T)_P$. The temperature dependence of $G$ is evaluated from the respective dependence of the three summands in (4.3)

$$G = U + PV - TS.$$

The internal energy $U(T)$ starts at $T = 0\,\mathrm{K}$ with some constant value $U_0$ which merely represents an offset of all parameters. In the low-temperature range the increase of $U(T)$ is essentially determined by the heat capacity of the (solid) system at constant volume, $C_V^{\mathrm{S}}$. The slope increases due to an increase of $C_V^{\mathrm{S}}(T)$. We may neglect here the small volume change of the solid at constant pressure and the consequential small contribution of $U(V(T))$. At the melting temperature $T_{\mathrm{SL}}$ (index SL for solid → liquid) and also at the boiling temperature $T_{\mathrm{LG}}$ (liquid → gaseous) the internal energy $U(T)$ increases by material-dependent steps $\Delta U_{\mathrm{SL}}$ and $\Delta U_{\mathrm{LG}}$, respectively: The bordering phases differ in internal energy. The thermal trend of $U$ in the liquid and gaseous phases is likewise described using the heat capacities $C_V^{\mathrm{L}}(T)$

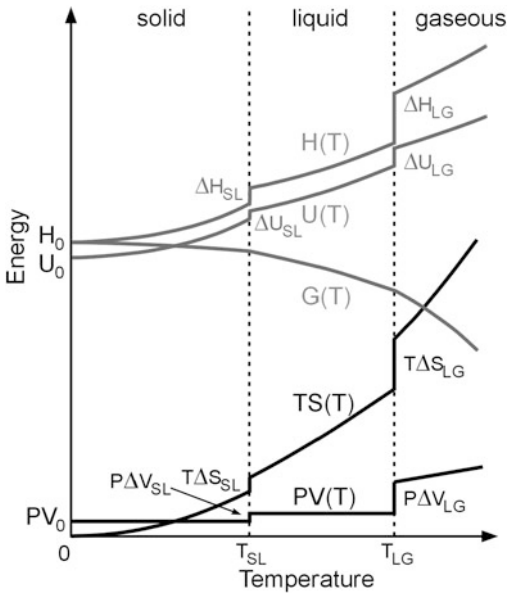


**Fig. 4.3** Temperature dependence of Gibbs energy $G$, internal energy $U$, enthalpy $H$, and the energies $TS$ and $PV$ at constant pressure for a single-component system. After [1]

and $C_V^{\mathrm{G}}(T)$, respectively. The entire temperature dependence of the first summand of $G(T)$ in (4.3) is then given by

$$U(T) = U_0 + \int_0^{T_{\mathrm{SL}}} C_V^{\mathrm{S}}(T)\,dT + \Delta U_{\mathrm{SL}} + \int_{T_{\mathrm{SL}}}^{T_{\mathrm{LG}}} C_V^{L}(T)\,dT + \Delta U_{\mathrm{LG}} + \int_{T_{\mathrm{LG}}}^{T} C_V^{\mathrm{G}}(T)\,dT. \tag{4.11}$$

For $T < T_{\mathrm{LG}}$ thereinafter summands are accordingly omitted. The trend of $U(T)$ is illustrated in Fig. 4.3.

The trend of the second summand of $G$ in (4.3) is given by $V(T)$ because $P$ is assumed to be constant. Since the thermal expansion coefficients in the solid and liquid phases are very small (typ. of order $10^{-6}$) we may assume a virtually constant volume. Melting and evaporation lead to a small step $\Delta V_{\mathrm{SL}}$ and a large step $\Delta V_{\mathrm{LG}}$. The dependence in the gas phase is approximated by the ideal gas law $V(T) \cong nRT/P$, $R$ being the universal molar gas constant.

Adding the first two summands of $G$ in (4.3) yields the *enthalpy* $H(T) = U(T) + PV(T)$. The thermal dependence is similar to that of $U(T)$ with slightly larger values due to positive values of $P$ and $V$, cf. Fig. 4.3. The step at the melting point $\Delta H_{\mathrm{SL}} = \Delta U_{\mathrm{SL}} + P\Delta V_{\mathrm{SL}}$ is the heat of fusion absorbed during melting at $T_{\mathrm{SL}}$. It is vice versa identical to the heat released during solidification. According convention a positive sign of $\Delta H$ indicates an endothermic reaction, where the system receives heat supplied from the surroundings. Similar considerations apply for evaporation and condensation expressed by $\Delta H_{\mathrm{LG}}$. $H(T)$ may be expressed by a similar relation as (4.11) when $U$ and $C_V$ are replaced by $H$ and $C_P$, respectively.

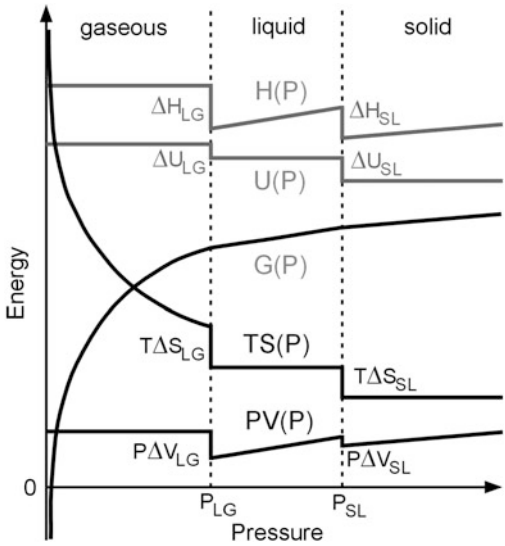


**Fig. 4.4** Pressure dependence of Gibbs energy $G$, internal energy $U$, enthalpy $H$, and the energies $TS$ and $PV$ at constant temperature for a single-component system. After [1]

The third summand of $G$ in (4.3) increases with $T$ according the *entropy* $S = \int C_P/T = \int C_P d\ln T$. $S_0$ is assumed to be zero. During the phase transitions at $T_{\mathrm{SL}}$ and $T_{\mathrm{LG}}$ the entropy $S$ experiences a steplike increase $\Delta H/T$. It should be noted that these steps have the same height as those in the function $H(T)$, since $\Delta H = T\Delta S$. $S$ may also be expressed by a similar relation as (4.11) when $U$, $C_V$, and $dT$ are replaced by $S$, $C_P$, and $d\ln T$, respectively.

We now put the three summands together to obtain Gibbs energy $G(T)$ according (4.3). As shown in Fig. 4.3 $G(T)$ is a monotonously decreasing function with a gradually increasing negative slope. $G(T)$ is continuous at the phase transitions but experiences a kink. Since $\mu = G/n$ we also know the trend of the chemical potential $\mu(T)$. We will consider this in more detail in Sect. 4.1.4.

In a second step we address the pressure dependence $G(P)_T$ evaluated from the respective dependence of the three summands in (4.3) at constant temperature.

Besides steps at phase transitions, $U(P)$ may be considered nearly constant in all phases at constant temperature. The second summand $PV(P)$ is approximately constant at low pressures due to the ideal gas law $V \cong nRT/P$. In the liquid and solid phases $V(P)$ is nearly constant. As $P$ increases $PV(P)$ hence rises approximately linearly, with a larger slope in the liquid phase. The enthalpy $H(P) = U(P) + PV(P)$ reproduces these slopes. The steps $\Delta H_{\mathrm{LG}}$ and $\Delta H_{\mathrm{SL}}$ again represent heats of condensation and solidification, respectively.

The trend of the third summand of $G$ in (4.3) $TS(P)$ is given by $S(P)$ at constant temperature. To obtain the trend at low pressure (gas phase) we apply the general Maxwell relation $(\partial S/\partial P)_T = -(\partial V/\partial T)_P$ and infer from the ideal gas law $(\partial V/\partial T)_P \cong nR/P$. Equalizing and integration yields $S(P) \cong -nR\ln P + S_0$, where $S_0$ is an integration constant. In the gas phase the trend decreases monotonously with a steep slope at small pressure due to the term $-\ln P$. In the

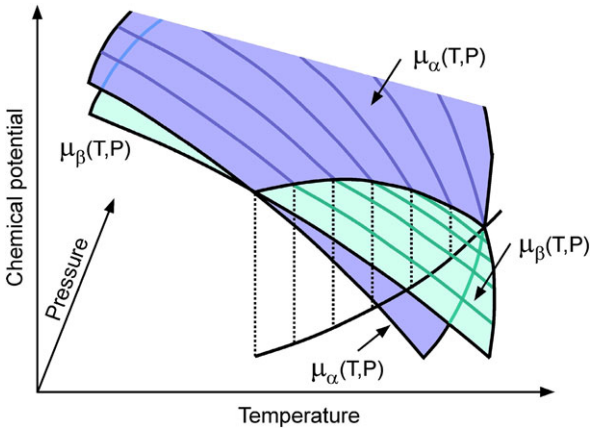


**Fig. 4.5** Chemical potentials $\mu_\alpha(T, P)$ and $\mu_\beta(T, P)$ of two phases $\alpha$ and $\beta$ near their intersection line, where both phases coexist. *Dotted vertical lines* indicate projection of the intersection line to the $P$–$T$ plane. After [1]

liquid and solid phases $(\partial V/\partial T)_P$ is quite small due to the small thermal expansion coefficient. $S(P)$ is considered nearly constant in these phases.

The sum adds up to the pressure dependence $G(P)_T$ illustrated in Fig. 4.4. $G(P)$ is a monotonously increasing function. At phase transitions $G(P)$ is continuous but experiences a kink. The same applies for the chemical potential $\mu(P) = G(P)/n$.

### 4.1.4 Phases Boundaries in a Single-Component System

We consider the chemical potential $\mu(T, P)$ at the boundary between two phases $\alpha$ and $\beta$ of a single-component system. The characteristics in the $P$–$T$ phase diagram is obtained from $\mu(T)_P = G(T)_P/n$ and $\mu(P)_T = G(P)_T/n$. We know from Sect. 4.1.3 that $\mu(P, T)$ is a curved plane which in each phase monotonously decreases along $T$ and increases along $P$. The slopes of $\mu_\alpha(T, P)$ and $\mu_\beta(T, P)$ differ in two different phases. The respective planes hence intersect. Along the intersection line the chemical potentials must be equal, $\mu_\alpha(T, P) = \mu_\beta(T, P)$. Adjacent to the line of intersection the respective lower plane refers to the stable phase. The stable phases change order upon crossing the section boundary: The respective other phase gets stabile. Figure 4.5 illustrates the situation.

The projection of the intersection line of the $\mu_\alpha(T, P)$ and $\mu_\beta(T, P)$ planes on the $P$–$T$ plane shown in Fig. 4.5 yields the boundary between phases $\alpha$ and $\beta$ depicted in Fig. 4.2. The characteristics of this boundary is described by the Clapeyron relation or, if a transition between a condensed (liquid or solid) to a gas phase is involved, by the Clausius-Clapeyron relation, named after B.P. Émile Clapeyron and Rudolf Clausius. The general Clapeyron equation follows from a variation $d\mu(T, P)$ of a state on the coexistence line that must fulfill the identity $d\mu_\alpha = d\mu_\beta$, or, by inserting $G/n$ for $\mu$,

$$\frac{1}{n}\left(\frac{\partial G_\alpha}{\partial T}\right)_P dT + \frac{1}{n}\left(\frac{\partial G_\alpha}{\partial P}\right)_T dP = \frac{1}{n}\left(\frac{\partial G_\beta}{\partial T}\right)_P dT + \frac{1}{n}\left(\frac{\partial G_\beta}{\partial P}\right)_T dP.$$

In the relation we may replace $(\partial G/\partial T)$ by $-S$ and $(\partial G/\partial P)$ by $V$. This yields a condition for the proportions of the two variables for a variation along the coexistence line,

$$dP = \frac{S_\beta - S_\alpha}{V_\beta - V_\alpha}\, dT.$$

The relation gives the slope $dP/dT$ of the coexistence curve. $\Delta S$ and $\Delta V$ are respectively the change of entropy and volume during a phase transition across the boundary. Since $\Delta S = \Delta H/T$ we may write

$$\frac{dP}{dT} = \frac{\Delta S}{\Delta V} = \frac{\Delta H}{T\Delta V}. \tag{4.12}$$

Here $\Delta H$ is the latent heat exchanged with the surroundings during the phase transition without change of temperature $T$. The Clapeyron equation (4.12) explains basic characteristics of the $P$–$T$ phase diagram Fig. 4.2. A transition from the gaseous phase to the liquid or the solid phase is accompanied by a large volume change $\Delta V$. According (4.12) the slopes of these two phase boundaries are therefore small. The heat of evaporation $\Delta H$ is a positive quantity just as the volume increase $\Delta V$. The slope $dP/dT$ is therefore also positive. Furthermore, the slope increases as $P$ increases due to a decrease of $\Delta V$ at higher pressure. Due to a larger heat of sublimation of a solid compared to the heat of evaporation of a liquid the slope of the solid-gas boundary is steeper than that of the liquid-gas boundary.

To obtain an idea of the relation $P(T)$ for a transition from a condensed phase to the gas phase, we roughly approximate the volume change by the volume of the gas formed, $\Delta V \cong V_{\text{gas}}$, and put $PV_{\text{gas}} \cong nRT$. Inserting the two approximations into (4.12) and taking $\Delta H$ as independent of $T$, we obtain $P(T)$ by integration, yielding

$$\ln\left(\frac{P}{P_0}\right) \cong \frac{-\Delta H}{nR}\left(\frac{1}{T} - \frac{1}{T_0}\right), \quad \text{or} \quad P \cong P_0 \exp\left(\frac{-\Delta H}{nR}\left(\frac{1}{T} - \frac{1}{T_0}\right)\right). \tag{4.13}$$

$\Delta H/n$ is the molar heat of evaporation or sublimation. We see that for the transition from a condensed to a gas phase the pressure approximately obeys an Arrhenius-like dependence over a limited temperature range. Vapor pressures are often tabled in terms of 2 parameters $a$ and $b$, obtained from (4.13) by using $\ln(x) = \ln(10) \times \log(x)$ and putting $b = -\Delta H/(nR\ln(10))$. The relation then reads $\log(P) = a - b/T$, with the parameter $a$ depending on the pressure unit.

The liquid-solid boundary is generally quite steep in the $P$–$T$ phase diagram due to a very small volume change $\Delta V$ during melting. Since the liquid phase may be more dense or less dense than the solid phase $\Delta V$ may have either sign. The slope $dP/dT$ of this boundary may hence be positive or negative.

### *4.1.5 Driving Force for Crystallization*

To induce a transition from a stable phase to another the parameters temperature and pressure have to be controlled such that the chemical potential in the target phase is

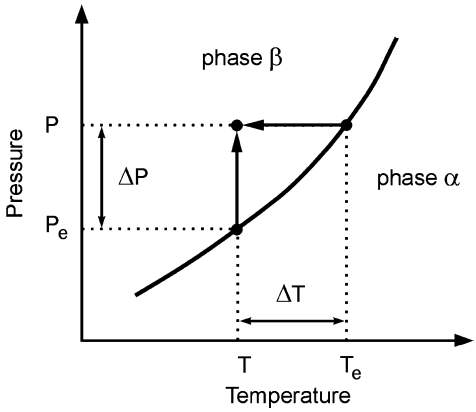


**Fig. 4.6** Crossing the phase boundary from a less stable phase $\alpha$ to a stable phase $\beta$ induced by supercooling $\Delta T$ at constant pressure or supersaturation $\Delta P$ at constant temperature

smaller than that in the initial phase. Particles from the initial phase will then cross the phase boundary toward the target phase to allow the system for approaching (the new) equilibrium conditions.

For a temperature variation at constant pressure the difference $\Delta T = T - T_e$ between the controlled temperature $T$ and the equilibrium temperature $T_e$ at the given pressure is a measure for the deviation from equilibrium. $\Delta T$ is a negative quantity and termed *supercooling*. In case of a liquid-solid equilibrium $T_e$ is the melting temperature.

The phase transition may as well be induced by varying the pressure by an amount $\Delta P = P - P_e$ at constant temperature. If the initial phase is the gaseous phase $\Delta P$ and $P_e$ are called *supersaturation* and saturation vapor-pressure, respectively. The achievement of equilibrium in the target phase via either of the two paths is illustrated in Fig. 4.6.

We consider the phase transition induced by supercooling $\Delta T = T - T_e$ at constant pressure in more detail. At fixed pressure phase $\alpha$ is above the equilibrium temperature $T_e$ more stabile than phase $\beta$, i.e. $\mu_\alpha(T) < \mu_\beta(T)$. Below $T_e$, however, $\mu_\beta(T) < \mu_\alpha(T)$ due to different slopes of the chemical potentials and their intersection at $T_e$, see Fig. 4.5. Phases $\alpha$ and $\beta$ may exchange particles via the common phase boundary. Since $\mu_\beta(T) < \mu_\alpha(T)$ below $T_e$, the system can lower the total enthalpy $G = G_\alpha + G_\beta = n_\alpha \mu_\alpha + n_\beta \mu_\beta$ by transferring particles from phase $\alpha$ to phase $\beta$: The amount of substance $n_\beta$ in the stable phase $\beta$ increases on expense of the amount of substance $n_\alpha$ in the less stable phase $\alpha$. The driving force for this phase transition is the difference in the chemical potential

$$\Delta\mu \equiv \mu_\beta - \mu_\alpha. \tag{4.14}$$

$\Delta\mu$ is called *growth affinity*, or *driving force for crystallization* if the stable phase $\beta$ is a solid phase. $\Delta\mu$ is a negative quantity, though it must be mentioned that $\Delta\mu$ is often chosen positive in literature. The relation between the driving force $\Delta\mu$ and the supercooling $\Delta T$ is illustrated in Fig. 4.7. We see that an increase of supercooling raises $\Delta\mu$ and thereby enhances the rate of substance crossing the phase boundary.

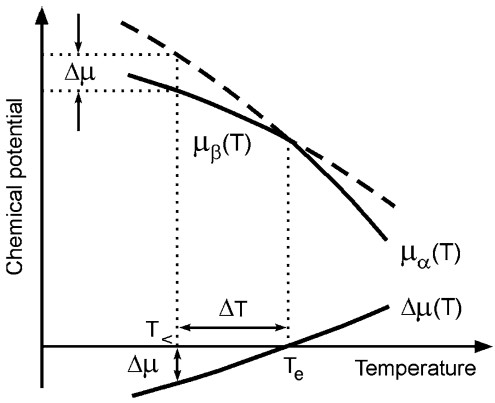


**Fig. 4.7** Temperature dependence of the chemical potential $\mu$ of phases $\alpha$ and $\beta$. The growth affinity $\Delta\mu$ designates the difference of the chemical potentials $\mu_\alpha$ and $\mu_\beta$ induced by a supercooling $\Delta T$ to a temperature $T_<$ below the equilibrium temperature $T_\mathrm{e}$

It should be noted that the respective instable phases may sometimes be experimentally observed to some extent. Such metastable state of a system is indicated by dashed lines in Fig. 4.7. Well-known examples are heating of a liquid above the boiling point (bumping) or supersaturated vapor in Wilson's cloud chamber. The effect is particularly pronounced for undercooled metal melts which may still be liquid some tens of degrees °C below the temperature of solidification. The phenomenon should not be confused with the size effect of melting point depression in nanoscale materials that originates from a high surface to volume ratio.

The driving force (4.14) may likewise be induced by a supersaturation $\Delta P = P - P_\mathrm{e}$ at constant temperature. For solidification from the liquid phase $P$ must be increased if the liquid-solid boundary has a positive slope $dP/dT$ and decreased otherwise. The driving force increases as $\Delta P$ is raised, similar to the dependence in supercooling discussed above.

To obtain an explicit relation for the temperature dependence of the driving force $\Delta\mu(\Delta T)$ we expand the function into a Taylor series at equilibrium temperature $T = T_\mathrm{e}$,

$$\Delta\mu(\Delta T) = \mu_\beta - \mu_\alpha \cong \left(\frac{\partial\mu_\beta}{\partial T} - \frac{\partial\mu_\alpha}{\partial T}\right)\Delta T + \left(\frac{\partial^2\mu_\beta}{\partial T^2} - \frac{\partial^2\mu_\alpha}{\partial T^2}\right)\frac{(\Delta T)^2}{2} + \cdots.$$

Replacing $n(\partial\mu/\partial T)_P = (\partial G/\partial T)_P$ by $-S = -H/T$ we obtain for the expressions in the second summand

$$\left(\frac{\partial^2\mu}{\partial T^2}\right)_P = -\frac{1}{n}\left(\frac{\partial S}{\partial T}\right)_P = -\frac{1}{nT}\left(\frac{\partial H}{\partial T}\right)_P = -\frac{C_P}{nT}.$$

Insertion into $\Delta\mu$ yields

$$\Delta\mu(\Delta T) = \frac{1}{n}\left(-\frac{\Delta H_\mathrm{trans}}{T_\mathrm{e}}\Delta T - \frac{\Delta C_P}{2T_\mathrm{e}}(\Delta T)^2 + \cdots\right). \tag{4.15}$$

In this relation $\Delta H_\mathrm{trans}$ and $\Delta C_P$ denote the latent heat exchanged with the surroundings during the phase transition and the difference of the specific heat at both sides of the phase boundary, respectively. We note that the driving force $\Delta\mu$ is not a

linear function of the supersaturation $\Delta T$, particularly for significant deviation from the equilibrium temperature $T_\mathrm{e}$ and a large difference of the specific heat in phases $\alpha$ and $\beta$.

In a similar way we obtain an explicit relation for the pressure dependence of the driving force $\Delta\mu(P)$ by expanding the function into a Taylor series at equilibrium pressure $P = P_\mathrm{e}$,

$$\Delta\mu(P) = \mu_\beta - \mu_\alpha \cong \left(\frac{\partial\mu_\beta}{\partial P} - \frac{\partial\mu_\alpha}{\partial P}\right)\Delta P + \left(\frac{\partial^2\mu_\beta}{\partial P^2} - \frac{\partial^2\mu_\alpha}{\partial P^2}\right)\frac{(\Delta P)^2}{2} + \cdots.$$

This approach yields a reasonable description of the transition between condensed phases like, e.g., liquid $\rightarrow$ solid. We replace $n(\partial\mu/\partial P)_T = V$ and $(-1/V)(\partial V/\partial P)_T = \kappa$ (isothermal expansion coefficient), obtaining

$$\Delta\mu(\Delta P) = \frac{1}{n}\big(\Delta V_\mathrm{e}\Delta P - (V_{\mathrm{e},\beta}\kappa_{\mathrm{e},\beta} - V_{\mathrm{e},\alpha}\kappa_{\mathrm{e},\alpha})(\Delta P)^2/2 + \cdots\big). \tag{4.16}$$

$\Delta V_\mathrm{e}/n$ designates the difference of the molar volumes at both sides of the phase boundary at equilibrium pressure $P_\mathrm{e}$. This quantity controls the driving force induced by a supersaturation $\Delta P$ as a first approximation.

The driving force $\Delta\mu(P)$ of a pressure-induced transition between a gas phase $\alpha$ and a solid phase $\beta$ may be obtained by integrating over the pressure. We neglect the much smaller solid molar volume and assume the validity of the ideal gas law,

$$\begin{aligned}\Delta\mu(\Delta P) &= \int_{P_\mathrm{e}}^{P} \frac{\partial(\Delta\mu)}{\partial P}\,dP = \int_{P_e}^{P} \frac{(V_\beta - V_\alpha)}{n}\,dP \cong \int_{P_\mathrm{e}}^{P} -V_\alpha\,dP \\ &\cong -\int_{P_\mathrm{e}}^{P} \frac{RT}{P}\,dP = -RT\ln(P/P_\mathrm{e}).\end{aligned}$$

In this case the driving force for crystallization is approximately proportional to the logarithm of the supersaturation ratio $P/P_\mathrm{e}$ of the gas phase $\alpha$.

### *4.1.6 Two-Component System*

Practical real systems usually comprise more than one component. The treatment of a multi-component system is quite complex. For simplicity we focus on binary systems, which consist of only two components. Such system still allows for describing basic phenomena occurring in multi-component systems. Prominent examples are solidification from a solution, e.g., in liquid phase epitaxy, or the solubility of impurities governing doping of semiconductors.

A *component* in a multi-component system is a chemically distinct constituent whose concentration may be varied *independently* in the various phases. The number of components $N_\mathrm{c}$ specifies how many substances are (at least) needed to describe the composition of the system in all phases. Thus, pure water ($H_2O$) forms a single-component system, though some dissociation into hydronium cations ($H_3O^+$) and hydroxyl anions ($OH^-$) occurs; the numbers of anions and cations are contrained

to be equal due to charge neutrality and may hence not vary independently. If the substances of a system do not react the number of components $N_c$ is simply given by the number of substances.

A system containing two components $A$ and $B$ with substance amounts $n_A$ and $n_B$ is usually characterized by its composition $x$. This quantity designates the mole fraction of one of the two components, say $x \equiv x_A$. Often $x$ refers to the solute in a solution, i.e. to the minority component $A$ in the substance formed by adding $A$ to $B$. The respective remaining composition $x_B$ follows from the condition $x_A + x_B = 1$, yielding $x_B = 1 - x$. $x = 0$ and $x = 1$ then designate the pure components $B$ and $A$, respectively.

Equilibrium of a binary system is described by a minimum of Gibbs energy $G = H - TS$ which depends on three independent variables, namely temperature $T$, Pressure $P$, and composition $x$. In the following we will consider the *molar* Gibbs energy $g$. According (4.1) and (4.5) $g$ is given by

$$\begin{aligned} g = G/n &= (\mu_A n_A + \mu_B n_B)/(n_A + n_B) = \mu_A x_A + \mu_B x_B \\ &= \mu_A x + \mu_B (1 - x) = (\mu_A - \mu_B)x + \mu_B . \end{aligned}$$

We assume a solution of $A$ and $B$ with composition $x$ formed at fixed temperature and pressure in a single phase. If the two components are just put together *without* intermixing or solving the molar Gibbs energy is a linear function $\overline{g}$ of the composition $x$ with the starting and ending vertex given by the chemical potentials $\mu_{0,B}$ and $\mu_{0,A}$ of the *pure* components $B$ and $A$, respectively (Fig. 4.8),

$$\overline{g}(x) = (\mu_{0,A} - \mu_{0,B})x + \mu_{0,B} . \tag{4.17}$$

If now the two components are mixed their particles interact. This is taken into account by an additive term, the molar Gibbs free energy of mixing $\Delta g_M$. In general $\Delta g_M$ contains contributions of both, a change of molar enthalpy $\Delta h_M$ and a change of molar entropy $\Delta s_M$ on mixing,

$$\Delta g_M = \Delta h_M - T \Delta s_M . \tag{4.18}$$

A particularly simple case is given by an *ideal solution*, where the interactions between unlike and like particles in the solution are the same. If the interaction energies in the solution are identical to those in the pure components, mixing will not change the overall enthalpy. No heat is then exchanged with the surroundings on mixing, $\Delta h_M = 0$. Due to molecular forces being independent on composition, mixing is not accompanied by a change in molar volume, $\Delta v_M = 0$. There is, however, a change in molar entropy $\Delta s_M$ on mixing. The molar Gibbs energy of an ideal solution is hence given by

$$g(x) = \overline{g} + \Delta g_M = \overline{g} - T \Delta s_M \quad \text{(ideal solution)}. \tag{4.19}$$

Ideal solutions are completely miscible. For a statistically random distribution of $A$ and $B$ particles the change in molar entropy is

$$\Delta s_M = -R(x_A \ln x_A + x_B \ln x_B) = -R\big(x \ln x + (1 - x)\ln(1 - x)\big)$$
(ideal solution),

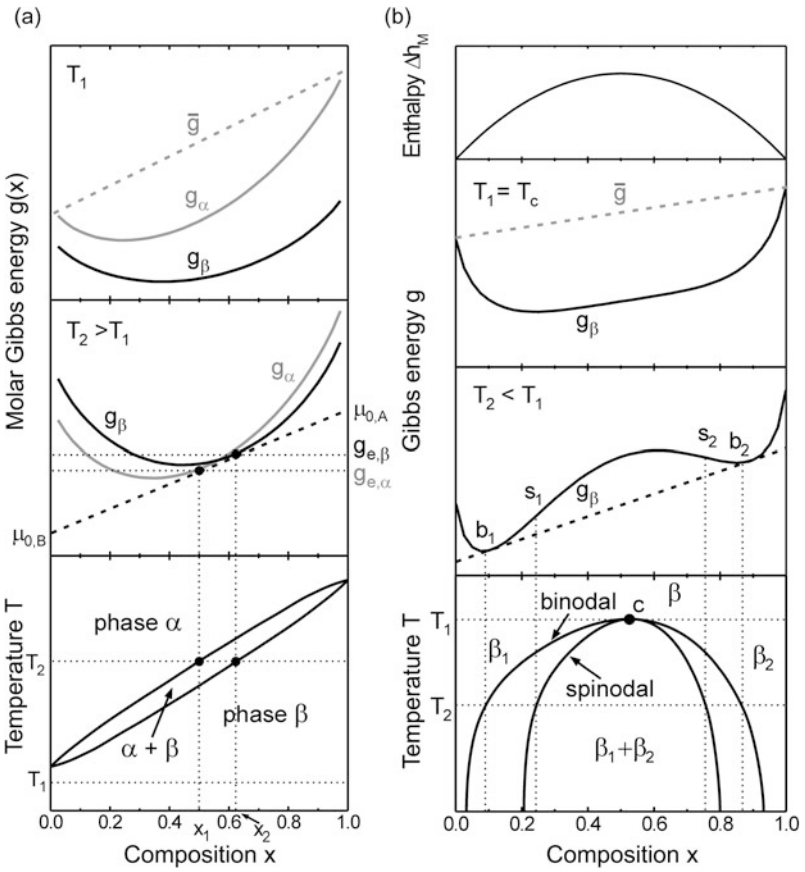


**Fig. 4.8** (**a**) Composition-dependent molar Gibbs energy of an ideal solution with phases $\alpha$ and $\beta$ at a low temperature $T_1$ (*top*) where only phase $\beta$ is stable, and a higher Temperature $T_2$ where phases $\alpha$ and $\beta$ coexist in equilibrium. *Bottom*: $T$–$x$ phase diagram with phases $\alpha$ and $\beta$ and a range of coexistence. (**b**) Real solution with contribution of an endothermal enthalpy on mixing (*top*), Gibbs energy of phase $\beta$ at a critical temperature $T_c$ and a lower temperature $T_2$. The phase diagram at the *bottom* shows two stable phases $\beta_1$ and $\beta_2$, an area of metastable compositions between the binodal and spinodal curves, and a range of spontaneous decomposition bounded by the spinodal

where $R$ is the gas constant. The mixing-induced change of molar entropy $\Delta s_M$ is a positive quantity, because the ln function yields negative values for $x$ ranging from 0 to 1. The term $-T\,\Delta s_M$ in $g(x)$ hence effects a deviation from the linear dependence $\overline{g}$ towards lower values. This decrease of molar Gibbs energy gets stronger for increased temperature, as illustrated for phase $\alpha$ of a two-component system in Fig. 4.8a (gray lines at $T_1$ and $T_2 > T_1$).

Figure 4.8a makes clear how the composition of a two-component system changes at a transition from a phase $\alpha$ (e.g., the liquid phase) to phase $\beta$ (solid). At a low temperature $T_1$ the system is in a solid state $\beta$: The molar Gibbs energy

of the solid $g_\beta(x)$ is smaller than $g_\alpha(x)$ for any composition $x$. As the temperature is increased both $g_\alpha(x)$ and $g_\beta(x)$ get smaller, cf. $g(T)$ depicted in Fig. 4.3. Since the temperature dependence in the liquid phase is stronger than in the solid phase $g_\alpha(x)$ decreases faster and will be tangent to $g_\beta(x)$ at a melting temperature $T_{\mathrm{melt},B}$. (The melting temperature $T_{\mathrm{melt},B}$ of component $B$ lies above $T_1$ at the lower left corner of the lens-shaped area between phases $\alpha$ and $\beta$ in Fig. 4.8a (bottom).) At $T_{\mathrm{melt},B}$ the pure component with the lower melting point starts melting, say component $B$. Above $T_{\mathrm{melt},B}$ the solid and liquid states will coexist within some concentration range $\Delta x$ and temperature range $\Delta T$ up to a maximum temperature $T_{\mathrm{melt},A}$, the melting point of pure component $A$. Above $T_{\mathrm{melt},A} g_\alpha(x) < g_\beta(x)$ for any composition $x$, i.e., the system is entirely in the liquid state $\alpha$.

At an intermediate temperature $T_2$ the liquid ($\alpha$) and solid ($\beta$) phases coexist between the compositions $x_1$ and $x_2$, see Fig. 4.8a. In this range $g_\beta(x) < g_\alpha(x)$ for smaller $x$, and $g_\alpha(x) < g_\beta(x)$ for larger $x$, see $g(x)$ at $T_2$. For a given composition $x$ between $x_1$ and $x_2$ the system attains lowest molar Gibbs energy with a mole fraction $x_1$ in the liquid phase $\alpha$ and a mole fraction $x_2$ in the solid phase $\beta$: $g$ takes an equilibrium value $g_\alpha(x_1) = g_{\mathrm{e},\alpha}$ at $x_1$ in phase $\alpha$, and in phase $\beta$ accordingly $g_\beta(x_2) = g_{\mathrm{e},\beta}$ at $x_2$. The molar Gibbs energy of the two-phase state lies on the common tangent $(\partial g_\alpha/\partial x)_{x1} = (\partial g_\beta/\partial x)_{x2}$ at the given composition $x$.

A different composition in two phases $\alpha$ and $\beta$ of a binary system in equilibrium represents a general feature of multicomponent systems. For an average composition $x$ a mole fraction $x_1$ is in phase $\alpha$ and a mole fraction $x_2$ in phase $\beta$. $x_1$ and $x_2$ are fixed for a given temperature for any value of $x$ between $x_1$ and $x_2$. The fraction of substance in phase $\alpha$ is given by $x_\alpha = (x_2 - x)/(x_2 - x_1)$, and the fraction of substance in phase $\beta$ is given by $x_\beta = (x - x_1)/(x_2 - x_1)$. In the example discussed above and in Fig. 4.8a $x_1 = 0.50$ and $x_2 = 0.62$ at $T_2$. This means a fraction $x_\alpha =$ 17 % of $A + B$ is in the liquid phase $\alpha$ and has a composition of 50 % of component $A$ in $A + B$, while $x_\beta = 83$ % is in the solid phase $\beta$ which has a composition of 62 % of $A$ in $A + B$. If $\alpha$ and $\beta$ are respectively the liquid and solid phases, then the line between regions $\alpha$ and $\alpha + \beta$ is called liquidus curve. It is built from all points $x_1$ as the temperature is varied. The line separating regions $\alpha + \beta$ and $\beta$ is then called solidus curve.

The quotient $k_0 \equiv x_\alpha/x_\beta$ is the equilibrium distribution-coefficient. It controls the solubility of diluted components and is used to describe any mixture, e.g. doping or alloying of crystals. Its value exceeds 1 if the coexistence boundary increases as the concentration of the considered component is increased.

In *real solutions* particle interactions $A$–$A$, $A$–$B$, and $B$–$B$ are all different. There is hence an enthalpy change $\Delta h_\mathrm{M} \neq 0$ upon mixing which may have either sign. A negative value signifies an exothermal reaction, where heat is generated during mixing due to an attractive interaction among the components. A positive value of $\Delta h_\mathrm{M}$ occurs for an endothermal reaction, where heat from the environment is consumed by the system for mixing. Such behavior indicates a diminishment of binding energy in the mixed system and a consequential tendency towards a separation into immiscible components.

Most real solutions are miscible over the entire or a certain range of composition $x$. If the components of the solution are randomly distributed (in crystalline

solid solutions with a random distribution of atoms on lattice sites), then the mixture is termed *regular solution*. Such real solutions have the same mixture-induced change of entropy $\Delta s_\mathrm{M}$ as an ideal solution. Due to a finite $\Delta h_\mathrm{M}$ the Gibbs energy of a regular solution differs from that of an ideal solution,

$$g(x) = \overline{g} + \Delta g_\mathrm{M} = \overline{g} + \Delta h_\mathrm{M} - T\,\Delta s_\mathrm{M} \quad \text{(regular, real solution)}. \tag{4.20}$$

The enthalpy change $\Delta h_\mathrm{M}$ is proportional to the concentrations $x$ and $(1-x)$ of the components of the system $A$ and $B$, respectively. It may be described by a parameter $\Omega$ characterizing the interaction among the components,

$$\Delta h_\mathrm{M}(x) = \Omega x(1-x) = \Omega\left(x - x^2\right). \tag{4.21}$$

Expression (4.21) represents a quadratic correction to the ideal Gibbs energy (4.19) for regular solutions with a maximum (or—for a negative $\Omega$ value—a minimum) at $x = 0.5$. The function is drawn for positive $\Delta h_\mathrm{M}$ in the top panel of Fig. 4.8b.

A negative enthalpy change $\Delta h_\mathrm{M}$ upon mixing—indicative for miscibility—leads to a decrease of Gibbs energy $\overline{g}$ in addition to that induced by the entropy change. There is then a quantitative change of Gibbs energy $g(x)$, but largely only a minor qualitative change in the shape of the function compared to the ideal case shown in Fig. 4.8a.

A positive enthalpy change $\Delta h_\mathrm{M} > 0$ counteracts the entropy change. A large enthalpy change upon mixing leads to a contribution comparable to the term $-T\,\Delta s_\mathrm{M}$ in the range of medium composition and at sufficiently low temperature. At low temperature the system is considered to be in the solid phase $\beta$. Below a critical temperature $T_\mathrm{c}$, Gibbs energy $g_\beta(x)$ then has a negative curvature ($\partial^2 g_\beta/\partial x^2 < 0$) in this range, leading to *two* minima $b_1$ and $b_2$.

The function $g_\beta(x)$ is drawn in Fig. 4.8b for a corresponding low temperature $T_2$. The minima $b_1$ and $b_2$ correspond to two chemical potentials $\mu_i = \frac{\partial g_\beta}{\partial x}|_{x_i}$ at the compositions $x_i$. In equilibrium $\mu_1 = \mu_2$ applies, and the chemical potentials are given by the common tangent drawn in Fig. 4.8b. Analogous to the case of the ideal system with two phases $\alpha$ and $\beta$ discussed above and in Fig. 4.8a, the lowest Gibbs energy of the solid phase $g_\beta(x)$ is attained if the system decomposes into two solid phases $\beta_1$ and $\beta_2$ with compositions $x_1$ and $x_2$ at $T_2$, respectively. Such behavior is referred to as *spinodal decomposition*. The minima $b_1$ and $b_2$ represent points for the given temperature of a curve termed *binodal*.

The minima $b_1$ and $b_2$ are separated by a local maximum in the range of medium composition and two inflection points $s_1$, $s_2$. The maximum represents an instable composition of the solid solution. Such maximum emerges as the temperature is decreased below a critical value $T_\mathrm{c}$. The homogeneous solid phase $\beta$ then spontaneously separates into two immiscible phases with compositions given by the binodal. The miscibility gap gets wider for lower temperature as illustrated at the bottom of Fig. 4.8b. Cooling of the solid therefore leads to a continuous change in the compositions of the two phases $\beta_1$ and $\beta_2$ along the binodal—provided the process is sufficiently slow to allow for establishing a thermal equilibrium. If the kinetics in the solid phase is not fast enough, the compositions of the solid phase $\beta$ may be

preserved in a metastable state below $T_c$. This feature may be employed in epitaxy to fabricate alloy layers, which cannot be grown using equilibrium-near techniques.

Regions of negative curvature of $g_\beta(x)$ lie within the inflection points of the curve ($\partial^2 g_\beta/\partial x^2 = 0$). The points are called the spinodes, and their locus as a function of temperature defines the spinodal curve. For compositions bounded by the spinodal, a homogeneous solution is unstable against infinitesimal fluctuations in composition, and there is no thermodynamic barrier to the decomposition into phases $\beta_1$ and $\beta_2$. For regular solutions the spinodal is given by

$$x(1-x) = RT/2\Omega.$$

Epitaxy of multicomponent systems is often performed at low temperatures, and phase separation leading to compositional fluctuations on a small scale may become an issue. The solid may still be deposited in a metastable state when the kinetics is sufficiently slow.

It must be noted that spinodal decomposition is significantly affected by elastic strain, which in epitaxial heterostructures is generated by lattice misfit. Experiments demonstrated that strained semiconductor alloys can be grown within the miscibility gap well below the critical temperature $T_c$ [2, 3]. Lowering of $T_c$ and narrowing of the immiscibility range bounded by the spinodal is described by an additive term in the bulk free energy that is proportional to the misfit $f$ (2.20a)–(2.20c) of the in-plane lattice parameter parallel to the layer-substrate interface [4–7]. The calculations show that the suppression of phase separation is related to the interaction parameter $\Omega$, which is found to depend nonlinearly on the composition of the alloy.

## 4.2 Crystalline Growth

Growth of a crystalline layer proceeds by the attachment of particles (atoms, molecules) to the surface. The driving force is provided by the chemical potential treated in the previous section. The growth process is basically described in terms of a structural model and kinetic processes which an impinging particle experiences until being incorporated into the crystal [8, 9]. In the *initial* stage of growth the formation of the new phase requires, however, some nucleation: small clusters of the particles forming nuclei of the solid. Once stable nuclei are formed the crystal grows according conditions controlled by properties of the applied phase transition and adjusted growth parameters. In the following we first consider the initial step in terms of the classical theory of nucleation.

### *4.2.1 Homogeneous Three-Dimensional Nucleation*

We discussed in Sect. 4.1 how a driving force may be created by varying temperature or pressure to make a solid phase more stable than a liquid or gas phase. If the

system was initially in a homogeneous phase, e.g., entirely liquid, the solid phase is *not* spontaneously formed when the equilibrium boundary is crossed. Instead, the initial phase remains at first in a metastable state of undercooling (of a liquid below the freezing point) or supersaturation (of a vapor below the condensation point). These states are indicated by dashed lines in Figs. 4.2 and 4.7. The reason for the persistence of the no longer most stable phase is the need to create an interface at the boundaries of the new phase. The formation of such interface consumes some energy, based on the *surface energy* of each phase. The stable new phase is only formed at sufficient undercooling or supersaturation. Any disturbance like, e.g., a slight agitation or charge, will reduce to some extent the required deviation from equilibrium. *Homogeneous nucleation* occurs spontaneously and randomly in a homogeneous initial phase. Nucleation is strongly facilitated in presence of preferential *nucleation sites*. Such site is any inhomogeneity in the metastable phase, e.g., a substrate or suspended minute particles. In the case of such *heterogeneous nucleation*, some energy is released by the partial destruction of the pre-existing interface.

Nucleation is the onset of the phase transition in small regions called nuclei: regions of the new phase with an interface at the boundaries to the initial phase. If a potential nucleus is too small, the energy that would be released by forming its volume is not enough to create its surface, and nucleation does not proceed. The critical size of a nucleus required for growth in homogeneous nucleation is described by thermodynamics. The creation of a nucleus is accompanied by a change of Gibbs energy $\Delta G_\mathrm{N}$. This quantity is composed of three contributions. First some amount of substance enters the new stable phase, liberating an energy $\Delta G_\mathrm{V}$ proportional to the volume of the nucleus. This process is favorable for the system, and $\Delta G_\mathrm{V}$ is hence a negative quantity. Second the interface between the new stable phase and the metastable surrounding phase must be created, yielding a positive cost $\Delta G_\mathrm{S}$. This contribution of surface free energy is proportional to the area of the interface.

The *surface free energy* $\gamma$ may be regarded as reversible work to form a unit area of surface (or interface) at equilibrium with constant system volume and number of components. For a crystal $\gamma$ is always a positive quantity, because otherwise the crystal phase would not be stable. In a solid the magnitude of the surface energy $\gamma$ per atom is roughly given by half the heat of melting per atom. This rule of thumb originates from the imagination that melting breaks all bonds of an atom, while only half of the bonds of a surface atom are broken. The surface free energy $\gamma$ is related to the surface stress tensor $\gamma^\mathrm{S}$ with the in-plane components $\gamma_{ij}^\mathrm{S}$, $i, j = 1, 2$. The $\gamma_{ij}^\mathrm{S}$ describe the work per unit area for an elastic strain of the surface and may have either sign. A negative sign for compressive strain indicates that work is released when the surface area decreases. The surface stress $\gamma_{ij}^\mathrm{S}$ designates the difference between the stress field in the bulk of the crystal $\sigma_{ij}^\mathrm{bulk}$ used in Hooke's law (2.10) and the modified stress field $\sigma_{ij}(z)$ in the region near the surface located at $z = 0$: $\gamma_{ij}^\mathrm{S} = \int (\sigma_{ij}(z) - \sigma_{ij}^\mathrm{bulk})\, dz$. The relation between surface stress $\gamma_{ij}^\mathrm{S}$ and the surface free energy $\gamma$ is given by the Shuttleworth relation

$$\gamma_{ij}^\mathrm{S} = \gamma \delta_{ij} + \left.\frac{\partial \gamma}{\partial \varepsilon_{ij}}\right|_{T,\mu_i},$$

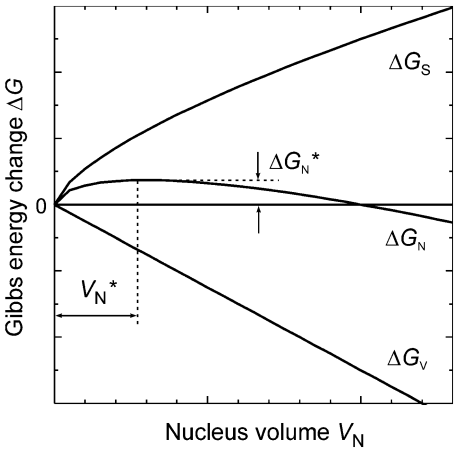


**Fig. 4.9** Change of Gibbs energy for creating a spherical nucleus with volume $V_N$ in homogeneous nucleation. $V_N^*$ and $\Delta G_N^*$ are the critical nucleus size and the critical work of nucleus creation, respectively

$\delta_{ij}$ being the Kronecker symbol and $\varepsilon_{ij}$ the in-plane components of the strain tensor [10]. In a liquid the second summand equals zero, because a liquid does not resist to strain: If the surface is increased (e.g. by tilting a half-filled vessel) material just flows from the bulk of the liquid to enlarge the surface. In a liquid surface energy $\gamma$ and surface stress $\gamma^S$ are equal.

A third term $\Delta G_E$ arises in the change of Gibbs energy $\Delta G_N$ upon creation of a nucleus if the nucleus is subjected to elastic stress. $\Delta G_E$ is a positive quantity which counteracts the favorable volume term $\Delta G_V$ and may even suppress nucleation if $\Delta G_E > |\Delta G_V|$. The total change of Gibbs energy is given by

$$\Delta G_N = \Delta G_V + \Delta G_S + \Delta G_E. \tag{4.22}$$

We consider an *unstrained* nucleus and neglect the last term $\Delta G_E$ to obtain a simple expression for the characteristics of homogeneous nucleation. Strain effects are considered in the next section. As a further simplification we assume an *isotropic* surface free energy $\gamma$ expressed by a constant energy per unit surface area. In our approach we consider a nucleus with spherical shape, which is realized for a liquid nucleus in the bulk of a vapor phase. In this case we obtain $\Delta G_S = \gamma \Delta S = \gamma 4\pi r^2$ and $\Delta G_V = (\Delta g/v)(4/3)\pi r^3$. Here $r$ is the radius of the nucleus and $\Delta S$ its surface. $v$ is the mole volume of the new phase and $\Delta g$ is the change of Gibbs energy of the system by creating one mole of the new phase. Equation (4.21) then reads

$$\Delta G_N = \Delta G_S + \Delta G_V = 4\pi\left(\gamma r^2 + (\Delta g/v) r^3/3\right) \quad \text{(unstrained spherical nucleus)}. \tag{4.23}$$

The molar change of Gibbs energy $\Delta g$ is negative because the new phase is the stable phase for the set conditions. The sum $\Delta G_N = \Delta G_V + \Delta G_S$ is drawn in Fig. 4.9 as a function of nucleus volume $V_N$.

We see from Fig. 4.9 that Gibbs energy initially *increases* during formation of the stable phase due to the unfavorable creation of the boundary to the initial phase. The favorable volume term counterbalances the energy cost of the phase boundary as the nucleus grows. Since increase of the absolute value of the volume term ($\propto r^3$)

preponderates that of the surface term ($\propto r^2$) Gibbs energy change $\Delta G_\mathrm{N}$ passes a maximum at some critical radius $r^*$ as the nucleus grows. The volume term eventually prevails over the energy cost of the phase boundary and Gibbs energy change induced by the creation of the nucleus becomes negative.

The critical nucleus size denoted by the critical volume $V_\mathrm{N}^*$ follows from the maximum condition of $\Delta G_\mathrm{N}$ in (4.23) and is attained at the critical radius

$$r^* = -\frac{2v\gamma}{\Delta g}. \tag{4.24}$$

$v$ designates the molar volume in the new stable phase and $\Delta g$ is the change of molar Gibbs energy for a transition to this phase. Inserting $r^*$ into (4.23) yields the corresponding critical work required to create such nucleus,

$$\Delta G_\mathrm{N}^* = (16/3)\pi\gamma^3(v/\Delta g)^2. \tag{4.25}$$

The critical free energy of nucleation $\Delta G_\mathrm{N}^*$ represents an activation energy for the formation of stable nuclei. The maximum condition of (4.23) $\partial(\Delta G_\mathrm{N})/\partial r = 0$ implies that the critical nucleus is in thermodynamic equilibrium with the metastable phase at $r = r^*$. The chemical potential of the nucleus is then identical to that of the surroundings. This equilibrium is labile: Gibbs energy degreases for both a decrease and an increase of nucleus size. Nuclei with a radius smaller than $r^*$ are instable and tend to disband. Above $r^*$ nuclei tend to grow since addition of particles to clusters larger than the critical radius releases, rather than costs, energy. Once $\Delta G_\mathrm{N}$ gets negative the nucleus is stable. Growth is then no longer limited by nucleation, albeit it may still be limited by supply of particles, i.e. by a limited diffusion, or by reaction kinetics. Growth of the stable phase is now more favorable until thermodynamic equilibrium is restored.

If we apply (4.24) to supercooling expressed by (4.15) we obtain an approximate expression for the critical radius $r^*$ of a nucleus depending on the deviation $\Delta T = T - T_\mathrm{e}$ from the equilibrium temperature $T_\mathrm{e}$, yielding

$$r^* \cong \frac{2\gamma v T_\mathrm{e}}{\Delta h_\mathrm{trans}\Delta T},$$

$\Delta h_\mathrm{trans}$ being the change of molar enthalpy by the phase transition, i.e., the molar heat of crystallization. In this relation only the linear term in (4.15) was considered, and we used $g = \mu$ for a single-component system. Implicitly we assumed that the properties of the system in the nucleus are identical to those in the macroscopic phase. We similarly may apply (4.24) to supersaturation conditions $\Delta P = P - P_\mathrm{e}$ described by (4.16), yielding

$$r^* \cong \frac{2\gamma v}{\Delta v_\mathrm{e}\Delta P}.$$

Here $\Delta v_\mathrm{e}$ is the difference of molar volume in the metastable and stable phases, respectively.

Homogeneous nucleation induces randomly a spontaneous phase transition in the initial phase. This may, e.g., occur in metalorganic vapor phase epitaxy if instable precursors react in the gas phase before being transported to the substrate. In epitaxy

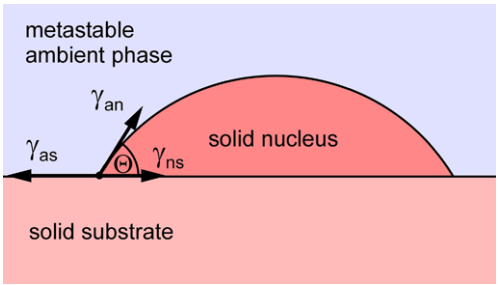


**Fig. 4.10** Nucleus created on a substrate. The balance of surface energies $\gamma$ leads to a wetting angle $\Theta$

such situation must generally be avoided to maintain control over growth. Epitaxial growth is therefore performed *below* the critical supersaturation or supercooling required for homogeneous nucleation.

### *4.2.2 Heterogeneous Three-Dimensional Nucleation*

Nuclei form in heterogeneous nucleation at preferential sites. In epitaxy such sites are provided by the crystalline substrate. Due to the presence of a pre-existing solid phase the interface area to the ambient metastable phase is reduced. The energy barrier to nucleation $\Delta G_{\mathrm{N}}^{*}$ is therefore substantially smaller. Since a part of the substrate is covered by the nucleus a new interface is created between nucleus and substrate. The total change of Gibbs energy $\Delta G_{\mathrm{N}}$ in heterogeneous nucleation is described by the sum of volume, surface and stress terms given in (4.22) in the same way as in homogeneous nucleation.

We again at first neglect elastic stress term $\Delta G_{\mathrm{E}}$ in (4.22) and consider its effect at the end of this section. We assume a nucleus with the shape of a spherical cap with radius $r$ on a substrate as depicted in Fig. 4.10. Such case is realized for a liquid nucleus on a structureless substrate. The balance of interface tensions at the line of contact between the three phases of metastable ambient (index a), nucleus (n), and substrate (s) is given by three quantities which represent the energies needed to create unit area of each of the three interfaces. From the figure we read Young's relation for the absolute values of tensions in balance $\gamma_{\mathrm{as}} = \gamma_{\mathrm{ns}} + \gamma_{\mathrm{an}} \cos\Theta$, or

$$\cos\Theta = \frac{\gamma_{\mathrm{as}} - \gamma_{\mathrm{ns}}}{\gamma_{\mathrm{an}}}. \tag{4.26}$$

The wetting angle $\Theta$ may vary between 0 and 180° depending on the degree of wetting corresponding to the affinity of nucleus and substrate materials. $\Theta$ hence determines the shape of the nucleus. The volume of a spherical cap is $(4/3)\pi r^3 \times f$, where the geometrical factor $f$ depends on $\Theta$ according

$$f = \left(2 - 3\cos\Theta + \cos^3\Theta\right)/4.$$

The shape factor reduces the volume of the nucleus with respect to homogeneous nucleation and accordingly the volume term of Gibbs energy change $\Delta G_{\mathrm{N}}$, yielding

$$\Delta G_{\mathrm{V}}^{\mathrm{hetero}} = f \times \Delta G_{\mathrm{V}}^{\mathrm{homo}}.$$

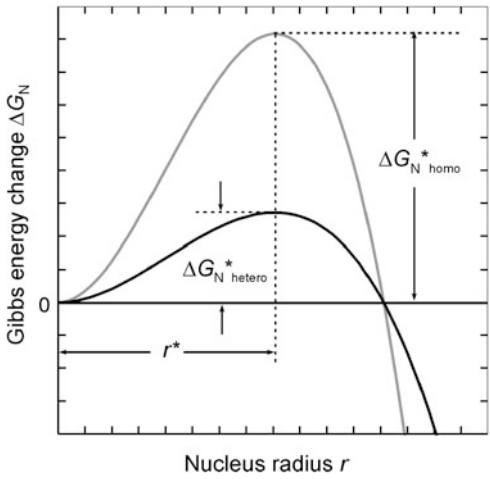


**Fig. 4.11** Change of Gibbs energy $\Delta G_N$ when creating unstrained spherical nuclei with radius $r$ in heterogeneous (*black curve*) and homogeneous nucleation (*gray*). $r^*$ is the critical nucleus radius

The surface term $\Delta G_S$ is now composed of two parts related to the interfaces ambient-nucleus and nucleus-substrate. Including the corresponding geometrical factors we obtain the critical nucleus size $r^*_{\text{hetero}}$ in the same way as in homogeneous nucleation, leading to $r^*_{\text{hetero}} = r^*_{\text{homo}}$ given by (4.24). The critical free energy of nucleation $\Delta G^*_{\text{N hetero}}$ for (unstrained) heterogeneous nucleation is then

$$\Delta G^*_{\text{N hetero}} = \frac{16\pi}{3} \frac{\gamma_{\text{an}}^3 v^2}{(\Delta g)^2} f. \tag{4.27}$$

Comparing (4.27) to (4.25) shows that $\Delta G^*_{\text{N hetero}}$ is reduced with respect to $\Delta G^*_{\text{N homo}}$ by the shape factor $f$ which is controlled by the three surface tensions. Note that there is a smaller amount of substance in the nucleus expressed by $f$ for given $r^*$ in heterogeneous nucleation. The relation of Gibbs energy change in hetero- and homogeneous nucleation is illustrated in Fig. 4.11.

Epitaxy is preferred on substrates which are well wet by the epitaxial layer, so as to obtain a large separation to homogeneous critical supersaturation or undercooling. Furthermore, usually a two-dimensional atomically flat layer-by-layer growth is intended in epitaxy, favored by such wetting.

### Effect of Strain

The structureless surface of the substrate assumed above is certainly oversimplified. The surface structure of the substrate provides specific sites for nucleating atoms. On a plane substrate such sites are defined by the potential created by the topmost substrate atoms. Section 2.2 pointed out how layer atoms accommodate to the lateral spacing of the substrate atoms. Such alignment also applies for nucleation at the initial stage of growth. The nucleus is consequently strained and accumulates a strain energy $\Delta G_E$, which is—according Hooke's law—proportional to the difference of the lateral equilibrium atom spacings of layer atoms and substrate atoms. The strain

$\varepsilon$ enters Gibbs energy $\Delta G_N$ of the nucleus in both the volume term $\Delta G_V$ and the surface term $\Delta G_S$ discussed in the previous section for the unstrained case. $\Delta G_V$ is reduced by an increased chemical potential in the nucleus originating from the strained atomic bonds. The surface energy $\Delta G_S$ of the strained nucleus is increased in a complex way due to the anisotropic nature of the strain and the effect of a partial elastic strain relaxation at side faces (compare Fig. 5.35a). As a consequence, the energy $\Delta G_N^*$ to form a nucleus of critical size is *increased* in the presence of strain. A simple explicit expression for the effect of the strain $\varepsilon$ on the critical free energy of nucleation $\Delta G_N^*$ was derived in Ref. [11] for the case of a Kossel crystal with first neighbor interactions in absence of the Poisson effect,

$$\Delta G^*_{\mathrm{N\ hetero,strained}} = \Delta G^*_{\mathrm{N\ hetero,unstrained}} \left(1 - \frac{\varepsilon}{E_1}\right)^2 \left(1 - \frac{2\varepsilon}{\Delta\mu}\right)^{-2}. \qquad (4.28)$$

The quantity $E_1$ is the first neighbor interaction of the bond between two adjacent atoms, and $\Delta\mu$ is the supersaturation. We note a singularity in (4.28) for $\Delta\mu$ equals $2\varepsilon$. At large strain the term $\Delta G_E$ in (4.23) which counteracts the favorable (negative) volume term $\Delta G_V$ in Gibbs energy $\Delta G_N$ will even suppress nucleation.

### *4.2.3 Growth Modes*

The surface energies leading to Young's relation (4.26) affect the initial stage of layer deposition on a substrate of different material. Epitaxy usually aims at depositing a layer with a smooth growth surface. This corresponds to a wetting angle of 0 in Young's relation, or $\gamma_{as} = \gamma_{ns} + \gamma_{an}$. If this condition applies or $\gamma_{as}$ exceeds the sum of the two other interface energies we obtain complete wetting of the layer on the substrate surface. The condition implies that layer atoms are more strongly attracted to the substrate than to themselves. Growth may then proceed in an atomically flat layer-by-layer mode referred to as Frank-Van der Merve growth mode. Figure 4.12 illustrates the initial stages of such two-dimensional layer growth for different thickness of deposited material. Nucleation in this case proceeds by the formation of *two-dimensional* islands or step advancement as outlined in Sects. 4.2.5 and 4.2.7.

A different surface morphology of the layer is observed if layer atoms are more strongly attracted to each other than to the substrate. This situation is expressed in Young's relation (4.26) by a wetting angle of $\pi$, or $\gamma_{ns} = \gamma_{as} + \gamma_{an}$. If this condition applies or $\gamma_{ns}$ is even larger, then the layer does not wet the substrate surface. The surface energy of layer plus substrate is minimized if a maximum of substrate surface (with a low surface energy $\gamma_{as}$) is *not* covered by layer material (which has a large surface energy $\gamma_{an}$). This results in a three-dimensional growth of the layer referred to as Volmer-Weber growth mode. Fig. 4.12 shows that the layer material is deposited in form of islands, which for thicker deposits eventually coalesce. Here, nucleation proceeds by 3D nuclei as pointed out in the preceding sections.

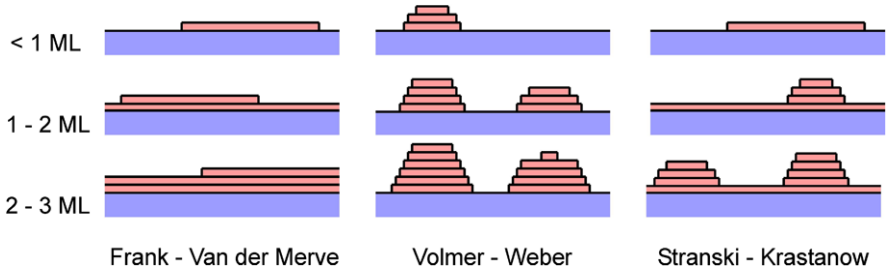


**Fig. 4.12** Schematic of the three growth modes, illustrated as a function of approximately equal coverage given in units of monolayers (ML)

Often an intermediate case is found referred to as Stranski-Krastanow growth mode (also termed layer-plus-island growth). Here the condition $\gamma_{as} \geq \gamma_{ns} + \gamma_{an}$ for Frank-Van der Merve growth applies solely for the first deposited monolayer (or the first few monolayers). After exceeding some critical coverage thickness the growth changes to the Volmer-Weber case where $\gamma_{ns} \geq \gamma_{as} + \gamma_{an}$ applies. Such change may be induced by the gradual accumulation of strain in the epitaxial layer (Sect. 2.2.6). The layer material then resumes growth in form of three-dimensional islands, leaving a two-dimensional wetting layer underneath. It should be noted that the critical thickness pointed out here lies usually below that required for the formation of misfit dislocations treated in Sects. 2.2.6 and 2.3. Stranski-Krastanow growth has gained much advertence in recent years, because it may be employed for growth of defect-free quantum dots. We therefore will consider this specific growth mode in more detail separately in Sect. 5.3.1.

The three growth modes depicted in Fig. 4.12 arise from a thermodynamic consideration of the interface energies. Additional growth modes have been introduced to account for frequently observed surface morphologies. On terraced surfaces *step-flow growth* may be found under suitable conditions; depending on growth parameters also *step bunching* may occur (Sect. 5.2.4). In the presence of screw dislocations *spiral growth* (Sect. 4.2.7) or *screw-island growth* is observed. Eventually for materials with low surface mobility of adatoms *columnar growth* may be obtained. Similar to Volmer-Weber growth islands nucleate, but they do not merge to continuous layers when growth proceeds. A mosaic crystal composed of numerous slightly tilted and twisted columnar crystallites is formed instead.

### *4.2.4 Equilibrium Surfaces*

The Stranski-Krastanow growth mode described above indicates that under certain conditions a rough or faceted surface is more stable than a flat surface. The reason is the pronounced dependence of the surface energy $\gamma$ of crystalline solids on the orientation of the surface. In absence of kinetic effects and defects the macroscopic shape of a solid is determined by a minimum of Gibbs free energy $G$ which includes

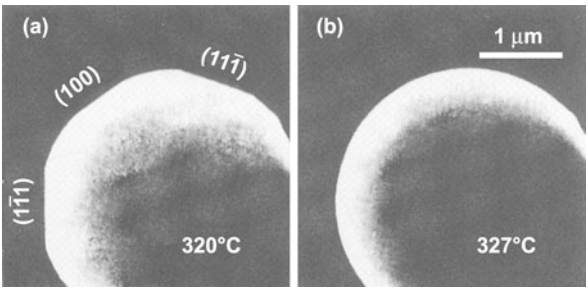


**Fig. 4.13** In-situ imaged scanning electron micrographs of a small lead particle slightly below (**a**) and above (**b**) the melting point. Indices in (**a**) signify equilibrium facets. Reproduced with permission from [12], © 1989 Elsevier

a term of its surface $G_{\text{surf}}$. The equilibrium shape is therefore given by a minimum of $G_{\text{surf}}$ for a given volume (or amount of substance),

$$G_{\text{surf}} = \oint_A \gamma(\mathbf{n})\, dA \rightarrow \text{minimum}, \tag{4.29}$$

where $\mathbf{n}$ is the surface normal of the respective part of the surface considered. In liquids $\gamma(\mathbf{n}) = \gamma$ is isotropic, and the equilibrium shape (in absence of gravity) is consequently a sphere which has minimum surface area. This is illustrated in Fig. 4.13 for a small lead particle annealed slightly below and above the melting point. A spherical shape is observed above the melting point (Fig. 4.13b), whereas the equilibrium shape of solid lead Pb in Fig. 4.13a shows sharp facets of the fcc structure.

In crystalline solids $\gamma(\mathbf{n})$ has pronounced minima for specific faces denoted by their Miller indices $(hkl)$. The equilibrium shape is therefore not given by a minimum surface area but by a minimum of $G_{\text{surf}}$. Such minimum is attained by a polyhedron built from these particular faces of minimum surface energy. While $\gamma$ of liquids may be readily obtained from capillary experiments, determination of $\gamma(\mathbf{n})$ from crystal surfaces is difficult. We employ a simple approach to obtain a qualitative estimate on the orientation dependence of $\gamma$.

We consider a Kossel crystal which assumes atoms as cubes that are bond by their six faces. Only next-neighbor bonding and only a single species of atoms are presumed. The surface energy is evaluated in the framework of the terrace-step-kink model (Sect. 5.2.1). According to this model a surface may be classified into the three categories *singular* (i.e., perfectly oriented low index plane), *vicinal* (i.e., slightly inclined with respect to a singular surface), and *rough*. Let us first consider a singular (001) surface of a Kossel crystal. The surface energy $\gamma$ is given by the sum of the energies of all bonds broken to create this surface, i.e.

$$\gamma = \frac{E_B}{2}\nu. \tag{4.30}$$

$\nu$ is the number of bonds on the surface per unit area, $E_B$ is the bond energy and the factor $\frac{1}{2}$ takes into account that 1 bond connects 2 atoms (i.e., actually *two* surfaces are created when a bulk crystal is cleaved into two parts). $E_B$ is related to

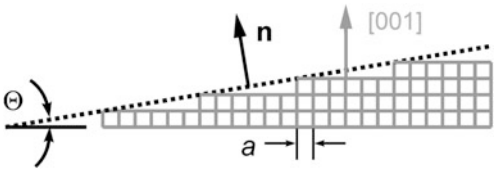


**Fig. 4.14** (**a**) Cross section of a Kossel crystal (*gray*) with a vicinal (016) surface (*black*, *dotted*), inclined by a small angle $\Theta$ with respect to the singular (001) plane

the sublimation energy $\Delta H_S$: Releasing an atom from the bulk requires breaking 6 next-neighbor bonds, leading to the relation

$$\Delta H_S = \frac{6}{2} E_B, \quad \text{or} \quad E_B = \frac{1}{3} \Delta H_S. \tag{4.31}$$

The number $\nu$ of bonds per unit area of a (001) surface with $n_1 \times n_2$ atoms along the two orthogonal lateral directions is just $\nu = n_1 \times n_2/(n_1 \times n_2 \times a^2) = 1/a^2$.

To obtain an expression for the orientation dependence of $\gamma$ we evaluate a vicinal surface which is inclined by a small angle $\Theta$ with respect to the (001) plane. Figure 4.14 shows such vicinal surface of a Kossel crystal. The surface consists of flat terraces separated by steps. We assume the steps are regularly spaced (i.e., absence of step-step interactions) and of monoatomic height.

The number $\nu$ of bonds per unit area of the vicinal surface is larger than that of the singular surface and given by

$$\nu = \frac{1}{a^2}(\cos\Theta + \sin\Theta).$$

Inserting this expression into (4.30) and using (4.31) yields

$$\gamma = \frac{\Delta H_S}{6a^2}(\cos\Theta + \sin\Theta). \tag{4.32}$$

Since the angle dependence in the brackets is always greater than unity, the surface energy of a vicinal surface always exceeds that of the corresponding singular surface. The excess energy originates from the ledge atoms located at the steps. These atoms have an additional missing bond with respect to atoms located on a terrace site.

Relation (4.32) leads to a geometrical construction to represent the surface energy of a solid: the *Wulff plot*. Equation (4.32) describes a circle (in three dimensions a sphere) with diameter $2r = \Delta H_S/(6a^2)$. In polar coordinates a circle which passes through the origin is given by

$$\gamma = 2r\cos(\Theta - \varphi) = 2r(\cos\Theta\cos\varphi + \sin\Theta\sin\varphi),$$

see Fig. 4.15a. If the origin of the circle lies on a line inclined by $\varphi = \pi/4$ with respect to a coordinate axis as illustrated in the figure we obtain an expression like (4.32). Due to the symmetry of the considered cubic crystal the entire three-dimensional representation of the surface energy $\gamma(\Theta)$ is actually described by eight interpenetrating spheres, the origins of which are lying on the four $\langle 111 \rangle$ axes. Figure 4.15 is a two-dimensional cross section of $\gamma(\Theta)$ for an azimuth angle of 0. We note that the surface energy $\gamma$ has pronounced minima (cusps) on the low-index $\langle 100 \rangle$ axes.

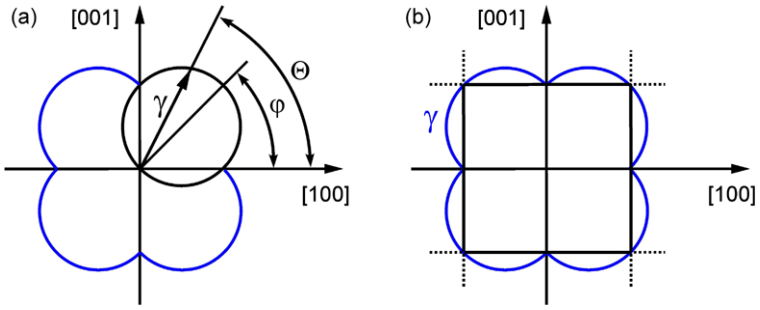


**Fig. 4.15** (**a**) Construction of the surface energy $\gamma(\Theta)$ of a Kossel crystal (*blue curves*) by *circles* passing through the origin. (**b**) Wulff plot of the equilibrium crystal shape (*black lines*), constructed from the surface energy given in (**a**)

The equilibrium shape of the Kossel crystal with next-neighbor bonds is found from the surface energy given in Fig. 4.15a by drawing lines from the origin to all possible crystallographic directions through the $\gamma$ plot. At a point of intersection with the surface of the plot, a plane is constructed perpendicular to the line. Such *Wulff plane* has an equal $\gamma$ as the crystal at the intersection point for the orientation given by the line. The equilibrium shape of the crystal is the inner envelope of all such possible Wulff planes. The construction is called *Wulff plot*. Figure 4.15b shows the Wulff plot of the Kossel crystal with next-neighbor bonds. Since the surface energy of the {100} faces is much lower than that of all other crystallographic faces, the polyhedron given by the inner envelope of all planes is a cube. This is no longer the case if also second-next neighbor interactions of the atoms are taken into account. Atoms in the considered cubic Kossel crystal have 12 second-next neighbor atoms located along the ⟨110⟩ directions. Their bonds are weaker than those of next-neighbor atoms. Consequently their contribution to the surface energy is also weaker. Figure 4.16 shows a two-dimensional representation of the first and second-nearest neighbor contributions to $\gamma$. The contribution $\gamma_2$ of the weaker second-nearest neighbor bonds to the surface energy $\gamma$ is constructed in the same way as that of nearest neighbor bonds $\gamma_1$, leading to a smaller $\gamma(\Theta)$ plot with cusps along the ⟨110⟩ bond directions. Consequently the sum $\gamma = \gamma_1 + \gamma_2$ has also (local) minima along these directions, and the Wulff plot results in a polyhedron with more faces than obtained in the case with only next-neighbor bonds.

The equilibrium crystal shape is generally composed of more crystallographic inequivalent facets if the distance of bonding forces increases. Surfaces of small surface energy $\gamma$ lead to larger facets. On the other hand the facets referring to surfaces with too large surface energy $\gamma$ lie far away from the origin in a Wulff plot and can hence not contribute to the equilibrium shape. The condition to appear in the equilibrium crystal shape of a cubic crystal in addition to the {001} facets reads for any surface *hkl*

$$\gamma_{hkl} < \frac{h+k+l}{\sqrt{h^2+k^2+l^2}} \times \gamma_{001}.$$

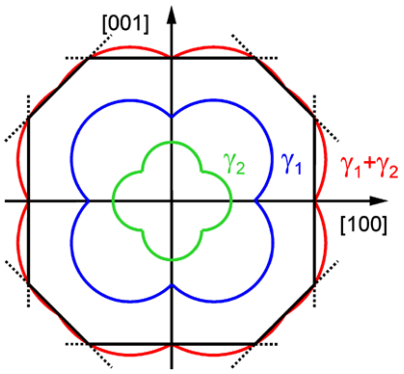


**Fig. 4.16** Surface energy $\gamma = \gamma_1 + \gamma_2$ of a cubic Kossel crystal with first ($\gamma_1$) and second ($\gamma_2$) nearest neighbor interactions taken into account. The *black polygon* represents a cross section of the equilibrium shape of the crystal

According this relation e.g. {111} facets appear on a cubic crystal if $\gamma_{111} < \sqrt{3}\gamma_{001}$ applies.

A general expression of the minimum surface-energy condition (4.29) may be given in terms of *Wulff's theorem*

$$\frac{\gamma_1}{r_1} = \frac{\gamma_2}{r_2} = \frac{\gamma_3}{r_3} = \cdots = \text{const.} \tag{4.33}$$

The expression is a concise summarization of Wulff's construction illustrated above. The indices in (4.33) represent the $(hkl)$ sets of the relevant surfaces, and $r$ is the absolute value of the vectors $r_{hkl}$ parallel to the corresponding surface normals $\mathbf{n}_{hkl}$ with $r_{hkl} \propto \gamma_{hkl}$.

Surface energies $\gamma(\mathbf{n})$ of solids are difficult to measure. During the 1990ies first principles calculations based on slab configurations have reached a maturity to yield sufficient numerical precision. It must be noted that $\gamma(\mathbf{n})$ for a given orientation depends significantly on the structure of the surface. The equilibrium structure may in turn depend on the chemical potential of the ambient. Data given in Table 4.1 represent the lowest values determined for different reconstructions. In the case of GaAs the reconstruction for the broadest range of the anion potential is given. Calculations for data given of the (100) face assumed ambient conditions $\mu_{\text{As}} = \mu_{\text{As}}^{\text{bulk}} - 0.3$ eV. Details of surface reconstructions are considered in Chap. 5.

The equilibrium crystal shape follows from the surface energies $\gamma(\mathbf{n})$. Applying Wulff's construction and using calculated surface energies for As-rich conditions we obtain the equilibrium shape of a GaAs crystal shown in Fig. 4.17a [14]. The polyhedron is composed of low-index planes reflecting the symmetry of the zincblende lattice. It should be noted that the (111) face and the $(\bar{1}\bar{1}\bar{1})$ face show a different dependence on the ambient chemical potential and hence vary differently in size as the chemical potential is changed. The cross section of the equilibrium crystal shape shown in Fig. 4.17b demonstrates the dependence on the chemical potential $\mu_{\text{As}}$. A high value of $\mu_{\text{As}}$ corresponds to an As-rich (i.e., Ga-poor) ambient. The corresponding shape (black polyhedron) is smaller than that expected for a Ga-rich environment (gray polyhedron): As-terminated surfaces have surfaces energies about 20 % smaller than those in a Ga-rich ambient [14].

**Table 4.1** Calculated surface energies $\gamma$ of low-index surfaces, data are given in J/m$^2$. Type of reconstruction noted at the listed data indicate the corresponding lowest-energy surface selected from various calculated configurations, $(1 \times 1)$ relaxed denotes an unreconstructed cleavage surface

| Solid | (100) | | (110) | | (111) | |
|---|---|---|---|---|---|---|
| Si[a] | 1.41 | $c(4 \times 4)$ | 1.70 | $(1 \times 1)$ relaxed | 1.36 | $7 \times 7$ |
| Ge[a] | 1.00 | $c(4 \times 4)$ | 1.17 | $(1 \times 1)$ relaxed | 1.01 | $c(2 \times 8)$ |
| GaAs[b] | ~0.96 | $\beta 2(2 \times 4)$ | 0.83 | $(1 \times 1)$ relaxed | 0.87 | $(2 \times 2)$ Ga vacancy |
| InAs[c] | 0.75 | $\beta 2(2 \times 4)$ | 0.66 | $(1 \times 1)$ relaxed | 0.67 | $(2 \times 2)$ In vacancy |
| InP[d] | ~0.99 | $\beta 2(2 \times 4)$ | 0.88 | $(1 \times 1)$ relaxed | 0.99 | $(2 \times 2)$ In vacancy |

[a]Ref. [13], [b]Ref. [14], [c]Ref. [15], [d]Ref. [16]

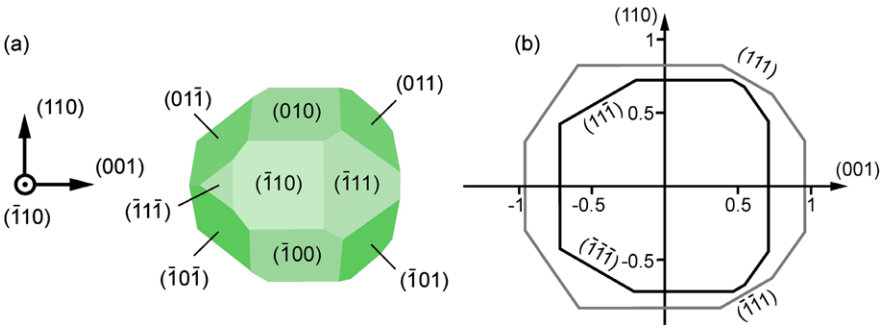


**Fig. 4.17** (**a**) Calculated equilibrium crystal shape of GaAs in As-rich ambient ($\mu_{As} = \mu_{As(bulk)}$). The polyhedron is constructed from the different surface energies of (100), (110), (111), and ($\bar{1}\bar{1}\bar{1}$) facets. (**b**) Cross sections calculated for different chemical potentials: *black lines* $\mu_{As} = \mu_{As(bulk)}$, *gray lines* $\mu_{As} = \mu_{As(bulk)} - 0.3$ eV. Energies are given in J/m$^2$. After [14]

Growth occurs at some deviation from thermodynamic equilibrium as pointed out in Sect. 4.1.5. For a single component system we obtained homogeneous critical nuclei with radius $r^*$ for a given driving force $\Delta\mu$. The respective relation (4.24) was derived assuming unstrained spherical nuclei and an *isotropic* surface energy $\gamma$. We now take different surface energies $\gamma_i$ of inequivalent facets into account, modifying (4.24) to

$$|\Delta\mu| = \frac{2v\gamma_i}{r_i}, \tag{4.34}$$

where $i$ denotes $(hkl)$ sets of the facets. At equilibrium the chemical potentials of all facets must be equal, leading to constant ratios $\gamma_i/r_i$, and consequently to Wulff's theorem (4.32). Equation (4.34) says that the critical size of stable nuclei decreases with increasing deviation $|\Delta\mu|$ from equilibrium.

The shape of a growing crystal deviates from the equilibrium crystal shape. From (4.34) we note that the differences to the equilibrium get smaller for large dimensions $r_i$. The driving force to maintain the equilibrium crystal shape therefore gets negligible for macroscopic crystals. Their shape is instead determined by

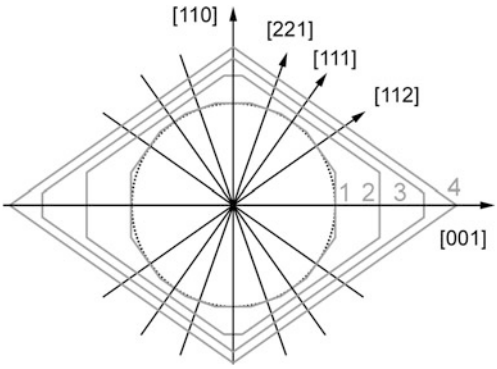


**Fig. 4.18** Facets of a growing crystal at successive stages. Different growth rates are assumed along the indicated directions, with a minimum along ⟨111⟩

kinetic conditions. Surfaces which grow most slowly eventually build the facets of a crystal, as pointed out below. The consequence of a slow growth rate of a facet is illustrated in Fig. 4.18. We assume slowest growth of {111} facets, and, for simplicity, an equal growth rate of a facet along a given crystallographic direction and the inverse direction, i.e., for $\{hkl\}$ and $\{\bar{h}\bar{k}\bar{l}\}$ facets. Starting from an initial stage 1 with almost spherical crystal shape made from the facets indicated in Fig. 4.18, we note that successively all faster growing facets disappear. At stage 4 only the slowly growing {111} facets remain.

Real crystals may deviate from the ideal growth form discussed above. Local differences in the supersaturation and transport to growing surfaces lead to differences in the growth rate of equivalent facets and consequently to different areas of these facets, i.e., to a parallel displacement of the facets with respect to the ideal form. Moreover, crystal defects may significantly accelerate the growth rate of facets. Particularly screw dislocations build a continuous source of surface steps which facilitate the attachment of particles impinging the surface and the subsequent incorporation into the crystal. Kinetic processes in the growth at steps are considered in Sect. 5.2.4.

### *4.2.5 Two-Dimensional Nucleation*

Flat surfaces have generally slow growth rates, because they hardly offer favorable sites like steps for the attachment of atoms from the ambient phase. In absence of terrace steps and defects like screw dislocations, growth of atomically flat surfaces in the layer-by-layer mode proceeds by clusters of adsorbed atoms with a sufficient size. They form *two-dimensional* (2D) nuclei which provide preferential sites for the attachment of further atoms at their perimeter. Which mode of nucleation, 2D or 3D, is thermodynamically preferred depends on the difference in interface energies and strain, cf. Sect. 4.2.3. 2D nuclei must exceed a critical size for stable growth in analogy to three-dimensional nuclei treated in the previous section.

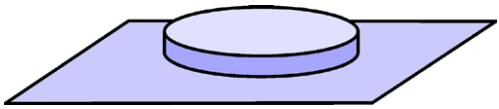

**Fig. 4.19** Two-dimensional nucleus of circular shape with monoatomic height on a flat surface

We consider the critical size of a two-dimensional nucleus for a one-component system. For simplicity we assume a circular shape of the 2D nucleus with radius $\rho$ and monoatomic height as depicted in Fig. 4.19.

The formation of a 2D cluster comprising an amount of substance $n$ changes Gibbs energy due to the transition from the ambient phase to the more stable solid phase by $\Delta G_n^{\mathrm{2D}} = n\Delta\mu$. Since in the assumed one-component system the 2D cluster grows on a surface made of atoms of the same kind no change of the interface energy of the system occurs. There is, however, a contribution $\Delta G_\gamma^{\mathrm{2D}}$ originating from the ledge atoms of the cluster. They have fewer neighbors and thus more unsaturated bonds, which add a positive destabilizing boundary free energy to the total free energy of the 2D cluster. The contribution $\Delta G_\gamma^{\mathrm{2D}}$ is the 1D analog of the surface free energy, which is generally measured as the surface tension. $\Delta G_\gamma^{\mathrm{2D}}$ can hence be considered as a line tension and is proportional to the length of the 2D cluster perimeter $2\pi\rho$, $\rho$ being the radius of the nucleus. A specific free step energy $\gamma_{\mathrm{p}}$ assumed to be isotropic is taken as proportionality factor. If one mole of atoms in a circular 2D island covers an area $a$, the change of Gibbs energy by the formation of a 2D cluster is given by

$$\Delta G_{\mathrm{N}}^{\mathrm{2D}} = \Delta G_n^{\mathrm{2D}} + \Delta G_\gamma^{\mathrm{2D}} = \frac{\pi\rho^2}{a}\Delta\mu + 2\pi\rho\gamma_{\mathrm{p}}. \tag{4.35}$$

The critical 2D nucleus size is obtained similar to the 3D case from the maximum condition of $\Delta G_{\mathrm{N}}^{\mathrm{2D}}$, yielding the critical radius of a two-dimensional nucleus

$$\rho^* = \frac{a\gamma_{\mathrm{p}}}{|\Delta\mu|}, \tag{4.36}$$

and the activation energy

$$\Delta G_{\mathrm{N}}^{\mathrm{2D}*} = \pi\frac{a\gamma_{\mathrm{p}}^2}{|\Delta\mu|}. \tag{4.37}$$

$a$ designates the specific area covered by one mole of atoms, and $\gamma_{\mathrm{p}}$ the excess energy per length of atoms located at the perimeter of the in 2D nucleus with respect to the energy of atoms located on a flat surface. The prefactor $\pi$ in (4.37) applies for a circular shape of the 2D nucleus and is to be replaced by another form factor for a different shape (e.g., $(1+\alpha)^2/\alpha$ for rectangular nuclei, $\alpha$ being the ratio of the side lengths). Relations (4.36), (4.37) are analogous to (4.24) and (4.25) obtained for three-dimensional nuclei. We note that the driving force $\Delta\mu$ enters the 2D activation linearly in the denominator, while a quadratic dependence is found in the 3D case (4.25). For a given small deviation from equilibrium $\Delta\mu$ the formation energy of a 2D nucleus is hence smaller than in homogeneous 3D nucleation.

The shape of 2D nuclei and subsequently growing islands is not necessarily given by the equilibrium crystal shape, due to the required deviation from equilibrium.

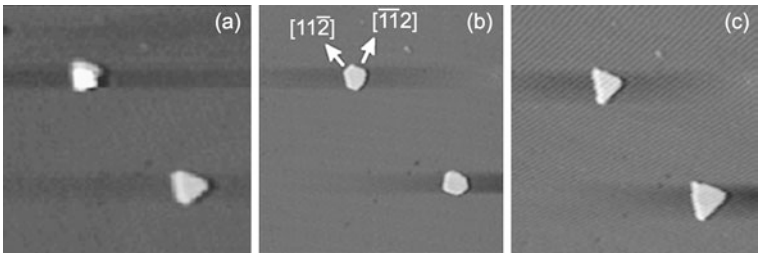


**Fig. 4.20** Scanning tunneling images of two-dimensional Si islands on Si(111) substrate, recorded during molecular beam epitaxy at 725 K (**a**, **c**) and after 18 min annealing at 775 K (**b**). The image size is $55 \times 55$ nm$^2$. Reproduced with permission from [17], © 2004 IOP

Furthermore, the shape is affected by the structure of the substrate surface and kinetic effects considered in more detail in Chap. 5. Evidence for such effects are given in Fig. 4.20.

The in situ recorded scanning tunneling micrographs show two Si islands growing on a Si(111) substrate [17]. During growth the islands clearly show a triangular shape (Fig. 4.20a). When the growth is interrupted and the temperature is raised, the lateral form gradually turns into a hexagon-like shape (Fig. 4.20b). Here, edges perpendicular to [11$\bar{2}$] are somewhat shorter than those perpendicular to [$\bar{1}$12], indicating a lower energy of the latter. When growth is resumed, the islands quickly adopt the initial triangular shape (Fig. 4.20c).

To provide some visual evidence for critical 2D nucleus formation, we consider the assembly of Co-Si clusters at 400 °C on a Si(111)-(7 × 7) surface. High speed scanning tunneling microscopy represents one such cluster as a single bright protrusion, though it probably contains 3 Si atoms and 6 Co atoms [18]. STM images show that the clusters are mobile on the Si surface [19]. Figure 4.21 shows a series of STM scans over $8 \times 8$ nm$^2$ captured in 5 s frames. We note a steady change of the imaged configuration, until the cluster labeled Y occupies the vacancy visible in Fig. 4.21c. The ring composed of 6 clusters is fairly stable. Eventually a cluster detaches (arrow in Fig. 4.21f) and the ring-structure decomposes. Studies reported in Ref. [19] show that the $i = 6$ configuration represents a critical nucleus for the studied system. Once one of the 6 clusters moves to occupy the vacant site in the center and a seventh cluster attaches to the ring, a stable nucleus with $i = 7$ clusters is formed.

The critical free energy of nucleation $\Delta G_{\mathrm{N}}^{2\mathrm{D}*}$ (4.37) represents an activation energy for the formation of 2D nuclei. The rate of formation per unit area of such nuclei is given by the Arrhenius dependence

$$j^{2\mathrm{D}} = j_0^{2\mathrm{D}} \exp\left(\frac{\Delta G_{\mathrm{N}}^{2\mathrm{D}*}}{kT}\right). \tag{4.38}$$

The prefactor $j_0^{2\mathrm{D}}$ follows from kinetic considerations of the nucleation process on an atomic scale.

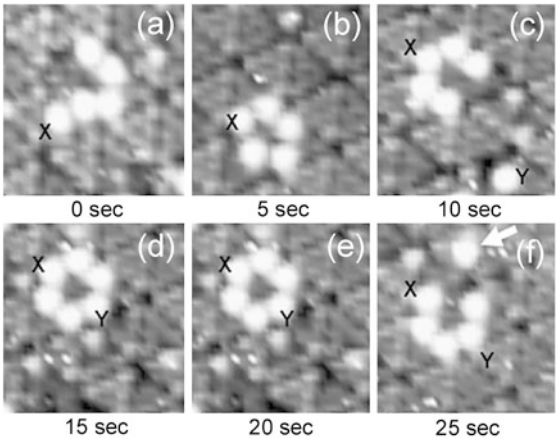


**Fig. 4.21** In situ recorded formation of a critical nucleus of Co-Si clusters (*white protrusions*) on a Si(111)-(7 × 7) surface. *X* and *Y* label two particular clusters. At (**d**) cluster *Y* has moved to complete a ring-like structure consisting of 6 clusters. Reproduced with permission from [19], © 2007 Royal Society of Chemistry Publishing

### *4.2.6 Island Growth and Coalescence*

Using $j^{2D}$ (given in units of $m^{-2} \times s^{-1}$) we obtain the total nucleation rate $J^{2D}$ on a surface of a given area $L \times L$ by the product $J^{2D} = j^{2D} \times L^2$. Two-dimensional growth of a layer proceeds by a lateral growth of 2D nuclei, which eventually coalesce and form a complete coverage of the surface by a new monolayer. The 2D nuclei grow by the attachment of atoms at the step formed at their perimeter. The time $T$ required to grow a monolayer thick complete coverage may therefore be expressed in terms of the velocity of step advancement $v_{step}$ by the relation $T \cong L/v_{step}$. The number of nuclei $N$ created during the time interval $T$ of one monolayer formation is then given by

$$N \cong j^{2D} \times L^2 \times T \cong j^{2D} \times L^3/v_{step}.$$

From this relation we may derive an estimate for the velocity $R$ of the growth front along the surface normal. The growth rate $R$ depends on whether only a single nucleus grows and eventually completes a new monolayer on the considered area $L^2$, or multinuclear (or even multilayer) growth occurs. In the first case a complete monolayer originates from only a single nucleus, i.e., the number of new forming additional nuclei is $N < 1$. This condition corresponds to $L < \sqrt[3]{v_{step}/j^{2D}}$, i.e., it is favored for a small area. The two-dimensional growth of the epilayer proceeds by a formation of a nucleus and its lateral growth until the completion of a monolayer, before the subsequent nucleus is created. The growth rate $R$ is then given by the total nucleation rate $J^{2D}$ times the thickness $d$ of the 2D nucleus, i.e.,

$$R = j^{2D} L^2 d \quad (N < 1, \text{ single nucleus}). \tag{4.39}$$

Generally the condition $N < 1$ does not apply, because the area of an epilayer is large (compared to the diffusion length of an atom on the surface) and supersaturation is not thus small to allow only for the creation of just a single nucleus. The more general case $N > 1$ for the number of nuclei $N$ created during the time interval $T$

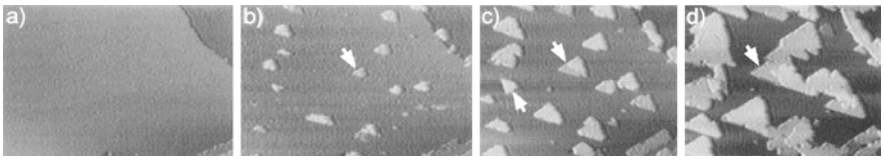


**Fig. 4.22** Growth of Si on Si(111) during chemical vapor deposition at 485 °C. The *arrows* in frames (**b**) to (**d**) mark an island which grows by an additional layer each image. The *left arrow* in (**c**) designates an island, which is rotated by 180° and represents the onset of a stacking fault. The image size is 200 × 180 nm$^2$. Reproduced with permission from [20], © 1993 Springer

of monolayer growth corresponds to $L > \sqrt[3]{v_{\text{step}}/j^{2\text{D}}}$. More than just one nucleus is formed, and all nuclei contribute to the growing layer. In such multinuclear layer-by-layer growth nuclei have a mean time $t$ to grow to 2D islands with a mean radius $l$ before meeting another growing 2D island originating from another nucleus. This time interval is of the order $t \cong l/v_{\text{step}} \cong 1/J^{2\text{D}} \cong (j^{2\text{D}} \times \pi l^2)^{-1}$. The mean radius may therefore be written $l \cong \sqrt[3]{v_{\text{step}}/(\pi j^{2\text{D}})}$. The growth rate $R$ is in this case given by

$$R \cong j^{2\text{D}} \pi l^2 d \cong d\sqrt[3]{\pi v_{\text{step}}^2 j^{2\text{D}}} \quad (N > 1, \text{ many nuclei}), \tag{4.40}$$

where $d$ is the thickness of the 2D nuclei. If growth is initiated on an flat surface without steps, the first nuclei appear simultaneously. When the isolated nuclei (which subsequently become islands) grow, their total perimeter increases. The total perimeter represents also the total step length. Layer growth proceeds by the overall advancement of this step via the attachment of atoms, which arrive at the surface from the ambient and diffuse laterally. Once the growing islands come into contact, they coalesce and their steps annihilate. The total step length therefore decreases at the onset of island coalescence. If no additional nucleation occurs on top of large and still growing 2D islands, the total step length reaches a minimum (0 without any nucleation) when the layer is completed. The total step length oscillates between a minimum and a maximum. Since the incorporation of atoms into the solid occurs at surface steps, also the growth rate oscillates. The oscillation period corresponds to the growth duration of one monolayer, i.e., $T \cong (\pi v_{\text{step}}^2 j^{2\text{D}})^{-1/3}$. Usually after deposition of a few monolayers there occurs gradually additional nucleation on large and still growing 2D islands, giving rise to growth on various heights. As a result, the oscillations are gradually damped and the growth rate eventually approaches a constant value. Such behavior is often observed in the intensity of the specular reflectivity of reflection high energy electron diffraction (RHEED) applied during growth in molecular-beam epitaxy (Sect. 7.3): A high diffraction intensity reflected from a smooth completed layer changes periodically with a low intensity reflected from a rough layer composed of many 2D islands.

Some of the growth features mentioned above are illustrated in the series of scanning tunneling micrographs Fig. 4.22, which were recorded in situ during homoepitaxial growth of Si/Si(111) [20]. The two-dimensional islands have a triangular shape, similar to those shown in Fig. 4.20a, c and those studied in more detail

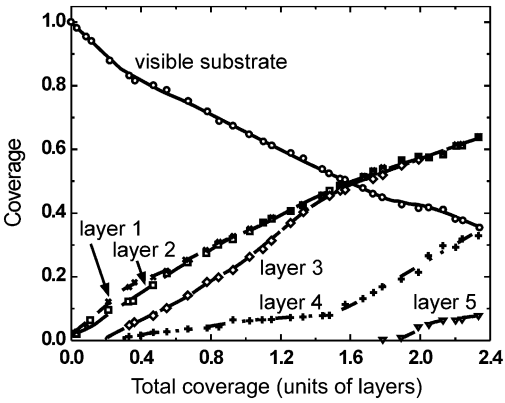


**Fig. 4.23** Buildup of the surface coverage in each layer during epitaxial growth. Distribution of coverages in the first five layers as counted from the Si/Si(111) growth sequence shown in Fig. 4.22. Reproduced with permission from [20], © 1993 Springer

in Sect. 5.2.8. In Fig. 4.22 epitaxy does not proceed in a layer-by-layer mode at the given growth conditions. Instead, additional nucleation occurs already before islands start to coalesce (arrow in the middle of the frames). We still observe lateral growth of the islands at their perimeter. Eventually the islands coalescence and the total perimeter decreases (Fig. 4.22d). The left arrow in Fig. 4.22c marks an island, which is rotated by 180° with respect to the other islands. This orientation corresponds to a stacking fault along the [111] growth direction. The chosen growth temperature is significantly lower than that usually applied in growth of silicon. This leads to structural defects, which are not annealed during further growth. In the case shown in Figs. 4.22c, d an antiphase domain boundary is formed when islands coalesce, cf. the schematic Fig. 2.25.

A measure for layer-by-layer growth is obtained if the coverage buildup of each layer is plotted as a function of the total coverage or of growth time. The curves in Fig. 4.23 correspond to the simultaneous growth of multiple monolayers visible in the series of Fig. 4.22. We note a set of curves with a slow progression: Even after deposition of 2.4 layers (which actually are bilayers in the stacking AaBbCc of the diamond structure of Si) 40 % of the substrate are still not covered. This is a further indicative for a low surface mobility of adatoms due to the low growth temperature applied for in situ characterization.

### *4.2.7 Growth without Nucleation*

The nucleation work pointed out in Sects. 4.2.2 and 4.2.5 (3D and 2D nucleation) impose a significant supersaturation required for nucleation and consequential layer growth. This is in remarkable disagreement with frequent experimental findings of growth occurring already at negligible supersaturation. The reason for such apparent discrepancy is found in the fact that growth occurs at *steps* on the surface, and surfaces without any steps are hardly realized. There are two major sources of persisting monoatomic surface steps: A vicinal orientation of the surface and screw dislocations.

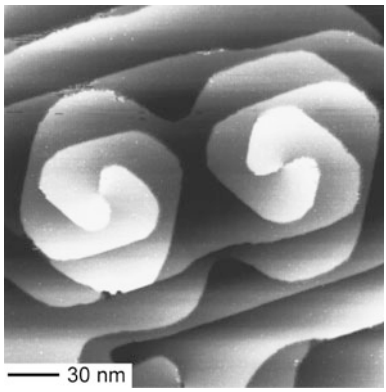


**Fig. 4.24** Screw dislocations on the Ga-face of a (0001) oriented GaN/sapphire layer with total Burgers vector $c[0001]$. The image size is $230 \times 230$ nm$^2$. Reproduced with permission from [22], © 1998 AVS

Wafer crystals cut with respect to a specific crystallographic orientation always have a slight misorientation. The result of such offcut is the formation of a vicinal surface composed of terraces and steps as illustrated in Fig. 4.14. For a typical offcut of $\Theta = 0.1$ degree the terrace width is $l = \tan^{-1}\Theta \times a \cong 2$ µm for an assumed typical thickness $a \cong 0.3$ nm of an epitaxial monolayer (for, e.g., zincblende material $a_{001} = \frac{1}{2}a_0$) and equally spaced steps. Such terrace width is usually well below the mean diffusion length of adatoms, allowing for atoms which arrived from the ambient at the surface to be attached at the terrace step. Consequently there is no need for nucleation to grow on a vicinal surface. The resulting growth proceeds by the advancement of more or less parallel steps and is referred to as *step-flow growth*. The effect is often designedly applied to facilitate layer growth in epitaxy. For this purpose wafers with a specified offcut in a desired direction to choose the terrace width and the kind of vicinal surface are used. Step-flow growth is discussed in more detail in terms of growth kinetics in Sect. 5.2.3.

A second source of steps persisting on a surface during growth is provided by screw dislocations (Sect. 2.3) [21]. It was found that the distance between two neighboring arms of the spiral is directly proportional to the size of a 2D nucleus which depends on the supersaturation. The slope of the growth spiral around the core of the screw dislocation is then direct proportional to the supersaturation. An example of screw dislocations in the metalorganic vapor-phase epitaxy of GaN/$Al_2O_3$ is given in Fig. 4.24 [22]. The scanning tunneling micrograph shows two adjacent screw dislocations with Burgers vectors $c[0001]$ pointing in the opposite direction to that of the screw dislocation on an N-face of GaN shown in Fig. 2.31b. Their counter-clockwise spirals combine, yielding a doubled Burgers vector.

We should note that even perfect crystal surfaces are generally not atomically flat and may intrinsically provide sites for a preferential attachment of atoms. Atomistic details are considered in Sect. 5.2.

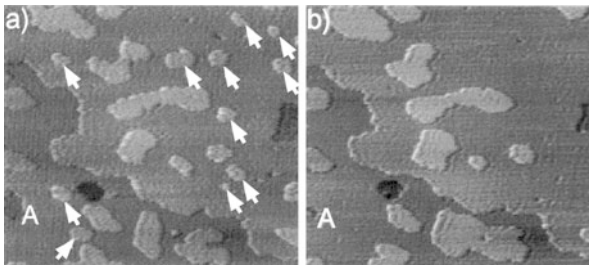


**Fig. 4.25** Ostwald ripening of 2D Si islands on Si(111). (**a**) Image scanned during growth at 520 °C, (**b**) image scanned after a 23 min interruption of the deposition at the same temperature. From [23]

### *4.2.8 Ripening Process After Growth Interruption*

The interruption of the growth process corresponds to a change of the chemical potential of the surface with respect to that of the ambient. Since growth occurs at a depart from thermal equilibrium, a sudden interruption of this process leaves the surface in a non-equilibrium state. An equilibration is therefore initiated comprising diffusion and evaporation–condensation processes. Changes of the surface morphology occurring during equilibration are often described by *Ostwald ripening*. The term denotes the evolution of an inhomogeneous structure (also in solid or liquid solutions) over time first described by Wilhelm Ostwald in 1896. Generally speaking, large particles (with a lower surface to volume ratio) grow in size, drawing material from smaller particles, which shrink. In the process, many small particles (or crystals, islands) formed initially slowly disappear, except for a few that grow larger, at the expense of the small particles. As a result, the broad size distribution of particles gradually gets more narrow as the mean particle size increases.

An example of Ostwald ripening initiated by an interruption of the homoepitaxial chemical vapor deposition of Si is shown in Fig. 4.25 [23]. All small islands with an unfavorable ratio of perimeter over area marked by an arrow in Fig. 4.25a dissolve. Their material feeds the larger islands remaining 23 min later, cf. Fig. 4.25b. In addition, holes in the main terrace tend to close (see, e.g., the hole near label A).

## 4.3 Problems Chap. 4

4.1 For solid silicon, the molar entropy is 18.8 J/(mol K) and the molar volume is 12.1 $cm^3$/mol at 1 bar and 298 K. Estimate the change in the chemical potential $\mu(P, T)$ for
   (a) a decrease in temperature by 5 K at $P = 1$ bar.
   (b) an increase in pressure by 5 bar at $T = 298$ K.

4.2 Differences in the bonding of InN compared to GaN or AlN lead to a large miscibility gap of solid solutions. We consider an unstrained $In_xGa_{1-x}N$ alloy described by a regular solution with an interaction parameter of 32 kJ/mol.
   (a) Calculate the molar Gibbs free energy of mixing for an indium composition $x = 0.2$ at 800 °C and 1200 °C.

(b) At which temperature is Gibbs free energy of mixing zero at the given composition?
(c) Determine the indium compositions for the locus of the spinodal at 800 °C.

4.3 Construct the cross section of a Wulff plot for GaAs in a {110} plane, using the surface energies given in Table 4.1. Consider only the listed facets, assuming for simplicity equal surface energies for $\{hkl\}$ faces of different polarity. Verify that the considered facets fulfill the condition $\gamma_{hkl} < \frac{h+k+l}{\sqrt{h^2+k^2+l^2}} \times \gamma_{011}$.

4.4 Consider a rectangular two-dimensional silicon island on a flat Si(001) surface, bound by two $S_A$ and two $S_B$ single-layer steps with step energies of 0.02 eV/$a$ and 0.1 eV/$a$, respectively, $a$ being the $1 \times 1$ surface lattice constant of 3.8 Å. Assume that the shape of the island reflects the ratio of the edge energies, and the length of an $S_\mathrm{b}$ side is 1.9 nm.
(a) Calculate the free step energy of the island boundary, neglecting the small contribution of the four edges. What would be the free step energy, if the island had the same area, but $S_B$ steps also had the step energy of $S_A$ steps?
(b) In a very simplified description the island of (a) is considered to have a circular shape of equal area bounded by a step with 0.02 eV/3.8 Å step energy. Calculate the number of atoms in the island, if the specific area of a layer is $3 \times 10^4$ m$^2$/mol. Determine the activation energy (in kJ/mol) for the formation of a stable two-dimensional nucleus, if the island exceeds the critical radius by a factor of 10.

4.5 The conditions for the epitaxy of (001)-oriented GaAs are set to a growth rate of 2 µm/h.
(a) Express the growth rate in units of monolayers per second.
(b) Estimate the approximate step velocity for layer-by-layer growth from multiple nuclei, if the nucleation rate is $1 \times 10^{13}$ m$^{-2} \times$ s$^{-1}$. What is the mean radius of the 2D islands just before coalescence?

## 4.4 General Reading Chap. 4

D.J.T. Hurle, *Handbook of Crystal Growth, vol. I, Fundamentals, Part 1. Thermodynamics and Kinetics* (North-Holland, Amsterdam 1993)
I.V. Markov, *Crystal Growth for Beginners* (World Scientific, Singapore, 2003)
A.A. Chernov (ed.), *Modern Crystallography, vol. III, Crystal Growth*. Springer Series Sol. State Sci., vol. 36 (Springer, Berlin, 1985)

## References

1. K.Th. Wilke, J. Bohm, *Kristallzüchtung* (Harry Deutsch, Thun/Frankfurt am Main, 1999) (in German)
2. M. Quillec, C. Daguet, J.L. Benchimol, H. Launois, $In_xGa_{1-x}As_yP_{1-y}$ alloy stabilization by the InP substrate inside an unstable region in liquid phase epitaxy. Appl. Phys. Lett. **40**, 325 (1982)

3. M.J. Jou, Y.T. Cherng, H.R. Jen, G.B. Stringfellow, Organometallic vapor phase epitaxial growth of a new semiconductor alloy: $GaP_{1-x}Sb_x$. Appl. Phys. Lett. **52**, 549 (1988)
4. W.A. Jesser, D. Kuhlmann-Wilsdorf, On the theory of interfacial energy and strain of epitaxial overgrowths in parallel alignment on single crystal substrates. Phys. Status Solidi **19**, 95 (1967)
5. D.M. Wood, A. Zunger, Epitaxial effects on coherent phase diagrams of alloys. Phys. Rev. B **40**, 4062 (1989)
6. S.Yu. Karpov, N.I. Podolskaya, I.A. Zhmakin, A.I. Zhmakin, Statistical model of ternary group-III nitrides. Phys. Rev. B **70**, 235203 (2004)
7. S.Yu. Karpov, Suppression of phase separation in InGaN due to elastic strain. MRS Internet J. Nitride Semicond. Res. **3**, 16 (1998)
8. W. Kossel, Zur Theorie des Kristallwachstums. Nachr. Akad. Wiss. Gött. Math.-Wiss. Kl., 135–143 (1927) (in German)
9. I.N. Stranski, Zur Theorie des Kristallwachstums. Z. Phys. Chem. **136**, 259 (1928) (in German)
10. R. Shuttleworth, The surface tension of solids. Proc. Phys. Soc. A **63**, 444 (1950)
11. I.V. Markov, *Crystal Growth for Beginners* (World Scientific, Singapore, 1995)
12. J.J. Métois, J.C. Heyraud, SEM studies of equilibrium forms: roughening transition and surface melting of indium and lead crystals. Ultramicroscopy **31**, 73 (1989)
13. A.A. Stekolnikov, J. Furthmüller, F. Bechstedt, Absolute surface energies of group-IV semiconductors: dependence on orientation and reconstruction. Phys. Rev. B **65**, 115318 (2002)
14. N. Moll, A. Kley, E. Pehlke, M. Scheffler, GaAs equilibrium crystal shape from first principles. Phys. Rev. B **54**, 8844 (1996)
15. N. Moll, M. Scheffler, E. Pehlke, Influence of stress on the equilibrium shape of strained quantum dots. Phys. Rev. B **58**, 4566 (1998)
16. Q.K.K. Liu, N. Moll, M. Scheffler, E. Pehlke, Equilibrium shapes and energies of coherent strained InP islands. Phys. Rev. B **60**, 17008 (1999)
17. B. Voigtländer, M. Kawamura, N. Paul, V. Cherepanov, Formation of Si/Ge nanostructures at surfaces by self-organization. J. Phys. Condens. Matter **16**, S1535 (2004)
18. M.A.K. Zilani, Y.Y. Sun, H. Xu, L. Liu, Y.P. Feng, X.-S. Wang, A.T.S. We, Reactive Co magic cluster formation on Si(111)-7 $\times$ 7. Phys. Rev. B **72**, 193402 (2005)
19. W.J. Ong, E.S. Tok, Configuration dependent critical nuclei in the self assembly of magic clusters. Phys. Chem. Chem. Phys. **9**, 991 (2007)
20. U. Köhler, L. Andersohn, B. Dahlheimer, Time-resolved observation of CVD-growth of silicon on Si(111) with STM. Appl. Phys. A **57**, 491 (1993)
21. W.K. Burton, N. Cabrera, F.C. Frank, The growth of crystals and the equilibrium structure of their surface. Philos. Trans. R. Soc. Lond. A **243**, 299 (1951)
22. A.R. Smith, V. Ramachandran, R.M. Feenstra, D.W. Grewe, M.-S. Shin, M. Skowronski, J. Neugebauer, J.E. Northrup, Wurtzite GaN surface structures studied by scanning tunneling microscopy and reflection high energy electron diffraction. J. Vac. Sci. Technol. A **16**, 1641 (1998)
23. U. Köhler, Kristallwachstum unter dem Rastertunnelmikroskop. Phys. Bl. **51**, 843 (1995) (in German)

# Chapter 5
# Atomistic Aspects of Epitaxial Layer-Growth

**Abstract** Crystal growth far from thermodynamic equilibrium is affected by kinetic barriers. This chapter describes nucleation and growth in terms of atomistic processes, which are characterized by such energy barriers. We consider the ideal and the real structure of a crystal surface, and discuss kinetic steps occurring during nucleation and growth. At the end of the chapter phenomena of self-organization employed for epitaxial growth of nanostructures are presented.

The description of growth treated in the previous chapter was based on macroscopic quantities: Thermodynamics describes collective motions of particles in terms of a macroscopic growth affinity. It accounts well for the direction a system tends to reach and describes conditions particularly near thermal equilibrium. Crystal growth is actually governed by a competition between kinetic and thermodynamic processes. Growth conditions in epitaxy are sometimes far from equilibrium and processes may largely be determined by kinetics. Particularly on a short time scale a kinetic description of growth on an atomic level may be more appropriate. The kinetics of epitaxial growth can usually be described by only a few categories of atomistic rate processes. Such processes strongly depend on the specific location of an atom on or near the surface. We therefore first consider the surface structure of a solid.

## 5.1 Surface Structure

The equilibrium conditions for surface atoms are different to those of bulk atoms due to the absence of neighboring atoms on one side. Therefore the atomistic structure of the surface does usually not coincide with that of the bulk. This is particularly true for semiconductors, which have pronounced directional bonds. By contrast metals have a chemical bond which is basically not directed, and in many cases the surface lattice corresponds to the bulk lattice. Starting with a simple model we will consider some examples of semiconductor-surface reconstructions to provide a basis for the description of growth on the atomic scale.

U.W. Pohl, *Epitaxy of Semiconductors*, Graduate Texts in Physics,
DOI 10.1007/978-3-642-32970-8_5, 

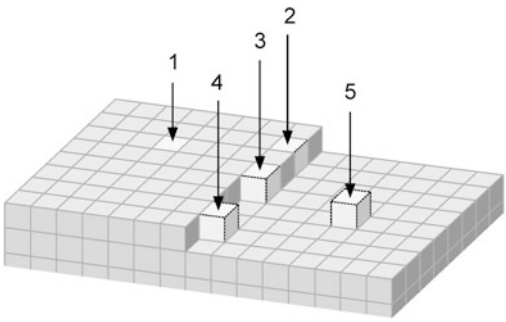


**Fig. 5.1** Important sites of an atom on a crystal surface. Numbers signify unsaturated nearest-neighbor bonds of atoms located at the marked sites: *1*—atom embedded in the uppermost surface layer, *2*—atom embedded into a step edge, *3*—atom at a kink site, *4*—atom attached to a step, *5*—atom adsorbed on the surface (adatom)

### *5.1.1 The Kink Site of a Kossel Crystal*

The Kossel crystal is a simple model which assumes the atoms as cubes (more generally the building blocks which may be atoms, ions, or molecules). In the most simple approach only nearest-neighbor interaction is assumed, i.e., only the bond at the face between adjacent cubes. Let us consider a surface with a monoatomic step as shown in Fig. 5.1. Atoms at different positions on the surface have different numbers of neighboring atoms. Consequently these atoms are differently bound to the surface. An atom embedded in the uppermost layer of a flat surface—at position 1 in Fig. 5.1—has 4 lateral bonds and 1 bond to the layer below, leaving just a single unsaturated bond. The atom embedded into the step (site 2) has only 3 lateral bonds and 1 vertical bond, leaving *two* bonds unsaturated. This atom is hence less tightly bound as that at site 1 and may more easily be detached from the surface.

A site of particular importance is position 3, the so-called *kink site*. We note that 3 bonds are unsaturated and 3 bond are attached to neighboring atoms of the solid. This means that exactly one half of the bonds is unsaturated. The three saturated bonds attach the atom to a half row of atoms (the row with the atom embedded at site 2), to a half crystal plane (the plane with the atom embedded at site 1), and to a half bulk crystal (the crystal underneath the atom), respectively. The kink position is therefore also referred to as half-crystal position. Crystal growth basically proceeds via the incorporation of atoms at this site. The work $\varphi_{\frac{1}{2}}$ required to detach an atom from a kink position is just half the work required to detach an atom located in the bulk.

We note that an attachment or detachment of an atom at a kink site leaves the number of unsaturated bonds at the surface unchanged: the initial configuration is reproduced. Since the number of unsaturated bond is associated with the surface energy no change occurs for an occupation of this site. This means that the work required to add or remove a kink atom is equal to the chemical potential of the crystal. This implies that the chemical potential of the atom at a kink site is equal to that of the crystal. Transferring an atom from the ambient to a kink site of the crystal surface (or vice versa) is therefore equal to the difference of the chemical potentials of the ambient and the crystal.

In thermodynamic equilibrium of a (large) crystal with an ambient the probabilities of attachment and detachment of a kink atom are equal. Sites which provide

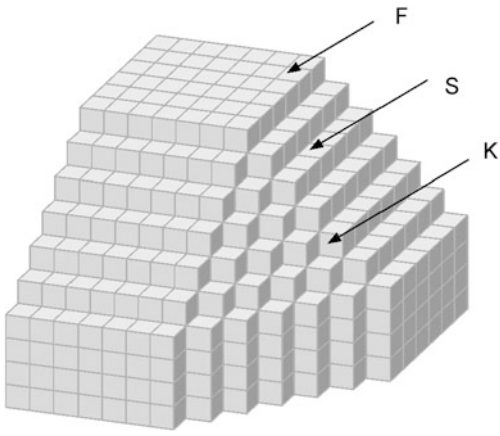


**Fig. 5.2** Kossel crystal with flat (*F*), stepped (*S*), and kinked (*K*) surfaces

more bonds (like, e.g., a hole in a surface at site 1 in Fig. 5.1) have a larger probability for attachment with respect to detachment. In equilibrium such sites are hence probably occupied. On the other hand sites with less bonds as a kink position like sites 4 and 5 have a smaller probability to be occupied in thermal equilibrium. As a consequence a crystal in thermal equilibrium with an ambient is bounded by flat faces: the equilibrium surfaces discussed in Sect. 4.2.4. It should be noted that perfect atomically flat surfaces do not exist at finite temperatures: The action of entropy always gives rise to some roughening.

### *5.1.2 Surfaces of a Kossel Crystal*

Crystal faces of different crystallographic orientation differ in their surface structure. We first consider the low-index faces of a Kossel crystal. A schematic of this model crystal with {100}, {110}, and {111} faces is given in Fig. 5.2.

The figure illustrates that the depicted low-index planes differ significantly with respect to their roughness on an atomic scale: {100} faces are perfectly flat and {111} faces are rough. Generally crystal surfaces can be classified into three groups, namely flat (F), stepped (S), and kinked (K). Low-index faces of all groups represent singular faces. The classification follows from a consideration of rows of atoms with a most dense arrangement. The direction of a dense packed row of atoms is referred to as nearest-neighbor periodic-bond-chain. Faces of any lattice which are parallel to at least *two* nearest-neighbor periodic-bond-chains are called F (flat) faces. Usually these faces have the highest surface density of atoms. In a Kossel crystal close-packed atoms are aligned along a ⟨100⟩ direction. F faces are therefore {100} faces. Each atom on such surface offers one unsaturated nearest-neighbor bond. Faces which comprise *one* nearest-neighbor periodic-bond-chain are called S (stepped) faces. S faces of a Kossel crystal with lowest indices are {110} faces like those depicted in Fig. 5.2. Each atom on such S face offers two unsaturated nearest-neighbor bonds. Faces which comprise *no* nearest-neighbor periodic-bond-chain are

**Table 5.1** Numbers of nearest neighbors $Z_i$ for an atom on a kink site for some lattices

| Lattice | $Z_1$ | $Z_2$ | $Z_3$ |
|---|---|---|---|
| Simple cubic | 3 | 6 | 4 |
| Diamond | 2 | 6 | 6 |
| Hexagonal close-packed | 6 | 3 | 1 |

called K (kinked) faces. K faces of a Kossel crystal with lowest indices are {111} faces. Each atom of a K face offers three unsaturated nearest-neighbor bonds.

In Sect. 4.2 we pointed out the importance of a step and, in particular, of a kink for growth of a crystal layer. Obviously, an F face does not offer such sites, and growth requires the formation of stable 2D nuclei. By contrast, the atomically rough K face offers a large number of kink sites. Growth on such face does not require the presence of 2D nuclei or structural defects. The growth rate is simply expected to increase with supersaturation, without any barrier to be surmounted. For a given supersaturation the growth rate of K faces will therefore be highest. The S face offers kink sites once an atom is attached. The density of kink sites is lower than on F faces, the growth rate will therefore be smaller. F faces will have the smallest growth rate due to the need of nucleation. According our discussion of the facets of a growing crystal illustrated in Fig. 4.18 we note that K faces are expected to disappear first, followed by S faces, leaving eventually the F faces. A growing Kossel crystal will thus eventually be bounded by {100} faces.

The model discussed so far may be extended by taking higher order interactions into account. If we include also second and third-nearest neighbor interactions, the detachment energy $\varphi_{\frac{1}{2}}$ from a kink position is given by the sum of the interaction energies $E_i$ and their respective coordination numbers $Z_i$,

$$\varphi_{\frac{1}{2}} = \frac{1}{2}(Z_1 E_1 + Z_2 E_2 + Z_3 E_3). \tag{5.1}$$

The coordination number is the number of $i$th nearest neighbors. A bulk atom in a cubic Kossel crystal has $Z_1 = 6$ nearest neighbors along $\langle 100 \rangle$, $Z_2 = 12$ second-nearest neighbors along $\langle 110 \rangle$, and 8 third-nearest neighbors along $\langle 111 \rangle$. At a kink site half of these neighbors exist, respectively. Our consideration of the half-crystal site and (5.1) may be applied to extend relation (4.31) between the bond energy (including higher order bonds) and the enthalpy of evaporation,

$$\Delta H_S \cong \varphi_{\frac{1}{2}}. \tag{5.2}$$

The considerations above basically also apply for other lattices. The numbers of neighboring atoms of $i$th order for an atom on a kink site of various lattices are listed in Table 5.1.

The directions of the periodic-bond-chains in the cubic diamond structure differ from those in the simple cubic structure: They are oriented along the six $\langle 110 \rangle$ directions and are thus not parallel to the next neighbor bonds. The related zincblende lattice has six periodic-bond-chains along $\langle 110 \rangle$ for each of the two ion types. F faces of the diamond and zincblende structures are {111} faces, while {100} faces and also

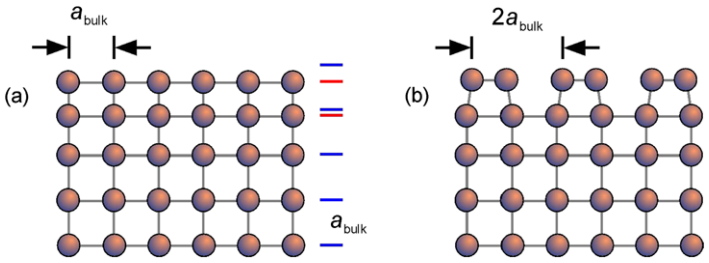


**Fig. 5.3** (**a**) Relaxation and (**b**) reconstruction of atoms at the surface of a crystalline solid. *Blue* and *red horizontal bars* at the side of schematic (**a**) mark vertical positions of the atomic net planes corresponding to the bulk and the relaxed surface, respectively

{110} faces are stepped. K faces are, e.g., {311} faces. Also the diamond structure and the hexagonal close-packed (hcp) structure are related: Both are derived from stacking net planes along a [0001] stacking axis (cf. Sect. 2.1). F faces of the hcp structure are hence the (0001) and $(000\bar{1})$ faces which correspond to the {111} faces of the diamond structure.

### *5.1.3 Relaxation and Reconstruction*

The atomic bonds in the uppermost layer of the surface of a solid differ significantly from those in the bulk due to the absence of neighboring atoms on one side. The altered equilibrium conditions for surface atoms lead to shifted atomic positions with respect to the bulk lattice. Two different effects in the rearrangement are to be distinguished: relaxation and reconstruction. *Relaxation* signifies a pure shift of atoms *normal* to the surface due to the missing attractive forces above the surface. Usually a compression occurs in the topmost few layers as illustrated in Fig. 5.3a. Relaxation leaves the lateral periodicity of the atom positions unchanged with respect to the bulk, i.e., the 2D surface unit cell corresponds to the unit cell of a truncated bulk crystal.

Usually surface atoms tend to restore some of the bonds broken to create the surface. Such rearrangement is accompanied by *lateral* shifts of atoms, i.e., a shift parallel to the surface. This kind of reordering is termed *reconstruction*. The 2D surface unit cell of a reconstructed surface does *not* correspond to the lateral part of the bulk 3D unit cell. In most cases the dimension of the surface unit cell differs from the bulk unit cell as depicted in Fig. 5.3b. Reconstruction includes also surface unit cells of unchanged lateral dimensions with a modified lateral order compared to the bulk.

The modified order of surface-near atoms is related to a change of the surface energy. Surface energy may be regarded as the energy difference between an ideal surface without any relaxation and reconstruction, and the actual surface. Vice versa, it is the energy required to rearrange all surface-near atoms of a relaxed and reconstructed surface to the order of the bulk lattice to form an ideal surface.

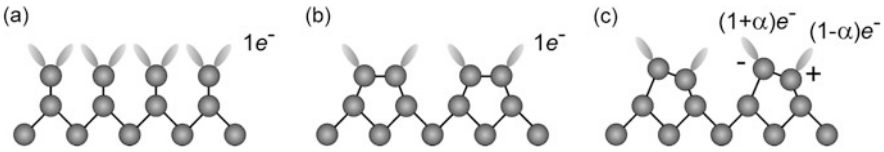


**Fig. 5.4** Schematic on the gradual formation of a surface reconstruction from an ideal surface (**a**) via dimerization with symmetric dimers (**b**) to relaxed, buckled dimers (**c**)

The ordering of atoms near the surface depends on the kind of bonds and is different for crystalline semiconductors and metals. Semiconductors usually have strongly directed covalent bonds, particularly those with a tetrahedral coordination. Atoms at the surface tend to saturate at least some of the unsaturated bonds to minimize the density of unfavorable dangling bonds. Semiconductors show a large variety of often quite complex reconstructions, some are illustrated below in Sect. 5.1.6. Metals, by contrast, have a delocalized electron gas yielding basically no directed bonds. As a consequence many metal surfaces do not reconstruct. It must be noted that the type of reconstruction does not only depend on the considered solid and (*hkl*) surface plane, but also to a large extent on preparation conditions.

A simple picture on the formation of a reconstructed surface is illustrated in Fig. 5.4. The figure assumes a tetrahedrally coordinated crystal bond by $sp^3$ hybrides. The ideal surface (Fig. 5.4a) may be considered to be created from a cut of the bulk crystal, leaving half-filled dangling bond orbitals at the surface. Each dangling bond is occupied by one electron. Such ideal surface is not stable, because a dangling bond represents an unfavorable energy state of the surface. The number of dangling bonds can be significantly reduced by the formation of surface dimers (Fig. 5.4b): Two unsaturated bond orbitals form one filled bridge-bond orbital parallel to the surface, respectively. The surface energy may be further minimized by a charge redistribution among the remaining dangling bonds. The formation of a more-than-half filled *s*-like and a less filled *p*-like dangling bond eventually leads to asymmetric dimers (Fig. 5.4c). The electron-charge transfer from the "down" atom to the "up" atom of the dimer changes the covalent bond of the symmetric dimer to a partially ionic bond [1]. Such relaxation of the dimer bond is referred to as *buckling*. The vertical shifts of the atoms are accompanied by lateral displacements towards one another.

### *5.1.4 Electron-Counting Model*

For tetrahedrally coordinated compound semiconductors such as GaAs a simple *electron counting model* has been developed to explain a wide variety of surface reconstructions [2]. This model accounts for the occupation of surface states and assumes no net surface charge for reordered surfaces with minimum energy. Bonding and nonbonding surface states *below* the Fermi energy must be filled, while the antibonding and nonbonding states *above* the Fermi energy must be empty. For the

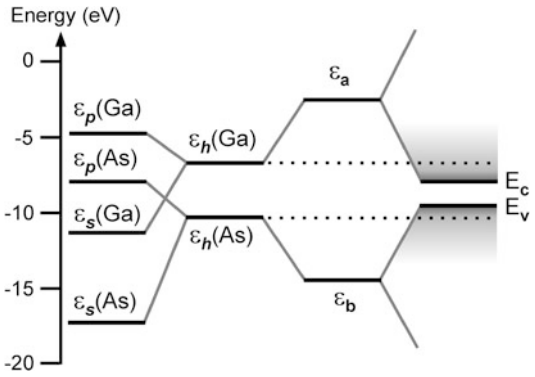


**Fig. 5.5** Energy levels $\varepsilon_h$ of $sp^3$ hybride dangling-bond orbitals of GaAs. The hybride energies are derived from the energies $\varepsilon_s$ and $\varepsilon_p$ of the atomic $s$ and $p$ orbitals of Ga and As, respectively. $E_c$ and $E_v$ denote conduction and valence bands of the GaAs bulk crystal. Data from [3]

given number of available electrons in the surface layer all dangling bonds on the electronegative element will then be full, and all those on the electropositive element of the compound semiconductor will be empty. This rule is generally applicable for any surface of a crystalline solid.

Formation and occupation of bond orbitals at the surface is illustrated for GaAs in Fig. 5.5 [3]. In the bulk crystal, bonds oriented towards their nearest neighbors are constructed from $sp^3$ hybrids with energies $\varepsilon_h = (3\varepsilon_s + \varepsilon_p)/4$ on each atom. The bond energy $\varepsilon_b$ within each bond results from the linear combination of the two hybrids $\varepsilon_h$ (Ga) and $\varepsilon_h$ (As) with lowest energy. Eventually the occupied valence band with maximum $E_v$ is formed from linear combinations of these orbitals. Correspondingly, the empty conduction band with minimum $E_c$ is built from antibonding linear combinations. At the surface, some hybrid orbitals cannot form bonds, and partially filled dangling bonds remain. Details depend on the considered surface. On (111) surfaces the surface atoms are bond to three atoms of the layer underneath, yielding three hybrid orbitals used for bonds and one dangling hybrid directed out of the material. For the electropositive Ga atom the energy of this hybrid lies near the conduction-band edge, leading to an empty state (Fig. 5.5). The hybrid of the electronegative As atoms on a $(\bar{1}\bar{1}\bar{1})$ surface (also denoted (111)B surface) lies below the valence-band edge and is consequently expected to be occupied. On the (001) surface *two* of the four $sp^3$ hybrids are used to form bonds to the crystal underneath. Linear combinations of the two remaining dangling-bond hybrids with lowest and highest energy yield a pure $p$ state and an $sp$ hybrid [3]. Both, Ga and As $p$ states lie above the conduction band according Fig. 5.5, leaving the $p$ dangling bond unoccupied. The $sp$-hybrid on As lies below the valence-band edge. In a relaxed state this applies also for the $sp$-hybrid on the Ga [3].

Any structure obeying the electron counting model exactly fills the electrons available in the surface layer into all dangling-bond states in the valence band, leaving all dangling-bond states in the conduction band empty. The surface will then be semiconducting, while partially filled dangling bonds may lead to a metallic surface. The electron counting rule also assures that no charge accumulates at the surface. The model can successfully explain principal reconstructions on many surfaces. It can, however, not decide among alternatives which fit the model. Moreover, also

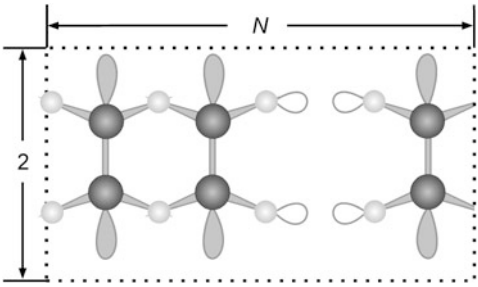


**Fig. 5.6** $(2 \times N)$ surface unit-cell with a missing dimer on a (001) face of a compound semiconductor with zincblende structure. Electronegative and electropositive elements are *dark* and *bright*, respectively. Bonds and dangling bonds are shaded if filled, empty bonds are open. After [2]

reconstructions may exist which are connected to a surface charge and do not obey the electron counting rule.

We illustrate the application of the electron counting model for the (As-rich) GaAs(001) surface [2]. Since numerous structures comply with the model, we need some reasonable assumption on the nature of the reconstruction as a starting point, obtained, e.g., from scanning tunneling micrographs. Such images show a surface unit cell in one specific direction being twice as long as the lateral part of the bulk unit cell, originating from the formation of surface dimers as depicted in Fig. 5.4. In the other lateral direction the surface unit-cell is a factor of $N$ longer than that of the bulk (Fig. 5.9). This periodicity arises from periodically missing dimers. The reconstruction is termed $(2 \times N)$ and leaves $D$ dimers in one unit cell with $D \leq N$, cf. Fig. 5.6.

The relation between $D$ and $N$ follows from a balance between the number of electrons required to fill the bonds and that of available electrons. Each As dimer bond requires 2 electrons, and another 2 for the filled dangling bond at each of the two As atoms of the dimer, yielding a total of 6 electron per dimer, or $6D$ electrons per unit cell. Furthermore, a total of $8D$ electrons per unit cell is required to bond all dimer As atoms to the Ga layer underneath. The dangling bonds on the electropositive Ga atoms in the second layer are empty. On the other hand, the number of available electrons results from the number of valence electrons $V_n$ of the electronegative element and $V_p$ of the electropositive element. The number of electrons in one unit cell available from the topmost three layers are therefore:

$2V_nD$ from the topmost layer comprising the As dimers, and
$\frac{1}{2}2V_pN$ from the second layer comprising Ga atoms, with the factor $\frac{1}{2}$ because half of the total electrons are involved in bonding to the bulk crystal underneath.

To balance the numbers of required and available electrons in a $(2 \times N)$ surface-unit cell, we thus yield the condition

$$6D + 8D = 2V_nD + V_pN. \tag{5.3}$$

In the case of the studied GaAs surface $V_n = 5$ and $V_p = 3$ applies. Inserting these numbers we eventually obtain

$$4D = 3N \quad \text{(for GaAs)}.$$

**Table 5.2** The 4 crystal systems and the 5 Bravais lattices in two-dimensional space. **a** and **b** are lattice vectors spanning the unit cell, $\alpha$ is the angle between the vectors

| System | Unit cell | Bravais lattices | Symmetry axes |
|---|---|---|---|
| Cubic | $\mathbf{a} = \mathbf{b}, \alpha = 90°$ | cubic | 1 fourfold axes of rotation or inversion parallel to $\mathbf{a} \times \mathbf{b}$ |
| Rectangular | $\mathbf{a} \neq \mathbf{b}, \alpha = 90°$ | primitive rectangular, centered rectangular | 1 twofold axes of rotation or inversion parallel to $\mathbf{a} \times \mathbf{b}$ |
| Hexagonal | $\mathbf{a} = \mathbf{b}, \alpha = 120°$ | hexagonal | 1 sixfold axes of rotation or inversion parallel to $\mathbf{a} \times \mathbf{b}$ |
| Oblique | $\mathbf{a} \neq \mathbf{b}, \alpha \neq 90°$ | oblique | 1 axes of inversion parallel to $\mathbf{a} \times \mathbf{b}$ |

The smallest periodicity fulfilling this condition and $D \leq N$ is $N = 4$ and $D = 3$. This yields a $(2 \times 4)$ reconstruction of 3 dimers and one missing dimer in a unit cell (Fig. 5.6). If we consider a (Se-rich) (001) surface of zincblende ZnSe we have $V_n = 6$ and $V_p = 2$. The energies of the hybrid orbitals of the electropositive Zn and that of the electronegative Se lie in the conduction and valence bands of the solid, respectively, similar to the GaAs case [3]. The electron counting model (5.3) yields in this case $N = D$. We therefore expect a $(2 \times 1)$ reconstruction with no missing dimers as a favorable candidate. The Zn-rich ZnSe(001) surface actually forms a $c(2 \times 2)$ reconstruction. Such reconstruction with Zn dimers is also consistent with the model, since a $c(2 \times 2)$ periodicity is formed from a complete layer of Zn dimers if each dimer row is displaced by one spacing in the $2\times$ direction with respect to the previous dimer row [2].

The surface reconstruction of a semiconductor may significantly be modified in the presence of metal adsorbates. Metals then act as an electron reservoir which donates or accepts the right number of electrons, when the surface assumes a specific reconstruction to fulfill the electron-counting model. The model was therefore more recently extended to account also for metal-induced reconstructions [4].

A couple of prominent surface reconstructions assumed by GaAs and Si surfaces are discussed in Sect. 5.1.6. Prior to that we point out the notation used to designate surface unit cells of reconstructions.

### *5.1.5 Denotation of Surface Reconstructions*

The surface of a solid represents a three-dimensional structure. The symmetry properties may though be described by two-dimensional operations. We therefore consider a two-dimensional lattice, which constitutes a 2D translational periodicity, and a basis representing the atomic structure of the recurring surface unit-cell. There are only 5 Bravais lattices in two dimensions, which constitute 4 crystal systems of differently shaped surface-unit cells. Table 5.2 gives the symmetry properties of the 5 two-dimensional Bravais lattices.

The 2D lattice describing the surface periodicity is related to the 3D lattice of the bulk crystal underneath. The relation is illustrated in Fig. 5.7.

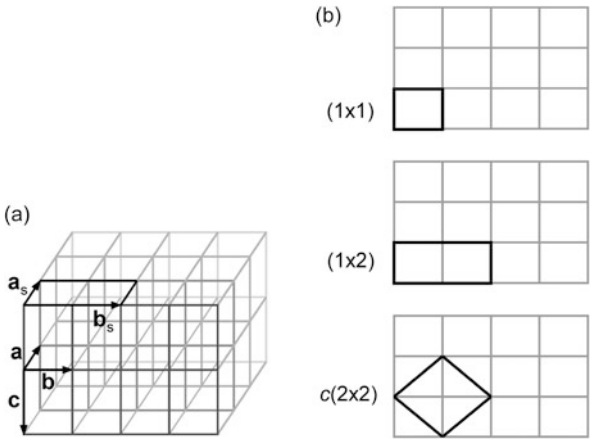


**Fig. 5.7** (**a**) Unit cells of surface and bulk lattices, defined by their corresponding vectors. (**b**) Some unit cells of the surface lattice (*black*) on the bulk lattice (*gray*)

**Table 5.3** Relation between matrix representation and corresponding shorthand terms for some surface lattices

| **M** | Shorthand term |
|---|---|
| $\left(\begin{smallmatrix}1&0\\0&1\end{smallmatrix}\right)$ | $(1 \times 1)$ |
| $\left(\begin{smallmatrix}1&0\\0&2\end{smallmatrix}\right)$ | $(1 \times 2)$ |
| $\left(\begin{smallmatrix}2&0\\0&2\end{smallmatrix}\right)$ | $(2 \times 2)$ |
| $\left(\begin{smallmatrix}1&1\\-1&1\end{smallmatrix}\right)$ | $c(2 \times 2)$ or $(\sqrt{2} \times \sqrt{2})R45°$ |

The surface lattice vectors $\mathbf{a}_s$, $\mathbf{b}_s$ may be expressed in terms of the two vectors $\mathbf{a}$, $\mathbf{b}$ which span the surface unit cell of a truncated bulk lattice,

$$\begin{pmatrix}\mathbf{a}_s\\ \mathbf{b}_s\end{pmatrix} = \mathbf{M}\begin{pmatrix}\mathbf{a}\\ \mathbf{b}\end{pmatrix} = \begin{pmatrix}m_{11} & m_{12}\\ m_{21} & m_{22}\end{pmatrix}\begin{pmatrix}\mathbf{a}\\ \mathbf{b}\end{pmatrix}. \tag{5.4}$$

The $(2 \times 2)$ matrix $\mathbf{M}$ provides an unambiguous relation between the surface and the bulk lattices. Usually the vectors $\mathbf{a}_s$ and $\mathbf{b}_s$ are multiples of the vectors $\mathbf{a}$, $\mathbf{b}$ (by convention $a_s < b_s$ if $a_s \neq b_s$). This leads to more convenient shorthand terms (Wood's notation), which comprise these multipliers and, if necessary, an angle by which the surface lattice is rotated with respect to the bulk lattice [5]. Let us consider, e.g., the $\{hkl\}$ surface of a solid $X$ with a surface lattice, which fulfills $\mathbf{a}_s = 2\mathbf{a}$, $\mathbf{b}_s = \mathbf{b}$. Such structure may be formed by surface dimers as depicted in Fig. 5.4. The corresponding surface is then described by the shorthand term $X\{hkl\}$ $(2 \times 1)$. Primitive and centered cells are indicated by adding $p$ or $c$, respectively, and a rotated cell is denoted by adding $R$ and the angle of rotation in units of degrees. Usually the $p$ for a primitive cell is suppressed. The relation between the matrix representation and corresponding shorthand terms is given in Table 5.3. It should be noted that the simplified notation is not always unambiguous. A centered cubic unit cell $c(2 \times 2)$ may as well be described by the unit cell $(\sqrt{2} \times \sqrt{2})R45°$.

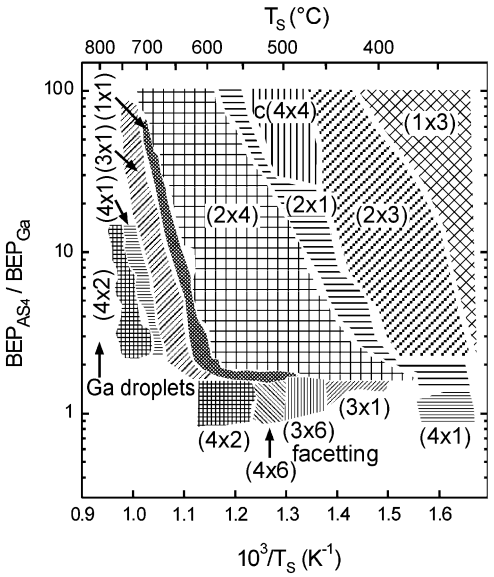


**Fig. 5.8** Existence range of surface reconstructions forming during the MBE of GaAs for various temperatures $T_S$ and beam equivalent pressure (BEP) ratios of the $As_4$ and Ga fluxes. Reproduced with permission from [6], © 1990 Elsevier

### *5.1.6 Reconstructions of the GaAs(001) Surface*

The electron counting rule pointed out in Sect. 5.1.4 selects favored structures for a specific surface. The actual reconstruction is further determined by experiments and calculations. Different reconstructions with different surface stoichiometries become thermodynamically stable, when the chemical potential of the ambient is varied. Moreover, different reconstructions may coexist on a given surface due to varied surface preparations and kinetic barriers for a reordering of surface atoms.

As an example we consider the technologically important (001) surface of GaAs already treated above for illustrating the electron-counting rule. Experimentally, many surface reconstructions were found depending on ambient conditions. Figure 5.8 shows experimental results for a growing GaAs(001) surface composed as a phase diagram [6]. Here, a vicinal surface tilted by 2° toward the $(1\bar{1}1)$ As plane was used to facilitate growth. This tilt leads to As-terminated steps. The structure was analyzed by reflection high-energy electron diffraction (RHEED) during molecular-beam epitaxy at a fixed Ga flux corresponding to a growth rate of 0.7 monolayer/sec GaAs. In the experiment the chemical potential was varied by the supplied flux of $As_4$ molecules, expressed in the diagram in terms of the beam equivalent pressure (BEP) ratio with respect to that of the Ga flux. In addition the temperature was varied as an independent basic growth parameter. We note that the conditions do not correspond to equilibrium.

The diagram Fig. 5.8 shows 14 different reconstructions which may be distinguished as As-rich surfaces ($(2 \times 4)$ or $(2 \times 1)$), as a transition range ($(3 \times 1)$ or $(1 \times 1)$), as Ga-rich surfaces ($(4 \times 1)$, $(4 \times 2)$, $(4 \times 6)$, or $(3 \times 6)$), as absorption structures of the type $c(4 \times 4)$, $(2 \times 3)$, $(1 \times 3)$, and surfaces where degradation occurs [6]. The transitions between all regions were found to be reversible and could

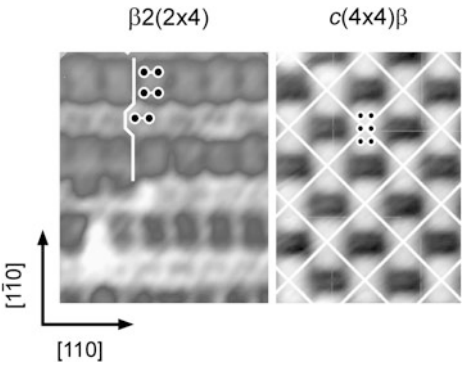


**Fig. 5.9** Filled-state STM image of (**a**) the $\beta 2(2 \times 4)$ and (**b**) the $c(4 \times 4)\beta$ reconstructions of the GaAs(001) surface. In (**a**) two As-As top dimers and an As-As trench dimer are marked. In (**b**) three As-As top dimers and the $c(4 \times 4)$ lattice mesh are marked. Reproduced with permission from [7] and [8], © 1999 and 2004 APS, respectively

be described by an Arrhenius law. Within a transition range often a coexistence of adjoining patterns was observed.

The periodicity of the surface unit cell is usually readily accessible in MBE from electron diffraction experiments. The arrangement of atoms within the unit cell often poses, however, a tricky problem. A variety of methods such as scanning tunneling microscopy, low-energy electron diffraction, and angle-resolved photoelectron spectroscopy has to be applied to obtain an unequivocal structural model. Two prominent reconstructions of the GaAs(001) surface imaged using high-resolution STM are shown in Fig. 5.9. Though many details can be identified on such images, the arrangement of the atoms at the surface may hardly be extracted.

Calculations of surface energies for various orientations and reconstructions help substantially to find and to understand the actual atomic structure of the surface unit cell. The stable equilibrium surface-reconstruction is that with the lowest surface free energy $\gamma A$. The surface of a compound semiconductor like GaAs may be nonstoichiometric with respect to the number of atoms of different species, and the surface free energy depends on the chemical potential $\mu_i$ for each species $i$. The surface may exchange atoms with the ambient which acts as a reservoir, and $\mu_i$ is the free energy per particle of species $i$ in the reservoir. In the experiment $\mu_i$ can be varied within the limits given by the bulk chemical potentials of the condensed phases of the species, $\mu_i < \mu_{i(\text{bulk})}$, because otherwise the elemental phase of species $i$ will form on the surface. In the case of GaAs this will be bulk As and bulk Ga. Furthermore, in equilibrium the sum of the chemical potentials of the species Ga and As must be equal the bulk energy per GaAs pair [9],

$$\mu_{\text{Ga}} + \mu_{\text{As}} = \mu_{\text{GaAs(bulk)}} = \mu_{\text{Ga(bulk)}} + \mu_{\text{As(bulk)}} + \Delta H_{\text{f}}^{\text{GaAs}},$$

$\Delta H_{\text{f}}^{\text{GaAs}}$ being the heat of formation of the GaAs bulk crystal. Using this relation the surface energy may be expressed as a function of the As chemical potential $\mu_{\text{As}}$. If $\mu_{\text{As}}$ is varied, different surface stoichiometries and related reconstructions get most stable. A large variety of atomic configurations exists for surface unit cells of each of the reconstruction periodicities shown in Fig. 5.8. Surface structures with low surface energies within some range of $\mu_{\text{As}}$ are given in Fig. 5.10. These structures all fulfill the electron counting rule (Sect. 5.1.4) and are semiconducting (filled anion and empty cation dangling bonds).

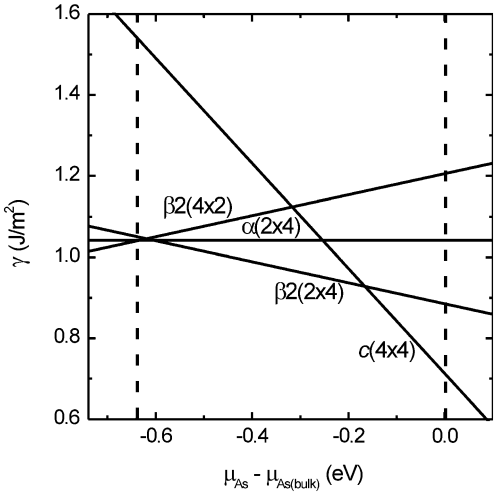


**Fig. 5.10** Surface energy of different low-energy GaAs(001) reconstructions, depending on the chemical potential of the arsenic. *Dashed lines* mark limits of the chemical potential difference $\mu_{\mathrm{As}} - \mu_{\mathrm{As(bulk)}}$. Data from [9]

The surface energies shown in Fig. 5.10 are calculated from the total energy $E_{\mathrm{tot}}$ according [9]

$$\gamma A = E_{\mathrm{tot}} - \mu_{\mathrm{GaAs}} N_{\mathrm{Ga}} - \mu_{\mathrm{As}}(N_{\mathrm{As}} - N_{\mathrm{Ga}}).$$

The stoichiometry of the surface $N_{\mathrm{As}} - N_{\mathrm{Ga}}$ determines the slope in a linear dependence on the chemical potential $\mu_{\mathrm{As}}$. The reconstructions noted in Fig. 5.10 are those with a low surface energy within the indicated allowed limits of $\mu_{\mathrm{As}}$. Particular phases of GaAs(001) reconstructions with given periodicity of the unit cell are indicated using a leading label like, e.g., $\alpha$ or $\beta 2$ [10, 11]. Starting from the Ga-rich $\beta 2(4 \times 2)$ reconstruction we note a progressive trend to a negative slope in the sequence towards the most As-rich $c(4 \times 4)$ surface for high $\mu_{\mathrm{As}} - \mu_{\mathrm{As(bulk)}}$ values. The $\alpha(2 \times 4)$ surface is stoichiometric, i.e., $N_{\mathrm{As}} = N_{\mathrm{Ga}}$, and does not depend on the chemical potential of As. The low-energy As-rich $\beta 2(2 \times 4)$ and $c(4 \times 4)$ surfaces are those generally used in the molecular-beam epitaxy and the metalorganic vapor-phase epitaxy of (001)-oriented GaAs, respectively.

The atomic structure of the four most favorable reconstructions indicated above are shown in Fig. 5.11. Both, Ga-Ga and As-As dimer bonds occur in the topmost layer of the displayed unit cells. They both have filled bonding and empty antibonding states.

The Ga-rich $\beta 2(4 \times 2)$ structure consists of two Ga-Ga dimers per unit cell oriented along [110] in the top layer and two missing As atoms in the second layer. An electron counting within the unit cell [12] yields a surface stoichiometry of $N_{\mathrm{As}} - N_{\mathrm{Ga}} = -\frac{1}{4}$ per $(1 \times 1)$ unit cell.

The stoichiometric $\alpha(2 \times 4)$ surface consists of two As-As top-layer dimers oriented along $[\bar{1}10]$, adsorbed on a complete Ga monolayer underneath. Two As-As dimers are missing in the row of top-layer dimers, and two Ga-Ga bonds are formed within the Ga monolayer where one As-As dimer is missing. It should be noted that another stoichiometric structure with a single As-As top-layer dimer termed $\alpha 2(2 \times 4)$ was found with an even lower energy than that depicted here [11].

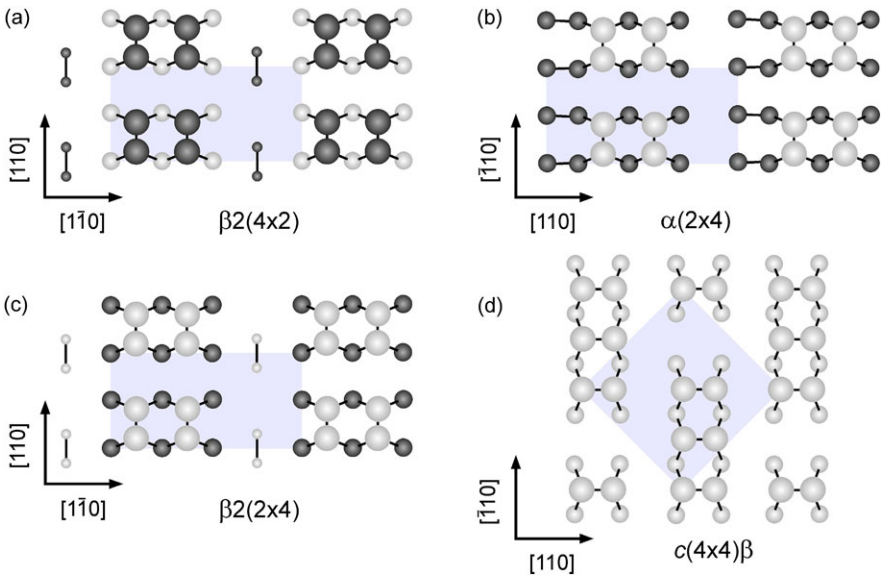


**Fig. 5.11** Models of the four GaAs(001) surface reconstructions considered in Fig. 5.10. The size of the atoms indicates the vertical position, *bright* and *dark atoms* represent As and Ga, respectively. *Shaded areas* indicate the surface unit-cells

The more As-rich $\beta 2(2 \times 4)$ structure is obtained from the $\alpha(2 \times 4)$ structure by removing two Ga atoms in the missing As-As dimer region, resulting in a stoichiometry of $N_{\mathrm{As}} - N_{\mathrm{Ga}} = \frac{1}{4}$ per $(1 \times 1)$ unit cell. The structure represents the counterpart of $\beta 2(4 \times 2)$, with Ga atoms exchanged for As atoms and vice versa.

The most As-rich $c(4 \times 4)\beta$ surface represents a double-layer structure consisting of As-As dimers oriented along the [110] direction and adsorbed on a full As monolayer, yielding a stoichiometry of $N_{\mathrm{As}} - N_{\mathrm{Ga}} = \frac{5}{4}$ per $(1 \times 1)$ unit cell. The commonly accepted model comprises a block of three dimers in a row along $[\bar{1}10]$, being interrupted by a dimer vacancy. As-Ga heterodimers are assumed to appear in the $c(4 \times 4)$ reconstruction as the chemical potential $\mu_{\mathrm{As}} - \mu_{\mathrm{As(bulk)}}$ is lowered towards less As-rich conditions and the $\beta 2(4 \times 2)$ structure is approached [13]. The $c(4 \times 4)$ reconstruction with three As-Ga top-layer dimers is referred to as $c(4 \times 4)\alpha$.

The reconstructions of the GaAs(001) surface considered above as some typical examples give an impression about the wealth of surface structures. More detailed information on surface reconstructions is found in, e.g., Refs. [14, 15].

### *5.1.7 The Silicon (111)(7 × 7) Reconstruction*

Silicon is the most important semiconductor for device technology. Chips for integrated circuits are fabricated from (001)-oriented Si wafers. Atoms in the uppermost layer of the unreconstructed {100} surface of the diamond structure have two

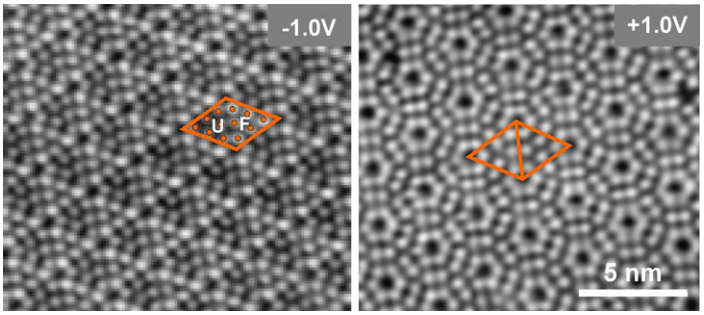


**Fig. 5.12** Scanning tunneling images of the Si(111)(7 × 7) surface for negative (*left*, *filled states*) and positive (*right*, *empty states*) sample bias. The *orange rhombs* mark a unit cell comprising 12 protruding adatoms, *U* and *F* denote unfaulted and faulted half-unit cell, respectively. Courtesy of M. Dähne, TU Berlin

dangling bonds each. The surface energy is lowered by formation of asymmetric buckled dimers as illustrated in Fig. 5.4c, leading to a Si(001)(2 × 1) reconstruction. Usually Si(001) wafers are chemically treated using a dilute HF-etch to remove surface defects. During such procedure dangling bonds are saturated by hydrogen. The H-terminated surface relaxes but does not reconstruct.

Some applications such as electric high-power applications employ the (111) surface of silicon. (111) is the primary cleavage plane of Si. When Si is cleaved in vacuum along this plane with a wedge kept parallel to the $\langle 11\bar{2}\rangle$ direction, a Si(111)(2 × 1) reconstruction is created. This reconstruction differs from that of the (100) surface by forming long pi-bonded chains in the first and second surface layers. Annealing above 300 °C converts the structure irreversibly into a (7 × 7) reconstruction, which represents an equilibrium phase. Much effort was spent over more than two decades to unravel the complex structure of this surface.

The Si(111)(7 × 7) surface unit-cell is 49 times larger than the unit cell of the ideal surface. An unreconstructed cell of this size would have 98 dangling bonds. The formation of the actual (7 × 7) structure comprises an extensive rearrangement of atoms and the addition of adatoms on top. Scanning tunneling micrographs show a pattern of 12 protruding adatoms in a unit cell and vacancies at the deep corner holes, see Fig. 5.12. Each adatom saturates three dangling bonds from the layer underneath and leaves one dangling bond. STM images recorded with a suitable bias show that the rhombic unit cell is composed of two triangular subunits.

The structure of the Si(111)(7 × 7) surface was eventually explained by the generally accepted DAS model derived from a detailed analysis of transmission electron diffraction [16]. The name DAS refers to the basic structural elements: 15 dimers (D), 12 adatoms (A), 1 stacking fault (S). The model has also been confirmed by computation, yielding an energy gain of 60 meV per (1 × 1) unit cell with respect to the (2 × 1) reconstruction [17]. A top view of the unit cell according the DAS model is given in Fig. 5.13. The uppermost atoms are indicated by largest size, and we recognize the 12 adatoms visible in the STM image Fig. 5.12. We also note the corner holes in the top layer. The model shows an apparent difference in the left and

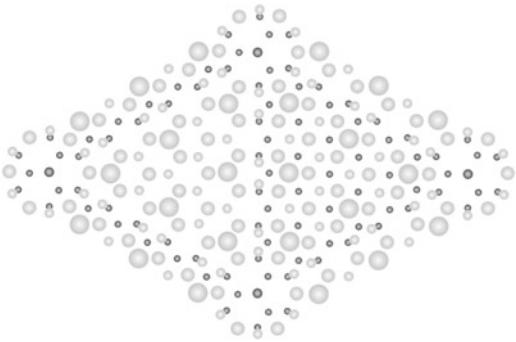

**Fig. 5.13** Structure of the Si(111)(7 × 7) surface unit-cell according to the dimer-adatom-stacking fault model. Atoms in layers of decreasing height are represented by decreasing size, *dark atoms* represent unreconstructed atoms of the uppermost bulk layer underneath the surface layers

right triangles of the unit cell. In the right half we see the uppermost atoms of the bulk crystal underneath the surface layers drawn with a dark shading. This yields an $ABC$ stacking order with respect to the first two surface layers, thereby continuing the cubic diamond structure of bulk Si. The uppermost bulk atoms are not visible in the left triangle, because they are hidden by the surface layers due to an $ABAB$ stacking order. The left part of the unit cell has consequently a hexagonal order, i.e., the sequence is faulted with respect to the structure of bulk Si. The faulted and non-faulted triangular subunits are each surrounded by 3 vacancies at the corners and 9 dimers, three of them located at the separating domain boundary, which is oriented along the vertical short diagonal in Fig. 5.13.

The DAS model leaves only 19 unsaturated dangling bonds per unit cell: 12 for the adatoms, 6 from three-fold coordinated rest atoms lying in the layer below the adatoms, and 1 from the atom below the vacancy at the corner. A number of similar DAS reconstructions in a $(2n + 1) \times (2n + 1)$ pattern have also been observed in non-equilibrium conditions, including $5 \times 5$ and $9 \times 9$ reconstructions [18]. The preference for the $(7 \times 7)$ reconstruction is attributed to an optimal balance of charge transfer and stress.

## 5.2 Kinetic Process Steps in Layer Growth

The non-equilibrium process of growth is governed by a competition between kinetics and thermodynamics. As the size of heterostructures approaches the nanometer-scale regime, atomic-level control is becoming crucial. Kinetic growth processes may to a large extend be described by the terrace-step-kink model already used in Sect. 4.2.4 to characterize surface energies. We will first employ this simplified model to consider growth kinetics, and include the effect of the actually more complex surface structure as described above in a second step.

### *5.2.1 Kinetics in the Terrace-Step-Kink Model*

The *terrace-step-kink* (TSK) *model* of a surface [19] (also termed *terrace-ledge-kink* (TLK) *model*) is based on the idea that the energy of an atom's position on

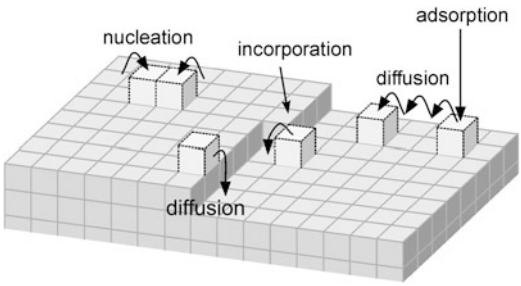


**Fig. 5.14** Schematic of atomistic rate processes in epitaxial growth. The step-down diffusion differs from the indicated lateral diffusion

a crystal surface is determined by its bonding to neighboring atoms. Processes on an atomistic scale hence involve the counting of broken and formed bonds. In the framework of the TSK model the kinetics of growth is described by rates of transition steps, which atoms undergo on the surface. The complex process of epitaxy is largely determined by only a few categories of such processes. Some processes of particular importance are illustrated for the surface of a Kossel crystal in Fig. 5.14.

Growth proceeds by a number of consecutive steps as indicated in Fig. 5.14. Atoms arrive from the ambient and are adsorbed on the surface. They may then diffuse over the surface until they cease to diffuse by one of several processes. Such processes are re-evaporation (or re-solution in case of a liquid ambient), nucleation of (2D or 3D) islands, attachment to existing islands or to defects like a step on the surface. In the framework of the considered model the adatom diffusion on the surface is described by rates of hopping from one site to an adjacent site. The vibrational motion of an adatom on the surface is regarded as an attempt at such a hop. Since many attempts are required to produce a single hop, a factor is introduced representing the probability per attempt to hop, yielding an effective hopping rate $k(T)$. The rate may also be expressed in terms of a mean residence time $\tau(T) = k^{-1}(T)$. Each thermally activated kinetic process of epitaxy is governed by characteristic parameters entering an Arrhenius dependence with an activation energy $E$,

$$\tau^{-1}(T) = \nu_0 e^{-\frac{E}{k_B T}}. \tag{5.5}$$

$E$ is the barrier which has to be surmounted in the process. The prefactor $\nu_0$ represents an attempt-rate constant for the given process.

Rate equations referring to a few basic processes are used in numeric Monte Carlo simulations to model the dynamics of growth and the evolution of the growth surface. Only the rate-limiting steps are included in the calculations. Faster processes are accounted for in average by using *effective* kinetic parameters. Parameters to control the supersaturation $\Delta\mu$ are usually the experimental variables $T$, the arrival rate of atoms $R$, and the material parameters of the kinetic processes describing diffusion, re-evaporation, and nucleation. The approach does not require a detailed knowledge of the atomic interactions and permits simulations including large time scales. Values for $\nu_0$ and $E$ (of the order of $10^{12}$ s$^{-1}$ and eV, respectively) for each process are estimated from, e.g., molecular dynamics, or they are taken as parameters to fit experimental results.

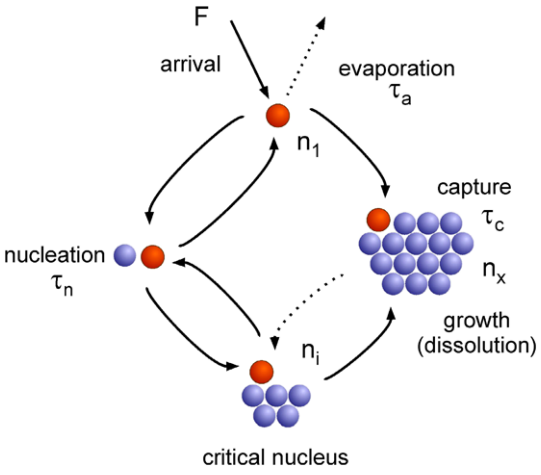


**Fig. 5.15** Processes considered for the kinetic description of growth

### 5.2.2 *Atomistic Processes in Nucleation and Growth*

The atomistic processes indicated in Fig. 5.14 are now described in more detail to account for nucleation and growth analogous to the thermodynamic approach discussed in Sect. 4.2. In our simplified approach [20] we neglect surface reconstructions, interdiffusion, and chemical reactions between substrate and deposit material. The assumed processes are indicated in Fig. 5.15.

Atoms arriving from the ambient on the surface at an externally controlled flux $F$ (atoms per unit area and per unit time) diffuse on the surface. They either meet other atoms to nucleate, or they are captured at a growing island (also denoted cluster) after a mean time $\tau_c$, or they re-evaporate after a mean adsorption residence time $\tau_a$. A nucleus will either loose adatoms after a mean time $\tau_n$, or grows to a critical size comprising $i$ atoms. The critical nucleus also may dissolve or grow to a stable island comprising $x > i$ atoms. Such islands will capture further adatoms but—under growth conditions—hardly loose atoms.

We trace an atom which arrives at the surface. At a high temperature the adatom will only stay on the surface for a short residence time $\tau_a$. This time is determined by the adsorption energy $E_a$ and may be written

$$\tau_a^{-1} = \nu_{a0} \exp\bigl(-E_a/(k_B T)\bigr), \tag{5.6}$$

$\nu_{a0}$ being an atomic surface vibration-frequency. For some materials relation (5.6) is complemented by a factor, which accounts for a dependence of the residence time on the material coverage on the substrate. During $\tau_a$ the adatom migrates in a random walk process consisting of a series of jumps to respective adjacent substrate sites. The mean-square displacement of the adatom during a period of duration $t$ depends on the hopping rate (or, mean hopping frequency) $\nu_d$ and is given by

$$\langle \lambda^2 \rangle = \nu_d a^2 t, \tag{5.7}$$

$a$ being the mean jump distance. Usually $a$ is the distance of two neighboring lattice sites on the surface. The number of hops during the considered period is $\nu_d t$.

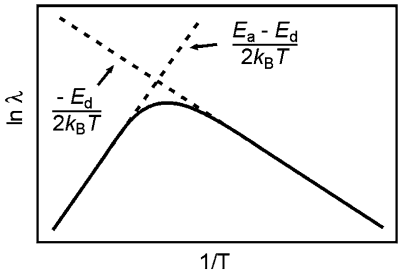


**Fig. 5.16** Temperature dependence of the surface diffusion length λ

Hopping to a neighboring site requires surmounting a potential barrier, cf. Fig. 5.23. This diffusion barrier $E_d$ is surmounted more easily at increased temperature due to an Arrhenius dependence of the hopping rate,

$$\nu_d = \nu_{d0} \exp\bigl(-E_d/(k_B T)\bigr). \tag{5.8}$$

The ratio of the mean-square displacement (5.7) to the duration of the period is the time-independent diffusion coefficient (or diffusivity) $D$,

$$D = \frac{\langle \lambda^2 \rangle}{\eta t} = \frac{\nu_d a^2}{\eta}, \tag{5.9}$$

where $\eta$ is the number of neighboring sites reachable by a single jump: For one-dimensional diffusion $\eta = 2$, while for 2D surface diffusion $\eta = 4$ on a square lattice and 6 on a hexagonal lattice. Using Einstein's relation of the diffusion length, $\lambda = \sqrt{D\tau}$, and (5.9), the displacement (root-mean-square value) from the arrival site to the site of eventual evaporation or incorporation reads

$$\lambda = \sqrt{D\tau} = \lambda_0 \exp\bigl((E_a - E_d)/(2k_B T)\bigr), \tag{5.10}$$

$\tau$ being the mean time of surface diffusion (basically $\tau_a$ at high $T$, $\tau_c$ at lower $T$). The pre-exponential factor $\lambda_0$ is a merged *effective* elementary jump distance, e.g., for $\tau = \tau_a$ given by $\lambda_0 = \sqrt{\nu_d 0/\nu_{a0}} \times a/\sqrt{\eta}$. Values of $\nu_{d0}$ are typically somewhat less than those of the corresponding parameter for adsorption $\nu_{a0}$, but of the same order. The barrier to be surmounted for desorption, $E_a$, is however usually much larger than the diffusion barrier $E_d$, and also several times exceeding thermal energies $k_B T$ at typical growth temperatures. The adatom will therefore migrate over a quite long distance $\lambda \gg a$ before evaporation. For small values of $1/T$ (in the high temperature range) the surface diffusion length λ increases exponentially with $1/T$ (or, decreases with $T$) as indicated by (5.10) and the straight line in the Arrhenius plot Fig. 5.16. The residence time in this desorption regime is short, and adatoms are likely to evaporate before being incorporated. At large values $1/T$ (low $T$) the slope in the Arrhenius dependence of $\lambda(T)$ changes sign. The residence time is large (5.6), at low $T$ adatoms are incorporated after diffusion and the competition by desorption gets negligible. Best epitaxial growth is often achieved for large diffusion length. This is obtained just below the onset of significant re-evaporation.

During surface diffusion the adatom encounters other atoms on the surface. The probability of such meeting depends on the areal density $n_1$ of single migrating

atoms, and the areal density of clusters containing more than one atom. In our approach we assume the clusters to be stationary, i.e., single adatoms are the only species which are mobile.

The clusters on the surface are divided according their size into subcritical clusters with atom numbers $j \leq i$, and stable clusters, $j > i$, the density of which is summed as

$$n_x = \sum_{j=i+1}^{\infty} n_j .$$

After an initial nucleation of stable clusters the subcritical clusters nucleate and dissolve in an approximate detailed balance. They are therefore not considered further in the evolution due to the local equilibrium condition $dn_j/dt = 0$ for $2 \leq j \leq i$. In the following we focus on the density of single atoms $n_1$ and that of stable clusters $n_x$.

The density $n_1$ of the mobile single atoms follows from a balance of processes described by an appropriate rate equation. As we read from Fig. 5.15, atoms arriving on the surface at a rate $F$ increase $n_1$, while nucleation ($\tau_n$), capture ($\tau_c$), and evaporation ($\tau_a$) decrease $n_1$. Furthermore, when larger stable islands cover a significant fraction $Z$ of the surface, arrival on top of an island is possible, thereby decreasing the part of atoms on the uncovered surface. The evolution of the single-atom density $n_1$ is therefore described by

$$dn_1/dt = +F(1-Z) - n_1/\tau_n - n_1/\tau_c - n_1/\tau_a = F(1-Z) - n_1/\tau, \qquad (5.11)$$

with $\tau^{-1} = \tau_n^{-1} + \tau_c^{-1} + \tau_a^{-1}$. The sum may be extended when additional loss processes for diffusing adatoms are to be taken into account. On the other hand, also less processes may be considered.

In the limit of *high temperature* the residence time $\tau_a$ gets very short, and nucleation and capture processes become negligible. Since also $Z = 0$ in this case, we obtain $dn_1/dt = F - n_1/\tau_a$. This yields for long times $t \gg \tau_a$ a stationary state ($dn_1/dt = 0$) with the solution

$$n_1 = F\tau_a .$$

The constant density in the high temperature limit reflects the balance of arrival and evaporation without nucleation or growth.

*Below* the high temperature limit loss of adatoms by attachment to growing stable islands is relevant. Once stable islands exist, the term $-n_1/\tau_c$ in (5.11) is generally much larger than the term $-n_1/\tau_n$. Neglecting the nucleation term $-n_1/\tau_n$ for $t \gg \tau_a$ the solution gets

$$n_1 = F(1-Z)(1/\tau_a - 1/\tau_c)^{-1} .$$

The mean time $\tau_c$ of the adatom capture at a stable island depends on their density $n_x$ and the diffusional flow,

$$\tau_c^{-1} = \sigma_x D n_x . \qquad (5.12)$$

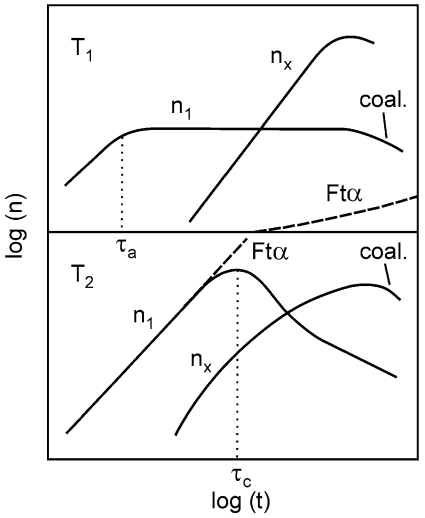


**Fig. 5.17** Density of single atoms $n_1$, stable clusters $n_x$, and the total number $Ft\alpha$ of atoms condensed on the surface as a function of time $t$ for a high temperature $T_1$ and a low temperature $T_2$. $\tau_a$ and $\tau_c$ indicate re-evaporation and capture times, respectively, the label *coal.* marks a decrease of $n_1$ and $n_x$ due to coalescence. After [20]

The capture numbers $\sigma_k$ of the stable clusters summed to a mean number $\sigma_x$ express the local decrease of $n_1(\mathbf{r}, t)$ near a $k$-sized cluster due to capture [21]. They are typically of order 5–10 and may regarded for a first appreciation as slowly varying quantities.

The density $n_x$ of stable clusters increases by a nucleation rate $J$ involving capture at critical clusters with $i$ atoms. The creation of new stable clusters is proportional to the density $n_i$ of the critical clusters with their capture number $\sigma_i$, and the density of single adatoms $n_1$ and their diffusivity $D$, yielding $J = \sigma_i D n_1 n_i$. On the other hand, as growth of a layer proceeds the density will reduce due to an impingement of stable clusters on each other. Such coalescence is accounted for by including a negative term proportional to the temporal change of coverage $Z$, leading to the rate equation [20]

$$dn_x/dt = +\sigma_i D n_1 n_i - 2n_x dZ/dt. \tag{5.13}$$

To solve the coupled equations (5.11) and (5.13) a relation between $Z$ and $n_x$ is needed. If the clusters grow two-dimensionally, we may put [20]

$$dZ/dt = \Omega^{2/3}\big((i+1)n_1/\tau_i + n_1/\tau_c + FZ\big), \tag{5.14}$$

where $\Omega$ is the atomic volume of the deposit and the stable-cluster nucleation rate $\tau_i^{-1} = \sigma_i D n_i$. The solution of the rate equations leads to the cluster densities schematically shown in Fig. 5.17.

Growth on a flat surface starts at coverage $Z = 0$. At a *high temperature* $T_1$ we note an initial rise of the single-atom density $n_1 \sim Ft$ lasting for $t < \tau_a$, followed by a constant value described by the high-temperature limit. The density of stable clusters $n_x$ starts at a negligible value at $t = \tau_a$, and increases for $t > \tau_a$ as given by the first term in (5.13), i.e., before coalescence. Both, $n_1$ and $n_x$ decrease as coalescence sets in. The condensation coefficient $\alpha(t)$, which denotes the fraction

**Table 5.4** Parameters $p$ and $E$ of (5.15) for the maximum density $n_x$ of stable two-dimensional clusters in various regimes of condensation. $i$ is the number of atoms in the critical cluster. From [20]

| Condensation regime | $p$ | $E$ |
|---|---|---|
| Extreme incomplete | $i$ | $E_i + (i+1)E_\mathrm{a} - E_\mathrm{d}$ |
| Initially incomplete | $i/2$ | $\frac{1}{2}(E_i + iE_\mathrm{a})$ |
| Complete | $i/(i+2)$ | $(E_i + iE_\mathrm{d})/(i+2)$ |

of atomic dose impinging on the surface and being incorporated into the deposit, is initially very small in this high temperature, and so also the total deposit $Ft\alpha$.

At a *low temperature* $T_2$ no re-evaporation occurs, i.e., $\alpha = 1$. In this temperature range the single-atom density $n_1$ plotted in Fig. 5.17 increases linearly until capture by previously nucleated clusters sets in, causing $n_1$ to pass a maximum at the mean capture time $\tau_\mathrm{c}$ and to decrease subsequently. The stable-cluster density $n_x$ increases after a nucleation period and eventually decreases due to coalescence.

The maximum density of stable clusters has the general form

$$n_x \sim (F/\nu)^p \exp\bigl(-E/(k_\mathrm{B}T)\bigr), \tag{5.15}$$

where the materials parameters $p$ and $E$ lead to different regimes of condensation [20]. Values for the regimes of extreme incomplete condensation, initially incomplete in an intermediate range, and complete condensation are given in Table 5.4. The three regimes refer to the conditions $\sigma_x D\tau_\mathrm{a} n_x \ll Z$, $Z < \sigma_x D\tau_\mathrm{a} n_x < 1$, and $\sigma_x D\tau_\mathrm{a} n_x \gg 1$, respectively, and define the meaning of a *high* and a *low* temperature for growth of the considered material.

We note from Table 5.4 that the condensation regimes are essentially determined by the relation between the materials parameters $E_i$, which signifies the energy difference between $i$ atoms in the adsorbed state and in stable clusters, the adsorption energy $E_\mathrm{a}$, and the critical cluster size $i$. At *extreme incomplete* condensation growth is slow due to strong re-evaporation and proceeds essentially by direct impingement. In the intermediate, *initially incomplete* regime stable clusters grow by diffusive capture in the initial state. Direct impingement becomes relevant at large coverage $Z$, leading to more complete condensation. This regime will often occur in practice. At *complete* condensation growth is fast, since re-evaporation is negligible.

### *5.2.3 Adatoms on a Terraced Surface*

Growth of a flat surface proceeds basically by the attachment of adatoms at steps. The steps may originate either from 2D nucleation as discussed above, or from screw dislocations, or from the terrace structure of a vicinal surface inclined with respect to a singular face by a small tilt angle. The rate of layer growth $r$, which represents

the velocity of a parallel displacement of the singular faces, is hence determined by the advancement of steps.

To obtain an expression for the velocity of step advance we consider growth conditions with an only minor contribution of nucleation. Such conditions may be found in step flow growth of a vicinal surface (Sects. 4.2.7, 5.2.4). This surface consists of terraces of width $l$ which are separated by steps of height $a$ (Fig. 4.14). Let us assume for simplicity that the steps are equidistant and straight. If the steps remain straight all the time, we obtain a one-dimensional problem. The steps are assumed perfect sinks for diffusing adatoms arriving from either side and have monoatomic height. Furthermore, the terrace width $l$ is assumed smaller than the mean displacement $\lambda$ of an adatom after arrival on the surface. If now a constant flux $F$ deposits a low density of adatoms $n$ on the surface (in the previous Sect. 5.2.2 labeled $n_1$), the adatoms will diffuse with some finite probability to an adjacent step where they are incorporated, and we may neglect nucleation on the terrace. For the given conditions the concentration of adatoms on the surface $n(x,t)$ is described by

$$\dot{n}(x,t) = Dn''(x,t) - \frac{1}{\tau_a} n(x,t) + F, \tag{5.16}$$

where $x$ is the lateral direction perpendicular to the steps, dot and double primes designate temporal derivative $\partial/\partial t$, and spatial derivative $\partial^2/\partial x^2$, respectively, $D$ is the surface diffusion constant (5.9), and $1/\tau_a$ denotes the evaporation probability (5.6). The change of the adatom density $n$ expressed by (5.16) is composed of the three terms surface diffusion, loss by evaporation, and deposition by the external flux $F$.

To solve (5.16) we need boundary conditions, which are to be fulfilled by $n(x,t)$. We consider steady state conditions, where $F$ is constant and $n$ does not change in time, i.e., $\dot{n}(x,t) = 0$. Steps are considered as perfect sinks. A fast incorporation of adatom at steps is fulfilled by the condition that $n$ equals a constant concentration $n_{eq}$ at a step to be reached at thermal equilibrium. Choosing the origin of $x$ at the center of a terrace, the condition reads

$$n(\pm l/2) = n_{eq}. \tag{5.17}$$

The steady-state solution of (5.16) is then given by

$$n(x) = \frac{\cosh(\kappa x)}{\cosh(\kappa l/2)} (n_{eq} - F\tau_a) + F\tau_a. \tag{5.18}$$

In (5.18) $\kappa$ is the inverse of the mean displacement, $\kappa = 1/\lambda = 1/\sqrt{D\tau_a}$. If the residence time $\tau_a$ is long, re-evaporation described by the second term in (5.16) becomes negligible. $\kappa$ is then small. If also $\kappa l/2$ is small, solution (5.18) can be approximated by a Taylor expansion, yielding

$$n(x) \cong n_{eq} + \left(F\tau_a\kappa^2/8\right)\left(l^2 - 4x^2\right) = n_{eq} + (F/8D)\left(l^2 - 4x^2\right) \quad (\kappa l/2 \text{ small}). \tag{5.19}$$

The steady-state solution (5.19) for negligible re-evaporation is shown in Fig. 5.18 (black curve). It is a parabola with a maximum centered in the middle of a terrace at $x = 0$ with values $n(\pm l/2) = n_{eq}$.

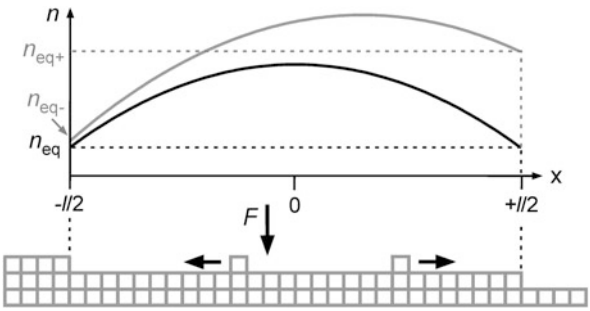


**Fig. 5.18** Density profile $n(x)$ of adatoms on a terraced surface under steady-state conditions provided by a constant flux $F$ and steps acting as sinks (*black curve*). *Gray curve*: $n(x)$ resulting from an uneven capture probability of up-steps and down-steps

The assumptions made to obtain the simple geometry expressed by (5.16) and the approximate solution (5.19) are quite extensive and may in practice often not be fulfilled. The requirement of a perfect sink may, e.g., be fulfilled by the left step in Fig. 5.18 but less well by the right step, because the latter requires a less probable down-step diffusion for incorporation. An unequal capture probability can be expressed by *two* equilibrium adatom-concentrations at the steps $n_{eq+}$ and $n_{eq-}$, leading to a similar solution as (5.19) with a parabola maximum being displaced from $x = 0$ by $\Delta x_{max} = D/(Fl)(n_{eq+} - n_{eq-})$. The respective profile $n(x)$ is drawn in Fig. 5.18 in gray; values for $n_{eq+}$ and $n_{eq-}$ are assumed larger than $n_{eq}$.

The mean adatom density $n$ in steady state conditions is obtained from (5.19) by integration over $n(x)$, yielding

$$n = \frac{1}{l}\int_{-l/2}^{+l/2} n(x)\,dx = n_{eq} + Fl^2/(12D). \tag{5.20}$$

In case of unequal capture probability at the steps $n_{eq} = (n_{eq+} + n_{eq-})/2$ in the right-hand side of (5.20).

### 5.2.4 Growth by Step Advance

We may treat the capture of adatoms at steps similar to the capture at stable clusters of density $n_x$. If we assume the steps acting as strong sinks, i.e., $n_{eq} = 0$, such treatment is accomplished by adding a term $-n_1/\tau_s$ to the right side of (5.11). $\tau_s$ is the mean time of adatom capture at a step. The mean single-adatom density $n_1$ given by (5.20) then corresponds to $F\tau_s$. Capture at steps now compete with capture at stable clusters and nucleation. Capture at a cluster occurs for an adatom arrival within a root-mean-square distance $\lambda_c = (D\tau_c)^{1/2}$. Near a step (ideal sink) nucleation is depressed. This zone on either side of a step is called *denuded zone*. Its width is given by $\lambda_c$. This consideration allows to express a condition for the transition from nucleation and 2D island growth at lower temperatures to step flow growth at higher temperatures. For dominating capture at clusters, $n_1$ is expressed by $F\tau_c$ with $\tau_c$ given by (5.12). Step flow becomes more dominant than nucleation on a terrace if

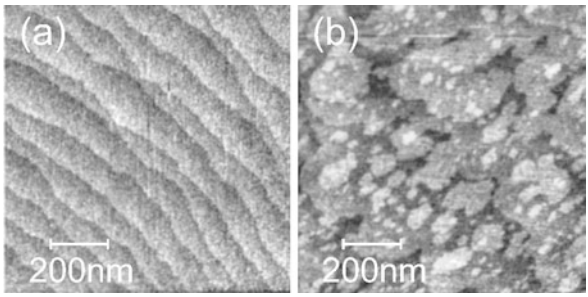


**Fig. 5.19** Atomic-force micrographs of 0.5 μm thick GaAs layers grown at (**a**) 570 °C, and (**b**) 530 °C

$\tau_s < \tau_c$. Inserting $n_1$ from (5.20) and (5.12), respectively, we see that this condition is met if

$$l^2/(12D) < (\sigma_x D n_x)^{-1}. \tag{5.21}$$

This inequality may be expressed in terms of the denuded-zone width $\lambda_c$ with $\tau_c$ from (5.12), yielding

$$\frac{l^2}{12}\frac{\sigma_x n_x}{1} = \frac{l^2}{\lambda_c^2}\frac{1}{12} < 1. \tag{5.22}$$

According (5.22) the transition from nucleation to step flow occurs if the width of the denuded zone $\lambda_c$ (which increases as the temperature increases) becomes larger than a fraction of about one third of the terrace length $l$.

The surface morphology of homoepitaxial GaAs layers grown at different temperatures is shown in Fig. 5.19. The sample grown in step-flow mode at a high temperature exhibits terraces with steps of atomic height, originating from an off-orientation of the substrate with respect to the [001] growth direction. The morphology of the sample grown at decreased temperature shown in Fig. 5.19b exhibits 2D island growth on terraces. The terrace edges are irregular, the large terrace width indicates a small off-orientation of the substrate. Note that no islands nucleate close to a step.

A simulation of the molecular-beam epitaxy of GaAs on GaAs(001) in the step-flow growth mode for appropriate growth conditions is given in Fig. 5.20. The growing (001) surface of the GaAs zincblende structure is polar: surfaces with terminations of Ga cations and As anions alternate periodically. For a slow $As_2$ incorporation rate assumed in the simulation, the As coverage (even numbered gray curves) lags behind the directly preceding Ga layer coverage (odd numbered black curves) until the near completion of a layer [22]. We note that the S-shaped curves of subsequent (bi)layers overlap: Nucleation of the next layer starts before the layer underneath is completed. Of the first monolayer's worth of Ga material delivered (at $\tau_{ML} \cong 0.9/\text{sec}$) about 95 % goes into the first Ga layer and 5 % into the next for the considered growth conditions. At fast $As_2$ incorporation, coverages of As layers *lead* the coverage of the preceeding Ga layers [22].

The advancement of a step results from the capture of adatoms from the upper and lower terrace. Let us consider the velocity of lateral advance $r_{step}$ of the step

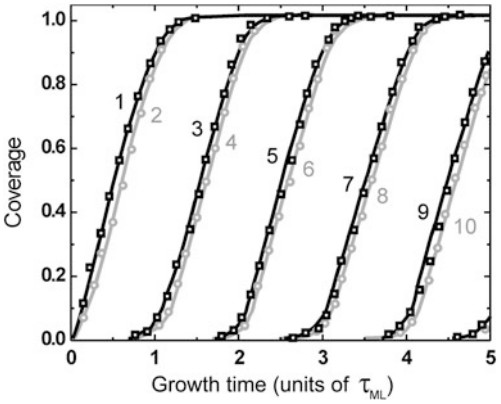


**Fig. 5.20** Simulated coverage in the molecular-beam epitaxy of GaAs/GaAs(001) for slow $As_2$ incorporation. *Odd* and *even numbered curves* refer to Ga and As layers, respectively. Reproduced with permission from [22], © 1986 APS

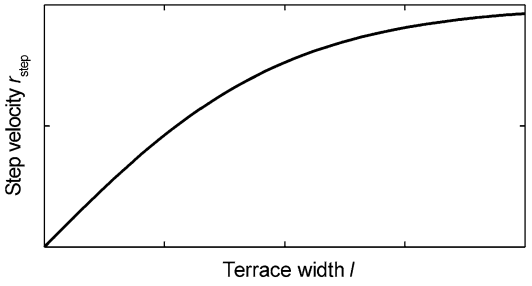


**Fig. 5.21** Steady-state velocity of lateral step advance $r_{step}$ depending on the terrace width $l$ for equidistant and straight steps

at the position $x = -l/2$. We again assume steady state conditions, i.e., adatoms diffuse much faster than steps move. Furthermore, we again consider terraces of equal width and an equal probability for capture from either terrace. The current density $j$ of adatoms arriving at the step follows from the gradient of the adatom density $n(x)$ at the step position $x = -l/2$,

$$j(-l/2) = -D\frac{d}{dx}n(-l/2). \tag{5.23}$$

Inserting the symmetric adatom density $n(x)$ from (5.18) we obtain

$$j(-l/2) = D\kappa(F\tau_a - n_{eq})\tanh(-\kappa l/2). \tag{5.24}$$

The step velocity $r_{step}$ results from the (equal) contributions from the upper and the lower terrace separated by the step,

$$r_{step} = a^2\big(j_{upper}(-l/2) + j_{lower}(-l/2)\big) = 2a^2 j(-l/2), \tag{5.25}$$

$a^2$ being a unit area of the terrace. The velocity $r_{step}$ depends on the terrace width, because larger terraces collect more adatoms from the ambient, cf. Fig. 5.21. For small $\kappa l/2$ (long residence time $\tau_a$) (5.24) simplifies to

$$j(-l/2) = D(F\tau_a - n_{eq})\kappa^2 l/2. \tag{5.26}$$

The linear relation $j \propto l$ is reflected in the constant slope of $r_{step}$ for small terrace width $l$ in Fig. 5.21.

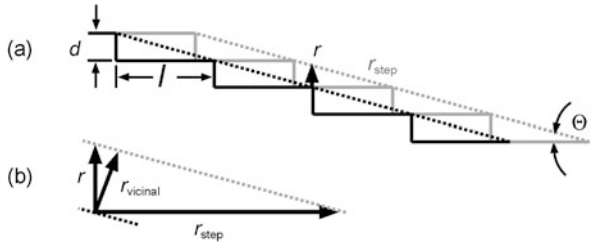


**Fig. 5.22** (**a**) Relation between the lateral growth rate $r_{step}$ of steps on a vicinal surface and the growth rate $r$ of the related singular layer. *Black* and *gray lines* represent cross sections of the surface at two times, the *dotted lines* indicate the vicinal surface. (**b**) Magnified scheme showing the relation between the growth rates of steps, singular surface and vicinal surface

We now consider the growth rate $r$ of a flat crystal surface. Growth proceeds essentially by the attachment of adatoms at steps. The steps may either originate from 2D nucleation, or screw dislocations, or from the terrace structure of a vicinal surface inclined with respect to a singular face by a small tilt angle $\Theta$ (Fig. 4.14). The advancement of steps therefore determines the rate of layer growth $r$, which represents the velocity of a parallel displacement of the singular faces. The relation between the lateral advancement of steps and growth rate $r$ is illustrated for a vicinal surface in Fig. 5.22. The figure depicts a cross section of the terraced surface at a time $t_1$ (black lines) and a later time $t_2$ (gray lines). During $t_2 - t_1$ the steps are laterally displaced via adatom attachment by some amount $s$, yielding the velocity $r_{step} = s/(t_2 - t_1)$.

The growth rate $r$ of the singular layer (i.e., the mean vertical displacement of the horizontal terraces in Fig. 5.22a) follows from $r_{step}$ via the tilt angle $\Theta$ of the vicinal layer. For steps of height $d$ and terraces of width $l$ the tilt angle is given by $\tan\Theta = d/l$. Since also $\tan\Theta = r/r_{step}$, we obtain

$$r = r_{step}\tan\Theta = (d/l)r_{step}. \tag{5.27}$$

The growth rate $r_{vicinal}$ of the vicinal layer (i.e., the velocity of a parallel displacement of the layer indicated by dotted lines in Fig. 5.22) may be read from the enlarged scheme Fig. 5.22b. Since $\Theta$ is also the angle between $r$ and $r_{vicinal}$, the relation is given by

$$r_{vicinal} = r\cos\Theta = r_{step}\sin\Theta. \tag{5.28}$$

### *5.2.5 The Ehrlich-Schwoebel Barrier*

Diffusion of an adatom on a flat or terraced surface is of particular importance in the kinetics of growth. Surface diffusion by a random walk process on a *flat* surface was described by (5.10). Until now we assumed that steps or stable 2D clusters capture adatoms from their top and from their bottom with the same probability. In fact, diffusion across a flat surface generally differs from diffusion across a

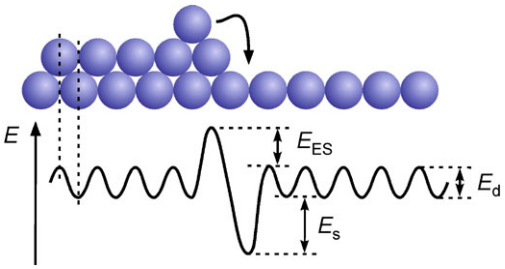


**Fig. 5.23** Cross section of a monoatomic surface step and schematic of the potential associated with the diffusion of an adatom across the surface. Energies $E_d$, $E_s$, and $E_{ES}$ refer to the activation of surface diffusion, binding to a step, and the Ehrlich-Schwoebel barrier, respectively

step, as first pointed out by G. Ehrlich [24], R.L. Schwoebel [25], and co-workers. Adatom capture from the upper and lower terrace at a step hence also differ. Such unequal capture probability causes the asymmetry in the adatom density discussed in Sect. 5.2.3. We consider the diffusion barrier provided by a step and consequences for two-dimensional growth.

An intuitive picture of the so-called Ehrlich-Schwoebel barrier of diffusion across a step is given in Fig. 5.23. As an adatom moving on the upper terrace approaches the step it has to overcome a pronounced maximum of the potential to step down. The reason is a fewer number of nearest neighbors in the transitions state of the hop over the ledge compared to that in flat-surface diffusion. We note from Fig. 5.23 that the Ehrlich-Schwoebel barrier $E_{ES}$ is actually the *difference* in the activation energy for hopping across the step and hopping across a flat surface. Once the adatom has surmounted the barrier $E_{ES}$ it enters a position at the step edge with an increased binding energy $E_s$. The increase originates from the larger number of nearest neighbors at the lower edge of the step.

Step down of an adatom may also occur by another process with a potentially lower barrier: The adatom located at the position on top drawn in Fig. 5.23 pushes the edge atom underneath away to the right and takes its place. This *exchange process* may provide an efficient parallel channel to the step-down process discussed above. Both processes have always higher barriers than diffusion on a flat surface. In the following we focus on the usual Ehrlich-Schwoebel barrier depicted in Fig. 5.23.

We note from Fig. 5.23 a distinct difference for step-down and step-up diffusion. In the first case the adatom approaches a *descending* step and experiences a repulsive step-edge barrier of height $E_{ES}$, which tends to reflect the adatom. By contrast, an adatom approaching an *ascending* step (i.e., migrating from the right to left towards the step in Fig. 5.23) experiences a trapping potential $E_s$ accompanied by a subsequent barrier $E_{ES}$. Such potential landscape tends to capture the adatom at the step.

Incorporation of diffusing adatoms into the crystal was mentioned in Sect. 5.1.1 to occur preferentially at kink positions. To fulfill such requirement an adatom caught at a step by the binding potential illustrated in Fig. 5.23 needs to diffuse along the step until meeting a kink position. We consider this one-dimensional dif-

fusion analogous to the surface diffusion on a terrace. Let us assume a single adatom diffusing along a step towards a kink formed by an additional row of atoms (i.e., a kink with *positive* sign, cf. Fig. 5.1). To *pass* the kink site and continue diffusion along the step the adatom has to hop around the kink. Obviously the kink provides a barrier in addition to the activation barrier for the one-dimensional diffusion along a straight step, and also in addition to the Ehrlich-Schwoebel barrier discussed above. Qualitatively, the potential looks like that for two-dimensional diffusion *across* the step depicted in Fig. 5.23. Due to this analogy the barrier is termed the *Kink Ehrlich-Schwoebel barrier*, and the constraint of the 1D diffusion by this barrier is referred to as the *Kink Ehrlich-Schwoebel effect*.

The barriers for diffusion *across* a step and *along* a step both affect the morphology of the surface. The first effect may particularly affect the distribution of steps, while the latter may control the structure of a step. Both effects are addressed in the following.

### 5.2.6 *Effect of the Ehrlich-Schwoebel Barrier on Surface Steps*

In the discussion on growth by step advance Sect. 5.2.4 we assumed a terraced surface with equidistant and straight steps. Qualitative arguments show that both conditions may be oversimplified. It has in fact been observed in experiments as well as in computer simulations that the step-flow mode is only metastable. Let us consider step-flow growth of an ideal vicinal surface with equidistant steps, and *absence* of an Ehrlich-Schwoebel barrier (Fig. 5.24a). Adatoms from an upper and a lower terrace will then be captured at a step with equal probability, and due to a constant width of all terraces all steps advance with the same velocity $r_{\text{step}}$. We recall from (5.25) and (5.26) that the velocity is proportional to the widths of upper and lower terrace, $r_{\text{step}} \propto (l_{\text{upper}} + l_{\text{lower}})$. If now one step lags behind its regular position for any reason (e.g., some fluctuation) the area of the lower terrace in front increases and that of the upper terrace behind decreases, see Fig. 5.24b. The lower, wider terrace in front of the step will collect more adatoms, and distributes one half of this surplus to the considered step and the other half to the step ahead. The upper, smaller terrace accordingly collects less adatoms. The lack is equal to the surplus at the lower terrace. Less adatoms are hence supplied from the upper terrace to the considered step and also to that behind. As a consequence, the decreased velocity of the considered step remains unchanged. In addition, the velocity of the step ahead is slightly accelerated, and the velocity of the step behind is slightly delayed. The equidistant arrangement of steps is therefore not stable in absence of an Ehrlich-Schwoebel barrier. Eventually bunches of steps appear on the surface, cf. Fig. 5.24c. Such process is termed *step bunching*.

In *presence* of an Ehrlich-Schwoebel barrier adatoms are basically captured from the lower terrace at a step. A delayed step will then be supplied with more adatoms from the lower (wider) terrace ahead and its velocity will increase. On the other hand, a faster step is supplied less and its speed decreases. The Ehrlich-Schwoebel barrier therefore stabilizes an equidistant train of steps during step-flow growth.

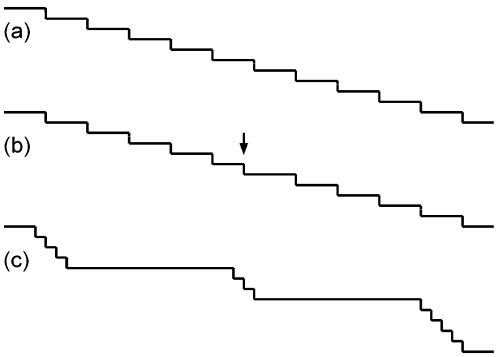


**Fig. 5.24** (**a**) Surface cross-section during stable step-flow growth in presence of Ehrlich-Schwoebel barriers. (**b**) Step delayed behind its regular position (*arrow*) and (**c**) eventually forming bunches of steps in absence of Ehrlich-Schwoebel barriers

Conditions are reversed if no flux is supplied to the surface. During evaporation of adatoms the Ehrlich-Schwoebel barrier destabilizes a regularly stepped surface and leads to the formation of step bunches. Steps move in reverse direction due to detachment of atoms and subsequent evaporation. If now a step is delayed, the lower terrace gets more narrow than the upper terrace. The flux of evaporation is then reduced, leading to a further decrease of step velocity.

Surface steps were by now considered straight and assumed to move during step-flow growth on the hole like a rigid entity. Experiments and theoretical analyses show that such condition is not stable in practice. A step will generally be perfectly straight only at $T = 0$ K. As the temperature is increased, at finite temperature the action of entropy produces a roughening addressed in the next section. The overall shape of a step is basically preserved by such change which occurs on a small scale.

On a larger scale the shape of a straight step was found to be unstable during step-flow growth, if the adatom attachment from the upper and lower terraces differ. G.S. Bales and A. Zangwill pointed out that surface diffusion in presence of an Ehrlich-Schwoebel barrier gives rise to a morphological instability of straight steps, leading to a distinct wavy shape [26]. The qualitative reason for the *Bales-Zangwill instability* is analogous to that considered above to explain the debunching effect of the Ehrlich-Schwoebel barrier on a sequence of steps during step-flow growth.

We recall from (5.25) that the step velocity $r_{\text{step}}$ is proportional to the sum of the current density of adatoms $j_{\text{upper}}$ from the upper terrace to the step and $j_{\text{lower}}$ from the lower terrace, $r_{\text{step}} = a^2(j_{\text{upper}} + j_{\text{lower}})$. Furthermore, we note that the current density $\mathbf{j}$ on either side of the step is proportional to the gradient of the adatom density $n$ near the step, $\mathbf{j} = -D\partial n/\partial \mathbf{r}$. Let us now assume a step deviates at one section from the perfect straight shape and has, say, a warpage in the direction along $r_{\text{step}}$ (like point A in Fig. 5.25). The lines of isoconcentration of the adatom density $n$ on the lower terrace are then more dense in front of the warpage than on the straight parts of the step. The adatom density is even less dense in front of notches (like point B in Fig. 5.25). A high density of isoconcentration lines in front of point A corresponds to an increased current density $j_{\text{lower}}$ towards the step at this point. In *absence* of an Ehrlich-Schwoebel effect this surplus of adatoms from the lower terrace is exactly balanced by a lack of adatoms from the upper terrace: Behind the

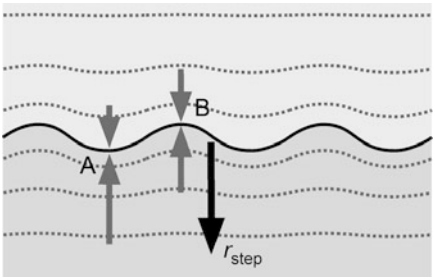


**Fig. 5.25** Monoatomic wavy step (*solid black line*) viewed from top. *Light gray* and *gray shaded area* indicate upper and lower terrace, respectively. The *dotted lines* are isoconcentration lines of adatoms, *gray arrows* represent adatom fluxes towards the step being proportional to the gradient of adatom concentration. *A* and *B* denote respectively points of enhanced and diminished adatom inflow at the step compared to a straight step

warpage on the upper terrace the density of isoconcentration lines of $n$ is decreased, and so $j_{\text{upper}}$. Without an Ehrlich-Schwoebel effect all parts of the distorted step will travel with the same velocity $r_{\text{step}}$. The *presence* of an Ehrlich-Schwoebel barrier will, however, reduce the compensating contributions from the upper terrace. As a result, the dominating contributions from $j_{\text{lower}}$ lead to an increased growth rate at a convex section of the step (point A) and a decreased growth rate a concave section (point B). This positive feedback amplifies perturbations of a straight step. Eventually, the line tension at the step that increases with the step length limits the feedback, and a wavy shape as indicated in Fig. 5.25 develops.

The Bales-Zangwill instability is discussed quantitatively and in more detail in [26, 27]. We confine ourselves to the qualitative arguments given above. A wavy step structure can be recognized in Fig. 5.19; the effect is particularly strong at decreased temperature (Fig. 5.19b), where also low barriers act more effective due to a lowered adatom mobility. It should be noted that a meander pattern of step may also be induced by a Kink-Ehrlich-Schwoebel effect [28, 29].

### *5.2.7 Roughening of Surface Steps*

A surface step will generally be perfectly straight only at $T = 0$ K. As the temperature is increased, a finite contribution of entropy will decrease Gibbs free energy and kinks separated by straight parts will appear. This roughening provides kink sites for the incorporation of adatoms into the layer during growth. We consider the structure of a straight step of monoatomic height on the (001) surface of a cubic Kossel crystal oriented along the [100] direction [19]. Figure 5.26 shows a top view on a straight step at position (a), where one atom was moved from an embedded step site to a site attached to the step. To evaluate the energy cost of this operation in the framework of the terrace-step-kink model we count the number of broken and formed next-neighbor bonds. Three bonds with an energy $E_{\text{B}}$ each were broken, and

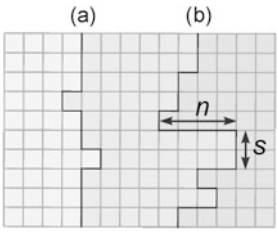


**Fig. 5.26** Schematic of monoatomic steps on a Kossel crystal viewed from top, a *lighter gray shading* indicates higher lying terraces. (**a**) Kinks generated by moving one embedded ledge atom of a straight step to a position attached to the step. (**b**) Step with kinks of several atom units

one bond for the attachment at the step was formed, yielding a net amount of $2E_B$. Counting of the kinks created yields (from bottom to top in Fig. 5.26 at position (a)) $1^+$, $1^-$, $1^-$, $1^+$, i.e., two positive and two negative kinks. We thus obtain an energy of $E_B/2$ necessary to form a kink.

The probability of having a kink or a straight part of the step depends on the energy per kink. Denoting the probabilities for (monoatomic) positive kinks, negative kinks, and straight parts $p_+$, $p_-$, and $p_0$, respectively, we obtain [19]

$$\frac{(1/2)(p_+ + p_-)}{p_0} = \exp\left(-\frac{E_B/2}{kT}\right), \quad p_+ + p_- + p_0 = 1. \tag{5.29}$$

The mean distance between kinks is given by $y_0 = a/(p_+ + p_-)$, $a$ being the unit spacing. Inserting (5.29) yields

$$y_0 = \frac{a}{2}\exp\left(\left(\frac{E_B/2}{k_B T}\right) + 2\right) \approx \frac{a}{2}\exp\left(\frac{E_B/2}{k_B T}\right). \tag{5.30}$$

The mean distance $y_0$ between kinks decreases as the temperature is raised. Note that at common growth temperatures usually $E_B \gg k_B T$ applies. Considerations above assumed kinks of a single atom unit and steps without any mutual interaction arising from long-range strain fields.

We illustrate the effect of step roughening for the interesting vicinal surface of Si(001). The Si(001) surface reconstructs to a $(2 \times 1)$ surface unit-cell by forming rows of dimerized atoms. Dimer rows on terraces that are separated by a monoatomic step (or by an odd number of such steps) are perpendicular to each other due to the structure of the diamond lattice (Sect. 2.1.4). If the singular Si(001) surface is tilted by a small angle (below $\sim 1°$) toward a [011] direction, adjacent monoatomic steps are hence not equivalent. It should be mentioned that larger miscuts (2–10°) and heating to typical growth temperatures above 600 °C leads to double-layer steps, which are not considered here. There exist two kind of monoatomic steps: those labeled $S_A$ steps (single A steps) have dimers on the lower terrace directed parallel to the step, while the dimerization direction on the lower terrace at $S_B$ steps runs perpendicular to the steps, cf. Fig. 5.27. Calculations show that the formation energy per length of $S_A$ steps is much lower ($\sim 0.01 \pm 0.01$ eV/atom) than that of $S_B$ steps ($\sim 0.15 \pm 0.03$ eV/atom) [30]. This finding was

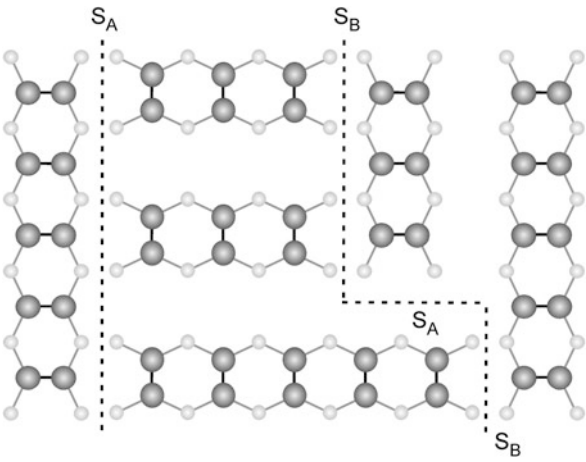


**Fig. 5.27** Top view on monoatomic steps of a vicinal Si(001) surface. The height decreases from *left* to *right*. On each terrace *dark gray dimers* and *gray atoms* lie on the topmost layer and the layer underneath, respectively

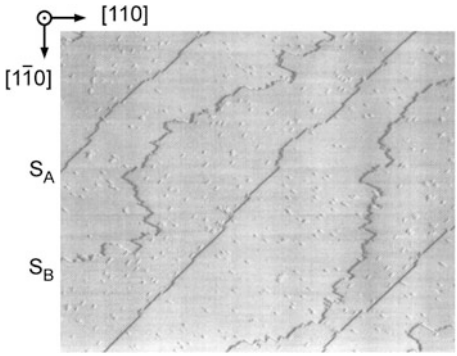


**Fig. 5.28** Scanning-tunneling micrograph of a Si(001) surface miscut 0.3° towards [100]. The surface was annealed at 600 °C for 5 min prior to quenching to room temperature. Steps are descending from the *upper left* to the *lower right corner*. Reproduced with permission from [31], © 1990 APS

basically confirmed by scanning-tunneling microscopy, yielding an upper-bound estimate of $\sim 0.028 \pm 0.002$ eV/atom for $S_A$ steps and $\sim 0.09 \pm 0.01$ eV/atom for $S_B$ steps [31].

Due to the symmetry of the Si(001) surface each kink must have a length of multiples of $2a$, and the same holds for the distance between kinks. We note from Fig. 5.27 that kinks in one type of step are made of segments of the other type of step. The two types of steps have different energies associated with the formation of kinks and consequentially also different morphology: $S_A$ steps are smooth and $S_B$ steps are rough, see Fig. 5.28.

The equilibrium distribution of steps and kinks was analyzed from images like that of Fig. 5.28 [31]. In the analysis a kink is any inside corner followed by an outside corner or vice versa. Separations $s$ and lengths $n$ of kinks are defined as shown in Fig. 5.26. Resulting distributions of kink separations $s$ and kink lengths $n$ of an $S_B$ step are displayed in Fig. 5.29. The probability $p(s)$ of finding two adjacent kinks separated by $s$ atoms follows from the probability $p_k$ that a kink exists times

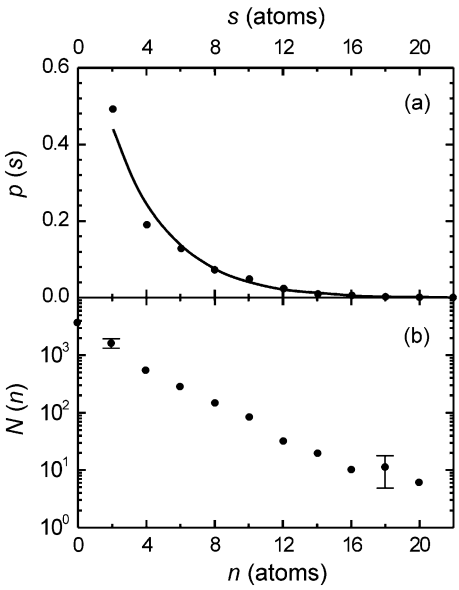


**Fig. 5.29** (**a**) Probability of two adjacent kinks separated by $s$ atoms depending on their separation for an $S_B$ step on Si(001) prepared at 600 °C. The *solid line* is function (5.31) with $p_k$ taken from the measured kink density. (**b**) Number of kinks of length $n$ as a function of kink length $n$. Reproduced with permission from [31], © 1990 APS

the probability that *no kink* (i.e., $(1 - p_k)$) is nearby in a range $\pm s$ atoms. The exact relation is given by

$$p(s) = p_k(1 - p_k)^{s/2-1}. \tag{5.31}$$

This function is drawn in Fig. 5.29a. In the plot $p_k$ equals the number of kinks of $S_B$ steps counted from STM images divided by the total number of possible kink sites. We observe that (5.31) describes the measured probability distribution $p(s)$ very well, indicating that kinks may be considered independent in this experiment. The validity of this assumption is also reflected in Fig. 5.29b, showing an exponential dependence of the number $N$ of kinks of length $n$ atoms from the length, i.e., $N \sim \exp(-E(n)/(kT))$, where $E(n)$ is the energy of a kink of length $na$. $E(n)$ was shown to be related to the formation energy per length of a step $E_S$ according $E(n) = nE_S + \text{const}$ [31]. $E_S$ corresponds to an $S_A$ step for kinks in an $S_B$ step (and vice versa) due to the symmetry of the diamond lattice as illustrated in Fig. 5.27. The $E(n)$ offset, i.e., the const $= 0.08 \pm 0.02$ eV, may be considered as an additional energy due to the corner of a kink. The lower formation energy per length $E_S$ of $S_A$ steps leads to a small kink energy $E(n)$ in $S_B$ steps, and consequently according (5.30) to a smaller mean distance $y_0$ between kinks as compared to $S_A$ steps.

### 5.2.8 *Growth of a Si(111)(7 × 7) Surface*

Surface kinetics considered so far assumed adatoms arriving on the surface to migrate and eventually nucleating islands or being incorporated on a regular lattice

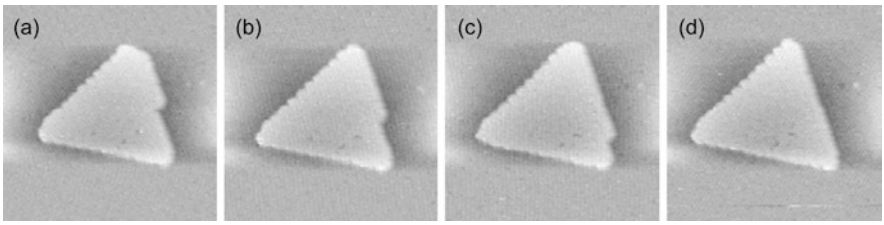


**Fig. 5.30** Homoepitaxial growth of a two-dimensional island on a (7 × 7) reconstructed Si(111) surface recorded at 575 K using scanning tunneling microscopy. The image size is 500 × 500 Å$^2$. Reproduced with permission from [33], © 1998 APS

site at a step. The nucleation theory outlined above in Sect. 5.2.2 is often successfully applied to describe epitaxy of metals. Metal surfaces often do not reconstruct, and surface diffusion and capture to form a stable nucleus may be the only relevant processes which determine the growth morphology. We know, however, from Sect. 5.1 that the arrangement of surface-near atoms may strongly deviate from that inside the bulk solid. Such reconstruction is particularly prominent on semiconductor surfaces. Compared to an unreconstructed surface an additional energy barrier must hence be surmounted to form a stable nucleus [32]. How are surface atoms rearranged from sites in reconstruction to regular lattice sites during growth? The complexity of surface reconstructions pointed out in Sects. 5.1.6 and 5.1.7 indicate that this question does not have a general answer. Only few studies provide a microscopic insight into the complex growth kinetics of reconstructed semiconductors. We consider growth steps for the two examples previously also treated to illustrate surface reconstructions.

The (7 × 7) reconstruction of the Si(111) surface is a prominent surface structure. According the DAS model the complex reconstruction comprises 15 dimers, 12 adatoms, and 1 stacking fault, cf. Fig. 5.13. During growth the atoms of the surface reconstruction have to be rearranged to the bulk structure. We first consider an experimental observation of the epitaxial growth of a two-dimensional island. Figure 5.30 shows a sequence of STM images recorded at 575 K during MBE growth on a (7 × 7) reconstructed Si(111) surface [33]. Details of the reconstruction are not resolved in the images. We note a pronounced macro kink at the right edge of the island that gradually moves downwards, thereby eventually completing a laterally enlarged triangular island. Atomically resolved images proved that the fast growing stripe has the width of a (7 × 7) unit cell (27 Å).

The stability of the island during the sequence shown in Fig. 5.30 indicates a fast growth of the additional row. This is confirmed by the growth dynamics evaluated from such in situ STM images given in Fig. 5.31 [33]. The lower curve shows the experimentally observed size of a single island expressed in units of half the rhombic (7 × 7) unit cell. We note pronounced plateaus indicating a stable configuration of the island, and a rapid increase of the island size between the plateaus. These periods of fast growth correspond to the addition of a row like that shown in the sequence of Fig. 5.30. The stable islands occur at triangular "closed shell" configurations, i.e., at sizes of $n^2$ half-unit-cells. At these numbers isosceles triangles appear, cf. Fig. 5.32.

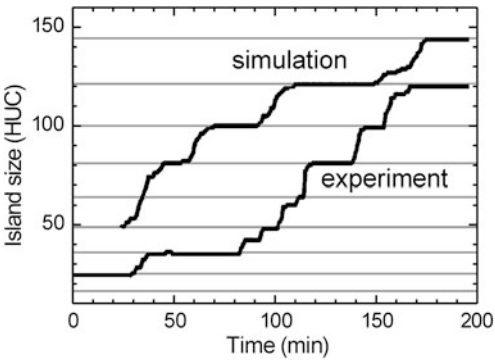


**Fig. 5.31** Evolution of a single island on a Si(111) (7 × 7) surface. *Lower* and *upper curve* refer to experimental data and a kinetic Monte Carlo simulation, respectively. The island size is given in numbers of half-unit-cells (HUC), *gray horizontal lines* marks sizes of $n^2$ HUC. Reproduced with permission from [33], © 1998 APS

The observed island growth is related to the structure of the surface reconstruction. The rhombic (7 × 7) unit cell of the Si(111) (7 × 7) surface is composed of two triangular half-unit-cells (HUC): One unfaulted half (U-HUC) with a near-surface layer sequence identical to the bulk underneath, and a faulted half (F-HUC) with a stacking fault (the right and left triangles in Fig. 5.13, respectively). During growth the reconstructed atoms have to rearrange toward the bulk structure. In the unfaulted HUC these are the atoms in the uppermost layer. In the faulted HUC the stacking fault must be removed in addition. Atom rearrangement in the faulted half is therefore associated with a higher energy barrier than in the unfaulted half of the (7 × 7) unit cell [34].

A model of the growth sequence is illustrated in Fig. 5.32. A triangular two-dimensional island on Si(111) (7 × 7) is surrounded by *faulted* half-unit-cells denoted F in Fig. 5.32 (the initial nucleation is assumed to be favored on an unfaulted unit cell). Growth of the island hence requires the overgrowth of a faulted HUC. Surmounting the unfavorable high energy barrier causes the delay observed in the dynamics Fig. 5.31. Once an F-HUC nucleates the adjacent U-HUC can be overgrown more easily. Overgrowth of the next F-HUC is facilitated by the macro kink depicted in Fig. 5.32: The new F-HUC has a shorter edge length than the F-HUC which nucleated before (1 side instead of 2). Neighboring faulted and unfaulted half-unit-cells aside the island are overgrown in a quick succession until an enlarged island comprising $n^2$ half-unit-cells in total is completed.

The experimentally observed growth behavior is well reproduced by a kinetic Monte Carlo simulation [33]. The simplified model assumes a honeycomb lattice consisting of alternating F and U sites, and material to be transported towards the island in HUC units. The attachment barrier $E$ is assumed to depend on both, the type of the underlying HUC (F or U), and the number $n_{\mathrm{edge}}$ of nearest-neighbor HUC already attached to the island, $E = E_{\mathrm{U/F}} - n_{\mathrm{edge}} \times E_{\mathrm{edge}}$. Rates for hopping and attachment are modeled in terms of Arrhenius expressions with energies chosen to yield the best agreement with experimental data. The result shown in Fig. 5.31 features a similar dynamics as the island evolution observed in the experiment.

Nucleation of the half-unit-cells was addressed in spatially more refined models [35, 36]. Nucleation of a 2D island is considered to proceed in three steps, starting with a small stable cluster in a HUC of the Si(111) (7 × 7) surface. The cluster raises

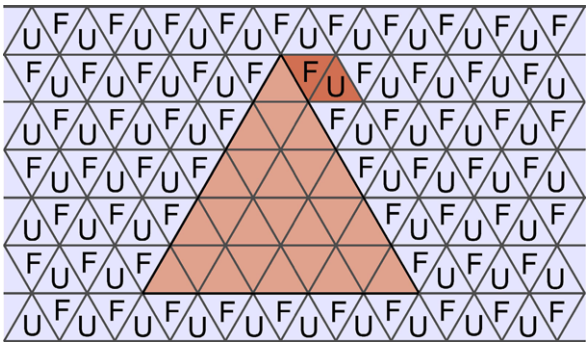

**Fig. 5.32** Arrangement of faulted (F) and unfaulted (U) half-unit-cells of a (7 × 7) reconstructed Si(111) surface around a triangular two-dimensional Si island (*dark gray*)

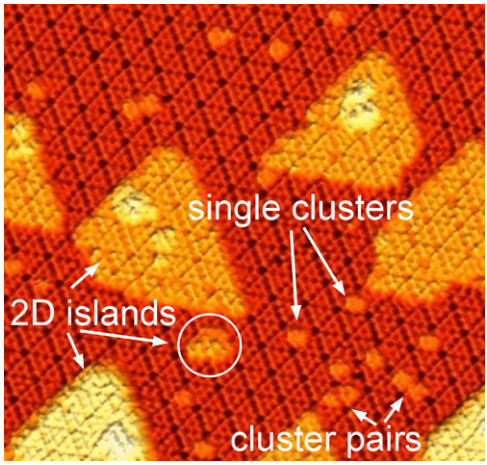


**Fig. 5.33** STM image of a (7 × 7) reconstructed Si(111) surface after deposition of 0.2 bilayers of Si showing clusters, cluster pairs, and 2D islands. The smallest island (*circle*) has the size of one unit cell. The image size is 425 × 425 Å$^2$. Reproduced with permission from [36], © 2007 APS

the adatom binding energy in adjacent HUCs, leading to a preferential formation of a second cluster in a neighboring HUC of the same unit cell. Eventually an additional adatom is attached to the cluster pair, and the (7 × 7) reconstruction is locally removed [36]. The species cluster, cluster pair, and 2D island are well reproduced in the STM image Fig. 5.33.

### *5.2.9 Growth of a GaAs(001) β2(2 × 4) Surface*

A very detailed scenario of kinetic processes occurring during nucleation and growth of reconstructed surfaces was obtained by combining experimental STM results with kinetic Monte Carlo simulations [37, 38]. Advanced modeling emloyed rates obtained from density-functional theory (DFT) calculations [38]. Monte Carlo simulations can bridge the time scales from individual kinetic steps to macroscopic growth, while DFT calculations yield kinetic parameters from first principles. The studies focus on homoepitaxial growth of GaAs on a As-rich GaAs(001)-$\beta 2(2 \times 4)$

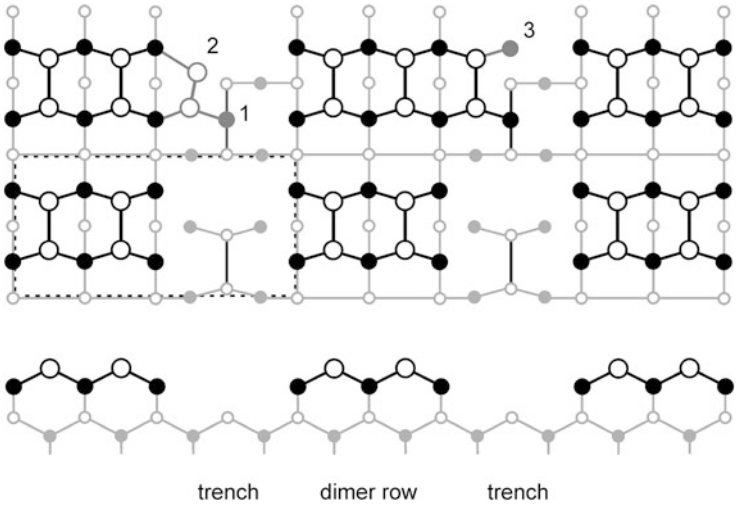


**Fig. 5.34** Side and plan views of a $\beta 2(2 \times 4)$ reconstructed GaAs(001). The unit cell is indicated by *dashed lines*, *filled* and *open symbols* represent Ga and As atoms, respectively. *Numbers* label initial growth steps

surface from beams of atomic Ga and $As_2$ molecules. The two species behave quite different on the surface. Ga atoms adsorb with a sticking coefficient of unity on the As-rich surface [39], leading to a growth rate which is controlled by the Ga flux. On the other hand, the chemically rather stable $As_2$ binds only weakly to an As-rich GaAs surface [39, 40]. It adsorbs only after deposition of Ga [41] and diffusion to adjacent sites [38]. Diffusion and incorporation of Ga has thus a strong impact on the adsorption and incorporation of arsenic.

The $\beta 2(2 \times 4)$ reconstructed GaAs(001) surface consists of rows with topmost As-As dimers, separated by trenches, cf. Fig. 5.34. Diffusion of Ga adatoms is anisotropic with lowest activation energy for hopping processes along the trenches [42]. From calculations it was found that the terminating $As_2$ dimers of the $\beta 2(2 \times 4)$ reconstruction, particularly those in the trenches, act as traps for diffusing Ga adatoms: Ga atoms are immobilized for about $10^{-8}$ s, much longer than the time scale for hopping of order $10^{-12}$–$10^{-9}$ s. At such Ga adsorption site a gas-phase $As_2$ molecule can readily adsorb by forming one bond to the adsorbed Ga atom and two bonds to Ga atoms with unsaturated bonds that are located at the side walls of the $\beta 2(2 \times 4)$ trenches. The new As-As dimer complex becomes more stable by attaching another diffusing Ga adatom in the trench. Growth on the reconstructed surface hence preferentially nucleates at the side walls of the trench and largely proceeds by partially filling the trenches, followed by island nucleation on surface regions where a filling of the trenches has occurred [43]. The first steps of the mentioned process are depicted in Fig. 5.34. The surface unit-cell marked in the figure contains an As-As dimer in the trench. In one of the favored Ga diffusion channels the bond of these dimers is broken by Ga as depicted at position 1 in the top panel of Fig. 5.34 [42]. The new bonds relax the position of the two As atoms to their bulk

position. The Ga atom at position 1 favors a subsequent $As_2$ adsorption at the trench side-wall as indicated at position 2. A dangling bond of As may then be saturated by a further Ga atom in the trench at position 3.

The outlined nucleation steps describe the main route occurring at standard conditions of molecular beam epitaxy of GaAs(001) at 800 K. The prevailing processes change when the growth temperature is changed [38].

The examples of homoepitaxial growth on the $\beta 2(2 \times 4)$ reconstructed GaAs(001) surface and the $(7 \times 7)$ reconstructed Si(111) surface indicated that the classical nucleation theory may sometimes be too simplified for describing the complex processes of semiconductor growth. Still the simple theory provides useful guidelines to interpret growth phenomena and to optimize growth conditions.

## 5.3 Self-organized Nanostructures

The reduction of the dimensionality of a solid leads to a modification of the electronic density-of-states. The effect of size quantization requires characteristic length scales in the range of typically 10 nm defined by the de-Broglie wavelength as outlined in Sect. 3.3.2. Fabrication of such small structures with high material quality may hardly be accomplished by lateral patterning of quantum wells. Etching or implantation techniques inevitably introduce defects, which deteriorate the electronic properties of a nanostructure. Therefore a number of techniques were developed particularly in the 1990ies employing self-organization phenomena during epitaxial growth. The approaches are based on an anisotropy of surface migration of supplied atoms, originating from a non-uniform driving force like, e.g., strain, that tends to minimize the total energy of the system. Thereby structurally or compositionally non-uniform crystals with dimensions in the nanometer range may be coherently formed without structural defects. Some of these techniques have attracted much attention for the fabrication of quantum wires and quantum dots, and are outlined in the following.

### *5.3.1 Stranski-Krastanow Island Growth*

Stranski-Krastanow growth is one of the three fundamental growth modes introduced in Sect. 4.2.3. The characteristic feature is a transition of an initially two-dimensional layer-by-layer growth to three-dimensional growth. The size of the three-dimensional islands formed by such transition lies for many semiconductors in the range required for quantum dots (QDs) as expressed by (3.37). The transition of 2D to 3D layer growth may be induced by strain upon depositing a 2D layer on

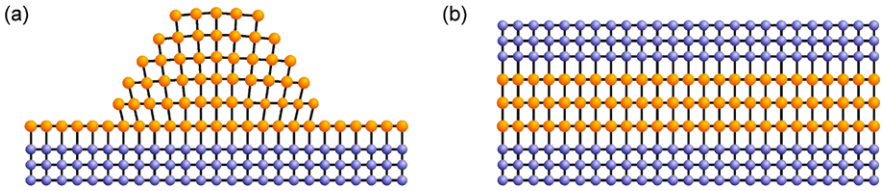


**Fig. 5.35** Scheme illustrating elastic strain relaxation in (**a**) a quantum dot and (**b**) a quantum well. *Yellow* and *blue circles* represent atoms of size-quantized materials and barrier materials, respectively

a substrate with a different lateral lattice constant. Since a coherent layer adopts the lateral atomic spacing of the substrate, strain accumulates with increasing thickness. Above a critical layer thickness the strain is relaxed plastically by introduction of misfit dislocations (Sect. 2.2.6). Below this critical thickness under suitable conditions a considerable part of the strain may be relaxed *elastically*, i.e. without introduction of dislocations, by the formation of three-dimensional surface structures. Such reorganization of a flat surface into a system of tilted facets implies an enlargement of the surface area. The driving force of the Stranski-Krastanow growth mode is therefore a minimization of the total strain and surface energy [44]. The elastic strain relaxation in an uncovered 3D island is illustrated in Fig. 5.35a. We note that the strain is inhomogeneous, giving rise to shear deformations in addition to hydrostatic strain components. This feature is in contrast to a strained quantum well depicted in Fig. 5.35b. The quantum well exhibits a constant, homogeneous biaxial strain in the entire layer.

Elastic strain relaxation generally leads to an energy decrease of the structure. The contribution of the surface energy upon faceting of a flat surface may, by contrast, be positive or negative. The sign follows from a simple advisement. Consider, e.g., a (001) surface with area $A$ and a surface energy $\gamma_{001}$ as illustrated in Fig. 5.36. This surface will gain energy upon a faceting with {110} facets, if the surface energy $\gamma_{011}$ of these facets fulfills the condition $\sqrt{2}\gamma_{011} < \gamma_{001}$. The prefactor $\sqrt{2}$ is the increase of surface area of a faceted {011} surface with respect to the flat (001) surface.

The total energy gain of three-dimensional islands with respect to a two-dimensional deposition is given by strain and surface energy contributions of both, the reorganized part of the material and the part remaining in the wetting layer after the Stranski-Krastanow transition. The wetting layer is a fraction of the deposited strained material of at least one monolayer thickness. This part remains as a two-dimensional layer on the substrate and does not migrate to the faceted part due to a lower surface energy of the deposit as discussed in Sect. 4.2.3.

We consider the total energy gain per unit volume obtained, if a two-dimensional deposit of nominal thickness $\theta_0$ (in units of monolayers) reorganizes to a single faceted three-dimensional island on a wetting layer (WL) of thickness $\theta$, cf. Fig. 5.37. The contributions sensitively depend on the shape of the island. For

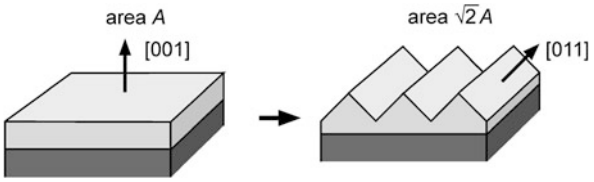


**Fig. 5.36** Faceting of a (001) surface with area $A$ to a surface of total area $\sqrt{2}A$ with {011} facets

simplicity we assume an island with the shape of a pyramid with a quadratic base of length $L$ as often found in experiment. The gain can be expressed as [45]

$$\frac{E_{\text{total}}}{V} = \varepsilon^{\text{elast}}_{\text{island}} - \varepsilon^{\text{elast}}_{\text{layer}} + \frac{A\gamma_{\text{facet}} - L^2\gamma_{\text{WL}}(\theta_0)}{V} + \left(\frac{1}{\rho} - L^2\right)\frac{\gamma_{\text{WL}}(\theta) - \gamma_{\text{WL}}(\theta_0)}{V}, \tag{5.32}$$

with the elastic energy densities $\varepsilon^{\text{elast}}_{\text{island}}$ and $\varepsilon^{\text{elast}}_{\text{layer}}$ of the island and the uniformly strained layer, respectively. The third term describes the change in surface energy due to the island: $\gamma_{\text{facet}}$ is the surface energy of the island facets, $A$ is their area, and $L$ the island base length. The volume of the pyramidal shaped island $V$ follows from mass conservation and is given by

$$V = \frac{1}{\rho}(\theta_0 - \theta)d_{\text{ML}} = \frac{1}{6}L^3 \tan\alpha,$$

where $\rho$, $d_{\text{ML}}$, and $\alpha$ are the areal density of the islands (in units $\text{cm}^{-2}$), the thickness of one monolayer, and the tilt angle of the facets. The fourth term in (5.32) accounts for the change of wetting layer energy as the thickness decreases from $\theta_0$ to $\theta$. The relation $\gamma_{\text{WL}}(\theta)$ computed for thin reconstructed InAs layers on GaAs substrate is shown in Fig. 5.38a [45]. The prefactor $(1/\rho - L^2)$ effectuates that this term solely applies for the free surface *besides* the island (i.e., the area *not* covered by the island). The sum of all four contributions is given in Fig. 5.38b. Values refer to pyramidal InAs islands with relaxed, but unreconstructed {110} facets and a $\beta 2(2 \times 4)$ reconstructed (001) surface of the wetting layer, grown on (001) oriented GaAs.

The calculated energy gain per unit volume upon island formation given in Fig. 5.38b shows that major contributions originate from the elastic energy relief, i.e., from the first two terms in (5.32). This negative part scales with the island volume. The surface energy described by the third term in (5.32) is an unfavorable positive energy with a decreasing contribution for larger islands due to a $\propto V^{2/3}$ dependence. The wetting-layer contribution represented by the fourth term in (5.32) is also positive. Besides island volume it depends on island density and the coverage. The importance of facet edges was controversial in literature [44, 46]; the calculation presented in Fig. 5.38b yields an only minor contribution.

The total energy density given by the sum of all contributions has an energy minimum for a particular island size as indicated by an arrow in the figure. Such minimum is important for obtaining a narrow size distribution for an ensemble of islands. It should be noted that a theory considering only the two contributions of elastic relaxation (negative, $\propto V$) and island surface-energy (positive, $\propto V^{2/3}$) does


**Fig. 5.37** Reorganization of a uniformly strained layer of $\theta_0$ monolayers thickness to an island with pyramidal shape on a remaining wetting-layer thickness of $\theta$ monolayers. $L$ and $\alpha$ are the base length of the island and the tilt angle of the island facets, respectively

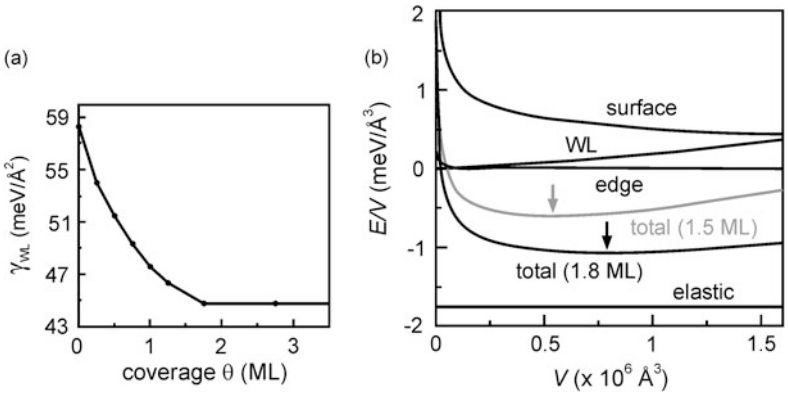


**Fig. 5.38** (**a**) Calculated formation energy of a strained InAs wetting layer on (001)-oriented GaAs as a function of coverage $\theta$. (**b**) Total energy gain by island formation with various contributions for $\rho = 10^{10}$ cm$^{-2}$ areal density and $\theta_0 = 1.8$ monolayers InAs layer coverage on GaAs (*black lines*). The *gray line* refers to the total energy gain for $\theta_0 = 1.5$ monolayers. *Arrows* mark the minima of the total energy curves, *WL* denotes the contribution of the wetting layer. Reproduced with permission from [45], © 1999 APS

not yield a finite equilibrium size. For sufficient high coverages the volume term always prevails and favors steady island growth as previously discussed in nucleation and ripening (Sects. 4.2.1, 4.2.8).

Stranski-Krastanow growth induced by strain represents a quite universal behavior. Self-organized formation of islands is found for both, compressively and tensely-strained layers in various materials systems and crystal structures. Table 5.5 and Fig. 5.39 give some examples. The mismatch is defined by (2.20a), yielding a negative sign for compressively strained islands. Usually substrate material is also employed for covering the islands after formation. The material is then generally termed matrix. Often the island material is alloyed with matrix material to reduce the strain, yielding a parameter for controlling the transition energy of confined excitons.

Self-organized Stranski-Krastanow growth was particularly studied for fabricating InAs and $In_{1-x}Ga_xAs$ quantum dots in a GaAs matrix [51]. The InAs lattice constant exceeds that of GaAs by ∼7 %, and the critical thickness for elastic relaxation of such a highly strained 2D InAs layer on a GaAs(001) substrate to 3D

**Table 5.5** Some semiconductor materials used for strain-induced, self-organized Stranski-Krastanow formation of islands

| Island/matrix | Ge/Si | InAs/GaAs | GaN/AlN | PbSe/PbTe |
|---|---|---|---|---|
| Structure | Diamond | Zincblende | Wurtzite | Sodium chloride |
| Orientation | (001) | (001) | (0001) | (111) |
| Mismatch | −3.6 % | −7 % | −2.5 % | +5.5 % |

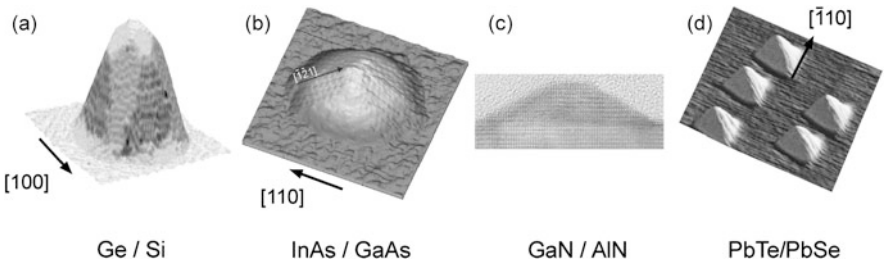


**Fig. 5.39** Free standing self-organized islands formed by Stranski-Krastanow growth in various strained heteroepitaxial materials: (**a**) Ge/Si(001) [47], (**b**) InAs/GaAs(001) [48], (**c**) GaN/AlN(0001) [49], (**d**) PbTe/PbSe(111) [50]. The AFM images are vertically not to scale with respect to the lateral scale

islands is only about 1.5 InAs layers. Once this critical layer thickness is exceeded, islands form with a high areal density of typically $10^{10}$–$10^{11}$ cm$^{-2}$.

The Stranski-Krastanow transition from 2D growth of a strained layer to 3D growth of islands occurs quite abrupt, albeit it may be delayed by kinetic barriers constituted by suitable growth conditions. During molecular-beam epitaxy the 2D–3D transition can be monitored in situ using reflection high-energy electron diffraction: The streaky reflection pattern indicating reflection from a flat 2D surface changes to a spotty pattern created by three-dimensional surface structures [52]. Atomic force micrographs taken for different coverages of InAs yield virtually no islands below the critical coverage $\theta_c$, and a sharp increase of the density of islands $\rho$ above $d_c$ following a relation $\rho \sim (\theta - \theta_c)^{\alpha}$ [53]. The dependence of island density on InAs coverage $\theta$ is shown in Fig. 5.40.

The shape of islands created by Stranski-Krastanow growth depends on the material system and also on the growth conditions. For uncovered islands in several materials systems the shape is found to undergo a transition upon increase of volume, which increases for thicker coverage. Generally a transition with a continuous introduction of steeper facets at the island edge is expected [54], particularly due to the strain concentrating at the base perimeter. Experimental results for the two most studied materials InAs/GaAs(001) and Ge/Si(001) are given in Fig. 5.41. Small and large islands, referred to as pyramids with shallow facets and domes with steep facets, respectively, were found. The gray scale in the figure indicates the local slope of the facets.

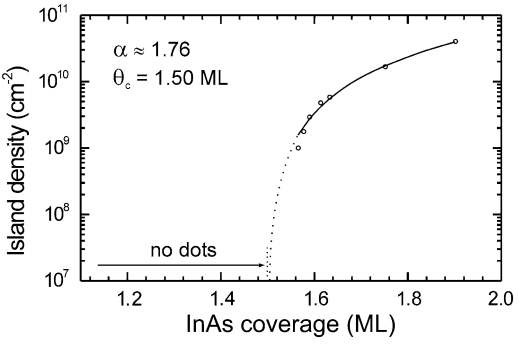


**Fig. 5.40** Density of self-organized islands formed by Stranski-Krastanow growth during molecular-beam epitaxy at 530 °C with a low growth rate of 0.01 ML/s. Reproduced with permission from [53], © 1994 APS

Figure 5.41 indicates that islands with distinctly different sizes may coexist. A bimodal size distribution of island ensembles with well separated maxima of the mean sizes is often observed. The finding indicates some departure from thermodynamic equilibrium due to the presence of kinetic barriers in the formation process. Island formation using Stranski-Krastanow growth is usually performed at quite low growth temperatures.

For quantum-dot applications in devices Stranski-Krastanow islands are covered by a capping layer. Usually the same material as that underneath the islands is employed. The morphology of the islands is generally strongly modified during the capping procedure, unless special deposition conditions are found to preserve the initial shape. While strain favors the formation of steep facets in the case of free standing islands, deposition of a mismatched material on top of the islands reverses this trend: Generally the islands tend to become flat during cap layer deposition. Often quantum dots with a shape of truncated pyramids are formed. A microscopic picture of the capping dynamics of InAs/GaAs/(001) islands was obtained from scanning tunneling microscopy [55]. The process is illustrated in Fig. 5.42. Initially the deposited Ga atoms tend to migrate away from the islands' apex and accumulate at the base due to a better lattice match of the GaAs cap layer material. Indium from the apes starts to alloy with Ga near the base, thereby releasing strain and increasing entropy. Eventually GaAs covers the remaining material of the island, yielding a surface morphology depending on the deposition rate of the cap layer.

The effect of cap layer deposition on the island shape is illustrated in Fig. 5.43. The STM images show (110) cross sections of InAs islands in GaAs matrix material grown using MBE under the same conditions as applied for the free standing island shown in Fig. 5.39b. The GaAs cap layer was deposited with a rate of 0.15 ML/s at the same low temperature of 510 °C as the InAs islands after applying 10 s growth interruption. The shape changed from a pyramid with shallow facets to a truncated pyramid with a flat (001) top and steeper side facets [56]. Such shape was also found for structures grown using MOVPE [57] and is typical for buried InAs/GaAs islands.

Often a growth interruption is applied after deposition of the island material and prior to deposition of the cap layer. The interruption intends to equilibrate the ensemble of islands for obtaining a narrow distribution of sizes. Usually the mean size of the resulting quantum dots increases as the duration of the growth interruption

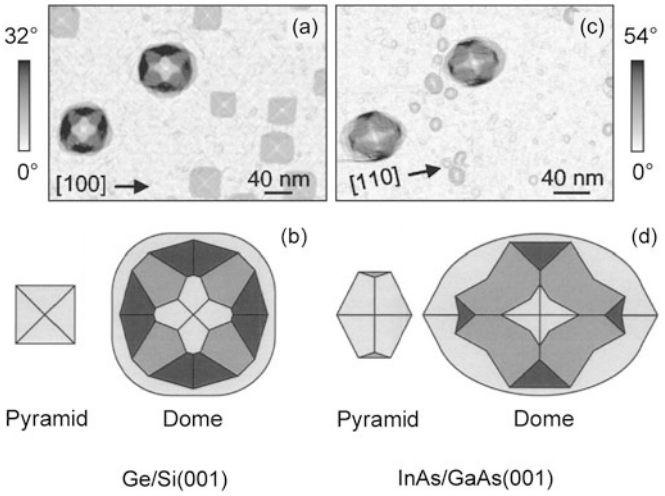


**Fig. 5.41** Shape of uncapped Ge/Si (**a**, **b**) and InAs/GaAs islands (**c**, **d**). Steeper facets are marked by a *darker gray tone*: *light gray*, *gray* and *dark gray* denote {105}, {113}, and {15 3 23} facets for Ge/Si and {137}, {101}, and {111} facets for InAs/GaAs, respectively. Reproduced with permission from [58], © 2004 APS

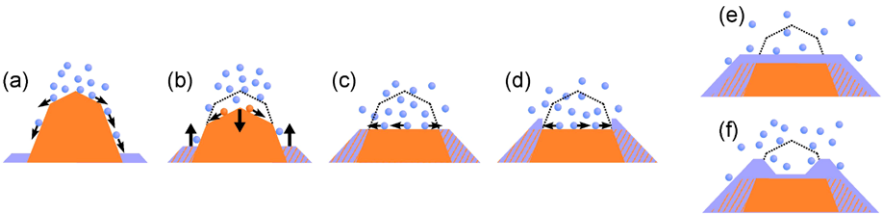


**Fig. 5.42** Schematic of the overgrowth process of InAs/GaAs islands. *Orange* and *blue* mark In and Ga Column-III elements, respectively. *Shaded regions* indicate intermixed InGaAs materials. Cap layer morphology obtained for a low capping rate is illustrated in (**e**), for a high capping rate in (**f**). Reproduced with permission from [55], © 2006 APS

increases. Such ripening is a further indicative of kinetic limitations in the usually applied growth procedure.

### *5.3.2 Thermodynamics Versus Kinetics in Island Formation*

Stranski-Krastanow growth in a regime with a major influence of kinetics sometimes leads to experimental findings which appear inconsistent. Size and density of islands for a given deposition thickness are important parameters which are readily obtained experimentally. At low deposition temperature the diffusion length of adatoms is short and the nucleation rate is high. Consequently small islands form with a high areal density. In this *kinetic regime* the islands grow larger and the

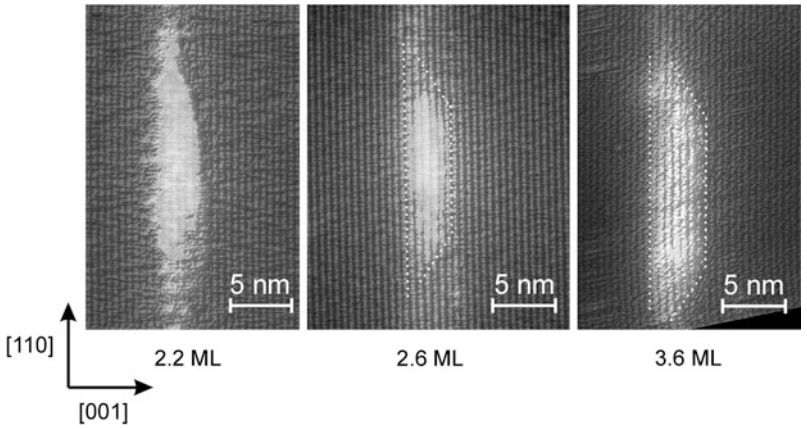


**Fig. 5.43** Cross section STM images of small InAs/GaAs(001) islands formed from various InAs coverages and buried by GaAs. The *dotted white lines* indicate the truncated pyramid shape. Courtesy of M. Dähne, TU Berlin

density accordingly decreases for a given deposition thickness as the temperature is increased. Such trend is usually observed in island formation using Stranski-Krastanow growth. On the other hand, in the *thermodynamic regime* at high temperature the size is expected to decrease in favor of a larger areal density as the deposition temperature is increased [59, 60]. Numerical results of corresponding equilibrium calculations are given in the inset of Fig. 5.44a. The maximum of the distribution function shifts to smaller island sizes and broadens as the temperature is increased. The same result is obtained from kinetic Monte Carlo (KMC) simulations shown in the main panel of Fig. 5.44 [61]. In the KMC simulation a long duration for equilibration of the island ensemble (35 s) was assumed.

The temporal evolution of the island sizes is displayed in Fig. 5.44b. The KMC simulation was performed on a lattice with $250 \times 250$ atoms and assumed an initial coverage of 4 %, randomly deposited at a flux of 1 ML/s. Adatoms diffuse by nearest neighbor hopping and may cross island edges by surmounting a Schwoebel barrier. Strain near an island is accounted for by including a position-dependent energy correction in the Arrhenius expression of the hopping rate. In the initial stage we find small islands at low temperature, whereas larger (and fewer) islands are formed at higher temperatures: The mean diffusion length increases at higher temperature, and nucleation of new islands is suppressed. Nucleation is hence the dominating process for a short duration of the evolution, a clear indication for a kinetically controlled growth. Right after deposition the island ensemble begins to equilibrate. At low temperature a slow increase of the mean island size is found. Such ripening proceeds much faster at higher temperature. Eventually the size distribution attains an equilibrium value. We note from Fig. 5.44b that the average island size now *decreases* as the temperature is increased, in agreement with equilibrium results shown in Fig. 5.44a. The study thus evidences a crossover from an initial kinetically controlled regime to thermodynamic equilibrium after an equilibration period.

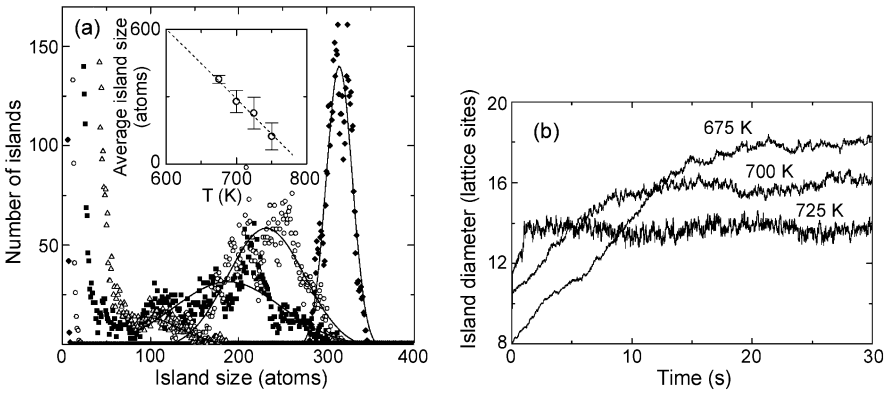


**Fig. 5.44** (**a**) Equilibrium distribution of island sizes for $T = 675$ K (*diamonds*), 700 K (*circles*), 725 K (*squares*), and 750 K *triangles*) obtained from Monte Carlo simulations on a $250 \times 250$ grid. *Solid lines* are numerical fits. *Inset*: Results from thermodynamic theory. (**b**) Simulated evolution of the mean island size for various temperatures. Reproduced with permission from [61], © 2001 APS

### *5.3.3 Wire Growth on Non-planar Surfaces*

One-dimensional structures in the nanometer-scale may be fabricated by employing a variety of growth-related phenomena [62]. Two different methods are pointed out here.

The realization of quantum wires is a challenging task. A 1D wire has a larger interface/volume ratio than a 2D quantum well and consequently makes high demands for structural quality. Interface fluctuations on a length scale of the exciton Bohr radius easily lead to localization referred to as zero-dimensional regime. Progress and true 1D properties of confined carriers was particularly achieved using V-shaped wires fabricated using patterned substrates as depicted in Fig. 3.25. The techniques utilizes the dependence of the Ga surface diffusion-length and GaAs growth rate on the crystallographic orientation of GaAs surfaces.

The diffusion length $\lambda_{\mathrm{Ga}}$ of Ga adatoms is—in a certain temperature range—approximately described by a dependence $\lambda_{\mathrm{Ga}} \propto \exp(-E_{\mathrm{eff}}/(k_{\mathrm{B}}T))$, with an effective activation energy $E_{\mathrm{eff}}$ depending on the orientation of the surface. From molecular beam epitaxy of GaAl/AlGaAs superlattices on various GaAs facets grown under Column-III limited flux conditions the following order of diffusion lengths was concluded [63]:

$$\begin{aligned}\lambda_{\mathrm{Ga}}(001) &\approx \lambda_{\mathrm{Ga}}(\bar{1}\bar{1}\bar{3})\mathrm{B}\\ &< \left\{\lambda_{\mathrm{Ga}}(\bar{1}\bar{1}\bar{1})\mathrm{B}, \lambda_{\mathrm{Ga}}(\bar{3}\bar{3}\bar{1})\mathrm{B}, \lambda_{\mathrm{Ga}}(013), \lambda_{\mathrm{Ga}}(113)A\right\}\\ &< \lambda_{\mathrm{Ga}}(159) \approx \lambda_{\mathrm{Ga}}(114)\mathrm{A} \approx \lambda_{\mathrm{Ga}}(111)\mathrm{A}\\ &< \lambda_{\mathrm{Ga}}(110).\end{aligned}$$

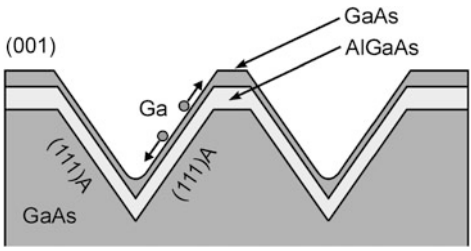


**Fig. 5.45** Schematic of GaAs wire formation on a V-shaped patterned substrate with an AlGaAs barrier layer

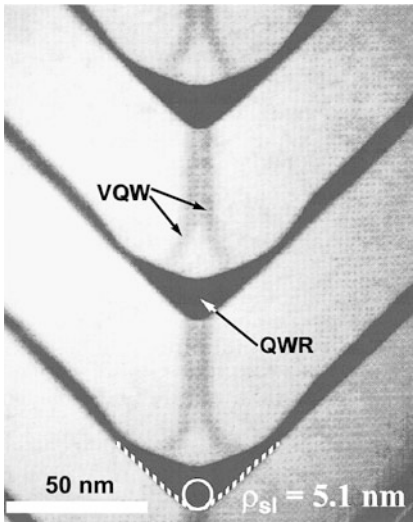


**Fig. 5.46** Cross-section transmission-electron micrograph of a vertically stacked GaAs/$Al_{0.42}Ga_{0.58}As$ quantum wires. The *white circle* marks the radius of curvature of the bottom wire interface. Reproduced with permission from [68], © 1995 AIP

The Ga diffusion length increases in the order of GaAs surfaces related to (001), $(\bar{1}\bar{1}\bar{1})$B, (111)A, and (110) orientations. $\lambda_{Ga}(001)$ was about 0.5 μm for the investigated growth at 620 °C.

On a non-planar GaAs substrate Ga adatoms migrate towards a surface with the minimum $\lambda_{Ga}$ and are incorporated there. The growth rate of facets with a larger diffusion length is therefore decreased. This effect was employed to fabricate V-shaped quantum wires [64] and also ridge quantum-wires [65, 66]. Figure 5.45 illustrates the effect of wire formation. Growth is performed on a GaAs substrate with V-shaped grooves fabricated using lithography and anisotropic wet etching. Usually grooves on a GaAs(001) substrate oriented along the $[\bar{1}10]$ direction and composed of two {111}A side walls are used. A lower AlGaAs barrier layer is then grown on the patterned substrate. The adatom diffusion-length during AlGaAs growth is quite short and does not show a pronounced facet formation; the V-groove bottom therefore remains quite sharp. In the subsequent GaAs growth Ga adatoms impinging on the {111}A side walls tend to migrate with a long diffusion length to facets with a short diffusion length. Thereby the growth rate is enhanced at the bottom of the V-groove, and a (001) facet and accompanying {311} facets are generated. Adatom migration towards the center at the V-groove bottom is supported by an additional

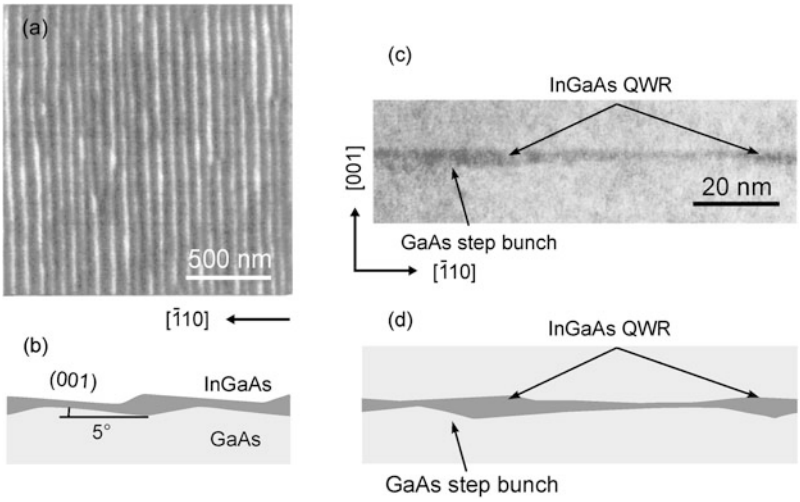


**Fig. 5.47** Formation of quantum wires from 3 nm thick InGaAs deposition on GaAs (001) misoriented 5° towards [1̄10]. (**a**) Atomic force micrograph of an $In_{0.1}Ga_{0.9}As$ layer grown on the stepped GaAs surface; adopted from [62]. (**b**) Magnified schematic of the cross section of image (**a**). (**c**) Cross-section transmission-electron micrograph and (**d**) schematic of an $In_{0.15}Ga_{0.85}As$ layer covered by a thick GaAs barrier layer. Reproduced with permission from [70], © 1997 Elsevier

capillary effect [67]. Eventually the GaAs layer is capped by an upper AlGaAs barrier, leaving buried regions of an enhanced thickness which act as quantum wires.

During growth of the upper AlGaAs layer the diffusion length of Ga adatoms is again quite short. This leads to a sharpening of the V-groove bottom, and eventually to a shape similar to that existing before the deposition of the GaAs layer. The growth sequence may then be repeated, so as to create a vertical stack of quantum wires as shown in Fig. 5.46. The dark regions in the AlGaAs layers labeled VQW (vertical QW) represent Ga-rich parts with a lower bandgap.

Self-organized growth was also applied on non-patterned substrates to fabricate quantum wires. We consider the use of step bunches which may appear on surfaces as pointed out in Sect. 5.2.6. Quantum wires forming at step bunches were studied for virtually unstrained GaAs/AlGaAs [69], but as well for strained wire/barrier materials such as InGaAs/GaAs [70], InGaAs/InP, and SiGe/Si [71] on various low-index surfaces. The strain-induced interaction among steps in superlattice wire-structures was shown to favor the ordering of step bunching [72], leading to wires with regular lateral spacing [71]. The formation of wire material at steps of the barrier material may be attributed to the process of step-flow growth (Sect. 5.2.4) and the lower surface energy of the wire material. Furthermore, elastic relaxation of strained wire material is enhanced at step edges.

Formation of InGaAs quantum wires on a vicinal GaAs (001) surface misoriented by 5° towards the [1̄10] direction is illustrated in Fig. 5.47. The vicinal GaAs surface forms step bunches of ∼6.1 nm height and 70 nm spacing running along [110].

The terraces correspond to singular (001) faces. Metalorganic vapor-phase epitaxy of 3 nm thick InGaAs on this GaAs surface basically reproduces the stepped surface morphology [70]. InGaAs quantum wires form after growth of an upper GaAs barrier layer. The cross-sectional TEM image Fig. 5.47c shows ∼6 nm thick quantum wires with a lateral width of ∼25 nm. The thickness of the persisting quantum well on the (001) facets is ∼1.3 nm, yielding a growth enhancement of a factor of 4 at the step edges.

## 5.4 Problems Chap. 5

5.1 Consider a Kossel crystal with the shape of a cube with edge length $n \times a$, consisting of atom cubes with edge length $a$.
   (a) Determine the number of atoms $N_i$ which differ in energy. Assume only nearest-neighbor bonds and distinguish between atoms in the bulk, on the faces (but not at corners or edges), at the edges (not at a corner), and at corners. Calculate $N_i$ for $n$ equals 10 and 1000, and check that the total number equals $n^3$.
   (b) The number of bonds for the different types of atoms noted in (a) differs. With 1 bond of energy $E_b$ shared by 2 neighbored atoms, a bulk atom has an energy $E = 6 \times E_b \times \frac{1}{2} = 3E_b$. Calculate the respective energies for the different types of atoms. The contribution of atoms at the surface (= faces, corners, and edges) to the total energy $E_{tot}$ of all atoms decreases as the size of the crystal increases. Find the fraction of their energy contribution to $E_{tot}$ for $n = 10^1$ to $10^4$ in steps by a factor of 10. Compare the result for a large number $n$ to that obtained when only bulk and face atoms are considered.

5.2 The $\beta 2(2 \times 4)$ reconstruction of the As-rich GaAs(001) surface contains two As dimers in the 1st (top) layer and one in the 3rd layer. The reconstruction complies with the electron-counting model similar to the missing-dimer $(2 \times 4)$ surface discussed in the text (cf. Fig. 5.11).
   (a) Apply electron counting for the $\beta 2(2 \times 4)$ reconstruction by listing the required and the available electrons in the topmost 4 layers, assuming dangling Ga bonds empty and dangling As bonds filled. How many electrons are involved?
   (b) Repeat (a) for the related Ga-rich $\beta 2(4 \times 2)$ reconstruction. In this surface the As atoms are exchanged for Ga atoms and vice versa, yielding two Ga dimers in the first and one in the third layer (cf. Fig. 5.11). Does the $\beta 2(4 \times 2)$ reconstruction comply with the electron-counting rule?

5.3 The surface diffusion of Ga is the rate-determining process in the epitaxy of GaAs under excess arsenic pressure. An experiment on the temperature-dependent surface-diffusion length $\lambda$ yields the following four data points for an Arrhenius plot of $\lambda$/cm versus 1000/T/K: $5.3 \times 10^{-6}$, 1.00; $7.5 \times 10^{-6}$, 1.05; $7.0 \times 10^{-6}$, 1.20; $5.5 \times 10^{-6}$, 1.25. Assume that the diffusion length of the first two data points in the high-temperature range is solely governed by

the diffusion barrier, and the latter data points also reflect a pure exponential behavior which is additionally affected by the adsorption energy.
(a) Calculate the energy of the diffusion barrier and the adsorption energy.
(b) Find two different temperatures where the diffusion length equals $4.0 \times 10^{-6}$ cm.

5.4 We consider adatoms on a Si surface.
(a) How long is the residence time of an adatom at 1000 °C? Assume 2.0 eV adsorption energy and a typical atomic vibration frequency of $10^{13}$ Hz. Find the surface diffusivity, if the mean diffusion length of $4 \times 10^{-5}$ cm is limited by the residence time. What is the diffusion length at 800 °C, if the diffusion barrier is half the adsorption energy?
(b) Step-flow growth occurs, if the surface diffusion-length exceeds well the terrace width. Find the height of a (not reconstructed) single Si(001) monolayer and the angle for a small miscut along [100] required to produce equidistant terraces with 200 nm width and 1 monolayer high steps. Find the rate for the advancement of the step for 1 μm/h growth rate on the Si surface.

5.5 An InAs island of pyramidal shape with 10 nm base length, bound by unreconstructed (110) side facets, is formed on a 1.40 monolayer thick wetting layer on GaAs substrate. The lattice parameter of InAs is approximately 6.1 Å. Neglect the strain in the following assessments.
(a) Estimate the number of In and As atoms in the island.
(b) Which thickness has the initially deposited two-dimensional InAs layer before the formation of the islands, if $4 \times 10^{10}$ cm$^{-2}$ islands are generated?
(c) What were the thickness of the initially deposited two-dimensional InAs layer, if islands of the same areal density as in (b) were generated, but with a shape of a spherical cap? The diameter and contact angle of these islands are assumed to be 10 nm and 45°, respectively (compare to Fig. 4.10). How many In and As atoms contains one of these islands?

## 5.5 General Reading Chap. 5

A. Pimpinellei, J. Villain, *Physics of Crystal Growth* (Cambridge University Press, Cambridge, 1998)
W.K. Burton, N. Cabrera, F.C. Frank, The growth of crystals and the equilibrium structure of their surfaces. Philos. Trans. R. Soc. Lond. A **243**, 299–358 (1951)
K. Oura, V.G. Lifshits, A.A. Saranin, A.V. Zotov, M. Katayama, *Surface Science—An Introduction*, 1st edn. (Springer, Berlin, 2003)
H. Ibach, *Physics of Surfaces and Interfaces* (Springer, Berlin, 2006)
F. Bechstedt, *Principles of Surface Physics* (Springer, Berlin 2003)

## References

1. D.J. Chadi, Atomic and electronic structures of reconstructed Si(100) surfaces. Phys. Rev. Lett. **43**, 43 (1979)

2. M.D. Pashley, Electron counting model and its application to island structures on molecular-beam epitaxy grown GaAs(001) and ZnSe(001). Phys. Rev. B **40**, 10481 (1989)
3. W.A. Harrison, Theory of polar semiconductor surfaces. J. Vac. Sci. Technol. **16**, 1492 (1979)
4. S. Yuan, L. Zhang, H. Chen, E. Wang, Z. Zhang, Generic principle for the prediction of metal-induced reconstructions of compound semiconductor surfaces. Phys. Rev. B **78**, 075305 (2008)
5. E.A. Wood, Vocabulary of surface crystallography. J. Appl. Phys. **35**, 1306 (1964)
6. L. Däweritz, R. Hey, Reconstruction and defect structure of vicinal GaAs(001) and $Al_xGa_{1-x}As(001)$ surfaces during MBE growth. Surf. Sci. **236**, 15 (1990)
7. V.P. LaBella, H. Yang, D.W. Bullok, P.M. Thibado, P. Kratzer, M. Scheffler, Atomic structure of the GaAs(001)-(2 × 4) surface resolved using scanning tunneling microscopy and first-principles theory. Phys. Rev. Lett. **83**, 2989 (1999)
8. A. Ohtake, P. Kocán, J. Nakamura, A. Natori, N. Koguchi, Kinetics in surface reconstructions on GaAs(001). Phys. Rev. Lett. **92**, 236105 (2004)
9. N. Moll, A. Kley, E. Pehlke, M. Scheffler, GaAs equilibrium crystal shape from first principles. Phys. Rev. B **54**, 8844 (1996)
10. J.E. Northrup, S. Froyen, Structure of GaAs(001) surfaces: the role of electrostatic interactions. Phys. Rev. B **50**, 2015 (1994)
11. W.G. Schmidt, S. Mirbt, F. Bechstedt, Surface phase diagram of (2 × 4) and (4 × 2) reconstructions of GaAs(001). Phys. Rev. B **62**, 8087 (2000)
12. N. Chetty, R.M. Martin, Determination of integrals at surfaces using the bulk crystal symmetry. Phys. Rev. B **44**, 5568 (1991)
13. E. Penev, P. Kratzer, M. Scheffler, Atomic structure of the GaAs(001) surface: first-principles evidence for diversity of heterodimer motifs. Phys. Rev. Lett. **93**, 146102 (2004)
14. F. Bechstedt, R. Enderlein, *Semiconductor Surfaces and Interfaces* (Akademie Verlag, Berlin, 1988)
15. K. Oura, V.G. Lifshits, A.A. Saranin, A.V. Zotov, M. Katayama, *Surface Science: An Introduction* (Springer, Berlin, 2003)
16. K. Takayanagi, Y. Tanishiro, S. Takahashi, M. Takahashi, Structure analysis of Si(111)-7 × 7 reconstructed surface by transmission electron diffraction. Surf. Sci. **164**, 367 (1985)
17. K.D. Brommer, M. Needels, B.E. Larson, J.D. Joannopoulos, Ab initio theory of the Si(111)-(7 × 7) surface reconstruction: a challenge for massively parallel computation. Phys. Rev. Lett. **68**, 1355 (1992)
18. R.S. Becker, J.A. Golovchenko, G.S. Higashi, G.S. Swartzentruber, New reconstructions on silicon (111) surfaces. Phys. Rev. Lett. **57**, 1020 (1986)
19. W.K. Burton, N. Cabrera, F.C. Frank, The growth of crystals and the equilibrium structure of their surfaces. Philos. Trans. R. Soc. Lond. A **243**, 299 (1951)
20. J.A. Venables, G.D.T. Spiller, M. Hanbrücken, Nucleation and growth of thin films. Rep. Prog. Phys. **47**, 399 (1984)
21. J.A. Venables, Rate equation approaches to thin film nucleation kinetics. Philos. Mag. **27**, 693 (1973)
22. S.V. Ghaisas, A. Madhukar, Role of surface molecular reactions in the growth mechanism and the nature of nonequilibrium surfaces: a Monte Carlo study of molecular-beam epitaxy. Phys. Rev. Lett. **56**, 1066 (1986). A comprehensive essay is given in [23]
23. A. Madhukar, S.V. Ghaisas, The nature of molecular beam epitaxial growth examined via computer simulations. CRC Crit. Rev. Solid State Mater. Sci. **14**, 1 (1988)
24. G. Ehrlich, F.G. Hudda, Atomic view of surface self-diffusion: tungsten on tungsten. J. Chem. Phys. **44**, 1039 (1966)
25. R.L. Schwoebel, E.J. Shipsey, Step motion on crystal surfaces. J. Appl. Phys. **37**, 3682 (1966)
26. G.S. Bales, A. Zangwill, Morphological instability of a terrace edge during step-flow growth. Phys. Rev. B **41**, 5500 (1990). Erratum referring to one equation cf. G.S. Bales, A. Zangwill, Phys. Rev. B **48**, 2024 (1993)
27. A. Pimpinelli, J. Villain, *Physics of Crystal Growth* (Cambridge University Press, Cambridge, 1998)

28. O. Pierre-Louis, M.R. D'Orsogna, T.L. Einstein, Edge diffusion during growth: the Kink-Ehrlich-Schwoebel effect and resulting instabilities. Phys. Rev. Lett. **82**, 3661 (1999)
29. M.V.R. Murty, B.H. Cooper, Instability in molecular beam epitaxy due to fast edge diffusion and corner diffusion barriers. Phys. Rev. Lett. **83**, 352 (1999)
30. D.J. Chadi, Stabilities of single-layer and bilayer steps on Si(001) surfaces. Phys. Rev. Lett. **59**, 1691 (1987)
31. B.S. Schwartzentruber, Y.-W. Mo, R. Kariotis, M.G. Lagally, M.B. Webb, Direct determination of step and kink energies on vicinal Si(001). Phys. Rev. Lett. **65**, 1913 (1990)
32. R.G.S. Pala, S. Liu, Critical epinucleation on reconstructured surfaces and first-principle calculation of homonucleation on Si(100). Phys. Rev. Lett. **95**, 136106 (2005)
33. B. Voigtländer, M. Kästner, P. Smilauer, Magic islands in Si/Si(111) homoepitaxy. Phys. Rev. Lett. **81**, 858 (1998). A movie on island growth is accessible at www.fz-juelich.de/video/voigtlaender
34. W. Shimada, H. Tochihara, Step-structure dependent step-flow: models for the homoepitaxial growth at the atomic steps on Si(111)7 × 7. Surf. Sci. **311**, 107 (1994)
35. H. Tochihara, W. Shimada, The initial process of molecular beam epitaxial growth of Si on Si(111)7 × 7: a model for the destruction of the 7 × 7 reconstruction. Surf. Sci. **296**, 186 (1993)
36. S. Filimonov, V. Cherepanov, Y. Hervieu, B. Voigtländer, Multistage nucleation of two-dimensional Si islands on Si(111)-7 × 7 homoepitaxy during MBE growth. Phys. Rev. B **76**, 035428 (2007)
37. M. Itoh, G.R. Bell, B.A. Joyce, D.D. Vvedensky, Transformation kinetics of homoepitaxial islands on GaAs(001). Surf. Sci. **464**, 200 (2000)
38. P. Kratzer, M. Scheffler, Reaction-limited island nucleation in molecular beam epitaxy of compound semiconductors. Phys. Rev. Lett. **88**, 036102 (2002)
39. C.T. Foxon, B.A. Joyce, Interaction kinetics of $As_2$ and Ga on {100} GaAs surfaces. Surf. Sci. **64**, 293 (1977)
40. P. Kratzer, C.G. Morgan, M. Scheffler, Density-functional theory studies on microscopic processes of GaAs growth. Prog. Surf. Sci. **59**, 135 (1998)
41. E.S. Tok, J.H. Neave, J. Zhang, B.A. Joyce, T.S. Jones, Arsenic incorporation kinetics in GaAs(001) homoepitaxy revisited. Surf. Sci. **374**, 397 (1997)
42. A. Kley, P. Ruggerone, M. Scheffler, Novel diffusion mechanism on the GaAs(001) surface: the role of adatom-dimer interaction. Phys. Rev. Lett. **79**, 5278 (1997)
43. P. Kratzer, C.G. Morgan, M. Scheffler, Model for the nucleation in GaAs homoepitaxy derived from first principles. Phys. Rev. B **59**, 15246 (1999)
44. V.A. Shchukin, N.N. Ledentsov, P.S. Kop'ev, D. Bimberg, Spontaneous ordering of arrays of coherent strained islands. Phys. Rev. Lett. **75**, 2968 (1995)
45. L.G. Wang, P. Kratzer, M. Scheffler, N. Moll, Formation and stability of self-assembled coherent islands in highly mismatched heteroepitaxy. Phys. Rev. Lett. **82**, 4042 (1999)
46. N. Moll, M. Scheffler, E. Pehlke, Influence of surface stress on the equilibrium shape of strained quantum dots. Phys. Rev. B **58**, 4566 (1998)
47. A. Rastelli, M. Kummer, H. Von Känel, Reversible shape evolution of Ge islands on Si(001). Phys. Rev. Lett. **87**, 256101 (2001)
48. J. Márquez, L. Geelhaar, K. Jacobi, Atomically resolved structure of InAs quantum dots. Appl. Phys. Lett. **78**, 2309 (2001)
49. T. Xu, L. Zhou, Y. Wang, A.S. Özcan, K.F. Ludwig, GaN quantum dot superlattices grown by molecular beam epitaxy at high temperature. J. Appl. Phys. **102**, 073517 (2007)
50. M. Pinczolits, G. Springholz, G. Bauer, Direct formation of self-assembled quantum dots under tensile strain by heteroepitaxy of PbSe on PbTe (111). Appl. Phys. Lett. **73**, 250 (1998)
51. S. Ruvimov, P. Werner, K. Scheerschmidt, U. Gösele, J. Heydenreich, U. Richter, N.N. Ledentsov, M. Grundmann, D. Bimberg, V.M. Ustinov, A.Yu. Egorov, P.S. Kop'ev, Zh.I. Alferov, Phys. Rev. B **51**, 14766 (1995)
52. Y. Nabetani, T. Ishikawa, S. Noda, A. Sasaki, Initial growth stage and optical properties of a three-dimensional InAs structure on GaAs. J. Appl. Phys. **76**, 347 (1994)

53. D. Leonard, K. Pond, P.M. Petroff, Critical layer thickness for self-assembled InAs islands on GaAs. Phys. Rev. B **50**, 11687 (1994)
54. I. Daruka, J. Tersoff, A.-L. Barabási, Shape transition in growth of strained islands. Phys. Rev. Lett. **82**, 2753 (1999)
55. G. Costantini, A. Rastelli, C. Manzano, P. Acosta-Diaz, R. Songmuang, G. Katsaros, O.G. Schmidt, K. Kern, Interplay between thermodynamics and kinetics of InAs/GaAs(001) quantum dots. Phys. Rev. Lett. **96**, 226106 (2006)
56. H. Eisele, A. Lenz, R. Heitz, R. Timm, M. Dähne, Y. Temko, T. Suzuki, K. Jacobi, Change of InAs/GaAs quantum dot shape and composition during capping. J. Appl. Phys. **104**, 124301 (2008)
57. U.W. Pohl, K. Pötschke, A. Schliwa, F. Guffarth, D. Bimberg, N.D. Zakharov, P. Werner, M.B. Lifshits, V.A. Shchukin, D.E. Jesson, Evolution of a multimodal distribution of self-organized InAs/GaAs quantum dots. Phys. Rev. B **72**, 245332 (2005)
58. G. Costantini, A. Rastelli, C. Manzano, R. Songmuang, O.G. Schmidt, K. Kern, H. von Känel, Universal shapes of self-organized semiconductor quantum dots: striking similarities between InAs/GaAs(001) and Ge/Si(001). Appl. Phys. Lett. **85**, 5674 (2004)
59. V.A. Shchukin, N.N. Ledentsov, D. Bimberg, Entropy effects in self-organized formation of nanostructures, in *NATO advanced workshop on atomistic aspects of epitaxial growth*, ed. by M. Kortla, et al. (Kluwer, Dordrecht, 2002)
60. V.A. Shchukin, N.N. Ledentsov, D. Bimberg, *Epitaxy of Nanostructures* (Springer, Berlin, 2004)
61. M. Meixner, E. Schöll, V.A. Shchukin, D. Bimberg, Self-assembled quantum dots: crossover from kinetically controlled to thermodynamically limited growth. Phys. Rev. Lett. **87**, 236101 (2001)
62. X.-L. Wang, V. Voliotis, Epitaxial growth and optical properties of semiconductor quantum wires. J. Appl. Phys. **99**, 121301 (2006)
63. T. Takebe, M. Fujii, Y. Yamamoto, K. Fujita, T. Watanabe, Orientation-dependent Ga surface diffusion in molecular beam epitaxy of GaAs on GaAs patterned substrates. J. Appl. Phys. **81**, 7273 (1997)
64. R. Bhat, E. Kapon, D.M. Hwang, M.A. Koza, C.P. Yun, Patterned quantum well heterostructures grown by OMCVD on non-planar substrates: applications to extremely narrow SQW lasers. J. Cryst. Growth **93**, 850 (1988)
65. S. Koshiba, N. Noge, H. Akiyama, T. Inoshita, Y. Nakamura, A. Shimizu, Y. Nagamune, M. Tsuchiya, H. Kano, H. Sasaki, Formation of GaAs ridge quantum wire structures by molecular beam epitaxy on patterned substrates. Appl. Phys. Lett. **64**, 363 (1994)
66. T. Sato, I. Tamai, H. Hasegawa, Growth kinetics and modeling of selective molecular beam epitaxial growth of GaAs ridge quantum wires on pre-patterned nonplanar substrates. J. Vac. Sci. Technol. B **22**, 2266 (2004)
67. G. Biasiol, A. Gustafsson, K. Leifer, E. Kapon, Mechanisms of self-ordering in nonplanar epitaxy of semiconductor nanostructures. Phys. Rev. B **65**, 205306 (2002)
68. A. Gustafsson, F. Reinhardt, G. Biasiol, E. Kapon, Low-pressure organometallic chemical vapor deposition of quantum wires on V-grooved substrates. Appl. Phys. Lett. **67**, 3673 (1995)
69. S. Hara, J. Motohisa, T. Fukui, H. Hasegawa, Quantum well wire fabrication method using self-organized multiatomic steps on vicinal (001) GaAs surfaces by metalorganic vapor phase epitaxy. Jpn. J. Appl. Phys. **34**, 4401 (1995)
70. S. Hara, J. Motohisa, T. Fukui, Formation and characterization of InGaAs strained quantum wires on GaAs multiatomic steps grown by metalorganic vapor phase epitaxy. J. Cryst. Growth **170**, 579 (1997)
71. K. Brunner, Si/Ge nanostructures. Rep. Prog. Phys. **65**, 27 (2002)
72. L. Bai, J. Tersoff, F. Liu, Self-organized quantum-wire lattice via step flow growth of a short-period superlattice. Phys. Rev. Lett. **92**, 225503 (2004)

# Chapter 6
# Doping, Diffusion, and Contacts

**Abstract** The ability to control the conductivity is an essential feature of semiconductors. This chapter points out the basics for the control of the free carrier concentration and discusses the nature of limiting factors. The integrity of doping profiles and of interfaces in heterostructures depends on the stability of atoms against a change of lattice site. We briefly consider fundamentals of diffusion and discuss some basic mechanisms governing the diffusivity of atoms in a crystal. The chapter concludes with concepts for ohmic metal-semiconductor contacts.

Device applications of semiconductors require control of the free carrier concentration and application of ohmic contacts for carrier injection or extraction. The conductivity of a semiconductor can be varied over a wide range from semi-insulating to semi-metallic by the introduction of impurities. The substitutional replacement of a semiconductor atom by, e.g., a dopant atom with a chemical valence incremented by one introduces an additional electron and a positive charge at the ion core. For suitable dopant species the electron may thermally be released at room temperature due to a small binding energy, allowing for adjusting the conductivity via the concentration of impurities. The same applies for the creation of free holes by substitutional dopants with a lower chemical valence. The simple concept works particularly well for low doping levels and many semiconductors with a bandgap below about 2 eV. Section 6.1 points out the essentials for conductivity control, limits imposed by thermodynamics, and the nature of limiting factors.

Doping profiles are often created via diffusion by providing a concentration gradient of the doping species. Diffusion phenomena also control the abruptness of semiconductor interfaces. The underlying concepts are treated in Sect. 6.2.

Ohmic contacts are usually fabricated by evaporation of a contact metal on heavily doped semiconductor layers. Besides such non-epitaxial techniques also epitaxial contact structures may provide a solution in special cases. Basic concepts for ohmic metal-semiconductor contacts are discussed in Sect. 6.3.

## 6.1 Doping of Semiconductors

The use of semiconductors in electronic and optoelectronic devices requires the reliable control of bipolar conductivity. Typical concentrations of impurities employed

U.W. Pohl, *Epitaxy of Semiconductors*, Graduate Texts in Physics,
DOI 10.1007/978-3-642-32970-8_6, 

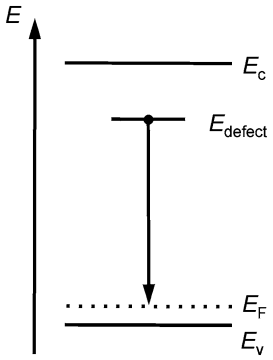


**Fig. 6.1** Compensation of $p$-type doping by a native donor defect, which introduces an occupied level $E_{\text{defect}}$ near the conduction band

for doping are in the $10^{15}$–$10^{20}$ cm$^{-3}$ range, compared to about $5 \times 10^{22}$ atoms/cm$^3$ of the host semiconductor. Doping of shallow impurities for both, donors and acceptors is usually well achieved for semiconductors with a sufficiently small bandgap energy such as Si. In contrast, wide-bandgap semiconductors with a gap energy above ~2 eV like, e.g., many II–VI compounds and group-III nitrides can typically be doped either $n$-type or $p$-type, but not both. It is exceedingly difficult to achieve $n$-type conductivity in ZnTe or $p$-type conductivity in ZnO. Fundamental problems arise from various origins. The solubility of dopants imposes limits for incorporation, a large ionization energy may hamper activation, native defects may compensate an intentional doping, dopants may change their character depending on the incorporation site or lattice relaxation, and eventually hydrogen may passivate dopants. Many of these processes are related to the bandgap energy, and are hence particularly pronounced in wide bandgap semiconductors. The effect is illustrated in Fig. 6.1 for the compensation of $p$-type doping by a native donor defect. The intentional $p$-type doping moves the Fermi level $E_{\text{F}}$ to the valence-band edge $E_{\text{v}}$. The creation of a point defect made of host atoms like, e.g., an interstitial atom consumes some formation energy, but the transfer of the electron from its occupied donor level $E_{\text{defect}}$ near the conduction band $E_{\text{c}}$ to the Fermi level may recoup this energy. Since the energy gained by such compensation is of the order of the bandgap energy, the tendency for native defect compensation increases as the bandgap increases.

Dopant incorporation during epitaxial growth may occur far from thermal equilibrium, potentially allowing to achieve a net doping which cannot be achieved under equilibrium-near conditions. In the following we treat basic concepts to obtain conductivity control.

### *6.1.1 Thermal Equilibrium Carrier-Densities*

The density of electrons $n$ in the conduction band at temperature $T$ is given by the Fermi-Dirac distribution function $f_n$ and depends on the density of energy levels in the conduction band $D_{\text{c}}(E)$ and the value of the Fermi energy $E_{\text{F}}$,

$$n = \int_{E_{\text{c}}}^{\infty} D_{\text{c}}(E) \frac{1}{e^{(E-E_{\text{F}})/k_{\text{B}}T} + 1} dE. \tag{6.1}$$

The Fermi energy $E_\mathrm{F}$ of charge carriers is also referred to as chemical potential $\mu$. A similar expression as (6.1) holds for the density of holes $p$ in the valence band with density-of-states $D_\mathrm{v}$ and a distribution function $f_h = 1 - f_n$,

$$p = \int_{-\infty}^{E_\mathrm{v}} D_\mathrm{v}(E)\left(1 - \frac{1}{e^{(E-E_\mathrm{F})/k_\mathrm{B}T}+1}\right)dE. \tag{6.2}$$

Equations (6.1) and (6.2) are simplified, if the position of the chemical potential is not in the vicinity of one of the band edges, i.e., if conditions $E_\mathrm{c} - E_\mathrm{F} \gg k_\mathrm{B}T$ or $E_\mathrm{F} - E_\mathrm{v} \gg k_\mathrm{B}T$ hold, respectively. Such semiconductors are called nondegenerate. The Fermi distribution may then be replaced by the Boltzmann distribution by omitting the term "+1" in the denominator. Due to the exponential factors in the simplified integrals only energies within $k_\mathrm{B}T$ at the band edges give significant contributions. The band edges are then well described by a quadratic approximation, yielding the density of states

$$D_{\mathrm{c,v}}(E) = \frac{\sqrt{2}m_{\mathrm{e,h}}^{*\,3/2}}{\hbar^3\pi^2}\sqrt{|E - E_{\mathrm{c,v}}|} \tag{6.3}$$

with the effective masses of electrons $m_\mathrm{e}^*$ and holes $m_\mathrm{h}^*$. The effective masses include potentially occurring degeneracy and anisotropy. For Si, e.g., the conduction band is 6-fold degenerate and comprises longitudinal and transversal mass components, yielding $m_\mathrm{e}^* = 6^{2/3} \times (m_t^2 \times m_l)^{1/3}$. Similarly, the hole mass includes heavy-hole and light-hole contributions (the split-off hole is usually not occupied), yielding $m_\mathrm{h}^* = (m_\mathrm{hh}^{3/2} + m_\mathrm{lh}^{3/2})^{2/3}$.

Using the density of states (6.3), Eqs. (6.1) and (6.2) for the carrier densities read

$$n = 2\left(\frac{m_\mathrm{e}^* k_\mathrm{B}T}{2\pi\hbar^2}\right)^{3/2} e^{-(E_\mathrm{c}-E_\mathrm{F})/k_\mathrm{B}T} = D_\mathrm{c}^\mathrm{eff} e^{-(E_\mathrm{c}-E_\mathrm{F})/k_\mathrm{B}T}, \tag{6.4a}$$

$$p = 2\left(\frac{m_\mathrm{h}^* k_\mathrm{B}T}{2\pi\hbar^2}\right)^{3/2} e^{-(E_\mathrm{F}-E_\mathrm{v})/k_\mathrm{B}T} = D_\mathrm{v}^\mathrm{eff} e^{-(E_\mathrm{F}-E_\mathrm{v})/k_\mathrm{B}T}. \tag{6.4b}$$

The prefactors of the exponential functions in (6.4a), (6.4b) are the effective densities of states at the edges of conduction and valence bands $D_\mathrm{c}^\mathrm{eff}$ and $D_\mathrm{v}^\mathrm{eff}$, respectively. The dependence on the until now unknown position of the chemical potential disappears from the *product* of the carrier densities,

$$n \times p = 4\left(\frac{k_\mathrm{B}T}{2\pi\hbar^2}\right)^3 \left(m_\mathrm{e}^* m_\mathrm{h}^*\right)^{3/2} e^{-E_\mathrm{g}/k_\mathrm{B}T}, \tag{6.5}$$

where $E_\mathrm{g} = E_\mathrm{c} - E_\mathrm{v}$ is the bandgap energy. This relation is called the *law of mass action* and applies for nondegenerate semiconductors. It means that at a given temperature the density of one carrier type is given by the density of the other. The position of the Fermi energy $E_\mathrm{F}$ within the bandgap follows from (6.4a), (6.4b). If we resolve (6.4a) for $E_\mathrm{c} - E_\mathrm{F}$ we obtain

$$E_\mathrm{c} - E_\mathrm{F} = k_\mathrm{B}T \ln\left(\frac{D_\mathrm{c}^\mathrm{eff}}{n}\right). \tag{6.5a}$$

In devices the electron density $n$, and consequently $E_F$, is controlled by doping and basically given by the density of ionized donors $N_D$ and acceptors $N_A$, i.e., $n \approx N_D - N_A$. But also in an undoped semiconductor the Fermi level is not fixed.

If in a pure crystal the contribution of impurity donors or acceptors to the carrier densities is negligible, the semiconductor is called *intrinsic*. In this case each electron in the conduction band originates from the valence band, $n = p \equiv n_i$. The value of the intrinsic carrier density $n_i$ at any temperature is given by the square root of (6.5). We note that the intrinsic carrier concentration decreases exponentially as the bandgap increases. At $T = 300$ K we find values of, e.g., Ge ($E_g = 0.67$ eV, $n_i \approx 10^{13}$ cm$^{-3}$), Si (1.12 eV, $\sim 10^{10}$ cm$^{-3}$), GaAs (1.43 eV, $\sim 10^{6}$ cm$^{-3}$), and GaP (2.26 eV, $\sim 10^{0}$ cm$^{-3}$), illustrating the trend. In the intrinsic case the position of the chemical potential, $E_F$, follows from the charge neutrality condition $n = p$ and (6.1), (6.2), yielding

$$E_F = E_v + \frac{E_g}{2} + \frac{3}{4} k_B T \ln\left(\frac{m_h^*}{m_e^*}\right) \quad \text{(intrinsic case)}. \tag{6.6}$$

At $T = 0$ the chemical potential lies in the middle of the energy gap. Since $m_h^*$ is typically less than an order of magnitude larger than $m_e^*$, the last term in (6.6) is of order $k_B T$. This is usually much less than $E_g$, leading to a near midgap position of $E_F$ at finite temperatures.

To control conductivity *impurities* are introduced in the crystal as sources of free carriers. The semiconductor is then called *extrinsic*. For efficient doping the energy level introduced by a dopant should lie in the bandgap near the band edge to allow for thermal activation at the intended operating temperature. Such impurities are referred to as *shallow impurities*. In a nondegenerate semiconductor the density of band states $D_v(E)$ or $D_c(E)$ is not considerably altered by doping.

Shallow donor impurities are well described in analogy to a hydrogen atom. A substitutional donor has a higher chemical valence than the replaced host atom. A single donor introduces a positive charge at the ion core and an additional electron. The binding energy of the electron is strongly reduced compared to the Rydberg energy $Ry = 13.6$ eV of hydrogen due to the electron motion in the medium of the semiconductor with a dielectric constant $\varepsilon_r$. Replacing in the hydrogen problem $\varepsilon_0$ by $\varepsilon = \varepsilon_r \varepsilon_0$, $\varepsilon_r$ being the (relative) permittivity of the semiconductor, and the free electron mass $m_0$ by the effective mass $m_e^*$, we obtain the binding energy of the donor electron in the ground state

$$E_D^b = \frac{m_e^*}{m_0} \frac{1}{\varepsilon_r^2} \times Ry. \tag{6.7}$$

$E_D^b$ is also referred to as donor Rydberg energy or donor ionization energy. The position of the donor energy in the bandgap is $E_D = E_g - E_D^b$. Taking typical values $m_e^* \approx m_0/10$ and $\varepsilon_r \approx 10$ we obtain binding energies of the order 10 meV. Donors which fulfill the approximation (6.7) are referred to as *effective-mass donors*.

The effective-mass and dielectric constant corrections lead to a donor Bohr radius

$$a_B^* = \frac{\varepsilon_r m_e^*}{m_0} \times a_B, \tag{6.8}$$

**Table 6.1** Binding energies of donors ($E_D^b$) and acceptors ($E_A^b$) in Si, GaAs (donor data from [3], $C_{Ga}$ and acceptors from [4]), and ZnSe (donor data from [5], acceptor data from [6], $Li_i$ from [7])

| Host | Bandgap $E_g$ (eV) | Donor Rydberg $E_D^b$ (meV) | | Acceptor Rydberg $E_A^b$ (meV) | |
|---|---|---|---|---|---|
| Si | 1.12 | $P_{Si}$ | 45 | $B_{Si}$ | 45 |
| | | $As_{Si}$ | 49 | $Al_{Si}$ | 57 |
| | | $Sb_{Si}$ | 39 | $Ga_{Si}$ | 65 |
| GaAs | 1.42 | $S_{As}$ | 5.9 | $Be_{Ga}$ | 28 |
| | | $Te_{As}$ | 5.8 | $Mg_{Ga}$ | 29 |
| | | $Sn_{Ga}$ | 5.8 | $Zn_{Ga}$ | 31 |
| | | $C_{Ga}$ | 5.9 | $C_{As}$ | 27 |
| ZnSe | 2.67 | $Al_{Zn}$ | 25.7 | $N_{Se}$ | ∼110 |
| | | $Ga_{Zn}$ | 27.5 | $P_{Se}$ | ∼87 |
| | | $In_{Zn}$ | 28.2 | $As_{Se}$ | ∼105 |
| | | $Li_i$ | ∼26 | $Li_{Zn}$ | ∼114 |

with the hydrogen Bohr radius $a_B = 0.53$ Å. Inserting typical values noted above yields an order of 50 Å. The electron orbit hence extends over many lattice constants. In such a case the description of a screened donor Coulomb potential by the effective dielectric constant $\varepsilon_r$ is a good approximation. The usually small differences found for different shallow donors, termed chemical shift, are accounted for by a central cell correction to the coulomb potential.

An acceptor impurity has a lower chemical valence than a host atom. The missing electron is represented by a hole, which is bound to the excess negative charge of the acceptor core. An application of the hydrogen analogy to a shallow acceptor impurity must account for the more complicated structure of the valence band (Sect. 3.1). The dispersion of holes near the center of the Brillouin zone of semiconductors with zincblende or diamond structure is often described by the Luttinger parameters $\gamma_1$, $\gamma_2$, and $\gamma_3$ [1]. $1/\gamma_1$ is a multiplying factor (of order $10^{-1}$) in the acceptor binding energy $E_A^b$ described analogous to (6.7) for the light and heavy holes. To obtain the acceptor ionization energy an additional multiplication by a function $f(\gamma_1, \gamma_2, \gamma_3)$ is required, $f$ covering values between 1 and 5. A more detailed treatment is given, e.g., in [2]. Rydberg energies of some dopants in semiconductors are given in Table 6.1.

We restrict ourselves to $n$-type doping with shallow donors to discuss the effect of doping. Electrons in the conduction band originate either from ionized donors or from the valence band, $n = N_D^+ + p$. $N_D^+$ denotes the density of positively charged donors, which lost their electron by thermal activation. The value follows from the total density of donors $N_D$ and an electron occupation of donors depending on the activation energy $E_D^b$. Furthermore, the degeneracy $g$ for the occupation of the donor ground-state must be included in the Fermi distribution function, yielding

$$N_D^+ = N_D\left(1 - \frac{1}{\frac{1}{g}e^{(E_D - E_F)/k_B T} + 1}\right) \quad \text{(only donors)}. \tag{6.9}$$

For effective-mass donors $g = 2$ due to an occupation with an electron of either spin (up or down). We now consider the semiconductor at low temperatures and neglect the small intrinsic contribution of $p$ electrons, i.e., $n_\mathrm{i} \ll N_\mathrm{D}^+$, yielding

$$n = N_\mathrm{D}^+ \quad \text{(low temperatures)}. \tag{6.10}$$

At low temperatures most donors are not ionized, and the occupation of the conduction band is described by Boltzmann statistics used in (6.4a). We hence may express the chemical potential in (6.9) by

$$e^{E_\mathrm{F}/k_\mathrm{B}T} = \left(n/D_\mathrm{c}^\mathrm{eff}\right) e^{E_\mathrm{c}/k_\mathrm{B}T}. \tag{6.11}$$

This leads to a quadratic equation for the free carrier concentration

$$n^2 + \frac{1}{g} D_\mathrm{c}^\mathrm{eff} e^{-E_\mathrm{D}^\mathrm{b}/k_\mathrm{B}T} n - \frac{1}{g} D_\mathrm{c}^\mathrm{eff} e^{-E_\mathrm{D}^\mathrm{b}/k_\mathrm{B}T} N_\mathrm{D} = 0 \tag{6.12}$$

with the solution

$$n = 2N_\mathrm{D} \left( 1 + \sqrt{1 + 4g \frac{N_\mathrm{D}}{D_\mathrm{c}^\mathrm{eff}} e^{E_\mathrm{D}^\mathrm{b}/k_\mathrm{B}T}} \right)^{-1}. \tag{6.13}$$

In the limit of very low temperatures the condition $4g(N_\mathrm{D}/D_\mathrm{c}^\mathrm{eff}) e^{E_\mathrm{D}^\mathrm{b}/k_\mathrm{B}T} \gg 1$ applies. Equation (6.13) then simplifies to

$$n \cong \sqrt{(1/g) N_\mathrm{D} D_\mathrm{c}^\mathrm{eff}} e^{-E_\mathrm{D}^\mathrm{b}/2k_\mathrm{B}T} \quad \text{(ionization regime)}. \tag{6.14}$$

In this low temperature range sufficient donors still have their electron and may be ionized if the temperature is increased. The ionization energy can be derived from the slope of an Arrhenius plot of the carrier density versus reciprocal temperature, see Fig. 6.2. From (6.14) we obtain $E_\mathrm{D}^\mathrm{b} = -2k_\mathrm{B} d(\ln n)/d(1/T)$.

Once all donors are ionized, the carrier density saturates. $n$ is given by the donor concentration and remains constant independent on temperature,

$$n = N_\mathrm{D}^+ = N_\mathrm{D} \quad \text{(saturation regime)}. \tag{6.15}$$

As the temperature is further increased the carrier concentration again raises due to a thermal activation of electrons from the valence band. The intrinsic carrier concentration increases with a much steeper slope $-E_\mathrm{g}/2k_\mathrm{B}$ in the Arrhenius plot given in Fig. 6.2. In this high-temperature range we hence find

$$n \propto e^{-E_\mathrm{g}/(2k_\mathrm{B}T)} \quad \text{(intrinsic regime)}. \tag{6.16}$$

Pure doping of solely one kind of carriers does hardly occur. In practice dopant atoms of one kind are partially compensated by a smaller number of dopants of the other kind. Let us assume donors with a concentration $N_\mathrm{D}$ being partially compensated by residual acceptors with concentration $N_\mathrm{A}$. Since acceptors provide low-energy states for donor electrons, even at lowest temperatures all acceptors are ionized, i.e. $N_\mathrm{A}^- = N_\mathrm{A}$. Consequently the number of donors which may release their electron to the conduction band is reduced by this number, yielding instead of (6.10) now $n = N_\mathrm{D}^+ - N_\mathrm{A}^-$. The most evident change in the free carrier concentration $n$ is

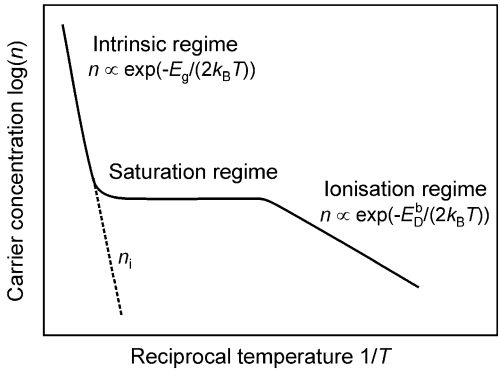


**Fig. 6.2** Arrhenius plot of the carrier concentration $n$ in the conduction band of an uncompensated $n$-type semiconductor. $n_i$ denotes the contribution of intrinsic carriers

given by a decrease of the plateau in the saturation regime to the value $n = N_D - N_A$. Furthermore, for a given carrier concentration the mobility is reduced in a compensated semiconductor due to additional scattering at ionized dopants. An additional effect is the appearance of a second ionization regime with a slope $-E_D^b/k_B$ instead of $-E_D^b/2k_B$ in the Arrhenius plot at the low-temperature end.

### *6.1.2 Solubility of Dopants*

Doping of a semiconductor host with impurities requires a sufficiently high solubility for the introduction on the intended lattice site. The solubility of a dopant is inherently connected to the dissociation of the impurity atom into an ionized state and a carrier, and is therefore associated with the Fermi level [8]. If, e.g. a donor atom is introduced, energy is gained by incorporating the electron of the donor at the Fermi level. The energy gain decreases at higher doping concentration, because the Fermi level increases by doping. A comparable situation occurs for acceptors. Low dopant concentrations are therefore more readily achieved than high concentrations, and the problem gets increasingly severe as the bandgap energy increases. Incorporation of the dopant at other sites than intended may then get more favorable, and even the formation of phases composed of impurity and host atoms with a configuration deviating from that of the semiconductor may occur.

The creation of a defect is generally connected to the incorporation or removal of atoms from other parts of the crystal, its surface, or the environment. Since this finding and the treatment below apply for both, impurities and native defects, we will just denote them defects in the following. The creation—or annihilation—of a defect is considered by a coupling to subsystems or reservoirs, which donate or accept atoms and, in case of charged defects, also electrons. The equilibrium is described by respective chemical potentials.

We consider the introduction of an impurity by connecting the semiconductor to a reservoir of dopant atoms. The probability of incorporation is related to the

formation energy of a respective defect in the crystal. In thermal equilibrium the concentration $[D_i]$ of the dopant (or any defect) in the semiconductor is given by

$$\left[D_i^q\right] = N \exp\left(-\frac{E_{\text{form}}(D_i^q)}{k_B T}\right). \tag{6.17}$$

$E_{\text{form}}(D_i^q)$ is the formation energy of the defect $D_i$ in the charge state $q$. $N$ is the number of sites where the defect can form, e.g., the number of substitutional cation $A$ sites of an $AB$ compound semiconductor in case of dopant incorporation of this site. The defect formation energy depends on the chemical potential of the species involved in the creation of the defect and the change of Gibbs free energy required to create the defect. An additional term accounts for the charge of the defect. The general expression reads

$$E_{\text{form}}\left(D_i^q\right) = \Delta G_{\text{form}}\left(D_i^q\right) + \sum_j n_j \mu_{j\,(\text{reservoir})} + q E_F, \tag{6.18}$$

where $q$ is the charge state (e.g., $-1$) and $E_F$ is the Fermi energy with respect to the valence band edge $E_v$. The index $j$ in the sum of (6.18) goes over all chemical species involved in the defect creation. The number $n_j$ of species $j$ is positive if an atom is removed from the semiconductor and negative if it is added. $\mu_j$ are the respective chemical potentials. The energy to substitute, e.g., a negatively charged Li acceptor for Zn in a ZnSe semiconductor reads

$$E_{\text{form}}\left(\text{Li}_{\text{Zn}}^-\right) = \Delta G_{\text{form}}\left(\text{Li}_{\text{Zn}}^-\right) + \mu_{\text{Zn}} - \mu_{\text{Li}} - E_F.$$

The change of Gibbs free energy $\Delta G_{\text{form}}(D_i^q)$ is given by

$$\Delta G_{\text{form}}\left(D_i^q\right) = \Delta E_0 - T\Delta S + P\Delta V, \tag{6.19}$$

$\Delta E_0$ being the difference between the electronic ground-state energy of the system with and without the defect. Correspondingly $\Delta S$ and $\Delta V$ are the respective entropy and volume changes due to the creation of the defect. The contributions related to a volume change and the entropy change are usually expected to yield only minor corrections and not considered. A positive sign of $\Delta G_{\text{form}}$ denotes an energy cost to create the defect.

The charge state of the defect will be that with lowest formation energy. Depending on $E_F$ the defect may be in different charge states. The energy where the defect changes the charge state from $q$ to $q'$ is referred to as charge transfer energy $E^{q/q'}$. Figure 6.3 illustrates how the formation energy depends on the charge state $q$ and the Fermi energy $E_F$, which is varied between valence and conduction band. In the example given in Fig. 6.3 the defect is negatively charged if $E_F$ lies above $E^{0/-}$, because in this range $E_{\text{form}}(D^-) < E_{\text{form}}(D^0)$. Below $E^{0/-}$ the defect is in its neutral charge state. The level in the bandgap $E^{0/-}$ is the value of the Fermi energy at which the two charge states $E_{\text{form}}(D^0)$ and $E_{\text{form}}(D^-)$ have the same energy.

The quantities noted in the equations above are accessible by first-principles calculations. The electrical interaction of the defect is treated analogous to the chemical interaction of atoms with their atomic reservoirs: The defect donates or accepts electrons from the electron reservoir of the semiconductor. A negative charge denotes

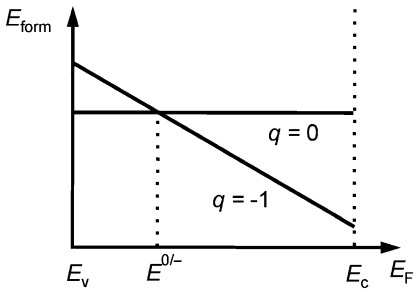


**Fig. 6.3** Formation energy of a defect in a neutral and a negative charge state. The Fermi level $E_F$ is varied between the energy of the valence band $E_v$ and the conduction band $E_c$

that the defect accepts $q$ electrons. The position of the Fermi energy is calculated self-consistently by applying (6.18) for all relevant defects and accounting for the condition of charge neutrality

$$\text{net charge} = 0 = p - n - \sum_i n_i^{\text{electron}} \left[ D_i^q \right]. \tag{6.20}$$

$p$ and $n$ are the hole and electron densities, and $n_i^{\text{electron}}$ is the number of excess electrons in the defect $D_i^q$. Details of the computational approach are given in Ref. [9] for the example of ZnSe doping. Within this framework performed in a supercell geometry the change of Gibbs free energy $\Delta G_{\text{form}}$ in (6.18) is the total energy of a supercell containing the defect minus the energy of a supercell of the pure bulk semiconductor. For an elementary semiconductor like Si the chemical potential, $\mu_{\text{Si}}$, is fixed, while for an $AB$ compound semiconductor this applies for the *sum* of the constituents $\mu_{AB} = \mu_A + \mu_B$, leaving an individual summand variable.

Bounds on chemical potentials arise from the phases that can be formed by the constituents. For the *host atoms* the upper bound is given by formation of the respective elements. In ZnSe, e.g., $\mu_{\text{Zn}}^{\text{max}} = \mu_{\text{Zn(bulk)}}$: Further increase above this level will preferentially lead to the formation of Zn metal. The same applies for $\mu_{\text{Se}}^{\text{max}}$. A lower bound is imposed by the heat of formation $\Delta H_{\text{form}}$ of the semiconductor and the fixed sum of the chemical potentials noted above. For our example we obtain $\mu_{\text{ZnSe}} = \mu_{\text{Zn(bulk)}} + \mu_{\text{Se(bulk)}} + \Delta H_{\text{form}}(\text{ZnSe})$, yielding $\mu_{\text{Zn}}^{\text{min}} = \mu_{\text{Zn(bulk)}} + \Delta H_{\text{form}}(\text{ZnSe})$. Note that $\Delta H_{\text{form}} < 0$ for the stable semiconductor. For the *dopant* the various compounds which the impurity can form including host atoms must be considered. For the example of a $p$-type doping of ZnSe using Li the most stringent bound is found to be given by the formation of the $LiSe_2$ compound [10], yielding the constraint on the chemical potential $2\mu_{\text{Li}} + \mu_{\text{Se}} = \mu_{\text{Li}_2\text{Se}} = 2\mu_{\text{Li(bulk)}} + \mu_{\text{Se(bulk)}} + \Delta H_{\text{form}}(\text{Li}_2\text{Se})$.

To obtain the solubility and doping effect of a dopant we have to include all relevant configurations and charge states of the impurity as expressed by (6.18). To be specific we continue to analyze the Li acceptor in ZnSe [10]. Besides the substitutional site $\text{Li}_{\text{Zn}}^-$ where Li acts as an acceptor we particularly find two interstitial sites $\text{Li}_{\text{i}}^+$ were it acts as a shallow donor. Calculations show that the tetrahedral site surrounded by Se is by 0.2 eV more favorable than the respective site with Zn atoms. The substitutional Se site may be excluded due to a very large formation energy.

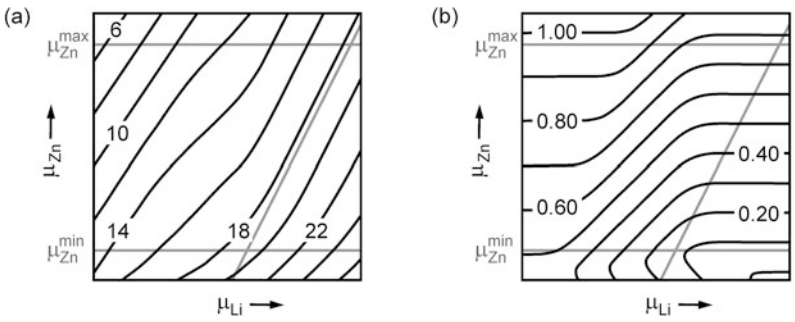


**Fig. 6.4** (**a**) Total Li concentration $\log_{10}$[Li] in a ZnSe:Li semiconductor doped at 600 K. Values depend on the chemical potentials of Li and Zn, and are given in $cm^{-3}$. (**b**) Fermi level resulting from the Li doping shown in (**a**). Values are given in eV and refer to the top of the valence band. Reproduced with permission from [10], © 1993 APS

Results of first-principles calculations for Li doping of ZnSe are displayed in Fig. 6.4 [10]. The contour plot Fig. 6.4a shows the total concentration of Li in ZnSe at an equilibrium temperature of 600 K, corresponding to the typical low growth temperature of ZnSe. Figure 6.4b gives the resulting Fermi energy.

In Fig. 6.4a the bounds of the chemical potentials of Zn and Li are indicated by straight gray lines. The formation of the $Li_2Se$ compound leads to the bound for $\mu_{Li}$ with a slope of 2 due to the dependence of $\mu_{Li_2Se}$ from $\mu_{Li}$ noted above. $Li_2Se$ islands were actually found to form during molecular beam epitaxy of heavily doped ZnSe:Li [11]. The calculated maximum of Li concentration of ZnSe:Li is slightly above $10^{18}$ $cm^{-3}$ [10]. The coinciding slope of the contour lines near the $Li_2Se$-related bound is accidental and originates from the incorporation of *two* Li atoms (one substitutional, one interstitial) for the removal of *one* Zn atom. The highest Li concentration ($1.7 \times 10^{19}$ $cm^{-3}$) is obtained at the crossover point of a minimum accessible Zn chemical potential $\mu_{Zn}^{min}$ and a maximum accessible Li chemical potential before formation of $Li_2Se$. At this point the calculation yields fewer than 3 % of the introduced Li atoms on an interstitial site and the most abundant native ZnSe defect of the Se antisite $Se_{Zn}^{2+}$ (a donor) with two orders of magnitude concentration below that of Li. Native defect concentrations become sizeable only below the physically meaningful limit $\mu_{Zn}^{min}$ and lead to a bending of the contour lines. If the equilibrium temperature is lowered the concentrations of all defects reduce. Reduction factors of about 5, $10^1$, and $10^2$ for substitutional Li, interstitial Li, and the Se antisite, respectively, are found as the temperature decreases by 100 °C [10].

The Fermi energy resulting from the Li concentration of Fig. 6.4a is shown in Fig. 6.4b. We note that the Fermi level decreases at fixed $\mu_{Li}$ as the Zn chemical potential is lowered. This trend results from the increasingly favored incorporation of Li on a Zn site and is also reflected in the Li concentration of Fig. 6.4a. If $\mu_{Li}$ is increased at fixed $\mu_{Zn}$ we note from Fig. 6.4b that the decrease of the Fermi level tends to saturate despite the further increase of the total Li concentration shown in Fig. 6.4a. The reason is a steady increase by compensating interstitial Li donors that

limits the hole concentration. The effect is minimized by decreasing the Zn chemical potential.

Results outlined above for the specific case of Li exemplify the general behavior of dopant impurities. For any dopant limits of the solubility are imposed by the compounds that can be formed by the participating atoms. The relevant bound of the dopant chemical potential is imposed by the phase with minimum heat of formation. Saturation of the Fermi-level position occurs when compensating species are formed. Such species are extrinsic species of amphoteric dopants or intrinsic native defects and are addressed in the following sections.

In addition to isolated point defects treated above basically also *complexes* may affect the electrical properties. The concentration of a given complex (e.g., a pair of substitutional and an interstitial Li denoted $(Li_{Zn}^{-}, Li_{i}^{+})$) gets significant if the binding energy exceeds the larger of the two formation energies of the individual defects out of which the complex is formed [10]. This makes it less likely that complexes have a significant influence, since complexes with a low binding energy tend to dissociate at growth temperatures.

### *6.1.3 Amphoteric Dopants*

An amphoteric dopant is one that can act as either a donor or an acceptor. The word "amphoteric" originates from the Greek word amphoteroi (αμφοτεροι) and means "having two characters". Amphoteric behavior can occur if the dopant occupies different lattice sites like lithium in ZnSe as illustrated above. Prominent examples are group-IV impurities (C, Si, Ge, Sn) in III–V semiconductors that form donors on group-III sites and acceptors on group-V sites. Obviously incorporation of an undesired site limits the intended doping effect. Such compensation due to the same chemical species is referred to as *autocompensation*.

The discussion of the amphoteric behavior of Li in the preceding section indicates that the degree of compensation depends on the applied equilibrium conditions. Anion-poor conditions applied during doping of III–V semiconductors by group-IV impurities favor incorporation on an anion site, while anion-rich conditions favor incorporation on a cation site. This behavior is demonstrated in Fig. 6.5a for the incorporation of carbon in GaAs during metalorganic vapor-phase epitaxy [12]. C doping originates from the organic $CH_3$ ligands of the Ga source trimethylgallium $Ga(CH_3)_3$. A low V/III ratio in the gas phase of the applied arsenic source $AsH_3$ to $Ga(CH_3)_3$ leads preferentially to $C_{As}$ acceptors, while a high ratio favors $C_{Ga}$ donors.

Ge is an impurity with a pronounced amphoteric character in III–V semiconductors. Both *n*- and *p*-type conductivity can hence be obtained depending on growth conditions. Besides the V/III ratio incorporation is also strongly affected by kinetics on the growth surface. GaAs surfaces stabilized by As favor incorporation on a Ga site yielding a $Ge_{Ga}$ donor. This represents the usual case of molecular beam epitaxy on (001) GaAs surfaces at temperatures below 630 °C, i.e., below the congruent sublimation temperature of GaAs. Above this temperature Ga-rich surfaces

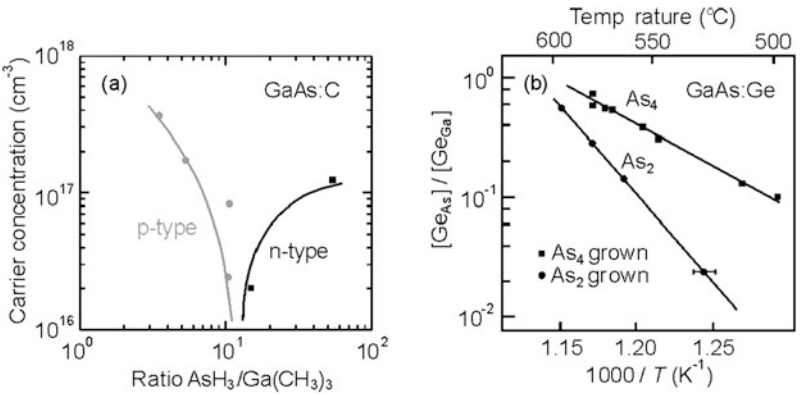


**Fig. 6.5** (**a**) Doping of GaAs with C from organic ligands in metalorganic vapor-phase epitaxy for a varied ratio of arsenic and gallium sources in the gas phase. Data points are from [12]. (**b**) Autocompensation ratio of the doping of GaAs with Ge in molecular beam epitaxy at varied temperature for different arsenic species. Reproduced with permission from [13], © 1982 Springer

occur leading to $Ge_{As}$ acceptors. Even below 630 °C a gradual increase of the concentration of Ge on As is observed as the temperature is raised [13]. This behavior is shown in Fig. 6.5b. Temperature increase leads to a gradual reevaporation of As from the surface and hence increased occupation of Ge on As sites, i.e., to compensating acceptors. The more reactive $As_2$ species are expected to yield a higher As coverage of the surface and hence a smaller compensation ratio.

Amphoteric behavior may also occur for a defect on a given lattice site, i.e., without occupation of different inequivalent sites. If the defect has several levels in the bandgap like, e.g., Au in Ge, its character depends on the position of the Fermi level. We illustrate such behavior below for a native defect pair.

### *6.1.4 Compensation by Native Defects*

Native defects represent an equilibrium phenomenon and occur in any solid. The abundance of intrinsic charged point defects has a strong impact on the electronic properties of semiconductors. Such defects comprise vacancies, interstitial atoms, and, in case of compound semiconductors, antisites. In compound semiconductors the abundance of native defects is particularly sensitive to a deviation from stoichiometry. With about $5 \times 10^{22}$ cm$^{-3}$ atomic sites even a slight deviation from perfect stoichiometry as small as $10^{-4}$ leads to a defect concentration in the range $10^{18}$ cm$^{-3}$. Generally native defects which accommodate deviation from stoichiometry are those that compensate *majority* carriers. Since the energy gained by such compensation increases as the bandgap energy increases, early work on wide-gap semiconductors focused particularly on self-compensation by native defects [14]. Certainly the effect contributes significantly to doping problems, albeit autocompensation and solubility may impose more rigorous limits.

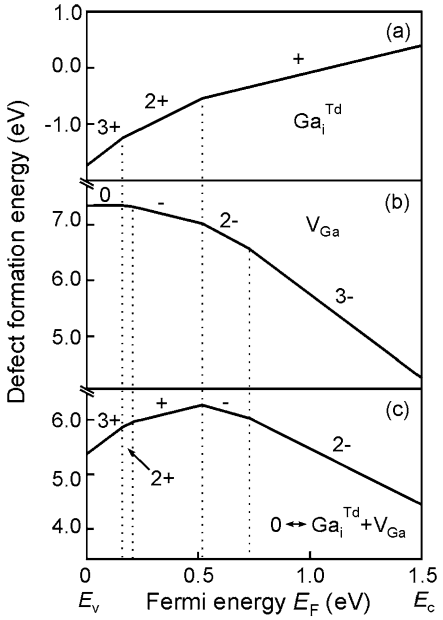


**Fig. 6.6** Calculated formation energies of defects in GaAs. (**a**) Isolated interstitial Ga atom $Ga_i$ at a tetrahedral site with 4 nearest As atoms, (**b**) isolated vacancy at the Ga site $V_{Ga}$, and (**c**) a vacancy-interstitial pair $Ga_i + V_{Ga}$. Defect energies in (**a**) and (**b**) are arbitrarily normalized. The origin of the Fermi-energy scale is set to the maximum of the valence band $E_v$. After [15]

We study the effect of a native defect for the vacancy-interstitial pair in GaAs created by a Ga atom which moved from a regular lattice site to an interstitial position. The pair formation is described by the reaction $0 \leftrightarrow Ga_i + V_{Ga}$. Calculated energies are given in Fig. 6.6 [15]. The ionization levels are in qualitative agreement with more recent calculations [16, 17]. Both isolated defects of the vacancy-interstitial pair have several charge-transfer energies in the band gap. For a Fermi level near the valence-band edge in $p$-type GaAs, the interstitial $Ga_i$ defect with three-fold positive charge has lowest formation energy. The defect hence traps holes, thereby compensating the extrinsic doping. As the Fermi level is increased, less holes are trapped by $Ga_i$ due to an increased formation energy and gradually more electrons are trapped by the vacancy $V_{Ga}$ defect. As a result, the charge state of the vacancy-interstitial pair gets more negative. We note that the formation energy depicted in Fig. 6.6c decreases for *either* high doping. Both, $p$-type and $n$-type doping are hence compensated by the vacancy-interstitial pair.

The equilibrium concentration of intrinsic defects is given by (6.17) which was also used to describe extrinsic defects. The abundance of native defects hence depends on temperature, doping level, and the deviation from ideal stoichiometry. The dependence on the doping level, i.e., on the electron chemical potential is illustrated in Fig. 6.6. We now turn toward the dependence on the chemical potentials of the atoms. Limits for the stoichiometry are imposed by thermodynamics. We express these bounds by applying the approach discussed in Sect. 6.1.2 for impurity doping of ZnSe. The chemical potentials of the constituents Ga and As may not exceed their respective bulk values, i.e., $\mu_{Ga}^{max} = \mu_{Ga(bulk)}$, $\mu_{As}^{max} = \mu_{As(bulk)}$, and their sum equals the chemical potential of bulk GaAs, $\mu_{Ga} + \mu_{As} = \mu_{GaAs}$. The

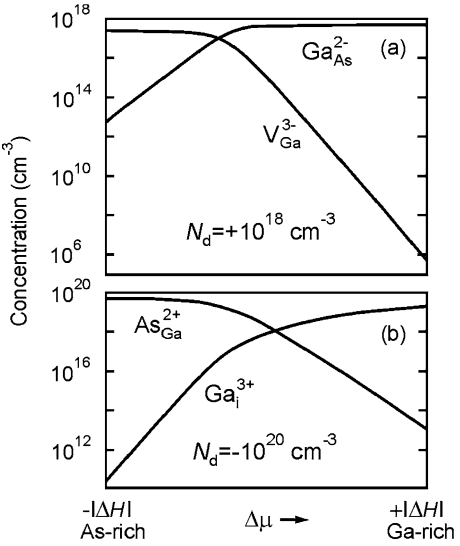


**Fig. 6.7** (**a**) Calculated equilibrium concentration of the Ga vacancy and the Ga antisite as a function of the difference of the chemical potentials of Ga and As atoms under $n$-type conditions at 827 °C. (**b**) Concentration of the Ga interstitial and the As antisite for $p$-type conditions at 827 °C. Reproduced with permission from [18], © 1991 APS

difference of the chemical potentials $\Delta\mu = \mu_{Ga} - \mu_{As} - (\mu_{Ga(bulk)} - \mu_{As(bulk)})$ is then limited by the heat of formation $\Delta H_{form}(GaAs)$ of bulk GaAs from elemental Ga and As, $|\Delta\mu| \leq |\Delta H_{form}|$, with $|\Delta H_{form}| = |\mu_{GaAs} - \mu_{Ga(bulk)} - \mu_{As(bulk)}|$. We recall that $\Delta H_{form} < 0$, because GaAs is a stable compound. Ga-rich and As-rich bounds of $\Delta\mu$ are given by $\Delta\mu = +|\Delta H_{form}|$ and $\Delta\mu = -|\Delta H_{form}|$, respectively.

We consider some native defects in GaAs for a fixed doping level and temperature. Figure 6.7a shows the concentration of the Ga vacancy $V_{Ga}$ and the Ga antisite $Ga_{As}$ in $n$-type GaAs [18]. For high doping $V_{Ga}$ is triply negatively charged as shown in Fig. 6.6. In the As-rich limit $V_{Ga}^{3-}$ is the dominant defect with a concentration of about 1/3 of the effective doping level $N_d$ [18]. Under these conditions the formation energy is so low that about one such defect is formed for every three electrons introduced by doping. We find a strong decrease of the $V_{Ga}^{3-}$ abundance by more than 10 orders of magnitude as $\Delta\mu$ is increased toward Ga-rich conditions. Two reasons account for this finding. First, the formation energy of $V_{Ga}$ increases. This effect is accompanied by a decrease of the electron chemical potential that further increases the formation energy of $V_{Ga}^{3-}$ [18]. Second, As-rich conditions provide an effective sink for removed Ga atoms at the surface. This counteracts thermal equilibrium for Ga interstitial atoms and consequently, by the law of mass action, enhances the concentration of vacancies.

The decrease of $V_{Ga}^{3-}$ in Ga-rich $n$-type GaAs is accompanied by an increase of the antisite $Ga_{As}$, the formation energy of which linearly decreases as $\Delta\mu$ is raised. It becomes the dominat defect in the Ga-rich limit and acts also as a compensating electron trap under these conditions.

In strongly $p$-type doped GaAs the dominant native defect under Ga-rich conditions is the interstitial Ga atom $Ga_i$ at a tetrahedral site with 4 nearest As atoms. At this doping level it acts as a triple hole trap. Below $10^{17}$ cm$^{-3}$ $p$-type doping it mainly appears in the singly charged state [18]. Decreasing $\Delta\mu$ toward As-rich

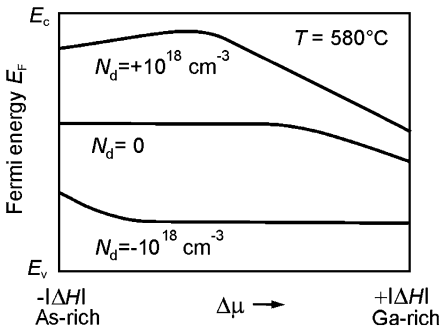


**Fig. 6.8** Calculated position of the Fermi energy in GaAs as a function of the difference of the chemical potentials of Ga and As atoms for three fixed doping levels $N_\mathrm{d} = N_\mathrm{D}^+ - N_\mathrm{A}^-$. Reproduced with permission from [18], © 1991 APS

conditions leads to a decrease of the $\mathrm{Ga_i^{3+}}$ abundance, accompanied by an increase of the As antisite $\mathrm{As_{Ga}^{2+}}$, which also acts as a hole trap.

Charged native defects have an influence on the position of the Fermi level due to the charge neutrality condition (6.20). The effect on $E_\mathrm{F}$ becomes obvious by explicitly expressing the hole and electron densities in terms of Boltzmann statistics,

$$\begin{aligned} N_\mathrm{d} &= N_\mathrm{D}^+ - N_\mathrm{A}^- \\ &= D_\mathrm{c}^\mathrm{eff} \exp\bigl(-(E_\mathrm{c} - E_\mathrm{F})/k_\mathrm{B}T\bigr) - D_\mathrm{v}^\mathrm{eff} \exp\bigl(-(E_\mathrm{F} - E_\mathrm{v})/k_\mathrm{B}T\bigr) \\ &\quad + \sum_i n_i^\mathrm{electron}\bigl[D_i^q\bigr]. \end{aligned} \tag{6.21}$$

Here $[D_i^q]$ is the concentration of a native defect, and $D_\mathrm{c}^\mathrm{eff}$ and $D_\mathrm{v}^\mathrm{eff}$ are the effective conduction-band and valence-band densities of states defined in (6.4a)–(6.4b). Figure 6.8 shows the calculated dependence of the Fermi-level position on native defects created by a variation of the stoichiometry [18]. We note significant variations of $E_\mathrm{F}$ for fixed concentrations of excess free charge carriers. The strong decrease for Ga-rich conditions in $n$-type GaAs ($N_\mathrm{d} = +10^{18}$ cm$^{-3}$) originates from charge compensation by the antisite defect $\mathrm{Ga_{As}^{2-}}$, the slight increase on the As-rich side originates essentially from the vacancy $\mathrm{V_{Ga}^{3-}}$.

### *6.1.5 DX Centers*

A number of impurities introduce levels in the bandgap that are far away from the conduction-band and valence-band edges. Due to their large ionization energy they are able to trap free charge carriers, thereby increasing the resistivity of a semiconductor. Prominent examples are transition metals like Cr or Fe in GaAs or InP. According to the position of the charge-transfer level in the bandgap they are classified into donor-like or acceptor-like centers. A common feature is a strong localization of their wave-function compared to that of shallow impurities. Deep centers affect many properties of semiconductors, e.g., they compensate doping, reduce minority-carrier lifetime and diffusion length, and lead to a reduced carrier mobility.

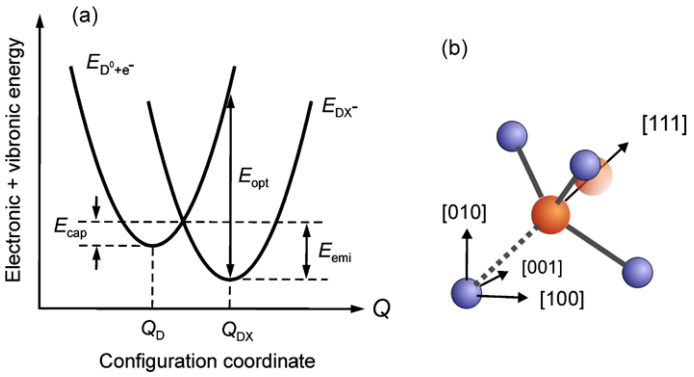


**Fig. 6.9** (**a**) Configuration-coordinate diagram representing the total energy of a DX center and a substitutional donor. (**b**) Structural model of a DX center. The *dotted line* indicates the bond which breaks when the tetrahedrally coordinated impurity (*red*) is displaced along a ⟨111⟩ direction to a position depicted by the transparent atom

There exists a large variety of different kind of centers introducing deep levels in semiconductors. We focus here on a specific kind of deep centers related to a structural instability of impurities. The motivation to emphasize these so-called DX centers is their amphoteric character, which converts an intentional shallow dopant to a deep-level impurity.

The label DX refers to a complex of a donor D and an unknown (at the time of discovery) intrinsic defect X. A comparable case for acceptors is referred to as AX center. Experiments found a large energy difference between the optical and thermal ionization energies, indicating that the deep state is strongly coupled to the crystal lattice [19].

The generally accepted model of a DX center in a tetrahedrally coordinated compound semiconductor is illustrated in Fig. 6.9. The donor has two configurations: A substitutional site where it acts as a shallow donor, and a relaxed site where one of the four bonds with two electrons is broken and the impurity is displaced along one of the ⟨111⟩ directions [20]. The broken bond creates two dangling bonds which may be occupied by up to four electrons. The (neutral) donor thus can hold its own extra electron and accept an additional electron according the reaction $D^0 + e^- \rightarrow DX^-$. Since the ionization of a shallow donor is described by $D^0 \rightarrow D^+ + e^-$, an electron transfer between the donors is given by the sum of the two reactions, yielding

$$2D^0 \rightarrow D^+ + DX^-. \tag{6.22}$$

The two donors do not need to be in close proximity to each other. Reaction (6.22) indicates that one half of all donor atoms may exist in the broken-bond configuration and compensates thereby the free electrons released from the other half in the substitutional shallow configuration.

Donor centers which yield an exothermic reaction according (6.22) are also referred to as negative-$U$ centers. $U$ denotes the effective electron-electron correlation energy of the two centers. A negative correlation energy is obtained if the energy

gained by the lattice distortion is larger than the energy cost for the electron repulsion.

The instability of specific dopants against formation of DX centers is assigned to a large Jahn-Teller distortion of the highly symmetric substitutional site. The strength of the effect depends on the bonding character and hence on both, the dopant *and* the host crystal. Ga, e.g., forms a stable substitutional donor on a Zn site in ZnSe, but is instable against formation of a DX center in ZnTe [21]. For a (meta-stable) Ga-related DX center in ZnSe the corresponding parabola ($E_{\mathrm{DX}^-}$) in the configuration-coordinate diagram has a minimum at $Q_{\mathrm{DX}}$ with a *higher* energy than the minimum of the parabola ($E_{\mathrm{D}_0+\mathrm{e}^-}$) at $Q_{\mathrm{D}}$.

Substitutional Si in GaAs forms a stable donor on a Ga site, while it builds a well-studied DX center in $\mathrm{Al}_x\mathrm{Ga}_{1-x}\mathrm{As}$ for compositions $x > 0.22$ (below this value the DX level lies in the conduction band) [19]. Electron capture into the DX center is thermally activated with a composition-dependent energy barrier $E_{\mathrm{cap}}$ (>0.2 eV) as depicted in Fig. 6.9a. The barrier $E_{\mathrm{emi}}$ for thermal emission of carriers from the DX center is larger (∼0.4 eV). Carriers may as well be released by optical absorption with a large photon energy $E_{\mathrm{opt}}$ (>1 eV). Optically released carriers remain in the conduction band (for days) due to a very low recapture rate and generate a persistent photoconductivity. Other donors like, e.g., Te, Se, and Sn show similar DX characteristics. The model outlined in Fig. 6.9 accounts well for the experimental findings.

### *6.1.6 Fermi-Level Stabilization Model*

The amphoteric character of intrinsic defects and the formation of related deep levels illustrated above leads to a phenomenological model to account for the widely differing doping ability of semiconductors. The *Fermi-level stabilization model*, also termed *amphoteric defect model* or *doping pinning rule*, points out trends for intrinsic limitations to account for, e.g., the difficulties for achieving *n*-type ZnTe or *p*-type ZnO. The model ties in with the empirical rule of naturally fixed energy levels of transition-metal impurities in different semiconductors (Sect. 3.2.3). Similarly, clear evidence for the localized nature of native defects is found. The Fermi-level stabilization model therefore assumes that doping limitations reflect the absolute position of the valence and conduction band edges with respect to a fixed reference energy like, e.g., the vacuum level. Doping restrictions are hence *not* assigned to the size of the bandgap per se or to properties of particular dopants.

The reference level for the natural alignment of the band edges with respect to the ability of doping is termed Fermi-level stabilization energy $E_{\mathrm{FS}}$. Indication for such an internal reference was concluded from semiconductors, which were heavily damaged with gamma rays or electrons [22]. For a high density of damage, where material properties are controlled by native defects, the Fermi level was found to stabilize at a certain energy and becomes insensitive to further damage. This energy $E_{\mathrm{FS}}$ is located at an energy of about 4.9 eV below the vacuum level for the studied

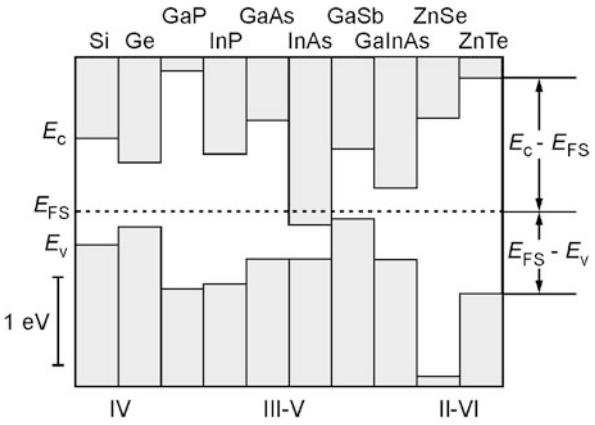


**Fig. 6.10** Valence band maxima and conduction band minima of various semiconductors aligned with respect to their internal Fermi-level stabilization energy $E_{FS}$. Data from [24]

tetrahedrally bonded semiconductors [23]. The internal reference $E_{FS}$ allows to arrange the bands of all semiconductors on a common energy scale. Figure 6.10 shows the band alignment of some tetrahedrally coordinated semiconductors.

The position of $E_{FS}$ with respect to the band edges depicted in Fig. 6.10 affects the ability to achieve high carrier concentration of a given type. The formation energy of compensating native defect depends on the difference between the Fermi energy and the stabilization energy $E_{FS}$. If $E_{FS}$ lies close to the valence band, the Fermi level should easily be moved into the valence band by $p$-type doping without significant formation of compensating defects. Consequently high $p$-type carrier concentration is expected. On the other hand, a large energy difference to the conduction band will lead to a high abundance of compensating defects if $E_F$ is raised by $n$-type doping, resulting in solely poor $n$-type carrier concentration. The asymmetry of $p$ and $n$-type doping increases as the bandgap increases.

Experimental data of maximum carrier concentrations achieved are given in Fig. 6.11. Electron and hole concentrations are normalized by the effective density of states $D_c^{\text{eff}}$ and $D_v^{\text{eff}}$, respectively. Normalized values are used, because electron concentrations are given by $n = D_c^{\text{eff}} \times F_{1/2}[(E_F - E_c)/k_B T]$ and hole concentrations $p$ accordingly with $D_v^{\text{eff}}$ and $(E_v - E_F)$, where $F_{1/2}$ is the Fermi integral. Figure 6.11 clearly shows that the achieved normalized doping levels decrease as the energy separation between the stabilization energy $E_{FS}$ and the band edges $E_c$ or $E_v$ increase. The data can be roughly described by the empirical relation [24]

$$cc_{\max}/D^{\text{eff}} = a \times \exp\bigl(b|E_{FS} - E_{\text{band edge}}|\bigr).$$

Here, $cc_{\max}$ is the maximum carrier concentration $n$ or $p$ with the related effective density of states and the related band-edge energies $E_c$ or $E_v$, and the parameters are $a_n = 2.7 \times 10^3$, $b_n = -5.5\ \text{eV}^{-1}$, $a_p = 4.0 \times 10^2$, $b_p = -6.1\ \text{eV}^{-1}$.

The maximum carrier concentrations achieved in experiments can be expressed in terms of pinning energies $E_{\text{pin}}^{(n)}$ and $E_{\text{pin}}^{(p)}$ of the Fermi energy in $n$-type and $p$-type

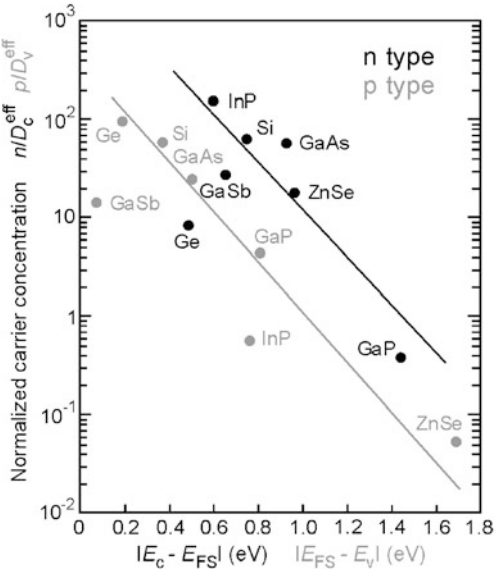


**Fig. 6.11** Experimental maximum carrier concentrations for $n$-type (*black circles*) and $p$-type semiconductors (*gray circles*) as a function of the energy difference between $E_{FS}$ and either the conduction-band edge $E_c$, or the valence-band edge $E_v$, respectively. The solid lines are fits. Data taken from [24]

semiconductors, respectively. In the approximation of single parabolic bands the maximum net free carrier concentration $cc_{max}$ is given by [25]

$$cc_{max} = \frac{(2m^*_{(n/p)})^{3/2}}{2\pi^2} \int_0^\infty \frac{\sqrt{E}\, dE}{\exp((E - E_{pin}^{(n/p)})/k_B T) + 1}.$$

The equation is inverted to obtain the pinning energies $E_{pin}^{(n)}$ and $E_{pin}^{(p)}$ from the experimental $cc_{max}$ data. The resulting pinning energies are given in Fig. 6.12 for various III–V and II–VI compound semiconductors. We note a fairly small scatter in the pinning energy, if the bands are aligned with respect to an absolute reference energy.

### *6.1.7 Delta Doping*

Epitaxial growth allows for fabricating highly doped buried layers with a very small thickness in the range of atomic monolayers referred to as *delta doping* ($\delta$ doping) [26, 27]. The spacially inhomogeneous doping profile provides free carriers and an electrical potential which differs from that of the conventional homogeneous doping. Many characteristics of semiconductor structures related to potential fluctuations like, e.g., free carrier mobility of luminescence linewidth, perform better applying delta doping. The most prominent application is the enhancement of conductivity in a layer, where the carriers are not subjected to impurity scattering at the ionized dopant cores. The mobility of carriers in this layer is strongly increased, similar to the modulation-doping technique based on band bending at heterojunctions.

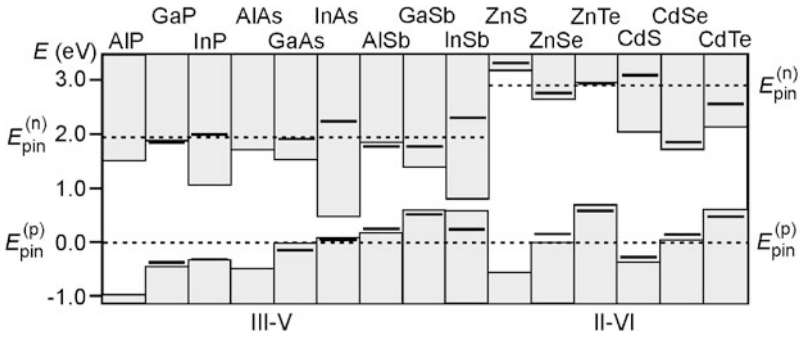


**Fig. 6.12** Pinning energies (*black bars*) calculated from experimental maximum carrier concentrations. *Dotted lines* are averaged pinning energies. Bands are aligned with respect to calculated offsets, zero is set at the valence band edge of GaAs for III–V and that of ZnSe for II–VI compounds. Data are from [25]

The effect of delta doping requires a confinement of the doping atoms within a layer thickness well below a relevant length scale, which usually is given by the de Broglie wavelength of free carriers. In practice doping profiles with a width of 3 nm and below can be considered like a delta function. Note that this width corresponds to only five lattice constants. To achieve such narrow profiles, impurity redistribution processes like diffusion or segregation must largely be suppressed. This usually implies deposition at lowered temperature to avoid thermally activated diffusion. The doping procedure basically proceeds by an initial interruption of the epitaxy of the undoped semiconductor, followed by the deposition of the highly doped layer. Eventually the growth of the undoped material is resumed. Growth parameters like temperature, partial pressures and material supply have to be adjusted such that the doping profile is preserved. Due to the two-dimensional character of the doping layer it is often referred to as doping sheet.

The profile of delta doping is described by two parameters: The location of the dopand sheet $z_{2D}$ and the areal density of doping atoms in the sheet $n_{2D}$ or $p_{2D}$. To be specific we consider donor dopants and a complete ionization. The 2D donor density $n_{2D}$ may be estimated from growth parameters used to obtain a 3D bulk carrier concentration $n$ by scaling with the thickness $r \times t$ of the doping sheet,

$$n_{2D} = nrt.$$

Here $r$ is the growth rate and $t$ the duration of the doping-sheet deposition. The relation applies well if the incorporation efficiency of dopants is not affected by the preceding growth interruption. The effective 3D concentration of donors $n_{3D}$ is obtained from $n_{2D}$ of a homogeneously doped sheet by considering the mean distance between donors in the sheet $(n_{2D})^{-1/2}$ and assuming the same mean distance in 3D bulk, yielding

$$n_{3D} = (n_{2D})^{3/2}. \tag{6.23}$$

In semiconductors with delta doping the concentration of dopants varies strongly over short distances. The free carrier concentration is then spread much further than

the profile of doping atoms. This feature is different to a slowly varying doping concentration, where the free-carrier profile follows the doping profile. Let us assume in a first approximation that all (ionized) doping atoms are located within a single atomic layer in the $xy$ plane located at $z = z_{2D}$ with a density $n_{2D}$. The doping profile is then described by $n(z) = n_{2D}\delta(z - z_{2D})$, $\delta$ being the delta function. The two-dimensional charge $e \times n_{2D}$ of the doping sheet creates a one-dimensional electric potential $V(z)$ which is calculated using Poisson's equation,

$$\frac{\partial^2 V}{\partial z^2} = -\frac{en(z)}{\varepsilon}. \tag{6.24}$$

$\varepsilon = \varepsilon_r \varepsilon_0$ is the permittivity of the semiconductor. Twofold integration yields the potential

$$V(z) = \frac{en(z)}{2\varepsilon}|z - z_{2D}|. \tag{6.25}$$

We note that $V$ is a linear and symmetric function of $z$ and is V-shaped with $V(z_{2D}) = 0$. For an interaction with *negative* free carriers $V \leq 0$. The slope of the potential $V(z)$ represents the electric field created by the ionized impurity atoms in the doping sheet, $E = -\partial V/\partial z = \text{const}$. It depends on the doping density and the permittivity, yielding typical values exceeding $10^6$ V/m. Such strong fields lead to a strong attractive interaction with free carriers: The potential $V(z)$ forms a narrow well with a width of the order of the de Broglie wavelength. Similar to the narrow square potential treated in Sect. 3.3 we obtain size quantization with discrete energy levels. We should note that the shape of the potential actually deviates from a simple V. The delta-doped semiconductor is neutral, because the charge of the doping sheet is balanced by the opposite charge of the released free carriers. The electric field therefore approaches 0 at some distance from the sheet. Figure 6.13 depicts a self-consistent solution of an effective-mass calculation of carriers confined in a potential which is created by delta doping [28]. The calculation assumes data of GaAs with an electron mass $m^* = 0.067m_0$.

The donor-doping profile $n(z)$ illustrated in Fig. 6.13a creates a local bending of the conduction-band edge $E_c$ that confines free electrons to discrete energies $E_i$. For the parameters assumed in the calculation four energy levels $E_0$ to $E_3$ are occupied with fractions of 61 %, 24 %, 11 %, and 4 %, respectively. We note a steep and nearly constant slope of the confining potential in a close vicinity to the doping sheet, and an approach to a constant value at some distance. The spatial extent of the carrier wave-function is much wider than the thickness of the doping sheet (~50 Å in the ground state vs. 2 Å, even more in the excited states). This finding leads to a more precise condition for delta doping: The distribution of doping atoms must be significantly more narrow than the spatial extent of carriers confined in the ground state. Obviously a factor 10 thicker doping sheet will lead to quite similar results in the present example.

The effect of delta doping on the Hall mobility of free carriers is illustrated in Fig. 6.14 [29]. The 2D mobility was measured using the two-dimensional electron gas created in the channel of a GaAs field-effect transistor [30]. Bulk values of

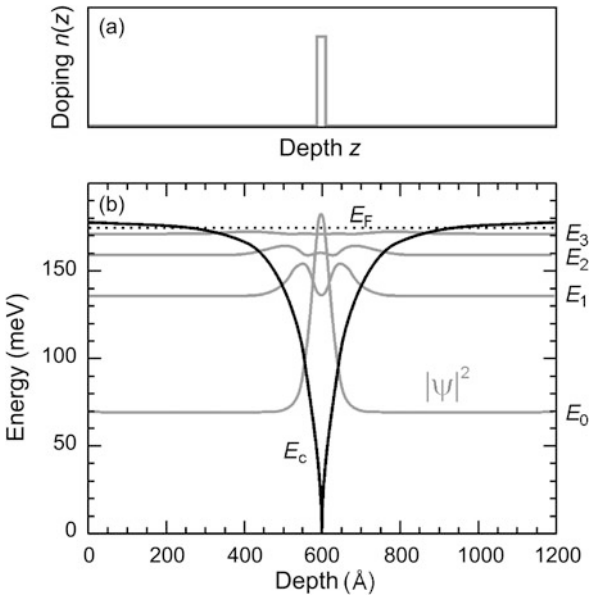


**Fig. 6.13** (**a**) Schematic of delta-doping profile. (**b**) Calculated effective-field potential well ($E_c$) and confined carrier distribution $|\psi|^2$ of an $n$-type delta-doping sheet with 2 Å thickness and $5 \times 10^{12}$ cm$^{-2}$ density. $E_F$ denotes the Fermi energy. Reproduced with permission from [28], © 1990 AIP

the donor concentration $n_{3D}$ corresponding to the 2D values of the delta-doping sheet were calculated from (6.23) and used in the abscissa of Fig. 6.14. The 2D mobility $\mu_{2D}$ is related to the doping-dependent mobility of bulk GaAs which is taken from the empirical expression $\mu_{3D} = \mu_L(1 + (n_{3D}/10^{17}\ \text{cm}^{-3})^{1/2})^{-1}$, $\mu_L = 10^4\ \text{cm}^2/(\text{Vs})$ being the mobility limit due to lattice scattering [31].

Figure 6.14 shows that the mobility of free carriers in the two-dimensional electron gas significantly exceeds that of bulk free carriers at high doping concentrations $n_{3D}$. The increase of mobility is assigned to various features of the 2D carriers. From an only weak dependence of the mobility $\mu_{2D}$ on temperature a reduced scattering at ionized impurities was concluded [29]. The carriers in the 2D electron gas have a high degeneracy on their energy levels $E_i$, connected to high kinetic energies parallel to the plane of the doping sheet. Carriers with energies close to the Fermi surface are most sensitive to scattering. Their energies $E_F - E_i$ exceed well the thermal energy $k_B T$, leading to a reduced temperature-dependent impurity scattering. A further contribution originates from a decreased overlap of odd-numbered carrier wave-functions with the delta-doping plane of impurities. Wave functions $\psi_1, \psi_3, \ldots$ have a node at the position of the doping sheet (cf. Fig. 6.13b) and hence experience much less impurity scattering. Also the overlap of symmetric even-numbered excited wave functions $\psi_2, \psi_4, \ldots$ is much smaller than that of the ground state $\psi_0$, and even the spatial extent of the ground state is significantly larger than the thickness of the doping sheet.

The delta-doping technique is used to improve the performance of electronic devices. The low impurity scattering in modulation-doped field-effect transistors (MOD FET, also termed HEMT, high electron-mobility transistor) can be further reduced by delta doping. In a conventional MOD FET a homogeneously doped

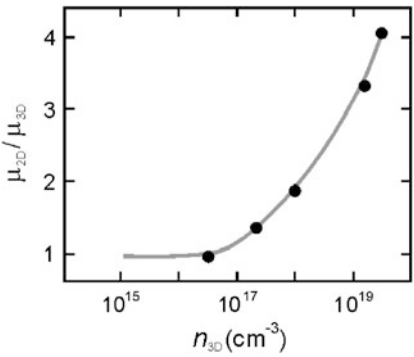


**Fig. 6.14** Relative mobility enhancement of delta-doped $n$-type GaAs with respect to homogeneously doped $n$-type GaAs measured at 300 K. Data from [29]

wide-bandgap layer (usually AlGaAs) provides free carriers, which are trapped at the heterojunction to an adjacent undoped layer with a smaller bandgap (GaAs). The carriers are two-dimensionally confined at the interface due to band bending in the undoped layer [32]. Employing delta doping instead of homogeneous doping allows for a large and well-defined separation between free carriers and doping impurities. Since band bending is also induced by a delta-doping layer, also homostructure FETs with a two-dimensional electron gas in the channel can be fabricated [e.g., [30]].

## 6.2 Diffusion

Atoms in a crystal may not stay fixed on their site. In presence of a concentration gradient and at sufficiently high temperature atoms redistribute by diffusion, thereby changing the interface abruptness in heterostructures and the spatial distribution of defects. The effect is utilized, e.g., for the indiffusion of dopants into semiconductors via the surface, but may also be detrimental for epitaxial nanostructures. Atoms diffuse via different mechanisms, which are controlled by temperature, partial pressure, and material composition. Since various diffusion paths usually act simultaneously and diffusivity may depend on defect concentration, diffusion is a complex subject. We will outline basic phenomena and illustrate some examples.

### *6.2.1 Diffusion Equations*

The diffusion of an atom incorporated in a crystal is described similar to the surface diffusion of an adatom considered in Sect. 5.2.2. Each jump of the atom to an adjacent site is the result of an attempt to leave the actual site and the success probability to surmount the potential barrier $\Delta E$ which tends to keep the atom at its site. The *diffusion coefficient* $D$ is likewise given by the product of the mean square value of the displacement $\lambda^2$ and the rate of successful jumps $\nu$, yielding

$$D = \lambda^2 \nu = \lambda^2 \nu_0 \exp\bigl(-\Delta E/(k_\mathrm{B}T)\bigr) = D_0 \exp\bigl(-\Delta E/(k_\mathrm{B}T)\bigr). \qquad (6.26)$$

The *diffusion constant* $D_0 = \lambda^2 \nu_0$ has usually an only small temperature dependence compared to the exponential term and is often assumed constant with respect to temperature. Note that $D_0$ may still vary spatially in an inhomogeneous solid.

To obtain an expression for the motion of a diffusing atom we first consider a macroscopic view of the diffusion of impurities in a solid; an atomistic approach is discussed below in Sect. 6.2.2. We assume an impurity concentration $c$ which varies only along a single coordinate $z$ and a random diffusion of an impurity which is not affected by other impurities. In this case the net flux of impurities $j$ per unit area and unit time also varies only along $z$ and is given by *Fick's first law*,

$$j(z) = -D\frac{d}{dz}c(z). \tag{6.27}$$

The flux of impurities $j(z)$ is proportional to the gradient of the impurity concentration $c(z)$ and directed toward the low-concentration region (cf. the negative sign). Since the atoms move in such a way as to even the gradient up, the one-dimensional form of Fick's law is sufficient to describe the flux. We note that there is no net flux if the impurity concentration is constant. The diffusion coefficient $D$ depends in a simple case not on the impurity concentration $c$ and also not on the spatial position $z$ (but still on the temperature). This case describes a *linear* Fick diffusion. A dependence $D(c, z)$ due to experimental conditions leads to a *non-linear* Fick diffusion also described by (6.27).

The impurity flux must comply with the *continuity condition*. The net flow into any volume element equals the increase of impurity concentration per unit time in this volume element,

$$\frac{\partial}{\partial z}j(z) = -\frac{\partial}{\partial t}c(z,t). \tag{6.28}$$

Inserting (6.27) into the one-dimensional continuity equation (6.28) yields the diffusion equation known as *Fick's second law*,

$$\frac{\partial}{\partial z}\left(D\frac{\partial c(z,t)}{\partial z}\right) = \frac{\partial c(z,t)}{\partial t}. \tag{6.29}$$

If the diffusion coefficient $D$ is constant with respect to $z$, then (6.29) simplifies to

$$D\frac{\partial^2 c(z,t)}{\partial z^2} = \frac{\partial c(z,t)}{\partial t}. \tag{6.30}$$

The solution to Fick's second law depends on the boundary conditions which are given by the experiment.

We consider some solutions of the one-dimensional diffusion equation in the form of (6.30) for different experimental conditions; a more comprehensive treatment is given in Ref. [33]. The first example is the indiffusion of impurities from the surface with a surface concentration kept constant at a value $c_0$. Such condition may be given by applying an external constant vapor pressure of impurity atoms on the surface. The impurity concentration in the solid depends only on the distance $z$ from the surface, which is assumed to be located at $z = 0$. The resulting boundary conditions read

$$c(z = 0, t) = c_0 \quad \text{for all } t, \quad \text{and} \quad c(z, t) = 0 \quad \text{for } z > 0 \text{ and } t = 0.$$

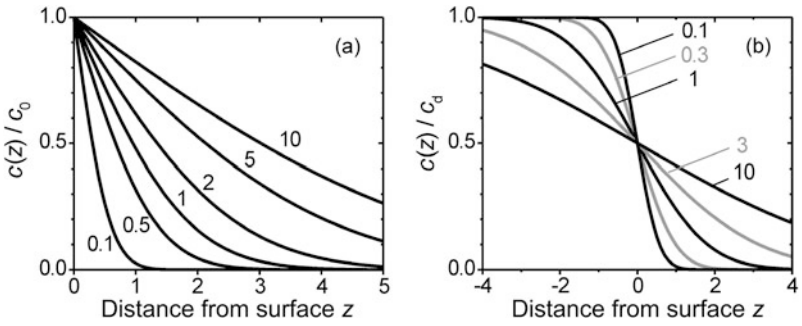


**Fig. 6.15** Solutions of the one-dimensional diffusion equation for two different boundary conditions. Concentration profiles $c(z)$ are given for varied values of the quantity $Dt$ as indicated on the curves. (**a**) Impurity distribution in an initially (at $Dt = 0$) undoped solid for a surface concentration kept constant at a value $c_0$. (**b**) Distribution for a solid being initially homogeneously doped with an impurity concentration $c_d$ at $z < 0$ and undoped at $z > 0$

The solution of the diffusion equation (6.30) for these conditions is

$$c(z,t) = c_0 \,\mathrm{erfc}\left(\frac{z}{2\sqrt{Dt}}\right),$$

where erfc is the complementary error function. The diffusion profile $c(z,t)$ depends on the diffusion coefficient $D(T)$ and the duration of the indiffusion process $t$. Profiles for varied values of the product $Dt$ are shown in Fig. 6.15a. The concentration profiles $c(z)$ show a progressive indiffusion of impurities for increasing process time $t$. The material is constantly supplied from the external vapor phase via the surface, such that $c(z = 0, t) = c_0$ during the entire process.

In our second example the source of impurities is assumed to be located within the solid. We consider a solid being doped with impurities with an (initially) constant concentration $c_d$ in a range $z < 0$ up to an interface located at $z = 0$. Beyond the interface at $z > 0$ the solid is assumed to be undoped. The boundary conditions are now

$$c(z) = c_d \quad \text{for } z < 0 \quad \text{and} \quad c(z) = 0 \quad \text{for } z > 0 \text{ for } t = 0.$$

The solution of the diffusion equation (6.30) in this case is given by

$$c(z,t) = \frac{c_d}{2}\,\mathrm{erfc}\left(\frac{z}{2\sqrt{Dt}}\right).$$

The result is quite similar to the first case. In contrast to the first example the total amount of impurities diffusing in the solid now is constant. Impurities diffusing across the interface hence increase the concentration $c$ at $z > 0$ on expense of $c$ at $z < 0$. The initial step-function-like profile gradually smoothness and has the shape of the complementary error function as shown in Fig. 6.15b. The impurity concentration at the interface remains fixed at $c(z = 0, t) = c_d/2$. The example resembles the first one as long as the doped part can be considered semi-infinite thick with respect to the diffusion length $\sqrt{Dt}$.

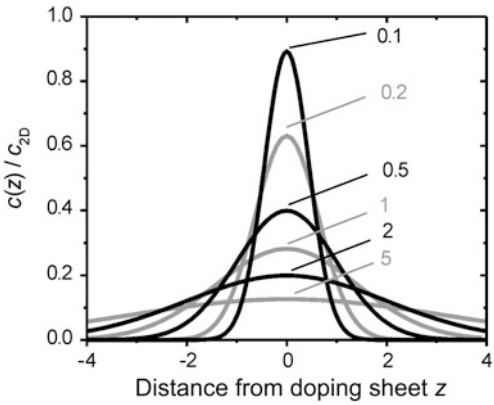


**Fig. 6.16** Impurity concentration-profiles for a doping sheet located at $z = 0$ initially (at $Dt = 0$) described by a $\delta$-function-like profile. Numbers on the curves signify respective values of $Dt$

In our third example a delta-doping sheet within an undoped solid is assumed to represent the source of impurities. The total impurity concentration $c_{2D}$ is initially (at $t = 0$) located in the two-dimensional $(xy)$-plane at $z = 0$. The boundary conditions are in this case

$$c(z,t) = c_{2D}\delta(z) \quad \text{for } t = 0, \quad \text{and} \quad \int_{z=-\infty}^{\infty} c(z,t) = c_{2D} = \text{const} \quad \text{for all } t > 0.$$

The solution of the diffusion equation (6.30) for this geometry is given by

$$c(z,t) = \frac{c_{2D}}{2\sqrt{\pi\, Dt}} \exp\left(-\frac{z^2}{4Dt}\right).$$

The total amount of impurities diffusing in the solid is constant like in the previous example. The initial $\delta$-function-like profile gradually broadens to a Gaussian distribution as illustrated in Fig. 6.16. The broadening is characterized by the increasing standard deviation of the distribution $\sigma = \sqrt{2Dt}$.

### *6.2.2 Diffusion Mechanisms*

The diffusion of atoms in a crystal depends on many experimental parameters in addition to the temperature, such as the material composition, the position of the Fermi level, or the concentration of point defects. An understanding of these dependences requires a microscopic view on the diffusion mechanisms. We consider some important mechanisms separately, even though usually a combination of these diffusion paths occurs in practice. Often the dominant mechanism provides a reasonable description of the diffusion process at least in some limited temperature range.

In a perfect crystal which does not contain point or line defects, the only mechanisms for atom diffusion on lattice sites are the exchange and ring mechanisms illustrated in Fig. 6.17a. Since many bonds need to be broken simultaneously in these collective mechanisms, they are associated with a very high activation energy for

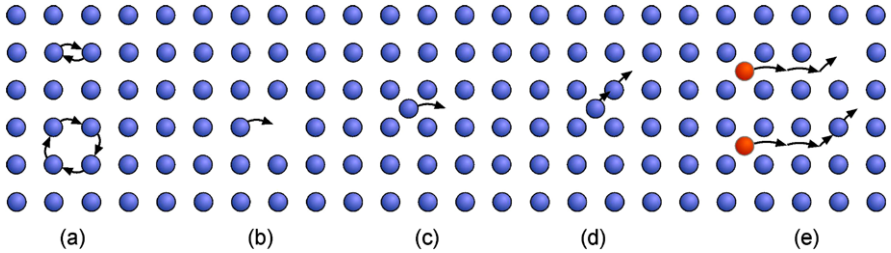


**Fig. 6.17** Schematic illustration of diffusion mechanisms. (**a**) *Top*: exchange mechanism, *bottom*: ring mechanism. (**b**) Vacancy mechanism. (**c**) Interstitial mechanism. (**d**) Interstitialcy mechanism. (**e**) Substitutional-interstitial mechanisms, *top*: Frank-Turnbull mechanism, *bottom*: kick-out mechanism

the migration and do not play a significant role in practice. Mechanisms involving defects are much more effective for both, diffusion of impurities and self-diffusion of crystal species. We focus on the effect of point defects and do not include phenomena in the presence of line defects.

*Vacancy mechanism*: Any crystal at finite temperature contains vacant lattice sites, which provide an efficient path of diffusion via substitutional sites. The elementary jump of an atom into a neighboring vacancy is depicted in Fig. 6.17b. Diffusion of substitutionally dissolved impurities or self-diffusion via this path is still slow compared to other mechanisms. Examples of slow impurity diffusors are the common Column III and Column V dopants in silicon as shown below in Fig. 6.18.

*Interstitial mechanism*: If atoms exist on interstitial sites, they can migrate by jumping from one interstitial site to another as illustrated in Fig. 6.17c. This mechanism is particularly favorable for small impurity atoms, which do not need to greatly displace crystal atoms from their regular lattice site. The mechanism is very efficient. Prominent fast diffusors are interstitially dissolved Cu, Li, H, or Fe in silicon [34]. Their large diffusivities are shown in Fig. 6.18.

*Interstitialcy* or *indirect interstitial mechanism*: This path is more likely for impurities with a similar size as lattice atoms or for self-diffusion. The mechanism implies a cooperative motion of two atoms as shown in Fig. 6.17d. An interstitial atom moves into a lattice site by pushing an atom, which originally occupied this site, to a neighboring interstitial site.

*Substitutional-interstitial mechanism*: This effective diffusion mechanism in semiconductors may apply for impurity atoms $A$ which can be incorporated on both a substitutional site $A_s$ and an interstitial site $A_i$ (hybrid solutes). Such impurities can diffuse via one of the two types of this mechanism depicted in Fig. 6.17e. The Frank-Turnbull (or, dissociative) mechanism involves vacancies $V$ according the reaction [35]

$$A_i + V \leftrightarrow A_s. \tag{6.31}$$

The kick-out mechanism involves self-interstitials $I$ (interstitials of crystal species) according the reaction [36, 37]

$$A_i \leftrightarrow A_s + I. \tag{6.32}$$

The diffusivity of $A_\mathrm{i}$ is generally much larger than that of $A_\mathrm{s}$, while the solubility and hence also the equilibrium concentration $c_\mathrm{i}$ on interstitial sites is much less than on lattice sites $c_\mathrm{s}$. An efficient incorporation of impurities $A$ may then proceed by a fast interstitial diffusion for many consecutive jumps, eventually followed by the occupation of a regular lattice site. This process differs from the interstitialcy mechanism, where the atom in the interstitial position remains there for only a single step. The Frank-Turnbull and kick-out mechanisms are prevailing diffusion paths for many substitutionally dissolved fast diffusing elements in Column-IV and III–V semiconductors. Well established examples are the diffusion of Cu, Ag, and Au in Ge via the Frank-Turnbull mechanism and that of Au, Zn, Pt, and S in Si via the kick-out mechanism.

### *6.2.3 Effective Diffusion Coefficients*

Usually several of the diffusion mechanisms outlined above act simultaneously. Since diffusion coefficients vary over many orders of magnitude depending on experimental conditions the dominating path may already provide a reasonable description. We illustrate some dependences of the diffusivity for the important diffusion mechanisms with participating point defects. In compound semiconductors single point defects are vacancies, interstitials, and antisites. Their equilibrium concentrations depend on the parameters temperature, partial pressures, and composition, which are mutually related by the phase diagram. In this section we assume the concentration $C_\mathrm{defect}$ as given quantities to point out their effect on diffusivity.

*Vacancy mechanism*: One diffusion jump of this mechanism requires the presence of one vacancy $V$. The diffusion coefficient $D$ of the migrating species is therefore proportional to the concentration of vacancies $C_V$. An atom with no adjacent vacancy can also move, if first a vacancy diffuses to a neighboring lattice site. The diffusion coefficient $D$ is therefore also proportional to the diffusion coefficient $D_V$ of the vacancies, eventually yielding

$$D \propto C_V D_V .$$

*Substitutional-interstitial mechanism*: There are two types of this mechanism as outlined in the previous section. In the *Frank-Turnbull* mechanism (Fig. 6.17e, top) the diffusivity of the impurity $A$ is essentially given by the (large) diffusivity $D_\mathrm{i}$ of the (small) fraction $A_\mathrm{i}$ dissolved on interstitial sites. The marginal contribution of substitutional impurities $A_\mathrm{s}$, which either diffuse directly via the vacancy mechanism or interact with self-interstitials, is neglected. According (6.31) the diffusion mechanism involves the three species $A_\mathrm{i}$, $A_\mathrm{s}$, and vacancies $V$. The diffusivity of $A_\mathrm{s}$ depends on the incorporation rate of impurities $A$ on a lattice site. It is determined by the slower process of either supplying interstitials $A_\mathrm{i}$ or vacancies $V$ from the sample surface. If the supply of interstitials limits the process due to experimental conditions (i.e., $C_\mathrm{i}^\mathrm{eq} D_\mathrm{i} \ll C_V^\mathrm{eq} D_V$), the effective diffusivity of the *Frank-Turnbull* mechanism is given by [34, 38]

$$D_{\text{eff}}^{\lim(\text{i})} = \left(\frac{C_{\text{i}}^{\text{eq}}}{C_{\text{i}}^{\text{eq}} + C_{\text{s}}^{\text{eq}}}\right) D_{\text{i}}$$
$$\approx \left(C_{\text{i}}^{\text{eq}}/C_{\text{s}}^{\text{eq}}\right) D_{\text{i}} \quad \text{(Frank-Turnbull, limited by interstitials)}.$$

$C_{\text{i}}^{\text{eq}}$ and $C_{\text{s}}^{\text{eq}}$ being the local equilibrium concentrations of $A_{\text{i}}$ and $A_{\text{s}}$, respectively. The index lim(i) denotes the limitation by the supply with interstitials. If the supply of vacancies limits the process (i.e., $C_V^{\text{eq}} D_V \ll C_{\text{i}}^{\text{eq}} D_{\text{i}}$), the local equilibrium concentration of vacancies $C_V^{\text{eq}}$ controls the effective diffusivity according

$$D_{\text{eff}}^{\lim(V)} = \left(C_V^{\text{eq}}/C_{\text{s}}^{\text{eq}}\right) D_V \quad \text{(Frank-Turnbull, vacancy-limited)}.$$

The *kick-out* type of the substitutional-interstitial mechanism involves the species $A_{\text{i}}$, $A_{\text{s}}$, and self-interstitials $I$ according (6.32). Now the diffusivity of $A_{\text{s}}$ depends on the rate of in-diffusion of $A_{\text{i}}$ and the out-diffusion of self-interstitials. When a slow in-diffusion of $A_{\text{i}}$ controls the process, $C_{\text{i}}^{\text{eq}} D_{\text{i}} \ll C_I^{\text{eq}} D_I$ holds and the diffusion coefficient is identical to $D_{\text{eff}}^{\lim(\text{i})}$ of the Frank-Turnbull mechanism noted above. If the out-diffusion of self-interstitials limits the process, the diffusivity becomes [34]

$$D_{\text{eff}}^{\lim(I)} \cong \left(C_I^{\text{eq}}/C_{\text{s}}^{\text{eq}}\right)\left(C_{\text{s}}^{\text{eq}}/C_{\text{s}}\right)^2 D_I \quad \text{(kick-out, self-interstitial-limited)},$$

where $C_I^{\text{eq}}$ is the local equilibrium concentration of self-interstitials $I$ and $C_{\text{s}} = C_{\text{s}}(\mathbf{r})$ is the actual local concentration of substitutional impurities $A_{\text{s}}$. A simultaneous operation of diffusion mediated by self-interstitials *and* vacancies leads for $C_{\text{i}}^{\text{eq}} D_i \gg (C_I^{\text{eq}} D_I + C_V^{\text{eq}} D_V)$ to a combined effective diffusivity composed of both parts, i.e. $D_{\text{eff}} = D_{\text{eff}}^{\lim(I)} + D_{\text{eff}}^{\lim(V)}$. Using such effective diffusivities the diffusion via the various substitutional-interstitial mechanisms can be described by a single effective process using Fick's diffusion equation (6.29).

*Effect of charge*: The diffusivity of a point defect $D_{\text{defect}}$ depends strongly on its charge state. Since defects in semiconductors are usually charged, this property must be included into the terms discussed above. A stable charged point defect must possess an electronic level in the fundamental energy gap [37]. If a charged defect has several charge states, the thermal equilibrium concentrations of the differently charged defects depend on the position of the Fermi level. This feature is related to the dependence of the defect formation energy as illustrated in Fig. 6.6 for some native point defects in GaAs.

The substitutional-interstitial mechanism represents the diffusion of an impurity-defect complex. The interaction of the impurity and the defect depends on the charge state of the defect and the impurity, and so also the diffusivity of the complex. The Frank-Turnbull reaction (6.31) of an interstitial impurity $A_{\text{i}}^{l+}$ with charge $l+$, an $m$-fold negatively charged vacancy $V^{m-}$, and a substitutional impurity $A_{\text{s}}^{n-}$ with charge $n-$ reads [34]

$$A_{\text{i}}^{l+} + V^{m-} \leftrightarrow A_{\text{s}}^{n-} + (l - m + n)h.$$

$h$ denotes the holes created or consumed in this reaction due to the charge balance condition, and $l$, $m$, $n$ are integers. In compound semiconductors the vacancy is here

assumed to be located on the same sublattice in which the substitutional impurity $A_s$ is dissolved. Charged species were introduced in literature to describe the diffusion of Zn in GaAs according the reaction $Zn_i^+ + V_{Ga} \leftrightarrow Zn_s^- + 2h^+$, and since then the Frank-Turnbull process involving charged species is also referred to *Longini mechanism* [39]. For the kick-out mechanism the relation is given by

$$A_i^{l+} \leftrightarrow A_s^{n-} + I^{m+} + (l - m + n)h.$$

Diffusivities following from the charge-including reactions depend on the supply of the charged defects similar to the reactions without charge discussed above. If the supply of interstitials $A_i$ limits the process, we obtain [34]

$$D_{\text{eff}}^{\lim(i)} = (|n| + 1)\left(\frac{C_i^{\text{eq}}(C_s^{\text{eq}})}{C_s^{\text{eq}}}\right)\left(\frac{C_s}{C_s^{\text{eq}}}\right)^{|n|\pm l} D_i$$

(Frank-Turnbull with charged defects, interstitial-limited).

A positive sign in the exponent applies for substitutional acceptors, a negative for substitutional donors. The reaction does not depend on the charge $m$ of the vacancy. The equation accounts for a (possibly) locally varying electron or hole concentration, yielding an also locally varying concentration $C_i^{\text{eq}}$ of charged interstitials $A_i^{l+}$. Similar to the uncharged case the same equation applies to the kick-out mechanism when a slow in-diffusion of $A_i$ limits the incorporation rate of $A_s$. If the incorporation rate of $A_s$ in the Frank-Turnbull process with charged defects is limited by the supply of vacancies, then the effective diffusivity of $A_s$ impurities is described by [34]

$$D_{\text{eff}}^{\lim(V)} = (|n| + 1)\left(\frac{C_V^{\text{eq}}(C_s^{\text{eq}})}{C_s^{\text{eq}}}\right)\left(\frac{C_s^{\text{eq}}}{C_s}\right)^{\pm m-|n|} D_V$$

(Frank-Turnbull with charged defects, vacancy-limited).

When in the kick-out mechanism with charged defects the incorporation of $A_s$ is limited by the supply of self-interstitials, the effective diffusivity is analogously given by

$$D_{\text{eff}}^{\lim(I)} = (|n| + 1)\left(\frac{C_I^{\text{eq}}(C_s^{\text{eq}})}{C_s^{\text{eq}}}\right)\left(\frac{C_s^{\text{eq}}}{C_s}\right)^{\pm m-|n|-2} D_I$$

(kick-out with charged defects, self-interstitial-limited).

If the diffusion coefficient of each charged complex is independent of that of other complexes, the resulting effective diffusion coefficient is given by a linear combination of the diffusivities of all complexes. This leads eventually to an effective diffusion coefficient, which in the general case is composed of the effective diffusion coefficients of all defect complexes with all occurring charge states. We abbreviate the notation for effective diffusivities of the two substitutional-interstitial mechanisms (6.31) and (6.32) by $D_{\text{eff}}(AV)$ for the Frank-Turnbull type and $D_{\text{eff}}(AI)$ for the kick-out type, and include the various charge states of vacancies $V^0, V^-, V^{2-}, \ldots,$

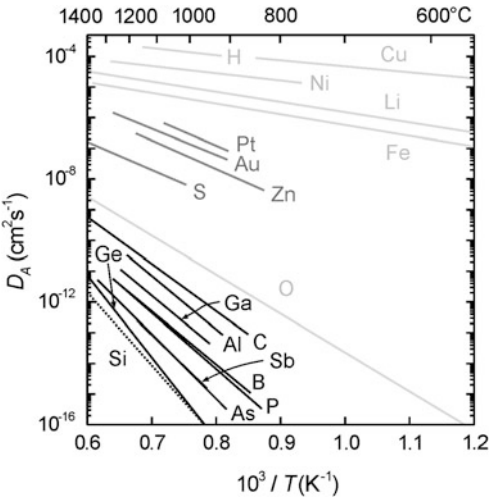


**Fig. 6.18** Diffusion coefficients $D_A$ of impurities $A$ in Si. *Black lines* refer to elements which mainly dissolve substitutionally and diffuse via the vacancy or interstitialcy mechanism. *Gray lines* represent data of hybride elements which diffuse via the substitutional-interstitial mechanism. *Light gray lines* give data of elements diffusing via the direct interstitial mechanism. The *dotted line* represents Si self-diffusion. Data from [40], Li, Fe, and Ga from [41]

$V^+$, $V^{2+}$, ... and the same for self-interstitials $I$. We then may write for the general case

$$D_{\text{eff}} = \sum_{z_{V,\min}}^{z_{V,\max}} D_{\text{eff}}\left(AV^{z_V}\right) + \sum_{z_{I,\min}}^{z_{I,\max}} D_{\text{eff}}\left(AI^{z_I}\right).$$

In the sums the charge states of the native defects characterized by the integers $z_V$ and $z_I$ start at the most negative values $z_{V,\min}$ and $z_{I,\min}$ occurring in the considered semiconductor, and end at the corresponding most positive values.

The relations discussed in this section point up the complexity of diffusion phenomena in semiconductors. A clear description is usually restricted to specific elements and a limited temperature range. Diffusivities of some impurity atoms in silicon are shown in Fig. 6.18.

The diffusion coefficients shown in the Arrhenius plot are described by the relation (6.26) and vary over many orders of magnitude. We note the very high diffusivity of the elements moving via the interstitial mechanism (light gray lines, except for O) and the slowly moving substitutional impurities diffusing via the vacancy mechanism or the interstitialcy mechanism (black lines). Such elements are favorable for fabricating stable doping profiles.

### *6.2.4 Disordering of Heterointerfaces*

Epitaxial growth procedures have proved their ability to fabricate atomically sharp heterointerfaces. Such interfaces provide strong gradients in the distribution of different atom species and hence a driving force for disordering by diffusion. There may even exist growth conditions which counteract the formation of atomically

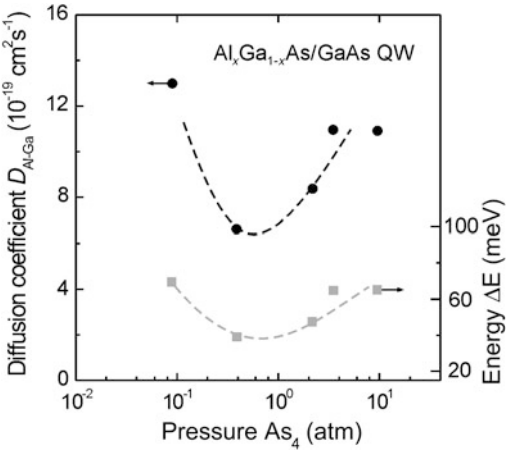


**Fig. 6.19** Energy shift $\Delta E$ of the photoluminescence from an $Al_{0.25}Ga_{0.75}As$/GaAs quantum well annealed for 25 h at 825 °C at various values of the $As_4$ ambient pressure (*gray squares*). The *black circles* are corresponding calculated diffusion coefficients of the Al-Ga interdiffusion. *Dashed lines* are guides to the eye. From [43]

sharp interfaces. Furthermore, also the preservation of sharp interfaces is important, e.g., during device processing of heterostructures. On the other hand, a well-directed locally enhanced layer disordering was employed for both studying diffusion mechanisms and defining lateral confinement for photons and charge carriers in optoelectronic devices. We consider disordering of heterointerfaces in more detail for $Al_xGa_{1-x}As$-based heterostructures to illustrate the effect of experimental conditions on the diffusivity outlined in the previous section.

The self-diffusion of Ga in GaAs was found to be quite low under intrinsic conditions. A similar diffusivity was found for Ga self-diffusion $D_{Ga}(n_i)$ and Ga-Al interdiffusion $D_{Al\text{-}Ga}(n_i)$ obtained from AlGaAs/GaAs heterostructures, both being well described by (6.26) with a diffusion constant $D_0 = 2.9 \times 10^8$ cm$^2$/s and a fairly high activation energy $\Delta E \cong 6$ eV [42]. Such values correspond to a diffusion length $\sqrt{Dt}$ of 1 nm for 30 h diffusion at 1100 K. Since the self- and interdiffusion on the Column III sublattice must proceed through native defects of the crystal, the diffusivity depends on the As pressure applied during the annealing at elevated temperature. Pressure-depending interdiffusion coefficients were derived from an evaluation of the photoluminescence energy-shift measured for annealed $Al_{0.25}Ga_{0.75}As$/GaAs quantum well samples [43]. The diffusion of Al and Ga across the heterointerfaces of the 13 nm thick quantum well leads to a change of the confinement potential, resulting in a blue-shift of the energy levels.

Figure 6.19 shows that both, a high *and* a low $As_4$ ambient pressure applied during annealing leads to an enhanced $D_{Al\text{-}Ga}$ interdiffusion coefficient. The increase of $D_{Al\text{-}Ga}$ is generated by the change of the native defect concentration via the sample surface. Six single point defect species may occur in GaAs. A shift of the crystal stoichiometry to the As-poor side favors the creation of As vacancies $V_{As}$, Ga interstitials $I_{Ga}$, and Ga antisites $Ga_{As}$. As-rich point defects are Ga vacancies $V_{Ga}$, As interstitials $I_{As}$, and As antisites $As_{Ga}$. Corresponding defects apply for Al which occupies the same sublattice as Ga, leading to the more general notation for Column III defects, e.g., Column III vacancies $V_{III}$.

A consistent description including also Fermi-level effects was obtained by considering the Column III self-diffusion as being due to neutral and singly ionized Column III vacancies $V_{\mathrm{III}}$ and Column III interstitials $I_{\mathrm{III}}$ [44]. A creation of such a defect pair can occur according the reaction

$$0 \leftrightarrow I_{\mathrm{III}} + V_{\mathrm{III}} \quad \text{and} \quad C_{\mathrm{I_{III}}} C_{\mathrm{V_{III}}} = k_1.$$

The second equation expresses the law of mass action with the concentrations $C$ of the participating defects and a temperature-dependent constant $k_1$. Under As-rich conditions the crystal surface can act as a sink for the interstitials $I_{\mathrm{III}}$, thereby increasing the concentration of vacancies $C_{V_{\mathrm{III}}}$. Under As-poor conditions, evaporation of As at the surface leads to a local excess of Ga atoms, which can diffuse into the crystal and increase the concentration of interstitials $C_{I_{\mathrm{III}}}$ according the reaction

$$0 \leftrightarrow I_{\mathrm{III}} + \frac{1}{4}\mathrm{As}_4^{\mathrm{vapor}} \quad \text{and} \quad C_{I_{\mathrm{III}}} P_{\mathrm{As_4}}^{1/4} = k_2.$$

Both $V_{\mathrm{III}}$ and $I_{\mathrm{III}}$ can lead to Column III self-diffusion, yielding a diffusivity

$$D_{\mathrm{III}} = c_1 C_{V_{\mathrm{III}}} D_{V_{\mathrm{III}}} + c_2 C_{I_{\mathrm{III}}} D_{I_{\mathrm{III}}} = c_3 P_{\mathrm{As_4}}^{1/4} D_{V_{\mathrm{III}}} + c_4 P_{\mathrm{As_4}}^{-1/4} D_{I_{\mathrm{III}}}.$$

The $c_i$ are constants containing the temperature-dependent constants $k_j$. In the second equation we used the law of mass action involving $k_2$. The equation describes the trend of the pressure-dependent diffusivity shown in Fig. 6.19. Under As-poor conditions the diffusivity is increased by Column III interstitials $I_{\mathrm{III}}$, while under As-rich conditions Column III vacancies $V_{\mathrm{III}}$ enhance the diffusivity.

The diffusivity is also affected by doping. A shift of the Fermi level from the intrinsic position can increase the self-diffusion by orders of magnitude. Evidence for a combined effect of doping and ambient pressure on heterointerfaces applied during annealing is given in Fig. 6.20. The TEM images show cross sections of $n$-type (left, $n = 10^{18}$ cm$^{-3}$) and $p$-type (right, $p = 8 \times 10^{18}$ cm$^{-3}$) AlGaAs/GaAs superlattices, which were annealed for 10 h at elevated temperature [45]. The $n$-type structure shows some interdiffusion for an anneal under As-poor conditions, and a much stronger layer intermixing in As-rich ambient. In contrast, the $p$-type structure shows a complete intermixing for As-poor conditions, while the superlattice remains stable in As-rich ambient. Experiments with compensated doping (i.e., simultaneous doping with donors *and* acceptors) confirmed that the enhancement of the interdiffusivity is controlled by the position of the Fermi level and not by the presence of impurity atoms [46].

The experimental results point to the participation of charged defects in the effective diffusivity $D_{\mathrm{III}}$. Their equilibrium concentration depends on their energy position in the bandgap with respect to the Fermi level. Considering only neutral and singly ionized vacancies $V_{\mathrm{III}}$ and interstitials $I_{\mathrm{III}}$ yields for the donor-like interstitials $I_{\mathrm{III}}$ the relation $C_{I_{\mathrm{III}}^+}/C_{I_{\mathrm{III}}^0} = \exp((E_{\mathrm{D}} - E_{\mathrm{F}})/(k_{\mathrm{B}}T))$, and for the acceptor-like vacancies $V_{\mathrm{III}}$ the ratio $C_{V_{\mathrm{III}}^-}/C_{V_{\mathrm{III}}^0} = \exp((E_{\mathrm{F}} - E_{\mathrm{A}})/(k_{\mathrm{B}}T))$ [44]. The difference of the ionization energy and the Fermi level in the exponential terms represents the energy gain when the native defect is charged, cf. Fig. 6.1 and Sect. 6.1.2. If the Fermi level is decreased by extrinsic $p$-type doping, the donor-like interstitials $I_{\mathrm{III}}$

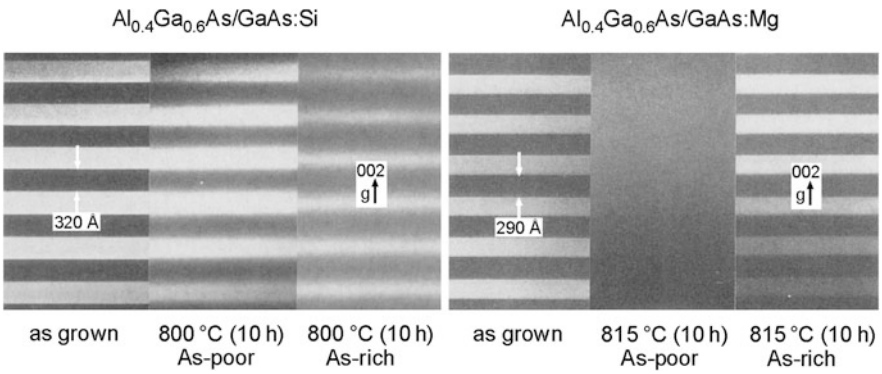


**Fig. 6.20** Transmission electron micrographs of cross sections of Si-doped (*left*) and a Mg-doped (*right*) $Al_{0.4}Ga_{0.6}As/GaAs$ superlattices. The images show the as-grown structures and the structures after annealing for 10 h under either As-poor or As-rich conditions. Reproduced with permission from [45], © 1988 MRS

are positively charged and attain an increased solubility and corresponding high concentration $C_{I_{III}^+}$. In $n$-type heterostructures the solubility and thereby concentration of acceptor-like charged vacancies $V_{III}^-$ is increased. Introducing respective diffusivities of the charged native defects, the effective diffusion constant for Column III self-diffusion noted above only for undoped defects is extended and reads [44]

$$D_{III} = c_5 P_{As_4}^{1/4}\left(D_{V_{III}^0} + D_{V_{III}^-}\exp\left((E_F - E_A)/(k_B T)\right)\right) + c_6 P_{As_4}^{-1/4}\left(D_{I_{III}^0} + D_{I_{III}^+}\exp\left((E_D - E_F)/(k_B T)\right)\right).$$

According this relation the diffusivity increases when $p$-type AlGaAs heterostructures are annealed in an As-poor ambient, because both effects increase the concentration of interstitials $I_{III}$. The diffusivity increases also when $n$-type structures are annealed in an As-rich ambient. In this case both effects increase the concentration of vacancies $V_{III}$.

The effect of the Fermi-level position on the effective diffusivity is more pronounced for multiple charged defects. A cubic dependence of $D_{III}$ on the electron concentration, e.g., points to the participation of a triply charged defect $V_{III}^{3-}$ [42]. A definite assignment to a specific charged defect is though difficult, because both the enthalpy of formation and the enthalpy of migration enter the effective diffusivity, and *both* quantities change if the charge state of a defect changes due to a shift of the Fermi-level [44].

The spatially selective modification of heterostructure interfaces by layer disordering was also employed for device fabrication. By applying masks on the surface, a laterally selective intermixing of quantum well heterostructures is obtained. The corresponding change of the bandgap and the refractive index with respect to the not intermixed regions can be used to locally confine charge carriers and photons. If, e.g., a sample containing a quantum-well is exposed to intermixing conditions except along a stripe, the lateral regions adjacent to the stripe have a larger bandgap

and a lower refractive index. These effects were used to fabricate, e.g., index-guided edge-emitting lasers of III–V [47, 48] and II–VI [49] semiconductors. Techniques employed for selective intermixing comprise impurity-induced layer disordering (IILD) by introducing dopants [50], impurity-free vacancy disordering (IFVD) by supplying vacancies [47], and ion-implantation-induced composition disordering (IID).

## 6.3 Metal-Semiconductor Contact

Any electronic semiconductor device requires an electric contact between the semiconductor and a metal. A metal-semiconductor junction may have either rectifying or ohmic characteristics, depending on the two materials which are brought into contact. The problem is closely related to the band alignment of a semiconductor heterostructure treated in Sect. 3.2. We will introduce the characteristics of a classical ideal metal-semiconductor contact, nonideal effects, and some approaches to fabricate ohmic junctions.

### *6.3.1 Ideal Schottky Contact*

We consider a rectifying metal-semiconductor contact in the framework of the model introduced by W. Schottky [51] and N.F. Mott [52]. According the simple Schottky-Mott model the properties of the junction are determined by the work function $e\phi_{\mathrm{m}}$ of the metal and that of the semiconductor $e\phi_{\mathrm{sc}}$. Since $\phi_{\mathrm{m}}$ may be larger or smaller than $\phi_{\mathrm{sc}}$ and the latter depends on the type of semiconductor ($n$ or $p$), we have to distinguish four cases. We first consider a metal—$n$-type semiconductor junction with $\phi_{\mathrm{m}} > \phi_{\mathrm{sc}}$. Figure 6.21a shows the energy-band diagram of the two solids before contact, taking the vacuum level $E_{\mathrm{vac}}$ as reference energy. Since the work functions of the metal and the semiconductor differ, electrons will flow from the side with a high Fermi energy to that with a lower Fermi energy for equilibration if a contact is made. The difference $\phi_{\mathrm{m}} - \phi_{\mathrm{sc}}$ is referred to as *contact potential*. In the case depicted in Fig. 6.21a electrons are transferred to the metal, leaving positively charged donors without a balancing negative charge in the $n$-type semiconductor. A positive space charge is thereby built up in the interface-near region of the semiconductor, leading to a bending of the band edges over a width $w$, which is depleted from free electrons. Outside the depletion layer the semiconductor is neutral. The positive space charge in the semiconductor is balanced by an equal negative charge at the metal surface. The dipole potential equilibrates the contact potential. In thermal equilibrium these quantities are equal and the Fermi energy is constant through the junction. We note from Fig. 6.21b that now a barrier $e\phi_{\mathrm{Bn}}$ exists at the junction. The height of this Schottky barrier is given by the band bending $eV_{\mathrm{bi}}$, the so-called built-in potential barrier, and the energy spacing between the Fermi level and the conduction-band edge in the semiconductor,

$$e\phi_{\mathrm{Bn}} = e(V_{\mathrm{bi}} + \phi_{\mathrm{sc}} - \chi) = e(\phi_{\mathrm{m}} - \chi), \tag{6.33}$$

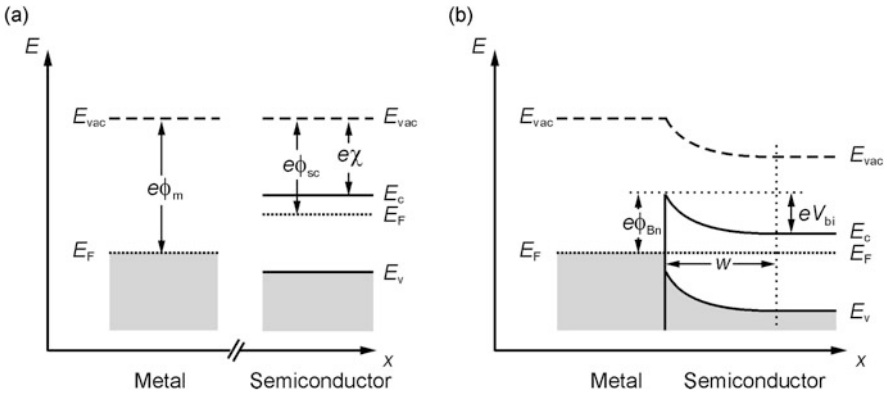


**Fig. 6.21** Energy-band diagram of an ideal junction between a metal with a large work function $e\phi_m$ and an $n$-type semiconductor with a smaller work function $e\phi_{sc}$. (**a**) Before contact, (**b**) in contact without an external bias. $e\phi_m$ and $w$ denote the height of the Schottky barrier and the width of the space-charge region, respectively. *Gray shadings* indicate occupied bands

$e\chi$ being the electron affinity of the semiconductor as depicted in Fig. 6.21a. Equation (6.33) shows that the built-in potential equals the contact potential, $V_{bi} = \phi_m - \phi_{sc}$. Values of work functions and electron affinities for some solids are given in Table 6.2.

The width of the space-charge region $w$ may be calculated in the Schottky-Mott model under the abrupt approximation, i.e., assuming that the charge density in this region is given by the constant concentration of the donors, $\rho = en_D$. Outside the space-charge region the semiconductor is neutral and $\rho = 0$. The potential in the semiconductor is obtained from the one-dimensional Poisson equation

$$\frac{d^2V}{dx^2} = -\frac{\rho}{\varepsilon},$$

where $\varepsilon = \varepsilon_r \times \varepsilon_0$ is the permittivity. Taking the location of the junction along $x$ and $E_c$ in the bulk of the semiconductor as origin, integration leads to

$$V(x) = \frac{en_D}{\varepsilon}\left(wx - \frac{1}{2}x^2\right) - V_{bi}. \tag{6.34}$$

The width of the depletion region $w$ is obtained from the condition $V(x = w) = 0$, yielding

$$w = \left(\frac{2\varepsilon V_{bi}}{en_D}\right)^{1/2}. \tag{6.35}$$

In (6.35) we assumed a complete ionization of donors in the space-charge region and a zero bias across the junction. If the thermal distribution of the majority carriers is taken into account, the charge density $\rho = en_D$ is replaced by $\rho = en_D(1 - \exp[eV(x)/(k_BT)])$. $V_{bi}$ in (6.35) is then replaced by $(V_{bi} - k_BT/e)$. If an external bias $V_{ext}$ is applied to the metal-semiconductor junction, this quantity

**Table 6.2** Work functions $\phi_m$ of some metals and electron affinities $\chi$ of some semiconductors. Metal data from [53], semiconductors from [54]

| Metal | $e\phi_m$ (eV) | Semiconductor | $e\chi$ (eV) |
|---|---|---|---|
| Al | 4.28 | Ge | 4.00 |
| Au | 5.10 | Si | 4.05 |
| Ni | 5.15 | SiC (4H) | 4.05 |
| Pd | 5.12 | GaAs | 4.07 |
| Pt | 5.65 | InP | 4.38 |
| Ti | 4.31 | GaN | 4.10 |
| W | 4.54 | ZnSe | 4.09 |

is also added. The more complete expression then reads

$$w = \left( \frac{2\varepsilon(V_{bi} - V_{ext} - k_B T/e)}{e n_D} \right)^{1/2}$$
(external bias and thermal carrier distribution included). (6.36)

Application of an external bias $V_{ext}$ such that the semiconductor is negative with respect to the metal (forward bias) lowers the barrier to $e(V_{bi} - V_{ext} - k_B T/e)$, while a reverse bias leaves the barrier $e\phi_{Bn}$, in this first-order model, unaffected. The Schottky barrier hence represents an asymmetric resistance for the current across the junction. The junction has a rectifying character, it represents a *Schottky diode*.

The treatment above refers to a metal—$n$-type semiconductor junction. We now compare the four basic cases of $\phi_m > \phi_{sc}$, $\phi_m < \phi_{sc}$, and contacts to either an $n$-type or a $p$-type semiconductor. If the junction to the $n$-type semiconductor is made using a metal with a *smaller* work function $\phi_m < \phi_{sc}$, electrons will flow from the metal to the semiconductor for equilibration. In thermal equilibrium (without external bias), when the Fermi energy is constant across the junction, a negative space charge in the semiconductor balances an equal positive charge at the junction in the metal. Figure 6.22b depicts the resulting band bending in the semiconductor. There exits no barrier for an electron flow from the $n$-type semiconductor to the metal, and a small barrier $e(\phi_{sc} - \chi)$ for the reverse direction. Such a contact has nearly ohmic character.

A comparable case is the metal—$p$-type semiconductor junction for a *larger* work function of the metal $\phi_m > \phi_{sc}$ depicted in Fig. 6.22c. When the contact is made, electrons flow from the semiconductor to the metal to equilibrate the Fermi level $E_F$. The band bending in the semiconductor originating from the space charge of the positively ionized donors is qualitatively similar to the case assumed in Fig. 6.22a, but now there exists no barrier for an electron flow from the metal to the $p$-type semiconductor, and an only small barrier $e(\chi - \phi_{sc})$ exists for the reverse direction. This contact is nearly ohmic.

The last case of the metal—$p$-type semiconductor junction for a *smaller* work function of the metal $\phi_m < \phi_{sc}$ depicted in Fig. 6.22d has similarities to the first case shown in Figs. 6.22a and 6.21. The band bending in the semiconductor $eV_{bi}$ due to an equilibrating electron flow from the metal to the semiconductor leads to

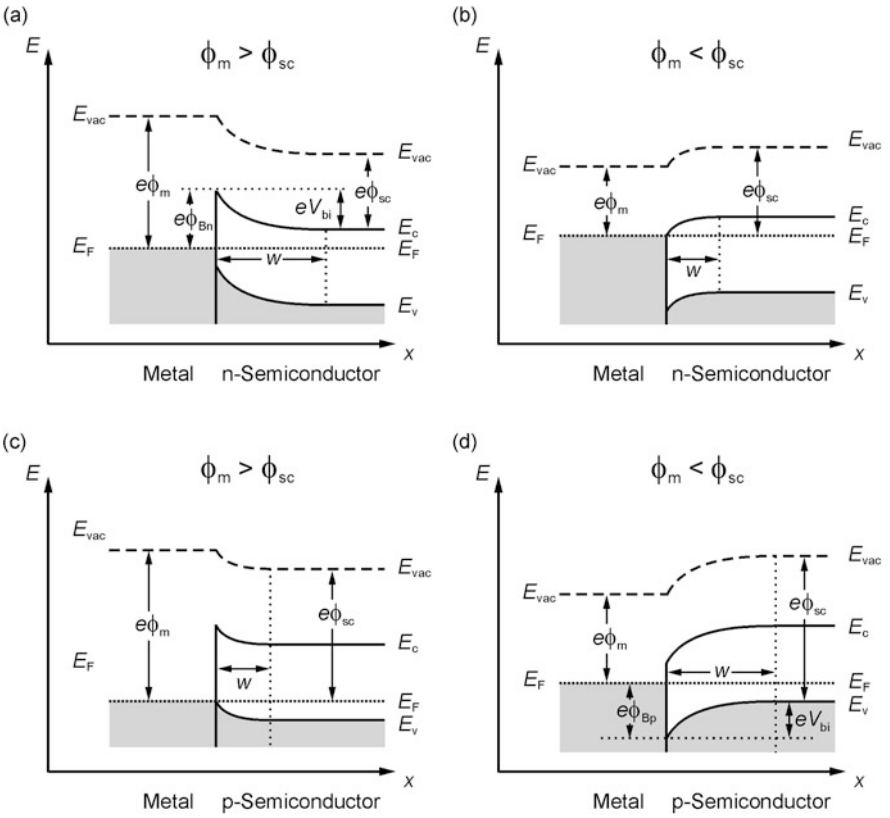


**Fig. 6.22** Energy-band diagrams of ideal junctions between metal and an either $n$-type semiconductor (**a**, **b**) or a $p$-type semiconductor (**c**, **d**). Metal work functions $e\phi_m$ being larger (**a**, **c**) or smaller (**b**, **d**) than the work functions of the semiconductors $e\phi_{sc}$ are assumed

the Schottky barrier $e\phi_{Bp} = e(\chi - \phi_m)$. The barrier for the flow of holes is lowered to $e(V_{bi} - V_{ext})$ when an external bias $V_{ext}$ is applied such that the semiconductor is positive with respect to the metal. For the reverse bias the barrier $e\phi_{Bp}$ remains virtually unaffected, leading to a rectifying characteristics of this junction.

The height of the Schottky barriers in cases (a) and (d) above is somewhat reduced, if the *Schottky effect* is taken into account. A free carrier in the semiconductor with charge $-e$ experiences an image-charge effect near the junction to the metal, because the metal surface is an equipotential surface. This modifies the potential distribution similar to the case if an image charge $+e$ were equidistant to the junction on the metal side. The reduction of the Schottky barrier $\Delta\phi$ by this effect depends on the external bias and is given by the resulting electric field, $\Delta\phi = (e|\mathbf{E}|/(4\pi\varepsilon_r\varepsilon_0))^{1/2}$. The Schottky effect is hence diminished by the large relative permittivity $\varepsilon_r$ of semiconductors and usually quite small ($\sim$10–20 meV). Since real metal-semiconductor junctions are dominated by other effects the Schottky effect is not detailed here.

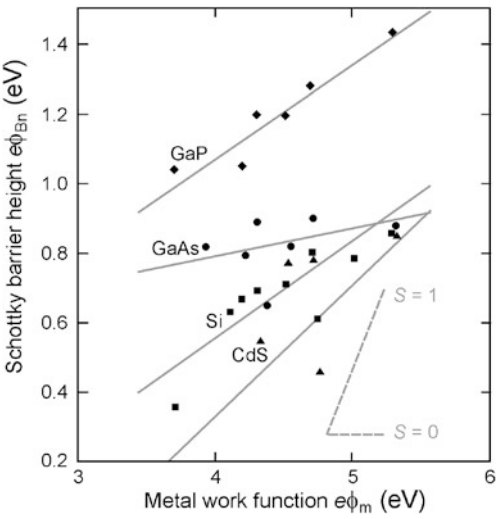


**Fig. 6.23** Schottky barrier heights for various junctions between *n*-type semiconductor and metal. *Gray solid lines* are least-square fits to experimental data, *dashed lines* indicate the slope for slope parameters $S$ equal 1 and 0. Data from [55]

### *6.3.2 Real Metal-Semiconductor Contact*

The Schottky-Mott model pointed out above predicts the Schottky-barrier height $e\phi_B$ to be the difference between the semiconductor electron affinity $e\chi$ and the metal work function $e\phi_m$. Consequently the slope parameter $S = \delta\phi_B/\delta\phi_m$, which describes the variation of the barrier height of a given semiconductor with different metal contacts, is unity in this ideal case. Experimental Schottky barrier heights are, however, often only weakly dependent on the metal work function. Some typical results for are plotted in Fig. 6.23 for various semiconductors versus the work function of the applied metal. The steep dashed line indicates the expected ideal dependence of the Schottky barrier on the metal work function, i.e., $S = 1$. We note that the experimental slopes given in the figure are significantly smaller and differ among the semiconductors.

It is found that metal junctions to semiconductors with ionic bonding display a large dependence of the barrier height on the metal work function with only little deviation from the ideal behavior ($S = 1$). On the other hand, metal junctions to semiconductors with a predominantly covalent bonding lead to an only weak dependence of the barrier height on the metal work function ($S$ small). Experimental slope parameters $S$ are given in Fig. 6.24 for a number of semiconductors. The ionicity of the bonding is expressed in terms of the difference in electronegativity $\Delta\chi = \chi_A - \chi_B$ of the atoms (or, more precisely, anions and cations) $A$, $B$ of the semiconductor.

The low dependence of the Schottky-barrier height on the metal work-function is referred to as *Fermi-level pinning*. The phenomenon can be understood qualitatively in terms of a model based upon localized states located at the interface between semiconductor and metal. Let us consider such interface states (also termed surface states) with a distribution of electronic levels in the bandgap of the semiconductor. The distribution may be characterized by an energy $e\phi_0$, the so-called

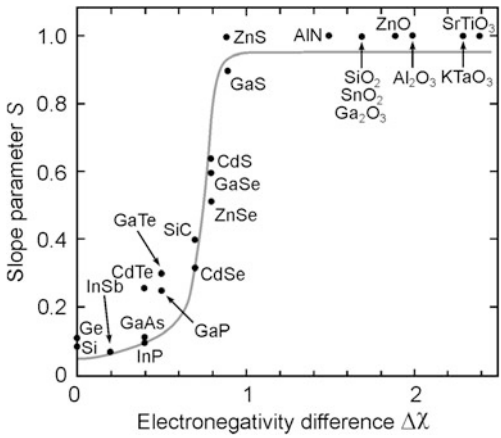


**Fig. 6.24** Slope parameter $S$ for various $n$-type semiconductor/metal junctions plotted versus the electronegativity difference of the constituents of the semiconductor. The *gray curve* is a guide to the eye. Adapted from [56]

charge-neutrality level. States below this level are assumed neutral if they are filled with electrons, and states lying above are assumed neutral if they are empty. If the density of such interface states near $e\phi_0$ is large, then adding electrons to the semiconductor or extracting them from the semiconductor does not alter the position of the Fermi energy. The Fermi level is *pinned*. When the contact between the metal and the semiconductor is made, both, addition of electrons and extraction of electrons are accommodated by the interface states, leaving the Fermi level virtually unchanged. The Schottky barrier height is then independent of the metal used, and given by

$$e\phi_{\mathrm{B}} = E_{\mathrm{g}} - e\phi_0,$$

$e\phi_0$ being the charge-neutrality level.

Two basically different models on the physical nature of the interface states have been proposed. The *model of virtual gap states* (ViGS, also referred to as metal induced gap states MIGS) assumes that the wave functions of the metal electrons have exponentially decaying tails into the semiconductor [57, 58]. These virtual states are located in the bandgap and decay on an atomic scale with a charge decay length of some Å, making the first few layers of the semiconductor locally metallic: The local density-of-states in the semiconductor bandgap is filled with a smooth density of gap states. The gap states are related to those bands of the semiconductor that are nearest in energy. ViGS which are related to the valence band are then occupied, and those with conduction-band character are empty. At an effective midgap point $E_{\mathrm{B}}$ gap states change from primarily valence character to conduction character. The Fermi level is pinned at or near this energy $E_{\mathrm{B}}$, yielding local charge neutrality. A relatively low number of ViGS (about one per 100 atoms at the interface) is required to produce the pinning effect. The strength of the ViGS model is its simplicity. Without adjustable parameters it could reasonably predict experimentally observed pinned Shottky barrier heights for a number of metal-semiconductor combinations and explain why more ionic semiconductors do not show a universal barrier height. Some results are listed in Table 6.3.

**Table 6.3** Schottky barrier height $e\phi_{Bn}^{theo}$ for an $n$-type semiconductor-Au metal junction and effective midgap point $E_B$ calculated from the model of virtual gap states. Experimental barrier heights refer to Au metal. Data from [58], $E_B$ from [59]

| | $E_g$ (eV) | $E_B$ (eV) | $e\phi_{Bn}^{theo}$ (eV) | $e\phi_{Bn}^{exp}$ (Au) (eV) |
|---|---|---|---|---|
| Ge | 0.66 | 0.18 | 0.48 | 0.59 |
| Si | 1.12 | 0.36 | 0.76 | 0.83 |
| GaAs | 1.56 | 0.70 | 0.74 | 0.94 |
| ZnS | 3.60 | | 1.40 | 2.00 |

The ViGS model assumes a featureless interface between metal and semiconductor, neglecting structural details or the formation of strong local chemical bonds across the interface. Experiments on a variety of different junctions demonstrated, however, a systematic dependence of the barrier height on the chemical reactivity of the interface [60, 61]. Moreover, Fermi level pinning was already obtained with a metal coverage much less than one monolayer. For reactive metals the position of the Fermi level was found to be largely independent of the metal used. Such findings lead to a different approach emphasizing the role of defects at the interface.

The *defect model* assumes that the Fermi-level pinning originates from localized electronic states originating from defects near the interface [61]. Such defects are, e.g., vacancies in the semiconductor. The energy for the formation of the defect can be created by the heat of condensation of surface adatoms or from the heat of formation of compounds made from metal and semiconductor atoms forming at the interface. A low number of defects (order of one per 100 interface atoms) is required to pin the Fermi energy, analogous to the ViGS model. There exist numerous experimental and theoretical studies on the microscopic nature of such defects and quite a number of related detailed models. Many chemical trends could be explained for specific junctions of semiconductors to metals. Sometimes both, ViGS model *and* defect model are needed to explain the data. No general model accounting for the rich variety of phenomena has been reached to date. The density of interface states cannot be predicted with any degree of certainty. The Schottky barrier height must therefore be considered a parameter which must experimentally be determined.

We should note that the fundamental mechanism for Fermi-level pinning is essentially the same for both, ViGS model and defect model. The concept is based upon energy levels in the gap of the semiconductor near the interface that can accommodate carriers flowing across the interface for equilibration of the electronegativity when the contact is made. The charge transferred between the metal and the semiconductor creates an interface dipole, which pins the Fermi level and hence controls the Shottky barrier height.

### *6.3.3 Practical Ohmic Metal-Semiconductor Contact*

Practical contacts should have a negligible resistance compared with that of the semiconductor device of which the contact forms part. Such contacts are often re-

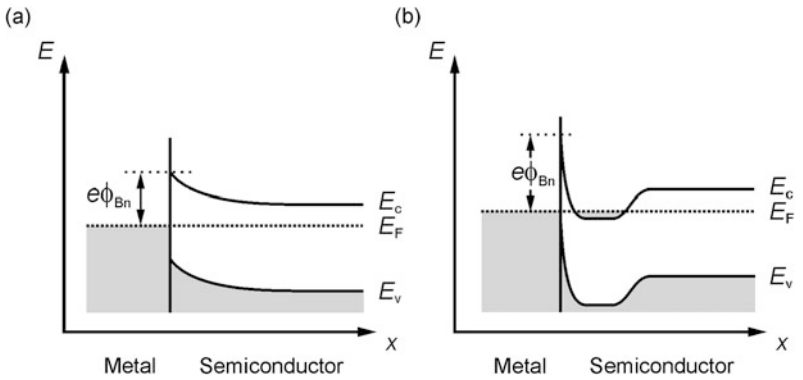


**Fig. 6.25** Schematics of concepts for fabricating ohmic contacts: (**a**) formation of a low barrier height, (**b**) application of a thin layer with a high doping level

ferred to as *ohmic contacts*, i.e., non-rectifying contacts. The *IV* characteristics of a device with low-resistance contacts is determined by the resistance of the semiconductor. The linearity of the contact is then actually not essential. The contact should, furthermore, not inject minority carriers.

The model of an ideal Schottky contact pointed out in Sect. 6.3.1 provides useful guidelines for fabricating a practical contact. The two basic approaches used to obtain a low contact resistance are depicted in Fig. 6.25. The first principle shown in Fig. 6.25a is based on the formation of a low Schottky-barrier height $e\phi_{\mathrm{Bn}}$. This requires—in absence of pinning effects—a metal with a very small work function for a junction to an $n$-type semiconductor, and a metal with a very large work function for a junction to an $p$-type semiconductor, cf. Fig. 6.22. The implementation of the concept is usually hampered by the problem of finding a metal with a suitable work function. The task is particularly difficult for $p$ contacts to semiconductors with a wide band gap.

The majority of practical contacts is therefore based on the approach of using a thin, heavily doped semiconductor layer adjacent to the metal as illustrated in Fig. 6.25b. The width of the depletion region of such layer is very thin, as expressed by (6.35). The contact resistance is then dominated by the tunneling of carriers through the barrier.

The metal-semiconductor contact is characterized by the specific differential resistance $R_{\mathrm{c}}$ at zero bias,

$$R_{\mathrm{c}} = \left(\frac{dI}{dV}\right)^{-1}_{V=0}. \tag{6.37}$$

In the commonly applied approach depicted in Fig. 6.25b the tunneling current across the thin barrier comprises not only electrons with an energy close to the Fermi level (the so-called field emission dominating at very low temperatures), but also thermally excited electrons. The resulting current is known as *thermionic field emission*. Its maximum passes the barrier at an energy $E_{\mathrm{m}}$ above the conduction

**Table 6.4** Typical metallization layers applied for practical contacts to III–V semiconductors

| Type of conductivity | Contact material | Composition (%) |
|---|---|---|
| *n* | AuGe | 88 : 12 |
| *n* | AuSn | 95 : 5 |
| *p* | AuBe | 99.1 : 0.9 |
| *p* | AuZn | 95 : 5 |

band, where the tunneling probability is larger than at $E_F$ due to a thinner barrier [62]. For this case the contact resistance is proportional to

$$R_c \sim \exp\left(\frac{2}{\hbar}\sqrt{\frac{\varepsilon m^*}{n_D}}\phi_{Bn}\right), \tag{6.38}$$

where $\varepsilon$ is the permittivity of the semiconductor. We note the strong dependence on doping and on the height of the Schottky barrier.

Due to the large importance of ohmic contacts for semiconductor devices some standard technology has been developed. Generally a contact metal containing also some dopant material is evaporated onto the semiconductor surface like, e.g., AuZn on *p*-type GaAs. Table 6.4 summarizes some standard metallizations applied for contacts to III–V compound semiconductors. Often these contact layers are alloyed into the semiconductor at the respective eutectic temperature. In addition, further metal layers are usually added to improve the adhesion to the semiconductor and to lower the total contact resistance. An example is the layer sequence AuGe (100 nm)/Ni (50 nm)/Au (200 nm), where Ni provides good adhesion due to a low surface energy, and Au lowers the resistance.

### *6.3.4 Epitaxial Contact Structures*

In some cases no suitable metallization for forming an ohmic contact can be found. The reason may be an unfavorable Fermi-level pinning or the lack of a metal with a suitable work function. A metal contact to, e.g., *p*-type ZnSe proved difficult, because no metal with a sufficiently large work function was found to avoid the formation of a Schottky barrier $e\phi_{Bp}$ for hole injection according Fig. 6.22d. In such cases a heteroepitaxial contact structure may provide a viable solution. The presented examples intend to introduce some basic concepts rather than representing general recipes.

The principle of an epitaxial contact structure is based on the introduction of a material between the metal and the semiconductor that accommodates the difference in metal and semiconductor work functions and avoids Fermi-level pinning. There exist various implementations of the idea. A simple approach is the application of a heavily doped thin semiconductor layer on top of the semiconductor used in the device. Such structure was reported for a contact to *n*-type GaAs and is shown in Fig. 6.26 [63].

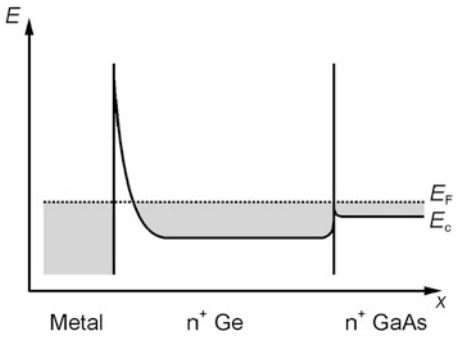


**Fig. 6.26** Energy-band diagram of a heterojunction structure for a low-resistance ohmic contact

By inserting a heavily doped Ge layer between Au metal and GaAs, the large Schottky barrier forming at the metal/$n$-GaAs junction is split into two smaller barriers. The smaller metal/$n$-Ge barrier height is, furthermore, quite thin due to the heavy-doping ability of the narrow-gap semiconductor Ge ($n \geq 10^{20}$ cm$^{-3}$). A contact resistance below $10^{-7}$ $\Omega$cm$^2$ was reported for such non-alloyed contact [63].

Another concept is the application of a semiconductor material which provides a good contact to a metal and can be alloyed during growth with the semiconductor used in the device. An alloy layer is then inserted the composition of which is graded from the semiconductor forming the interface with the metal to that used in the device. The principle of this approach is illustrated in Fig. 6.27.

The example depicted in Fig. 6.27 employs the property of InAs with an untypical Fermi-level pinning in the conduction band. Therefore a good ohmic contact with a small Schottky barrier $e\phi_{Bn} < 0$ can be made to $n$-type InAs as shown in Fig. 6.27b. The simple insertion of such a layer between the metal and $n$-type GaAs with a Fermi level pinned in the gap will not avoid the high Schottky barrier, which is then formed at the interface between the two semiconductors as illustrated in Fig. 6.27c. The problem may be solved by replacing the abrupt junction between the semiconductors by an $n$-type ternary $In_xGa_{1-x}As$ layer with a composition graded from $x = 1$ to $x = 0$ [64]. For the example given in Fig. 6.27 a contact resistance in the range $10^{-6}$ $\Omega$cm$^2$ was reported. The principle was also applied to other materials. An ohmic $p$ contact to ZnSe with a resistance in the mid $10^{-2}$ $\Omega$cm$^2$ range was accomplished, e.g., by applying a Au metallization to $p$-type BeTe and using a pseudograded $p$-type BeTe/ZnSe superlattice [65]. Within the superlattice with 20 monolayer (ML) pseudoperiod the thickness of individual layers was varied in 1 ML steps starting at 19 ML BeTe + 1 ML ZnSe and ending at 1 ML BeTe + 19 ML ZnSe. The purpose of this superlattice was to mimic a random alloy for smoothly grading the valence-band offset.

An approach apparently similar to pseudograding but representing actually a different concept of an epitaxial contact structure is based on resonant tunneling within a multi-quantum well (MQW) structure. The principle of the approach is depicted for a $p$-type contact to ZnSe in Fig. 6.28. The metal-semiconductor junction is made to $p$-type ZnTe, which can be degenerately doped $p$-type and forms a good ohmic (tunnel) contact to Au for hole injection. A ZnTe/ZnSe MQW structure is placed

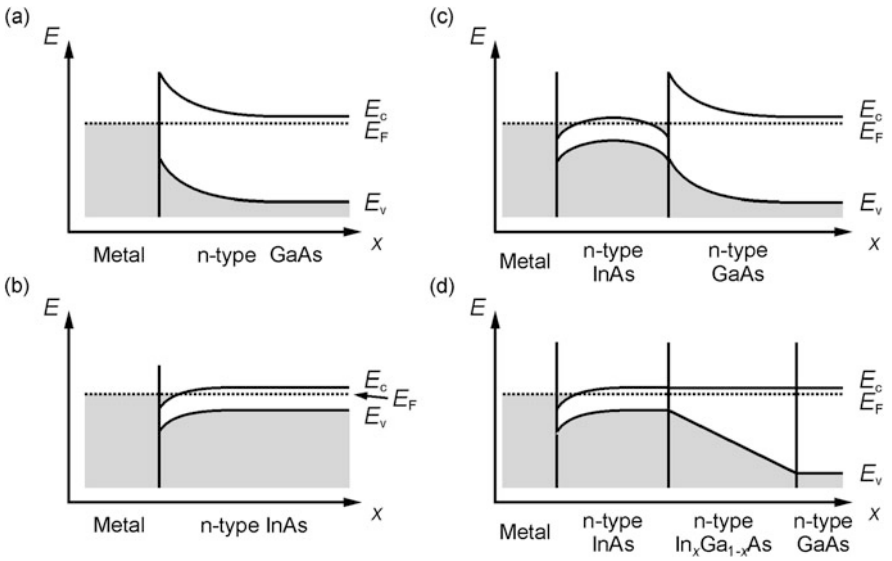


**Fig. 6.27** Energy-band diagrams illustrating the concept of ohmic contact formation using a layer with a graded band gap: Metal contact to (**a**) $n$-type GaAs, (**b**) $n$-type InAs, (**c**) $n$-type GaAs with an inserted $n$-type InAs layer and abrupt interface, (**d**) $n$-type GaAs with an additional graded $n$-type $In_xGa_{1-x}As$ layer and non-abrupt interfaces

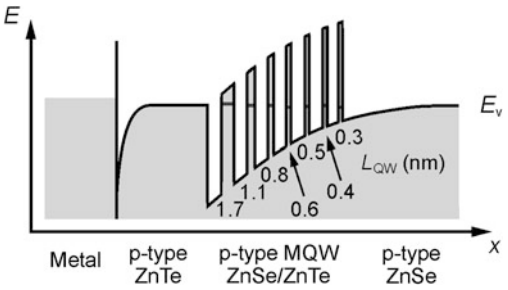


**Fig. 6.28** Energy-band diagram depicting the concept of a resonant-tunneling contact using a multiple-quantum well (MQW) region. *Dark gray horizontal lines* represent the lowest quantized energy levels for holes

between ZnTe and ZnSe to accommodate the large valence-band offset of about 0.5 eV between these binaries. The widths $L_{QW}$ of the ZnTe quantum wells in this structure are designed such that the lowest hole levels align to the energies of the valence-band maxima of ZnTe and ZnSe, yielding a sequence of gradually narrowing quantum wells separated by 2 nm thick ZnSe barriers as shown in Fig. 6.28 [66]. Current transport is provided by resonant tunneling through the aligned QW levels. For the structure depicted in Fig. 6.28 also a contact resistance in the mid $10^{-2}\ \Omega\,cm^2$ range was obtained.

An issue of any contact is mechanical and thermal stability besides the band alignment and a low contact resistance as discussed above. The lattice mismatch of semiconductors applied in epitaxial contact structures must therefore also be considered. A high density of structural defects is usually detrimental to the contact life-

time. The InAs/GaAs and ZnTe/ZnSe junctions mentioned in the examples above introduce large strain due to ∼7 % misfit in both cases, while the Ge/GaAs and BeTe/ZnSe junctions are well lattice-matched and expected to contain a low density of defects.

## 6.4 Problems Chap. 6

6.1 (a) Find the intrinsic carrier concentrations in InAs and InP at 77 K and 300 K. Use band parameters given in Problem 2 of Chap. 3 and effective masses $m_e$, $m_{hh}$, and $m_{lh}$ (all in units of the free-electron mass $m_0$) for InAs 0.02, 0.41, 0.03, and for InP 0.08, 0,60, 0.12, respectively.

(b) Calculate for both intrinsic semiconductors the temperature, where the Fermi energy deviates by +50 meV from the midgap position.

6.2 Compute the effective densities of states at the band edges, and estimate the maximum carrier concentration for electrons and holes in InP at 300 K using the Fermi-level stabilization model. Apply a Fermi-level stabilization energy of 0.76 eV above the valence-band edge, band parameters given in Problem 2 of Chap. 3, and the effective mass parameters given in the previous problem.

6.3 An undoped GaAs layer is grown at 700 °C on $p$-type GaAs bulk homogeneously doped with $1 \times 10^{18}$ cm$^3$ Be atoms. The Be atoms redistribute due to the concentration gradient at the interface. Assume that the diffusion process is well described by a simple Fick diffusion with a single diffusion constant of $2 \times 10^{-5}$ cm$^2$/s and an activation energy of 1.95 eV.

(a) How long does it take at the given temperature to obtain a softened Be concentration profile at the interface with a width (for drop from 90 % to 10 % of the initial concentration) of 200 nm? Approximate values of the complementary error function are ($x$, erfc($x$): 0.0, 1.00; 0.2, 0.78; 0.4, 0.57; 0.6, 0.40; 0.8, 0.26; 1.0, 0.16; interpolate to obtain rough values in between).

(b) Diffusion slows down if the temperature is lowered. Which temperature is needed to double the time for obtaining the same softening of the concentration profile?

(c) Find the width of the drop of the softened Be concentration profile (drop from 90 % to 10 %) after an exposure of the interface (with initially step-like profile) at 700 °C for 24 hours.

(d) Which Be concentration exists in the GaAs layer at a distance of 100 nm from the initial interface after the exposure at 700 °C for 24 hours?

6.4 Consider a contact of platinum to $n$-type Si with $2 \times 10^{16}$ cm$^{-3}$ donors—all ionized at a temperature of 300 K—in the framework of the Schottky-Mott model. Si has a relative permittivity of 11.7 and—at the given temperature—an effective density of states of $2.8 \times 10^{19}$ cm$^{-3}$.

(a) Calculate the barrier height, the energy difference between the conduction-band edge and the Fermi level in the bulk of Si, and the contact potential.

(b) What is the width of the depletion region without an externally applied voltage? What is the width of the space charge if a voltage of 1.0 V is

applied in the forward direction? What is the width for a bias of 1.0 V in the reverse direction?

(c) What is the space-charge width without external bias at 400 K?

6.5 A contact resistance of $5\times10^{-4}\ \Omega \times \mathrm{cm}^2$ is measured for a junction between Al and $n$-Si highly doped to $2 \times 10^{19}\ \mathrm{cm}^{-3}$ at room temperature. Estimate the contact resistance if the doping level can be further raised to $1 \times 10^{20}\ \mathrm{cm}^{-3}$, assuming no interface states occur. The effective mass of the density of states and the relative permittivity of Si are $1.2 \times m_0$ and 11.7, respectively.

## 6.5 General Reading Chap. 6

E.F. Schubert, *Doping in III–V Semiconductors* (Cambridge University Press, Cambridge, 1993)
D. Shaw (ed.), *Atomic Diffusion in Semiconductors* (Plenum Press, New York, 1973)
B. Tuck, *Atomic Diffusion in III–V Semiconductors* (Adam Hilger, Bristol, 1988)
P. Heitjans, J. Kärger (eds.), *Diffusion in Condensed Matter—Methods, Materials, Models* (Springer, Berlin, 2005)
H. Mehrer, *Diffusion in Solids—Fundamentals, Methods, Materials, Diffusion-Controlled Processes* (Springer, Berlin, 2007)
W. Mönch, *Semiconductor Surfaces and Interfaces*, 3rd edn. (Springer, Berlin, 2001)
S.L. Chuang, *Physics of Photonic Devices*, 2nd edn. (Wiley, Hoboken, 2009)

## References

1. J.M. Luttinger, Quantum theory of cyclotron resonance in semiconductors: general theory. Phys. Rev. **102**, 1030 (1956)
2. E.F. Schubert, *Doping in III–V Semiconductors* (Cambridge University Press, Cambridge, 1993)
3. V.A. Karasyuk, D.G.S. Beckett, M.K. Nissen, A. Villemaire, T.W. Steiner, M.L.W. Thewalt, Fourier-transform magnetophololuminescence spectroscopy of donor-bound excitons in GaAs. Phys. Rev. B **49**, 16381 (1994)
4. M. Grundmann, *The Physics of Semiconductors* (Springer, Berlin, 2006)
5. M. Isshiki, T. Kyotani, K. Masumoto, W. Ichida, S. Suto, Emissions related to donor-bound excitons in highly purified zinc selenide crystals. Phys. Rev. B **36**, 2568 (1987)
6. H.E. Ruda, Theoretical study of hole transport in ZnSe. J. Appl. Phys. **59**, 3516 (1986)
7. R.N. Bhargava, R.J. Seymour, B.J. Fitzpatrick, S.P. Herko, Donor-acceptor pair bands in ZnSe. Phys. Rev. B **20**, 2407 (1979)
8. H. Reiss, Chemical effects due to the ionization of impurities in semiconductors. J. Chem. Phys. **21**, 1209 (1953)
9. D.B. Laks, C.G. Van de Walle, G.F. Neumark, P.E. Blöchl, S.T. Pantelides, Native defects and self-compensation in ZnSe. Phys. Rev. B **45**, 10965 (1992)
10. C.G. Van de Walle, D.B. Laks, G.F. Neumark, S.T. Pantelides, First-principles calculations of solubilities and doping limits: Li, Na, and N in ZnSe. Phys. Rev. B **47**, 9425 (1993)
11. Z. Zhu, H. Mori, M. Kawashima, T. Yao, Planar doping of p-type ZnSe layers with lithium grown by molecular beam epitaxy. J. Cryst. Growth **117**, 400 (1992)
12. M. Tao, A kinetic model for metalorganic chemical vapor deposition from trimethylgallium and arsine. J. Appl. Phys. **87**, 3554 (2000)
13. H. Künzel, J. Knecht, H. Jung, K. Wünstel, K. Ploog, The effect of arsenic vapour species on electrical and optical properties of GaAs grown by molecular beam epitaxy. Appl. Phys. A **28**, 167 (1982)
14. G. Mandel, Self-compensation limited conductivity in binary semiconductors. Phys. Rev. **134**, A1073 (1964)

15. G.A. Baraff, M. Schlüter, Electronic structure, total energies, and abundances of the elementary point defects in GaAs. Phys. Rev. Lett. **55**, 1327 (1985)
16. R.W. Jansen, O.F. Sankey, Theory of relative native- and impurity-defect abundances in compound semiconductors and the factors that influence them. Phys. Rev. B **39**, 3192 (1989)
17. F. El-Mellouhi, N. Mousseau, Self-vacancies in gallium aresenide: an ab initio calculation. Phys. Rev. B **71**, 125207 (2005)
18. S.B. Zhang, J.E. Northrup, Chemical potential dependence of defect formation energies in GaAs: application to Ga self-diffusion. Phys. Rev. Lett. **67**, 2339 (1991)
19. P.M. Mooney, Deep donor levels (DX centers) in III–V semiconductors. J. Appl. Phys. **67**, R1 (1990)
20. D.J. Chadi, K.J. Chang, Energetics of DX-center formation in GaAs and $Al_xGa_{1-x}As$ alloys. Phys. Rev. B **39**, 10063 (1989)
21. D.J. Chadi, Doping in ZnSe, ZnTe, MgSe, and MgTe wide-band-gap semiconductors. Phys. Rev. Lett. **72**, 534 (1994)
22. W. Walukiewicz, Intrinsic limitations to the doping of wide-gap semiconductors. Physica B **302**, 123 (2001)
23. W. Walukiewicz, Fermi level dependent native defect formation: consequences for metal-semiconductor and semiconductor-semiconductor interfaces. J. Vac. Sci. Technol. B **6**, 1257 (1988)
24. E. Tokumitsu, Correlation between Fermi level stabilization positions and maximum free carrier concentrations in III–V compound semiconductors. Jpn. J. Appl. Phys. **29**, L698 (1990)
25. S.B. Zhang, The microscopic origin of the doping limits in semiconductors and widegap materials and recent developments in overcoming these limits: a review. J. Phys. Condens. Matter **14**, R881 (2002)
26. C.E.C. Wood, G. Metze, J. Berry, L.F. Eastman, Complex free-carrier profile synthesis by "atomic-plane" doping of MBE GaAs. J. Appl. Phys. **51**, 383 (1980)
27. E.F. Schubert, *Doping in III–V Semiconductors* (Cambridge University Press, Cambridge, 2005)
28. E.F. Schubert, Delta doping of III–V compound semiconductors: fundamentals and device applications. J. Vac. Sci. Technol. A **8**, 2980 (1990)
29. E.F. Schubert, J.E. Cunningham, W.T. Tsang, Electron-mobility enhancement and electron-concentration enhancement. Solid State Commun. **63**, 591 (1987)
30. E.F. Schubert, A. Fischer, K. Ploog, The delta-doped field-effect transistor. IEEE Trans. Electron Devices **33**, 625 (1986)
31. C. Hilsum, Simple empirical relationship between mobility and carrier concentration. Electron. Lett. **10**, 259 (1974)
32. W. Walukiewicz, H.E. Ruda, J. Lagowski, H.C. Gatos, Electron mobility in modulation-doped heterostructures. Phys. Rev. B **30**, 4571 (1984)
33. J. Crank, *The Mathematics of Diffusion*, 2nd edn. (Clarendon Press, Oxford, 1975)
34. U.M. Gösele, Fast diffusion in semiconductors. Annu. Rev. Mater. Sci. **18**, 257 (1988)
35. F.C. Frank, D. Turnbull, Mechanism of diffusion of copper in germanium. Phys. Rev. **104**, 617 (1956)
36. U. Gösele, W. Frank, A. Seeger, Mechanism and kinetics of the diffusion of gold in silicon. Appl. Phys. **23**, 361 (1980)
37. T.Y. Tan, U. Gösele, S. Yu, Point defects, diffusion mechanisms, and superlattice disordering in gallium arsenide-based materials. Crit. Rev. Solid State Mater. Sci. **17**, 47 (1991)
38. W.R. Wilcox, T.J. LaChapelle, Mechanism of gold diffusion in silicon. J. Appl. Phys. **35**, 240 (1964)
39. R.L. Longini, Rapid zinc diffusion in gallium arsenide. Solid-State Electron. **5**, 127 (1962)
40. H. Bracht, Diffusion mechanisms and intrinsic point-defect properties in silicon. Mater. Res. Soc. Bull. **25**(6), 22 (2000)
41. T.Y. Tan, U. Gösele, Diffusion in semiconductors, in *Diffusion in Condensed Matter*, ed. by P. Heitjans, J. Kärger (Springer, Berlin, 2005)

42. T.Y. Tan, U. Gösele, Mechanisms of doping-enhanced superlattice disordering and of gallium self-diffusion in GaAs. Appl. Phys. Lett. **52**, 1240 (1988)
43. L.J. Guido, N. Holonyak Jr., K.C. Hsieh, R.W. Kaliski, W.E. Plano, R.D. Burnham, R.L. Thornton, J.E. Epler, T.L. Paoli, Effects of dielectric encapsulation and As overpressure on Al-Ga interdiffusion in $Al_xGa_{1-x}As$-GaAs quantum-well heterostructures. J. Appl. Phys. **61**, 1372 (1987)
44. D.G. Deppe, N. Holonyak Jr., Atom diffusion and impurity-induced layer disordering in quantum-well III–V semiconductor heterostructures. J. Appl. Phys. **64**, R93 (1988)
45. D.G. Deppe, L.J. Guido, N. Holonyak, Impurity-induced layer disordering in $Al_xGa_{1-x}As$-GaAs quantum well heterostructures. Mater. Res. Soc. Symp. Proc. **126**, 31 (1988). Cf. also Ref. [44]
46. M. Kawabe, N. Shimizu, F. Hasegawa, Y. Nannichi, Effects of Be and Si on disordering of the AlAs/GaAs superlattice. Appl. Phys. Lett. **46**, 849 (1985)
47. D.G. Deppe, L.J. Guido, N. Holonyak Jr., K.C. Hsieh, R.D. Burnham, R.L. Thornton, T.L. Paoli, Stripe-geometry quantum well heterostructure $Al_xGa_{1-x}As$-GaAs lasers defined by defect diffusion. Appl. Phys. Lett. **49**, 510 (1986)
48. P.D. Floyd, C.P. Chao, K.-K. Law, J.L. Merz, Low-threshold lasers fabricated by alignment-free impurity-induced disordering. IEEE Photonics Technol. Lett. **5**, 1261 (1993)
49. M. Straßburg, O. Schulz, U.W. Pohl, D. Bimberg, S. Itoh, K. Nakano, A. Ishibashi, M. Klude, D. Hommel, A novel approach to improved green emitting II–VI lasers. IEEE J. Sel. Top. Quantum Electron. **7**, 371 (2001)
50. W.D. Laidig, N. Holonyak, M.D. Camras, H. Hess, J.J. Coleman, P.D. Dapkus, J. Bardeen, Disorder of an AlAsGaAs superlattice by impurity diffusion. Appl. Phys. Lett. **38**, 776 (1981)
51. W. Schottky, Vereinfachte und erweiterte Theorie der Randschicht-Gleichrichter (Simplified and extended theory of boundary-layer rectifiers). Z. Phys. **118**, 539 (1942) (in German)
52. N.F. Mott, Note on the contact between a metal and an insulator or semiconductor. Math. Proc. Camb. Philos. Soc. **34**, 568 (1938)
53. W. Martienssen, H. Warlimont, *Springer Handbook of Condensed Matter and Materials Data* (Springer, Berlin, 2004)
54. Web-archive of semiconductor parameters of the Ioffe Physico-Technical Institute, St. Petersburg, Russian Federation. http://www.ioffe.rssi.ru/SVA/NSM/Semicond/
55. A.M. Cowley, S.M. Sze, Surface states and barrier height of metal-semiconductor systems. J. Appl. Phys. **36**, 3212 (1965)
56. S. Kurtin, T.C. McGill, C.A. Mead, Fundamental transition in the electronic nature of solids. Phys. Rev. Lett. **22**, 1433 (1969)
57. V. Heine, Theory of surface states. Phys. Rev. **138**, A1689 (1965)
58. J. Tersoff, Schottky barrier heights and the continuum of gap states. Phys. Rev. Lett. **52**, 465 (1984)
59. J. Tersoff, Recent models of Schottky barrier formation. J. Vac. Sci. Technol. B **3**, 1157 (1985)
60. L.J. Brillson, Transition in Schottky barrier formation with chemical reactivity. Phys. Rev. Lett. **40**, 260 (1978)
61. W.E. Spicer, P.W. Chye, P.R. Skeath, C.Y. Su, I. Lindau, New and unified model for Schottky barrier and III–V insulator interface states formation. J. Vac. Sci. Technol. **16**, 1422 (1979)
62. F.A. Padovani, R. Stratton, Field and thermionic-field emission in Schottky barriers. Solid-State Electron. **9**, 695 (1966)
63. R. Stall, C.E.C. Wood, K. Board, L.F. Eastman, Ultra low resistance ohmic contacts to $n$-GaAs. Electron. Lett. **15**, 800 (1979)
64. J.M. Woodall, J.L. Freeouf, G.D. Pettit, T. Jackson, P. Kirchner, Ohmic contacts to $n$-GaAs using graded band gap layers of $Ga_{1-x}In_xAs$ grown by molecular beam epitaxy. J. Vac. Sci. Technol. **19**, 626 (1981)
65. F. Vigué, P. Brunet, P. Lorenzini, E. Tournié, J.P. Faurie, Ohmic contacts to $p$-type ZnSe using a ZnSe/BeTe superlattice. Appl. Phys. Lett. **75**, 3345 (1999)
66. F. Hiei, M. Ikeda, M. Ozawa, T. Miyajima, A. Ishibashi, K. Akimoto, Ohmic contacts to $p$-type ZnSe using ZnTe/ZnSe quantum wells. Electron. Lett. **29**, 878 (1993)

# Chapter 7
# Methods of Epitaxy

**Abstract** The fabrication of a semiconductor heterostructure with atomically sharp interfaces requires epitaxial growth. This chapter focuses on the widely applied growth techniques of liquid-phase epitaxy (LPE), metalorganic vapor-phase epitaxy (MOVPE), and molecular-beam epitaxy (MBE). The usually equilibrium-near LPE process is illustrated for different cooling procedures. For the growth employing MOVPE we consider properties of source precursors and processes of mass transport. The section on MBE concentrates particularly on vacuum requirements, the effusion of beam sources, and the uniformity of deposition.

The heterostructures discussed in the previous chapters represent the basis of advanced semiconductor devices. Such structures comprising quantum wells and superlattices can only be fabricated by epitaxial growth processes. Different methods for epitaxial growth have been established. They are basically named after the nutrition phase supplying the material for the growth of the solid phase. Prominent methods are techniques applying growth from the vapor phase. Vapor-phase epitaxy (VPE) is usually classified by the transport mechanism of the gaseous species: physical-vapor deposition (PVD), or chemical-vapor deposition (CVD). CVD is often further classified according the chemistry of the source gases, such as metalorganic CVD (MOCVD, also termed metalorganic VPE, MOVPE, or organometallic VPE, OMVPE), chloride VPE (ClVPE), and hydride VPE (HVPE). PVD represents the vaporization of source material in vacuum. Again different methods are applied such as thermal evaporation, laser ablation, or sputtering. The most prominent PVD technique is molecular-beam epitaxy (MBE), where beams of species are provided by thermal heating in effusion cells.

Besides the rich variety of VPE techniques epitaxy is also performed from the liquid and even from the solid phase. In liquid-phase epitaxy (LPE) growth is performed from a liquid solution or a melt. Solid-phase epitaxy (SPE) is a transition between the solid amorphous and crystalline phases of a material. This kind of crystallization is primarily used for the annealing of crystal damage.

Each of the mentioned epitaxy methods has its strengths and weaknesses. We will focus on the widely applied techniques of liquid-phase epitaxy, metalorganic vapor-phase epitaxy, and molecular-beam epitaxy. Most electronic and optoelectronic devices are fabricated using one of these methods. The principles applied in the three

U.W. Pohl, *Epitaxy of Semiconductors*, Graduate Texts in Physics,
DOI 10.1007/978-3-642-32970-8_7, 

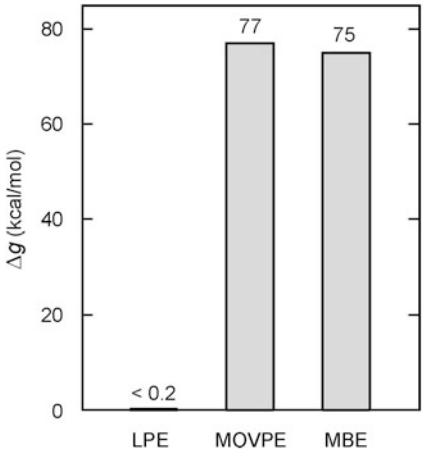


**Fig. 7.1** Estimated Gibbs free energy differences between reactants and products for the epitaxy of GaAs at 1000 K using various growth methods. Calculation of the thermodynamic driving forces assumed for liquid-phase epitaxy (LPE) a supercooling below 10 K. In metalorganic vapor-phase epitaxy (MOVPE) growth with $Me_3Ga$ and $AsH_3$ precursors, and in molecular-beam epitaxy (MBE) growth with Ga and $As_4$ species is assumed. Data from [1]

growth techniques are quite different. LPE operates usually close to thermodynamic equilibrium, while MOVPE and MBE occurs quite far from equilibrium. Figure 7.1 illustrates the apparent difference of the driving forces for the epitaxy of GaAs.

The equilibrium-near conditions in the LPE imply the possibility of reversible processes to occur at the growth interface. The LPE process is well described by thermodynamics. We note a much larger driving force in the MOVPE process. Here, growth is mostly not controlled by thermodynamics, but by the slow mass transport of reactants through the vapor to the growth interface. Similar conditions apply for the MBE process.

## 7.1 Liquid-Phase Epitaxy

In liquid-phase epitaxy (LPE) a crystalline layer usually grows from a supersaturated liquid solution on a substrate. The process has similarities to the seeded growth of bulk crystals from the melt, so that much experience could be transferred to LPE in the past. LPE is a mature technology which is widely used in industry, while it was largely replaced in universities by more flexible techniques like MBE or MOVPE. LPE has a number of advantages over other growth techniques, the most unique features being:

- LPE enables growth of layers with an extraordinary high structural perfection.
- High growth rates can be applied in the LPE growth process.

Since growth conditions of LPE processes are close to thermodynamic equilibrium, atoms can efficiently migrate to the growth interface and find energetically

optimum positions for incorporation. This may result in crystalline layers with a very low density of point and dislocation defects. Compound semiconductor layers grown by LPE exhibited point defects densities orders of magnitudes lower than layers grown by other growth techniques. The carrier lifetime in such layers is consequently quite high. Red-emitting GaAs-based LEDs with highest efficiency and high-performance $\gamma$-ray detectors based on HgCdTe are presently fabricated using LPE. Today a significant part of the world's LED production is covered by LPE, and LPE is the major growth method for fabricating magneto-optic layers. The technique was successfully applied to a large variety of materials, such as compound semiconductors (III–V, II–VI, IV–IV) and magnetic or superconducting oxides.

LPE is particularly useful for growing thick layers, also due to high deposition rates up to 1 μm/minute. On the other hand, LPE is less appropriate for fabricating nanostructures like quantum wells. The interface quality depends very strongly on crystallographic misorientation and lattice misfit. Rough interfaces are often also obtained due to back-dissolution. Another restriction of LPE is the limitation to materials which are miscible at growth temperature.

### *7.1.1 Growth Systems*

There exist several methods to bring the substrate into contact with the growth solution prepared for epitaxial growth, and to separate them at the end of layer growth. They can be classified into the techniques of tipping, dipping, and sliding boat. They basically differ in the way to bring the substrate into contact with the solution. The material used for the fabrication of the crucible or the boat depends on the materials to be grown. Usually graphite is used for semiconductor growth systems, while platinum is applied for growing oxide materials like garnets. The schematics of the three mentioned techniques are illustrated below for epitaxy on single substrates. Today LPE is actually used for industrial mass production in upscaled systems employing multiple large-area substrates.

#### Tipping System

The tipping system was the earliest LPE system applied for growing III–V semiconductors [2]. The schematic of a tipping apparatus is given in Fig. 7.2. The set-up consists of a boat containing the source material solved in a saturated molten solution, a reactor tube allowing to control the gaseous ambient, and a furnace for precise temperature control. The furnace is tiltable such that the growth solution can either be separated from the substrate (position (a) in Fig. 7.2) or placed over the substrate (position (b)). The growth process starts by equilibrating the growth solution in position (a). After completing this step the temperature of the furnace is reduced and the furnace is tipped to position (b). The solution runs over the substrate and layer growth starts. After growing a layer of sufficient thickness, the furnace is tipped

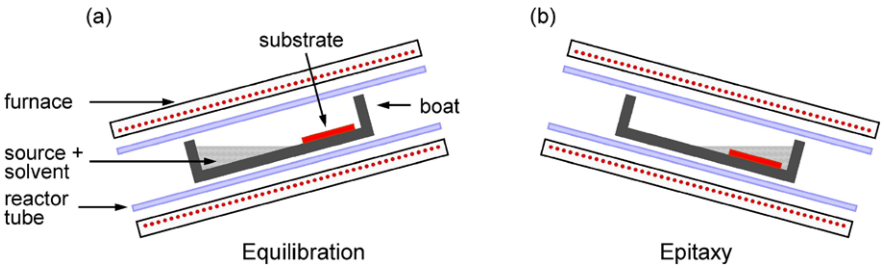


**Fig. 7.2** Tipping apparatus for liquid-phase epitaxy. (**a**) Position for equilibrating the growth solution, (**b**) furnace tipped to the position for epitaxial growth on the substrate

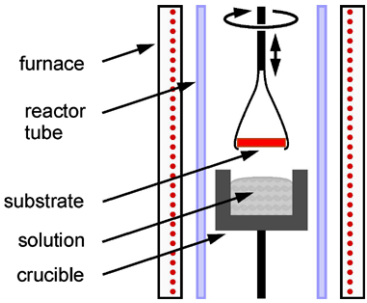


**Fig. 7.3** Dipping LPE apparatus for liquid-phase epitaxy. In systems with horizontally mounted substrate rotation may be applied to set up convection in the solute

back to position (b) and the solution rolls off the layer. The removal of the solution is not quite reliable, a major drawback of the technique. Moreover, the system allows for growing only a single layer. The simple tipping technique was particularly useful for initial early experiments.

### Dipping System

The principle of the dipping technique is illustrated in Fig. 7.3. The substrate is mounted on a substrate holder equipped with lift and rotation mechanisms in a horizontal or a vertical position. Layers are grown by dipping the substrate into the solution. The rotation mechanism is employed in the horizontal rotating-disk configuration to control the convection of the solute atoms in the liquid. It may also be used for removal of the solution by spinning off at the end of layer growth.

Dipping systems are useful if thick layers are to be grown. A further advantage particularly for substrates with volatile components is that the substrate can be kept at a decreased temperature prior to growth. The dipping technique is widely applied for the LPE of oxide materials. The popular sliding-boat technique employed for growing semiconductors is not used to grow oxide layers, because platinum used as a boat material does not slide on platinum. Furthermore, no substrate rotation is applied for semiconductor growth due to the sensitivity of the solution surface to oxidation.

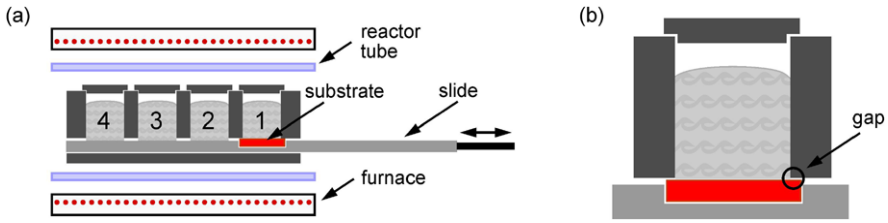


**Fig. 7.4** (**a**) Sliding boat LPE apparatus. Numbers signify solutions with different compositions. (**b**) Location of the critical gap between the substrate and crucible containing the solution

### Sliding-Boat System

The sliding-boat technique is quite versatile and allows for multiple-layer growth. It is widely applied for the LPE of compound semiconductors. A schematic of a sliding-boat apparatus is given in Fig. 7.4a. The boat consists of two parts: a base, which carries the substrate in a recess, and wells in a block, which contain the solutions for growing successively different layers. Either the block with the wells or the base are movable, such that the solutions can be placed over the substrate. Similar to the previous systems the boat is located in a reactor tube for providing control of the gaseous ambient, and in a furnace for precise temperature control. The wells of the different solutions may be covered with caps as indicated in the figure.

Proper adjustment of the gap between the block containing the solutions and the substrate accommodated in the slide is a critical issue of the siding-boat technique. If the clearance depicted in Fig. 7.4b is too wide, mixing with an adjacent solution and aftergrowth effects may occur. If, on the other hand, the gap is too small, the grown layers are scratched when the slide is moved. This limits also the maximum total thickness of the epitaxial layer sequence which can be grown by the sliding-boat technique. Typical gaps are in the range of 25 to 100 μm.

## *7.1.2 Congruent Melting*

We consider a melting process in a completely miscible two-component system to prepare the discussion of the LPE process. The phase diagram of the system composed of two components $A$ and $B$ is given in Fig. 7.5.

There are two liquidus curves: one separating the region of all liquid $A$ and $B$ at higher temperatures from a region at small concentrations of $B$ (i.e., high concentrations of $A$) where a fraction of $A$ is solid and in equilibrium with liquid $A$ and liquid $B$. Another liquidus curve at higher concentration of $B$ separates the all liquid region from a region with solid $B$ and liquid $A$ and $B$. At an even lower temperature $T_E$ a solidus line bounds the regions with either only $A$ or $B$ solid from an all solid region. At the eutectic point denoted E the liquidus and solidus curves intersect. At this point all three phases (all) Liquid, Solid of $A$, and Solid

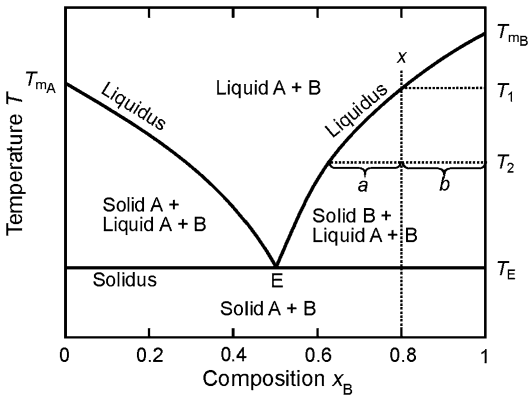


**Fig. 7.5** Phase diagram of a two-component system at constant pressure. The abscissa values give the fraction of component $B$ with respect to the sum $A + B$

of $B$ coexist in equilibrium. The phase rule (4.10) states that this point is invariant at a selected fixed pressure: The number of independent variables $N_f$ is determined by the number of components $N_c$ and the number of coexisting phases $N_p$, $N_f = N_c - N_p + 2 = 2 - 3 + 2 = 1$. If the temperature or the composition is changed at the given fixed pressure, then the number of phases $N_p$ is reduced to 2.

At the composition $x_B = 0$ we obtain a one-component system of pure component $A$. This system melts at only one temperature, the melting temperature $T_{mA}$. Correspondingly the pure one-component system $B$ at $x_B = 1$ melts at $T_{mB}$. For all compositions between these end points melting of the system begins at one temperature, the eutectic temperature $T_E$. Except for the eutectic composition melting occurs over a *range* of temperatures between $T_E$ and the temperature of the liquidus curve at the given composition; the eutectic composition melts only at $T_E$. It is important to note that in a closed system in equilibrium the composition does not change during melting or, vice versa, during crystallization.

To illustrate this rule we consider a crystallization of the system along the dotted line at $x_B = 0.8$ drawn in Fig. 7.5. Above the solidus line the system is a liquid mixture of 80 % of component $B$ and 20 % of component $A$. When the temperature is lowered, crystals of component $B$ begin to form at $T_1$. The more $T$ is lowered, the more of component $B$ crystallizes. Since the overall composition is fixed at $x_B = 0.8$ and crystals only form from component $B$, the liquid becomes gradually more enriched in $A$ due to the loss of liquid $B$. The 20 % composition of $B$ is hence composed of solid $B$ and liquid $B$. The fraction of $B$ in the solid state increases for decreasing temperature. At a temperature $T_2$ marked in Fig. 7.5 this fraction is given by the lever rule $x_{B,\text{solid}} = a/(a + b)$. The liquid fraction of $B$ is correspondingly $x_{B,\text{liquid}} = b/(a + b)$, and $A$ is all liquid. We note from Fig. 7.5 that section $b$ remains constant and $a$ increases as the temperature is lowered towards $T_E$. Thus, the proportional distance between the initial composition represented by the dotted line and the solidus curve gives the amount of solid $B$ formed at a given temperature below $T_1$. The composition of the all Liquid region changes as given by the solidus line. For decreasing temperature the Liquid contains gradually less $B$ due to loss into the pure $B$ solid. Still the overall composition

$x_B = (B_{\text{solid}} + B_{\text{liquid}})/(A_{\text{liquid}}(+A_{\text{solid}} = 0))$ remains fixed at 0.8. At $T_E$ also $A$ begins to crystallize, keeping $x_B$ constant (i.e., $A_{\text{solid}} \neq 0$). In a cooling process the temperature would remain constant at $T_E$ until all of $A$ is solid. The final solid is a mixture of 80 % $B_{\text{solid}}$ and 20 % $A_{\text{solid}}$.

### *7.1.3 LPE Principle*

The fundamental processes of liquid-phase epitaxy are similar to those of seeded growth of bulk crystals from a solution or a melt. There are major advantages of LPE growth from a solution rather than growing from a melt. Lower growth temperatures can be applied, leading to improved structural perfection and stoichiometry. In addition, the vapor pressure of volatile components in compound semiconductors is much reduced at temperatures far below melting, the interdiffusion of heterointerfaces is decreased, and detrimental effects of thermal expansion differences of substrate and epitaxial layer are reduced. Furthermore, solution growth allows a more precise control of low growth rates for improved thickness adjustment, and unwanted spontaneous nucleation is reduced.

For a discussion of the basics we consider a part of the phase diagram of a congruently melting binary solid $AB$ and the formation of a solid from a liquid solution of $B$ atoms solved in a solvent $A$. Since the LPE process is usually controlled by varying the temperature, $T$ is plotted as the independent variable. At a given temperature $T_{e2}$ labeled in Fig. 7.6a the liquidus curve shows the equilibrium composition $x_{e2}$ of $B$ atoms in the saturated liquid at point $L_e$. The liquid composition $x_{e2}$ is connected with a unique composition of the solid $x_S$. Points at the left of the liquidus, like $L^+$ above $L_e$, correspond to metastable states of a supersaturated or a supercooled liquid solution for the given temperature $T_{e2}$. Points at the right of the liquidus like $L^-$ correspond to undersaturated liquid solutions at $T_{e2}$. The deviation from thermal equilibrium can be expressed by the relative supersaturation

$$\sigma = \frac{x_{e1} - x_{e2}}{x_{e2}}, \tag{7.1}$$

where $x_{e1}$ represents the actual concentration in the bulk of the liquid solution (i.e., far away from a phase boundary to a solid) being supersaturated at $T_{e2}$, and $x_{e2}$ is the equilibrium concentration at $T_{e2}$. We discussed in Sect. 4.2 that nucleation of a solid in a homogeneous liquid phase requires a minimum driving force, or supersaturation, to take place. This quantity is the critical work $\Delta G^*_N$ for creating stable nuclei of critical size which can grow. In the phase diagram, the region between the corresponding critical supersaturation and the liquidus curve is a metastable region which can be used for heteronucleation, because the critical free energy of heteronucleation $\Delta G^*_{N\,\text{hetero}}$ is significantly smaller than that of nucleation in a homogeneous (liquid) phase. Thus, if a supersaturated solution at point $L^+$ in Fig. 7.6a is brought into contact with a solid, e.g., a substrate, then the solid tends to grow. Vice versa, a contact to an undersaturated solution at point $L^-$ tends to dissolve the

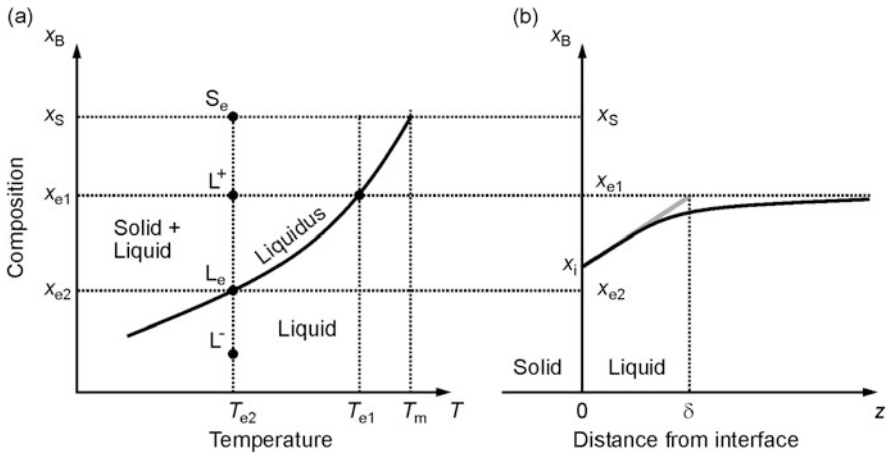


**Fig. 7.6** (**a**) Phase diagram of a two-component system. Points $L^+$ and $L^-$ signify a liquid in supersaturated and undersaturated states at temperature $T_{e2}$, respectively, $x_{e2}$ is the equilibrium liquid composition corresponding to an equilibrium solid composition $x_S$. $T_m$ is the melting temperature of the solid. (**b**) Concentration profile of composition $x_B$ in the supersaturated liquid solution near the solid-liquid interface located at $z = 0$. $\delta$ denotes the diffusion boundary, the *gray line* represents the composition gradient at the interface

solid. The width of the metastable region varies greatly for different solvent-solute systems, depending on the complexity of the crystallizing material, hydrodynamics, and other factors. While metallic semiconductor solutions support only a few degrees of undercooling $\Delta T_s = T_{e1} - T_{e2}$, undercoolings up to 150 °C are possible for oxides. For this reason LPE processes of these materials differ strongly.

We consider a solid $B$ in contact with a supersaturated solution at temperature $T_{e2}$. Figure 7.6b shows the concentration $x_B(z)$ of component $B$ in the liquid phase near the boundary to the solid. At the interface the concentration $x_i$ is smaller than the concentration $x_{e1}$ in the bulk of the liquid solution, because the solution depletes from $B$ atoms due to incorporation into the solid. Usually kinetic limitations at the growing surface prevent $x_i$ from attaining the equilibrium value $x_{e2}$. Away from the liquid-solid boundary the composition of the liquid approaches the prepared liquid bulk value $x_{e1}$.

In an LPE process the supersaturation is created either by cooling or by solvent evaporation of a saturated solution. During growth, a *diffusion boundary layer* of thickness $\delta$ is formed at the growth front, in which a concentration gradient and a temperature gradient exist. Growth species of the solute diffuse towards the liquid-solid interface, and solvent species diffuse contrariwise towards the bulk of the solution. Besides diffusion also hydrodynamic flow occurs near the interface. While hydrodynamic flow is more effective than diffusion in the bulk of the solution, its contribution decreases towards the interface and becomes negligible at the growth front. $\delta$ describes the concentration gradient in the solution at the interface, $(\partial x_B/\partial z)_{z=0} = (x_{e1} - x_i)/\delta$, cf. Fig. 7.6b. The thickness $\delta$ of the diffusion boundary

layer is determined by the hydrodynamic flow, and the process within this layer is solely controlled by diffusion. Thus, $\delta$ eventually determines the growth rate.

The theory of diffusion-limited growth has been widely applied to describe the LPE process. It assumes that the rate-limiting step is mass transport, i.e., the diffusion of solute species to the growth interface. For simplicity we consider the growth of a one-component system like, e.g., growth from single solute species $B$ in a solvent $A$. Such description applies as well for the growth unit of a multicomponent system, if the growth is limited by low rate constants of one of the solute constituents in this unit. Under such conditions, the concentration of the growth unit in the liquid $x_{\mathrm{L}}(z,t)$ (termed $x_B$ for the system described in Fig. 7.6b) is described by the solution of the one-dimensional diffusion equation [3]

$$\frac{\partial x_{\mathrm{L}}}{\partial t} = D\frac{\partial^2 x_{\mathrm{L}}}{\partial z^2} + v\frac{\partial x_{\mathrm{L}}}{\partial z}. \tag{7.2}$$

$D$ is the diffusion coefficient of the solute species in the solvent and $z$ is the distance to the solid-liquid interface as depicted in Fig. 7.6b. In a multicomponent system $D$ refers to the limiting component of the growth unit. The second term on the right-hand side describes convection, where $v$ is the growth velocity resulting from convection and the growth rate. In dipping processes convection is often enforced by substrate rotation to draw growth units in the normal direction towards the substrate and to control the thickness of the boundary layer by the rotation rate $\omega$.

The simultaneously occurring diffusion of heat in the solid and liquid phases is described by an equation similar to (7.2),

$$\frac{\partial T}{\partial t} = K\frac{\partial^2 T}{\partial z^2} + v\frac{\partial T}{\partial z},$$

where $T$ is the temperature and $K$ is the thermal diffusivity. Thermal gradients due to the dissipation of the crystallization heat and to temperature differences in the setup have a major effect in growth *from the melt*. In solution growth usually isothermal conditions prevail, and heat diffusion may be neglected.

### *7.1.4 LPE Processes*

We focus on the diffusion of growth species expressed by (7.2). If no convective field is set up by substrate rotation, the convection term is quite small. This is particularly fulfilled for small growth rates (order of 1 µm/h). We assume that convection is not enforced and neglect this term. We restrict our consideration to semi-infinite growth solutions, where the dimensions of the crucible or boat do not affect the process. This is a good approximation for growth times $t < l^2/D$, where $l$ is the depth of the growth solution and $D$ is the diffusion constant of the growth species. The concentration in the liquid $x_{\mathrm{L}}(z,t)$ is then described by the solution of

$$\frac{\partial x_{\mathrm{L}}}{\partial t} = D\frac{\partial^2 x_{\mathrm{L}}}{\partial z^2}. \tag{7.3}$$

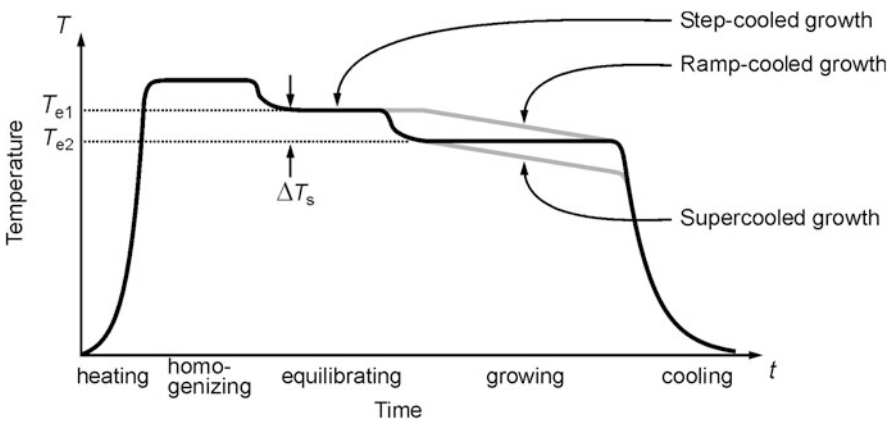


**Fig. 7.7** Temperature profiles of various LPE growth processes. Profiles drawn in *gray* are alternatives to that applied for step-cooled growth drawn in *black*

The solution of (7.3) depends on the boundary conditions of the growth process. Initially, the solute concentration is homogeneous, i.e., the concentration of the growth unit in the liquid $x_L(z, t = 0) = x_{e1}$ for all $z$. We assume fast kinetics at the liquid-solid interface, such that the solute concentration at the interface $x_i$ during growth equals the equilibrium concentration $x_{e2}$ at any time, $x_L(z = 0, t) = x_i(t) = x_{e2}(t)$.

Once the concentration profile $x_L$ is known, the growth rate $r$ is obtained by mass conservation, yielding

$$r = \frac{D}{(x_s - x_i)} \left( \frac{\partial x_L}{\partial z} \right)_{z=0}. \tag{7.4}$$

Here $x_s$ is the concentration of growth units in the solid and $x_i \approx x_{e2}$ (for fast kinetics) is the interfacial concentration. Often $x_i \ll x_s$ applies, and $x_i$ in the denominator is neglected. The thickness of the grown layer $d(t)$ results from integrating the growth rate,

$$d = \int_0^t r(t')\, dt'. \tag{7.5}$$

The temperature applied during growth may be a function of the growth time $t$, depending on the growth technique. There are various methods to adjust the temperature for producing the required supersaturation. Some temperature profiles are depicted in Fig. 7.7.

The process of liquid-phase epitaxy generally starts with heating the solution, followed by a period of homogenizing. The latter is of particular importance, since volatile impurities are baked out in this time. Hereafter, the temperature of the solution is lowered for equilibration, and then growth is started. Major temperature profiles applied for LPE growth are pointed out in the following.

*Step-cooling growth*: During equilibration the solution attains a uniform solute concentration $x_{e1}$ corresponding to a liquidus temperature $T_{e1}$, cf. Fig. 7.6. At

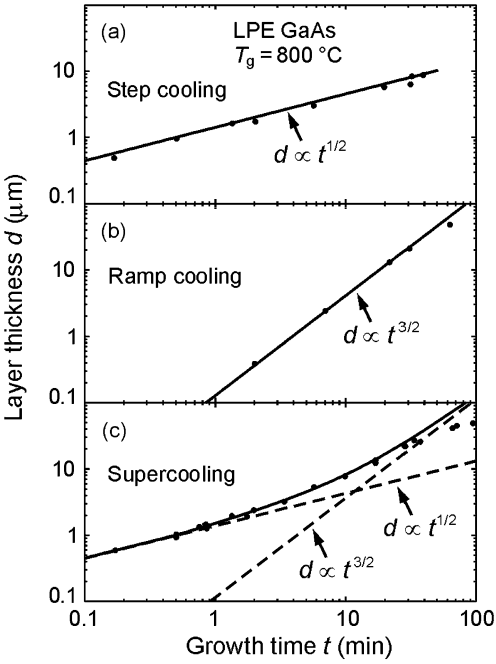


**Fig. 7.8** Layer thickness $d$ as a function of growth time $t$ for the liquid-phase epitaxy of GaAs. (**a**) Layers grown by the step-cooling process. *Points* are measured data, the *line* is calculated from (7.7). (**b**) Layers grown by ramp cooling, the *line* is calculated from (7.9). (**c**) Layers grown by supercooling, the *continuous line* is calculated from (7.10). Reproduced with permission from [4], © 1974 Elsevier

growth start the temperature is lowered to $T_{e2} = T_{e1} - \Delta T_s$ as illustrated in Fig. 7.7. Thereby the equilibrium concentration changes to a value $x_{e2}$ given by the liquidus curve at $T_{e2}$, and the solution, which is still at $T_{e1}$, is supersaturated. Inserting the slope of the liquidus curve $m = \partial T_e / \partial x_e$ and assuming a small $\Delta T_s$ such that the liquidus curve is approximately linear, we can express the equilibrium concentration on the substrate surface at $T_{e2}$ by $x_L(z = 0, t) = x_{e2} = x_{e1} - \Delta T_s / m$. For this condition and the boundary condition $x_L(z, t = 0) = x_{e1}$ the solution $x_L(z, t)$ to (7.3) is given by the error function [4]

$$\frac{x_L - x_{e2}}{x_{e1} - x_{e2}} = \mathrm{erf}\left(\frac{z}{2\sqrt{Dt}}\right). \tag{7.6}$$

From (7.4) and (7.5) eventually the layer thickness is obtained as a function of the growth time, yielding [4]

$$d(t) = \frac{2\Delta T_s}{m x_s}\left(\frac{D}{\pi}\right)^{1/2} t^{1/2} \quad \text{(step cooling)}, \tag{7.7}$$

$m$ being the slope of the liquidus curve and $x_s$ is the concentration of growth units in the solid. We note that the layer thickness does not linearly increase with time, i.e., the growth rate is not constant. Experimental results for the LPE of GaAs using step cooling are given in Fig. 7.8a. GaAs was grown from a Ga-rich solution, i.e., Ga was also employed as solvent. The epitaxy was performed at 800 °C applying an undercooling $\Delta T_s = 5$ °C. The straight line was calculated from (7.7) and describes well the measured data [4].

*Ramp-cooling growth*: The process starts with equilibration at a temperature $T_{e1}$, yielding $x_L(z, t = 0) = x_{e1}$. The temperature of the solution is then lowered at a linear rate $\alpha$, such that $T(t) = T_{e1} - \alpha t$. If the total cooling interval is small, the slope of the liquidus curve $m = \partial T_e / \partial x_e$ is approximately constant and the equilibrium composition on the liquidus curve is a linear function of temperature. We then obtain the boundary condition $x_L(z = 0, t) = x_{e1} - (\alpha/m)t$. For these conditions the solution $x_L(z, t)$ to (7.3) is given by the complementary error function

$$x_L = x_{e1} - 4(\alpha t/m) i^2 \mathrm{erfc}\left(\frac{z}{2\sqrt{Dt}}\right), \tag{7.8}$$

and by inserting into (7.4) and (7.5) the resulting layer thickness is [4]

$$d(t) = \frac{4\alpha}{3 m x_s}\left(\frac{D}{\pi}\right)^{1/2} t^{3/2} \quad \text{(ramp cooling)}. \tag{7.9}$$

We note that the time dependence of $d(t)$ differs from the square-root dependence obtained for step cooling (7.7). Experimental data for ramp-cooling LPE of GaAs are given in Fig. 7.8b. A cooling rate $\alpha = 0.6$ °C/min was applied, and the given growth temperature $T_g$ refers to the midpoint of the growth interval.

*Supercooling growth*: This process is a combination of step and ramp cooling processes. An undercooling temperature step of $\Delta T_s$ is introduced in addition to the temperature lowering at a linear rate $\alpha$, yielding the boundary condition $x_L(z = 0, t) = x_{e1} - \Delta T_s/m - (\alpha/m)t$. The solution $x_L(z, t)$ to (7.3) is accordingly a combination of both processes, yielding the time-dependent layer thickness [4]

$$d(t) = \frac{1}{m x_s}\left(\frac{D}{\pi}\right)^{1/2}\left(2\Delta T_s t^{1/2} + \frac{4}{3}\alpha t^{3/2}\right) \quad \text{(supercooling)}. \tag{7.10}$$

LPE data of GaAs grown by supercooling given in Fig. 7.8c confirm the expected dependence. In the experiments temperature steps $\Delta T_s = 5$ °C and cooling rates $\alpha = 0.6$ °C/min were applied.

The chosen process depends on the requirements of the material to be grown, the phase diagram, the morphology of the layer structure, and other parameters. The introduction outlined in this section illustrates that LPE relies on well-established data of the liquid-solid phase equilibrium. The technique is certainly challenging due to stringent demands of growth parameters, and the development of a growth process for a new layer structure requires much more time than for the more popular techniques of MOVPE and MBE pointed out in the next sections. On the other hand, liquid-phase epitaxy bares the potential for fabricating epitaxial layers with the highest possible structural perfection and homogeneity.

## 7.2 Metalorganic Vapor-Phase Epitaxy

Metalorganic vapor-phase epitaxy (MOVPE), also termed metalorganic chemical vapor deposition (MOCVD; sometimes O and M in the acronyms are exchanged),

is the most frequently applied CVD technique for semiconductor device fabrication. Industrial large scale reactors presently have the capacity for a simultaneous deposition on fifty 2-inch wafers, and a majority of advanced semiconductor devices is produced using this technique. Applications of MOVPE are not restricted to semiconductors, but also include oxides, metals, and organic materials. The technique emerged in the 1960ies [5–9], when epitaxy was dominated by liquid-phase epitaxy, chloride vapor-phase epitaxy, and molecular-beam epitaxy (Sect. 7.3) did not exist in its present form. Complex sample structures with abrupt interfaces down to the monolayer range and excellent uniformity may today be fabricated using either MOVPE or MBE, though application of MOVPE is advantageous in realizing graded layers or, e.g., in arsenide-phosphide alloys and nitride semiconductors.

### *7.2.1 Metalorganic Precursors*

A common feature of chemical vapor-phase techniques is the transport of the constituent elements in the gas phase to the vapor-solid interface in form of volatile molecules. In MOVPE these species consist of metalorganic compounds, and the transport is made by a carrier gas like hydrogen at typically 100 mbar total pressure. The gaseous species dissociate thermally at the growing surface of the heated substrate, thereby releasing the elements for layer growth. The dissociation at the surface is generally assisted by chemical reactions.

The net reaction for the MOVPE of GaAs using the standard source compounds trimethylgallium and arsine reads

$$\mathrm{Ga(CH_3)_3 + AsH_3 \rightarrow GaAs + 3CH_4\uparrow}. \tag{7.11}$$

The reaction is actually much more complicate and comprises many successive steps and species in the chemistry of deposition [10] like, e.g., some steps of precursor decomposition

$$\mathrm{Ga(CH_3)_3 \rightarrow Ga(CH_3)_2 + CH_3 \rightarrow GaCH_3 + 2CH_3 \rightarrow Ga + 3CH_3}.$$

Major species occurring in the gas phase near the substrate surface are indicated in Fig. 7.14. The source compounds employed for MOVPE must meet some basic requirements. Their stability is low to allow for decomposition in the process, but still sufficient for long term storage. Furthermore the volatility should be high, and a liquid state is favorable to provide a steady state source flow. Most source molecules have the form $MR_n$, where $M$ denotes the element used for MOVPE, and $R$ are alkyls like methyl $CH_3$. By choosing a suitable organic ligand, the bond strength to a given element $M$ can be selected to comply with the requirements of MOVPE for the solid to be grown. The metal-carbon bond strength depends on the electronegativity of the metal $M$ and the size and configuration of the ligand $R$ [11]. As a thumb rule the bond strength decreases as the number of carbon atoms bond to the central carbon in the alkyl is increased. This trend is also reflected in the dissociation energy of the first carbon-hydrogen bond given in Table 7.1 [12].

**Table 7.1** Dissociation energy $E$ of the carbon-hydrogen bond for radicals $R$ used in MOVPE source molecules

| $R$ | $E$ (kJ/mol) | $R$ | $E$ (kJ/mol) |
|---|---|---|---|
| methyl (Me) | 435 | iso-propyl | 398 |
| ethyl (Et) | 410 | tert-butyl ($^t$Bu) | 381 |
| $n$-propyl | 410 | allyl | 368 |

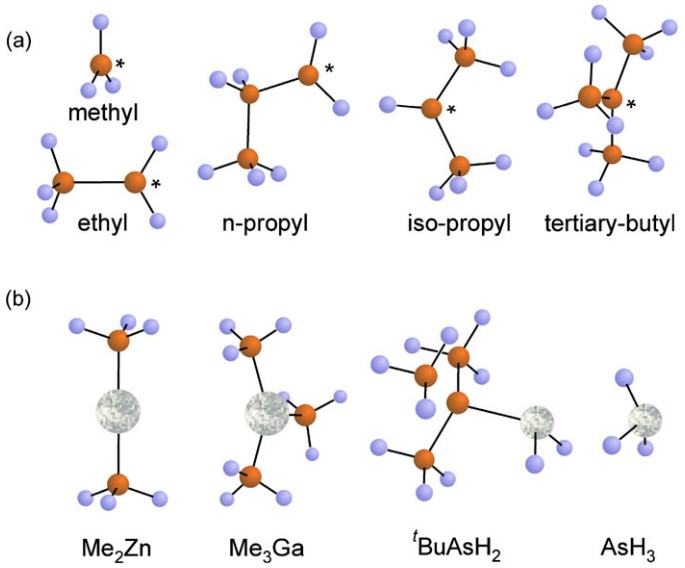


**Fig. 7.9** (**a**) Alkyl radicals used as organic ligands in source molecules, and (**b**) some source molecules for metalorganic vapor phase epitaxy. *Red* and *blue* spheres represent carbon and hydrogen atoms, respectively, the location for a bond to an element $M$ at the radicals is indicated by an *asterisk*

Organic radicals $R$ most frequently used for MOVPE precursors are depicted in Fig. 7.9a, some metalorganic precursors are given in Fig. 7.9b.

Besides metalorganic sources also hydrides like arsine are employed as precursors. Their use is interesting since they release hydrogen radicals under decomposition that can assist removal of carbon-containing radicals from the surface. A major obstacle is their high toxicity and their very high vapor pressure, requiring extensive safety precautions. To reduce the hazardous potential, hydrides are increasingly replaced by metalorganic alternatives, e.g., arsine by tertiarybutylarsine, where one of the three hydrogen radicals is replaced by a tertiarybutyl radical. Thereby the vapor pressure is strongly reduced, yielding usually liquids at ambient conditions. In addition the toxicity decreases significantly.

Partial pressures for some standard precursors used in the MOVPE of As-related III–V semiconductors are given in Table 7.2. The values are expressed in terms of

**Table 7.2** Equilibrium vapor-pressure data of some metalorganic compounds used for III–V MOVPE (Vapor-pressure data taken from data sheets of several precursor suppliers)

| Element | Precursor | Vapor pressure | | |
|---|---|---|---|---|
| | | $a$ | $b$ (K) | $P_{\mathrm{eq\,MO}}$ (mbar) at 20 °C |
| Al | trimethylaluminum | 8.349 | 2135 | 11.5 |
| Ga | trimethylgallium | 8.195 | 1703 | 241 |
| | triethylgallium | 8.208 | 2162 | 6.7 |
| In | trimethylindium (solid) | 10.645 | 3014 | 2.3 |
| P | tertiarybutylphosphine | 7.711 | 1539 | 187 (10 °C) |
| As | tertiarybutylarsine | 7.368 | 1509 | 109 (10 °C) |
| Sb | trimethylantimony | 7.833 | 1697 | 110 |
| | triethylantimony | 8.029 | 2183 | 3.8 |
| N | dimethylhydrazine | 8.771 | 1921 | 164 |

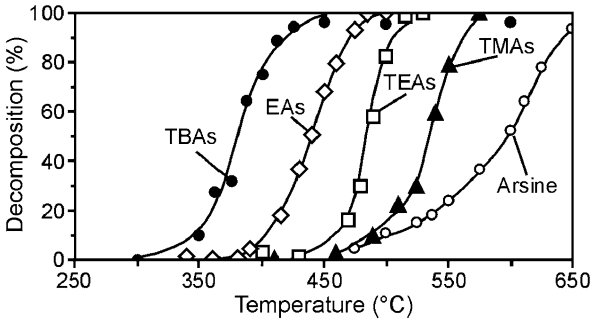


**Fig. 7.10** Decomposition of As precursors, the labels *TBAs*, *Eas*, *TEAs* and *TMAs* denote tertiarybutyl-As, ethyl-As, triethyl-As, and trimethyl-As, respectively. Reproduced with permission from [15], © 1991 Elsevier

the parameters $a$ and $b$ to account for the exponential temperature dependence of the vapor pressure according to

$$\log(P_{\mathrm{eq\,MO}}) = a - b/T, \tag{7.12}$$

where the equilibrium pressure of the metalorganic source $P_{\mathrm{eq\,MO}}$ and the temperature of the source $T$ are given in units of mbar and K, respectively. Hydrides $AsH_3$ and $PH_3$ are stored at 20 °C as liquids under pressures of 15 bar and 40 bar, respectively, and introduced as gases to the MOVPE setup.

Precursor molecules may decompose by a number of pyrolytic mechanisms, the most simple being free radical homolysis, i.e., a simple bond cleavage. Since the $M$-H bond is generally stronger than the $M$-C bond, metalorganic alternatives of the stable hydrides decompose at lower temperatures—a further incentive for their use. Results of pyrolysis studies for various As precursors, performed in an isothermal flow tube, are given in Fig. 7.10. The bond strength thumb rule noted above is well reflected in these curves.

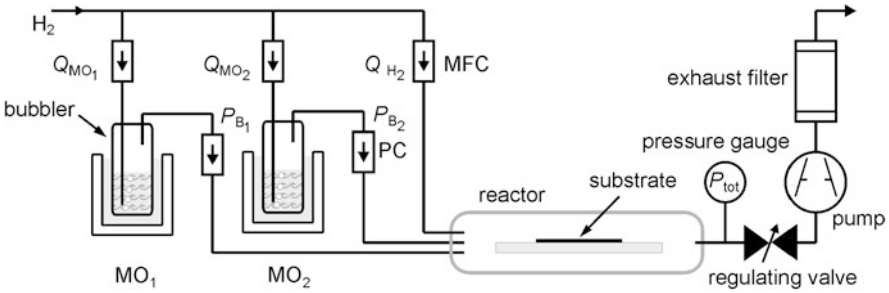


**Fig. 7.11** Schematic diagram of a metalorganic vapor phase epitaxy apparatus. Hydrogen is used as carrier gas and introduced into the metalorganic sources $MO_1$ and $MO_2$. MFC and PC denote mass-flow and pressure controllers, respectively

### *7.2.2 The Growth Process*

Most metalorganic sources are liquids which are stored in bubblers. For transport to the reactor a carrier gas (usually hydrogen) with a flow $Q_{\mathrm{MO}}$ is introduced by a dip tube ending near the bottom, see Fig. 7.11. At a fixed temperature the metalorganic liquid forms an equilibrium vapor pressure $P_{\mathrm{eq\,MO}}$ given by (7.12), and the bubbles of the carrier gas saturate with precursor molecules. At the outlet port of the bubbler a pressure controller is installed, which acts like a pressure-relief valve and allows to define a fixed pressure $P_{\mathrm{B}}$ ($> P_{\mathrm{eq\,MO}}$) in the bubbler, thereby decoupling the bubbler pressure from the equilibrium vapor pressure of the MO source. Also the total pressure $P_{\mathrm{tot}}$ in the reactor is controlled independently. The partial pressure of a metalorganic source in the reactor $P_{\mathrm{MO}}$ results from the mentioned parameters by

$$P_{\mathrm{MO}} = \frac{Q_{\mathrm{MO}}}{Q_{\mathrm{tot}}} \times \frac{P_{\mathrm{tot}}}{P_{\mathrm{B}}} \times P_{\mathrm{eq\,MO}}, \tag{7.13}$$

$Q_{\mathrm{tot}}$ denoting the total flow in the reactor. The two fractions in (7.13) are employed to control the partial pressure $P_{\mathrm{MO}}$ of the source in the reactor. For sources used as dopants or compounds with very high vapor pressures an additional dilution by mixing with a controlled flow of carrier gas is applied. The gaseous hydrides are directly controlled by their flow $Q_{\mathrm{Hyd}}$, and (7.13) simplifies to

$$P_{\mathrm{Hyd}} = \frac{Q_{\mathrm{Hyd}}}{Q_{\mathrm{tot}}} \times P_{\mathrm{tot}}. \tag{7.14}$$

The total flow in the reactor $Q_{\mathrm{tot}}$ results from the sum of all component flows plus the flow of the carrier gas which is additionally introduced into the reactor by a separate mass-flow controller. This flow is generally much higher than that of all sources, and the sum of all source partial pressures $P_{\mathrm{MO}}$ and $P_{\mathrm{Hyd}}$ is consequently much smaller than the total pressure in the reactor $P_{\mathrm{tot}}$. The reactor pressure $P_{\mathrm{tot}}$ is controlled as an independent parameter by a control valve attached to an exhaust pump behind the reactor (Fig. 7.11). The flow rate is usually specified in terms of a mass flow $dm/dt$ (in units of g/min or mol/min) or volume flow $dV/dt$ (standard

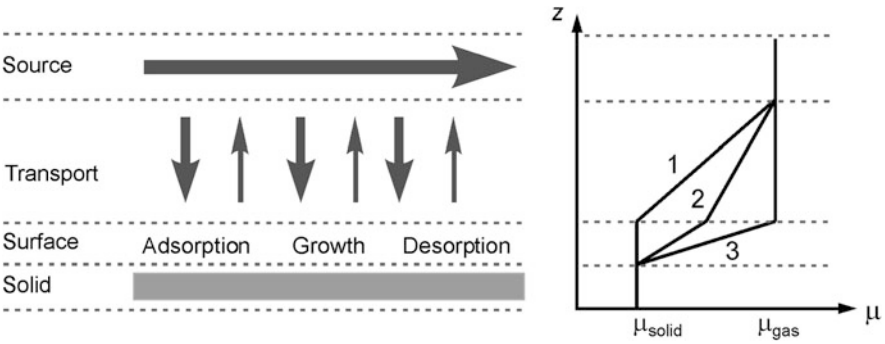


**Fig. 7.12** Scheme of the chemical potential $\mu$ near the surface of the growing solid during MOVPE. Path *1* signifies growth controlled by mass transport, paths *3* and *2* denote growth being limited by interface reactions and the general case, respectively

cubic centimeters per minute, sccm), both defined at some standard conditions with respect to temperature and pressure.

The complete treatment of the MOVPE growth process involves numerous gas phase and surface reactions, in addition to hydrodynamic aspects. Such complex studies require a numerical approach, and solutions were developed for specific processes like MOVPE of GaAs from trimethylgallium and arsine [10, 13, 14]. We will first draw a more general picture of the growth process.

Growth represents a nonequilibrium process. The driving force is given by a drop in the chemical potential $\mu$ from the input phase to the solid. For the discussion of the MOVPE process a description by consecutive steps as depicted in Fig. 7.12 is convenient. The reactants in the carrier gas represent the source. Near the solid surface a vertical diffusive transport component originates from reactions of source molecules and incorporation into the growing layer. All processes from adsorption at the surface to the incorporation are summarized to interface reactions. Finally excess reaction products desorb from the interface by diffusion.

The slowest process of the successive steps limits the growth rate. Without considering mechanisms of growth in detail, processes limited by either transport or kinetics can be well distinguished. Figure 7.13 shows on a logarithmic scale the dependence of the GaAs growth rate from the reciprocal substrate temperature. At low temperature experiment and simulation show an exponential relation, indicating that thermally activated processes limit the growth rate. Precursor decomposition and interface growth reactions lead to a pronounced temperature dependence, the slope $\propto -\Delta E/(k_B T)$ yields an activation energy $\Delta E$ near 19 kcal/mole for the given process. This regime is referred to as *kinetically limited growth*. The gas phase supplies precursors to the surface at a rate well exceeding the rate of growth reactions. As the temperature is increased, the growth rate becomes nearly independent on temperature. In this range precursor decomposition and surface reactions are much faster than mass transport from the source to the interface of the growing solid. Since diffusion in the gas phase depends only weakly on temperature, this process is called *transport-limited growth*. Mass transport in this regime depends

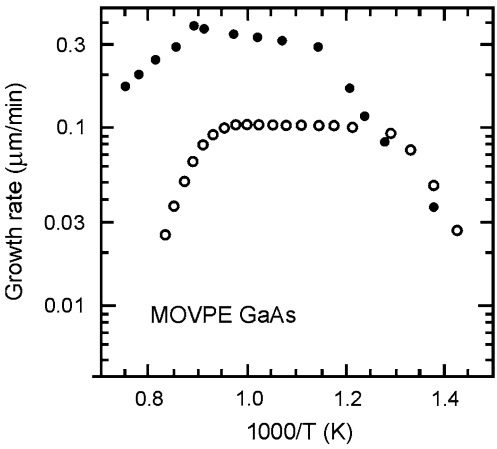


**Fig. 7.13** Growth rate in the MOVPE of (001)-oriented homoepitaxial GaAs layers as a function of reciprocal temperature. Trimethylgallium and arsine are used as precursors. *Full* and *open circles* represent measured data from [16] and model predictions from [10], respectively

on the geometry of the reactor, because flow field and temperature profile above the substrate affect cracking and arrival of precursors at the interface. This fact accounts for the difference in the maximum growth rates in Fig. 7.13. In the high-temperature range growth rates decrease due to enhanced desorption and parasitic deposition at the reactor walls, inducing a depletion of the gas phase.

MOVPE is usually performed in the mid-temperature range of transport limited growth, where variations of the substrate temperature have only a minor effect on the growth rate, the composition of alloys, and on the doping level. For arsenide and phosphide semiconductors the range is typically between 500 °C and 800 °C, for nitrides above 1000 °C.

The decomposition of the precursors at the heated substrate and subsequent reactions leads to a large number of species in the gas phase and on the surface. We consider some results of a detailed study of the elementary processes for the homoepitaxial growth of GaAs on (111)A-oriented substrates [14]. The model for the MOVPE from trimethylgallium and arsine source compounds according the net reaction (7.11) included 60 species and more than 200 reactions in the gas phase, and a total of 19 species and more than 100 processes at the surface. The model considered the flow, heat and mass transfer in a vertical reactor with forced convection like that shown in Fig. 7.15b. The gaseous reactants enter through a nozzle placed at right angles to the heated substrate. The gas flows toward the substrate and then flows radially outward. Gas inlet at 298 K is assumed, with inlet pressures of $3.4 \times 10^{-4}$ bar for $Ga(CH_3)_3$ and $6.8 \times 10^{-3}$ bar for $AsH_3$, a total flow rate of 1.5 standard liter per minute at 1 bar total reactor pressure, and a substrate temperature of 1000 K. Surface processes are considered for two different sites: the planar Ga-face of the (111)-oriented GaAs surface and ledge sites at monoatomic steps on the surface. Basic predictions of this model were verified experimentally.

The results demonstrate that the sites on the planar (111)A GaAs surface are basically occupied by $AsH_n$ species with a decreasing fractional coverage for $n = 2, 3$ at increased temperature, and a low, only slightly varying occupancy by AsH and As. $Ga(CH_3)_2$ and $GaCH_3$ species occupy ledge sites [14]. The rate-controlling steps

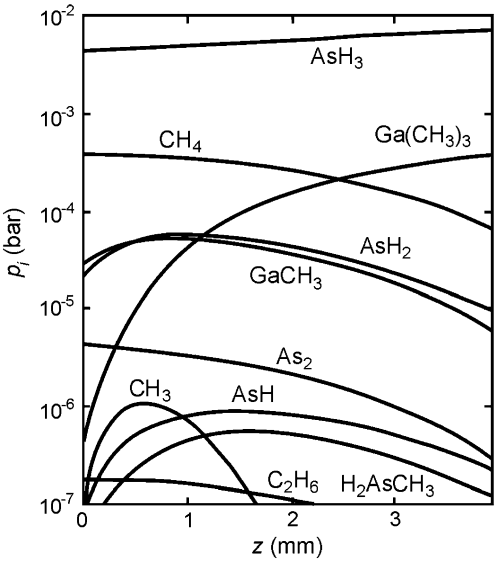


**Fig. 7.14** Calculated partial pressures $P_i$ of major species $i$ in the gas phase for the metalorganic vapor-phase epitaxy of GaAs from $Ga(CH_3)_3$ and $AsH_3$ precursors on GaAs (111)A substrate. $z$ designates the vertical distance from the growth surface, which is kept at 1000 K. Reproduced with permission from [14], © 1988 Elsevier

for the modeled MOVPE of GaAs strongly depend on the substrate temperature. At low temperature the growth rate is controlled by the activation energy of surface kinetics involving $Ga(CH_3)_n$ species ($n = 0, 1$), and reactions in the gas phase are not important. The rate-limiting step at 773 K is the removal of $CH_3$ radicals from $Ga(CH_3)_2$ adsorbed at a ledge site. As the temperature is raised to intermediate values between 900 K and 1000 K, surface reactions become fast and mass transport and gas-phase reactions become dominant. The reaction of $AsH_3$ with $CH_3$ radicals to $AsH_2$ and $CH_4$ in the gas phase enhances the decomposition of $Ga(CH_3)_3$ by removing the radicals. At high temperatures above 1000 K, deposition of arsenic in the form of $As_2$ and a reduced adsorption of $GaCH_3$ impose kinetic barriers.

The composition of the gas phase at a substrate temperature of 1000 K is given in Fig. 7.14. We note that the partial pressures of major species vary strongly in the vicinity of the substrate surface [14]. The amount of the readily decomposing Ga precursor $Ga(CH_3)_3$ drops to very small values, while the partial pressure of the stable arsine $AsH_3$ decreases only slightly. The concentration of $CH_3$ radicals remains low, mainly due to the consuming gas-phase reaction with $AsH_3$ noted above and the parallel reaction $CH_3 + H_2 \Leftrightarrow CH_4 + H$. GaAs growth at this high temperature occurs basically by adsorption of monomethylgallium $GaCH_3$ at ledge sites and subsequent surface reaction with AsH or with As.

### *7.2.3 Mass Transport*

The access of supplied precursor molecules to the growth surface occurs by various transport processes. Diffusion and convection in the presence of large temperature

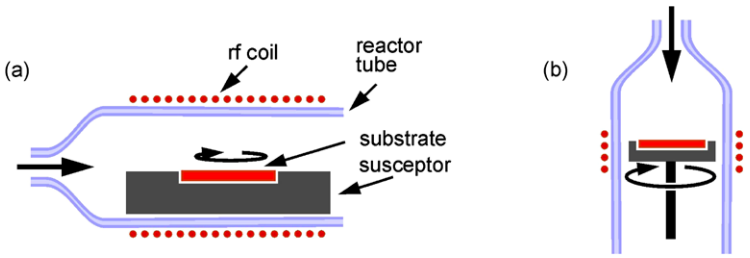


**Fig. 7.15** Reactor types applied in the metalorganic vapor-phase epitaxy. (**a**) Horizontal reactor with inductive heating of the susceptor which carries the substrate. The *circular arrow* indicates the wafer rotation. (**b**) Schematic of a vertical reactor

and concentration gradients affect the growth rate and uniformity of layer composition. The transport processes depend strongly on the configuration of the reactor and the adjustment of operating parameters. The main geometries of MOVPE reactors are shown in Fig. 7.15. Horizontal and vertical reactors are used, and both designs are also upscaled for simultaneous multiwafer epitaxy. For simplicity we consider single-wafer setups. Reactor vessels are made of quartz glass or steel. The reactor walls are usually kept cold to minimize unwanted deposition at the walls. The wafer is placed on a (graphite) susceptor, which often is inductively heated by a radio-frequency (rf) generator via an rf coil for coupling. Usually wafer rotation (typ. 30 rpm) is applied during deposition to even out gas supply and heating nonuniformities for achieving a laterally uniform growth rate. In vertical reactors also rotation at high speed is used (>500 rpm) to emulate a rotating-disk flow.

Both reactor types depicted in Fig. 7.15 are designed for a laminar gas flow. Typical operating conditions with a total pressure $P_{\mathrm{tot}}$ of $10^2$ Pa (low-pressure MOVPE) or $10^5$ Pa (atmospheric-pressure MOVPE) yield about $10^1$ cm/s mean gas velocity (somewhat higher at low pressure, also depending on the total flow in the reactor $Q_{\mathrm{tot}}$), leading to a flow well below the onset of turbolence.

The description of the mass transport in the gas phase consists of three-dimensional nonlinear, coupled partial differential equations. The conservation of momentum, energy, total mass and individual species is expressed by the Navier-Stokes, the energy transport, and mass continuity equations, respectively. In addition, the system is specified by the equation of state for the involved gases and suitable boundary conditions. The large temperature gradient created by the heated susceptor and the cold walls, and the gradient of species concentrations originating from decomposition and chemical reactions lead to strong diffusion processes and a coupling of mass transport and thermal transport. A correct treatment of mass transport is very complex, because the coupled equations must be solved simultaneously. Furthermore, a complete description must also account for the chemical reactions illustrated in the previous section. An analytical solution of such complex problem is not feasible. Experimental data have, however, been well described by extensive numerical modeling. Results of a comprehensive numerical treatment for some typical reactor geometries are given in Ref. [13]. Since general guidelines for the

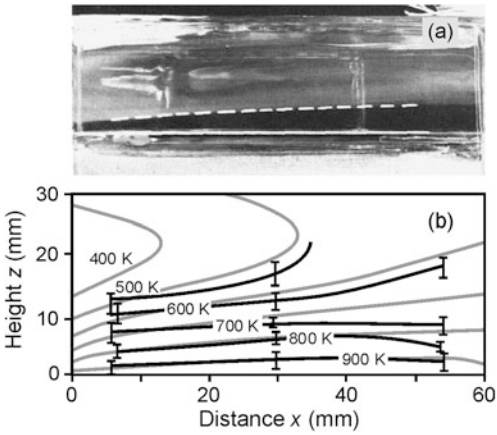


**Fig. 7.16** Flow visualization and isotherms in MOVPE reactors. (**a**) Horizontal reactor with 8 l/min total flow of $H_2$ and $TiO_2$ particles above a susceptor kept at 1000 K. Reproduced with permission from [21], © 1986 Elsevier. (**b**) Measured (*black lines*) and calculated isotherms (*gray lines*) above the susceptor kept at 1000 K for 8 l/min inlet $H_2$ flow at 1000 mbar total pressure. Reproduced with permission from [17], © 1990 Elsevier

dependences of growth parameters are difficult to extract from numerical solutions, simplified analytical approaches are quite popular. Comparison with experimental and numerical data demonstrate that the results obtained from such models are often wrong and misleading. We focus on hydrodynamic aspects of the carrier gas and do not consider the complex chemistry. Some justification for this reasonable approach is given by the usually small partial pressures of the species.

The flow conditions in a horizontal reactor are visualized in Fig. 7.16a. The flow lines are traced by micron-sized $TiO_2$ particles, which are produced by leading $H_2$ carrier gas with $TiCl_4$ into a bubbler filled with $H_2O$. The image shows Mie scattering of light illuminating the glass reactor. The white line at the bottom indicates the top of the graphite susceptor, which is heated to 1000 K. The gas is introduced from the left at room temperature with a flow of 8 l/min at $10^5$ Pa total pressure. We note the dark region limited by the dashed line, indicating that the flow does not enter the hottest region above the substrate. This region is often termed boundary layer, because an apparently similar phenomenon of this name is observed in the isothermal parallel flow over a flat plate as illustrated in Fig. 7.17.

The temperature distribution in the horizontal MOVPE reactor was measured using Raman scattering from rotational transitions of the $H_2$ carrier gas [17]. We note in Fig. 7.16b the strong temperature gradient at the bottom above the susceptor. At the selected high flow rate the hight-$T$ isotherms are fairly parallel to the susceptor, while a larger wedge-shaped dark region in flow visualization and accordingly more inclined isotherms are found at lower flow rate. The experimental data agree well with calculated results obtained using the finite elements method. Heat conduction in the reactor wall, heat transfer to the surroundings, and radiative heat transfer were included in the calculations to obtain such close agreement.

We now take a closer look to the boundary layer which develops at a plate in an isothermal laminar flow. Figure 7.17 depicts the velocity field near the surface of the flat plate, which is placed in the homogeneous gas flow moving with a constant free-stream velocity $u_\infty$. The boundary conditions for the solution of the (two-dimensional) hydrodynamic steady-state equation of continuity and the equation of

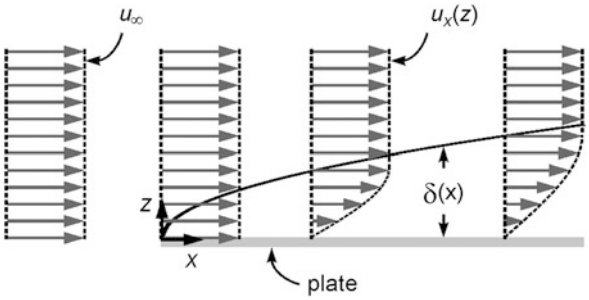


**Fig. 7.17** Development of a boundary layer of thickness $\delta(x)$ above the surface of a plate of negligible thickness, placed in an isothermal laminar flow of constant velocity $u_\infty$. The flow field below the plate is mirror inverted with respect to that above the plate and not drawn. The *arrows* give the distribution of the velocity $u_x$ over the distance from the plate $z$ at three different locations $x$

motion are given by the general assumption, that the fluid velocity at solid-fluid interfaces equals the velocity with which the solid surface moves itself: the fluid clings to the solid surface. In our case the plate is fixed, hence the $x$ component of the velocity at the surface (at $z = 0$) is $u_x = 0$. Moreover, far away from the plate (for all $x$ at large $z$) and at the very leading edge of the plate (at $x = 0$) the velocity is unaffected, $u_x = u_\infty$.

In the hydrodynamic problem illustrated in Fig. 7.17 a boundary layer of thickness $\delta(x)$ develops between the surface of the plate and the constant flow field far away from the plate. $\delta(x)$ is conventionally defined by the distance from the surface at which the velocity component $u_x$ becomes 99 % of the free-stream velocity $u_\infty$. Below $\delta(x)$, i.e., in the region of the boundary layer, the velocity $u_x$ gradually decreases to 0 as postulated from the boundary condition for the solid-fluid interface. The velocity distribution $u_x(x, z)$ is approximately given by [18]

$$u_x \cong \left(\frac{3}{2}\left(\frac{z}{\delta(x)}\right) - \frac{1}{2}\left(\frac{z}{\delta(x)}\right)^3\right)u_\infty; \quad 0 < z < \delta(x) \tag{7.15}$$

where the thickness of the boundary layer is

$$\delta(x) \cong 5\sqrt{\frac{\eta}{\rho u_\infty}x}. \tag{7.16}$$

Here $\eta$ and $\rho$ are the dynamic viscosity and the mass density of the gas, respectively. Function (7.15) is drawn as dashed line in Fig. 7.17. The thickness of the boundary layer is proportional to the square root of the distance $x$ down the plate along the direction of the flow, where $x$ is measured from the leading edge of the plate. We note the similarity between the dark region in the flow above the hot susceptor marked in Fig. 7.16a and the boundary layer of the plate in the isothermal flow shown in Fig. 7.17. Calling the dark region in Fig. 7.16a a boundary layer might meanwhile be misleading. Numerical simulations clearly demonstrate that the origin of the vertical flow component away from the hot susceptor is actually thermodiffusion (thermophoresis). The suddenly heated gas near the susceptor expands and becomes less dense. In the presence of gravity the gas rises due to buoyancy.

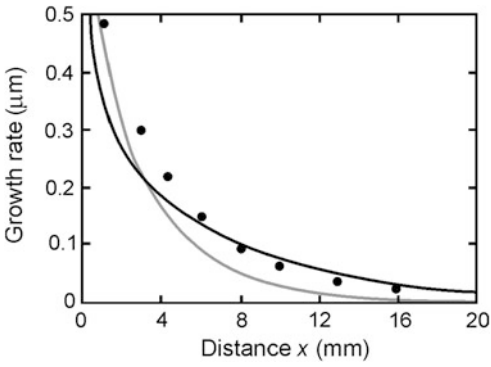


**Fig. 7.18** Effect of thermal diffusion on the growth rate of GaAs in a horizontal MOVPE reactor. *Symbols* give experimental data, showing a decreasing growth rate due to a depletion of Ga species in the gas phase. The *black* and *gray lines* are numerically predicted growth rates with and without thermal diffusion, respectively. Reproduced with permission from [19], © 1988 Elsevier

The effect of buoyancy-driven convection on the distribution of the GaAs growth rate along the flow direction in a horizontal reactor was evaluated by numerical modeling with and without the thermal-diffusion term included [19]. The growth rate under the selected experimental conditions was controlled by gas phase transport of the Ga component via diffusion and flow, and a significant gas-phase depletion was found [20]. The numerical results given in Fig. 7.18 show that thermal diffusion decreases the growth rate at the front edge of the susceptor, because the heavy reactant molecules are driven away due to buoyancy in the strong temperature gradient. The depletion of the gas phase from reactants is thereby diminished, leading to an increase of the growth rate in the downstream range. The influence of natural convection is reduced at lower total pressure.

### Model of a Stagnant Boundary Layer

Extensive numerical treatment of the hydrodynamic conditions in the reactor yields a good description of experimental data, but it delivers only little insight into dependences of growth parameters. We consider the popular (stagnant) boundary-layer model to indicate qualitatively some tendencies. Since the assumptions of the simple model are too restrictive to yield reliable relations, we should consider the results merely as a rough guideline to understand some trends.

The model of a stagnant boundary layer interprets the region above the hot susceptor visualized in Fig. 7.16a as a stagnant layer, where mass transport occurs solely by diffusion. This means that the horizontal velocity component of the flow $u_x$ is assumed to drop to zero below the upper bound of this layer as illustrated in Fig. 7.19.

The growth rate of the epilayer depends on the amount of source material supplied to the surface. The diffusive flux $\mathbf{j}_i$ of material component $i$ is given by the diffusion along the partial pressure gradient $\partial P_i/\partial \mathbf{r}$ and the termodiffusion along the temperature gradient $\partial T/\partial \mathbf{r}$. The comparably small effect of thermodiffusion is neglected, and the partial pressures are assumed to drop over the stagnant layer of thickness $d$ from their values $P_i$ in the source to values $P_i^{\text{interface}}$ at the interface

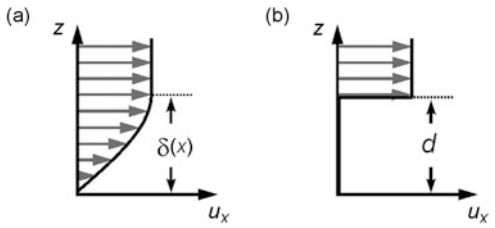


**Fig. 7.19** Comparison of (**a**) the boundary layer of thickness $\delta$ of a flow above the surface of a fixed surface, and (**b**) the condition assumed in the boundary-layer model applied to describe the diffusion of source material from the flow over a stagnant layer of thickness $d$ to the growing surface in the MOVPE. The *arrows* signify the flow velocity $u_x$

to the solid. A linear decrease of the partial pressure of component $i$ is assumed, yielding a pressure gradient expressed by $(P_i - P_i^{\text{interface}})/d$. Only diffusion normal to the surface is considered. Ficks's first law then becomes a simple expression for the flux from the source above the stagnant layer to the surface [22],

$$j_i = \frac{D_i}{k_B T d}\left(P_i - P_i^{\text{interface}}\right). \tag{7.17}$$

$D_i$ is the diffusion constant of species $i$ in the carrier gas. The factor $D_i/(k_B T d)$ may be considered as an effective coefficient of mass transport for component $i$.

Due to the supersaturation set to induce growth, the partial pressures of the components at the inlet of the reactor $P_i$ are much higher than the equilibrium-near values at the interface to the solid $P_i^{\text{interface}}$. For III–V compounds like GaAs this means $P_{\text{III}} P_{\text{V}} \gg P_{\text{III}}^{\text{interface}} P_{\text{V}}^{\text{interface}}$. Furthermore, the Column-V precursors are far more volatile than the Column-III species (except for Sb-sources). III–V semiconductors are hence usually grown with a large excess of Column-V species, i.e., $P_{\text{V}}/P_{\text{III}} \gg 1$. At the interface to the solid the same number of Ga and As atoms is permanently removed from the gas phase due to the requirement of stoichiometric growth. Ga is therefore nearly depleted at the interface, while the arsenic partial pressure is only slightly reduced. These conditions lead to the relations of the partial pressures at the interface and the reactor inlet $P_{\text{III}}^{\text{interface}} \ll P_{\text{III}}$, and $P_{\text{V}}^{\text{interface}} \approx P_{\text{V}}$. The flux of Column-III species $j_{\text{III}}$ arriving at the surface then reads

$$j_{\text{III}} = \frac{D_{\text{III}} P_{\text{III}}}{k_B T d}. \tag{7.18}$$

Since all Column-III species are incorporated into the solid, the growth rate $r$ is controlled by the flux of Column-III species, $r \propto j_{\text{III}}$. Experimental evidence for the linear dependence is shown in Fig. 7.20.

The dependences of the growth rate on the total reactor pressure $P_{\text{tot}}$ and on the total flow in the reactor $Q_{\text{tot}}$ are estimated by substituting the thickness of the boundary layer $\delta$ in (7.16) for the stagnant layer thickness $d$ in (7.18). The diffusion

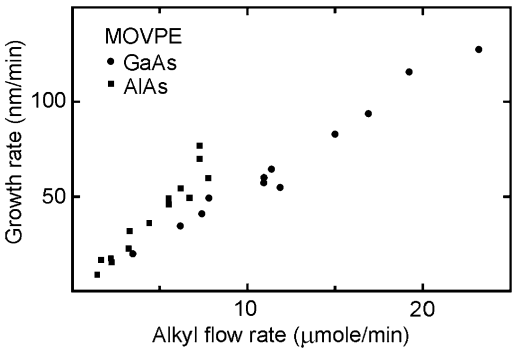


**Fig. 7.20** Growth rate of GaAs (*circles*) and AlAs (*squares*) depending on the Column-III alkyl supply trimethylgallium or trimethylaluminum, respectively, at constant arsine supply. Reproduced with permission from [29], © 1984 Elsevier

constant $D$ in the gas phase is inverse to $P_{\text{tot}}$, and the density $\rho$ is proportional to $P_{\text{tot}}$, yielding

$$r \propto P_{\text{III}} \sqrt{\frac{u_\infty}{P_{\text{tot}}}}. \tag{7.19}$$

Taking (7.13) into account we note that $r$ is proportional to the flow of carrier gas through the bubbler $Q_{\text{MO}}$ of the Column-III source. Equation (7.19) predicts a growth rate being *independent* on the total reactor pressure if all other parameters are kept constant, because both $P_{\text{III}}$ ($\propto P_{\text{tot}}$, cf. (7.13)) and $u_\infty$ (inverse to $P_{\text{tot}}$) are implicit functions of the reactor pressure. The dependence of $r$ on the flow $Q_{\text{tot}}$ is also determined by the implicit dependences of $P_{\text{III}}$ (inverse to $Q_{\text{tot}}$) and $u_\infty$ ($\propto Q_{\text{tot}}$), yielding a decrease of the growth rate $\propto Q_{\text{tot}}^{-1/2}$ as the total flow in the reactor $Q_{\text{tot}}$ is increased. We should not take these predictions literally and just regard them as some trends. Deviations are particularly expected at low pressures and low flow velocities, where the boundary-layer thickness is in the range of the reactor height.

## 7.3 Molecular Beam Epitaxy

Molecular beam epitaxy (MBE) is a physical-vapor deposition technique, which is widely applied in research labs and industrial production. The constituent elements of the crystalline solid are transported from the source(s) to the substrate using molecular beams. A molecular beam is a directed ray of neutral atoms or molecules in a vacuum chamber. In MBE the beams are usually thermally evaporated from solid or liquid elemental sources. Various names are used particularly for the epitaxy of compound semiconductors, if gas sources are employed as source materials: metalorganic MBE (MOMBE), if metalorganic compounds like those applied in MOVPE (Sect. 7.2.1) are used for metals and conventional sources for anions, gas-source MBE (GSMBE), if hydrides for anions and metals are employed, and chemical beam epitaxy (CBE) for the supply with all gas sources.

In early experiments during the 1950ies and 60ies various beam techniques were used for the crystalline and epitaxial deposition of II–VI [23], IV–VI [24], and III–V

[25, 26] semiconductors. In the late 60ies a study on the surface kinetics of Ga and As species in the epitaxy of GaAs provided a first insight into the growth mechanisms [27], and soon later epitaxial growth of GaAs layers with high quality was achieved [28].

### *7.3.1 MBE System and Vacuum Requirements*

The characteristic feature of MBE is the mass transport in molecular or atomic beams. A vacuum environment is required to ensure that no significant collisions occur among the beam particles and between beam and background vapor. A schematic diagram of an MBE system is given in Fig. 7.21.

The vacuum is generated in a chamber by pumps and cryoshrouds. Usually effusion cells mounted opposite to the substrate produce beams of different species by evaporation. The duration of the exposure on the substrate is individually controlled by shutters for a rapid change of material composition or doping. The substrate is mounted on a heated holder and can be loaded and unloaded under vacuum conditions by a manipulating mechanism. A gauge can be placed at the position of the substrate to measure and calibrate the beam-equivalent pressure (BEP) produced by the individual sources. The vacuum environment maintained during epitaxy provides an excellent opportunity for in situ monitoring of the growth process. Virtually any MBE system is equipped with an electron-diffraction setup. Usually reflection high-energy electron diffraction (RHEED) with an electron beam nearly parallel to the growth surface is applied, yielding structural information on the surface crystallography during surface preparation and during epitaxy. The location of the electron gun and the monitoring screen is indicated in Fig. 7.21.

Molecular beam epitaxy is performed in ultra high vacuum (UHV), i.e., at a residual-gas pressure below $10^{-7}$ Pa ($10^{-9}$ mbar). The need for such low pressure originates from the required purity of epitaxial semiconductors. To obtain a relation for the maximum admissible pressure in the MBE chamber, we first consider the number of particles from the residual gas impinging on the substrate surface, and then relate this quantity to the particles of the molecular beams used to grow the epitaxial layer.

A number of $N$ particles (molecules or atoms) that impinge on a surface with area $A$ per time $\Delta t$ produce a flux $F$ given by

$$F = \frac{N}{A\Delta t}. \tag{7.20}$$

During the time interval $\Delta t$ only particles with the velocity $v_x$ and a maximum distance $\Delta x = v_x \Delta t$ can reach the surface, yielding for the flux

$$F = \frac{N v_x}{A\Delta x} = \frac{N}{V} v_x. \tag{7.21}$$

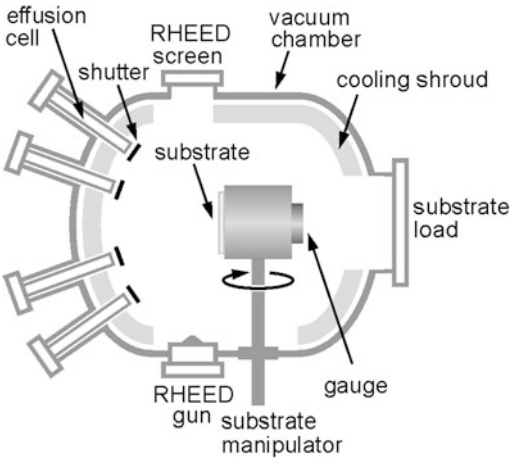


**Fig. 7.21** Schematic representation of a molecular-beam epitaxy system. The *circular arrow* indicates the positioning of the gauge at the location of the substrate to calibrate the beam-equivalent pressure of the effusion cells which contain different source materials

According (7.21) only particles contained in the volume $V$ arrive on the surface during $\Delta t$. The velocity $v_x$ of the ensemble of particles depends on the temperature $T$ and is given by the Maxwell-Boltzmann-distribution

$$f(v_x)\,dv_x = \sqrt{\frac{2}{\pi}}\left(\frac{m}{k_\mathrm{B}T}\right)^{3/2} v_x^2 e^{-mv_x^2/(2k_\mathrm{B}T)}\,dv_x, \tag{7.22}$$

where $m$ is the mass of the particles and $k_\mathrm{B}$ is Boltzmann's constant. The area below the distribution function $f(v_x)$ over an interval $dv_x$ denotes the fraction of particles with a velocity between $v_x$ and $v_x + dv_x$, and $f(v_x)$ is normalized to yield all particles for an integration over all velocities, $\int_0^\infty f(v_x)\,dv_x = 1$. Using (7.22) we obtain for the flux

$$F = \int_0^\infty \left(\frac{N}{V}\right) v_x f(v_x)\,dv_x = \frac{N}{V}\left(\frac{k_\mathrm{B}T}{2\pi m}\right)^{1/2}. \tag{7.23}$$

The flux $F$ is proportional to the particle density $N/V$ and the square root of $T/m$. The particle density may approximately be expressed in terms of the pressure $P$ by using the state equation of the ideal gas $PV = Nk_\mathrm{B}T$, eventually yielding

$$F = \frac{P}{\sqrt{2\pi k_\mathrm{B} m T}} = 8.332 \times 10^{22} \times \frac{P}{\sqrt{MT}}\left(\frac{\text{particles}}{\text{m}^2\,\text{s}}\right). \tag{7.24}$$

$M$ is the mole mass given by Avogadro's number $N_\mathrm{A}$, $M = mN_\mathrm{A}$. The second equation of (7.24) is given in SI units for all quantities.

For simplicity we assume only a single species producing the residual gas pressure, and we take oxygen $O_2$ with a mole mass $M = 32.0$ g/mol. At room temperature (300 K) we then obtain from (7.24) a pressure-dependent residual gas flux $F_{O_2} = 2.69 \times 10^{22} \times P_{O_2}$ ($O_2$ molecules $\mathrm{m}^{-2}\,\mathrm{s}^{-1}$), or twice this number for individual O species corresponding to a flux $F_\mathrm{O}$. We now relate the flux $F_\mathrm{O}$ produced by the residual gas (assumed here to be given solely by $O_2$) to the flux $F_\mathrm{MBE}$ of the beam(s) in typical MBE conditions and the requirement for purity in the layer. A semiconductor has about mid $10^{22}$ atoms/cm$^3$. Let us assume that each residual

gas atom arriving at the growing surface is incorporated into the epitaxial layer, and a maximum of mid $10^{17}$ impurities/cm$^3$ may not be exceeded. This leads to the requirement

$$\frac{F_O}{F_{MBE}} = 10^{-5} = \frac{5.38 \times 10^{22} P_{O_2}}{10^{19}} = 5.38 \times 10^3 P_{O_2}.$$

Resolving for $P_{O_2}$, the relation yields a maximum pressure $1.86 \times 10^{-8}$ Pa. This is a pressure in the UHV regime. A range $10^{-8}$ Pa to $10^{-9}$ Pa corresponds to the typical residual gas pressure in an MBE chamber. The impurity level found in epitaxial layers grown under such conditions is actually significantly lower than the postulated mid $10^{17}$ cm$^{-3}$. The sticking coefficients of typical residual gas species are usually much less than the assumed unity.

The requirement of UHV conditions arising from the purity requirement also ensures the beam nature of the molecular sources. The condition of a sufficiently large mean free path of effused particles in the range of typical dimensions of the MBE setup (order $10^{-1}$ m) is already fulfilled in a pressure range below $10^{-1}$ Pa.

To reach ultrahigh vacuum, all materials used in the vacuum chamber must have very low evolution of gas and a high chemical stability. Tantalum and molybdenum are widely used for shutters, heaters, and other components. The entire MBE chamber is baked out typically at 200 °C for 24 h any time after having vented the system. Spurious fluxes of atoms and molecules from the walls of the chamber are minimized by a cryogenic cooling shroud chilled using liquid nitrogen as indicated in Fig. 7.21.

### *7.3.2 Beam Sources*

The variety of source materials needed for MBE led to the development of different kind of sources with operation principles depending on the nature of the material. For the production of beams from solid or liquid materials usually Knudsen cells (K-cells) are employed. They are based on radiative heating and are limited to a maximum temperature of ∼1300 °C for thermal evaporation. Sources for higher temperatures mostly use electron-beam evaporation, albeit also laser-induced evaporation and plasma ion sources were employed. Gaseous species are directly introduced or decomposed in gas sources. Sources for condensed and gaseous particles are considered in the following.

#### Sources for Condensed Materials

MBE sources for condensed (solid or liquid) source materials are usually based on thermal evaporation described by a—sometimes modified—Knudsen equation (7.27). The *ideal Knudsen cell* is an isothermal enclosure which contains the solid

or liquid source material in thermodynamic equilibrium with its vapor at the pressure $P_{\mathrm{eq}}$. Effusion occurs through a *small* orifice with an area much smaller than that of the evaporation surface of the source material, and the flux passing this aperture equals the flux of material which leaves the condensed phase to maintain the equilibrium pressure. The diameter of the aperture is also small compared to the mean free path of the particles in the gas phase at $P_{\mathrm{eq}}$, and its wall thickness should be infinitely thin. All gaseous particles reaching the aperture from the inner side then escape to the vacuum chamber. The equilibrium pressure $P_{\mathrm{eq}}$ in the Knudsen cell depends on the temperature. For a pure source material in a closed enclosure with a temperature-independent evaporation enthalpy $\Delta H$ the dependence can be expressed by the Clausius–Clapeyron relation

$$P_{\mathrm{eq}}(T) = P_0 \exp\left(-\frac{\Delta H}{k_{\mathrm{B}}}\left(\frac{1}{T} - \frac{1}{T_0}\right)\right), \tag{7.25}$$

where $P_0$ is the equilibrium pressure at some temperature $T_0$. The effusion rate $\Gamma_{\max}$ of the aperture is given by the product of the aperture area $A$ and the flux $F$ which passes the aperture. Using (7.24) we obtain

$$\Gamma_{\max} = \frac{P_{\mathrm{eq}} A}{\sqrt{2\pi k_{\mathrm{B}} m T}}\left(\frac{\text{particles}}{\text{s}}\right). \tag{7.26}$$

Equation (7.26) represents the maximum effusion rate which can be achieved at a given cell temperature $T$. If the residual gas pressure $P_{\mathrm{res}}$ in the MBE chamber cannot be neglected, the equilibrium pressure in (7.26) is replaced by the difference pressure $(P_{\mathrm{eq}} - P_{\mathrm{res}})$ to express the effective effusion from the orifice area, yielding the *Knudsen equation*

$$\Gamma = \frac{(P_{\mathrm{eq}} - P_{\mathrm{res}}) A}{\sqrt{2\pi k_{\mathrm{B}} m T}}\left(\frac{\text{particles}}{\text{s}}\right), \tag{7.27}$$

$A$ being the aperture area. A real Knudsen cells may have a smaller effusion rate, and correction factors are introduced to account for the non-ideal behavior. A dimensionless evaporation coefficient $a$ accounts for the microscopic condition of the evaporation surface and is taken as an additional experimentally determined correction factor to the effusion obtained from the Knudsen equation (7.27). Another limitation of a real cell is given by the infinitesimal thin orifice assumed for the ideal Knudsen cell. The orifice of a real Knudsen cell has a finite thickness, leading to diffuse scattering of particles at its side walls. This affects the angular distribution of the flux as illustrated in Fig. 7.22.

The ideal Knudsen cell with infinitely thin orifice wall ($L = 0$) effuses particles with a cosine angular dependence expressed by

$$\Gamma(\vartheta)/\omega = \Gamma(0)\cos\vartheta, \tag{7.28}$$

the angle $\vartheta$ referring to the direction normal to the orifice as shown in Fig. 7.22; $\omega$ is the unit solid angle comprising the considered flux. For a flux leaving the orifice of the cell at an angle $\vartheta$ the orifice area appears smaller by a factor $\cos\vartheta$, leading to this dependence. Equation (7.28) is referred to as Knudsen's cosine law of effusion.

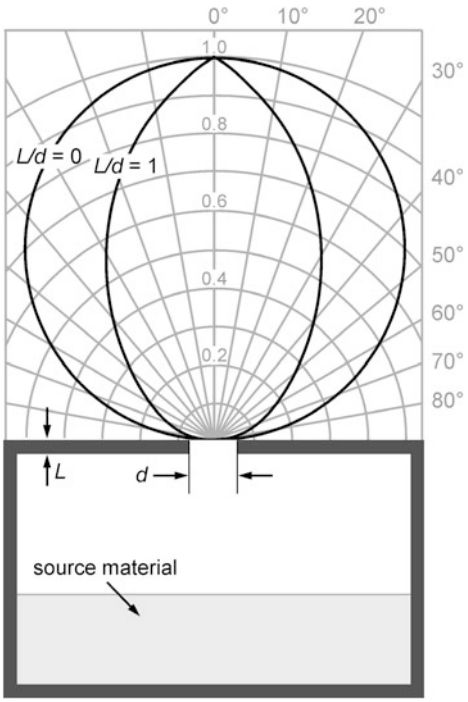


**Fig. 7.22** Angular distribution of particles effused from a Knudsen cell with ideally thin orifice (wall thickness to diameter ratio $L/d = 0$) and a thick orifice wall with a ratio $L/d = 1$. Data from [30]

The constant $\Gamma(\vartheta = 0)$ is related to the total effusion rate $\Gamma$, yielding $\Gamma(0) = \Gamma/\pi$. An orifice with a *finite* thickness $L$ and diameter $d$ leads to some collimation of the particle beam. Consequently the angular distribution gradually narrows as the ratio $L/d$ increases. The effect is shown in Fig. 7.22 for a ratio of unity.

For a given assembly of a substrate in front of an effusion cell the particle flux per unit area of the substrate $G$ can be derived from (7.27), (7.28). If the substrate is placed at a distance $l$ from the aperture directly in line (i.e., at $\vartheta = 0$), $G$ is given by $G = \Gamma/(\pi l^2)$.

The beam flux of a Knudsen cell can be calculated from the Knudsen equation (7.27) and does not depend on the quantity of source material in the cell. Knudsen cells are hence also used for flux calibration. The schematic of a Knudsen cell is depicted in Fig. 7.23a. A Knudsen cell contains a crucible made of pyrolytic boron nitride pBN, graphite, quartz, or tungsten, equipped with a cap which can be removed for filling the source material. Heating is provided by a filament coil or a heater foil (often made of metal tantalum, Ta). A radiation shield fabricated from multiple refractory metal foil (Ta or Mo) reduces heat losses. A water-cooling shield may be added to prevent heating of the cell environment. The temperature of the source material is controlled by a thermocouple, which is in intimate contact with the crucible of the cell and adjusts the heater power via a feed-back loop. Typically thermocouples of the thermally stable alloys W-Re (5 % and 26 %) are used to measure the temperature.

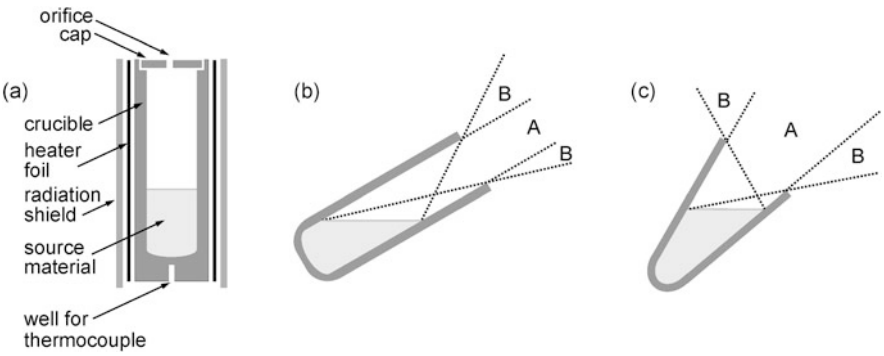


**Fig. 7.23** (**a**) Schematic of a Knudsen cell used as MBE source for condensed materials. (**b**) Cylindrical and (**c**) conical crucibles with liquid charges and limits of flux areas indicated by *dotted lines*. *A* and *B* denote areas of full flux and partially shadowed flux, respectively

Knudsen cells are widely used in MBE as evaporators for elementary sources with relatively low partial pressure (e.g. Ga, Al, As, Hg), but they suffer from a number of limitations. We know from (7.27) that the effusion flux is proportional to the aperture area. Since the aperture of a Knudsen cell must be small, the flux intensity is quite restricted for most materials at moderate cell temperatures. At high cell temperature, however, excessive outgassing of cell materials degrades the purity of the source flux. Another problem is the loss of heat at the cap, leading to a temperature decrease at the orifice. Consequently evaporants tend to condensate at the orifice and change effusion conditions.

Improved cell designs do not use a cap, providing a large aperture for effusion. This allows for operation with a large flux at moderate cell temperature leading to low flux contamination. The angular flux distribution of such a cell differs from that of a Knudsen cell. In particular, the flux distribution depends on the charging level of the cell. The beam is gradually collimated by the side walls of the crucible as the source material depletes. This effect is similar to that produced by a thick orifice wall shown in Fig. 7.22. Furthermore, source cells are usually mounted slantingly to allow for multiple-source arrangements. The surface normal of the source material in a cell is then inclined with respect to the crucible axis. Consequently the shadowing effects of the crucible walls are asymmetric and so is the angular flux distribution. The schematics of source cells with cylindrical or conical crucibles are depicted in Fig. 7.23b, c. Cylindrical crucibles allow for a larger charge of source material, and a better uniformity was reported for liquid charges such as Ga and Al [31]. The effect of a collimating shadowing is indicated by dotted lines in the figure. Area *B* denotes the penumbra, where only a part of the evaporant surface contributes to the flux. This area is particularly sensitive to the charge level. Conical crucibles have a large area *A* where the whole evaporant surface contributes to the flux.

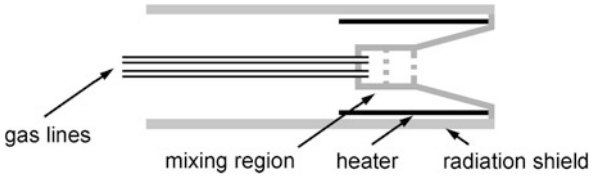


**Fig. 7.24** Schematic of an inlet cell used for gaseous source materials in MBE. A heated region at gas mixing is used to prevent condensation or to decompose stable hydride molecules

### Gaseous Sources

The use of gaseous source materials in MBE offers a couple of advantages. The lifetime of the source is not limited like that of condensed materials installed in the MBE system. Source gases are externally stored in cylinders and can readily be exchanged. Furthermore, the flux can be precisely controlled by pressure or mass-flow controllers which are also used in MOVPE setups. This allows also for a simple control of flux changes for, e.g., controlling alloy composition.

A gas source consists of the gas-control system and a cell for the gas inlet into the MBE chamber. The gas-control system resembles that used in MOVPE or VPE systems. In the system either the mass-flow through the inlet tube or the pressure in the tube (which then has a fine nozzle) is controlled using mass-flow or pressure controllers, respectively. One inlet cell may comprise multiple gas lines of either hydrides (like $AsH_3$) or metalorganic compounds (like $Ga(CH_3)_3$). In a multiple gas cell gases are mixed and then introduced into the vacuum chamber. Metalorganic compounds are generally thermally less stable than hydrides and decompose at the heated substrate surface. The vacuum inlet cell for metalorganics is therefore a simple gas-feed nozzle. A heater in front of the nozzle provides moderate heating up to about 100 °C to prevent condensation of the gas in the cell. Hydrides usually require decomposition temperatures exceeding the substrate temperature at typical MBE conditions. They must therefore be decomposed in the vacuum inlet cell. Thermal dissociation is accomplished in a ceramic cracking stage of the cell by heating to high temperature (up to 1000 °C) or by catalytic decomposition on a metal surface at somewhat lower temperature. The assembly of such a stage is illustrated in Fig. 7.26. The gas outlet may be formed by a conical crucible defining the angle of the beam aperture. The schematic of an inlet cell for gaseous source materials is given in Fig. 7.24.

### Dissociation Stage

Thermal dissociation as used in hydride cells may also be applied for decomposition of the evaporant molecules of condensed sources. In this case the source is equipped with an additional heated stage. Elemental sources for arsenic and phosphorous, e.g., produce a temperature-dependent mixture of dimers and tetramers. $As_2$ and $P_2$ dimer molecules are considered beneficial for the MBE of arsenides and phosphides.

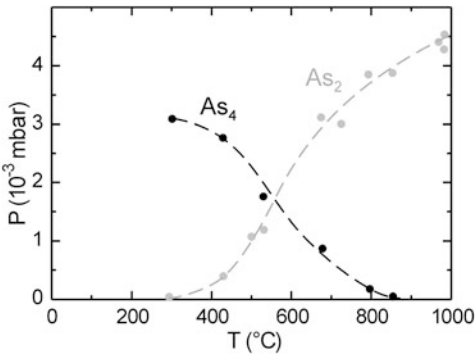


**Fig. 7.25** Thermal dissociation of arsenic tetramers to dimers in a cracker stage. The *dashed curves* are guides to the eye. Data are from [32]

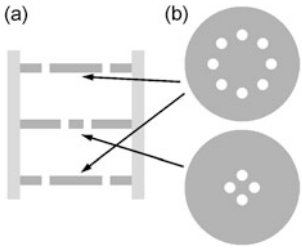


**Fig. 7.26** Schematic of a thermal dissociation stage employed to decompose hydrides of a gas inlet cell or molecules effused from an attached evaporation source. (**a**) Side view, (**b**) plan view of baffles

A cracker stage therefore dissociates $As_4$ and $P_4$ molecules and provides a pure beam of dimers. Typical temperatures for efficient cracking of both $As_4$ and $P_4$ are within the range 800–1000 °C. The thermal dissociation of $As_4$ tetramers to $As_2$ dimers in the cracker zone of an effusion cell kept at 327 °C is shown in Fig. 7.25.

The cracker region consists of a baffle assembly made of refractory metal (Ta), ceramic (pBN) or graphite, heated to a temperature much higher than that of the cell which evaporates the source material. The assembly provides multiple collision paths for the molecules. The schematic of the cracking region is depicted in Fig. 7.26.

### *7.3.3 Uniformity of Deposition*

The uniformity of beam fluxes at the plane of the substrate surface is important to obtain a well-defined thickness, composition and doping of layers over the entire wafer of an epitaxial structure. Besides the angular flux distribution of a source treated above the uniformity of the deposition on the substrate depends on the geometry of the source-substrate assembly.

We illustrate the dependence for a point source with a cosine flux distribution as shown in Fig. 7.22. The flux distribution of such source arriving at the plane of the substrate surface is depicted in Fig. 7.27. The off-center distance $x$ indicated in the figure is a consequence of the usual multiple source arrangement of an MBE system outlined in Fig. 7.21. We note a strong variation of the flux intensity across the

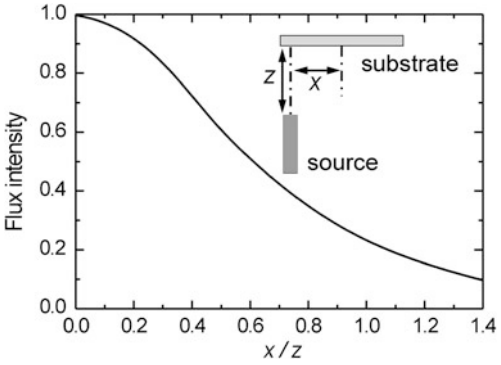


**Fig. 7.27** Calculated normalized flux intensity of the source at the surface plane of the substrate, depending on the displacement $x$ of the source axis with respect to the substrate center and the distance $z$ of the source orifice to the surface plane. A source with a cosine angular flux distribution is assumed. After [33]

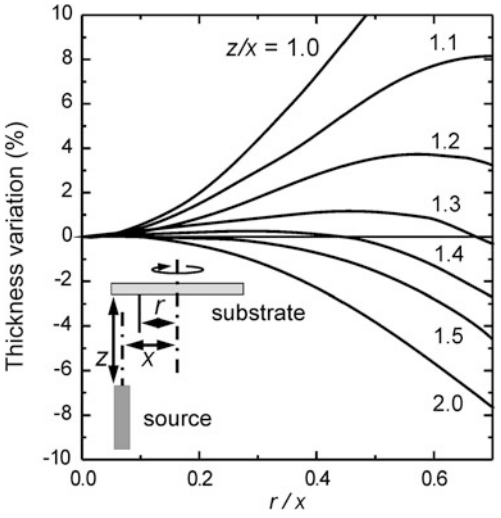


**Fig. 7.28** Calculated deviation of the deposition thickness from the value at the substrate center a $x = 0$, depending on the radial distance $r$ to the substrate axis and the distance $z$ of the source orifice to the substrate surface. Values apply for substrates rotating about the axis as indicated in the *inset* and a source with a cosine angular flux distribution. After [33]

substrate area, depending also on the vertical distance $z$ between substrate surface and orifice outlet of the source cell.

To obtain a largely homogeneous deposition on the substrate a rotation is applied as indicated by the circular arrow in the inset of Fig. 7.28. The flux is distributed rotationally symmetric on the substrate by averaging over the revolution around the axis. In principle a deposition uniformity better than 1 % is then possible. The effect depends on the ratio of the source distance $z$ versus the source displacement $x$ as shown in Fig. 7.28. The ratio $z/x$ of MBE setups is within the range 1.1 to 2. The calculated curves apply for point sources with a cosine flux distribution. Optimum condition for the assembly of multiple source cells is a symmetric arrangement of all cells with respect to the rotation axis.

The theoretical model considered above provides a reasonable rule-of-thumb for the design of MBE systems. In actual sources shadowing as illustrated in Fig. 7.23 and other effects affect the flux distribution. Source configurations are therefore also empirically optimized. Besides deposition uniformity, which improves as $z$ is

increased, also source yield, which improves for small $z$, and other factors are taken into account.

### 7.3.4 Adsorption of Impinging Particles

In the MBE growth process generally both, kinetic and thermodynamic processes are important. Since sources and substrate have different temperatures, no global equilibrium exists for the entire system. Particles effused from a source have an energy distribution according the temperature of this specific source. If the particles impinge on the substrate surface they thermalize to the substrate temperature. Particles desorbing again from the surface were found to reflect an energy distribution according the substrate temperature. This indicates that the time for thermalization is much less than the time required to grow one monolayer. Such finding justifies to assume an at least partial or local equilibrium on a time scale relevant for the growth process. The relevant equilibrium temperature is that of the substrate.

In the description of kinetic steps discussed in Sect. 5.2 the re-evaporation of particles from the surface was taken into account. The fraction given by the number of particles sticking to the surface and being incorporated during epitaxy $N_{\text{sticking}}$ with respect to the total number of impinging particles of a considered species $N_{\text{total}}$ is referred to as the *sticking coefficient* $s$ of this species,

$$s = \frac{N_{\text{sticking}}}{N_{\text{total}}}. \tag{7.29}$$

$s$ may also depend on the flux of other species and may have any value between zero and unity. An example is the sticking coefficient of $As_2$ molecules on the growing GaAs surface, that sensitively depends on the Ga flux as outlined in Sect. 5.2.9.

The sticking of particles on the surface is described by an adsorption energy as applied in (5.6). Usually the terms *physisorption* and *chemisorption* are used to account for smaller and larger energies, respectively, although chemical interactions occur in both kind of adsorptions and the two terms are not well defined. The terms are still useful for an overall description of surface processes to express different mobilities of a considered adatom species diffusing on the surface. A more rigorous definition in surface science refers physisorption solely to Van-der-Waals interactions. For a simplified description of MBE growth a two-step condensation process of an impinging particle is assumed implying two sticking coefficients for a given species referring to the two adsorption energies. The high surface mobility often found for species arriving at the surface is then assigned to a physisorbed state with a larger desorption probability, and incorporation to the chemisorbed state.

The kinetic processes occurring during molecular-beam epitaxy strongly depend on the specific material grown. Details of these processes are quite complex and reasonably known for only few examples. The scenario of molecular beam epitaxy of GaAs treated in Sect. 5.2.9 indicates the challenge of the task, and also demonstrates the achievement accomplished by combining advanced experimental and theoretical techniques.

## 7.4 Problems Chap. 7

7.1 Liquid-phase epitaxy of GaAs is generally performed on the Ga-rich side with low concentrations $x_{As}$ of As (as solute) dissoluted in Ga used as solvent. GaAs is grown in a step-cooling process with the solution at 805 °C (homogeneously in the bulk) and the solid-liquid interface at an equilibrium temperature of 800 °C. Assume that the liquidus curve $x(T)$ of the binary Ga-As system can be approximated by the empirical relation $x_{As} = 2352.8 \times \exp(-12404\ \mathrm{K/T})$.

(a) What is the approximate concentration of As in the liquid directly at the interface to the solid GaAs? What is the excess As concentration in the bulk of the liquid due to the supercooling?

(b) What is the diffusion coefficient of As in liquid Ga, if the diffusion length, given by the solution thickness of 0.5 cm, is covered in a mean time of 104 min?

(c) Compute the thickness of the GaAs layer homoepitaxially grown after a time of 100 s and after a time of 200 s.

7.2 A GaAs layer is grown by metalorganic vapor-phase epitaxy using trimethyl-gallium (TMGa) and tertiarybutyl-arsenic (TBAs) precursors. The total flow rate in the reactor is 3 slm (standard liters per minute, i.e., 3000 sccm = 3000 $cm^{-3}$/min at 0 °C and 1013 mbar), the total pressure is 100 mbar.

(a) What is the flow rate required for the Ga source to obtain a partial pressure of 3 Pa in the reactor, if the bubbler is kept at −10 °C and 1 bar ($10^5$ Pa) pressure?

(b) Which mass has one molecule of TMGa? Which mass of TMGa is consumed during 1 hr of growth at the flow rate found in (a)? Assume ideal-gas behavior and a mole volume of 22.4 l at standard conditions; atomic masses of Ga, C and H are 69.7, 12.0, and 1.0 grams/mole, respectively.

(c) Which temperature is required for the tertiarybutyl-arsenic bubbler for a V/III ratio of 5 in the gas phase? A flow of 62.5 sccm and a bubbler pressure of 1500 mbar are applied.

7.3 Assume a total flow rate of 3 slm (standard liters per minute at 0 °C and 1013 mbar) hydrogen, homogeneously heated in a MOVPE reactor to 600 °C at 100 mbar total pressure.

(a) What is the free-stream velocity, if the cross-section area of the reactor is 40 $cm^2$ and surface effects are neglected? What would be the free-stream velocity at standard conditions?

(b) Calculate the approximate thickness of a boundary layer 10 cm behind the leading edge of a fixed plate placed in the homogeneous hydrogen flow of (a) at 600 °C. Assume a dynamic viscosity of 17 μPa s, ideal-gas behavior with a mole volume of 22.4 l at standard conditions, and 2.0 grams/mole atomic mass.

(c) Let the growth rate of a GaAs layer be controlled by the partial pressure of the Ga precursor. How will an increase of the temperature from 600 °C to 700 °C approximately change the growth rate in the regime limited by mass transport? Assume an empirical temperature dependence of the diffusion coefficient described by a factor $(T/T_0)^{1.8}$, $T$ given in K.

7.4 A (001)-oriented Si layer is grown using molecular-beam epitaxy.
(a) What is the areal density of Si atoms on a (001) plane?
(b) What flux per unit substrate-area is required to grow a 0.2 μm thick layer in 1 hour? Assume a sticking coefficient of unity and ignore the formation of surface reconstructions which continuously reproduce during growth.
(c) Which effusion rate produces the flux density of (b)? Assume the substrate is mounted at a distance of 12 cm from the cell and is directly in line with the aperture.
(d) Estimate the substrate area with a deviation $\leq 5$ % from the maximum deposition thickness, if a cosine law applies. Note that the substrate is planar: a beam inclined by an angle $\vartheta$ has a longer path and, furthermore, supplies atoms to a larger area for a considered cross-section.

7.5 A (001)-oriented GaAs layer is grown using MBE with a growth rate controlled by the Ga flux. The Ga Knudsen cell is kept at 960 °C, producing an equilibrium pressure of $2.5 \times 10^{-3}$ mbar. The cell orifice has 0.8 cm diameter and the distance to the substrate is 13 cm.
(a) Calculate the areal flux density of Ga atoms at the substrate. Ga has 70 grams/mole atomic mass.
(b) Which growth rate of GaAs results from the areal flux density of (a)?
(c) Which cell temperature is required to double the growth rate of (b), if the enthalpy of Ga vaporization is $2.56 \times 10^5$ J/mol?

## 7.5 General Reading Chap. 7

M.A. Hermann, W. Richter, H. Sitter, *Epitaxy* (Springer, Berlin, 2004)
P. Capper, M. Mauk, *Liquid Phase Epitaxy of Electronic, Optical and Optoelectronic Materials* (Wiley, Chichester, 2007)
G.B. Stringfellow, *Organometallic Vapor-Phase Epitaxy*, 2nd edn. (Academic Press, New York, 1999)
J.E. Ayers, *Heteroepitaxy of Semiconductors: Theory, Growth, and Characterization* (CRC, Boca Raton, 2007)
A.C. Jones, P. O'Brien, *CVD of Compound Semiconductors* (VCH, Weinheim, 1997)

## References

1. G.B. Stringfellow, Fundamental aspects of vapor growth and epitaxy. J. Crystal Growth **115**, 1 (1991)
2. H. Nelson, Epitaxial growth from the liquid state and its application to the fabrication of tunnel and laser diodes. RCA Rev. **24**, 603 (1961)
3. E.A. Giess, R. Ghez, Liquid-phase epitaxy, in *Epitaxial Growth Part B*, ed. by J.W. Matthews (Academic Press, New York, 1975), pp. 183–213
4. J.J. Hsieh, Thickness and surface morphology of GaAs LPE layers grown by supercooling, step-cooling, equilibrium-cooling, and the two-phase solution techniques. J. Cryst. Growth **27**, 49 (1974)
5. W. Miederer, G. Ziegler, R. Dötzer, Verfahren zum tiegelfreien Herstellen von Galliumarsenidstäben aus Galliumalkylen und Arsenverbindungen bei niedrigen Temperaturen. German Patent 1,176,102, filed 25.9.1962

6. W. Miederer, G. Ziegler, R. Dötzer, Method of crucible-free production of gallium arsenide rods from alkyl galliums and arsenic compounds at low temperatures. U.S. Patent 3,226,270, filed 24.9.1963
7. H.M. Manasevit, W.I. Simpson, The use of metal-organics in the preparation of semiconductor materials on insulating substrates: I. Epitaxial III–V gallium compounds. J. Electrochem. Soc. **12**, 66C (1968)
8. H.M. Manasevit, The use of metalorganics in the preparation of semiconductor materials: growth on insulating substrates. J. Cryst. Growth **13/14**, 306 (1972)
9. R.W. Thomas, Growth of single crystal GaP from organometallic sources. J. Electrochem. Soc. **116**, 1449 (1969)
10. T.J. Mountziaris, K.F. Jensen, Gas-phase and surface reaction mechanisms in MOCVD of GaAs with trimethyl-gallium and arsine. J. Electrochem. Soc. **138**, 2426 (1991)
11. G.B. Stringfellow, *Organometallic Vapor-Phase Epitaxy*, 2nd edn. (Academic Press, New York, 1999)
12. R.T. Morrison, R.N. Boyd, *Organic Chemistry*, 5th edn. (Allyn & Bacon, New York, 1987)
13. K.F. Jensen, Transport phenomena in vapor phase epitaxy reactors, in *Handbook of Crystal Growth*, ed. by D.R.T. Hurle (Elsevier, Amsterdam, 1994), pp. 541–599
14. M. Tortowidjojo, R. Pollard, Elementary processes and rate-limiting factors in MOVPE of GaAs. J. Cryst. Growth **93**, 108 (1988)
15. G.B. Stringfellow, Fundamental aspects of vapor growth and epitaxy. J. Cryst. Growth **115**, 1 (1991)
16. D.H. Reep, S.K. Ghandhi, Deposition of GaAs epitaxial layers by organometallic CVD. J. Electrochem. Soc. **130**, 675 (1983)
17. D.I. Fotiadis, M. Boekholt, K.F. Jensen, W. Richter, Flow and heat transfer in CVD reactors: comparison of Raman temperature measurements and finite element model predictions. J. Cryst. Growth **100**, 577 (1990)
18. R.B. Bird, W.E. Steward, E.N. Lightfood, *Transport Phenomena* (Wiley, New York, 1960)
19. J. Ouazzani, K.-C. Chiu, F. Rosenberger, On the 2D modelling of horizontal CVD reactors and its limitations. J. Cryst. Growth **91**, 497 (1988)
20. J. van de Ven, G.M.J. Rutten, M.J. Raaijmakers, L.J. Giling, Gas phase depletion and flow dynamics in horizontal MOCVD reactors. J. Cryst. Growth **76**, 352 (1986)
21. L. Stock, W. Richter, Vertical versus horizontal reactor: an optical study of the gas phase in a MOCVD reactor. J. Cryst. Growth **77**, 144 (1986)
22. R.B. Bird, W.E. Stewart, E.N. Lightfoot, *Transport Phenomena* (Wiley, New York, 1962)
23. R.J. Miller, C.H. Bachmann, Production of cadmium sulfide crystals by coevaporation in a vacuum. J. Appl. Phys. **29**, 1277 (1958)
24. R.B. Schoolar, J.N. Zemel, Preparation of single-crystal films of PbS. J. Appl. Phys. **35**, 1848 (1964)
25. K.G. Günther, Aufdampfschichten aus halbleitenden III–V-Verbindungen. Z. Naturforsch. **13a**, 1081 (1958) (in German)
26. J.E. Davey, T. Pankey, Epitaxial GaAs films deposited by vacuum evaporation. J. Appl. Phys. **39**, 1941 (1968)
27. J.R. Arthur Jr., Interaction of Ga and $As_2$ molecular beams with GaAs surfaces. J. Appl. Phys. **39**, 4032 (1968)
28. A.Y. Cho, Film deposition by molecular-beam techniques. J. Vac. Sci. Technol. **8**, S31 (1971)
29. M. Mizuta, T. Iwamoto, F. Moriyama, S. Kawata, H. Kukimoto, AlGaAs growth using trimethyl and triethyl compound sources. J. Cryst. Growth **68**, 142 (1984)
30. P. Clausing, Über die Strahlformung bei der Molekularströmung. Z. Phys. **66**, 471 (1930) (in German)
31. T. Yamashita, T. Tomita, T. Sakurai, Calculations of molecular beam flux from liquid source. Jpn. J. Appl. Phys. **26**, 1192 (1987)

32. R.F.C. Farrow, P.W. Sullivan, G.M. Williams, C.R. Stanley, in *Proc. 2nd Int. Symp. Molecular Beam Epitaxy and Related Clean Techniques*, Tokyo (1982), p. 169
33. R.A. Kubiak, S.M. Newstead, P. Sullivan, Technology and design of molecular beam epitaxy systems, in *Molecular Beam Epitaxy: Applications to Key Materials*, ed. by R.F.C. Farrow (Noyes Publications, Park Ridge, 1995)

# Appendix
# Answers to Problems

2.1 (a) $f = 24.8\ \%$
(b) $4a_{\mathrm{GaAs}} \approx 5a_{\mathrm{GaN}}$, $f = -0.2\ \%$
(c) $a_{\mathrm{wurtzite}} = 4.0$ Å, use $a_{\mathrm{hex}} = a_{\mathrm{cub}}/\sqrt{2}$

2.2 (a) $f = +49.1\ \%$, $f_{\mathrm{alternative1}} = -32.9\ \%$
(b) $f = -14.0\ \%$ ($f_{\mathrm{alternative1}} = 16.2\ \%$)
(c) $f_1 = -1.8\ \%$, $f_2 = -0.5\ \%$
(d) $f_a = -3.5\ \%$, $f_c = -3\ \%$

2.3 (a) $x = 0.475 - 1.016y$
(b) $y_{\max} = 0.468$, $x_{\max} = 0.475$
(c) $(\mathrm{Al}_{0.475}\mathrm{In}_{0.525}\mathrm{As})_z\ (\mathrm{Ga}_{0.468}\mathrm{In}_{0.532}\mathrm{As})_{1-z}$

2.4 (a) $f = 0.24\ \%$
(b) $x = 0.5\ \%$
(c) $\varepsilon_{\parallel} = +0.15\ \%$
(d) $x = 8.41\ \%$, $f = -0.15\ \%$

2.5 (a) $\varepsilon_{\perp} = +0.15\ \%$
(b) $\Delta V/V = -2.1 \times 10^{-3}$
(c) $d_{\mathrm{unstrained}} = 3.272$ Å, $d_{\mathrm{strained}} = 3.270$ Å, the diagonal of the zincblende unit cell of $a_0\sqrt{3}$ length comprises 3 anion-cation (111) layers in *ABC* sequence, the nearest (111) layer distance is thus $1/3 \times \sqrt{3} \times a_0 = a_0/\sqrt{3}$
(d) $n = 100.3$
(e) $(E/A)_1 = 0.131\ \mathrm{J/m^2}$, $(E/A)_2 = 2.10\ \mathrm{J/m^2}$
(f) $E/V_{EZ} = 7.36 \times 10^{-11}\ \mathrm{J/m^3}$

2.6 (a) $t = 11.52$ Å $= 4$ ML
(b) $y = 0.3755$

2.7 (a) $E_{\mathrm{screw}}/L = 7.10 \times 10^{-6}\ \mathrm{J/m}$
(b) $E_{\mathrm{edge}}/L = 3.03 \times 10^{-5}\ \mathrm{J/m}$
(c) $E_{60^\circ}/L = 1.38 \times 10^{-5}\ \mathrm{J/m}$

2.8 (a) From Fig. 2.15: $t_{\mathrm{c}} \approx 6 \times 10^2 \times a_{\mathrm{s}} = 330$ nm
(b) $t_{\mathrm{c}2}/t_{\mathrm{c}1} = 0.90$
(c) $f = 2 \times 10^{-4}$

2.9 (a) $\Delta\Theta_{\mathrm{relaxed}} = -342$ sec, $\Delta\Theta_{\mathrm{strained}} = -744$ sec

U.W. Pohl, *Epitaxy of Semiconductors*, Graduate Texts in Physics,
DOI 10.1007/978-3-642-32970-8, © Springer-Verlag Berlin Heidelberg 2013

(b) $\Delta\Theta_{\text{relaxed}} = -528$ sec, $\Delta\Theta_{\text{strained}} = -1100$ sec
(c) $I(004)/I(115) \approx 3.6$

2.10 (a) $x_1 = 18.5$ %
(b) $x_2 = 25.1$ %, $x_3 = 22.6$ %

3.1 (a) $x = 48.5$ %, $E^{\Gamma} = 1.92$ eV (direct), order (increasing $E$) $E^{\Gamma}$, $E^{\text{L}}$, $E^{\text{X}}$, VCA: $E^{\Gamma}$, $E^{\text{X}}$, $E^{\text{L}}$
(b) $x = 30.5$ %, crossing $E^{\Gamma}$ and $E^{\text{X}}$, $E = 2.20$ eV

3.2 $\Delta E_{\text{c}}(77\text{ K}) = 0.25$ eV, $\Delta E_{\text{c}}(300\text{ K}) = 0.26$ eV

3.3 (a) $n = 4.45 \times 10^{12}$ cm$^{-2}$
(b) $\varepsilon_{\parallel} = -2.62$ %, $n_{\text{tot}} = 4.41 \times 10^{12}$ cm$^{-2}$

3.4 (a) $\Delta E_{\text{v}} = -0.24$ eV, $\Delta E_{\text{c}} = -0.13$ eV
(b) $\Delta E_{\text{v}} = +0.24$ eV, $\Delta E_{\text{c}} = -0.01$ eV
(c) using $b^{\text{theo}} = -1.90$ eV: $E_{\text{v,lh}} - E_{\text{v,hh}} = 0.35$ eV, splitting exceeds calculated offsets significantly—the strain is very large, $E^{\text{X}}_{\text{lh}} < E^{\text{X}}_{\text{hh}}$, $\Delta E_{\text{v}} = 0.45$ eV, $\Delta E_{\text{c}}$ is unchanged

3.5 (a) $E_{\text{g}}(77\text{ K}) = 1.51$ eV, $E_{\text{g}}(300\text{ K}) = 1.42$ eV
(b) $E_{\text{g,eff}} = 1.55$ eV
(c) $\Delta E_{\text{g,eff}} = \pm 8$ meV

4.1 (a) $\Delta\mu = 94$ J/K
(b) $\Delta\mu = 6.1$ J/K

4.2 (a) $\Delta g_{\text{m}}(800\text{ °C}) = 0.66$ kJ, $\Delta g_{\text{m}}(1200\text{ °C}) = -1.00$ kJ
(b) $T = 959$ °C
(c) $x_1 = 0.17$, $x_2 = 0.83$

4.3 Elements of the plot: axes [100], [011], and [111] lie in a common $(1\bar{1}0)$ plane considered here. Angles from [100] are 54.7° to [111] and 90° to [011], distances from the origin to respective Wulff planes are $r_{100} = 1.16 \times r_{011}$ and $r_{111} = 1.05 \times r_{011}$. The facets meet the condition, {110}: 0.83 J/m$^2$ < $\sqrt{2} \times 0.96$ J/m$^2$ = 1.36 J/m$^2$, {111}: 0.87 J/m$^2$ < $\sqrt{3} \times 0.96$ J/m$^2$ = 1.66 J/m$^2$

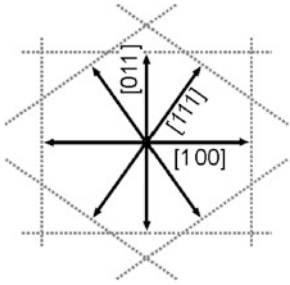


4.4 (a) $\Delta G^{\text{2D}}_{\gamma} = 2.0$ eV, for $\gamma_{\text{S}_\text{B}} = \gamma_{\text{S}_\text{A}}$ is $\Delta G^{\text{2D}}_{\gamma} = 0.9$ eV
(b) $N = 362$, $\Delta\mu \approx 1.1$ kJ/mol

4.5 (a) $R \approx 2$ ML/s (1.98 ML/s)
(b) $v = 61$ nm/s, $l = 251$ nm

5.1 (a) bulk $(n-2)^3$, faces $6 \times (n-2)^2$, edges $12 \times (n-2)$, corners $12 \times 1$, sum 1000 for $n = 10$, $10^9$ for $n = 1000$

(b) bulk $3E_b$, face $2.5E_b$, edge $2E_b$, corner $1.5E_b$, fractions $4.34 \times 10^{-1}$ for $n = 10^1$, $4.93 \times 10^{-2}$ for $10^2$, $4.99 \times 10^{-3}$ for $10^3$, $5.00 \times 10^{-4}$ for $10^4$; virtually unchanged without edge and corner atoms, e.g., $4.985 \times 10^{-3}$ instead of $4.993 \times 10^{-3}$ for $10^3$, i.e., the small fraction of edge and corner atoms gets negligible

5.2 The figure shows a top view of all atoms in the first 4 layers of a unit cell for the two reconstructions (no atom hidden), the largest in the 1st layer, open and filled symbols for either As and Ga, respectively, (in $\beta 2(2 \times 4)$), or vice versa (in $\beta 2(4 \times 2)$); dimers are encircled. Electron numbers see list, showing both reconstructions comply with the ECR

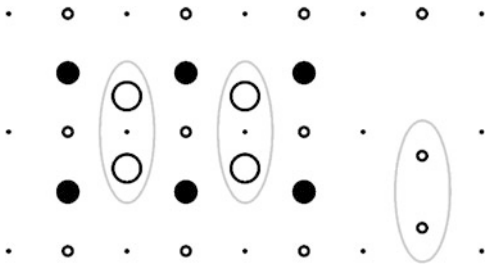

| Layer | Atoms | Electrons for $\beta 2(2 \times 4)$ | | Electrons for $\beta 2(4 \times 2)$ | |
|---|---|---|---|---|---|
| | | Required | Available | Required | Available |
| 1 | 2 dimers | 28 | 20 | 20 | 12 |
| 2 | 6 atoms | 24 | 18 | 32 | 30 |
| 3 | 6 atoms + | 24 | 30 | 24 | 18 |
| | 1 dimer | 14 | 10 | 10 | 6 |
| 4 | 8 atoms | | 12 | | 20 |
| sum | | 90 | 90 | 86 | 86 |

5.3 (a) $E_d = 1.2$ eV, $E_a = 2.0$ eV
(b) 1041 K and 759 K

5.4 (a) $\tau_a = 8.2 \times 10^{-6}$ s, $\lambda_2 = 1.9 \times 10^{-4}$ cm
(b) $\Theta = 0.039°$, $r_{step} = 0.4$ mm/s

5.5 (a) $n_{In} = n_{As} = 2937$ atoms
(b) $d = 1.62$ ML
(c) $n_{In} = n_{As} = 396$ atoms, $d = 1.43$ ML

6.1 (a) $n_{InAs}(77\ K) = 4.3 \times 10^3\ cm^{-3}$, $n_{InAs}(300\ K) = 7.5 \times 10^{14}\ cm^{-3}$, $n_{InP}(77\ K) = 2 \times 10^{-17}\ cm^{-3} \approx 0\ cm^{-3}$, $n_{InP}(300\ K) = 1.2 \times 10^7\ cm^{-3}$
(b) $T_{InAs}$ 255 K (−18 °C), $T_{InP}$ 373 K (100 °C)

6.2 $D_c^{eff} = 5.8 \times 10^{17}\ cm^{-3}$, $D_v^{eff} = 1.3 \times 10^{19}\ cm^{-3}$, $n_{max} = 6 \times 10^{19}\ cm^{-3}$, $p_{max} = 5 \times 10^{19}\ cm^{-3}$

6.3 (a) $t = 1.82 \times 10^4$ s $\approx 5$ h
(b) $T_2 = 672$ °C
(c) $w = 435$ nm
(d) $c = 2.8 \times 10^{17}$ cm$^{-3}$

6.4 (a) $e\phi_{Bn} = 1.60$ eV, $E_c - E_F \approx 0.19$ eV, $eV_{bi} = 1.41$ eV
(b) $w_0 = 3.0 \times 10^{-7}$ m $\approx 300$ nm, $w_{forward} \approx 1.6 \times 10^{-7}$ m, $w_{reverse} \approx 3.9 \times 10^{-7}$ m
(c) slightly reduced by 2 %

6.5 $R_{c2} = 1.6 \times 10^{-6}\ \Omega\,\text{cm}^2$

7.1 (a) $x_{interface} \approx 0.0224 = 2.24$ %, $x_{excess} \approx 0.0012 = 0.12$ %
(b) $D = 4 \times 10^{-5}$ cm$^{-2}$/s
(c) $d_{100\,s} \approx 1.7$ µm, $d_{200\,s} \approx 2.4$ µm

7.2 (a) $Q_{TMGa} = 17.2$ sccm
(b) $m_{TMGa\ molecule} = 1.9 \times 10^{-22}$ g, $m_{TMGa} = 0.28$ g consumption in 1 h
(c) $T_{TBAs} = 10$ °C

7.3 (a) $u \approx 40$ cm/s, $u_{standard} = 1.25$ cm/s
(b) $\delta \approx 20$ cm
(c) $r_2/r_1 \approx 1.09$

7.4 (a) $n_{Si} = 6.8 \times 10^{14}$ cm$^{-2}$
(b) $G = 2.8 \times 10^{14}$ cm$^{-2}$ s$^{-1}$
(c) $\Gamma = 2.0 \times 10^{17}$ s$^{-1}$
(d) $A \approx 18$ cm$^2$

7.5 (a) $G = 8.5 \times 10^{14}$ cm$^{-2}$ s$^{-1}$
(b) $r = 1.4$ µm/h
(c) double the Ga equilibrium pressure, $T_{Ga} = 995$ °C

# Index



U.W. Pohl, *Epitaxy of Semiconductors*, Graduate Texts in Physics,
DOI 10.1007/978-3-642-32970-8, © Springer-Verlag Berlin Heidelberg 2013

# Fundamental Physical Constants

| Quantity | Symbol | Value | SI Unit |
|---|---|---|---|
| Avogadro constant | $N_A$ | $6.02214 \times 10^{23}$ | $mol^{-1}$ |
| Bohr radius | $a_B$ | $5.29177 \times 10^{-11}$ | m |
| Boltzmann constant | $k_B$ | $1.38065 \times 10^{-23}$ | J/K |
| Elementary charge | $e$ | $1.60218 \times 10^{-19}$ | As |
| Electron mass | $m_0$ | $9.10938 \times 10^{-31}$ | kg |
| Molar gas constant | $R = k_B \times N_A$ | 8.31446 | J/(mol K) |
| Permeability in vacuum | $\mu_0$ | $4\pi \times 10^{-7}$ | Vs/(Am) |
| Permittivity in vacuum | $\varepsilon_0$ | $8.85419 \times 10^{-12}$ | As/(Vm) |
| Planck constant | $h$ | $6.62607 \times 10^{-34}$ | Js |
| | $\hbar = h/2\pi$ | $1.05457 \times 10^{-34}$ | Js |
| Proton mass | $m_p$ | $1.67262 \times 10^{-27}$ | kg |
| Rydberg energy | $R_\infty = m_0 e^4/(2\hbar^2)$ | $2.17987 \times 10^{-18}$ | J |
| Speed of light in vacuum | $c$ | $2.99792 \times 10^{8}$ | m/s |
| Unified atomic mass unit | $u = \frac{1}{12} m(C_6^{12})$ | $1.66054 \times 10^{-27}$ | kg |
| 1 Electron volt | eV | $1.60218 \times 10^{-19}$ | J |
| 1 Angstrom | Å | $1.00000 \times 10^{-10}$ | m |

Source: CODATA internationally recommended values of the fundamental physical constants, http://physics.nist.gov/cuu/Constants/index.html.

U.W. Pohl, *Epitaxy of Semiconductors*, Graduate Texts in Physics,
DOI 10.1007/978-3-642-32970-8, © Springer-Verlag Berlin Heidelberg 2013